frontiers | Research Topics

Women in biomaterials science 2023

Edited by
Silviya Petrova Zustiak, Sylvia Natividad-Diaz and Jenny Robinson

Published in
Frontiers in Biomaterials Science

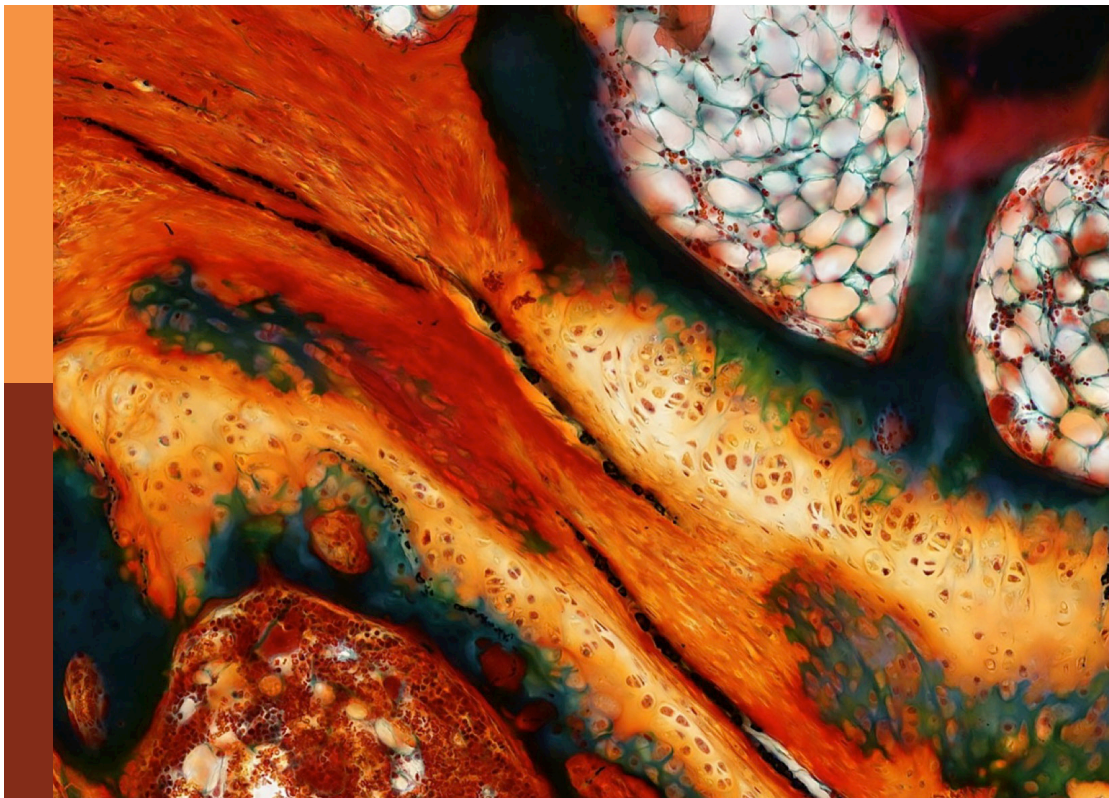

ISSN 1664-8714
ISBN 978-2-8325-5416-6
DOI 10.3389/978-2-8325-5416-6

About Frontiers

Frontiers is more than just an open access publisher of scholarly articles: it is a pioneering approach to the world of academia, radically improving the way scholarly research is managed. The grand vision of Frontiers is a world where all people have an equal opportunity to seek, share and generate knowledge. Frontiers provides immediate and permanent online open access to all its publications, but this alone is not enough to realize our grand goals.

Frontiers journal series

The Frontiers journal series is a multi-tier and interdisciplinary set of open-access, online journals, promising a paradigm shift from the current review, selection and dissemination processes in academic publishing. All Frontiers journals are driven by researchers for researchers; therefore, they constitute a service to the scholarly community. At the same time, the *Frontiers journal series* operates on a revolutionary invention, the tiered publishing system, initially addressing specific communities of scholars, and gradually climbing up to broader public understanding, thus serving the interests of the lay society, too.

Dedication to quality

Each Frontiers article is a landmark of the highest quality, thanks to genuinely collaborative interactions between authors and review editors, who include some of the world's best academicians. Research must be certified by peers before entering a stream of knowledge that may eventually reach the public - and shape society; therefore, Frontiers only applies the most rigorous and unbiased reviews. Frontiers revolutionizes research publishing by freely delivering the most outstanding research, evaluated with no bias from both the academic and social point of view. By applying the most advanced information technologies, Frontiers is catapulting scholarly publishing into a new generation.

What are Frontiers Research Topics?

Frontiers Research Topics are very popular trademarks of the *Frontiers journals series*: they are collections of at least ten articles, all centered on a particular subject. With their unique mix of varied contributions from Original Research to Review Articles, Frontiers Research Topics unify the most influential researchers, the latest key findings and historical advances in a hot research area.

Find out more on how to host your own Frontiers Research Topic or contribute to one as an author by contacting the Frontiers editorial office: frontiersin.org/about/contact

Women in biomaterials science 2023

Topic editors

Silviya Petrova Zustiak — Saint Louis University, United States
Sylvia Natividad-Diaz — University of Texas at El Paso, United States
Jenny Robinson — University of Washington, United States

Citation

Zustiak, S. P., Natividad-Diaz, S., Robinson, J., eds. (2024). *Women in biomaterials science 2023*. Lausanne: Frontiers Media SA. doi: 10.3389/978-2-8325-5416-6

Table of contents

frontiers | Frontiers in Biomaterials Science

TYPE Editorial
PUBLISHED 30 August 2024
DOI 10.3389/fbiom.2024.1469485

OPEN ACCESS

EDITED AND REVIEWED BY
Paulo Bartolo,
Nanyang Technological University, Singapore

*CORRESPONDENCE
Silviya P. Zustiak,
silviya.zustiak@slu.edu
Jennifer L. Robinson,
jrobins1@uw.edu

RECEIVED 23 July 2024
ACCEPTED 20 August 2024
PUBLISHED 30 August 2024

CITATION
Zustiak SP and Robinson JL (2024) Editorial: Women in biomaterials science 2023.
Front. Biomater. Sci. 3:1469485.
doi: 10.3389/fbiom.2024.1469485

Editorial: Women in biomaterials science 2023

Silviya P. Zustiak[1]* and Jennifer L. Robinson[2,3]*

[1]Department of Biomedical Engineering, Saint Louis University, St Louis, MO, United States, [2]Department of Orthopaedic Surgery and Sports Medicine, University of Washington, Seattle, WA, United States, [3]Department of Mechanical Engineering, University of Washington, Seattle, WA, United States

KEYWORDS

biomaterials, women, infection, tissue engineering, endometriosis

Editorial on the Research Topic
Women in biomaterials science 2023

We are excited to present the second edition of the "*Women in Biomaterials Science*" Research Topic, which features four original research manuscripts and six review articles. This Research Topic aims to promote the work of women researchers across Biomaterials Science and to encourage more women to pursue careers in the field. Each paper in this 2nd edition has a female corresponding author, all but one of the lead authors are female, and a total of twenty-nine female scientists are represented as co-authors. The Research Topic covered in this Research Topic are diverse and cover the technical range of nanomaterials to 3D human-sized biomaterial models as well as biomaterial applications from combatting infections to the treatment of uniquely female conditions including endometriosis and cervical dysplasia.

Not surprisingly, the Research Topic features several conditions anatomically unique to women. A paper by lead author Amberlyn Simmons from the lab of Dr. Sarah Stabenfeldt, considers sex as a biological variable in the context of nanomaterials in acute brain injury imaging and treatment (Simmons et al.). The authors conclude that biological sex affects nanomedicine distribution, toxicity, and efficacy in a manner specific to the nanoparticle system and yet critical gaps in knowledge still exist. Lead author Maneesha Sahni from the lab of Dr. Emily Day, reviews nanoparticle-based diagnostics and treatments for endometriosis, an incurable disease characterized by tissue growth outside of the uterine cavity (Sahni and Day). Nanomaterials have the potential to be more effective and less invasive than existing therapeutic approaches. A project by lead author Ines Cadena from the lab of Dr. Kaitlin Fogg, details an affordable and effective ethanol ablation treatment for cervical dysplasia, a cancerous growth on the cervix often caused by human papilloma virus (Cadena et al.). Specifically, the authors used gelatin methacrylate to build a human-sized 3-dimensional (3D) *in vitro* model which mirrors the architecture of cervical dysplasia and demonstrated that localized injection of ethyl cellulose-ethanol gel retains the drug inside the tumor killing cancer cells, while sparing healthy cells.

Another set of papers focused on using biomaterials to combat the growing threat of antibiotic-resistant bacterial infections. Lead author Dr. Mary Beth Browning Monroe reviews the use of smart materials in the surveillance and treatment of wound infections (Monroe and Fikhman). Smart materials that respond to the unique pH, temperature, and enzymatic changes induced by bacteria in wounds can be coupled with mechanisms to kill the bacteria, such as drug release, or to signal infection and ultimately improve treatment outcomes. Lead author Carolina Gomez Casas from the lab of Dr. Anita Shukla, reviews the

approach of using immunomodulatory biomaterials to treat bacterial infections, since bacteria adopt immune evasion strategies for survival, which in turn cause persistent or recurrent infections (Gomez Casas and Shukla). The review emphasizes strategies targeting the innate immune system, such as metal ion releasing coatings, stimuli-responsive polymeric coatings, interleukin releasing surfaces, and immunomodulatory nanoparticles and hydrogels for the treatment of wound infections. Lead author Halle Lutz from the lab of Dr. Ashley Brown, reviews biomaterials for the treatment of thromboinflammation induced by sepsis, a life-threatening disease with pathophysiology involving interplay between endothelial cells, platelets, and leukocytes (Lutz and Brown). To address the disease complexity, biomaterials can be designed to target and affect multiple pathways and systems and safely inhibit excessive inflammation while maintaining hemostasis.

Several original research articles describe the development of biomaterials for tissue engineering applications. Lead author Michaela Licciadello from the lab of Dr. Chiara Tonda-Turo, used aligned electroconductive polycaprolactone/polyaniline fibers produced via electrospinning in the development of an *in vitro* nervous tissue model (Licciardello et al.). The scaffold was able to support neural stem cell attachment and growth and foster differentiation into the neuronal phenotype. Lead author Jodi Graf from the labs of Drs. April Kloxin and Catherine Fromen, used both 2D and 3D biomaterial-based culture systems to understand how, under similar stimuli, immortalized macrophages cell lines and primary cells respond (Graf et al.). Overall, the authors noted differences in baseline marker expression between cell lines, phenotypical and functional differences in cell lines compared to primary macrophages of the same origin, and differences in macrophage polarization in 2D vs. 3D cell culture, highlighting the need for careful consideration of cell origin for specific applications. Lead author Eya Ferchichi from the lab of Dr. Silviya Zustiak, developed a library of gelatin methacrylate-polyethylene glycol diacrylate hydrogels for use in mechanosensing applications (Ferchichi et al.). Specifically, a design of experiments approach was used to perform detailed analysis on the interplay between chemical composition and scaffold properties as well as scaffold properties and cell behavior, such as human glioblastoma cell spreading and therapy responsiveness. Lastly, a review from the lab of Dr. Janet Zoldan from lead author Nikhith Kalkunte, discusses the use of machine learning in cardiac tissue engineering (Kalkunte et al.). The authors suggest that machine learning can improving the phenotyping and functionality of human induced pluripotent stem cells, which are critical for cardiac regeneration therapy, via robust mathematical models and predictions.

In summary, the papers in this Research Topic illustrate a diversity of ideas and approaches and exciting biomaterials science aimed to address emerging challenges from female researchers in the biomaterials field.

Author contributions

SZ: Writing–original draft, Writing–review and editing. JR: Writing–review and editing.

Funding

The author(s) declare that no financial support was received for the research, authorship, and/or publication of this article.

Conflict of interest

The authors declare that the research was conducted in the absence of any commercial or financial relationships that could be construed as a potential conflict of interest.

The author(s) declared that they were an editorial board member of Frontiers, at the time of submission. This had no impact on the peer review process and the final decision.

Publisher's note

frontiers | Frontiers in Biomaterials Science

TYPE Review
PUBLISHED 16 November 2023
DOI 10.3389/fbiom.2023.1279358

OPEN ACCESS

EDITED BY
Jenny Robinson,
University of Washington, United States

REVIEWED BY
Brendan Harley,
University of Illinois at Urbana-Champaign, United States
Kaitlin Fogg,
Oregon State University, United States

*CORRESPONDENCE
Emily S. Day,
emilyday@udel.edu

RECEIVED 17 August 2023
ACCEPTED 30 October 2023
PUBLISHED 16 November 2023

CITATION
Sahni M and Day ES (2023), Nanotechnologies for the detection and treatment of endometriosis.
Front. Front. Biomater. Sci. 2:1279358.
doi: 10.3389/fbiom.2023.1279358

Nanotechnologies for the detection and treatment of endometriosis

Maneesha Sahni[1] and Emily S. Day[1,2,3]*

[1]Department of Biomedical Engineering, University of Delaware, Newark, DE, United States, [2]Department of Materials Science and Engineering, University of Delaware, Newark, DE, United States, [3]Center for Translational Cancer Research, Helen F. Graham Cancer Center and Research Institute, Newark, DE, United States

Endometriosis is an incurable gynecologic disease characterized by endometrial-like tissue growth outside of the uterine cavity. It affects approximately 10% of reproductive age women, who endure pelvic pain during periods and/or sexual intercourse and who suffer from reduced fertility and diminished quality of life due to the side effects of current treatments. To improve the management and prognosis of endometriosis patients, researchers have recently begun to develop nanoparticle-based diagnostics and treatments that are more effective and less invasive than existing approaches. This review discusses the current state of the field and highlights considerations for the continued development of nanotechnologies for the diagnosis and treatment of endometriosis.

KEYWORDS

women's health, reproductive health, nanoparticles, nanomedicine, diagnostics, therapeutics, gynecologic health

1 Introduction

Approximately 10%–15% of reproductive-aged women and girls around the world are diagnosed with endometriosis (Eisenberg et al., 2018). Endometriosis is an inflammatory disease where endometrium-like tissue, which usually lines the inside of the uterus in a healthy patient, grows outside of the uterus where it can spread to other organs including the ovaries, fallopian tubes, bladder, and bowel (Figure 1) (Ellis et al., 2022). This abnormal tissue growth develops into cysts, known as endometriotic lesions, as well as scar tissue. In a eutopic, or healthy, endometrial lining, endometrial cells provide the pathway for a fertilized embryo to attach during the onset of pregnancy (Reed et al., 2018; Liu and Lang, 2011). During a standard menstrual cycle, the hormones produced by the ovaries stimulate these cells, which causes them to grow and divide. In the absence of fertilization/pregnancy, the endometrial cells die and are shed and exit through the vagina, which is the process commonly known as the menstrual cycle or period. In endometriosis patients, the endometriotic lesions in heterotopic tissues contain the same endometrial cells, which respond to the ovarian hormones the same way they would respond in a eutopic uterus. This causes the lesions to thicken and swell with blood at specific points in the menstrual cycle, which causes inflammation, pain, and discomfort. Symptomatic women commonly experience pain during menstruation, sexual intercourse, urination and/or bowel movements (Ellis et al., 2022). Unfortunately, accurately diagnosing endometriosis based on these symptoms alone remains a clinical challenge.

It is unknown why some women develop endometriosis and others do not, but there are multiple factors and theories behind what contributes to endometriosis onset and

development. One possible cause is retrograde menstruation, which is when menstrual blood travels back through the fallopian tubes instead of outward through the cervix and vagina (Figure 1) (Agostinis et al., 2021). This backflow of blood can result in the implantation and growth of endometrial cells outside the uterus. Another possible cause could be cellular metaplasia, which is when cells outside the uterus differentiate into endometrial-like cells due to an environmental stimulus such as hormones or immunological factors (Giroux and Rustgi, 2017). For example, some studies suggest increased estrogen levels could be an inducing factor for endometriosis. Finally, certain hereditary and/or physical factors can increase the risk of a woman developing endometriosis, such as having a mother, sister, or daughter with endometriosis, having an abnormal uterus, starting menstruation before the age of 11, and having either shorter menstrual cycles that are less than 27 days or heavy and long menstrual periods lasting more than 7 days (Tsamantioti and Heba, 2023).

There is a need for noninvasive diagnostics and a cure for endometriosis. Current treatment options provide temporary relief, such as pain management through the intake of anti-inflammatory medications like ibuprofen (Tsamantioti and Heba, 2023). Or, if hormone imbalance is involved, women may be prescribed hormonal treatments such as oral contraceptives. Another form of treatment is surgically excising the endometriotic lesions, which can help alleviate pain and discomfort and return affected organs back to their original state. Surgical excision of endometriotic lesions can also improve women's fertility by removing the source of inflammation that affected the functionality of the ovaries, fallopian tubes, and/or uterus (Ellis et al., 2022). Additionally, surgery can overcome endometriosis-induced distortion or blockage of the fallopian tubes, which limits their ability to capture the egg after ovulation, thus contributing to infertility. In some instances, surgical excision is combined with ablation to destroy the lining of the uterus, which reduces the heavy menstrual bleeding associated with endometriosis. Ablation methods include electrical ablation, radiofrequency ablation, cryoablation, hydrothermal ablation, microwave ablation, and balloon therapy. While effective, endometrial ablation may not be suitable for women who wish to become pregnant because it increases risk to both the mother and baby. Beyond surgical excision of lesions to improve fertility, other noninvasive treatments for infertility caused by endometriosis include oral or injectable medicines to stimulate super-ovulation, insemination, and *in vitro* fertilization (Lee et al., 2020). Despite the benefits of surgical treatment of endometriosis, complications can occur during or after the surgery and lesions can reoccur, with about 27% of patients needing multiple surgical procedures (Park et al., 2022). Hence, improved treatment methods are still required.

In terms of diagnostics, the two main techniques currently used by healthcare providers to confirm a diagnosis of endometriosis are a surgical procedure known as laparoscopy or advanced imaging modalities. In laparoscopy, a surgeon inflates the abdomen using a harmless gas, creates a small incision in the abdomen, and then uses a laparoscope to inspect the reproductive organs, intestines, and other nearby areas to identify any signs of endometriosis. Alternatively, imaging techniques including ultrasound and magnetic resonance imaging (MRI) can be utilized to try to non-invasively detect endometriosis, but these are limited by cost and lack the needed resolution for accurate identification of endometriotic lesions (Tsamantioti and Heba, 2023).

Given the limitations of current diagnostic and treatment methods, researchers and clinicians are searching for new ways to better manage endometriosis. Previously, nanoparticle-based contrast agents and drug carriers have shown great promise in improving the diagnosis and treatment of various diseases. Now, researchers are interested in applying these tools to applications in women's health (Lloyd-Parry et al., 2018; Nelson et al., 2021; Swingle et al., 2023). One challenge in the development of new diagnostics and therapeutics for endometriosis is the paucity of preclinical animal models that accurately represent the human disease. Most studies rely on rodent models wherein endometriotic cells or donor uterine tissue are transplanted subcutaneously or intraperitoneally

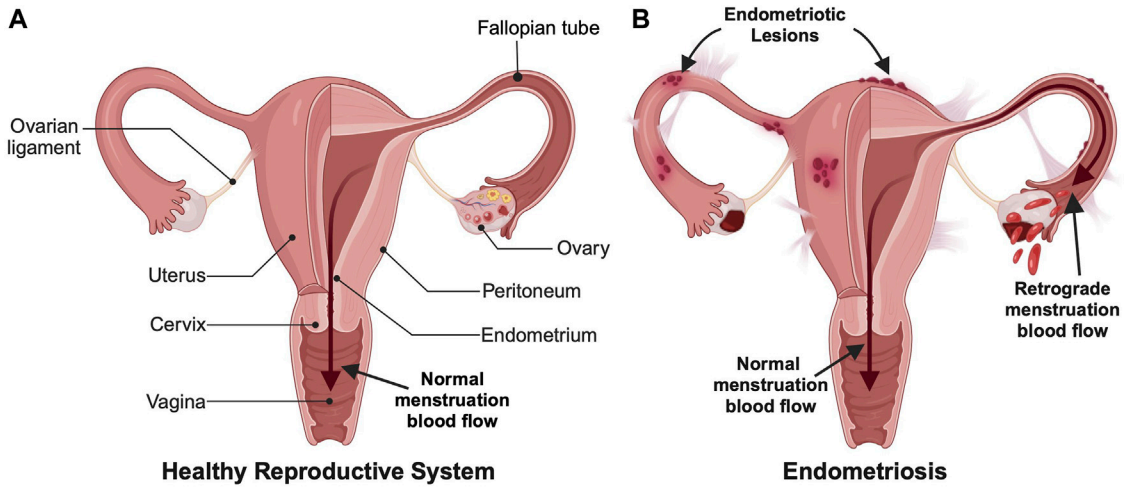

FIGURE 1
Comparison of **(A)** a healthy female reproductive system and **(B)** an endometriotic reproductive system. Endometriosis involves both endometrial lesions that form outside the uterine cavity and retrograde menstruation, which are commonly used for diagnosis. (Created with BioRender.com).

into recipient animals to induce disease. An alternative model is macaques which can naturally develop the disease, but these are more expensive and less readily accessible. Despite their drawbacks, these models have proven useful in the preclinical evaluation of nanoparticle-based tools to manage endometriosis. In the following sections, recent preclinical studies into the use of nanotechnologies for the diagnosis and treatment of endometriosis are discussed.

2 Diagnostics

This section discusses the development of nanotechnologies to noninvasively diagnose endometriosis and determine its level of severity. Section 2.1 introduces nanotechnologies for biomarker detection, while Section 2.2 describes nanoparticle contrast agents for imaging of endometriosis lesions.

2.1 Nanotechnologies as biosensors for endometriosis biomarker detection

The detection of biomarkers, including proteins and/or genetic material, is an appealing non-invasive approach to diagnose endometriosis. Previous studies have shown that endometriosis patients have a distinct microbial makeup in their peritoneal fluid and feces when compared to healthy patients (Ellis et al., 2022). Based on these observations, *Ruminococcus* in the gut and *Pseudomonas* in the peritoneal fluid may serve as diagnostic signatures for endometriosis. Additionally, the follicular fluid of endometriosis patients has dysregulated cytokine profiles with significant upregulation of IL-1β and IL-6 and lower concentrations of anti-inflammatory cytokine IL-12 and inflammatory cytokine IL-10, as well as lower expression of the cell adhesion molecule E-cadherin (Ellis et al., 2022). Finally, endometriosis patients have abnormally elevated levels of Cancer Antigen 125 (CA125) in serum (above 35 units per mL), so the CA125 assay is currently utilized to diagnose endometriosis (Kalyani et al., 2021). Recently however, CA19-9 has emerged as a more promising biomarker compared to CA125 due to its improved sensitivity and specificity (Kurdoglu et al., 2009; Hsu et al., 2010). In the future, nanotechnology-based biosensors that detect the presence or absence of such biomarkers in patient samples derived from blood, urine, feces, or other fluids could provide more accurate and less invasive diagnosis of endometriosis than existing surgical or imaging methods.

Before introducing specific examples of nanotechnology-based biosensors for endometriosis, it is important to understand the basic concept and benefits of these tools *versus* traditional sensors. Typically, biosensor assays use a reporter (such as an antibody tagged with a fluorophore) to detect the presence of a specific antigen (such as CA19-9 in serum). Nanoparticle-based systems can increase the sensitivity and signal-to-noise ratio of these assays by either increasing the readout (e.g., elevating the fluorescence quantum yield) or increasing the strength of binding to the targeted molecule. This extends into other detection methods as well, including those based on absorbance, electrical measurements, and more. A few examples of electrochemical immunosensors that have been reported to date are described below.

One team developed a bio-nanocomposite to detect CA19-9 in serum. The sensor consisted of multiwalled carbon nanotube (MWCNT) and magnetite (Fe_3O_4) nanoparticles dispersed in chitosan (CS), which were coupled to anti-CA19-9 antibodies and then placed onto a glassy carbon electrode using glutaraldehyde as a cross-linker (Kalyani et al., 2021). The electrical signals were recorded upon addition of serum containing CA19-9 antigen using square wave voltammetry in the presence of redox marker $[Fe(CN)_6]^{3-/4-}$ solution, and the sensing was validated using ELISA (enzyme linked immunosorbent assay) techniques. This sensor could detect CA19-9 across a range of 0.00083 to 83 IU/mL, which spans most of the physiological range (one study reported the mean serum CA19-9 level in endometriosis patients is ~15 IU/mL for stage 1 disease and ~108 IU/mL for stage IV disease (Harada et al., 2002). Other studies have shown supportive data for the elevated levels of CA19-9 in serum, especially in advanced stages of the disease, with values ranging from 16.81 IU/mL for stage I to 111.66 IU/mL for stage IV (Tuten et al., 2014; Kalyani et al., 2021). Accordingly, this test has potential application in early-stage diagnosis and/or treatment monitoring.

Gold nanoparticles (AuNPs) are also attractive for use in immunosensors due to their speed of synthesis, high conductivity, and ease of antibody labeling for biomolecule detection. Graphene is another material with advantageous properties for immunosensing applications including exceptional mechanical strength, large surface area, and high electrical conductivity. When reduced to graphene oxide (GO), the surface functional groups of GO interact with metal nanoparticles including AuNPs, allowing for the production of effective electrochemical sensors based on these nanocomposites. Sangili et al. developed a label-free immunosensor wherein glassy carbon electrodes (GCE) were modified with AuNP/reduced-GO, then further modified with anti-CA125 antibodies using a layer-by-layer assembly process (Figure 2) (Sangili et al., 2020). Bovine serum albumin (BSA) was used to block nonspecific active sites, then samples containing CA-125 (either phosphate buffered saline (PBS) with CA-125 at known concentrations or patient blood samples) were added for 45 min at 37°C. Thereafter, the analyte was detected using square wave voltammetry techniques. This sensor could detect CA-125 across a range of 0.0001–300 IU/mL, with a limit of detection (LOD) of 0.000042 IU/mL, and it showed excellent correlation with ELISA validation techniques when evaluated using patient samples. Moreover, the sensor had a broader detection range and lower LOD than previous immunosensors and the standard ELISA method. Hence, there is great promise for use of this and other immunosensors and biomarkers in the clinical screening of endometriosis. In the future, such low-cost, point-of-care diagnostic tools could improve patient access to screening.

2.2 Imaging techniques

Beyond biomarker detection, imaging techniques can be employed to diagnose endometriosis through lesion visualization. As mentioned earlier, current clinical imaging techniques include MRI and ultrasound. These and other imaging modalities can assist researchers and clinicians in learning more about the etiology and

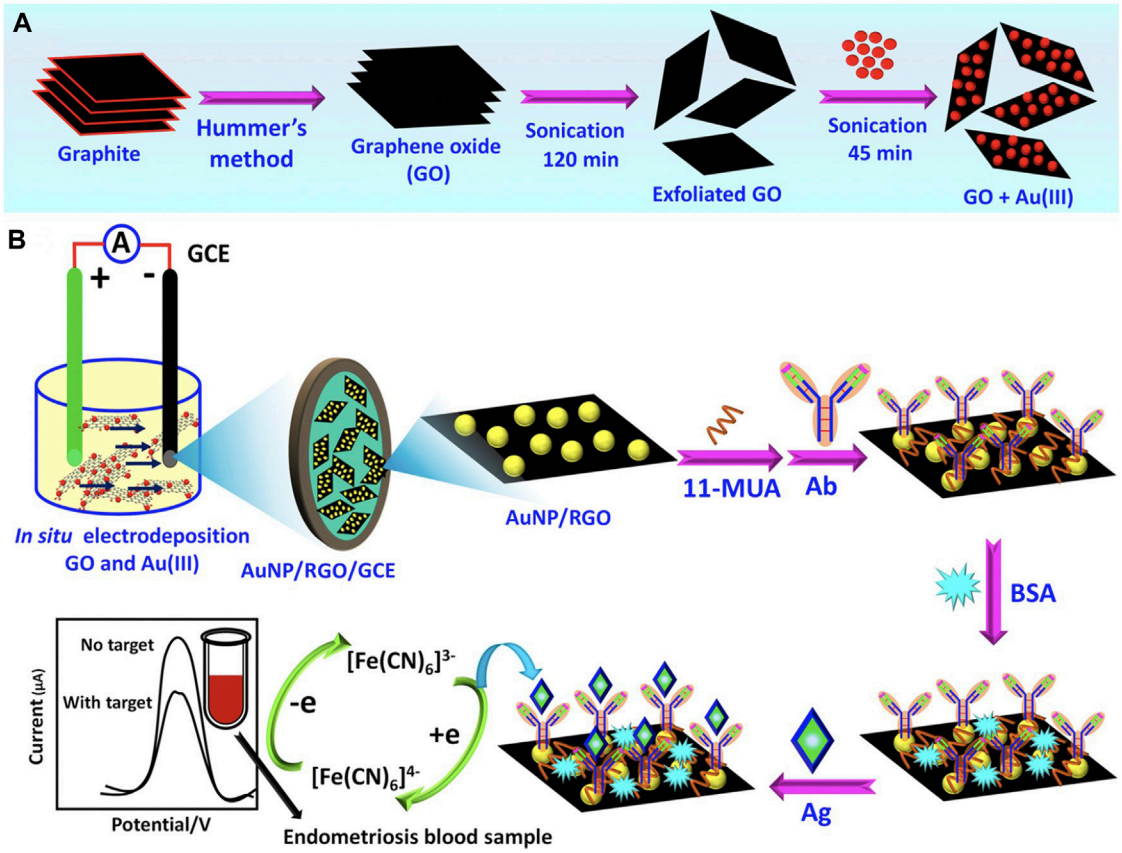

FIGURE 2
Overview of a nanocomposite designed to detect CA-125 in patient samples. **(A)** First, graphene oxide (GO) and Au^{3+}(AuIII) composites were prepared as depicted. **(B)** Prepared GO + AuIII composites were used to make glassy carbon electrodes (GCE) modified with AuNP/reduced graphene oxide (AuNP/RGO/GCE). Next, 11-mercaptoundecanoic acid (11-MUA) was used to facilitate attachment of anti-CA125 antibodies. After blocking nonspecific active sites with bovine serum albumin (BSA), CA-125 antigens (Ag) (diluted in PBS or within patient blood samples) were added to the sensors and square wave voltammetry analysis was implemented to quantify CA-125. Adapted with permission from Sangili A, *et al. ACS Applied Bio Materials.* 2020; 3 (11): 7620–30. Copyright 2020, American Chemical Society.

pathogenesis of the disease. Nanoparticle contrast agents that are coated with ligands that facilitate binding to endometrial cells or associated reproductive tissue structures can be used to enhance and improve these imaging techniques by providing more sensitive and accurate visualization and localization of the disease (Ellis et al., 2022). Some nanoparticles, such as those based on iron oxide or gold, have inherent properties that allow them to enhance the contrast of magnetic or optical imaging techniques. Other systems encapsulate molecules such as fluorescent dyes to achieve contrast enhancement between diseased and healthy tissues/cells. A key advantage of nanoparticle-enhanced imaging techniques is that they require a simple injection or infusion of the material, followed by non-invasive imaging of the tissues of interest. This is advantageous *versus* invasive laparoscopy techniques but requires effective delivery of the contrast agent to the targeted lesions. The main limitation of nanoparticle contrast agents is that they may be retained in the body with unknown long-term consequences. Clinicians and patients must carefully consider both the benefits and potential risks of nanoparticle contrast agents when deciding whether to use these materials for lesion detection.

In a recent study, scientists developed magnetic iron oxide (Fe_3O_4) nanoparticles, which have high relaxivity, low toxicity, and exceptional contrast enhancement, as negative contrast agents for T2-weighted MRI of endometriosis (Zhang et al., 2014). In this work, the Fe_3O_4 nanoparticles were modified with hyaluronic acid (HA) to facilitate targeting of CD44 receptors that are overexpressed on endometriotic cells (Zhang et al., 2014). Endometriosis was surgically induced in rats by autologous transplantation. Four weeks post-surgery, rats received intravenous (IV) HA-Fe_3O_4 nanoparticles, then MRI was performed. By 2 h post-injection, there was significant darkening of the walls of the lesions in mice that received HA-Fe_3O_4 nanoparticles and were imaged using turbo spin-echo fat-suppressed T2-weighted MRI (Figure 3). The presence of the nanoparticles in the lesions was confirmed by quantifying Fe concentration and by staining excised tissues with Prussian blue. More nanoparticles were found in the ectopic endometrium as compared to eutopic endometrium, validating the use of CD44 as a marker for lesion targeting (Zhang et al., 2014).

Related to this work, Lee et al. reported the use of ultrasmall superparamagnetic iron oxide nanoparticles to detect intraperitoneal endometriosis lesions in an experimental rat model by MRI (Lee et al., 2012). These could detect lesions 3 mm or greater in size. More recently, Park et al. developed

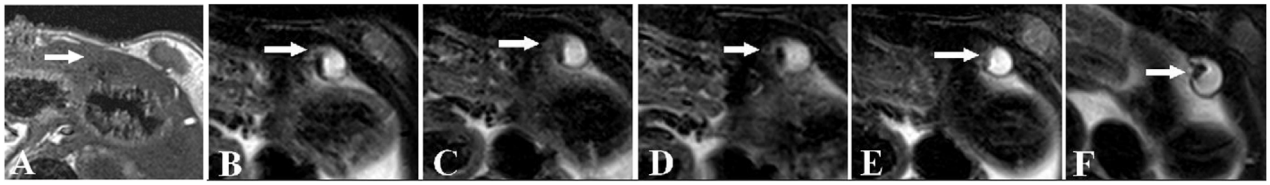

FIGURE 3
MRI images of rat ectopic endometriotic lesions at various time points post IV injection of HA-modified-Fe_3O_4 nanoparticles. **(A)** T1 weighted image of ectopic uterine tissue (EUT) (indicated by white arrow), which appeared as an ill-defined cystic mass with low signal. **(B)** Fat-suppressed (FS)-T2 weighted image of EUTs before nanoparticle injection. The EUTs showed a slightly higher signal intensity surrounded by the fibrous walls' intermediate signals. In FS-T2 weighted images at **(C)** 15 min, **(D)** 30 min, **(E)** 60 min, and **(F)** 120 min post nanoparticle injection the lesion walls and lesion to background contrast are more visibly identifiable. Reproduced with permission from Zhang H, *et al. PLOS ONE*. 2014; 9 (4): e94718. Copyright 2014, PLOS ONE.

hexagonal iron oxide nanoparticles coated with a peptide targeting vascular endothelial growth factor receptor-2 (VEGFR-2) for the targeted imaging and treatment of endometriosis (Park et al., 2022). Studies performed in mice bearing transplants of macaque endometriotic tissue showed that, following IV administration, the nanoparticles could enhance both T2-weighted MRI and fluorescence contrast of endometriosis lesions (Park et al., 2022). The therapeutic uses of these nanoparticles will be discussed in Section 3, but the results point toward the exciting potential of nanotechnology-based platforms to improve the detection and treatment of endometriosis.

Finally, one study investigated the use of silicon naphthalocyanine loaded poly (ethylene glycol)-poly(ε-caprolactone) (SiNc-PEG-PCL) nanoparticles for fluorescence imaging of endometriosis (Moses et al., 2020). SiNc was selected as the contrast agent because it has greater fluorescence intensity and photostability than other dyes like indocyanine green. When encapsulated, the SiNc fluorescence was quenched, but upon nanoparticle uptake by endometrial cells, the SiNc molecules were released, activating their fluorescence and providing high signal-to-noise ratio (Figure 4A). *In vivo* studies were performed using an FDA-approved intraoperative imaging system, demonstrating the potential for nanoparticle-based contrast agents to enhance surgical detection and/or excision of endometriotic lesions (Figures 4B–F) (Moses et al., 2020). This system was also utilized for photothermal ablation of lesions, as discussed in Section 3. Compared to MRI, fluorescence imaging has reduced depth of penetration, but the fast acquisition, ease of use, and ability to be incorporated into routine surgical procedures are major benefits towards clinical implementation.

3 Treatment

Surgical ablation of endometriotic lesions via laparoscopy is the primary treatment option for patients with endometriosis. However, this treatment is invasive and incomplete removal of diseased tissue could lead to free endometriotic cells that can develop into recurrent lesions. Nanoparticles loaded with therapeutic agents and modified with targeting molecules can enable precise and effective treatment of endometriosis to avoid recurrence while also minimizing systemic side effects. The types of therapeutic agents that can be delivered with nanoparticles to treat endometriosis include anti-inflammatory drugs, hormonal therapies, and immunomodulating molecules. Alternatively, nanoparticles that produce heat when activated with light or an applied magnetic field can thermally ablate endometriosis lesions. This approach is less invasive than surgical ablation and may improve patient outcomes by yielding immunogenic cell death that minimizes recurrence. Each of these therapeutic strategies show promise to improve patient care.

3.1 Nanoparticle-enhanced photothermal therapy

Nanoparticle-enhanced photothermal therapy (PTT) is a treatment wherein photoresponsive nanoparticles are administered into the body and once they have accumulated at the disease site a near-infrared (NIR) laser tuned to the nanoparticles' peak resonance wavelength is applied to the region, which causes the temperature of the targeted tissue to increase above 42°C as the particles convert the light energy into heat. PTT has been successfully applied to the treatment of solid-tumor cancers in both preclinical and human clinical studies (Riley et al., 2017; Rastinehad et al., 2019), and now researchers are investigating its potential to manage endometriosis (Giroux and Rustgi, 2017; Moses et al., 2020). A key benefit of PTT over drug-based therapies is that treatment is confined to areas where both the nanoparticles are laser light are combined—accordingly, the off-target effects of PTT are extremely low. Additionally, cells treated with heat are less prone to development of resistance, which results in improved overall response. Below, specific examples of nanoparticles developed for PTT of endometriosis are discussed.

Section 2 introduced the use of SiNc-PEG-PCL nanoparticles as fluorescence probes for endometriosis detection (Moses et al., 2020). Excitingly, these materials can also generate heat when exposed to NIR light, allowing their use for combination imaging and PTT of endometriosis. Both *in vivo* and *in vitro* testing were conducted to determine the efficacy of PTT with this system. When macaque endometriotic stromal cells were incubated with 30 μg/mL SiNc-NPs for 48 h and then irradiated with 780 nm light (0.9 W/cm^2, 15 min), the temperature of the cells rose to ~53°C, resulting in >95% cell death (Moses et al., 2020). In the absence of irradiation, the cells remained viable, demonstrating the system's cytocompatibility. *In vivo* studies were performed using mice bearing four endometriosis grafts each. The mice were

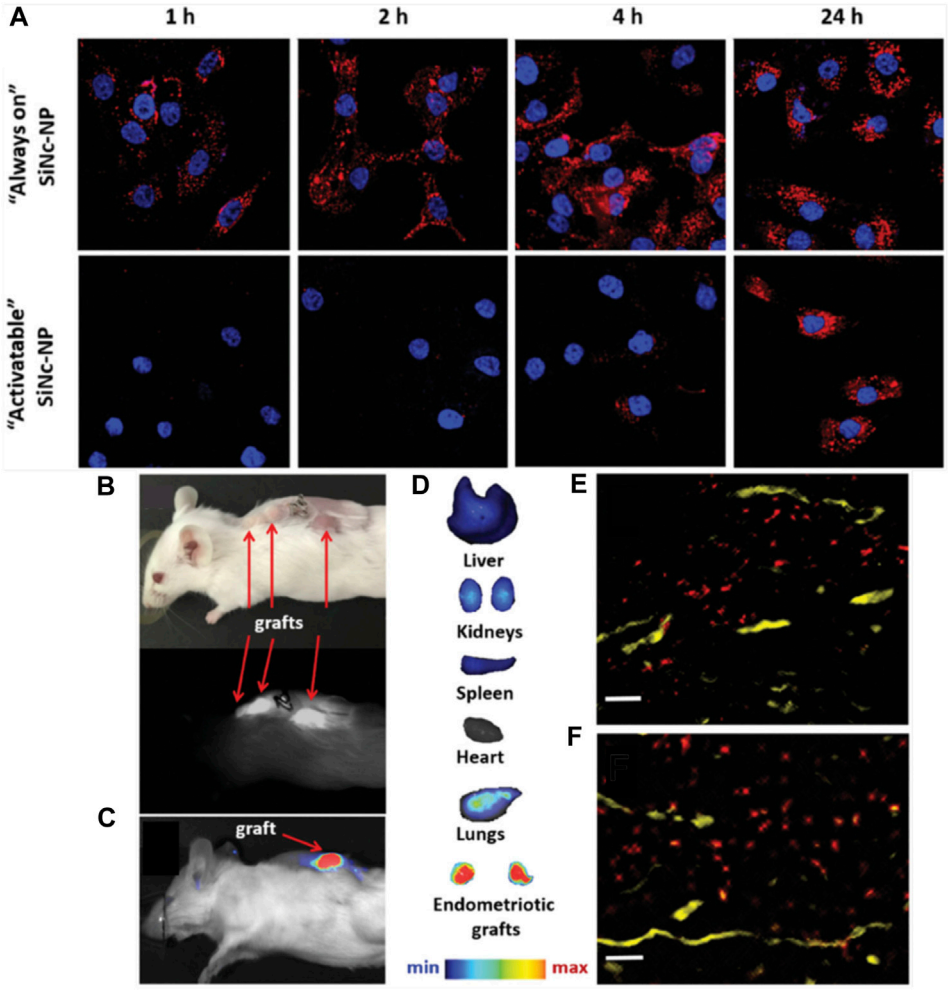

FIGURE 4
Detection of endometriosis with activatable SiNc-PEG-PCL nanoparticles. **(A)** Fluorescence microscopy images of macaque endometriotic stromal cells incubated with "always on" SiNc-NP (top row) or "activatable" SiNc-NP (bottom row) for 1, 2, 4, and 24 h. The red and blue colors reflect the fluorescence signal generated by SiNc and NucBlue (nuclei staining), respectively. **(B)** Photograph (top) and NIR fluorescence image (bottom), recorded with Fluobeam 800, of a mouse bearing endometriotic grafts 24 h after IV injection of "activatable" SiNc-NP. **(C, D)** NIR fluorescence images of a mouse bearing endometriotic graft **(C)** and excised tissues **(D)** recorded with Pearl Impulse Small Animal Imaging System 24 h after IV injection of "activatable" SiNc-NP. **(E, F)** Fluorescence microscopy images of sections of endometriotic grafts collected 24 h after IV injection of SiNc-NP. Red indicates NIR fluorescence generated by SiNc-NP. Yellow represents blood vessels stained with fluorescently labeled anti-CD31 antibodies. Scale bars = 50 µm. Adapted with permission from Moses A, *et al. Small.* 2020; 16 (18): 1906936. Copyright 2020, Wiley VCH.

intravenously injected with 3 mg SiNc/kg, and 24 h later two grafts per mouse were irradiated (780 nm light, 0.9 W/cm^2, 15 min). Irradiated lesions experienced temperature rises to 47°C and were completely eradicated within 4 days after a single treatment with no recurrence during the study's 7-week timeframe (Moses et al., 2020). These data indicate the SiNc system holds promise for the combined imaging and treatment of endometriosis.

Similar promising results were obtained by Guo *et al.*, who developed a system for targeted PTT of endometriosis based on hollow gold nanoshells (HAuNS) coated with TNYL peptides that bind EphB4 receptors that are overexpressed in endometriosis lesions (Guo et al., 2017) (Figure 5A). When non-targeted HAuNS or TNYL-HAuNS were intravenously administered into mice bearing bilaterial endometriosis lesions, the TNYL-HAuNS displayed nearly 2-fold higher accumulation in the lesions based on inductively coupled plasma-mass spectrometry (ICP-MS) analysis of gold content in the tissues. In follow-up experiments, mice with endometriosis lesions received intravenous saline, HAuNS, or TNYL-HAuNS, followed by NIR irradiation of the lesions at levels ranging from 0 to 2 W/cm^2 and times ranging from 0 to 10 min. A dosage-dependent response of the lesion volume was observed (Figures 5B, C), with the most effective treatment being TNYL-HAuNS combined with 2 W/cm^2, 10 min irradiation. This combination inhibited lesion volume by 92.7%, compared to 77.2% for HAuNS under the same irradiation conditions. Saline combined with laser had minimal effect, demonstrating that PTT was mediated by the targeted HAuNS and not by the light alone (Guo et al., 2017). Overall, this study, combined with that of Moses et al., demonstrates that PTT presents an effective and safe treatment for endometriosis that is worthy of further investigation (Guo et al., 2017; Moses et al., 2020).

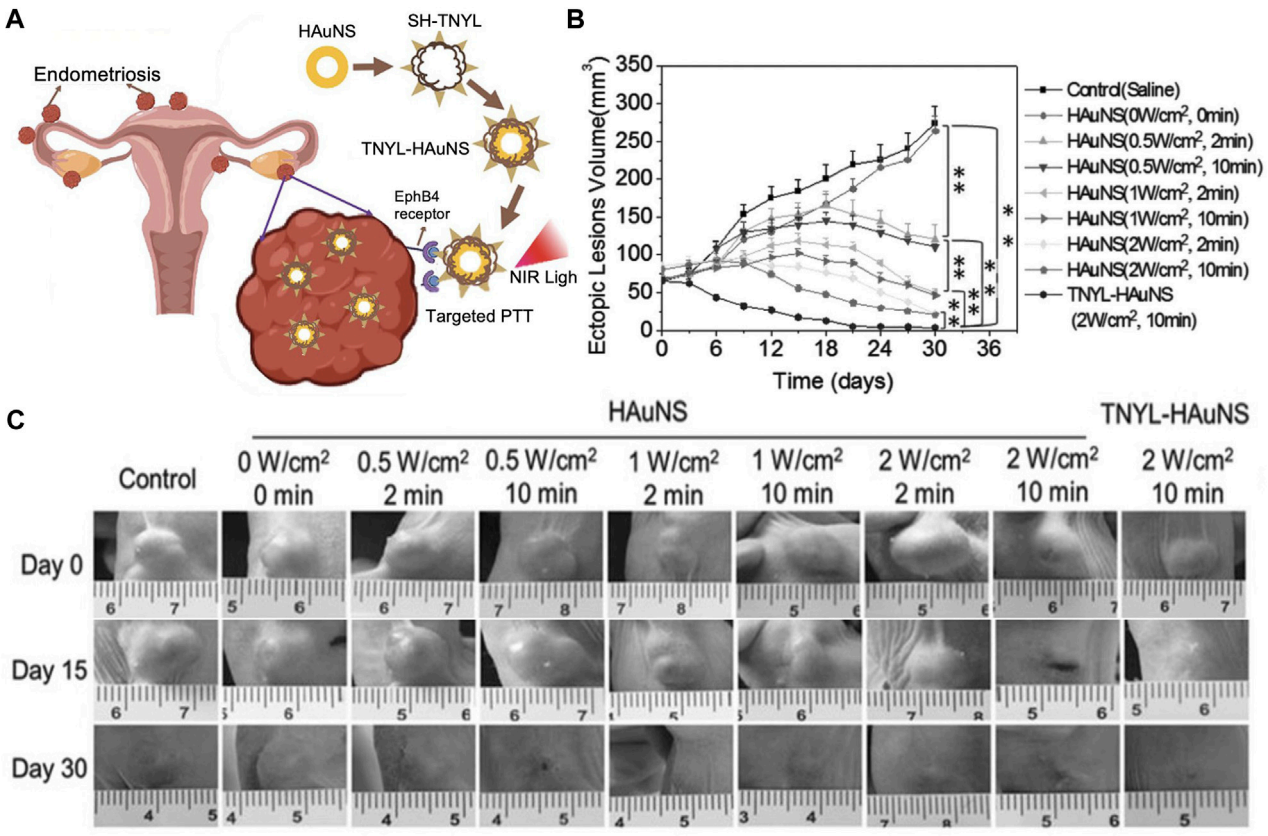

FIGURE 5
Photothermal therapy of endometriosis mediated by TNYL-targeted HAuNS. **(A)** Scheme depicting the ability of TNYL-HAuNS to bind EpHB4 receptors that are overexpressed in endometriosis lesions. Irradiation of the bound nanoparticles with NIR light facilitates photothermal ablation of the lesions. **(B)** Lesion growth curves for various treatment groups monitored every 6 days for 36 days. The TNYL-HAuNS treatment combined with 2 W/cm^2, 10 min irradiation with a 780 nm laser significantly inhibited lesion growth (n = 6/group). **(C)** Representative images of lesions in mice from each treatment group at days 0, 15, and 30 post irradiation. **(A)** Adapted with permission Luo L, *et al. Small,* 2023; 2207694, Copyright 2023 Wiley VCH and **(B, C)** adapted with permission from Guo X, *et al. Small,* 2017; 13 (15): 1603270, Copyright 2017 Wiley VCH.

3.2 Magnetic hyperthermia

While PTT has shown promise in endometriosis management, it suffers from the limited tissue penetration of NIR light, which is on the order of less than a few centimeters. An alternative approach without these limits is magnetic hyperthermia, which uses an alternating magnetic field (AMF) to activate magnetic nanoparticles and thereby produce heat (Park et al., 2022). Park et al. developed hexagonal iron oxide nanoparticles doped with a small amount of cobalt for improved heating efficiency and encapsulated these NPs in poly(ethylene glycol)-block-poly(ε-caprolactone) (PEG-PCL)-based nanocarriers that were further modified with peptides to target VEGFR-2 (also known as KDR) to enable targeted magnetic hyperthermia of endometriosis (Park et al., 2022). They chose to target VEGFR-2/KDR because its expression is elevated in endometriosis lesions when compared to the eutopic endometrium. Both *in vitro* and *in vivo* experiments were conducted to evaluate the potency of the KDR-targeted magnetic nanoparticles (MNs). When primary cells isolated from macaque endometriosis lesions (which were confirmed to overexpress KDR by qPCR) were incubated with the non-targeted or KDR-targeted MNs, those exposed to KDR-MNs heated more rapidly in the presence of AMF owing to improved cellular binding (Figures 6A, B). In turn, the magnetic hyperthermia mediated by targeted MNs more potently suppressed endometriosis cell viability (Figure 6C). This efficacy was maintained *in vivo*, as mice with endometriosis xenografts that were treated with KDR-targeted MNs and AMF exhibited intralesion temperatures above 50°C during treatment. This heating completely eradicated the lesions (Figure 6D), which did not respond to AMF or KDR-MNs alone (Park et al., 2022). While this study did not directly compare graft volume following treatment with non-targeted MNs *versus* KDR-targeted MNs, it suggests that targeted magnetic hyperthermia could provide a safe, non-surgical approach to eliminate deep-seated endometriosis lesions.

3.3 Drug-based therapy

Although there are drugs currently used to assist with management of endometriosis, none are curative and they lack stability and specificity. Oxidative stress, angiogenesis, and extracellular matrix degradation are characteristics of endometriosis, so nanoparticle-based drug carriers that attack

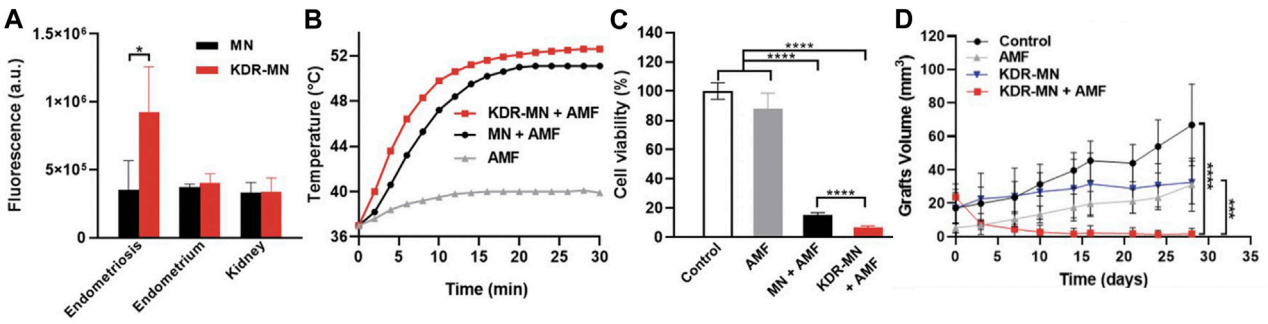

FIGURE 6
Magnetic hyperthermia of endometriosis mediated by KDR-targeted magnetic nanoparticles (KDR-MN). **(A)** Flow cytometry analysis of cellular uptake (mean ± standard deviation) of dye-labeled non-targeted magnetic nanoparticles (MN, black bar) and KDR-MNs (red bar) by macaque endometriosis stroma cells, endometrium cells, and kidney cells after 24-h incubation. *$p < 0.05$ by unpaired t-test ($n = 5$). **(B)** Temperature profiles of endometriosis cells treated with only applied magnetic field (AMF, gray curve), non-targeted MNs + AMF (black curve), or KDR-MNs + AMF (red curve). Nanoparticles were applied for 24 h at 25 μg Fe/mL and AMF was applied 30 min at 420 kHz (26.9 kA/m). **(C)** Viability of endometriosis cells after the treatments applied in **(B)**. Data are means ± standard deviation. Statistical comparisons were performed with one-way ANOVA ($n = 20$, ****$p < 0.0001$). **(D)** Graft volume *versus* time in mice treated with saline (control, $n = 4$), AMF only ($n = 4$), KDR-MN only ($n = 4$), or KDR-MN + AMF ($n = 5$). Data are means ± standard deviation and a one-way ANOVA was used for statistical analysis (***$p < 0.001$, ****$p < 0.0001$). Reproduced with permission from Park Y, *et al. Small*, 2022; 18 (24): 2107808, Copyright 2022, Wiley VCH.

these underlying mechanisms of the disease could provide better outcomes. For example, nanoparticles could be used to improve the delivery of compounds with antioxidant or antiangiogenic properties or drugs that can inhibit matrix metalloproteinases (MMPs) (Friend, 2017). Promising drug candidates include epigallocatechin gallate (EGCG) and doxycycline, which have antioxidant and antiangiogenic capabilities and can inhibit MMPs, but which lack the stability necessary for clinical use and thus could benefit from a nanocarrier (Yuxue et al., 2023). Towards this goal, Singh et al. loaded both EGCG and doxycycline in poly (lactic-co-glycolic) acid (PLGA) nanoparticles (Singh et al., 2015). When tested in mice with endometriosis induced by intraperitoneal injection of donor mouse uterine tissue, the dual drug-loaded nanoparticles outperformed nanoparticles loaded with either agent individually. In addition to reducing lesion size and number, the EGCG/doxycycline-loaded nanoparticles reduced MMP activity, oxidative stress, and angiogenesis in the lesions, indicating the drugs were working through the expected mechanism of action. These exciting results demonstrate the promise of PLGA nanoparticles to improve drug therapy for endometriosis, although the study did not provide direct comparison against drugs that were not encapsulated in nanoparticles. In separate work, PLGA nanoparticles have been loaded with copaiba oleoresin (CPO), a natural product derived from *Copaifera landgroffii* with anti-inflammatory capabilities (de Almeida et al., 2016). *In vitro,* the CPO-loaded nanoparticles reduced endometrial stromal cell viability, while unloaded nanoparticles had no toxic effects. This reiterates that PLGA nanocarriers appear to be a safe choice of vehicle for drug delivery to combat endometriosis.

As noted above, a key characteristic of endometriosis is oxidative stress, which results in higher concentrations of reactive oxygen species and lipid peroxide markers as the disease progresses. Congruently, the concentration of antioxidants is lower in serum and peritoneal fluids of endometriosis patients (Friend, 2017). To counteract these effects, one could administer antioxidant drugs (either freely or encapsulated in nanoparticles) or nanoparticles that have inherent antioxidant properties. For instance, cerium oxide (CeO_2) nanoparticles, also known as nanoceria, react catalytically with superoxide and hydrogen peroxide, and have thus been tested in mice with induced endometriosis. The nanoceria not only decreased oxidative stress and inhibited angiogenesis in this model, but also protected against endometriosis-related adverse effects on oocytes, which is critical for successful pregnancy (Chaudhury et al., 2013). Thus, nanoceria are a promising alternative to drug-loaded PLGA for endometriosis management.

While the above examples aimed to use nanomedicine to treat the underlying cause of endometriosis, other nanoparticle designs have been developed for pain management. A-317491 is a selective antagonist of P2X ligand-gated ion channel 3 (P2X3), a receptor in the ERK signaling pathway that has been implicated in endometriosis pain (Ding et al., 2017; Moses et al., 2021). Given its function, researchers loaded A-317491 in nanostructured lipid carriers (NLCs) that were then coated with chitosan oligosaccharide-g-stearic acid (CSOSA) to form CSOSA/NLC/A-317491 (Yuan et al., 2017). Mechanical and heat paw withdrawal tests were used to measure the hyperalgesia of control or endometriosis rats that were previously injected with either saline or CSOCA/NLC/A-317491. The treatment attenuated pain over a period lasting 8–24 h, which was longer than the 2-to-4-h pain relief provided by A-317491 salt. However, whether the effects of the CSOSA/NLC/A-317491 could extend over a longer prior was not evaluated. Nevertheless, this study shows the potential of nanomedicine to alleviate side effects such as pain that are associated with endometriosis.

3.4 Gene therapy

Gene therapy is being widely explored as an approach to treat various conditions. In some forms of gene therapy, specific genes are transferred to a set of target cells (via plasmid DNA or messenger

RNA (mRNA) delivery) to modify or compensate for a genetic defect (Yuxue et al., 2023). Alternatively, small interfering ribonucleic acid (siRNA) or microRNA molecules can be delivered to silence the expression of overactive genes at the mRNA level. Since nucleic acids cannot be delivered freely owing to their poor stability and unfavourable pharmacokinetic profile, nanocarriers have been utilized as safe and effective delivery vehicles. With respect to endometriosis treatment, the types of nanocarriers that have been tested in gene therapy applications include polymeric nanoparticles, extracellular vehicles (EVs), micelles, and more (Chaichian et al., 2022; Zhao et al., 2012; Wang et al., 2014; Zhao et al., 2016).

In one study, researchers developed stearic acid-grafted chitosan oligosaccharide micelles (CSO-SA) to deliver pigment epithelium-derived factor (PEDF) plasmids to endometriosis lesions (Zhao et al., 2012). PEDF is a protein with anti-angiogenic functions, so plasmids encoding PEDF would be expected to counteract the angiogenic features of endometriosis. In a rat model of peritoneal endometriosis, the CSO-SA/PEDF nanoparticles distributed to endometriotic lesions and, after 2 weeks of treatment, the rats showed a decrease of ~50% in the volume of endometriotic lesions (Zhao et al., 2012). Moreover, there was a significant reduction in microvessel density labelled by von Willebrand factor without a decrease in α-Smooth Muscle Actin-positive mature vessels in rats treated with CSO-SA/PEDF in comparison to controls. These data indicate that PEDF plasmid delivered via CSO-SA carriers can counteract the angiogenesis associated with endometriosis.

In a similar approach, researchers examined the use of polyamidoamine (PAMAM) dendrimers to deliver plasmids encoding endostatin, a potent inhibitor of angiogenesis (Wang et al., 2014). When directly injected into GFP-expressing subcutaneous endometriosis lesions in nude mice, the endostatin plasmid-loaded PAMAM dendrimers significantly reduced lesion size in comparison to control mice based on analysis of GFP fluorescence intensity at days 15, 20, 25 and 30 and by measurement of lesion weight at day 30. The endostatin-loaded PAMAM also reduced microvessel density based on immunohistochemistry analysis (Wang et al., 2014). Future studies that build on this work should evaluate the potency of endostatin plasmids when delivered via dendrimers or other nanocarriers in a systemic, rather than direct, manner, as this would be a more clinically relevant method of administration.

Beyond using plasmid DNA to increase the expression of desired genes, another potential opportunity to advance the treatment of endometriosis is to silence the expression of specific mRNA molecules using siRNA. This approach was explored by Zhao *et al.,* who delivered siRNA against aquaporin 2 (AQP2) using carriers composed of polyethylenimine (PEI) and chitosan oligosaccharide (CSO) (Zhao et al., 2016). Aquaporins (AQPs), transmembrane proteins spread across various tissues, play a crucial role in regulating water transport across cell membranes. Aquaporin 2 (AQP2) is abundantly expressed in endometriosis tissues, and it contains an estrogen-response element in the promoter sequence (Moses et al., 2021). As a result, estrogen stimulation has been shown to significantly increase the migration, invasion, adhesion, and proliferation of immortalized human endometrial adenocarcinoma cells, while AQP2-siRNA significantly reduces these features (Moses et al., 2021). This led Zhao *et al.* to develop PEI-CSO nanoparticles modified with hyaluronic acid (HA), which targets CD44, as AQP2 siRNA delivery vehicles for endometriosis treatment (Yuxue et al., 2023). After 2 weeks of therapy, the size of endometriosis cysts in treated rats was significantly lower in the (CSO-PEI/siRNA)HA group than in the control group. While promising, this study lacked comparison to a control with scrambled/non-targeting siRNA and it did not include analysis of AQP2 mRNA or protein expression to confirm the effect on cyst size was due to the delivered siRNA yielding knockdown of AQP2. Future work should include these controls and experiments to further validate the potential of this approach.

3.5 Immunotherapy

Regulating specific immune cells that contribute to disease progression is another promising approach to combat endometriosis. Thus far, studies have focused on macrophages or T cells. Macrophages are of interest because they can recognize and clear endometrial cells from the peritoneal cavity (Moses et al., 2021). The polarization of the macrophages is critical, as a high concentration of M2 macrophages promotes fibrosis and angiogenesis, which contributes to endometriosis development (Li et al., 2021). While transplantation with M1 macrophages has been shown to reduce the growth of endometrial lesions, transplantation with M2 macrophages promotes lesion development (Bacci et al., 2009). Based on this knowledge, Li et al. postulated that M1 macrophage-derived nanovesicles (M1NVs) could reprogram M2 macrophages to the M1 phenotype to suppress endometriosis in a mouse model (Li et al., 2021). Excitingly, the M1NVs reduced the migration of endometrial stromal cells obtained from endometriosis patients *in vitro* and, through the repolarization of M2 macrophages to M1 macrophages, inhibited the disease in a mouse model without any side effects (Figure 7). M0NVs did not elicit this same effect. Although M1NVs have not been investigated further, they show great potential as an option for endometriosis treatment.

Antsiferova et al. conducted another macrophage manipulation-based study (Antsiferova et al., 2013). They evaluated which of two different nanocarriers, unmodified mesoporous silica nanoparticles (UNPs) and aminopropyl modified silica nanoparticles (AMNPs), would be best suited to deliver the immunomodularity drug GMDP (glucosaminyl muramyldipeptide (N-acetylglucosaminyl-N-acetylmuramyl-L-alanyl-D-isoglutamine)) to macrophages collected from the peritoneal fluid of women with endometriosis (Antsiferova et al., 2013). Both particle types demonstrated significant cellular uptake and low cytotoxicity, but when used to deliver GMDP the AMNPs yielded more robust activation of several pattern recognition receptors (including CD36 (scavenger receptor B), CD204 (scavenger receptor A1), NOD2 (nucleotide-binding oligomerization domain 2) receptors, and RAGE (receptor for advanced glycation end products)) in treated peritoneal macrophages compared to free GMDP or GMDP-UNPs. The GMDP-AMNPs also increased expression of MMP-9 (matrix metalloproteinase-9), which helps macrophages degrade the extracellular matrix of cells being targeted for phagocytosis. Unfortunately, this study did not progress into *in vivo* testing, but it will be interesting to see how this technology advances in future work.

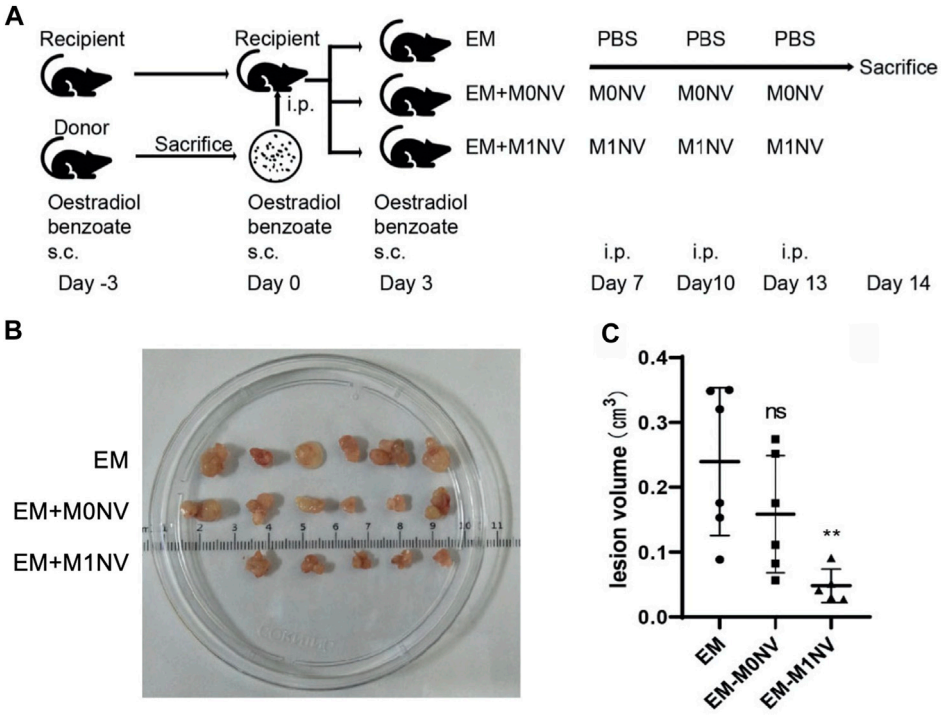

FIGURE 7
Use of M1NVs to inhibit endometriosis in a mouse model. **(A)** Diagram showing the experimental steps for *in vivo* testing. Oestradiol benzoate was administered to synchronize the cycle 3 days before intraperiteoneal (i.p.) injection of uterus fragments obtained from donor mice. Three days after i.p. injection, mice received oestradiol benzoate again to enhance endometriosis development. Thereafter, they were treated with PBS (EM control), M0NVs, or M1NVs as shown. The dose of NVs was 50 μg/mouse. **(B)** Ectopic lesions excised from mice in each treatment group at day 14. **(C)** The M1NV treatment significantly reduced lesion volume compared to the other treatments (PBS or M0NVs) (ns: no significance when compared with EM, $^{**}p < 0.01$ when compared with EM). Reproduced with permission from Li Q, *et al. Fronters in Immunology.* 2021; 12: 707784.

T cells are another potential target for immunotherapy of endometriosis. In particular, $CD4^+$ $CD25^+$ regulatory T cells (Tregs) are directly involved in the upkeep of the body's immune system. Multiple studies have shown there is an increased concentration of $CD4^+$ $CD25^+$ Tregs in the peritoneal fluid (PF) of women with endometriosis. Liu et al. investigated the potential for PLGA nanoparticles loaded with anti-CTLA-4-antibodies to inhibit the progression of endometriosis in a murine model (Liu et al., 2017). Blocking CTLA-4 with antibodies can limit the activation of $CD4^+$ $CD25^+$ Tregs. Using flow cytometry, the percentage of $CD4^+$ $CD25^+$ Tregs in PF treated with anti-CTLA-4/PLGA or free anti-CTLA-4 was measured. At day 3, there was no significant difference between groups, but at days 7 and 14 there were significantly fewer $CD4^+$ $CD25^+$ Tregs in samples treated with the nanocarriers compared to the free antibodies. In follow-up studies, ectopic endometrial cells (EEC) were co-cultured with $CD4^+$ $CD25^+$ Tregs isolated from PF and exposed to anti-CTLA-4/PLGA or free anti-CTLA-4. EEC proliferation and invasion were measured via ELISA and Matrigel invasion assays, respectively. The antibody nanocarrier treatment significantly suppressed EEC proliferation and invasion, and the effect was more pronounced than that of free antibodies, which the authors attributed to the sustained release from the PLGA (Liu et al., 2017). These results, coupled with observed reductions in the expression of IL-10 and TGF-beta cytokines, suggest anti-CTLA-4/PLGA could be a promising nanomedicine for endometriosis therapy.

4 Discussion/future outlook

As there is no cure for endometriosis and a paucity of treatments with long-lasting effects, it is essential to develop novel approaches to combat the disease. Further, too many women go undiagnosed for years due to a lack of accurate and simple diagnostic tools, and it is even more challenging to characterize the severity of the disease. These unmet needs have recently led to an influx of researchers working to develop improved treatment and diagnostic options for endometriosis, including approaches based on nanotechnology. Table 1 summarizes the technologies discussed in this review. Nanoparticles have numerous advantages in that many are biocompatible and can be easily modified with desired cargo, targeting ligands, or imaging agents. This has led to a great deal of progress towards developing non-invasive, accurate diagnostic tools and safe, effective treatments for endometriosis. Indeed, as discussed in this review, new treatments based on hyperthermia, drug delivery, gene therapy, and immunotherapy have shown substantial promise thanks to the unique characteristics of nanomedicines. Likewise, new sensors and imaging agents have shown promise to support earlier detection, which would transform patient care.

Despite these exciting advances, there is still work to be done. Regarding biosensors, there are many potential non-invasive biomarkers that require more testing to validate their use in endometriosis diagnostics, especially miRNA and siRNA, which

TABLE 1 Summary of the nanotechnology-enabled diagnostics and treatments for endometriosis presented in this review.

	System components	Application	Key results	Citation
Biosensing	Multiwalled carbon nanotubes and Fe_3O_4 NPs dispersed in chitosan, coupled to anti-CA19-9 antibodies, and placed on glassy carbon electrodes	Detection of CA19-9 in serum via electrochemical immunosensing	Detectable range of 0.00083 to 83 IU/mL	Kalyani et al. (2021)
	Glassy carbon electrodes modified with gold NPs, reduced graphene oxide, and CA-125 antibodies	Detection of CA-125 in blood via electrochemical immunosensing	Detectable range of 0.0001 to 300 IU/mL	Sangili et al. (2020)
Imaging	Fe_3O_4 NPs coated with hyaluronic acid (HA) to target CD44 on endometriotic cells	Lesion visualization in a rat endometriosis model via FS-T2-weighted MRI	Significant MRI contrast enhancement of lesions by 2 h post-IV injection of NPs	Zhang et al. (2014)
	Ultrasmall superparamagnetic Fe_3O_4 NPs	MRI detection of intraperitoneal endometriosis lesions in a rat model	Successful detection of lesions >3 mm in size	Lee et al. (2012)
	Hexagonal Fe_3O_4 NPs coated with peptides targeting VEGFR-2	MRI and fluorescence imaging of lesions in mice bearing transplants of macaque endometriotic tissue	IV-administered NPs enhanced lesion contrast under both imaging modalities	Park et al. (2022)
	SiNc-PEG-PCL NPs (silicon naphthalocyanine loaded poly (ethylene glycol)-poly(ε-caprolactone) NPs)	Fluorescence imaging of endometriotic grafts in a murine model	Significant fluorescence observed in grafts 24 h post-IV injection of NPs using an FDA-approved intraoperative imaging system	Moses et al. (2020)
Therapy	SiNc-PEG-PCL NPs	PTT of endometriotic lesions in mice upon NP activation with 780 nm light	PTT yielded >95% cell death *in vitro* and complete disease eradication without recurrence over 7-week *in vivo*	Moses et al. (2020)
	TNYL-HAuNS (Hollow gold nanoshells modified with TNYL peptides that bind EphB4 receptors)	PTT of endometriosis in mice upon NP activation with 780 nm light	TNYL-HAuNS exhibited ~2-fold higher accumulation in lesions than non-targeted HAuNS; PTT inhibited lesion volume by 92.7%	Guo et al. (2017)
	Cobalt-doped hexagonal Fe_3O_4 NPs loaded in PEG-PCL carriers modified with peptides targeting VEGFR-2	Magnetic hyperthermia of endometriosis xenografts in mice	Complete eradication of lesions achieved *in vivo*	Park et al. (2022)
	Epigallocatechin gallate (EGCG) + Doxycycline loaded in PLGA NPs	Drug-based treatment of intraperitoneal endometriosis in a murine model	Treatment reduced lesion size and number and also decreased MMP activity, oxidative stress, and angiogenesis in lesions	Singh et al. (2015)
	Copaiba oleoresin (CPO)-loaded PLGA NPs	Anti-inflammatory drug-based therapy	Reduced endometrial stromal cell viability *in vitro*	de Almeida et al. (2016)
	CeO_2 NPs	Management of endometriosis in a murine model through the antioxidant properties of the NPs	Treatment decreased oxidative stress, inhibited angiogenesis, and protected against adverse effects on oocytes	Chaudhury et al. (2013)
	A-317491 loaded in nanostructured lipid carriers coated with chitosan oligosaccharide-g-stearic acid (CSOSA/NLC/A-317491)	Pain management in a rat model of endometriosis	Treatment attenuated pain over 8–24 h, compared to 2–4-h relief provided by A-317491 salt	Yuan et al. (2017)
	CSO-SA micelles loaded with PEDF plasmids	Anti-angiogenesis gene therapy of endometriosis in a rat model	Treatment decreased lesion volume by ~50% and significantly reduced microvessel density	Zhao et al. (2012)
	PAMAM dendrimers carrying endostatin plasmids	Anti-angiogenesis gene therapy of endometriosis in a subcutaneous murine model	NPs directly injected into lesions reduced lesion size at days 15, 20, 25, and 30 and decreased microvessel density	Wang et al. (2014)
	CSO-PEI nanocarriers coated with HA and carrying AQP2 siRNA	Gene regulation of endometriosis in a rat model	Endometriosis cysts were significantly smaller in (CSO-PEI/siRNA)HA-treated rats after 2 weeks of therapy	Yuxue et al. (2023)
	M1NVs (M1 macrophage-derived nanovesicles)	Immunotherapy of endometriosis in a mouse model by reprogramming M2 macrophages to an M1 phenotype	Successfully inhibited disease *in vivo* without any side effects	Li et al. (2021)
	Unmodified mesoporous silica NPs (UNPs) and aminopropyl modified silica NPs (AMNPs) loaded with the immunomodulatory drug GMDP	Immunotherapy *in vitro* using macrophages collected from the peritoneal fluid of women with endometriosis	Both NPs exhibited significant cellular uptake and low cytotoxicity, but GMDP-AMNPs increased immune activation	Antsiferova et al. (2013)

(Continued on following page)

TABLE 1 (*Continued*) Summary of the nanotechnology-enabled diagnostics and treatments for endometriosis presented in this review.

	System components	Application	Key results	Citation
	PLGA NPs loaded with anti-CTLA-4 antibodies	Endometriosis management through immunotherapy to limit the activation of $CD4^+$ $CD25^+$ Tregs	Treatment reduced percentage of Tregs in peritoneal fluid and decreased endometrial cell proliferation and invasion	Liu et al. (2017)

are underexplored (Zhang et al., 2020). With respect to imaging, although several techniques have been tested for cervical cancers and other reproductive/gynecologic diseases, their application to endometriosis remains to be investigated. Approaches including fluorescence imaging, photoacoustic imaging, computed tomography, and multimodal imaging have great promise to advance the detection and delineation of endometriosis (Luo et al., 2023a). Future work incorporating nanoparticles, particularly those targeted to specific biomolecules on endometriotic lesions, as contrast agents could greatly improve diagnostic imaging and staging of the disease. Moreover, systems that provide both imaging and treatment (such as those discussed that enable imaging and PTT) could greatly advance patient care and outcomes (Guo et al., 2017; Moses et al., 2020).

Future steps for treatment should include both innovations in the nanotherapy design and the development and incorporation of improved and more accurate animal models of the disease. Current animal models usually utilize mice and rats, but they do not develop endometriosis naturally and the pathogenesis of the disease is complex. A primate model would be better suited for testing endometriosis treatments as the primate reproductive system has more direct similarities to that of humans and researchers would be able to naturally induce endometriosis. In addition to validating nanomedicines for endometriosis in more accurate disease models, future work should test nanomedicines appropriately for safety, which is crucial to ensure their translatability to humans.

Beyond typical safety analyses that measure blood chemistry, serum cytokines, body weight, and other characteristics of treated animals, future studies should ensure treatments do not negatively impact fertility, as infertility is a major complication of endometriosis. There is still much to be learned surrounding the mechanisms of endometriosis-associated infertility, so initial steps will require these mechanisms be determined, and then interventions established. Women with endometriosis have increased levels of peritoneal fluid and IL-6 levels are increased in the PF; together, these decrease sperm motility by 40%–80% and also have other detrimental effects on embryo development and sperm (Oral et al., 1996; Harada et al., 2002). Given this knowledge, ensuring treatments can induce/maintain a healthy pelvic environment may be a critical requirement for reducing the infertility of endometriosis.

In conclusion, researchers are actively developing various diagnostic and therapeutic tools based on nanotechnologies which may someday improve the quality of life and care for endometriosis patients. Until now, the application of nanomedicine to women's health has been understudied. More research is needed for these technologies to realize their potential, but it will be immensely exciting to follow the field as it progresses and transforms the lives of women with endometriosis.

Author contributions

MS: Conceptualization, Investigation, Visualization, Writing–original draft, Writing–review and editing. ED: Conceptualization, Funding acquisition, Project administration, Supervision, Visualization, Writing–review and editing.

Funding

The authors declare financial support was received for the research, authorship, and/or publication of this article. Funding was provided by the National Institute of General Medical Sciences of the National Institutes of Health under award number R35GM149292.

Conflict of interest

The authors declare that the research was conducted in the absence of any commercial or financial relationships that could be construed as a potential conflict of interest.

Publisher's note

All claims expressed in this article are solely those of the authors and do not necessarily represent those of their affiliated organizations, or those of the publisher, the editors and the reviewers. Any product that may be evaluated in this article, or claim that may be made by its manufacturer, is not guaranteed or endorsed by the publisher.

Author disclaimer

The content is solely the responsibility of the authors and does not necessarily reflect the view of the National Institutes of Health.

References

Agostinis, C., Balduit, A., Mangogna, A., Zito, G., Romano, F., Ricci, G., et al. (2021). Immunological basis of the endometriosis: the complement system as a potential therapeutic target. *Front. Immunol.* 11 (January), 599117. doi:10.3389/fimmu.2020.599117

Antsiferova, Y., Sotnikova, N., and Elena, P. (2013). Different effects of the immunomodulatory drug GMDP immobilized onto aminopropyl modified and unmodified mesoporous silica nanoparticles upon peritoneal macrophages of

women with endometriosis. *BioMed Res. Int.* 2013 (December), e924362. doi:10.1155/2013/924362

Bacci, M., Capobianco, A., Monno, A., Cottone, L., Di Puppo, F., Camisa, B., et al. (2009). Macrophages are alternatively activated in patients with endometriosis and required for growth and vascularization of lesions in a mouse model of disease. *Am. J. Pathology* 175 (2), 547–556. doi:10.2353/ajpath.2009.081011

Chaichian, S., Abolfazl Mehdizadeh, K., Tehermanesh, k, pirhajati Mahabadi, V., Minaeian, S., and Eslahi, N. (2022). Effect of PLGA nanoparticle-mediated delivery of MiRNA 503 on the apoptosis of ovarian endometriosis cells. *Cell J.* 24, 697–704. doi:10.22074/cellj.2022.557554.1069

Chaudhury, K., Narendra Babu, K., Singh, A. K., Das, S., Amit, K., and Seal, S. (2013). Mitigation of endometriosis using regenerative cerium oxide nanoparticles. *Nanomedicine Nanotechnol. Biol. Med.* 9 (3), 439–448. doi:10.1016/j.nano.2012.08.001

de Almeida, B., Julianna Henriques da Silva, V. R., Soares Barbosa, S., Eurico Nasciutti, L., Mendes Cabral, L., Pereira de Sousa, V., et al. (2016). Development and pharmacological evaluation of *in vitro* nanocarriers composed of lamellar silicates containing copaiba oil-resin for treatment of endometriosis. *Mater. Sci. Eng. C* 64 (July), 310–317. doi:10.1016/j.msec.2016.03.094

Ding, S., Zhu, L., Tian, Y., Zhu, T., Huang, X., and Zhang, X. (2017). P2X3 receptor involvement in endometriosis pain via ERK signaling pathway. *PLOS ONE* 12 (9), e0184647. doi:10.1371/journal.pone.0184647

Eisenberg, Vh, Weil, C., Chodick, G., and Shalev, V. (2018). Epidemiology of endometriosis: a large population-based database study from a healthcare provider with 2 million members. *BJOG Int. J. Obstetrics Gynaecol.* 125 (1), 55–62. doi:10.1111/1471-0528.14711

Ellis, K., Munro, D., and Clarke, J. (2022). Endometriosis is undervalued: a call to action. *Front. Glob. Women's Health* 3 (May), 902371. doi:10.3389/fgwh.2022.902371

Friend, D. R. (2017). Drug delivery for the treatment of endometriosis and uterine fibroids. *Drug Deliv. Transl. Res.* 7 (6), 829–839. doi:10.1007/s13346-017-0423-2

Giroux, V., and Rustgi, A. K. (2017). Metaplasia: tissue injury adaptation and a precursor to the dysplasia–cancer sequence. *Nat. Rev. Cancer* 17 (10), 594–604. doi:10.1038/nrc.2017.68

Guo, X., Li, W., Zhou, J., Hou, W., Wen, X., Zhang, H., et al. (2017). Specific photothermal ablation therapy of endometriosis by targeting delivery of gold nanospheres. *Small* 13 (15), 1603270. doi:10.1002/smll.201603270

Harada, T., Kubota, T., and Aso, T. (2002). Usefulness of CA19-9 versus CA125 for the diagnosis of endometriosis. *Fertil. Steril.* 78 (4), 733–739. doi:10.1016/S0015-0282(02)03328-9

Hsu, A. L., Khachikyan, I., and Stratton., P. (2010). Invasive and noninvasive methods for the diagnosis of endometriosis. *Clin. Obstetrics Gynecol.* 53 (2), 413–419. doi:10.1097/GRF.0b013e3181db7ce8

Kalyani, T., Sangili, A., Nanda, A., Prakash, S., Kaushik, A., and Kumar Jana, S. (2021). Bio-nanocomposite based highly sensitive and label-free electrochemical immunosensor for endometriosis diagnostics application. *Bioelectrochemistry* 139 (June), 107740. doi:10.1016/j.bioelechem.2021.107740

Kurdoglu, Z., Gursoy, R., Kurdoglu, M., Erdem, M., Erdem, O., and Erdem, A. (2009). Comparison of the clinical value of CA 19-9 versus CA 125 for the diagnosis of endometriosis. *Fertil. Steril.* 92 (5), 1761–1763. doi:10.1016/j.fertnstert.2009.05.022

Lee, D., Seul, K. K., Jung, R. L., and Byung Chul, J. (2020). Management of endometriosis-related infertility: considerations and treatment options. *Clin. Exp. Reproductive Med.* 47 (1), 1–11. doi:10.5653/cerm.2019.02971

Lee, D.-E., Koo, H., Kwon, I. C., In-Cheol, S., Ryu, J. H., Kim, K., et al. (2012). Multifunctional nanoparticles for multimodal imaging and theragnosis. *Chem. Soc. Rev.* 41 (7), 2656–2672. doi:10.1039/C2CS15261D

Li, Q., Yuan, M., Xue, J., Huang, Y., Jing, L., Dong, L., et al. (2021). M1 macrophage-derived nanovesicles repolarize M2 macrophages for inhibiting the development of endometriosis. *Front. Immunol.* 12 (July), 707784. doi:10.3389/fimmu.2021.707784

Liu, H., and Lang, J. H. (2011). Is abnormal eutopic endometrium the cause of endometriosis? The role of eutopic endometrium in pathogenesis of endometriosis. *Med. Sci. Monit.* 17 (4), RA92–99. doi:10.12659/MSM.881707

Liu, Q., Ma, P. c., Liu, L., Ma, G., Ma, J., Liu, X., et al. (2017). Evaluation of PLGA containing anti-CTLA4 inhibited endometriosis progression by regulating CD4+CD25+Treg cells in peritoneal fluid of mouse endometriosis model. *Eur. J. Pharm. Sci.* 96 (January), 542–550. doi:10.1016/j.ejps.2016.10.031

Lloyd-Parry, O., Downing, C., Aleisaei, E., Jones, C., and Coward, K. (2018). Nanomedicine applications in women's health: state of the art. *Int. J. Nanomedicine* 13 (March), 1963–1983. doi:10.2147/IJN.S97572

Luo, L., Zhou, H., Wang, S., Pang, M., Zhang, J., Hu, Y., et al. (2023a). The application of nanoparticle-based imaging and phototherapy for female reproductive organs diseases. *Small* May, 2207694. doi:10.1002/smll.202207694

Moses, A. S., Demessie, A. A., Taratula, O., Korzun, T., Slayden, O. D., and Taratula, O. (2021). Nanomedicines for endometriosis: lessons learned from cancer research. *Small* 17 (7), 2004975. doi:10.1002/smll.202004975

Moses, A. S., Taratula, O. R., Lee, H., Luo, F. Z., Tanner, G., Korzun, T., et al. (2020). Nanoparticle-based platform for activatable fluorescence imaging and photothermal ablation of endometriosis. *Small* 16 (18), 1906936. doi:10.1002/smll.201906936

Nelson, K. M., N'Dea, I.-C., Hoffman, M. K., Gleghorn, J. P., and Day, E. S. (2021). Diseases and conditions that impact maternal and fetal health and the potential for nanomedicine therapies. *Adv. Drug Deliv. Rev.* 170 (March), 425–438. doi:10.1016/j.addr.2020.09.013

Oral, E., Aydin, A., Olive, D. L., and Huszar, G. (1996). Peritoneal fluid from women with moderate or severe endometriosis inhibits sperm motility: the role of seminal fluid components. *Fertil. Steril.* 66 (5), 787–792. doi:10.1016/S0015-0282(16)58637-3

Park, Y., Demessie, A. A., Luo, A., Taratula, O. R., Moses, A. S., Do, P., et al. (2022). Targeted nanoparticles with high heating efficiency for the treatment of endometriosis with systemically delivered magnetic hyperthermia. *Small* 18 (24), 2107808. doi:10.1002/smll.202107808

Rastinehad, A. R., Anastos, H., Wajswol, E., Jared, S., Winoker, J. P. S., Doppalapudi, S. K., et al. (2019). Gold nanoshell-localized photothermal ablation of prostate tumors in a clinical pilot device study. *Proc. Natl. Acad. Sci.* 116 (37), 18590–18596. doi:10.1073/pnas.1906929116

Reed, B. G., and Carr, B. R. (2018). *The normal menstrual cycle and the control of ovulation*. MDText.com, Inc. *Endotext*. South Dartmouth (MA) https://www.ncbi.nlm.nih.gov/books/NBK279054/.

Riley, R. S., and Day, E. S. (2017). Gold nanoparticle-mediated photothermal therapy: applications and opportunities for multimodal cancer treatment. *Wiley Interdiscip. Rev. Nanomedicine Nanobiotechnology* 9 (4). doi:10.1002/wnan.1449

Sangili, A., Kalyani, T., Chen, S.-M., Nanda, A., and Kumar Jana, S. (2020). Label-free electrochemical immunosensor based on one-step electrochemical deposition of AuNP-RGO nanocomposites for detection of endometriosis marker CA 125. *ACS Appl. Bio Mater.* 3 (11), 7620–7630. doi:10.1021/acsabm.0c00821

Singh, A. K., Chakravarty, B., and Chaudhury, K. (2015). Nanoparticle-assisted combinatorial therapy for effective treatment of endometriosis. *J. Biomed. Nanotechnol.* 11 (5), 789–804. doi:10.1166/jbn.2015.2020

Swingle, K. L., Adele, S., Ricciardi, W. H. P., and Mitchell, M. J. (2023). Delivery technologies for women's health applications. *Nat. Rev. Bioeng.* 1 (6), 408–425. doi:10.1038/s44222-023-00040-w

Tsamantioti, E. S., and Heba, M. (2023). "Endometriosis," in StatPearls. *Treasure island (FL* (StatPearls Publishing). http://www.ncbi.nlm.nih.gov/books/NBK567777/.

Tuten, A., Kucur, M., Imamoglu, M., Kaya, B., Serdar Acikgoz, A., Yilmaz, N., et al. (2014). Copeptin is associated with the severity of endometriosis. *Archives Gynecol. Obstetrics* 290 (1), 75–82. doi:10.1007/s00404-014-3163-2

Wang, N., Liu, B., Liang, L., Wu, Y., Xie, H., Huang, J., et al. (2014). Antiangiogenesis therapy of endometriosis using PAMAM as a gene vector in a noninvasive animal model. *BioMed Res. Int.* 2014, 1–11. doi:10.1155/2014/546479

Yuan, M., Ding, S., Meng, T., Lu, B., Shao, S., Zhang, X., et al. (2017). Effect of A-317491 delivered by glycolipid-like polymer micelles on endometriosis pain. *Int. J. Nanomedicine* 12 (November), 8171–8183. doi:10.2147/IJN.S146569

Yuxue, J., Sun, R., Fan, M., and Sheng, M. (2023). Applications of nanomaterials in endometriosis treatment. *Front. Bioeng. Biotechnol.* 11 (May), 1184155. doi:10.3389/fbioe.2023.1184155

Zhang, H., Li, J., Sun, W., Hu, Y., Zhang, G., Shen, M., et al. (2014). Hyaluronic acid-modified magnetic iron oxide nanoparticles for MR imaging of surgically induced endometriosis model in rats. *PLoS One* 9 (4), e94718. doi:10.1371/journal.pone.0094718

Zhang, L., Li, H., Yuan, M., Dong, L., Sun, C., and Wang, G. (2020). Serum exosomal MicroRNAs as potential circulating biomarkers for endometriosis. *Dis. Markers* 2020 (January), 1–10. doi:10.1155/2020/2456340

Zhao, M., Cheng, J.-L., Yan, J.-J., Chen, F.-Y., Sheng, J.-Z., Sun, D.-L., et al. (2016). Hyaluronic acid reagent functional chitosan-PEI conjugate with AQP2-SiRNA suppressed endometriotic lesion formation. Int. J. Nanomedicine, *March* 11, 1323–1336. doi:10.2147/IJN.S99692

Zhao, M.-D., Sun, Y.-M., Fu, G.-F., Du, Y.-Z., Chen, F.-Y., Yuan, H., et al. (2012). Gene therapy of endometriosis introduced by polymeric micelles with glycolipid-like structure. *Biomaterials* 33 (2), 634–643. doi:10.1016/j.biomaterials.2011.09.077

frontiers | Frontiers in Biomaterials Science

TYPE Mini Review
PUBLISHED 24 November 2023
DOI 10.3389/fbiom.2023.1285386

OPEN ACCESS

EDITED BY
Silviya Petrova Zustiak,
Saint Louis University, United States

REVIEWED BY
Akram Abbasi,
Brown University, United States

*CORRESPONDENCE
Mary Beth Browning Monroe,
mbmonroe@syr.edu

RECEIVED 29 August 2023
ACCEPTED 31 October 2023
PUBLISHED 24 November 2023

CITATION
Monroe MBB and Fikhman DA (2023), Mini-review antimicrobial smart materials: the future's defense against wound infections.
Front. Front. Biomater. Sci. 2:1285386.
doi: 10.3389/fbiom.2023.1285386

Mini-review antimicrobial smart materials: the future's defense against wound infections

Mary Beth Browning Monroe[1,2]* and David A. Fikhman[1,2]

[1]Biomedical and Chemical Engineering, Syracuse University, Syracuse, NY, United States, [2]BioInspired Syracuse, Institute for Living and Material Systems, Syracuse, NY, United States

The overuse of antibiotics to treat bacterial infections along with bacteria's propensity to form biofilm communities has resulted in an alarming rise in drug-resistant microbes. Current approaches to infection surveillance and biofilm clearance in wounds are severely limited, requiring new biomaterials-based strategies to address this problem. To that end, a range of antimicrobial smart materials have been developed that change their properties in response to bacteria-induced external stimuli, providing tools with an additional level of complexity for defending against microbes. Researchers have tried to tackle this issue using materials that respond to the unique pH, temperature, and enzymatic changes that are induced by bacteria in wounds. These environmental responses are coupled with mechanisms to kill surrounding bacteria and/or to signal infection. For example, bacteria-responsive biomaterial solubilization (transition from non-solubilized solid material to solubilized liquid solution), swelling (volumetric increase due to absorption of surrounding media), de-swelling, degradation, or shape change can be coupled with drug release and/or activation or biofilm disruption, inhibition, or destruction. These materials provide a foundation for future work and improvements related to enhanced infection surveillance, increased specificity of infection response, and effective clearance of biofilms from wound surfaces.

KEYWORDS

antimicrobial, smart materials, stimuli-responsive, wound infection, thermoresponsive, pH responsive, enzyme responsive

1 Introduction

By 2050, it is projected that drug-resistant infections will cause 10,000,000 deaths each year, more than all cancers combined (O'Neill, 2016). A major contributor to drug-resistance and wound infection complications is biofilms (Bowler et al., 2020). Chronic wounds, including diabetic ulcers, affect >5 million patients per year in the US. The cost of healing one chronic wound is ~$50,000, and diabetic ulcers are associated with ~70% of foot amputations (Paquette and Falanga, 2002; Boulton et al., 2005). Of many factors that delay healing in chronic wounds, infection plays a significant role (Siddiqui and Bernstein, 2010; Ventola, 2015). To further complicate this clinical need, ~50% of chronic wound patients with a limb threatening infection do not show systemic infection symptoms, delaying diagnosis and treatment (Lipsky et al., 2004). Burn wounds are also negatively impacted by infection. In the US, ~10,000 people die each year from burn-related infections, and biofilms are associated with 60% of burn injury deaths (Smith et al., 1994; Norbury et al., 2016).

Despite the prevalence of wound infections, there is no expert consensus on the standard of care for assessment and treatment (Young, 2021). Infection assessment via wound swabbing or

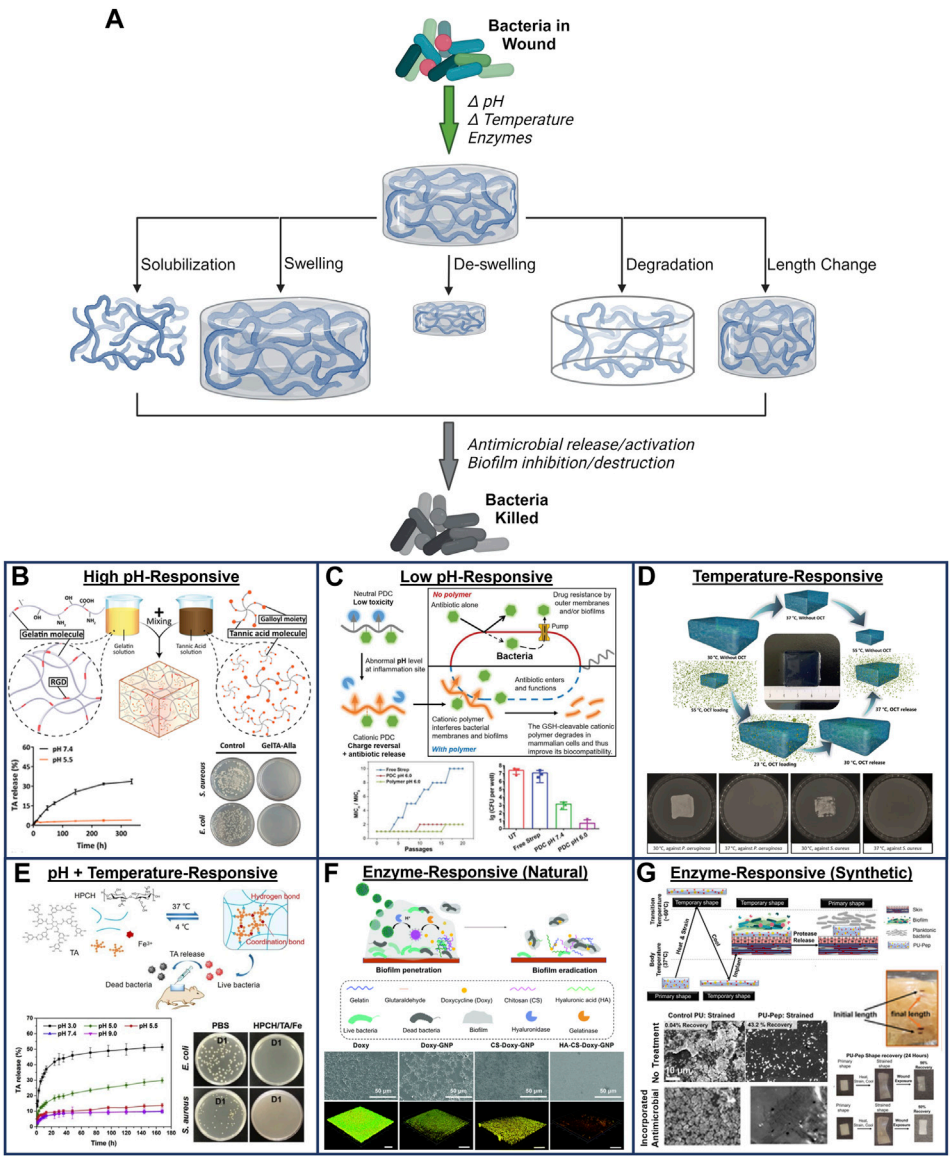

FIGURE 1
(A) Schematic representation of mechanisms for stimuli-responsive biomaterials to actively kill bacteria based on bacterial environmental cues. Created with Biorender.com. Representative bacterial environmentally-responsive systems. **(B)** Hydrogels that swell to release tannic acid at high pH to kill bacteria (from Ref. 36, © 2021 John Wiley & Sons, Inc.); **(C)** Cationic polymers that solubilize and release streptomycin at low pH to kill bacteria (from Ref. 40, © 2020 John Wiley & Sons, Inc.); **(D)** Lower critical solubility temperature hydrogels that de-swell at 37°C to release octenidine (from Ref. 49, © 2022 Royal Society of Chemistry); **(E)** Hydroxypropyl chitin hydrogels that crosslink at 37°C and release with tannic acid and ferric ions at low pH to kill bacteria (from Ref. 52, © 2020 Elsevier); **(F)** Gelatin nanoparticles coated with hyaluronic acid and chitosan. The chitosan swells at low pH to enable diffusion of bacterial hyaluronidase and gelatinase that degrades nanoparticles and triggers doxycycline release (from Ref. 57, © 2022 Royal Society of Chemistry); **(G)** Shape memory polyurethanes with poly (glutamic acid) in the backbone. Bacterial proteases degrade the poly (glutamic acid) to induce a shape change, which is a visible infection cue, prevents biofilm formation, and can be coupled with release of cinnamic acid to kill bacteria (from Ref. 62, © 2023 John Wiley & Sons, Inc.).

biopsies is susceptible to contamination with skin surface bacteria, may not effectively penetrate biofilms, and requires ~48 h to obtain a diagnosis (Young, 2021). Due to the overuse and misuse of antibiotics that contribute to drug resistance (Kardas et al., 2005; English et al., 2010), systemic antibiotic intake is not standardly recommended for treating wound infections (Bowler et al., 2001). Treating infections typically involves painful debridement and local antimicrobials, such as iodine or silver, that could hinder healing (Goldenheim, 1993; Kramer, 1999; Khansa et al., 2019). Furthermore, bacteria within biofilms are less amenable to treatment (Miller et al., 2011). Thus, new approaches are needed to improve wound infection surveillance and biofilm clearance.

One of the many ways to combat the rise of antibiotic resistant 'superbugs' is the use of antimicrobial biomaterials (Fasiku et al., 2020). Current research on antimicrobial polymers provides a number of potential paths, including incorporation of antimicrobial agents into the bulk or as coatings (Jain et al., 2014). Within the field of polymer science, stimuli-responsive or 'smart' materials provide a platform

TABLE 1 Summary of stimuli-responsive biomaterials for wound infection control.

pH-responsive materials					
Class	Material	Mechanism	Effects	Advantages	Disadvantages
Polyanions	Keratin (35)	Swelling at high pH releases ZnO nanoplates	6-log reduction in *S. aureus* & *E. coli* (*in vitro*)	+ *In vitro* efficacy	- No *in vivo* data - Not effective at low pH biofilm environment - Requires loaded drug - pH changes during infection are unreliable
	Gelatin (36)	Swelling at pH 7.4 releases tannic acid and allantoin	Reduced *S. aureus* & *E. coli* growth (*in vitro*)	+ Simple materials	
	Electrospun methacrylic acid co-polymers (37)	Bactericidal release at low, neutral, or high pH based on methacrylic acid content	Tunable antimicrobial effects on *S. aureus* & *E. coli* (*in vitro*)		
Polycations	Octapeptide nanofibers (38)	Solubilization at low pH destabilizes bacteria membranes and releases loaded drugs	Improved healing in MRSA biofilm infected mouse wound model	+ Promising *in vivo* results for infection clearance and healing	- Expense of peptide synthesis
	Antimicrobial peptides (39)	Solubilization at low pH destabilizes bacteria membranes	Reduced *Staph. aureus* & *E. coli* growth (*in vitro*)	+ Inherent antimicrobial activity (no need for loaded drugs)	- Requires mature biofilm formation (low pH)
	Synthetic polycations (40)	Solubilization at low pH induces pores in bacteria membranes and releases streptomycin	2–3 log reduction of *E. coli* (thigh), *P. aeruginosa* (lung), & MRSA (peritoneum) in mouse infection models		- pH changes during infection are unreliable
Supramolecular Hydrogels	Collagen-inspired peptide amphiphiles (41)	Nanofiber formation at low pH releases ferulic acid	Elimination of *E. coli* & *S. aureus* and improved healing (*in vitro*)	+ Promising *in vivo* results for infection clearance and healing + Inherent antimicrobial activity (no need for loaded drugs)	- Expensive &/or complex synthesis - Requires mature biofilm formation (low pH) - pH changes during infection are unreliable
	Amphiphilic pentapeptides (42)	Solubilization at low pH releases oregano oil and antimicrobial peptides	Improved healing in *S. aureus* infected mouse wound model		
	Carboxymethyl agarose with Ag+ (43)	Swelling at low pH releases Ag+	Reduced bacteria and improved healing in mouse wound model		
	Sodium alginate/poly (N-vinyl caprolactam) with tannic acid (44)	Solubilization at low pH releases tannic acid	Reduced bacteria (*in vitro*); Improved healing in rat wound model		
Temperature-Responsive Materials					
Class	Material	Mechanism	Effects	Advantages	Disadvantages
Lower Critical Solubility Temperature Polymer	PNIPAAm/poly (2-methacryloyloxyethyl phosphorylcholine) (49)	Deswelling at 37°C releases loaded antimicrobial	3-log reduction in *E. coli*, *P. aeruginosa*, *S. aureus*, & *S. epidermidis* (*in vitro*)	+ *In vitro* efficacy	- No *in vivo* data - Temperature changes during infection are unreliable - Requires loaded drug
Thermally-Actuated Shape Memory Polymer	Polyurethane (50–51)	Shape recovery at 40°C disrupts attached biofilms	Reduced *S. aureus* biomass and increased susceptibility to tobramycin (*in vitro*)	+ *In vitro* efficacy + Off-the-shelf material	- No *in vivo* data - Requires external healing and externally applied drug

(Continued on following page)

TABLE 1 (*Continued*) Summary of stimuli-responsive biomaterials for wound infection control.

pH-responsive materials					
Class	Material	Mechanism	Effects	Advantages	Disadvantages
Combined pH- & Temperature	Hydroxypropyl chitin with tannic acid (52)	Physically crosslinks at 37°C; releases tannic acid & Fe^{3+} at low pH	Reduced *E. coli* & *S. aureus* growth (*in vitro*); improved healing in mouse infected wound model	+ Promising *in vivo* results for infection clearance and healing	- Requires loaded drug
	PNIPAAm/poly (acrylic acid) (43)	Swelling at pH > 7.4 releases Ag	Reduced *S. aureus* growth (*in vitro* and *in vivo*)	+ Injectable and space-filling	- pH & temperature changes during infection are unreliable
Enzyme-Responsive Materials					
Class	Material	Mechanism	Effects	Advantages	Disadvantages
Natural Polymers	Hyaluronic acid (HA) (56)	HA degraded by hyaluronidase from bacteria to trigger prodrug release and antibiotic activation	Reduced *S. aureus* & *P. aeruginosa* growth and biofilm formation (*in vitro*)	+ *In vitro* efficacy	- No *in vivo* data
	Gelatin nanoparticles coated with HA & chitosan (57)	Chitosan is charged and swells in acidic biofilms to enable degradation by hyaluronidase/gelatinase and trigger antibiotic release	Penetrated *V. vulnificus* biofilms and killed bacteria (higher efficacy vs free drug *in vitro*)	+ Ability to use color change for infection surveillance	- Lack of enzyme specificity
	Gelatin with phospholipid vesicles (58)	Bacterial enzymes damage vesicle membranes to release antimicrobials &/or dye	Reduced *S. aureus* & *P. aeruginosa* growth (*in vitro*); visual (color) cue for infection	+ Simple materials	- Requires loaded drug
Synthetic Polymers	Poly (caprolactone)/poly (ethylene succinate) fibers (59)	Esters degraded by lipases from bacteria to release incorporated biocide	Reduced *S. aureus* & *E. coli* growth (*in vitro*)	+ *In vitro* efficacy	- No *in vivo* data
	Poly (ethylene glycol) with cephalosporin crosslinker (60–61)	β-lactamase from bacteria degrade hydrogels to induce release	Bacteria-responsive release of fluorescent nanoparticles (*in vitro* and *ex vivo*)	+ Ability to use shape change for infection surveillance	- Requires loaded or externally applied drug
	Segmented polyurethane with poly (glutamic acid) (62)	Bacterial enzymes degrade poly (glutamic acid) to trigger shape change and antimicrobial release	Bacteria-responsive visible shape change; biofilm inhibition; increased treatment efficacy (*in vitro*)	+ Improved enzyme specificity	- May only work with specific infections

for the inclusion of new functions into polymeric devices. Stimuli-responsive materials undergo large and abrupt changes in shape in response to environmental cues, including temperature, pH, or enzymes (Wei et al., 2017). These changes can be coupled with functions that aid in infection control, such as antimicrobial release or biofilm disruption and therefore could provide more precise tools for infection surveillance and treatment, Figures 1A–G. Smart biomaterials can be intrinsically antimicrobial based on their chemistry, they can have antimicrobial components incorporated into them, and/or they can be used to physically disrupt biofilms. There have been extensive efforts focused on smart materials that respond to externally-applied stimuli, including light (Yuan et al., 2022; Su et al., 2023), electric or magnetic fields (Zhu et al., 2019; Elbourne et al., 2020; Fragal et al., 2022), or ultrasound (LuTheryn et al., 2022; Fan et al., 2023), which show potential for improving infection control efforts. Here, we focus on smart biomaterials that independently respond to unique pH, temperature, and enzymatic environments induced by bacteria in wounds without the need for an external stimulus. Biomaterials that have been recently developed for infection control that undergo large and abrupt changes in the presence of bacteria are covered in this review and are summarized in Table 1.

2 pH-responsive smart biomaterials

pH is a logarithmic measure of hydrogen ions used to indicate acidic (1–6.9), neutral 7), or basic (7.1–14) conditions. Human skin exhibits a slightly acidic pH of 4.2–5.6, which discourages bacteria overgrowth (Schmid-Wendtner and Korting, 2006). Interior tissues that are exposed during wounding are typically at pH 7.4, but wound pH can vary based on host immune response and the presence of bacteria. In general, mammalian cell healing is more efficient in acidic conditions, while

bacteria prefer and promote alkaline environments (Weinrick et al., 2004; Shukla et al., 2007; Sharpe et al., 2009; Percival et al., 2014; Ono et al., 2015). Thus, infected wounds often have higher pH, while non-infected wounds have lower pH, providing an environmental cue for smart hydrogels.

2.1 Hydrogels based on polyanions and polycations

Hydrogels are water-soluble polymer networks that absorb large quantities of water. Hydrogels are typically biocompatible due to their high water content, enabling their extensive use in drug delivery and implantable biomaterials (Yang et al., 2018). Hydrogels are highly tunable and can be designed to change their solubility in water with changes in the environment, including pH. As solubility changes, hydrogel swelling is altered, which can be harnessed for environmentally-responsive drug delivery. pH-responsive hydrogels can be based on polyanions or polycations, which solubilize or swell to varying degrees based on the pKa of an ionic group in the polymer backbone. pH-responsive polyanions switch between a liquid polymer solution and a solid gel as the pH transitions from high to low. These solubility alterations occur as the polymer transitions between a charged, expanded state that is soluble at high pH and an uncharged, collapsed state that is insoluble at low pH. Polyanions can also be covalently crosslinked into insoluble 3D networks that swell (volumetric expansion due to absorption of surrounding media as chains expand) at high pH and de-swell (volumetric shrinking due to expulsion of media as chains collapse) at low pH. On the other hand, polycations move from a solution state at low pH to a solid gel state at high pH. Crosslinked polycations swell at low pH and de-swell and high pH. These properties can be employed in infection control to deliver antimicrobials upon swelling, de-swelling, or dissolution.

2.1.1 Polyanions

A recent example of pH-responsive hydrogels with controlled release of antimicrobials at basic conditions that mimic those of an infected wound is a keratin-based hydrogel that swells at high pH. Upon swelling, biocidal zinc oxide nanoplates are released, which resulted in a 6-log reduction in *Staphylococcus aureus* (*Staphylococcus aureus*) and *E. coli* (*Escherichia coli*) while maintaining high mammalian cytocompatibility (Villanueva et al., 2019). Ahmadian et al. developed a gelatin and tannic acid-based hydrogel system with low release of incorporated antimicrobials (tannic acid and allantoin) at low pH and higher release at physiological pH (7.4), Figure 1B (A et al., 2021). Combined release of both antimicrobials reduced *E. coli* and *S. aureus* growth.

In a synthetic approach, a methacrylic acid co-polymer with tunable pH response based on methacrylic acid content was employed to fabricate electrospun mesh scaffolds with pH sensitivity at low, neutral, and high pH (Miranda-Calderon et al., 2022). After loading the fibers with bactericidal agents, the authors show that drug release varies between the three chemistries based on pH, and antimicrobial properties can be tuned with both *S. aureus* and *E. coli*. This platform could allow for dressing selection based on real-time wound pH measurements.

2.1.2 Polycations

Although infection generally increases pH, bacteria in biofilms can survive in lower pH ranges than planktonic bacteria (Percival et al., 2014). Thus, infected wound pH may decrease over time as bacteria enter biofilms and the innate immune response takes over. To that end, the majority of pH-responsive antimicrobial wound dressings focus on polycations. Charged polycations are also inherently antimicrobial, which has been used extensively to complement released antimicrobial activity.

Antimicrobial peptides are often employed in polycation-based systems. Wang et al. recently reported an antimicrobial octapeptide that self-assembles into nanofibers at neutral pH and solubilizes in acidic conditions (Wang et al., 2019). The soluble peptide destabilizes bacteria membranes to aid in killing. Drug-loaded antimicrobial peptides promoted healing in a methicillin-resistant *S. aureus* (MRSA)-infected diabetic mouse wound model when applied 2 days after infection, indicating its potential efficacy as a chronic wound dressing. Another antimicrobial peptide was developed as an injectable wound dressing that forms a solid gel at physiological and high pH and solubilizes at pH 6 (Edirisinghe et al., 2023). By incorporating a non-natural AzAla tryptophan analog residue into the peptide sequence, antimicrobial properties were achieved against *E. coli* and *S. aureus*, which are activated upon solubilization at lower pH.

Using a synthetic approach, Ye et al. employed antimicrobial, pH responsive polycations that induce pores in bacterial membranes, Figure 1C (Ye et al., 2020). The polycation is neutral under physiological conditions but becomes positively charged to solubilize at low pH. Solubilization enabled controlled release of antibiotic streptomycin, which had enhanced transport through the resulting membrane pores, correlating with improved clearance of *E. coli*, *P. aeruginosa* (*Pseudomonas aeruginosa*), and MRSA (~two to three log reductions vs streptomycin delivery on its own) in mouse thigh, lung, and peritoneum infections, respectively, when applied 1 h after bacterial inoculation.

2.2 Supramolecular hydrogels

2.2.1 Peptide-based supramolecular hydrogels

Supramolecular hydrogels form a sub-class of pH-responsive materials that reversibly solidify based on specific, non-covalent interactions between components. One example includes supramolecular assembly of peptides into 3D networks. Pal and Roy employed collagen-inspired peptide amphiphiles to form nanoparticles with encapsulated antimicrobial ferulic acid (Pal and Roy, 2022). The nanoparticles are stable at neutral pH but undergo a structural transformation into nanofibers at pH 8.5, triggering ferulic acid release. The released antimicrobial effectively killed *E. coli* and *S. aureus*, while the peptide nanofibers showed beneficial effects for mammalian cell healing in *vitro* assays. Another group synthesized three amphiphilic pentapeptides that form supramolecular hydrogels that are stable at neutral pH (Chen et al., 2022). These hydrogels solubilize in acidic pH to provide an antimicrobial effect by combined exposure to the inherently antimicrobial peptides and release of encapsulated oregano oil. The hydrogels enhanced *S. aureus* infected wound closure in a mouse model by reducing bacterial loads in the wounds.

2.2.2 Other supramolecular hydrogels

A supramolecular hydrogel based on carboxymethyl agarose complexed with Ag+ was developed that is de-swollen at neutral pH and swells at acidic pH (Huang et al., 2020). The hydrogels release more Ag + as they swell to significantly reduce *S. aureus* and *E. coli* CFU counts *in vitro*. In a *S. aureus* infected mouse wound model, the Ag + -containing hydrogels reduced bacteria load and enhanced closure rates. Another supramolecular hydrogel was developed based on sodium alginate/poly (N-vinyl caprolactam) with incorporated tannic acid, which served as both a gelation binder and an antimicrobial (Preman et al., 2020). The scaffolds exhibited increased tannic acid release at low pH and were effective against several strains of Gram-negative and Gram-positive bacteria *in vitro* while enhancing healing in an *in vivo* rat wound model.

3 Thermally-responsive smart biomaterials

Normal, non-infected dermal wound temperatures are reported within the range of 30.2°C–33.0°C (Gethin et al., 2021). Wound inflammation can increase temperatures by 1.5°C–2.2°C, while infected wound temperatures are 4°C–5°C higher (Chanmugam et al., 2017). After successful infection treatment, dermal wound temperatures decrease back to 1°C within normal levels. Based on these temperature differentials, many approaches to smart antimicrobial wound dressings rely on thermally-responsive materials.

3.1 Lower critcal solubility temperature polymers

Polymers with lower critical solubility temperatures (LCST) are in solution at low temperatures due to dominant water/polymer interactions (Bernstein et al., 1977). As temperature is increased, hydrophobic interactions dominate to drive de-solubilization processes to form a solid scaffold. This approach is commonly used for injectable biomaterials, where a polymer is in a liquid solution state at room temperature and then solidifies after injection and heating to body temperature (Gandhi et al., 2015). This mechanism is particularly useful for space-filling applications in irregularly-shaped wounds. LCST polymers can also be crosslinked to swell and de-swell at low and high temperatures, respectively, without loss of overall structure. These dissolution and swelling processes can be coupled with antimicrobial release to aid in infection control.

Pan et al. combined a commonly used thermo-responsive polymer, poly (*N*-isopropylacrylamide) (PNIPAAm) with an antifouling polymer, poly (2-methacryloyloxyethyl phosphorylcholine) (PMPC) to obtain a dual-function hydrogel, Figure 1D (Pan et al., 2022). They took advantage of higher swelling at low temperature to efficiently load the hydrogels with an antimicrobial, octenidine, via diffusion. Upon heating to 37°C, the resulting de-swelling induced a 25-fold increase in octenidine release as compared with testing at normal skin temperatures of 30°C. This antimicrobial release resulted in a 3-log reduction in *E. coli*, *P. aeruginosa*, *S. aureus*, and *Staphylococcus epidermidis*.

3.2 Thermally-actuated shape memory polymers

Beyond thermo-responsive hydrogels, researchers have employed thermally-actuated shape memory polymers (SMPs) to disrupt biofilms. SMPs are type of 'smart' material that can be programmed and stored in a temporary shape and then return to their original, permanent state after application of an external stimulus, such as heat. Gu et al. grew *S. aureus* biofilms on strained polyurethane SMPs and then heated them to 40°C to induce shape recovery (i.e., shrinking) (Gu et al., 2016). The shape recovery process reduced *S. aureus* biomass from 5.4 to 0.07 $\mu m^3/\mu m^2$, and later studies showed that shape recovery with subsequent application of tobramycin reduced dispersed biofilm cell counts by 2,479X in comparison to static controls (Gu et al., 2016; Lee et al., 2018). These effects were attributed to the SMP shape change, which physically disrupted the biofilm structure to increase bacterial activity.

3.3 Combined pH- and thermo-responsive systems

Many researchers combine pH- and thermo-responsive materials for smart wound dressing development. In one approach, a composite hydrogel was developed based on hydroxypropyl chitin and tannic acid, Figure 1E (Ma et al., 2020). Upon heating to 37°C, the hydrogel transitions from a liquid solution into a solid, physically crosslinked gel, which aids in wound delivery by enabling space-filling of the wound volume by the liquid prior to gelation. The tannic acid is specifically released in acidic environments to provide antimicrobial protection in conjunction with incorporated ferric ion particles. The composite hydrogels were effective *in vitro* against *E. coli* and *S. aureus*, and they showed some benefits in healing in a mouse infected wound model. Using synthetic polymers, Haidari et al. combined PNIPAAm with poly (acrylic acid) (a polyanion) into a hydrogel loaded with silver nanoparticles (AgNPs) (Haidari et al., 2022). The materials exhibit a LCST of ~36°C, which the authors posit could enhance swelling at elevated infected dermal wound temperatures. The hydrogels had limited Ag^+ ion release at acidic pH and increased release at pH > 7.4. The AgNP release at higher pH resulted in correspondingly high antimicrobial efficacy against *S. aureus* both *in vitro* and *in vivo*.

4 Enzyme-responsive smart biomaterials

Bacteria release a number of proteases and other enzymes during infection to inactivate immune factors, break down tissues, and slow healing (Supuran et al., 2001; Lindsay et al.). Researchers have harnessed these processes to develop enzymatically-responsive biomaterials that respond to and kill bacteria.

4.1 Enzymatically-responsive natural polymers

An enzyme-responsive nanosystem was fabricated using mesoporous ruthenium nanoparticles as nanocarriers for a prodrug. The nanocarriers were encapsulated within hyaluronic acid (HA) (Liu et al., 2019). Hyaluronidase secreted by bacteria degrades the HA to trigger release of the prodrug, which then activates an antibiotic on the outer surface of the hydrogels. The nanosystem exhibited bactericidal and antibiofilm activity against drug-resistant *S. aureus* and *P. aeruginosa*. In a different approach with higher specificity towards biofilms, Wang and Shukla designed an antibiotic-loaded gelatin nanoparticle that is coated with HA and chitosan, Figure 1F. (Wang and Shukla) The chitosan becomes charged in the acidic biofilm environment, promoting swelling. As the hydrogel swells, hyaluronidase and gelatinase that are release by bacteria can more easily diffuse into the system. These enzymes degrade the HA and gelatin to provide biofilm-responsive antibiotic release. Nanoparticles were able to penetrate *Vibrio vulnificus* biofilms, eliminate the biofilm matrix, and kill bacteria with higher efficacy as compared with free drug treatment. Another system harnessed bacteria's capability to permeabilize eukaryotic cell phospholipid vesicle bilayer members using secreted α-hemolysin and phospholipase. In brief, antimicrobials and a self-quenching dye were encapsulated within cell-mimicking phospholipid vesicles, which were incorporated into a gelatin scaffold (Zhou et al., 2018). Upon exposure to *S. aureus* or *P. aeruginosa*, the vesicle membranes are damaged by bacterial proteases, which provides mechanisms to both kill bacteria via released antimicrobials and to enable visual surveillance of infection via dye color change.

4.2 Enzymatically-responsive synthetic polymers

In efforts to provide synthetic scaffolds that selectively release antimicrobials in the presence of bacteria, poly (caprolactone) and poly (ethylene succinate) nanofibers were fabricated with a biocide (Abdali et al., 2019). The synthetic polymers are degraded by lipase and acids secreted by bacteria, which induces release of the incorporated biocide and subsequent reduction of *S. aureus* and *E. coli*.

These described approaches show promise, but most of the targeted enzymes are also produced by mammalian cells, limiting specificity of the systems towards bacteria. Towards increasing specificity, a synthetic hydrogel system was designed with groups that are cleaved by β-lactamase that is produced by bacteria (Yu et al., 2020; Alkekhia et al., 2022). The hydrogels were biostable in physiological conditions and in common enzymes (i.e., collagenase and lipase) but degrade in the presence of β-lactamase-producing bacteria. This degradation process was coupled with the release of fluorescent nanoparticles in *vitro* and *ex vivo* models and can be used in the future to design β-lactamase-responsive drug delivery and/or diagnostic tools.

In a different approach, our group synthesized bacterial protease-responsive SMPs based on a segmented polyurethane with incorporated poly (glutamic acid), which is degraded by bacterial proteases to trigger shape recovery, Figure 1G (Ramezani and Monroe, 2023). Strained SMPs underwent visible shape recovery within ≤24 h in response to multiple bacteria strains (*S. aureus*, *S. epidermidis*, and *E. coli*), while remaining stable during exposure to mammalian fibroblasts. Shape recovery of strained samples prevented biofilm formation on the sample surfaces, and resulting attached planktonic bacteria had enhanced vulnerability to applied antimicrobials. Samples with physically incorporated antimicrobials simultaneously prevented biofilm formation and killed isolated bacteria. The shape change could serve as a combined infection surveillance tool and biofilm inhibitor to enable earlier and more effective infection treatment.

5 Discussion

Bacteria-responsive 'smart' systems are ever-expanding and highly promising in the wake of the antibiotic resistance crisis. pH and thermo-responsive approaches are more fully developed and show efficacy in *vivo* infection models, with the added benefit of simplified designs that do not rely on biological components. However, pH and temperature fluctuations during infection are generally small and unreliable, limiting specificity of these methods. Newer protease-responsive biomaterials could enhance specificity towards bacteria vs mammalian cells but are less developed. These materials can benefit from tools and information gained during the rise of mammalian enzyme-responsive biomaterials, such as the rapid synthesis and screening of peptide derivatives (Lin et al., 2021). In general, many antimicrobial approaches use antibiotics or antimicrobials that have limited efficacy against biofilms. Thus, future efforts should continue to consider the unique biofilm environment.

While bacterial infections are a significant clinical concern, fungi (yeast) infect billions of people every year with ~150 million severe and life threatening cases, resulting in ~1.7 million deaths annually (Bongomin et al., 2017; Houšť et al., 2020). With some exceptions within the biomaterials field, research on fungal infections is limited, and very few classes of antifungal drugs are available (Vera-González et al., 2020). New fungal species have emerged with resistance to currently available antifungals, and the Centers for Disease Control ranks drug-resistant *Candida* yeasts as a "serious antibiotic resistance threat" in the same threat level class as MRSA and multidrug-resistant *P. aeruginosa* (CDC, 2019). Based on these increasing threats to human health, it is essential that future efforts in smart biomaterials also turn their attention to fungal infections.

Some of the research highlighted here provides mechanisms for infection surveillance through color or shape change. However, infection assessment options are still limited. Future generations of bacteria-responsive biomaterials can provide valuable tools in complex wound dressings with simultaneous monitoring, surveillance, and treatment capabilities (Mostafalu et al., 2018; Ullah et al., 2023). These efforts will require multidisciplinary

work between biomaterials scientists, electrical and computer engineers, biologists, and clinicians.

Author contributions

MM: Supervision, Writing–original draft, Writing–review and editing. DF: Conceptualization, Methodology, Writing–original draft.

Funding

The author(s) declare that no financial support was received for the research, authorship, and/or publication of this article.

Conflict of interest

The authors declare that the research was conducted in the absence of any commercial or financial relationships that could be construed as a potential conflict of interest.

Publisher's note

All claims expressed in this article are solely those of the authors and do not necessarily represent those of their affiliated organizations, or those of the publisher, the editors and the reviewers. Any product that may be evaluated in this article, or claim that may be made by its manufacturer, is not guaranteed or endorsed by the publisher.

References

Abdali, Z., Logsetty, S., and Liu, S. (2019). Bacteria-responsive single and core–shell nanofibrous membranes based on polycaprolactone/poly(ethylene succinate) for on-demand release of biocides. *ACS Omega* 4, 4063–4070. doi:10.1021/acsomega.8b03137

Ahmadian, Z., Correia, A., Hasany, M., Figueiredo, P., Dobakhti, F., Eskandari, M. R., et al. (2021). A hydrogen-bonded extracellular matrix-mimicking bactericidal hydrogel with radical scavenging and hemostatic function for pH-responsive wound healing acceleration. *Adv. Healthc. Mat.* 10, 2001122. doi:10.1002/adhm.202001122

Alkekhia, D., LaRose, C., and Shukla, A. (2022). β-Lactamase-Responsive hydrogel drug delivery platform for bacteria-triggered cargo release. *ACS Appl. Mat. Interfaces.* 14, 27538–27550. doi:10.1021/acsami.2c02614

Bernstein, R. E., Cruz, C. A., Paul, D. R., and Barlow, J. W. (1977). LCST behavior in polymer blends. *Macromolecules* 10, 681–686. doi:10.1021/ma60057a037

Bongomin, F., Gago, S., Oladele, R. O., and Denning, D. W. (2017). Global and multi-national prevalence of fungal diseases—estimate precision. *J. Fungi* . 3, 57. doi:10.3390/jof3040057

Boulton, A. J. M., Vileikyte, L., Ragnarson-Tennvall, G., and Apelqvist, J. (2005). The global burden of diabetic foot disease. *Lancet London, Engl.* 366, 1719–1724. doi:10.1016/S0140-6736(05)67698-2

Bowler, P., Murphy, C., and Wolcott, R. (2020). Biofilm exacerbates antibiotic resistance: is this a current oversight in antimicrobial stewardship? *Antimicrob. Resist. Infect. Control.* 9, 162. doi:10.1186/s13756-020-00830-6

Bowler, P. G., Duerden, B. I., and Armstrong, D. G. (2001). Wound microbiology and associated approaches to wound management. *Clin. Microbiol. Rev.* 14, 244–269. doi:10.1128/CMR.14.2.244-269.2001

CDC (2019). Antibiotic resistance threats in the United States 2019. https://www.cdc.gov/drugresistance/pdf/threats-report/2019-ar-threats-report-508.pdf.

Chanmugam, A., Langemo, D., Thomason, K., Haan, J., Altenburger, E. A., Tippett, A., et al. (2017). Relative temperature maximum in wound infection and inflammation as compared with a control subject using long-wave infrared thermography. *Adv. Skin. Wound Care* 30, 406–414. doi:10.1097/01.asw.0000522161.13573.62

Chen, H., Cheng, J., Cai, X., Han, J., Chen, X., You, L., et al. (2022). pH-switchable antimicrobial supramolecular hydrogels for synergistically eliminating biofilm and promoting wound healing. *ACS Appl. Mat. Interfaces.* 14, 18120–18132. doi:10.1021/acsami.2c00580

Edirisinghe, D. I., D'Souza, A., Ramezani, M., Carroll, R. J., Chicón, Q., Muenzel, C. L., et al. (2023). Antibacterial and cytocompatible pH-responsive peptide hydrogel. *Molecules* 28, 4390. doi:10.3390/molecules28114390

Elbourne, A., Cheeseman, S., Atkin, P., Truong, N. P., Syed, N., Zavabeti, A., et al. (2020). Antibacterial liquid metals: biofilm treatment via magnetic activation. *ACS Nano* 14, 802–817. doi:10.1021/acsnano.9b07861

English, B. K., and Gaur, A. H. (2010). "The use and abuse of antibiotics and the development of antibiotic resistance," in *Hot top. Infect. Immun. Child. VI*. Editors A. Finn, N. Curtis, and A. J. Pollard (New York, NY, USA: Springer New York), 73–82. doi:10.1007/978-1-4419-0981-7_6

Fan, J., Xuan, M., Zhao, P., Loznik, M., Chen, J., Kiessling, F., et al. (2023). Ultrasound responsive microcapsules for antibacterial nanodrug delivery. *Nano Res.* 16, 2738–2748. doi:10.1007/s12274-022-4919-9

Fasiku, V. O., Hassan, D., Owonubi, S. J., Mukwevho, E., and Lolu Olajide, J. (2020). "Antibiotic polymer for biomedical applications (chapter 3)," in *Antibiot. Mater. Healthc.*, Editors V. Kokkarachedu, V. Kanikireddy, and H. Sadiku (Cambridge, Massachusetts, United States: Academic Press), 33–49. doi:10.1016/B978-0-12-820054-4.00003-3

Fragal, E. H., Fragal, V. H., Silva, E. P., Paulino, A. T., da Silva Filho, E. C., Mauricio, M. R., et al. (2022). Magnetic-responsive polysaccharide hydrogels as smart biomaterials: synthesis, properties, and biomedical applications. *Carbohydr. Polym.* 292, 119665. doi:10.1016/j.carbpol.2022.119665

Gandhi, A., Paul, A., Sen, S. O., and Sen, K. K. (2015). Studies on thermoresponsive polymers: phase behaviour, drug delivery and biomedical applications. *Asian J. Pharm. Sci.* 10, 99–107. doi:10.1016/j.ajps.2014.08.010

Gethin, G., Ivory, J. D., Sezgin, D., Muller, H., O'Connor, G., and Vellinga, A. (2021). What is the "normal" wound bed temperature? A scoping review and new hypothesis. *Wound Repair Regen.* 29, 843–847. doi:10.1111/wrr.12930

Goldenheim, P. D. (1993). An appraisal of povidone-iodine and wound healing. *Postgrad. Med. J.* 69 (Suppl. 3), S97–S105. http://europepmc.org/abstract/MED/8290466.

Gu, H., Lee, S. W., Buffington, S. L., Henderson, J. H., and Ren, D. (2016). On-demand removal of bacterial biofilms via shape memory activation. *ACS Appl. Mat. Interfaces.* 8, 21140–21144. doi:10.1021/acsami.6b06900

Haidari, H., Vasilev, K., Cowin, A. J., and Kopecki, Z. (2022). Bacteria-activated dual pH- and temperature-responsive hydrogel for targeted elimination of infection and improved wound healing. *ACS Appl. Mat. Interfaces.* 14, 51744–51762. doi:10.1021/acsami.2c15659

Houšť, J., Spížek, J., and Havlíček, V. (2020). Antifungal drugs. *Metab* 10, 106. doi:10.3390/metabo10030106

Huang, W.-C., Ying, R., Wang, W., Guo, Y., He, Y., Mo, X., et al. (2020). A macroporous hydrogel dressing with enhanced antibacterial and anti-inflammatory capabilities for accelerated wound healing. *Adv. Funct. Mat.* 30. doi:10.1002/adfm.202000644

Jain, A., Duvvuri, L. S., Farah, S., Beyth, N., Domb, A. J., and Khan, W. (2014). Antimicrobial polymers. *Adv. Healthc. Mat.* 3, 1969–1985. doi:10.1002/adhm.201400418

Kardas, P., Devine, S., Golembesky, A., and Roberts, C. (2005). A systematic review and meta-analysis of misuse of antibiotic therapies in the community. *Int. J. Antimicrob. Agents.* 26, 106–113. doi:10.1016/j.ijantimicag.2005.04.017

Khansa, I., Schoenbrunner, A. R., Kraft, C. T., and Janis, J. E. (2019). Silver in wound care-friend or foe? a comprehensive review. *Plast. Reconstr. Surg. Glob. Open.* 7, e2390. doi:10.1097/GOX.0000000000002390

Kramer, S. A. (1999). Effect of povidone-iodine on wound healing: a review. *J. Vasc. Nurs.* 17, 17–23. doi:10.1016/S1062-0303(99)90004-3

Lee, S. W., Gu, H., Kilberg, J. B., and Ren, D. (2018). Sensitizing bacterial cells to antibiotics by shape recovery triggered biofilm dispersion. *Acta Biomater.* 81, 93–102. doi:10.1016/j.actbio.2018.09.042

Lin, Y., Penna, M., Spicer, C. D., Higgins, S. G., Gelmi, A., Kim, N., et al. (2021). High-throughput peptide derivatization toward supramolecular diversification in microtiter plates. *ACS Nano* 15, 4034–4044. doi:10.1021/acsnano.0c05423

Lindsay, S., Oates, A., and Bourdillon, K. (2017). The detrimental impact of extracellular bacterial proteases on wound healing. *Int. Wound J.* 14, 1237–1247. doi:10.1111/iwj.12790

Lipsky, B. A., Berendt, A. R., Embil, J., and de Lalla, F. (2004). Diagnosing and treating diabetic foot infections. *Diabetes. Metab. Res. Rev.* 20, S56–S64. doi:10.1002/dmrr.441

Liu, Y., Lin, A., Liu, J., Chen, X., Zhu, X., Gong, Y., et al. (2019). Enzyme-responsive mesoporous ruthenium for combined chemo-photothermal therapy of drug-resistant bacteria. *ACS Appl. Mat. Interfaces* 11, 26590–26606. doi:10.1021/acsami.9b07866

LuTheryn, G., Hind, C., Campbell, C., Crowther, A., Wu, Q., Keller, S. B., et al. (2022). Bactericidal and anti-biofilm effects of uncharged and cationic ultrasound-responsive nitric oxide microbubbles on *Pseudomonas aeruginosa* biofilms. *Front. Cell. Infect. Microbiol.* 12, 956808. doi:10.3389/fcimb.2022.956808

Ma, M., Zhong, Y., and Jiang, X. (2020). Thermosensitive and pH-responsive tannin-containing hydroxypropyl chitin hydrogel with long-lasting antibacterial activity for wound healing. *Carbohydr. Polym.* 236, 116096. doi:10.1016/j.carbpol.2020.116096

Miller, C. N., Carville, K., Newall, N., Kapp, S., Lewin, G., Karimi, L., et al. (2011). Assessing bacterial burden in wounds: comparing clinical observation and wound swabs. *Int. Wound J.* 8, 45–55. doi:10.1111/j.1742-481X.2010.00747.x

Miranda-Calderon, L., Yus, C., Landa, G., Mendoza, G., Arruebo, M., and Irusta, S. (2022). Pharmacokinetic control on the release of antimicrobial drugs from pH-responsive electrospun wound dressings. *Int. J. Pharm.* 624, 122003. doi:10.1016/j.ijpharm.2022.122003

Mostafalu, P., Tamayol, A., Rahimi, R., Ochoa, M., Khalilpour, A., Kiaee, G., et al. (2018). Smart bandage for monitoring and treatment of chronic wounds. *Small* 14, 1703509. doi:10.1002/SMLL.201703509

Norbury, W., Herndon, D. N., Tanksley, J., Jeschke, M. G., and Finnerty, C. C. (2016). Infection in burns. *Surg. Infect. (Larchmt).* 17, 250–255. doi:10.1089/sur.2013.134

O'Neill, J. (2016). Tackling drug-resistant infections globally: final report and recommendations. https://apo.org.au/node/63983.

Ono, S., Imai, R., Ida, Y., Shibata, D., Komiya, T., and Matsumura, H. (2015). Increased wound pH as an indicator of local wound infection in second degree burns. *Burns* 41, 820–824. doi:10.1016/j.burns.2014.10.023

Pal, V. K., and Roy, S. (2022). Bioactive peptide nano-assemblies with pH-triggered shape transformation for antibacterial therapy. *ACS Appl. Nano Mat.* 5, 12019–12034. doi:10.1021/acsanm.2c03250

Pan, F., Zhang, S., Altenried, S., Zuber, F., Chen, Q., and Ren, Q. (2022). Advanced antifouling and antibacterial hydrogels enabled by controlled thermo-responses of a biocompatible polymer composite. *Biomater. Sci.* 10, 6146–6159. doi:10.1039/D2BM01244H

Paquette, D., and Falanga, V. (2002). Leg ulcers. *Clin. Geriatr. Med.* 18, 77–88. doi:10.1016/s0749-0690(03)00035-1

Percival, S. L., McCarty, S., Hunt, J. A., and Woods, E. J. (2014). The effects of pH on wound healing, biofilms, and antimicrobial efficacy. *Wound Repair Regen. Off. Publ. Wound heal. Soc. And. Eur. Tissue Repair Soc.* 22, 174–186. doi:10.1111/wrr.12125

Preman, N. K., Prabhu, A., Shaikh, S. B., Barki, R. R., Bhandary, Y. P., Rekha, P. D., et al. (2020). Bioresponsive supramolecular hydrogels for hemostasis, infection control and accelerated dermal wound healing. *J. Mat. Chem. B* 8, 8585–8598. doi:10.1039/D0TB01468K

Ramezani, M., and Monroe, M. B. B. (2023). Bacterial protease-responsive shape memory polymers for infection surveillance and biofilm inhibition in chronic wounds. *J. Biomed. Mat. Res. Part A.* 111, 921–937. doi:10.1002/jbm.a.37527

Schmid-Wendtner, M.-H., and Korting, H. C. (2006). The pH of the skin surface and its impact on the barrier function. *Skin. Pharmacol. Physiol.* 19, 296–302. doi:10.1159/000094670

Sharpe, J. R., Harris, K. L., Jubin, K., Bainbridge, N. J., and Jordan, N. R. (2009). The effect of pH in modulating skin cell behaviour. *Br. J. Dermatol.* 161, 671–673. doi:10.1111/j.1365-2133.2009.09168.x

Shukla, V. K., Shukla, D., Tiwary, S. K., Agrawal, S., and Rastogi, A. (2007). Evaluation of pH measurement as a method of wound assessment. *J. Wound Care.* 16, 291–294. doi:10.12968/jowc.2007.16.7.27062

Siddiqui, A. R., and Bernstein, J. M. (2010). Chronic wound infection: facts and controversies. *Clin. Dermatol.* 28, 519–526. doi:10.1016/j.clindermatol.2010.03.009

Smith, D. J. J., Thomson, P. D., Garner, W. L., and Rodriguez, J. L. (1994). Burn wounds: infection and healing. *Am. J. Surg.* 167, 46S–48S. doi:10.1016/0002-9610(94)90011-6

Su, Y., Andrabi, S. M., Shahriar, S. M. S., Wong, S. L., Wang, G., and Xie, J. (2023). Triggered release of antimicrobial peptide from microneedle patches for treatment of wound biofilms. *J. Control. Release.* 356, 131–141. doi:10.1016/j.jconrel.2023.02.030

Supuran, C. T., Scozzafava, A., and Mastrolorenzo, A. (2001). Bacterial proteases: current therapeutic use and future prospects for the development of new antibiotics. *Expert Opin. Ther. Pat.* 11, 221–259. doi:10.1517/13543776.11.2.221

Ullah, I., Wagih, M., Sun, Y., Li, Y., Hajdu, K., Courson, R., et al. (2023). Wirelessly powered drug-free and anti-infective smart bandage for chronic wound care. *IEEE Trans. Biomed. Circuits Syst.*, 1–16. doi:10.1109/TBCAS.2023.3277318

Ventola, C. L. (2015). The antibiotic resistance crisis: part 1: causes and threats. *P T* 40, 277–283.

Vera-González, N., Bailey-Hytholt, C. M., Langlois, L., de Camargo Ribeiro, F., de Souza Santos, E. L., Junqueira, J. C., et al. (2020). Anidulafungin liposome nanoparticles exhibit antifungal activity against planktonic and biofilm Candida albicans. *J. Biomed. Mat. Res. Part A.* 108, 2263–2276. doi:10.1002/jbm.a.36984

Villanueva, M. E., Cuestas, M. L., Pérez, C. J., Campo Dall′ Orto, V., and Copello, G. J. (2019). Smart release of antimicrobial ZnO nanoplates from a pH-responsive keratin hydrogel. *J. Colloid Interface Sci.* 536, 372–380. doi:10.1016/j.jcis.2018.10.067

Wang, J., Chen, X.-Y., Zhao, Y., Yang, Y., Wang, W., Wu, C., et al. (2019). pH-switchable antimicrobial nanofiber networks of hydrogel eradicate biofilm and rescue stalled healing in chronic wounds. *ACS Nano* 13, 11686–11697. doi:10.1021/acsnano.9b05608

Wang, Y., and Shukla, A. (2022). Bacteria-responsive biopolymer-coated nanoparticles for biofilm penetration and eradication. *Biomater. Sci.* 10, 2831–2843. doi:10.1039/d2bm00361a

Wei, M., Gao, Y., Li, X., and Serpe, M. J. (2017). Stimuli-responsive polymers and their applications. *Polym. Chem.* 8, 127–143. doi:10.1039/c6py01585a

Weinrick, B., Dunman, P. M., McAleese, F., Murphy, E., Projan, S. J., Fang, Y., et al. (2004). Effect of mild acid on gene expression in *Staphylococcus aureus*. *J. Bacteriol.* 186, 8407–8423. doi:10.1128/JB.186.24.8407-8423.2004

Yang, K., Han, Q., Chen, B., Zheng, Y., Zhang, K., Li, Q., et al. (2018). Antimicrobial hydrogels: promising materials for medical application. *Int. J. Nanomedicine.* 13, 2217–2263. doi:10.2147/IJN.S154748

Ye, M., Zhao, Y., Wang, Y., Yodsanit, N., Xie, R., and Gong, S. (2020). pH-responsive polymer–drug conjugate: an effective strategy to combat the antimicrobial resistance. *Adv. Funct. Mat.* 30, 2002655. doi:10.1002/adfm.202002655

Young, L. (2021). Identifying infection in chronic wounds. *Wound Pract. Res. J. Aust. Wound Manag. Assoc.*, doi:10.3316/informit.655721133752326

Yu, C., Alkekhia, D., and Shukla, A. (2020). β-Lactamase responsive supramolecular hydrogels with host–guest self-healing capability. *ACS Appl. Polym. Mat.* 2, 55–65. doi:10.1021/acsapm.9b00879

Yuan, Z., Gottsacker, C., He, X., Waterkotte, T., and Park, Y. C. (2022). Repetitive drug delivery using Light-Activated liposomes for potential antimicrobial therapies. *Adv. Drug Deliv. Rev.* 187, 114395. doi:10.1016/j.addr.2022.114395

Zhou, J., Yao, D., Qian, Z., Hou, S., Li, L., Jenkins, A. T. A., et al. (2018). Bacteria-responsive intelligent wound dressing: simultaneous *in situ* detection and inhibition of bacterial infection for accelerated wound healing. *Biomaterials* 161, 11–23. doi:10.1016/j.biomaterials.2018.01.024

Zhu, M., Hao, Y., Ma, X., Feng, L., Zhai, Y., Ding, Y., et al. (2019). Construction of a graphene/polypyrrole composite electrode as an electrochemically controlled release system. *RSC Adv.* 9, 12667–12674. doi:10.1039/c9ra00800d

frontiers | Frontiers in Biomaterials Science

TYPE Review
PUBLISHED 07 December 2023
DOI 10.3389/fbiom.2023.1305379

OPEN ACCESS

EDITED BY
Silviya Petrova Zustiak,
Saint Louis University, United States

REVIEWED BY
Elizabeth Cosgriff-Hernandez,
The University of Texas at Austin, United States
Juhi Samal,
Duke University, United States

*CORRESPONDENCE
Ashley C. Brown,
aecarso2@ncsu.edu

RECEIVED 01 October 2023
ACCEPTED 21 November 2023
PUBLISHED 07 December 2023

CITATION
Lutz H and Brown AC (2023), Biomaterials for treating sepsis-induced thromboinflammation. *Front. Front. Biomater. Sci.* 2:1305379. doi: 10.3389/fbiom.2023.1305379

Biomaterials for treating sepsis-induced thromboinflammation

Halle Lutz[1,3,4] and Ashley C. Brown[1,2,3]*

[1]Advanced Wound Healing Lab, Joint Department of Biomedical Engineering, North Carolina State University, Raleigh, NC, United States, [2]Joint Department of Biomedical Engineering, University of North Carolina at Chapel Hill, Chapel Hill, NC, United States, [3]Comparative Medicine Institute, North Carolina State University, Raleigh, NC, United States, [4]Department of Molecular Biomedical Sciences, North Carolina State University, Raleigh, NC, United States

Sepsis is a common and life-threatening disorder with an alarmingly high mortality rate. Unfortunately, this rate has not decreased significantly over the last decade and the number of septic cases is increasing each year. Despite sepsis affecting millions of people annually, there is still not an established standard of care. The development of a therapy that targets the thromboinflammation characteristic of sepsis is imperative. Until recently, research has focused on uncovering individual pathways to target. As more of the pathophysiology of sepsis has become understood and more biomarkers uncovered, the interplay between endothelial cells, platelets, and leukocytes has emerged as a critical event. Therefore, a multi-targeted approach is clearly required for designing an effective treatment for sepsis. The versatility of biomaterials offers a promising solution in that they can be designed to target and affect multiple pathways and systems and safely inhibit excessive inflammation while maintaining hemostasis. Already, studies have demonstrated the ability of biomaterials to target different processes and stages in sepsis-induced inflammation and coagulopathy. Moreover, some biomaterials offer inherent anti-inflammatory and hemostatic qualities. This review aims to discuss the most recent advancements in biomaterial development designed to address inflammation, coagulopathy, and thromboinflammation.

KEYWORDS

biomaterials, sepsis, inflammation, hemostasis, thromboinflammation, targeted delivery

1 Introduction

Sepsis is as life-threatening host response to infection, characterized by organ dysfunction (Semeraro et al., 2010; Angus and Poll, 2012; Singer et al., 2016), and this condition is estimated to cause almost 50 million cases globally each year (WHO, 2023). The causes for sepsis include any infectious organisms: bacteria, fungi, viruses, and parasites can all lead to sepsis (Rudd et al., 2020). Sepsis is most commonly caused by bacterial pneumonia, but intra-abdominal and urinary tract infections are also frequent underlying causes (Angus and Poll, 2012). These infections lead to uncontrolled inflammation, resulting in tissue damage and coagulopathy, organ dysfunction, and even death. People who are immunocompromised, such as babies, geriatric populations, and those on immunosuppressive treatments such as chemotherapy, are most at risk (Angus and Poll, 2012; Rudd et al., 2020; Weiss et al., 2020). The respiratory and cardiovascular systems are most severely affected. Clinical signs include difficulty breathing and low blood pressure.

Current treatment strategies depend on the individual and their clinical presentation, so a standard of care has not yet been established. Treatment often involves rescuing the cardiovascular and pulmonary systems through mechanical ventilation, vasopressor administration, and obtaining cultures to guide antimicrobial therapy (Angus and Poll, 2012; Weiss et al., 2020). Despite intensive treatment, sepsis remains a significant health concern, accounting for nearly 20% of all global deaths (WHO, 2023), with a high mortality rate of approximately 33% (Bauer et al., 2020). In the United States alone, hospitals spend over $24 billion each year on septic patient care (Rudd et al., 2020). Over the last decade, mortality rates have not lowered significantly (40% in 2009% vs. 34% in 2019) (Bauer et al., 2020) and the frequency of septic cases has risen every year by 13% on average (Tanne et al., 2002; Gaieski et al., 2013). These trends most likely result from increased life expectancies and the rise of antimicrobial resistance, both of which may contribute to sepsis becoming more difficult to treat (Cánovas-Cervera et al., 2023). Moreover, the relatively stagnant mortality rates in sepsis reflect the lack of significant advancements in therapeutics. Biomaterials and the design of multi-targeted therapeutics offer promising solutions to treating this complex disorder.

Biomaterials are most frequently considered for use as drug delivery vehicles with the aims of improving drug stability, prolonging blood circulation, and controlling spatiotemporal drug release to enhance local effects while minimizing systemic side effects. Accomplishing these goals ultimately improves patient outcomes and reduces drug-related toxicities and coagulopathies. Biomaterials offer inherent benefits based on their physical properties. For instance, silver is a natural antimicrobial, and when used as nanoparticles, it can amplify the antibacterial effects of antibiotics (Sun and Gupta, 2020; Vishwanath et al., 2022). This synergy allows for the use of lower antibiotic doses while achieving effective antibacterial responses. Biomaterials can be manipulated extensively to address several different diseases of different bodily systems as well. Material composition, size, shape, charge, molecular weight, and flexibility can all be optimized for specific purposes. With inflammation, nano-sized biomaterials can take advantage of the enhanced permeability and passively accumulate in inflamed tissues. For active targeting, ligands can be conjugated to biomaterials for selective binding. As for drug release, biomaterials can be designed to respond to changes in pH, temperature, shear forces, enzymes, radiation, and even ultrasonography and magnetic forces. For example, superparamagnetic iron oxide nanoparticles (SPIONs) have frequently been studied for drug delivery since they can be directed to specific areas for targeted drug delivery (Friedrich et al., 2021). Given these possibilities, the development of a biomaterial capable of effectively treating severe sepsis and associated thromboinflammation is imminent.

This review delves into investigations of state-of-the-art biomaterials and the challenges in the development of biomaterials for sepsis-induced thromboinflammation, as well as inflammation and hemostasis individually. Anti-inflammatory biomaterials have historically been engineered from either synthetic materials or cells. Excitingly, recent innovative biomaterials incorporate both synthetic and cellular components. Biomaterials addressing coagulopathy have also expanded to reflect that coagulation is a dynamic process involving both clot formation and lysis. This review will examine biomaterials for modulating the different stages of coagulation, including furthering hemostasis, preventing thrombosis, and enhancing fibrinolysis. Lastly, investigations into multifunctional therapeutic biomaterials for sepsis-induced thromboinflammation will be discussed.

2 Biomaterials for inflammation

The characteristic uncontrolled inflammatory response is initiated by the detection of the invading microbes through their pathogen-associated molecular patterns (PAMPs), such as lipopolysaccharide (LPS). Additionally, damage inflicted by the invading microbes to the host leads to the release of damage-associated molecular patterns (DAMPs), including high mobility group box 1 (HMGB1). These patterns bind to pattern recognition receptors (PRRs), which are displayed by both circulating innate immune cells and endothelial cells. These PRRs include Toll-like receptors (TLRs), C-type lectin receptors (CLRs), and NOD-like receptors (NLRs) (Lasola et al., 2020; Friedrich et al., 2021; Yu et al., 2022). This detection activates inflammatory signaling pathways, such as nuclear factor-kappa B (NF-κB), c-Jun N-terminal kinase (JNK), and p38 mitogen-activated protein kinase (MAPK). Activation of these pathways induces neutrophils, monocytes, and macrophages to phagocytize the pathogens and synthesize pro-inflammatory cytokines and chemokines, such as tumor necrosis factor-alpha (TNFα), interleukin-1 (IL-1), and interleukin-6 (IL-6) (Vuong et al., 2017; Huang et al., 2019). These inflammatory signals recruit more immune cells, induce vasodilation, and increase vascular permeability to promote immune cell infiltration (Semeraro et al., 2010; Jackson et al., 2019). Microbes and cytokines stimulate neutrophils to release neutrophil extracellular traps (NETs), which capture and kill microbes (DeBont et al., 2019). However, in sepsis, the excessive accumulation of immune cells is harmful to the body. The high leukocyte numbers release a "cytokine storm," resulting in tissue damage and paradoxically reduced pathogen clearance (Huang et al., 2019). This is largely due to activated natural killer (NK) cells, which amplify inflammation by secreting interferon-gamma (IFN-γ) and further tissue damage by releasing cytotoxic granzymes and perforins (Guo et al., 2018). NK cells also induce immune cell apoptosis with their ligands, ultimately reducing pathogen uptake and clearance (Michel et al., 2012; Thorén et al., 2012). The activated endothelium also increases its expression of adhesion molecules, including von Willebrand factor (vWF), P-selectins, vascular cell adhesion molecule-1 (VCAM-1), and platelet-endothelial cell adhesion molecule (PECAM)-1 (Greineder et al., 2013; Banka et al., 2023). These molecules enhance the binding of neutrophils, monocytes, and platelets, promoting coagulation and providing targets for site-specific nanoparticles. Biomaterials have also been developed to block inflammation from neutralizing PAMPs and removing reactive oxygen species to altering leukocyte recruitment and phagocytic capabilities and interactions (Lasola et al., 2020) (Figure 1).

2.1 Synthetic biomaterials for inflammation

Traditionally, biomaterials have been synthetic, including polymers, ceramics, and metals. Examples of commonly used

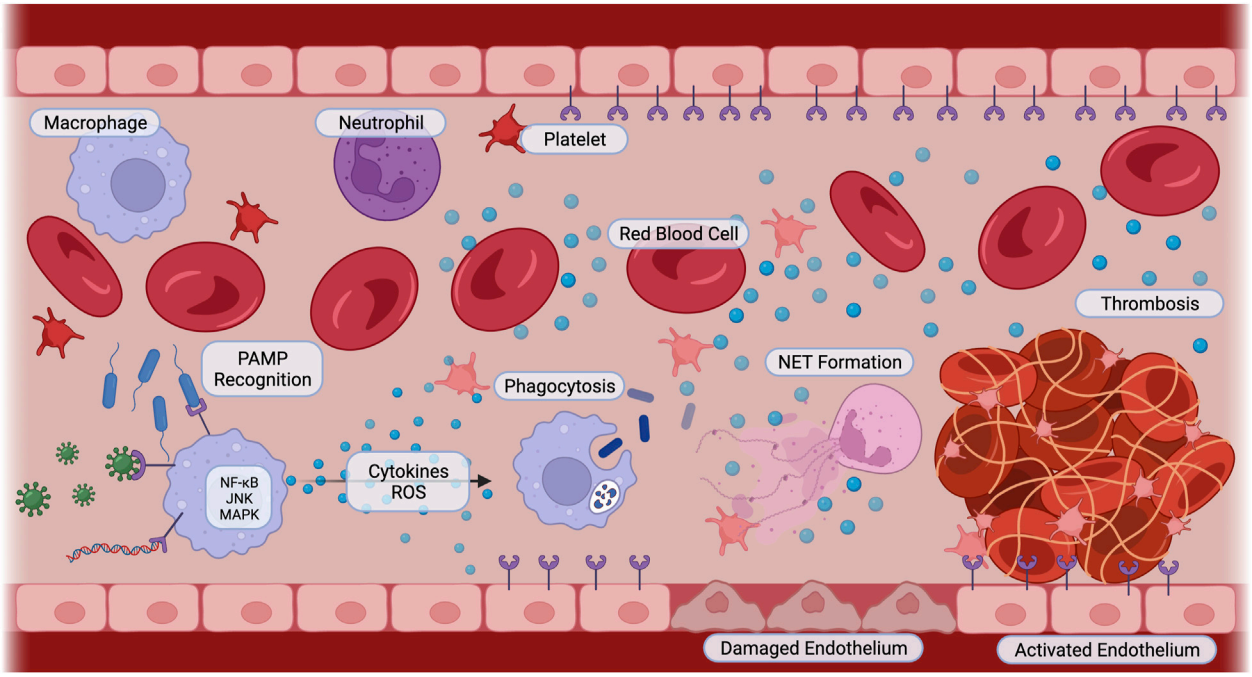

FIGURE 1
Sepsis Pathophysiology. Innate immune cells recognize pathogens such as bacteria, viruses, and parasitic DNA with pattern recognition receptors. Pro-inflammatory signaling cascades including NF-κB, JNK, and MAPK are activated. Cells secrete cytokines and reactive oxygen species, activating immune cells to phagocytize, neutrophils to release neutrophil extracellular traps, and platelets and endothelial cells to switch to a pro-coagulant phenotype. Cellular interactions amplify inflammation, cause endothelial cell damage, and induce thrombosis. Created with BioRender.

synthetic biomaterials for targeted drug delivery include lipid nanoparticles, liposomes, dendrimers, and poly(ethylene glycol) (PEG) conjugates (Greineder et al., 2013). Conjugating PEG to compounds or nanoparticles, also known as "PEGylation," is a common technique to improve the "stealth" of nanoparticles and increase circulation time (Sun et al., 2008; El Mohtadi et al., 2019; Yan et al., 2019; Huang et al., 2021; Nunoi et al., 2022). PEGylation creates a hydrophilic layer, sterically repelling proteins and thereby limiting the adsorption of opsonins that signal to immune cells to uptake and destroy (Kelley et al., 2016; Sobczynski et al., 2017). Moreover, the hydrophilic layer produced by PEGylation can increase drug solubility (Greineder et al., 2013). Of course, PEGylation has a drawback: studies have indicated that PEGylated products can lead to acquired immunogenicity, limiting its use for drugs that require repeat dosing (Kelley et al., 2016). Moreover, the acquired immunogenicity results in accelerated clearance of the particles from the bloodstream, limiting the "stealth" of the materials (El Mohtadi et al., 2019). Therefore, other polymers with stealth capabilities are also being investigated, including poly(propylene sulfoxide) which also has antioxidant properties (El Mohtadi et al., 2019), poly(2-oxazoline) (POx), and zwitterionic polymers (Fam et al., 2020). As of yet, none of these other polymers have been found to induce acquired immunogenicity nor result in accelerated blood clearance.

Several synthetic biomaterials are currently being investigated for attenuating inflammation in sepsis models (Table 1). The following studies emphasize the inherent anti-inflammatory abilities of empty biomaterials in ameliorating sepsis-induced pro-inflammatory cytokine release based on their physicochemical properties. Empty polymer nanoparticles, synthesized from poly(lactic-co-glycolic acid) (PLGA) and poly(lactic acid) (PLA), reduced TLR activation and subsequent pro-inflammatory cytokine release in an LPS-induced sepsis mouse model (Casey et al., 2019). Unloaded high-density lipoprotein nanoparticles targeted to VCAM-1 have been shown to inhibit leukocyte adhesion to activated endothelium, reducing proinflammatory cytokine release in an LPS-induced acute lung inflammation mouse model (Yu et al., 2022). Cargo-free liposomes developed from fish roe lipids similarly imparted anti-oxidant and anti-inflammatory effects in LPS-stimulated macrophages (Guedes et al., 2021). Similar in concept, eggshell membrane particles are under investigation for their anti-inflammatory properties, attributed to the proteins and carbohydrates they contain. In addition to reducing NF-κB activity and associated pro-inflammatory cytokines, these particles also increased anti-inflammatory cytokine interleukin-10 (IL-10) (Vuong et al., 2017). Other anti-inflammatory and antioxidant polymers that have demonstrated protection from LPS include N-acetylcysteine gels (Kim et al., 2021), graphene oxide-polypropylene nanoparticles (Fonticoli et al., 2023), and polyphenol gels (Luque et al., 2023), the latter two of which also have antibacterial benefits. In a cecal-puncture and ligation sepsis mouse model, dendrimers scavenged pro-inflammatory cytokines, resulting in a significantly improved survival rate of 100% (Shi et al., 2020). Bioactive glasses have also been examined for their anti-inflammatory and antibacterial potential (Nedelec et al., 2008). Mesoporous bioactive glass nanoparticles (MBGNPs) carrying cerium, an antioxidant, successfully demonstrated anti-inflammatory and antibacterial

TABLE 1 Biomaterials for Altering Inflammation. The composition, preparation methods, sizes, charges, and investigated anti-inflammatory properties of synthetic biomaterials, cell-derived biomaterials, and combined synthetic and cell-derived biomaterials. PLGA: poly(lactic-co-glycolic acid); PLA: polylatic acid; NAC: N-acetylcysteine; TMOS: tetramethoxysilane; CTAB: cetyltrimethylammonium bromide; PVA: poly(vinyl alcohol); PEG: polyethylene glycol; DAMP: damage-associated molecular pattern; PAMP: pathogen-associated molecular pattern; i.p.: intraperitoneal; i.t.: intratracheal; i.n.: intranasal; p.o.: per os; MHV: mouse hepatitis virus.

	Material composition	Preparation method	Size	Charge	Model	Investigated properties	Reference
Synthetic biomaterials	PLGA-PLA	Oil-in-water emulsion solvent evaporation	350 nm–500 nm	−40 to −50 mV	C57BL/6J mice; LPS i.p. (sepsis)	Interference with TLR signaling: NF-κB, IRF1, and STAT1 transcription factor activity Pro-inflammatory cytokine production Survival	Casey et al. (2019)
	High density lipoproteins	Lyophilization-rehydration	10 nm–15 nm	−7 to −15 mV	C57BL/6 mice; LPS i.p. (sepsis)	Interference with leukocyte-endothelial cell interactions: Cytotoxicity VCAM-1 specific targeting and accumulation Pro-inflammatory cytokine production Morphology and leukocyte infiltration	Yu et al. (2022)
	Roe-derived liposomes	MTBE method, lyophilization-rehydration	330 nm	−27 mV	L929 fibroblasts, THP-1 monocytes; LPS-stimulated	Antioxidant activity Cytotoxicity Pro-inflammatory cytokine production	Guedes et al. (2021)
Synthetic biomaterials	Eggshell membrane particles	Milling	<100 nm		U937-3xκB-LUC monocytes, THP-1-derived macrophages; LPS-stimulated	Inteference with NF-κB activity: NF-κB transcription factor activity Pro- and anti-inflammatory cytokine production Pro-inflammatory cell surface receptor expression	Vuong et al. (2017)
	NAC-loaded TMOS-CTAB	Sol-gel condensation	3.04 nm	−20.2 mV	Sprague Dawley rats; LPS i.t. (acute lung inflammation)	NF-κB and MAPK transcription factor activity Morphology and neutrophil infiltration Antioxidant activity Pro-inflammatory cytokine production	Kim et al. (2021)
	Graphene oxide-polypropylene	Ultrasonication, lyophilization-rehydration	717.7 nm–1.256 μm	−26.3 to −28.8 mV	Human gingival fibroblasts; LPS-stimulated	Cytotoxicity Activation of TLR4-MyD88-NF-κB-NLRP3 signaling pathway	Fonticoli et al. (2023)
Synthetic biomaterials	PVA Iongels	Self-assembly	220 nm–450 nm		Primary peritoneal macrophages from CD1 mice; LPS-stimulated	Cytotoxicity Hemolysis and agglutination Antioxidant activity Anti-inflammatory activity (via nitric oxide concentration) Antibacterial activity	Luque et al. (2023)

(Continued on following page)

TABLE 1 (*Continued*) Biomaterials for Altering Inflammation. The composition, preparation methods, sizes, charges, and investigated anti-inflammatory properties of synthetic biomaterials, cell-derived biomaterials, and combined synthetic and cell-derived biomaterials. PLGA: poly(lactic-co-glycolic acid); PLA: polylatic acid; NAC: N-acetylcysteine; TMOS: tetramethoxysilane; CTAB: cetyltrimethylammonium bromide; PVA: poly(vinyl alcohol); PEG: polyethylene glycol; DAMP: damage-associated molecular pattern; PAMP: pathogen-associated molecular pattern; i.p.: intraperitoneal; i.t.: intratracheal; i.n.: intranasal; p.o.: per os; MHV: mouse hepatitis virus.

	Material composition	Preparation method	Size	Charge	Model	Investigated properties	Reference
	PEG Telodendrimer	Solid-phase synthesis	25 nm–30 nm	Variable	BALB/c mice; cecal ligation and puncture (sepsis) RAW 264.7 macrophages; LPS-stimulated	LPS, cytokine, DAMP, and PAMP adsorption capability: NF-κB transcription factor activity Pro-inflammatory cytokine production Survival, hematology, and body temperature Selected protein adsorption	Shi et al. (2020)
	Loaded mesoporous bioactive glass nanoparticles	Microemulsion-assisted sol-gel condensation, template ion exchange	130 nm–150 nm		MC3T3-E1 preosteoblasts; RAW 264.7 macrophages; LPS-stimulated	Cytotoxicity Anti-inflammatory activity (via nitric oxide concentration) Antibacterial activity	Kurtuldu et al. (2021)
Cell-derived biomaterials	Dexamethasone-loaded macrophage-derived microvesicles	Ultracentrifugation	140 nm		C57BL/6 mice; LPS i.p. (sepsis) RAW 264.7 macrophages, primary glomerular endothelial cells from C57BL/6 mice; LPS-stimulated	NF-κB transcription factor activity Urine and serum enzymes, kidney morphology, collagen-deposition, and leukocyte infiltration Biodistribution Pro-inflammatory cytokine production Cell uptake	Tang et al. (2019)
	Piceatannol-loaded neutrophil-derived extracellular vesicles	Nitrogen cavitation	175 nm–200 nm	−15 to −20 mV	CD1 mice; LPS i.t. (acute lung inflammation) or i.p. (sepsis)	Interference with ICAM-1 endothelial cell expression: Endothelial cell targeting specificity Pro-inflammatory cytokine production Leukocyte infiltration, edema, and survival	Gao et al. (2017)
Synthetic and Cell-derived biomaterials	Gliclazide-loaded monocyte membrane covered PLGA	Extrusion	189.5 nm–292 nm	−10 to −34.1 mV	New Zealand white rabbits; 2% cholesterol (w/w) p.o. (atherosclerosis)	Hemolysis Toxicity Pro-inflammatory cytokine production Blood chemistry, histology, aortic plaque surface area, and macrophage infiltration	Karami et al. (2023)
	Lopinavir-loaded macrophage membrane covered PLGA	Sonication, ultracentrifugation	85.8 nm–102.2 nm	−12.4 to −42.4 mV	BALB/c mice; MHV i.n. (coronavirus) 293 T cells; S-pseudovirus	Pro-inflammatory cytokine production Leukocyte activation and NET formation Biodistribution Lung and liver targeting and accumulation Cytotoxicity Viral load	Tan et al. (2021)

(Continued on following page)

TABLE 1 (*Continued*) Biomaterials for Altering Inflammation. The composition, preparation methods, sizes, charges, and investigated anti-inflammatory properties of synthetic biomaterials, cell-derived biomaterials, and combined synthetic and cell-derived biomaterials. PLGA: poly(lactic-co-glycolic acid); PLA: polylatic acid; NAC: N-acetylcysteine; TMOS: tetramethoxysilane; CTAB: cetyltrimethylammonium bromide; PVA: poly(vinyl alcohol); PEG: polyethylene glycol; DAMP: damage-associated molecular pattern; PAMP: pathogen-associated molecular pattern; i.p.: intraperitoneal; i.t.: intratracheal; i.n.: intranasal; p.o.: per os; MHV: mouse hepatitis virus.

	Material composition	Preparation method	Size	Charge	Model	Investigated properties	Reference
	Dexamethasone-loaded macrophage-derived exosomes	Ultracentrifugation, electroporation	106.27 ± 11.40 nm	−34.80 ± 6.60 mV	DBA/1 mice; collagen-induced arthritis RAW 264.7 macrophages; LPS stimulated	Pro-inflammatory cytokine production Biodistribution Arthritis parameters (body weight, paw thickness, foot volume, bone density, trabecular thickness) Inflammatory cell infiltration	Yan et al. (2020)
	Hexyl 5-aminolevulinate hydrochloride-loaded neutrophil apoptotic body membrane covered mesoporous silica nanoparticles	Centrifugation; hypotonic treatment; sonication; base-catalyzed sol-gel method	200 nm	−15 mV	Sprague Dawley rats; myocardial infarction	Heart targeting efficiency Cardiac function, fibrosis, infarct size Toxicity Macrophage infiltration	Bao et al. (2022)
	Neutrophil membrane covered liposomes	Centrifugation; lipid film rehydration	143.6 ± 2.1 nm	−20.2 ± 0.8 mV	C57 mice; myocardial ischemia-reperfusion HUVECs, H9C2 cardiomyocytes, RAW 264.7 macrophages; hypoxia-reoxygenation	Pro-inflammatory cytokine production Apoptosis and proliferation Gene expression levels Neutrophil chemotaxis Biodistribution Cardiac function	Chen et al. (2022)
	Microglial membrane covered flavin mononucleotide-coated human serum albumin nanoparticles	Sonication; extrusion	106 nm	−15 to −20 mV	C57BL/6J mice; LPS i.p. (Alzhimer's disease)	Pro-inflammatory cytokine production Blood brain barrier permeability Biodistribution Cognitive ability (open field test, Y-maze test, Morris Water Maze)	Zhang et al. (2023)

activity against both gram-positive and gram-negative bacteria in *in vitro* assays (Kurtuldu et al., 2021). Similarly, MBGNPs loaded with gallium exhibited antibacterial and hemostatic benefits *in vitro* (Kurtuldu et al., 2022). In general, synthetic biomaterials are the easiest drug delivery vehicles to produce and have high manufacturing consistency, but cell-derived biomaterials also offer their own advantages (Witwer and Wolfram, 2021).

2.2 Cell-derived biomaterials for inflammation

Cell-derived biomaterials, including extracellular vesicles and cell-derived products, are being investigated as drug delivery vehicles for their inherent biocompatibility (Table 1). Exosomes are an exciting group of extracellular vesicles known as "natural nanoparticles." Exosomes are particularly promising due to their cell membrane proteins and natural cargo of nucleic acids, proteins, and lipids, meaning exosomes display parent cell-specific targeting and functions (Popowski et al., 2020). These particles' biocompatible membranes are also able to avoid immune recognition and reduce toxic effects (Lutz et al., 2021). Furthermore, exosome surfaces can be engineered to display ligands for improved targeting and controlled release and their cargo can be altered to carry pharmaceutical drugs (Lutz et al., 2019). In an LPS-induced sepsis mouse model, extracellular vesicles carrying a glucocorticoid reduced renal inflammation and fibrosis, and no side effects common with glucocorticoids were observed (Tang et al., 2019; Lasola et al., 2020). A significant challenge with extracellular vesicles are scaling up production to translating research findings to clinical doses. A potential solution being explored is nitrogen cavitation, which has shown promise by increasing extracellular vesicle production by 16-fold (Gao et al., 2017; Hahm et al., 2021; Ng et al., 2022). Additionally, extracellular vesicles generated using this method retained their ability to efficiently load drugs and deliver them effectively to reduce LPS-induced acute lung inflammation (Gao et al., 2017). Another cell-derived product is heparin, which is especially useful as a biomaterial for sepsis due to its antiviral activity and hemostatic properties (Kemp and Linhardt, 2010). Already, heparin has been found to reduce in-hospital mortality in septic patients by reducing inflammation and rescuing platelet counts over 28 days (Zou et al., 2022; Zhang Z et al., 2023).

Cell-based biomaterials are frequently examined in opposition to synthetic materials, for each type has its own advantages and disadvantages. After all, synthetic materials have more flexibility in terms of composition and designing the sizes and shapes for different applications. In contrast, modification of cell-derived materials are limited to certain sizes and shapes, such as 30–200 nm spherical exosomes (Gurung et al., 2021) or 7 μm discoid red blood cells (Muzykantov, 2013). Still, even with all the design options for synthetic materials, none have been shown to match the four-month lifespan of red blood cells in circulation (Chen et al., 2023). In terms of applications, synthetic materials have been found to provide better intracellular delivery (Muro et al., 2008), and in the context of sepsis, anti-inflammatory drug delivery to damaged tissues is critical. At the same time, red blood cells remain attractive for intravascular drug delivery in sepsis to deliver antithrombotic agents and cytokine inhibitors (Kolesnikova et al., 2013). Due to the unique advantages maintained by each type of biomaterial, research groups are investigating strategies to combine synthetic and cell-derived materials to produce more efficacious drug delivery systems.

One of the products of combined synthetic and cell-derived materials is the development of biomimetic nanoparticles (Table 1). These nanoparticles use membranes from platelets and other blood cells to encapsulate drug-carrying nanoparticles. Karami et al. investigated the ability of PLGA nanoparticles covered in monocyte membrane, carrying the anti-inflammasome drug Gliclazide, to reduce pro-inflammatory cytokine release in monocytes treated with LPS. They also found that in an atherosclerotic rabbit study, these "nanoghosts" shifted macrophages from a pro-inflammatory to anti-inflammatory phenotype and inhibited plaque development (Karami et al., 2023). Macrophage biomimetic nanoparticles have been studied as a therapeutic for COVID-19, which can progress into sepsis. These nanoparticles exhibited both anti-inflammatory and antiviral effects, ultimately resulting in improved survival in a mouse coronavirus model (Tan et al., 2021). However, further research in more relevant models is needed. While research into biomimetic materials specifically for sepsis-based inflammation is limited, many groups have demonstrated the potential of biomimetic nanoparticles for attenuating other inflammatory diseases, including osteoarthritis (Yan et al., 2020), myocardial infarction (Bao et al., 2022; Chen et al., 2022), and neuroinflammation (Zhang M et al., 2023), by suppressing pro-inflammatory cytokine secretion and enhancing the expression of anti-inflammatory cytokines.

2.3 Challenges for anti-inflammatory biomaterials

Despite the wide range of biomaterials investigated recently for controlling inflammation in sepsis, several obstacles persist in pre-clinical studies. Firstly, the models used for sepsis are too narrowly focused (Choi et al., 2023). Many studies rely on LPS-induced sepsis models and are limited to *in vitro* studies using monocytes and macrophages (Jin et al., 2019; Kong et al., 2019; Lee et al., 2020; Hemmingsen et al., 2021). Due to the extensive literature on the role of LPS in sepsis, it is obviously understandable to pursue investigations in an established model. However, sepsis can result from various infectious organisms, including viruses, fungi, and parasites and it would be remiss not to broaden studies to include these. With the advent of SARS-CoV-2, several studies have investigated COVID-19-related sepsis, but more sepsis models from different causes remain to studied. Moreover, LPS is specific to gram-negative bacteria and does not account for the pathogenicity and different inflammatory pathways activated by gram-positive bacteria, such as methicillin-resistant *Staphylococcus aureus* (MRSA) (Dickson and Lehmann, 2019). Even within bacterial species, different strains carry unique lipid A endotoxins, leading to varying interactions with cells and levels of toxicity (Dickson and Lehmann, 2019; Harm et al., 2019). Additionally, pre-clinical models often expose animals to their first infectious agents, while human sepsis patients must also combat opportunistic pathogens and underlying comorbidities. Another challenge is the need to shift research toward developing multitargeted biomaterials. Current strategies often focus on single-target approaches to minimalize side effects. However, sepsis is a complex disorder that affects multiple body systems and processes, necessitating a multitargeted solution.

3 Biomaterials for coagulopathy

One of the processes severely affected by sepsis is hemostasis. Under normal conditions, endothelial cells maintain an anticoagulant state and secrete platelet antagonists to prevent adhesion (Sloos et al., 2022). During sepsis or any inflammatory event, thrombosis is stimulated (Jackson et al., 2019). As previously noted, inflammation also activates the endothelial cells to increase their expression of adhesion proteins, thereby increasing the binding of neutrophils, monocytes, and platelets. Furthermore, the NETs released by neutrophils ensnare platelets as well as bacteria, promoting coagulation and clot formation. When injured, endothelial cells shift to a pro-coagulant state and secrete tissue factor, thrombin, and plasminogen activation inhibitor-1 (PAI-1) (Dudnick et al., 1991). The vasculature initially constricts, increasing platelet interactions with endothelial collagen (Cánovas-Cervera et al., 2023). The platelets activate and aggregate in a process known as primary hemostasis. Following, secondary hemostasis involves interactions between coagulation factors to stabilize the clot with fibrin formation (Raghunathan et al., 2022). In normal circumstances, once the damaged endothelium is repaired, the clot becomes subjected to fibrinolysis with tissue-plasminogen activator (tPA) converting inactive plasminogen to plasmin, which degrades and removes the clot. During sepsis, clot formation may be aberrant, resulting in clots that are either too weak to fulfill hemostasis or too strong to undergo lysis (Dudnick et al., 1991). Therefore, there is a need for biomaterials that can safely act on the endothelium to promote hemostasis and stimulate clot lysis as appropriate.

3.1 Hemostatic biomaterials

Currently, there are several pharmacologic treatments that are used to stabilize hemostasis, including desmopressin, aprotinin, and tranexamic acid. However, there is a need for drugs that directly promote hemostasis (Dudnick et al., 1991; Sloos et al., 2022). Another pro-hemostatic option is whole blood or platelet transfusions.

TABLE 2 Biomaterials for Coagulopathies. The composition, preparation methods, sizes, charges, and investigated hemostatic, anticoagulant, and fibrinolytic properties of biomaterials. pNIPAm: poly(N-isopropylacrylamide); AAC: acrylic acid; ULC: ultra-low crosslinked; DSPC: distearoylphosphatidylcholine; DSPE: 1,2-distearoyl-sn-glycero-3-phosphoethanolamine; VBP: vWF binding peptide; CBP: collagen binding peptide; PAH: poly(allylamine hydrochloride); BSA: bovine serum albumin; FMP: fibrinogen-mimetic peptide; TDI: 2,4-toluene diisocyanate; TCP: thrombin-cleavable peptide; i.v.: intravenous.

	Material composition	Preparation method	Size	Charge	Model	Investigated properties	Reference
Hemostatic biomaterials	pNIPAm-AAc ULC microgel with fibrin antibody fragments	Precipitation polymerization, EDC/Sulfo-NHS chemistry	1 μm		Sprague Dawley rats; femoral vessel injury	Enhancement of fibrin and clot formation: Fibrin-binding capabilities Fibrin clot formation and collapse Clot structure Clot contraction and stability	Brown et al. (2014)
	pNIPAm-co-AAc ULC microgel with fibrin knob B mimicking peptide	Precipitation polymerization, EDC/Sulfo-NHS chemistry	150 nm–1 μm		C57BL/6 mice; liver laceration	Facilitate fibrin B:b knob:hole binding to enhance clot formation and contraction: Clot fiber density, stability, and retraction Clot polymerization and degradation rates Blood loss and fibrin deposition in a liver laceration model Biodistribution Hematology Complement activation	Nandi et al. (2021)
	DSPC-DSPE liposomes with phosphatidylserine ligands	Thin-film rehydration and extrusion	100 nm–150 nm		C57BL/6 mice; anti-CD42b-induced thrombocytopenia C57BL/6 mice; cardiac puncture Sprague Dawley rats; liver laceration	Enhance thrombin and fibrin generation: Plasmin-specific targeting Thrombin and fibrin generation Fibrin clot formation and stability Bleeding time and blood loss, survival, thrombosis, and clot lysis	Sekhon et al. (2022)
Hemostatic biomaterials	Thrombin-loaded DSPC Liposomes with VBP and CBP	Maleimide-thiol reaction	175 nm		C57BL/6 mice; tail-clip C57BL/6 mice; liver laceration	Bind vWF and collagen to release thrombin and enhance clotting: Platelet activation and aggregation NET formation Complement activation Fibrin generation Bleeding time and blood loss vWF and collagen binding specificity Endothelial cell activation Clot formation time and rate	Girish et al. (2022)
	Hyaluronic acid with VBP and CBP	EDC/Sulfo-NHS chemistry			BALB/c mice; tail vein laceration	Bind activated platelets and promote accumulation at sites of endothelial injury: Platelet binding specificity Platelet accumulation and aggregation Bleeding time and blood loss	Gao et al. (2020)

(Continued on following page)

TABLE 2 (*Continued*) Biomaterials for Coagulopathies. The composition, preparation methods, sizes, charges, and investigated hemostatic, anticoagulant, and fibrinolytic properties of biomaterials. pNIPAm: poly(N-isopropylacrylamide); AAC: acrylic acid; ULC: ultra-low crosslinked; DSPC: distearoylphosphatidylcholine; DSPE: 1,2-distearoyl-sn-glycero-3-phosphoethanolamine; VBP: vWF binding peptide; CBP: collagen binding peptide; PAH: poly(allylamine hydrochloride); BSA: bovine serum albumin; FMP: fibrinogen-mimetic peptide; TDI: 2,4-toluene diisocyanate; TCP: thrombin-cleavable peptide; i.v.: intravenous.

	Material composition	Preparation method	Size	Charge	Model	Investigated properties	Reference
						Biodstribution Histology, hematology, and blood chemistry to assess toxicity Survival time	
	PAH and BSA with VBP, CBP, and FMP	Layer-by-layer	235 nm–240 nm	−16 to −25 mV	BALB/c mice; tail clip	Recruit activated platelets to sites of endothelial injury: Activated platelet and endothelium targeting specificity Shear-dependent aggregation Bleeding time Biodistribution Off-target microthrombi formation	Anselmo et al. (2014)
Anticoagulant biomaterials	Heparin and TDI	Interfacial polyaddition reaction with inverse miniemulsion	180 nm	−50 mV	HeLa cervix carcinoma cells, MCF-7 breast cancer cells, PC3 prostate cancer cells	Bind and activate ATIII: ATIII binding specificity Clotting time Cellular uptake	Baier et al. (2015)
	Heparin-coated colloidal mesoporous silica nanoparticles	Sol-gel synthesis	50 nm	−30 to −35 mV	*In vitro* assays	Bind and activate ATIII: ATIII binding specificity Heparin activity Coagulation time	Argyo et al. (2012)
	Hirudin and fibrin antibody fragment with factor Xa cross-linker	Cloning with M13 phage system			*In vitro* assays	Thrombin inhibition: Factor Xa-mediated hirudin release ATIII activity Clot size	Peter et al. (2000)
	Hirudin-loaded acrylamide and TCP nanogel with Clot-targeted peptide	One-pot synthesis, single emulsion polymerization	77 nm	Neutral	C57BL/6 mice; thromboplastin i.v. (pulmonary embolism) C57BL/6 mice; $FeCl_3$ topical (carotid arterial and mesenteric thrombosis)	Thrombin inhibition: Clot targeting TCP-mediated hirudin release Histology, collagen and fibrin deposition, survival, and bleeding time Hemolysis	Xu et al. (2020)
	Elastin-based protein micelles with GPIIb/IIIa antibodies	One pot transpeptidation with evolved sortase A	75 nm	−14 mV	C57BL/6J mice; laser-induced thrombosis	Thrombin inhibition: Clot targeting Platelet accumulation Thrombus formation	Kim et al. (2015)
	Serine Protease Inhibitor with GPIbα Antibody	Cloning			*Ex vivo* assays	Thrombin inhibition and interference with vWF binding: Thrombin and fibrin generation Platelet binding to vWF, agglutination, and aggregation ATP secretion	Sanrattana et al. (2022)

(Continued on following page)

TABLE 2 (*Continued*) Biomaterials for Coagulopathies. The composition, preparation methods, sizes, charges, and investigated hemostatic, anticoagulant, and fibrinolytic properties of biomaterials. pNIPAm: poly(N-isopropylacrylamide); AAC: acrylic acid; ULC: ultra-low crosslinked; DSPC: distearoylphosphatidylcholine; DSPE: 1,2-distearoyl-sn-glycero-3-phosphoethanolamine; VBP: vWF binding peptide; CBP: collagen binding peptide; PAH: poly(allylamine hydrochloride); BSA: bovine serum albumin; FMP: fibrinogen-mimetic peptide; TDI: 2,4-toluene diisocyanate; TCP: thrombin-cleavable peptide; i.v.: intravenous.

	Material composition	Preparation method	Size	Charge	Model	Investigated properties	Reference
	Hydroxychloroquine-loaded DSPE with P-selectin and neutrophil-elastase binding peptides	Thioether reaction, amide chemistry	200 nm		C57BL/6J mice; LPS i.v.	Inhibit neutrophil activation: Binding specificity to neutrophil-platelet complexes Circulation time Cytotoxicity NET formation Survival and thrombus weights in deep vein thrombosis model	Cruz et al. (2023)
Fibrinolytic biomaterials	Nattokinase-loaded polydopamine microspheres	Oxidative polymerization	>1 μm		*Ex vivo* assays	Fibrin degradation and plasmin generation: Activated platelet targeting Fibrinolysis Clotting time Platelet aggregation	Ye et al. (2018)

Unfortunately, this option is not always available due to donor shortages, high costs, and the risk of immunogenic reactions (Dudnick et al., 1991; Gao et al., 2020). Moreover, when available, platelets face a short storage life of only five to 7 days (Dudnick et al., 1991; Fernandez-Moure et al., 2018; Raghunathan et al., 2022; Gao et al., 2023). Lyophilization of blood products has been explored as a method to extend storage life and improve accessibility by enabling storage at higher temperatures. Lyo-protectants and cryo-protectants preserve platelet morphology and function. In several animal models, lyophilized platelets have been found to reduce bleeding time and blood loss (Cap and Perkins, 2011). Unfortunately, lyophilized platelets have been found to only last roughly 36 h in circulation before being cleared by macrophages, so while they may be useful in acute trauma, lyophilized platelets have limited use as a prophylactic (Raghunathan et al., 2022). Therefore, a branch of research has focused on developing biosynthetic blood cells, particularly platelet mimetics (Kelley et al., 2016). Some groups use platelet membranes to coat their nanoparticle surfaces, but as with extracellular vesicles, they face scale-up challenges. In this case, the lack of platelet availability from which to derive membranes was the primary obstacle (Raghunathan et al., 2022). To overcome the challenge of platelet membrane availability, some research groups coat nanoparticles with hemostatic proteins found on platelets, including fibrin knob B (Nandi et al., 2021), fibrin antibodies (Brown et al., 2014), phosphatidylserine (Sekhon et al., 2022), vWF-binding peptides, and collagen-binding peptides (Gao et al., 2020; Girish et al., 2022; Gao et al., 2023) (Table 2). These platelet-mimicking particles promote clotting, reduce blood loss, and decrease bleeding time in various models, including liver laceration, tail-clip injury, hemophilia, and human plasma from patients with coagulopathy.

3.2 Anticoagulant biomaterials

During systemic vascular injuries such as sepsis, blood clots can form and become lodged in the microvasculature, blocking blood flow, and causing ischemia. In clinical cases of thrombosis, anticoagulants are commonly administered. However, available anticoagulants have narrow therapeutic ranges and can interfere with hemostasis, posing a bleeding risk. As a result, the administration of anticoagulants, including heparin, antithrombin-III (ATIII), hirudin, activated protein C, thrombomodulin, and tissue factor pathway inhibitor, comes with a risk of bleeding, which can be equally life-threatening. Heparin is an attractive anticoagulant due to its binding with antithrombin-III, rending clots weak and easily lysed (Baier et al., 2015). Furthermore, heparin inhibits the complement system, thereby imparting "stealth" properties to nanoparticles hidden within and increasing blood circulation time (Argyo et al., 2012). Although studies have shown that heparin nanoparticles and heparin-coated nanoparticles increase clotting times, heparin carries a bleeding risk and also induces thrombocytopenia (Peter et al., 2000; Xu et al., 2020). Hirudin, a thrombin inhibitor independent of ATIII, is a potential heparin replacement. Hirudin can achieve anticoagulant activity without inducing thrombocytopenia and the magnitude of hirudin's effects is directly proportional to its dosage. In pulmonary embolism and arterial thrombosis mouse models, hirudin-loaded nanogels demonstrated clot-dependent release, inhibiting clot formation. Importantly, bleeding times were not significantly prolonged in tail-clip injuries (Xu et al., 2020). In these studies, the nanogels controlled hirudin release using thrombin-cleavable peptides.

Another approach to target active clot formation sites is to decorate delivery vehicles with antibodies or antibody-fragments specific to proteins expressed exclusively during endothelial injury. This method, nor its use in sepsis research, is new (Colman et al., 1988), but as understanding of sepsis and coagulopathy pathophysiology improves, novel targets and targeting ligands have recently developed. Polymeric micelles with a single-chain fragment variable antibody (scFv) that binds to GPIIb/IIIa, a glycoprotein receptor found only on activated platelets, accumulated at platelet-rich thrombi. When loaded with thrombomodulin, they effectively inhibited thrombus formation (W. Kim et al., 2015). Another strategy involved blocking platelet glycoproteins with an scFv to prevent

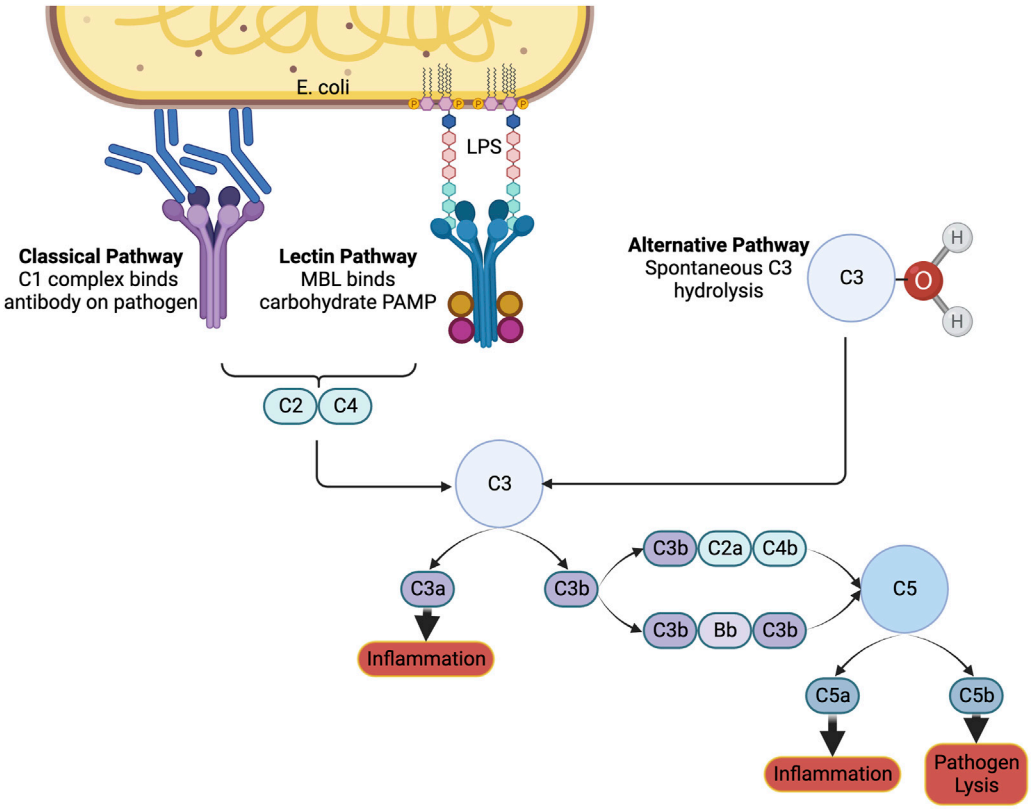

FIGURE 2
The complement system. The immune system can be notified of pathogens or foreign substances in the blood by activation of the complement system through the classical, lectin, or alternative pathways. A cascade of signals ultimately results in the formation of C3a and C5a, which induce inflammation, and C5b, which signals to immune cells to lyse the pathogen. Created with Biorender.

platelet interactions with thrombin and inhibit thrombus formation. Additional loading of an antithrombotic, an α1-antitrypsin variant, enhanced clot inhibition (Sanrattana et al., 2022). This particular set of studies is notable due to its multi-targeted strategy in both blocking platelet binding with scFv as well as inhibiting thrombin with the α1-antitrypsin variant. Following this multitargeted approach, a research group targeted clot formation from the trapping of activated platelets in NETs. This group developed nanoparticles with antibody fragments to selectively target and inhibit activated neutrophils from forming NETs. The nanoparticles were also loaded with hydroxychloroquine to inhibit platelet aggregation and adhesion, thereby inhibiting clot formation through two separate mechanisms (Cruz et al., 2023). Antibody fragments offer advantages such as avoiding cellular activation, minimizing immunogenicity, and binding with high specificity. However, it's important to note that while scFv-bound antithrombotic drugs localize at clots, their accessibility diminishes, potentially limiting their effectiveness and the ability to use lower dosages to reduce bleeding risk (Greineder et al., 2013).

3.3 Fibrinolytic biomaterials

Anticoagulants prevent thrombus formation, while fibrinolytics dissolve existing clots. The most common fibrinolytics are plasminogen activators, mainly tPA and urokinase. Unfortunately, as with anticoagulants, administration of plasminogen activators is associated with increased bleeding risk (Wang et al., 2020; Helms et al., 2023). Moreover, plasminogen activators are notorious for extremely short circulation times making their administration impractical in most cases. Delivery in a biomaterial vehicle can resolve both of these issues. Already, fusing tPA to PEG increases circulation time up to five times as long as naked tPA (M. Sun and Gupta, 2020) but doesn't affect tPA-induced hemorrhage (Greineder et al., 2013). When conjugated to an anti-fibrin antibody, tPA potency and selectivity improved, meaning further investigation is necessary to determine if a subclinical dose of tPA-bound anti-fibrin antibody could effectively dissolve clots and avoid bleeding (Runge et al., 1987). Thus far, delivery of subclinical tPA doses has yet to be examined, and this may be due to the discovery of nattokinase. Nattokinase, a plant-derived fibrinolytic with anti-inflammatory and antioxidant activities, directly degrades fibrin in clots without causing bleeding and inhibits platelet aggregation (Ye et al., 2018; Wu et al., 2020). Therefore, nattokinase overcomes the limitations of tPA without the need for additional modifications. Nattokinase is still a relatively novel fibrinolytic, so it is definitely a compound to keep an eye on as more studies examine its potential and establish its limits. As for urokinase, its clinical usage has thus far been limited to diagnosing sepsis and predicting prognosis based on blood level elevations of its receptor, soluble urokinase plasminogen activator receptor, correlating to disease severity (Sharma et al., 2020; Efat

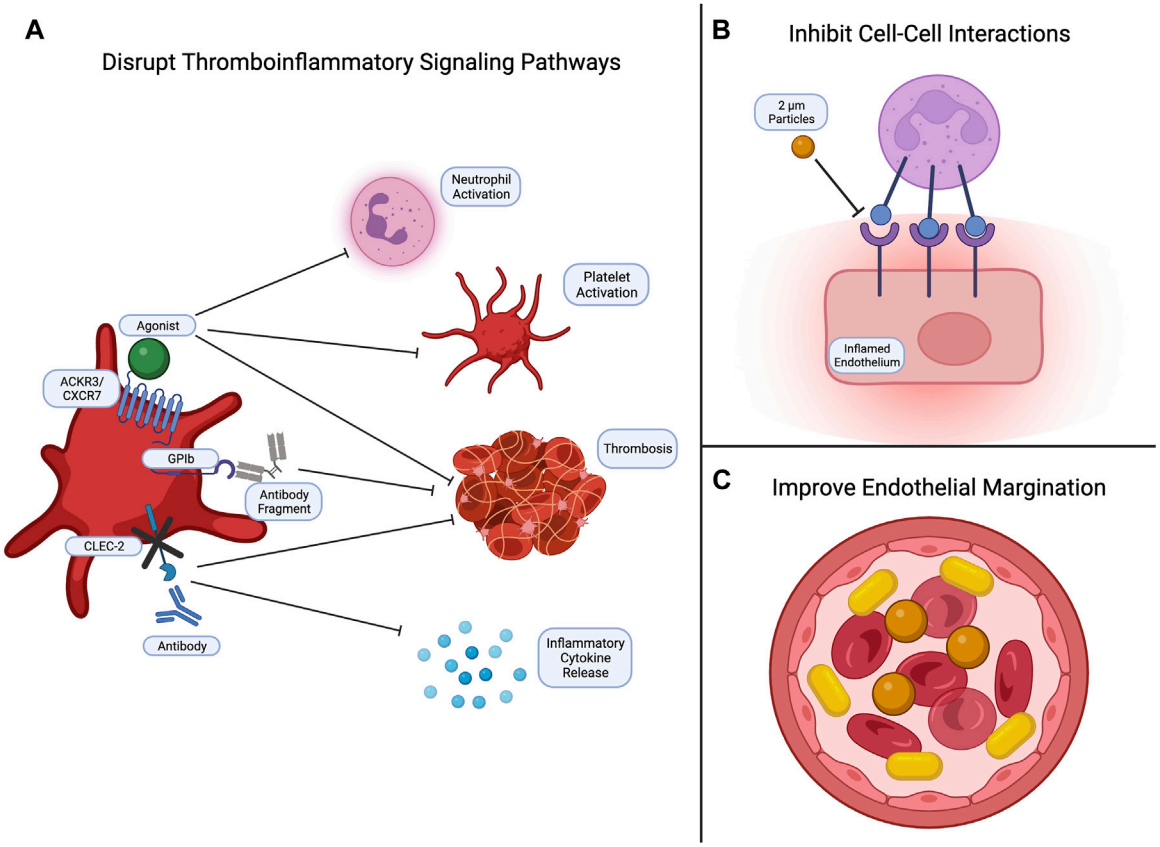

FIGURE 3
Common strategies for targeting thromboinflammation. Currently, efforts to inhibit thromboinflammation focus on **(A)** disrupting signaling pathways to reduce neutrophil and platelet activation, thrombus formation, and inflammatory cytokine release; **(B)** inhibiting cell-cell interactions, such as leukocyte-endothelial and leukocyte-platelet interactions; and **(C)** developing biomaterials with physical properties that enhance endothelial margination. Created with Biorender.

et al., 2021; Ma et al., 2023). Urokinase is not widely used as a thrombolytic due to its markedly reduced specificity for fibrin and increased bleeding risk in comparison to tPA (Adivitiya and Khasa, 2017; Kadir and Bayraktutan, 2020).

3.4 Challenges for biomaterials targeting coagulopathies

Special considerations are necessary for biomaterials administered intravenously to ensure compatibility with blood. The complement system plays a role in immune surveillance and recognizes foreign materials and pathogens (Figure 2). It can be activated through three different pathways: the classical, the lectin, and the alternative pathways. Each of these pathways result in the production of anaphylatoxins C3a and C5a (Maisha et al., 2020; Maisha et al., 2021). Once generated, these anaphylatoxins can trigger allergic reactions, including histamine release and vasodilation. When trying to improve clotting, vasodilation is counter-effective by increasing blood flow and minimizing platelet interactions with the endothelium. In severe sepsis, anaphylatoxins are already generated (Landsem et al., 2022) and administering therapeutic biomaterials may actually worsen a patient's condition. It is crucial to conduct *in vitro* testing for cell lysis of blood cells, platelet activation, plasma clotting, and C3a levels. Additionally, *in vivo* testing in an animal model with complement activation similar to that in humans is essential for anticipating adverse effects and advancing biomaterials (Harm et al., 2019; Maisha et al., 2020).

4 Biomaterials for thromboinflammation

As sepsis worsens, it can progress to thromboinflammation, which involves the inappropriate and unregulated formation of blood clots due to an extreme immune response (Banka et al., 2023). In more detail, inflammation activates the complement system and induces thrombosis (Vagionas et al., 2022). For example, activated neutrophils form neutrophil extracellular traps (NETs), which both activate platelets and entrap platelets, amplifying clot formation. Activated neutrophils also enhance platelet release from the bone marrow, contributing to thrombi formation (Petzold et al., 2022). In turn, activated platelets release pro-inflammatory signals, further increasing inflammation and injuring tissues in a pathologic cycle (Jackson et al., 2019; Senchenkova et al., 2019; Perrella et al., 2021). Thromboinflammation is a commonality in cardiovascular diseases, including atherosclerosis, COVID-19, and disseminated intravascular coagulation (DIC). In

TABLE 3 Biomaterials for Thromboinflammation. The composition, preparation methods, sizes, and investigated anti-thromboinflammatory properties of biomaterials. PEMA: poly(ethylene-co-maleic acid); PVA: polyvinyl alcohol.

Material composition	Preparation method	Size	Model	Investigated properties	Reference
PLGA-PEMA microparticles with E-selectin binding ligands	Emulsion-solvent evaporation	200 nm–4.5 μm	C57BL/6 mice; LPS i.p.	Interfere with leukocyte binding to platelets and endothelium: Leukocyte and platelet binding specificity Impaired cell binding to endothelium Biodistribution Neutrophil infiltration in LPS-induced sepsis model Liver toxicity	Banka et al. (2023)
tPA-loaded pNIPAm nanogels with fibrin antibody fragments	Precipitation polymerization, EDC/Sulfo-NHS chemistry	225 nm–275 nm	Sprague Dawley rats; LPS i.v. Sprague Dawley rats; LPS i.v. and liver laceration	Enhance clot maturation and promote existing clot lysis: Clot targeting Fibrinolysis Biodistribution Platelet count, fibrinogen and D-dimer concentration Clot formation and density Blood loss Clearance Toxicity via hematology and blood chemistry	Mihalko et al. (2021), (2022)
PLGA microspheres with E-selectin binding ligands and ICAM-1 antibodies	Co-solvent method	5.8 μm	*In vitro* assays	Leukocyte mimicking particles: Enhanced selectivity for inflamed endothelium Rolling and adhesion mimicry of leukocytes	Eniola and Hammer (2005)
PVA hydrogels with VCAM-1 and E-selectin antibodies	Precipitation polymerization, carbodiimide chemistry		Human umbilical vein endothelial cells	Greater binding retention to inflamed endothelium: Enhanced binding strength to activated endothelial cells	Rafat et al. (2012)

DIC, coagulation factors, platelets, and fibrinogen are consumed leading to the inappropriate formation of microthrombi and subsequent activation of fibrinolysis. Excessive platelet activation has been hypothesized to lead to platelet dysfunction and impaired response (Sloos et al., 2022). Clinically, this can present with prothrombotic and/or hemorrhagic phenotypes, resulting in contradictory treatment strategies. The concurrent ischemia, hemorrhage, and pro-inflammatory cytokines potentiate inflammation and injury, leading to multiple organ dysfunction syndrome (MODS). As expected, MODS is associated with a significantly worse prognosis (Helms et al., 2023). Therefore, there is an urgent need for the development of a single therapeutic that can simultaneously address inflammation, thrombosis, and hemorrhage.

To reduce thromboinflammation, studies have shown that cargo-free polystyrene microparticles can disrupt leukocyte adhesion to the endothelium in LPS models, emphasizing the importance in biomaterial physical characteristics (Banka et al., 2023) (Figure 3). Specifically, carriers with rod-like shapes and diameters between 2 and 5 microns demonstrate enhanced margination along the endothelium compared to spherical nanoparticles. This increased interaction with endothelial cells improves adhesion and targeting efficiency (Kelley et al., 2016; Van Der Meel et al., 2014; Y. Gao et al., 2020). At this moment, most studies focus on altering platelet signaling pathways involved in thromboinflammation by administering agonists or inhibitors. For example, increased expression of platelet chemokine receptor ACKR3/CXCR7 and administration of ACKR3/CXCR7 agonists reduced neutrophil activation, platelet activation, and thrombosis (Cebo et al., 2022). Another mechanism to reduce platelet-lymphocyte interactions is to eliminate platelet glycoprotein GPIb binding abilities to neutrophils. This was found to inhibit downstream Sema7a signaling and subsequent thrombus formation (Gauer et al., 2022). Alternatively, inhibition of CLEC-2 signaling by knocking out platelet expression of CLEC-2 or administering antibodies was found to inhibit thrombosis, reduce the release of pro-inflammatory mediators, and limit the severity of sepsis-related symptoms in mice (Meng et al., 2021).

Thrombosis can also lead to acute ischemic stroke, which currently only has one FDA approved therapy: tPA. As previously discussed, tPA presents a significant bleeding risk (Beyer et al., 2022). To address this, our research group has designed fibrin-targeting nanogels that site-specifically deliver anti-clotting drugs while also enhancing fibrin-crosslinking and clot formation. When loaded with tPA, we found that our nanogels accomplished a dual function of targeting and dissolving existing clots while promoting clotting at sites of hemorrhage, eliminating the bleeding risk posed by tPA (Mihalko et al., 2021; Mihalko et al., 2022). Other investigations using fibrin-specific systems have been similar in loading anti-fibrin antibody nanoparticles with fibrinolytics (Marsh et al., 2011), while more others target thrombi by decorating liposomes with anti-fibrin protein binders (Petroková et al., 2019) and conjugating anti-fibrin antibodies directly to fibrinolytics (Peter et al., 2000; El-Sherbiny et al., 2014). Recognizing the complexity of thromboinflammation, other strategies involve targeting different cell types. Some research groups have explored multitargeting by using nanoparticles with

multiple ligands to interact with multiple cell types and receptors. This approach enhances the specificity of nanoparticle interactions, drug release sites, and reduces systemic side effects (Eniola and Hammer, 2005; Rafat et al., 2012; Anselmo et al., 2014) (Table 3).

5 Discussion

Sepsis continues to be associated with high mortality, despite decades of research. Until recently, treatments for sepsis focused solely on reducing inflammation. Now, researchers understand that the pathophysiology of sepsis is driven by a close interplay between inflammation and hemostasis, termed "thromboinflammation" – a term first introduced only 25 years ago. As more information about thromboinflammation emerges, biomaterials continue to be the most promising solution for addressing thromboinflammation and treating sepsis. However, challenges remain in developing a single biomaterial that can effectively control inflammation, endothelial damage, and coagulopathy. Further examination and identification of the advantages of synthetic biomaterials and cell-derived biomaterials is necessary. Incorporating elements from each type of biomaterial appears effective in developing biomaterials that have improved blood circulation times and endothelial margination. Moreover, biomaterials have thus far been largely designed to target specific cell interactions, either reducing pro-inflammatory cytokines or preventing inappropriate thrombus formation separately. Recognizing the complexity of sepsis pathology and developing a multifunctional biomaterial is required to produce an effective therapy for this deadly disease.

Author contributions

HL: Conceptualization, Visualization, Writing–original draft, Writing–review and editing. AB: Funding acquisition, Project administration, Resources, Supervision, Writing–review and editing.

Funding

The author(s) declare financial support was received for the research, authorship, and/or publication of this article. This study is supported by NIH NHLBI R01HL146701, NIH NHLBI 1R01HL162809-01A1, and Grifols GATRA program.

Conflict of interest

The authors declare that the research was conducted in the absence of any commercial or financial relationships that could be construed as a potential conflict of interest.

Publisher's note

References

Adivitiya, and Khasa, Y. P. (2017). The evolution of recombinant thrombolytics: current status and future directions. *Bioengineered* 8 (4), 331–358. doi:10.1080/21655979.2016.1229718

Angus, D. C., and Poll, T. (2012). Severe sepsis and septic shock. *N. Engl. J. Med.* 369, 840–851. doi:10.1056/nejmra1208623

Anselmo, A. C., Modery-Pawlowski, C. L., Menegatti, S., Kumar, S., Vogus, D. R., Tian, L. L., et al. (2014). Platelet-like nanoparticles: mimicking shape, flexibility, and surface biology of platelets to target vascular injuries. *ACS Nano* 8 (11), 11243–11253. doi:10.1021/nn503732m

Argyo, C., Cauda, V., Engelke, H., Rädler, J., Bein, G., and Bein, T. (2012). Heparin-coated colloidal mesoporous silica nanoparticles efficiently bind to antithrombin as an anticoagulant drug-delivery system. *Chem. - A Eur. J.* 18 (2), 428–432. doi:10.1002/chem.201102926

Baier, G., Winzen, S., Messerschmidt, C., Frank, D., Fichter, M., Gehring, S., et al. (2015). Heparin-based nanocapsules as potential drug delivery systems. *Macromol. Biosci.* 15 (6), 765–776. doi:10.1002/mabi.201500035

Banka, A. L., Guevara, M. V., Brannon, E. R., Nguyen, N. Q., Song, S., Cady, G., et al. (2023). Cargo-free particles divert neutrophil-platelet aggregates to reduce thromboinflammation. *Nat. Commun.* 14 (1), 2462. doi:10.1038/s41467-023-37990-z

Bao, L., Dou, G., Tian, R., Lv, Y., Ding, F., Liu, S., et al. (2022). Engineered neutrophil apoptotic bodies ameliorate myocardial infarction by promoting macrophage efferocytosis and inflammation resolution. *Bioact. Mater.* 9, 183–197. doi:10.1016/j.bioactmat.2021.08.008

Bauer, M., Gerlach, H., Vogelmann, T., Preissing, F., Stiefel, J., and Adam, D. (2020). Mortality in sepsis and septic shock in europe, north America and Australia between 2009 and 2019-results from a systematic review and meta-analysis. *Crit. Care* 24 (1), 239–9. doi:10.1186/s13054-020-02950-2

Beyer, M., France, J., Lavik, E., Knight, R., and Lewandowski, C., (2022). Unaffected *ex vivo* clotting cascade by experimental hemostatic nanoparticles when introduced in the presence of recombinant tissue plasminogen activator. *Brain Circ.* 8 (4), 228. doi:10.4103/bc.bc_45_22

Brown, A., Stabenfeldt, S. E., Ahn, B., Hannan, R. T., Dhada, K. S., Herman, E. S., et al. (2014). Ultrasoft microgels displaying emergent platelet-like behaviours. *Nat. Mater.* 13 (12), 1108–1114. doi:10.1038/nmat4066

Cánovas-Cervera, I., Nacher-Sendra, E., Osca-Verdegal, R., Dolz-Andrés, E., Beltrán-García, J., Rodríguez-Gimillo, M., et al. (2023). The intricate role of non-coding RNAs in sepsis-associated disseminated intravascular coagulation. *Int. J. Mol. Sci.* 24 (3), 2582. doi:10.3390/ijms24032582

Cap, A. P., and Perkins, J. G. (2011). Lyophilized platelets: challenges and opportunities. *J. Trauma - Inj. Infect. Crit. Care* 70 (5 Suppl. L), 59–60. doi:10.1097/TA.0b013e31821a606d

Casey, L. M., Kakade, S., Decker, J. T., Rose, J. A., Deans, K., Shea, L. D., et al. (2019). Cargo-less nanoparticles program innate immune cell responses to toll-like receptor activation. *Biomaterials* 218 (June), 119333. doi:10.1016/j.biomaterials.2019.119333

Cebo, M., Dittrich, K., Fu, X., Manke, M. C., Emschermann, F., Rheinlaender, J., et al. (2022). Platelet ACKR3/CXCR7 favors antiplatelet lipids over an atherothrombotic lipidome and regulates thromboinflammation. *Blood* 139 (11), 1722–1742. doi:10.1182/blood.2021013097

Chen, J., Song, Y., Wang, Q., Li, Q., Tan, H., Gao, J., et al. (2022). Targeted neutrophil-mimetic liposomes promote cardiac repair by adsorbing proinflammatory cytokines and regulating the immune microenvironment. *J. Nanobiotechnology* 20 (1), 218–317. doi:10.1186/s12951-022-01433-6

Chen, M., Leng, Y., Li, X., Zhao, L., and Qu, Y., (2023). Red blood cells: a potential delivery system. *J. Nanobiotechnology* 21 (1), 288–319. doi:10.1186/s12951-023-02060-5

Choi, S.-H., Kim, S. Y., Kim, K. M., Mony, T. J., Bae, H. J., Kim, M. S., et al. (2023). Fermented sprouts of codonopsis lanceolata suppress LPS-induced inflammatory responses by inhibiting NF-κb signaling pathway in RAW 264.7 macrophages and CD1 mice. *Pharmaceutics* 15 (7), 1793. doi:10.3390/pharmaceutics15071793

Colman, R. W., Flores, D. N., De La Cadena, R. A., Scott, C. F., Cousens, L., Barr, P. J., et al. (1988). Recombinant alpha 1-antitrypsin Pittsburgh attenuates experimental gram-negative septicemia. *Am. J. Pathology* 130 (2), 418–426.

Cruz, M. A., Bohinc, D., Andraska, E. A., Alvikas, J., Raghunathan, S., Masters, N. A., et al. (2023). Nanomedicine platform for targeting activated neutrophils and neutrophil-platelet complexes using an α1-antitrypsin-derived peptide motif. *Nat. Nanotechnol.* 17 (9), 1004–1014. doi:10.1038/s41565-022-01161-w

DeBont, C. M., Boelens, W. C., and Pruijin, G. J. M. (2019). NETosis, complement, and coagulation: a triangular relationship. *Cell. Mol. Immunol.* 16, 19–27. doi:10.1038/s41423-018-0024-0

Dickson, K., and Lehmann, C. (2019). Inflammatory response to different toxins in experimental sepsis models. *Int. J. Mol. Sci.* 20 (18), 4341. doi:10.3390/ijms20184341

Dudnick, R., Martin, P., and Friedman, L. S. (1991). Management of bleeding ulcers. *Med. Clin. N. Am.* 75 (4), 947–965. doi:10.1016/S0025-7125(16)30423-0

Efat, A., Shoeib, S. A., Arafa, A. F., Dawod, A. A., Abd ElHafez, M. A., Abd ElMohsen, E. A., et al. (2021). Thrombo-inflammatory biomarkers to predict sepsis outcome. *Int. J. Immunopathol. Pharmacol.* 35, 205873842110485. doi:10.1177/20587384211048561

El Mohtadi, F., d'Arcy, R., Yang, X., Turhan, Z. Y., Alshamsan, A., and Tirelli, N. (2019). Main chain polysulfoxides as active 'stealth' polymers with additional antioxidant and anti-inflammatory behaviour. *Int. J. Mol. Sci.* 20 (18), 1–14. doi:10.3390/ijms20184583

El-Sherbiny, I., Elkholi, I. E., and Yacoub, M. H. (2014). Tissue plasminogen activator-based clot busting: controlled delivery approaches. *Glob. Cardiol. Sci. Pract.* 2014 (3), 46. doi:10.5339/gcsp.2014.46

Eniola, A. O., and Hammer, D. A. (2005). *In vitro* characterization of leukocyte mimetic for targeting therapeutics to the endothelium using two receptors. *Biomaterials* 26 (34), 7136–7144. doi:10.1016/j.biomaterials.2005.05.005

Fam, S. Y., Chee, C. F., Yong, C. Y., Ho, K. L., Mariatulqabtiah, A. R., and Tan, W. S. (2020). Stealth coating of nanoparticles in drug-delivery systems. *Nanomaterials* 10 (4), 787–818. doi:10.3390/nano10040787

Fernandez-Moure, J., Maisha, N., Lavik, E. B., and Cannon, J. W. (2018). The chemistry of lyophilized blood products. *Bioconjugate Chem.* 29 (7), 2150–2160. doi:10.1021/acs.bioconjchem.8b00271

Fonticoli, L., Diomede, F., Nanci, A., Fontana, A., Della Rocca, Y., Guadarrama Bello, D., et al. (2023). Enriched graphene oxide-polypropylene suture threads buttons modulate the inflammatory pathway induced by Escherichia coli lipopolysaccharide. *Int. J. Mol. Sci.* 24 (7), 6622. doi:10.3390/ijms24076622

Friedrich, B., Auger, J. P., Dutz, S., Cicha, I., Schreiber, E., Band, J., et al. (2021). Hydroxyapatite-coated SPIONs and their influence on cytokine release. *Int. J. Mol. Sci.* 22 (8), 4143. doi:10.3390/ijms22084143

Gaieski, D. F., Edwards, J. M., Kallan, M. J., and Carr, B. G. (2013). Benchmarking the incidence and mortality of severe sepsis in the United States. *Crit. Care Med.* 41 (5), 1167–1174. doi:10.1097/CCM.0b013e31827c09f8

Gao, J., Wang, S., and Wang, Z. (2017). High yield, scalable and remotely drug-loaded neutrophil-derived extracellular vesicles (EVs) for anti-inflammation therapy. *Biomaterials* 135, 62–73. doi:10.1016/j.biomaterials.2017.05.003

Gao, Y., Ikeda-Imafuku, M., Zhao, Z., Joshi, M., and Mitragotri, S. (2023). A polymer-based systemic hemostat for managing uncontrolled bleeding. *Bioeng. Transl. Med.* 8 (3), 1–11. doi:10.1002/btm2.10516

Gao, Y., Sarode, A., Kokoroskos, N., Ukidve, A., Zhao, Z., Guo, S., et al. (2020). A polymer-based systemic hemostatic agent. *Sci. Adv.* 6 (31), 1–12. doi:10.1126/sciadv.aba0588

Gauer, J. S., Ajjan, R. A., and Ariëns, R. A. S. (2022). Platelet–neutrophil interaction and thromboinflammation in diabetes: considerations for novel therapeutic approaches. *J. Am. Heart Assoc.* 11 (20), 1–14. doi:10.1161/JAHA.122.027071

Girish, A., Jolly, K., Alsaadi, N., de la Fuente, M., Recchione, A., An, R., et al. (2022). Platelet-inspired intravenous nanomedicine for injury-targeted direct delivery of thrombin to augment hemostasis in Coagulopathies. *ACS Nano* 16 (10), 16292–16313. doi:10.1021/acsnano.2c05306

Greineder, C. F., Howard, M. D., Carnemolla, R., Cines, D. B., and Muzykantov, V. R. (2013). Advanced drug delivery systems for antithrombotic agents. *Blood* 122 (9), 1565–1575. doi:10.1182/blood-2013-03-453498

Guedes, M., Vieira, S. F., Reis, R. L., Ferreira, H., and Neves, N. M. (2021). Fishroesomes as carriers with antioxidant and anti-inflammatory bioactivities. *Biomed. Pharmacother.* 140 (March), 111680. doi:10.1016/j.biopha.2021.111680

Guo, Y., Patil, N. K., Luan, L., Bohannon, J. K., and Sherwood, E. R. (2018). The biology of natural killer cells during sepsis. *Immunology* 153 (2), 190–202. doi:10.1111/imm.12854

Gurung, S., Perocheau, D., Touramanidou, L., and Baruteau, J. (2021). The exosome journey: from biogenesis to uptake and intracellular signalling. *Cell Commun. Signal.* 19 (1), 47–19. doi:10.1186/s12964-021-00730-1

Hahm, J., Kim, J., and Park, J. (2021). Strategies to enhance extracellular vesicle production. *Tissue Eng. Regen. Med.* 18 (4), 513–524. doi:10.1007/s13770-021-00364-x

Harm, S., Lohner, K., Fichtinger, U., Schildböck, C., Zottl, J., and Hartmann, J. (2019). Blood compatibility—an important but often forgotten aspect of the characterization of antimicrobial peptides for clinical application. *Int. J. Mol. Sci.* 20 (21), 5426. doi:10.3390/ijms20215426

Helms, J., Iba, T., Connors, J. M., Gando, S., Levi, M., Meziani, F., et al. (2023). How to manage Coagulopathies in critically ill patients. *Intensive Care Med.* 49 (3), 273–290. doi:10.1007/s00134-023-06980-6

Hemmingsen, L., Giordani, B., Pettersen, A. K., Vitali, B., Basnet, P., and Škalko-Basnet, N. (2021). Liposomes-in-Chitosan hydrogel boosts potential of chlorhexidine in biofilm eradication *in vitro*. *Carbohydr. Polym.* 262, 117939. doi:10.1016/j.carbpol.2021.117939

Huang, M., Cai, S., and Su, J. (2019). The pathogenesis of sepsis and potential therapeutic targets. *Int. J. Mol. Sci.* 20 (21), 5376. doi:10.3390/ijms20215376

Huang, Y., Gu, B., Salles-Crawley, I. I., Taylor, K. A., Yu, L., Ren, J., et al. (2021). Fibrinogen-mimicking, multiarm nanovesicles for human thrombus-specific delivery of tissue plasminogen activator and targeted thrombolytic therapy. *Sci. Adv.* 7 (23), eabf9033. doi:10.1126/sciadv.abf9033

Jackson, S. P., Darbousset, R., and Schoenwaelder, S. M. (2019). Thromboinflammation: challenges of therapeutically targeting coagulation and other host defense mechanisms. *Blood* 133 (9), 906–918. doi:10.1182/blood-2018-11-882993

Jin, L., Chen, C., Li, Y., Yuan, F., Gong, R., Wu, J., et al. (2019). A biodegradable Mg-based alloy inhibited the inflammatory response of THP-1 cell-derived macrophages through the TRPM7–PI3K–AKT1 signaling Axis. *Front. Immunol.* 10 (December), 1–15. doi:10.3389/fimmu.2019.02798

Kadir, R. R. A., and Bayraktutan, U. (2020). Urokinase plasminogen activator: a potential thrombolytic agent for ischaemic stroke. *Cell. Mol. Neurobiol.* 40 (3), 347–355. doi:10.1007/s10571-019-00737-w

Karami, Z., Mehrzad, J., Akrami, M., and Hosseinkhani, S. (2023). Anti-inflammation-based treatment of atherosclerosis using gliclazide-loaded biomimetic nanoghosts. *Sci. Rep.* 13 (1), 13880–13912. doi:10.1038/s41598-023-41136-y

Kelley, W. J., Safari, H., Lopez-Cazares, G., and Eniola-Adefeso, O. (2016). Vascular-targeted nanocarriers: design considerations and strategies for successful treatment of atherosclerosis and other vascular diseases. *Wiley Interdiscip. Rev. Nanomedicine Nanobiotechnology* 8 (6), 909–926. doi:10.1002/wnan.1414

Kemp, M. M., and Linhardt, R. J. (2010). Heparin-based nanoparticles. *WIRES Nanomed Nanobiotechnol* 2, 77–87. doi:10.1002/wnan.68

Kim, S., Rho, S. J., Song, S. H., and Kim, C. H., (2021). Biocompatible N-Acetyl-Nanoconstruct alleviates lipopolysaccharide-induced acute lung injury *in vivo*. *Sci. Rep.* 11 (1), 22662–22712. doi:10.1038/s41598-021-01624-5

Kim, W., Haller, C., Dai, E., Wang, X., Hagemeyer, C. E., Liu, D. R., et al. (2015). Targeted antithrombotic protein micelles. *Angew. Chem. - Int. Ed.* 54 (5), 1461–1465. doi:10.1002/anie.201408529

Kolesnikova, T., Skirtach, A. G., and Möhwald, H. (2013). Red blood cells and polyelectrolyte multilayer capsules: natural carriers versus polymer-based drug delivery vehicles. *Expert Opin. Drug Deliv.* 10 (1), 47–58. doi:10.1517/17425247.2013.730516

Kong, F., Lee, B. H., and Kun, W. (2019). 5-Hydroxymethylfurfural mitigates lipopolysaccharide-stimulated inflammation via suppression of MAPK, NF-κb and MTOR activation in RAW 264.7 cells. *Molecules* 24 (2), 275. doi:10.3390/molecules24020275

Kurtuldu, F., Kaňková, H., Beltrán, A. M., Liverani, L., Galusek, D., and Boccaccini, A. R. (2021). Anti-inflammatory and antibacterial activities of cerium-containing mesoporous bioactive glass nanoparticles for drug-free biomedical applications. *Mater. Today Bio* 12, 100150. doi:10.1016/j.mtbio.2021.100150

Kurtuldu, F., Mutlu, N., Boccaccini, A. R., and Galusek, D. (2022). Gallium containing bioactive materials: a review of anticancer, antibacterial, and osteogenic properties. *Bioact. Mater.* 17 (October 2021), 125–146. doi:10.1016/j.bioactmat.2021.12.034

Landsem, A., Emblem, Å., Lau, C., Christiansen, D., Gerogianni, A., Karlsen, B. O., et al. (2022). Complement C3b contributes to Escherichia coli-induced platelet aggregation in human whole blood. *Front. Immunol.* 13 (December), 1–16. doi:10.3389/fimmu.2022.1020712

Lasola, J., Kamdem, H., McDaniel, M. W., and Pearson, R. M. (2020). Biomaterial-driven immunomodulation: cell biology-based strategies to mitigate severe inflammation and sepsis. *Front. Immunol.* 11, 1726. doi:10.3389/fimmu.2020.01726

Lee, M. R., Kim, J., Park, J., Choi, J., Song, B., Choi, Y., et al. (2020). Protective role of fermented mulberry leave extract in LPS-induced inflammation and autophagy of RAW264.7 macrophage cells. *Mol. Med. Rep.* 22 (6), 4685–4695. doi:10.3892/mmr.2020.11563

Luque, G. C., Moya, M., Picchio, M. L., Bagnarello, V., Valerio, I., Bolaños, J., et al. (2023). Polyphenol iongel patches with antimicrobial, antioxidant and anti-inflammatory properties. *Polymers* 15 (5), 1076. doi:10.3390/polym15051076

Lutz, H., Hu, S., Dinh, P. U., and Cheng, K. (2019). Cells and cell derivatives as drug carriers for targeted delivery. *Med. Drug Discov.* 3, 100014. doi:10.1016/j.medidd.2020.100014

Lutz, H., Popowski, K. D., Dinh, P. U. C., and Cheng, K. (2021). Advanced nanobiomedical approaches to combat coronavirus disease of 2019. *Adv. NanoBiomed Res.* 1 (3), 2000063. doi:10.1002/anbr.202000063

Ma, J., Chen, X., Wang, X., Liang, J., Guo, L., Su, Y., et al. (2023). The accuracy of soluble urokinase-type plasminogen activator receptor for the diagnosis of neonatal sepsis: a meta-analysis. *Front. Med.* 10 (April), 1–9. doi:10.3389/fmed.2023.1169114

Maisha, N., Coombs, T., and Lavik, E. (2020). Development of a sensitive assay to screen nanoparticles *in vitro* for complement activation. *ACS Biomaterials Sci. Eng.* 6 (9), 4903–4915. doi:10.1021/acsbiomaterials.0c00722

Maisha, N., Naik, N., Okesola, M., Coombs, T., Zilberberg, R., Pandala, N., et al. (2021). Engineering PEGylated polyester nanoparticles to reduce complement-mediated infusion reaction. *Bioconjugate Chem.* 32 (10), 2154–2166. doi:10.1021/acs.bioconjchem.1c00339

Marsh, J. N., Hu, G., Scott, M. J., Zhang, H., Goette, M. J., Gaffney, P. J., et al. (2011). A fibrin-specific thrombolytic nanomedicine approach to acute ischemic stroke. *Nanomedicine* 6 (4), 605–615. doi:10.2217/nnm.11.21

Meng, D., Luo, M., and Liu, B. (2021). The role of CLEC-2 and its ligands in thromboinflammation. *Front. Immunol.* 12 (June), 688643. doi:10.3389/fimmu.2021.688643

Michel, T., Hentges, F., and Zimmer, J. (2012). Consequences of the crosstalk between monocytes/macrophages and natural killer cells. *Front. Immunol.* 3 (JAN), 403–406. doi:10.3389/fimmu.2012.00403

Mihalko, E. P., Nellenbach, K., Krishnakumar, M., Moiseiwitsch, N., Sollinger, J., Cooley, B. C., et al. (2022). Fibrin-specific poly(N-isopropylacrylamide) nanogels for targeted delivery of tissue-type plasminogen activator to treat thrombotic complications are well tolerated *in vivo*. *Bioeng. Transl. Med.* 7 (2), 1–16. doi:10.1002/btm2.10277

Mihalko, E. P., Sandry, M., Mininni, N., Nellenbach, K., Deal, H., Daniele, M., et al. (2021). Fibrin-modulating nanogels for treatment of disseminated intravascular coagulation. *Blood Adv.* 5 (3), 613–627. doi:10.1182/bloodadvances.2020003046

Muro, S., Garnacho, C., Champion, J. A., Leferovich, J., Gajewski, C., Schuchman, E. H., et al. (2008). Control of endothelial targeting and intracellular delivery of therapeutic enzymes by modulating the size and shape of ICAM-1-targeted carriers. *Mol. Ther.* 16 (8), 1450–1458. doi:10.1038/mt.2008.127

Muzykantov, V. R. (2013). Drug delivery carriers on the fringes: natural red blood cells versus synthetic multilayered capsules. *Expert Opin. Drug Deliv.* 10 (1), 1–4. doi:10.1517/17425247.2013.750292

Nandi, S., Mihalko, E., Nellenbach, K., Castaneda, M., Schneible, J., Harp, M., et al. (2021). Synthetic platelet microgels containing fibrin knob B mimetic motifs enhance clotting responses. *Adv. Ther.* 4 (5), 2100010. doi:10.1002/adtp.202100010

Nedelec, J. M., Courtheoux, L., Jallot, E., Kinowski, C., Lao, J., Laquerriere, P., et al. (2008). Materials doping through sol-gel chemistry: a little something can make a big difference. *J. Sol-Gel Sci. Technol.* 46 (3), 259–271. doi:10.1007/s10971-007-1665-0

Ng, C. Y., Kee, L. T., Al-Masawa, M. E., Lee, Q. H., Subramaniam, T., Kok, D., et al. (2022). Scalable production of extracellular vesicles and its therapeutic values: a review. *Int. J. Mol. Sci.* 23 (14), 7986. doi:10.3390/ijms23147986

Nunoi, H., Xie, P., Nakamura, H., Aratani, Y., Fang, J., Nishimura, T., et al. (2022). Treatment with polyethylene glycol–conjugated fungal d-amino acid oxidase reduces lung inflammation in a mouse model of chronic granulomatous disease. *Inflammation* 45 (4), 1668–1679. doi:10.1007/s10753-022-01650-z

Perrella, G., Nagy, M., Watson, S. P., and Heemskerk, J. W. (2021). Platelet GPVI (glycoprotein VI) and thrombotic complications in the venous system. *Arteriosclerosis, Thrombosis, Vasc. Biol.* 41 (11), 2681–2692. doi:10.1161/ATVBAHA.121.316108

Peter, K., Graeber, J., Kipriyanov, S., Zewe-Welschof, M., Runge, M. S., Kubler, W., et al. (2000). Construction and functional evaluation of a single-chain antibody fusion protein with fibrin targeting and thrombin inhibition after activation by factor xa. *Circulation* 101 (10), 1158–1164. doi:10.1161/01.CIR.101.10.1158

Petroková, H., Mašek, J., Kuchař, M., Vítečková Wünschová, A., Štikarová, J., Bartheldyová, E., et al. (2019). Targeting human thrombus by liposomes modified with anti-fibrin protein binders. *Pharmaceutics* 11 (12), 642. doi:10.3390/pharmaceutics11120642

Petzold, T., Zhang, Z., Ballesteros, I., Saleh, I., Polzin, A., Thienel, M., et al. (2022). Neutrophil 'plucking' on megakaryocytes drives platelet production and boosts cardiovascular disease. *Immunity* 55 (12), 2285–2299.e7. doi:10.1016/j.immuni.2022.10.001

Popowski, K., Lutz, H., Hu, S., George, A., Dinh, P.-U., and Cheng, K. (2020). Exosome therapeutics for lung regenerative medicine. *J. Extracell. Vesicles* 9 (1), 1785161. doi:10.1080/20013078.2020.1785161

Rafat, M., Rotenstein, L. S., You, J. O., and Auguste, D. T. (2012). Dual functionalized PVA hydrogels that adhere endothelial cells synergistically. *Biomaterials* 33 (15), 3880–3886. doi:10.1016/j.biomaterials.2012.02.017

Raghunathan, S., Rayes, J., and Sen Gupta, A. (2022). Platelet-inspired nanomedicine in hemostasis thrombosis and thromboinflammation. *J. Thrombosis Haemostasis* 20 (7), 1535–1549. doi:10.1111/jth.15734

Rudd, K. E., Johnson, S. C., Agesa, K. M., Shackelford, K. A., Tsoi, D., Kievlan, D. R., et al. (2020). Global, regional, and national sepsis incidence and mortality, 1990–2017: analysis for the global burden of disease study. *Lancet* 395 (10219), 200–211. doi:10.1016/S0140-6736(19)32989-7

Runge, M. S., Bode, C., Matsueda, G. R., and Haber, E. (1987). Antibody-enhanced thrombolysis: targeting of tissue plasminogen activator *in vivo*. *Proc. Natl. Acad. Sci. U. S. A.* 84 (21), 7659–7662. doi:10.1073/pnas.84.21.7659

Sanrattana, W., Smits, S., Barendrecht, A. D., van Kleef, N. D., El Otmani, H., Zivkovic, M., et al. (2022). Targeted serpin (TaSER): a dual-action antithrombotic agent that targets platelets for serpin delivery. *J. Thrombosis Haemostasis* 20 (2), 353–365. doi:10.1111/jth.15554

Sekhon, U., Swingle, K., Girish, A., Luc, N., de la Fuente, M., Alvikas, J., et al. (2022). Platelet-mimicking procoagulant nanoparticles augment hemostasis in animal models of bleeding. *Sci. Transl. Med.* 14 (629), 1–12. doi:10.1126/scitranslmed.abb8975

Semeraro, N., Ammollo, C. T., Semeraro, F., and Colucci, M. (2010). Sepsis-associated disseminated intravascular coagulation and thromboembolic disease. *Mediterr. J. Hematol. Infect. Dis.* 2 (3), e2010024. doi:10.4084/MJHID.2010.024

Senchenkova, E. Y., Ansari, J., Becker, F., Vital, S. A., Al-Yafeai, Z., Sparkenbaugh, E. M., et al. (2019). Novel role for the AnxA1-fpr2/ALX signaling Axis as a key regulator of platelet function to promote resolution of inflammation. *Circulation* 140 (4), 319–335. doi:10.1161/CIRCULATIONAHA.118.039345

Sharma, A., Ray, S., Mamidipalli, R., Jain, R., Ghalaut, M. S., and Choudhury, S. (2020). A comparative study of the diagnostic and prognostic utility of soluble urokinase-type plasminogen activator receptor and procalcitonin in patients with sepsis and systemic inflammation response syndrome. *Indian J. Crit. Care Med.* 24 (4), 245–251. doi:10.5005/jp-journals-10071-23385

Shi, C., Wang, X., Wang, L., Meng, Q., Guo, D., Chen, L., et al. (2020). A nanotrap improves survival in severe sepsis by attenuating hyperinflammation. *Nat. Commun.* 11 (1), 3384–3413. doi:10.1038/s41467-020-17153-0

Singer, M., Deutschman, C. S., Seymour, C. W., Shankar-Hari, M., Annane, D., Bauer, M., et al. (2016). The third international consensus definitions for sepsis and septic shock (Sepsis-3). *JAMA* 315 (8), 801–810. doi:10.1001/jama.2016.0287

Sloos, P. H., Vulliamy, P., van 't Veer, C., Gupta, A. S., Neal, M. D., Brohi, K., et al. (2022). Platelet dysfunction after trauma: from mechanisms to targeted treatment. *Transfusion* 62 (S1), S281–S300. doi:10.1111/trf.16971

Sobczynski, D. J., Fish, M. B., Fromen, C. A., and Carasco-Teja, M. (2017). Drug carrier interaction with blood: a critical aspect for highefficient vascular-targeted drug delivery systems. *Physiology Behav.* 176 (5), 139–148. doi:10.4155/TDE.15.38

Sun, M., and Gupta, A. S. (2020). Vascular nanomedicine: current status, opportunities, and challenges. *Seminars Thrombosis Hemostasis* 46 (5), 524–544. doi:10.1055/s-0039-1692395

Sun, X., Liu, Z., Welsher, K., Robinson, J. T., Goodwin, A., Zaric, S., et al. (2008). Nano-graphene oxide for cellular imaging and drug delivery. *Nano Res.* 1 (3), 203–212. doi:10.1007/s12274-008-8021-8

Tan, Q., He, L., Meng, X., Wang, W., Pan, H., Yin, W., et al. (2021). Macrophage biomimetic nanocarriers for anti-inflammation and targeted antiviral treatment in COVID-19. *J. Nanobiotechnology* 19 (1), 173–216. doi:10.1186/s12951-021-00926-0

Tang, T. T., Lv, L. L., Wang, B., Cao, J. Y., Feng, Y., Li, Z. L., et al. (2019). Employing macrophage-derived microvesicle for kidney-targeted delivery of dexamethasone: an efficient therapeutic strategy against renal inflammation and fibrosis. *Theranostics* 9 (16), 4740–4755. doi:10.7150/thno.33520

Tanne, D., Kasner, S. E., Demchuk, A. M., Koren-Morag, N., Hanson, S., Grond, M., et al. (2002). Markers of increased risk of intracerebral hemorrhage after intravenous recombinant tissue plasminogen activator therapy for acute ischemic stroke in clinical practice: the multicenter rt-PA acute stroke survey. *Circulation* 105 (14), 1679–1685. doi:10.1161/01.CIR.0000012747.53592.6A

Thorén, F. B., Riise, R. E., Ousbäck, J., Della Chiesa, M., Alsterholm, M., Marcenaro, E., et al. (2012). Human NK cells induce neutrophil apoptosis via an NKp46-and fas-dependent mechanism. *J. Immunol.* 188 (4), 1668–1674. doi:10.4049/jimmunol.1102002

Vagionas, D., Papadakis, D. D., Politou, M., Koutsoukou, A., and Vasileiadis, I. (2022). Thromboinflammation in sepsis and heparin: a review of literature and pathophysiology. *Vivo* 36 (6), 2542–2557. doi:10.21873/invivo.12991

Van Der Meel, R., Fens, M. H., Vader, P., van Solinge, W. W., Eniola-Adefeso, O., and Schiffelers, R. M. (2014). Extracellular vesicles as drug delivery systems: lessons from the liposome field. *J. Control. Release* 195, 72–85. doi:10.1016/j.jconrel.2014.07.049

Vishwanath, N., Whitaker, C., Allu, S., Clippert, D., Jouffroy, E., Hong, J., et al. (2022). Silver as an antibiotic-independent antimicrobial: review of current formulations and clinical relevance. *Surg. Infect.* 23 (9), 769–780. doi:10.1089/sur.2022.229

Vuong, T. T., Rønning, S. B., Suso, H. P., Schmidt, R., Prydz, K., Lundström, M., et al. (2017). The extracellular matrix of eggshell displays anti-inflammatory activities through NF-κB in LPS-triggered human immune cells. *J. Inflamm. Res.* 10, 83–96. doi:10.2147/JIR.S130974

Wang, J., Hajizadeh, N., Moore, E. E., McIntyre, R. C., Moore, P. K., Veress, L. A., et al. (2020). Tissue plasminogen activator (TPA) treatment for COVID-19 associated acute respiratory distress syndrome (ARDS): a case series. *J. Thrombosis Haemostasis* 18 (7), 1752–1755. doi:10.1111/jth.14828

Weiss, S. L., Peters, M. J., Alhazzani, W., Agus, M. S. D., Flori, H. R., Inwald, D. P., et al. (2020). Surviving sepsis campaign international guidelines for the management of septic shock and sepsis-associated organ dysfunction in children. *Intensive Care Med.* 46 (s1), 10–67. doi:10.1007/s00134-019-05878-6

WHO (2023). Sepsis. World Health Organization. 2023. Available at: https://www.who.int/news-room/fact-sheets/detail/sepsis.

Witwer, K. W., and Wolfram, J. (2021). Extracellular vesicles versus synthetic nanoparticles for drug delivery. *Nat. Rev. Mater.* 6 (2), 103–106. doi:10.1038/s41578-020-00277-6

Wu, H., Wang, Y., Zhang, Y., Xu, F., Chen, J., Duan, L., et al. (2020). Breaking the vicious loop between inflammation, oxidative stress and coagulation, a novel anti-thrombus insight of nattokinase by inhibiting LPS-induced inflammation and oxidative stress. *Redox Biol.* 32 (March), 101500. doi:10.1016/j.redox.2020.101500

Xu, X., Huang, X., Zhang, Y., Shen, S., Feng, Z., Dong, H., et al. (2020). Self-regulated hirudin delivery for anticoagulant therapy. *Sci. Adv.* 6 (41), 1–10. doi:10.1126/sciadv.abc0382

Yan, F., Zhong, Z., Wang, Y., Feng, Y., Mei, Z., Li, H., et al. (2020). Exosome-based biomimetic nanoparticles targeted to inflamed joints for enhanced treatment of rheumatoid arthritis. *J. Nanobiotechnology* 18 (1), 115–15. doi:10.1186/s12951-020-00675-6

Yan, X., Fang, W. W., Xue, J., Sun, T. C., Dong, L., Zha, Z., et al. (2019). Thermoresponsive *in situ* forming hydrogel with sol-gel irreversibility for effective methicillin-resistant Staphylococcus aureus infected wound healing. *ACS Nano* 13 (9), 10074–10084. doi:10.1021/acsnano.9b02845

Ye, W., Wang, N., Hu, K., Zhang, L., Liu, A., Pan, C., et al. (2018). Bio-inspired microcapsule for targeted antithrombotic drug delivery. *RSC Adv.* 8 (48), 27253–27259. doi:10.1039/c8ra04273j

Yu, M., Hong, K., Adili, R., Mei, L., Liu, L., He, H., et al. (2022). Development of activated endothelial targeted high-density lipoprotein nanoparticles. *Front. Pharmacol.* 13 (August), 1–14. doi:10.3389/fphar.2022.902269

Zhang, M., Chen, H., Zhang, W., Liu, Y., Ding, L., Gong, J., et al. (2023). Biomimetic remodeling of microglial riboflavin metabolism ameliorates cognitive impairment by modulating neuroinflammation. *Adv. Sci.* 10 (12), 1–21. doi:10.1002/advs.202300180

Zhang, Z., Yan, T., Ren, D., Zhou, J., Liu, L., Li, J., et al. (2023). Low-molecular-weight heparin therapy reduces 28-day mortality in patients with sepsis-3 by improving inflammation and coagulopathy. *Front. Med.* 10, 1157775. doi:10.3389/fmed.2023.1157775

Zou, Z., Huang, J. j., Luan, Y. y., Yang, Z. j., Zhou, Z. p., Zhang, J. j., et al. (2022). Early prophylactic anticoagulation with heparin alleviates mortality in critically ill patients with sepsis: a retrospective analysis from the MIMIC-IV database. *Burns Trauma* 10, tkac029. doi:10.1093/burnst/tkac029

frontiers | Frontiers in Biomaterials Science

TYPE Mini Review
PUBLISHED 10 January 2024
DOI 10.3389/fbiom.2023.1336842

OPEN ACCESS

EDITED BY
Jenny Robinson,
University of Washington, United States

REVIEWED BY
Rupak Madu Rajachar,
Marine Ecology and Telemetry Research (MarEcoTel), United States
Mary Beth Browning Monroe,
Syracuse University, United States

*CORRESPONDENCE
Anita Shukla,
anita_shukla@brown.edu

RECEIVED 11 November 2023
ACCEPTED 13 December 2023
PUBLISHED 10 January 2024

CITATION
Gomez Casas C and Shukla A (2024), Engineering immunomodulatory biomaterials to combat bacterial infections.
Front. Front. Biomater. Sci. 2:1336842.
doi: 10.3389/fbiom.2023.1336842

Engineering immunomodulatory biomaterials to combat bacterial infections

Carolina Gomez Casas and Anita Shukla*

School of Engineering, Center for Biomedical Engineering, Brown University, Providence, RI, United States

Modulating the immune system using engineered materials is an emerging strategy to combat bacterial infections. Bacteria adopt immune evasion strategies to ensure their survival, ultimately leading to persistence and recurrence of infections. With a rise in antimicrobial resistance and a decrease in antibiotic efficacy, host-directed therapies using immunomodulatory biomaterials are a promising approach to infection management. Here, we review biomaterials developed to modulate the immune system, with an emphasis on innate immunity. We specifically highlight the recent implementation of functionalized surfaces for immunomodulation, including metal ion releasing coatings, stimuli-responsive polymeric coatings, and interleukin releasing surfaces. We also describe immunomodulatory nanoparticles, including lipid-based nanoparticles, biomimetic nanoparticles, and inorganic nanocarriers. Lastly, we explore immunomodulatory hydrogels used primarily for the treatment of wound infections. These approaches offer new strategies for treating bacterial infections and enhancing existing antimicrobial approaches, all while avoiding complications associated with antimicrobial resistance.

KEYWORDS

biomaterials, immunotherapy, immunoengineering, nanoparticles, functionalized surfaces, hydrogels, bacteria, infection

1 Introduction

Bacterial infections are among the leading causes of death worldwide. In 2019, 1 in 8 deaths was caused by these infections, leading to 7.7 million deaths globally (Ikuta et al., 2022; Murray et al., 2022). The immune system, comprising of adaptive and innate immunity, serves as the primary host-defense mechanism against bacterial pathogens. The adaptive immune response eliminates pathogens by enabling the recognition of "non-self" antigens, mediated by antigen-specific T cells and B cells (Marshall et al., 2018). The innate response is a non-specific first line of defense that involves the rapid recruitment of phagocytic cells (e.g., macrophages, neutrophils, dendritic cells), basophils, eosinophils, and mast cells to the site of infection. Most innate immune effector cells possess pattern-recognition receptors (PRR) that recognize pathogen-associated molecular patterns (PAMPs) (Marshall et al., 2018; Paludan et al., 2020). Upon PAMP recognition, the various PRR families activate inflammatory signaling cascades, including the secretion of cytokines. Hematopoietin (Class I) cytokines, interferons (INFs), and tumor necrosis factor (TNF) cytokine families are key regulators of inflammation (Kany et al., 2019; Cho, 2022). Macrophages are one of the essential innate immune cells. The undifferentiated M0 macrophages have the ability

to polarize into pro-inflammatory, M1, and anti-inflammatory, M2 macrophages (Yao et al., 2019). The ability of macrophages to phagocytose and kill bacteria reduces the risk of infection (Li et al., 2019).

In addition to evading antibiotic mediated clearance, bacteria can manipulate innate immunity to promote infections (Diacovich and Gorvel, 2010). For example, they can modulate apoptosis/autophagy by altering apoptotic signaling pathways, interfere with Toll-like receptors (TLRs) to dampen inflammation, and they can alter reactive oxygen species (ROS) and reactive nitrogen intermediates (RNI) by producing ROS and RNI scavengers that ultimately suppresses innate immune activation (Finlay and McFadden, 2006; Diacovich and Gorvel, 2010; Chiang et al., 2018). Bacterial biofilms can also activate or impair macrophage activity, leading to macrophage secretion of pro-inflammatory and anti-inflammatory cytokines, and alter genetic switches to affect the activity of immune cells (González et al., 2018; Le et al., 2018; Kaya et al., 2020; Guzmán-Soto et al., 2021).

As the efficacy of existing antibiotics is rapidly declining in the face of rising antimicrobial resistance, there is growing interest in host-directed approaches against infections (Kalelkar et al., 2021; Super et al., 2021). With numerous advances spanning decades, the versatility of biomaterials enables the development of unique approaches to regulate the immune system with the potential to combat bacterial infections (Figure 1). Immunomodulatory biomaterials have been explored for a variety of disease states, with cancer and viral infections having garnered the greatest attention (Backlund et al., 2023; Yousefpour et al., 2023); the role of these materials in bacterial infections has been less explored. These materials can have a tremendous impact in combating bacterial infections and improving outcomes following these infections. Here, we explore biomaterials approaches taken for immunomodulation to treat bacterial infections, with a primary focus on the innate immune response. Specifically, we describe recent strategies involving functionalized surfaces, nanoparticle therapies, and hydrogels.

2 Immune modulation via functional surfaces

Surface functionalization strategies, including the application of biomaterials as surface coatings, can serve as a host immunomodulatory approach to mitigate bacterial infections, particularly implant-associated infections. These infections involve the attachment of bacteria on implant surfaces and eventual biofilm formation (Wang and Shukla, 2022; Deusenbery et al., 2023). Many strategies including metal ion releasing coatings, stimuli-responsive coatings, and interleukin releasing surfaces have shown great promise and are described here.

2.1 Metal ion releasing coatings

Copper (Cu) is among the most common elements integrated in metallic surface coatings for immunomodulation. It is involved in maintaining immune function by inducing macrophage polarization to an M1 phenotype (Huang et al., 2018; Wang et al., 2021; Huo et al., 2023). Cu also contributes to the generation of endogenous and exogenous ROS, enhancing bacterial killing (Li et al., 2016; Huang et al., 2019). In one example aimed at trapping and killing methicillin-resistant *Staphylococcus aureus* (MRSA) (a common source of implant-associated infections), Liu et al. developed a porous Cu-nanoparticle coated sulfonated polyetheretherketone (SPEEK) orthopedic implant (Liu et al., 2019). They found that the surface functionalized implant served as an immunomodulator by promoting M1 macrophage polarization. *In vitro* incubation of murine macrophage cell line, RAW264.7, on the orthopedic

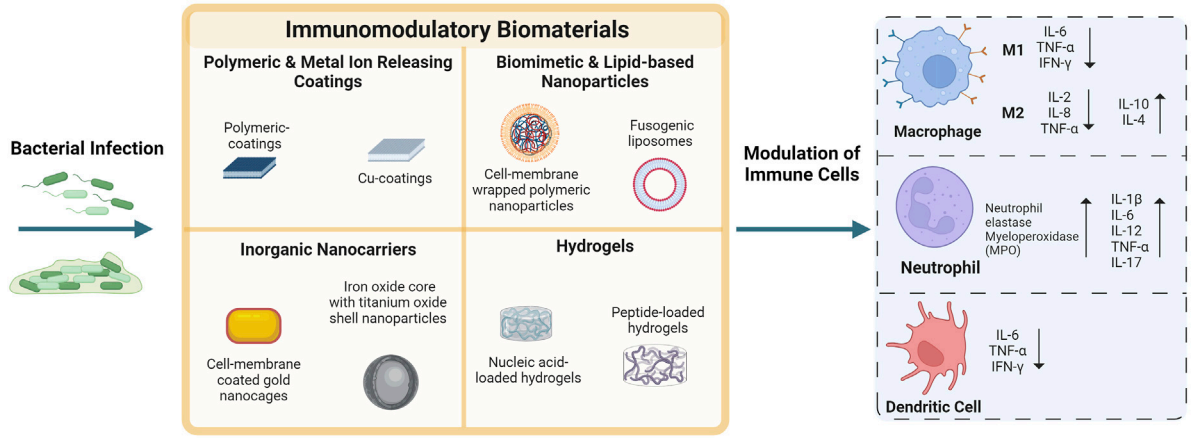

FIGURE 1
Biomaterials approaches to modulate the innate immune system and combat bacterial infections. Various biomaterial strategies have been used to modulate host immunity ranging from functionalized surfaces to nanoparticles and hydrogels, which are discussed in this article. Immune cells that are often the target of this biomaterials-mediated immune modulation, include macrophages (M1 and M2 polarization), neutrophils, and dendritic cells. The inflammatory response during a bacterial infection can be investigated by examining the secretion of pro-inflammatory and anti-inflammatory factors, including cytokines. Some of the common factors studied are shown in this figure (interleukin (IL), interferon-gamma (INF-γ), tumor necrosis factor-alpha (TNF-α), neutrophil elastase myeloperoxidase (MPO)). Created with BioRender.com.

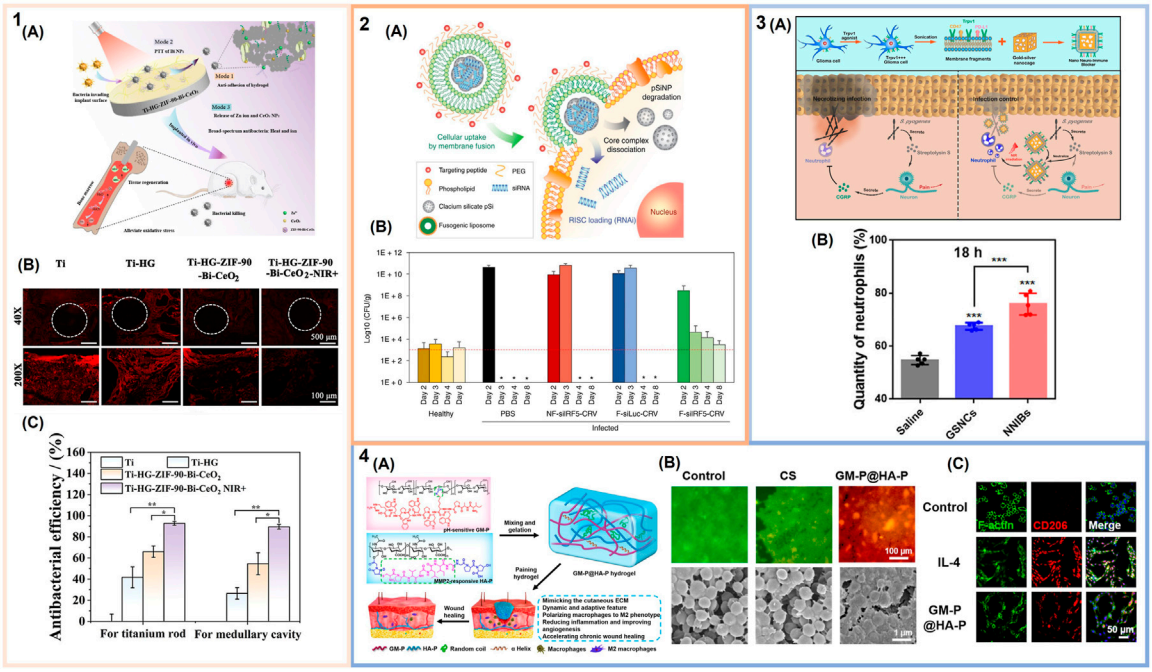

FIGURE 2
Immunomodulatory biomaterials for the treatment of bacterial infections. (1) Near infrared (NIR)-responsive polymer-based coatings: (1A) Schematic of immunomodulatory and antibacterial coating for the treatment of implant-associated infections. (1B) Quantification of the antibacterial efficacy of uncoated titanium (Ti) implants, Ti implants coated with hyaluronic acid/gelatin hydrogels, and Ti implants coated with these hydrogels loaded with bismuth (Bi) nanoparticles, zeolitic imidazolate framework-90 (ZIF-90), and cerium oxide (CeO_2) nanoparticles with and without NIR irradiation in a mouse femoral *Staphylococcus aureus* implant infection model. (1C) Anti-inflammatory effect of Ti-based implants assessed via fluorescence staining of intracellular reactive oxygen species (ROS) (red indicates generation of ROS) (adapted with permission from Ding et al. (2022). Copyright 2023 American Chemical Society). (2) Immunomodulatory lipid-based nanoparticles: (2A) Schematic illustrating the fusogenic nanparticle formulation and proposed macrophage uptake mechanism. (2B) *S. aureus* colony enumeration from healthy and infected lungs upon nanoparticle treatment (dashed line represents the average CFU from healthy mice) (adapted with permission from Kim et al. (2018). Copyright 2018; Springer Nature). (3) Inorganic nanocarriers to combat bacterial infections: (3A) Schematic of nano neuro-immune blockers (NNIBs). Top shows fabrication and implementation of the glioma cell membranes on gold-silver nanocages. Bottom depicts the proposed mechanism of action to neutralize *Streptococcus pyogenes* infections. (3B) Quantification of neutrophil recruitment to the site of infection after treatment with NNIBs or non-membrane coated nanocage core (GSNCs) and NIR irradiation (adapted with permission from Zhao et al. (2019). Copyright 2019 American Chemical Society). (4) Immunomodulatory hydrogel wound dressing: (4A) Schematic of the extracellular matrix mimetic hydrogels. (4B) Representative images of methicillin-resistant *S. aureus* (MRSA) biofilms upon treatment with the hydrogel (GM-P@HA-P) and a chitosan (CS) hydrogel control. Top shows the biofilms after laser scanning confocal microscopy (live bacteria = green; membrane damaged bacteria = red). Bottom shows scanning electron microscopy images of these biofilms. (4C) M2 polarization of RAW264.7 macrophages upon treatment with the immunomodulatory hydrogel. Laser scanning confocal microscopy images of the CD206 surface marker for M2 polarization in controls stimulated with or without IL-4 and macrophages treated with hydrogels. (From Liu et al. (2022).

implants with Cu functionalization revealed higher levels of inflammatory cytokine secretion (e.g., TNF-α and IL-6) compared to polyetheretherketone (PEEK) and SPEEK without Cu functionalization. Similarly, *in vitro* co-culture of RAW264.7 macrophages and MRSA exhibited greater macrophage phagocytic ability of MRSA compared to PEEK and SPEEK without Cu functionalization. Huang et al. developed a hybrid metal/ceramic coating on a titanium (Ti) substrate with micro- and nanoscale topographical features that incorporated Cu^{2+} (Huang et al., 2018). This surface coating was found to exhibit immunomodulatory properties, including M1 macrophage polarization indicated by increased production of IL-6 and inhibition of anti-inflammatory cytokines, IL-4 and IL-10, compared to non-Cu containing surfaces. Incubation of RAW264.7 macrophages on the Cu^{2+} containing surfaces with *S. aureus* led to an increase in macrophage phagocytic activity and enhanced bacterial killing after being phagocytosed in comparison to non-Cu containing surfaces.

Immunomodulatory coatings with metal ions have been investigated for treatment of osteomyelitis. One example consisted of using PEEK implants coated with Cu^{2+}-chelated polydopamine to modulate inflammation (Lyu et al., 2022). RAW264.7 cells incubated with the Cu-doped implants exhibited upregulation of pro-inflammatory genes (inducible nitric oxide synthase (*iNOS*) and *TNF*). Applying these materials in a rat implant MRSA osteomyelitis model showed a 50% decrease in bacterial burden along with mild inflammation for the Cu-containing implant compared to the PEEK-only implant. In another study aimed at treatment of osteomyelitis, Li et al. developed a cobalt (Co) doped titanium dioxide (TiO_2) semiconductor-based Ti implant coating to interrupt extracellular and intracellular proton transfer, while also releasing Co^{2+} ions that enhance the innate immune response via M1 macrophage polarization

(Li et al., 2019). The Co-containing implants significantly reduced bacterial adhesion to the implant compared with non-Co doped implants in a rat femoral MRSA osteomyelitis model.

2.2 Stimuli-responsive polymeric coatings

Polymeric coatings, comprised of both synthetic and biologically-derived polymers, generally offer broad physicochemical tunability, can serve as a depot for various bioactive components, and can be rendered responsive to intrinsic and extrinsic stimuli. For example, photothermally responsive polymeric coatings have been developed using photoresponsive polymers and/or nanocarriers for immunomodulation. In an attempt to eliminate bacterial biofilms, Ding et al. coated a polydopamine-modified Ti substrate with a hyaluronic acid/gelatin hydrogel coating loaded with a composite consisting of zeolitic imidazolate framework-90, cerium oxide (CeO_2) nanoparticles, and bismuth (Bi) nanoparticles (Ding et al., 2022). The hydrogel coating provided an anti-adhesive surface, while the Bi nanoparticles were included as the near infrared red (NIR)-responsive photothermal agent, and both the Bi and CeO_2 nanoparticles from the composite served as ROS scavengers (Figures 1A, 2). In a mouse femoral *S. aureus* implant infection model, Ti implants coated with the composite hydrogel led to an ~90% or greater reduction in *S. aureus* colonies in both the medullary cavity and on the Ti implant upon NIR irradiation compared to a Ti implant alone; use of the composite hydrogel coated implant also showed increased ROS scavenging (Figures 1B, C, 2). Similarly, ROS-scavenging coating formulations including nitric oxide releasing polymer coatings have been developed to modulate bacteria-induced inflammation (Pant et al., 2018; Li et al., 2020; Sapkota et al., 2023).

In another study by Ding et al., an antibiofouling polymeric coating of konjac gum and gelatin served as a carrier for self-assembled nanoparticles consisting of a hydrophobic tyrosine core and a hydrophilic tannic acid (TA) outer shell (Ding et al., 2023). The TA-derived nanocarrier exhibited NIR-responsive photothermal properties; upon NIR-irradiation moderate hyperthemia was observed along with bacterial cell membrane damage *in vitro*. Ti implants functionalized with this photothermally responsive coating were examined in a rat implant-associated *S. aureus* infection model, inflammatory cell infiltration of the tissue surrounding the implant showed a significant reduction in bacteria and neutrophils for irradiated coated implants compared to non-coated Ti implants. Further, immunofluorescent staining of macrophages in regions surrounding the implant 7 days post-infection confirmed that the coating had the ability to modulate inflammation by reversing M1 macrophages to an M2 phenotype, not observed for the non-coated Ti implants.

2.3 Interleukin releasing surfaces

Given their prominent role in inflammation, several strategies for antibacterial implant surface functionalization have directly incorporated either pro-inflammatory (e.g., IL-23 and IL-12) or anti-inflammatory (e.g., IL-4) cytokines (He et al., 2021; Lian et al., 2022; Pizarek et al., 2023). In one such example, He et al. designed a dual drug release system that eliminates bacteria, while also mitigating the pro-inflammatory response that occurs during this process. The drug delivery system comprised of IL-4 loaded TiO_2 nanotubes coated with a catechol-modified methacrylated gelatin hydrogel containing calcium peroxide (CaO_2) nanoparticles, which was applied to a Ti implant surface (He et al., 2021). CaO_2 nanoparticles undergo rapid degradation in acidic infection environments to yield hydrogen peroxide (H_2O_2); this ROS production, while eliminating bacterial pathogens, can also cause an undesirable increase in pro-inflammatory processes. IL-4 release from the coating helps mitigate inflammation by modulating the innate immune response. The coated Ti implants were examined in a murine subcutaneous *S. aureus* infection model. Samples were placed along the infection site, following which the soft-tissue was sutured. The CaO_2 nanoparticles embedded in the hydrogel coating with the IL-4 loaded TiO_2 nanotubes were found to reduce neutrophil infiltration during the bacterial infection compared to non-coated Ti implants. Additionally, enhanced expression of CD206 positive cells (a M2 macrophage marker) and decrease in iNOS and TNF-α levels upon treatment with the dual-drug delivery system coated implant, demonstrated M2 macrophage polarization compared to treatment with non-coated Ti implants.

In another interleukin delivery approach, Lian et al. fabricated a three-layer coating on a Ti implant. Here, a layer of sodium alginate containing IL-12-loaded liposomes was sandwiched between layers of the mineral, vaterite. The vaterite layers were loaded with the antibiotic, vancomycin (Lian et al., 2022). *In vitro*, the functionalized Ti surfaces reduced bacterial growth by 82%–87% and 89%–93% for methicllin-sensitive *S. aureus* (MSSA) and MRSA, respectively. To examine the sustained release of IL-12 and the ability of the three-layer coating to rebuild the immune system, a rat tibia implant MRSA infection model was implemented. The coated Ti was implanted in a MRSA infected tibia channel. The sustained release of IL-12 from the liposomes regulated the innate and adaptive immune responses. Specifically, IL-12 stimulated interferon-gamma (IFN-γ), which promotes differentiation of T cells to pro-inflammatory T helper type 1 cells (Vignali and Kuchroo, 2012). Overall, there was an ~99% bacterial clearance in the bone tissue treated with the three-layer coating implant compared to the infection-only with no implant control, the vaterite-only implant, and the vaterite with sodium-alginate implant.

3 Immunomodulatory nanoparticles

Nanoparticles have been widely explored for a range of drug delivery applications and are of great interest in immunomodulation due to the plethora of formulation approaches and tunability of composition (Ben-Akiva et al., 2018; Yousefpour et al., 2023). Several polymeric nanoparticle formulations have been developed for use in bacterial infections that focus on reprogramming macrophages from an

M2 phenotype to M1 via specific cytokine delivery (Yu et al., 2023) or inducing macrophage ROS production (Dai et al., 2022), among other approaches. We focus here on lipid-based nanoparticles, along with membrane wrapped polymeric nanoparticles, which are among the most commonly utilized immunomodulatory nanoparticles explored in the context of bacterial infection, along with discussing some of the inorganic nanoparticle approaches recently reported.

3.1 Lipid-based nanoparticles

Several immunomodulatory lipid-based nanoparticles have been designed to either interact with and eliminate the effects of bacterial toxins or for gene therapy. Examples of the former include the development of high density lipoprotein-mimicking nanoparticles (Foit and Thaxton, 2016) and antimicrobial peptide, LL37, containing lipid nanoparticles (Garcia-Orue et al., 2016) that neutralize lipopolysaccharide (LPS) toxins upon exposure to Gram-negative bacteria.

The most extensive use of lipid nanoparticles targeting the immune response during bacterial infections has been for the delivery of small interfering RNA (siRNA). Kim et al. developed a liposome formulation that fuses with the macrophage cell membrane to deliver siRNA to the perinuclear region against the M1 macrophage interferon regulatory factor 5 (*IRF5*) gene (Figure 2:2A) (Kube et al., 2017; Kim et al., 2018). These fusogenic nanocarriers were found to effectively eliminate a murine lung infection established using a lethal dose of *S. aureus* (Figure 2:2B). Two possible mechanisms of action were hypothesized, one involving inhibition of pro-inflammatory cytokine release from M1 macrophages and one in which M2 macrophage polarization occurs leading to an anti-inflammatory, restorative response. The same nanoparticle platform was later applied as a broad-spectrum immunotherapy against both MRSA and *Pseudomonas aeruginosa* murine muscle and lung infection models, respectively. In a MRSA-induced abscess infection model, there was a large decrease in abscess size along with significant bacterial clearance upon intravenous injection of the targeted fusogenic nanoparticle compared to controls including treatment with a buffer, a non-fusogenic liposome, a fusogenic liposome with siRNA against luciferase, and vancomycin, a common antibiotic. In the *P. aeruginosa* lung infection model, similar reduction in bacterial infection and decrease in inflammation was observed upon intravenous injection of the treatment with fusogenic nanoparticles, compared to treatment with a buffer, a non-fusogenic liposome, a fusogenic liposome with siRNA against luciferase, and tobramycin, a common antibiotic used to treat *P. aeruginosa* infections. The fusogenic nanocarrier proved to be a highly versatile anti-inflammatory therapeutic (Kim et al., 2021).

Messenger RNA (mRNA) has also been encapsulated inside lipid-nanoparticles to promote the production of specific proteins of interest and enhance macrophage bactericidal activity (Hou et al., 2021). For example, mRNA that encodes for antimicrobial peptide, IB367, and lysosomal protein, cathepsin B (CatB), was encapsulated in vitamin C lipid nanoparticles. These nanoparticles were used to condition macrophages prior to adoptive transfer in immunosupressed mice for the treatment of multidrug-resistant bacteria-induced sepsis (Hou et al., 2020). The CatB served as a transporter for the IB367, into lysosomes that can then fuse with phagocytic macrophages and elicit bactericidal activity. Notably, Hou et al. demonstrated a significantly greater bacterial clearance and improved mouse survival rate for immunosupressed septic mice induced by multi-drug resistant *S. aureus* and *Escherichia coli* receiving the engineered macrophages compared with macrophages that were not treated with the mRNA nanoparticles.

3.2 Biomimetic nanoparticles

Hybrid polymeric nanoparticles functionalized with cell membrane-derived coatings are being developed extensively for immunomodulation applications including treatment of bacterial infections due to their biomimetic properties. Polymeric nanoparticles have been wrapped with membranes derived from macrophages, neutrophils, natural killer cells, and red blood cells. For example, poly (lactic-co-glycolic acid) (PLGA) nanoparticle cores were wrapped with cell membranes derived from the J774 mouse macrophage cell line (Thamphiwatana et al., 2017). These macrophage-like nanoparticles were able to bind and neutralize LPS. Additionally, the membrane-wrapped nanoparticles sequestered pro-inflammatory cytokines, IL-6 and TNF-α, upon intraperitoneal injection in a murine uropathogenic *E. coli* sepsis model.

Membrane wrapped nanoparticles have also been used in bacterial infection vaccination strategies. Wang et al. demonstrated one of the earliest examples using red blood cell membranes to incorporate α-hemolysin (Hla), a major MRSA virulence factor. The toxin containing membrane was wrapped over a PLGA nanoparticle core (Wang et al., 2016). Subcutaneous injection of these nanoparticles in mice induced an anti-Hla antibody response, which led to protection of the mice upon introduction of a MRSA skin infection compared to those that received unloaded nanoparticles or a buffer control.

Recently, Li et al. developed a hyaluronic acid–polyethylenimine nanoparticle loaded with important microRNAs (miRNAs) identified as responsive for the immunoprotective effects of tumor-derived exosomes produced upon murine exposure to LPS (Li et al., 2022). These biomimetic nanoparticles enabled the therapeutic implementation of these miRNAs without necessitating the use of tumor-derived exosomes. The nanoparticles elicited sepsis protection and reduction in pro-inflammatory cytokine levels (IL-6, IL-8, and TNF-α) by ~50% in a non-human primate LPS-induced sepsis model compared to the control group that had received a saline infusion.

3.3 Inorganic nanocarriers

Inorganic nanocarriers have also been implemented to enhance the innate immune response and combat bacterial infections. Gold nanocages in particular, have been explored due to their versatility, from surface functionalization to photothermal properties. Zhao et al. developed nano neuro-

immune blockers (NNIBs) consisting of gold-silver nanocages coated with a glioma-derived cell-membrane. The cell membrane component contained virulence-factor inhibitors, developed to both reduce pain and enhance the innate immune response in necrotizing infections, while the nanocage itself served as a platform for photothermal therapy to regulate inflammation (Figure 2:3A) (Zhao et al., 2019). The nanocage formulation exhibits immunomodulatory properties by targeting calcitonin gene-related peptide (CGRP), which is associated with reduced immune cell recruitment. Subcutaneous injection of the NNIBs with NIR irradiation in a murine subcutaneous *Streptococcus pyogenes* infection model demonstrated CGRP inhibition and enhanced neutrophil recruitment by ~80% compared to a saline control group (Figure 2:3B). In another study, enhanced bacterial recognition through TLRs was achieved by adding a macrophage coating on a gold nanocage (Wang et al., 2018). In a murine subcutaneous *S. aureus* infection model, the immune cell coating increased retention at the site of infection by ~65% compared to a buffer control group due to the ability of the macrophage-nanoparticle coating to target and recognize PAMPs.

In addition to gold, other photoresponsive inorganic nanocarriers have been explored for immunodulation during bacterial infections. Zhang et al. developed a photocatalytic nanoparticle with an iron oxide (Fe_3O_4) core and TiO_2 shell that was used to take advantage of the macrophage recruitment process which follows neutrophil apoptosis and release of inflammatory cytokines (Zhang et al., 2020). The photocatalytic activity of these nanoparticles was confirmed *in vitro* using near-ultraviolet (NUV) irradiation of the neutrophils loaded with these particles via phagocytosis. In this case, NUV irradiation led to ROS production, inducing neutrophil apoptosis. Macrophage migration in response to ROS production was also assessed *in vitro* using a transwell assay, showing RAW264.7 cells migration towards the photocatalytic nanoparticles following NUV irradiation. Further, nanoparticle accumulation at an infection site was investigated in a MRSA necrotizing fasciitis mouse model. The photocatalytic nanoparticles showed an 85% localized accumulation 24 h post-treatment (involving a 3 min NUV irradiation immediately after sample injection), thus preventing bacterial infection and potential dissemination into the blood.

4 Immunomodulatory hydrogels

Immunomodulatory hydrogels for use in bacterial infections have focused primarily on the treatment of bacterial wound infections. Hydrogels are highly hydrated biomaterials that can be designed to be biocompatible and exhibit a wide range of tunable properties, including the ability to respond to environmental stimuli (Correa et al., 2021; Alkekhia et al., 2022). Nucleic acid-loaded hydrogels that reprogram macrophages to an M2 phenotype have been developed (Gribova et al., 2022), along with hydrogels that target IL-1 cytokines to regulate the inflammatory response in diabetic wound biofilm infections (Zhou et al. (2023)). Here, we briefly expand on peptide functionalized immunomodulatory hydrogels.

In one design, a hydroxyethyl cellulose hydrogel was functionalized with thrombin-derived C-terminal peptide, TCP-25, to treat *P. aeruginosa* and *S. aureus* wound infections (Puthia et al., 2020). TCP-25 exhibits both antimicrobial and anti-inflammatory properties via association with PAMPs, leading to a reduction in pro-inflammatory processes. In a porcine *S. aureus* partial thickness wound infection model, the TCP-25 hydrogel treatment was applied daily as a dressing for 4 days. Pigs treated with this hydrogel were found to exhibit a significant decrease in bacterial load and reduction in the secretion of IL-6 and TNF-α after 48 h compared to treatment with a non-TCP-25 functionalized hydrogel. In another study, Liu et al. synthesized extracellular matrix mimetic hydrogels that promote M2 macrophage polarization for the treatment of MRSA chronic wound infections. The hybrid hydrogel consisted of an antibacterial peptide conjugated to glucomannan (GM-P) using an acid-labile linkage to control local inflammation mediated by GM interaction with mannose receptors on macrophages (Liu et al., 2022) (Figure 2:4A). Additionally, to support tissue regeneration, the hydrogel incorporated a collagen tripeptide conjugated to hyaluronic acid via a matrix-metalloproteinase sensitive linkage (HA-P). This hydrogel exhibited ~98% and ~97% bacterial killing in a bacterial biofilm *in vitro* assay with MRSA and *E. coli*, respectively (Figure 2:4B). Further, the immunomodulatory hydrogel led to macrophage M2 polarization, with an increase in IL-4 production, helping to clear the infection in an *in vivo* MRSA-infected chronic wound healing model (Figure 2:4C).

5 Conclusion and outlook

Engineering immunomodulatory biomaterials is a promising strategy for the treatment of bacterial infections. It is now widely recognized that we have entered a post-antibiotic era (Kwon and Powderly (2021)). Alternative strategies to antibiotic treatment are critical for effective treatment of bacterial infections and to prevent further emergence of multi-drug resistant bacteria or “superbugs”. Development of immunomodulatory biomaterials that target the host-immune response are the likely solution to this global healthcare crisis. Here, we discussed biomaterials-mediated immunomodulation approaches from surface functionalization to nanoparticle therapies and hydrogels. While the majority of biomaterials explored thus far for treatment of bacterial infections have focused on macrophage polarization to control inflammation, it is important to note that additional myeloid and lymphoid cells are also promising immune response targets. Further research in bacterial immune evasion and the host-pathogen response is imperative for the development of successful host-directed therapies to modulate the immune system during bacterial infections.

Author contributions

CGC: Conceptualization, Investigation, Writing–original draft, Writing–review and editing. AS: Funding acquisition, Resources, Writing–original draft, Writing–review and editing.

Funding

The author(s) declare financial support was received for the research, authorship, and/or publication of this article. AS and CGC acknowledge support from Brown University and the Office of Naval Research (award N00014-22-1-2336).

Acknowledgments

AS and CGC thank Brown University Ph.D. student, Veronica LaMastro for useful discussions related to article content. Figure 1 was created with BioRender.com.

Conflict of interest

The authors declare that the research was conducted in the absence of any commercial or financial relationships that could be construed as a potential conflict of interest.

Publisher's note

References

Alkekhia, D., Larose, C., and Shukla, A. (2022). *β*-Lactamase-Responsive hydrogel drug delivery platform for bacteria-triggered cargo release. *ACS Appl. Mater. Interfaces* 14, 27538–27550. doi:10.1021/ACSAMI.2C02614

Backlund, C., Jalili-Firoozinezhad, S., Kim, B., and Irvine, D. J. (2023). Biomaterials-mediated engineering of the immune system. *Annu. Rev. Immunol.* 41, 153–179. doi:10.1146/ANNUREV-IMMUNOL-101721-040259

Ben-Akiva, E., Est Witte, S., Meyer, R. A., Rhodes, K. R., and Green, J. J. (2018). Polymeric micro- and nanoparticles for immune modulation. *Biomaterials Sci.* 7, 14–30. doi:10.1039/C8BM01285G

Chiang, C. Y., Uzoma, I., Moore, R. T., Gilbert, M., Duplantier, A. J., and Panchal, R. G. (2018). Mitigating the impact of antibacterial drug resistance through host-directed therapies: current progress, outlook, and challenges. *mBio* 9, e01932-17. doi:10.1128/MBIO.01932-17

Cho, J. Y. (2022). Recent advancements in microbial diversity: macrophages and their role in inflammation. *J. Clin. Exp. Hepatol.* 1–461. doi:10.1016/C2019-0-04189-1

Correa, S., Grosskopf, A. K., Lopez Hernandez, H., Chan, D., Yu, A. C., Stapleton, L. M., et al. (2021). Translational applications of hydrogels. *Chem. Rev.* 121, 11385–11457. doi:10.1021/ACS.CHEMREV.0C01177

Dai, X., Liu, X., Yang, L., Yuan, S., Xu, Q., Li, Y., et al. (2022). pH-Responsive non-antibiotic polymer prodrugs eradicate intracellular infection by killing bacteria and regulating immune response. *Colloids surfaces. B, Biointerfaces* 220, 112889. doi:10.1016/J.COLSURFB.2022.112889

Deusenbery, C., Gomez Casas, C., and Shukla, A. (2023). pH-responsive swelling micelles for the treatment of methicillin-resistant *Staphylococcus aureus* biofilms. *ACS Appl. Polym. Mater.* 5, 7400–7410. doi:10.1021/ACSAPM.3C01307

Diacovich, L., and Gorvel, J. P. (2010). Bacterial manipulation of innate immunity to promote infection. *Nat. Rev. Microbiol.* 8, 117–128. doi:10.1038/nrmicro2295

Ding, Y., Liu, G., Liu, S., Li, X., Xu, K., Liu, P., et al. (2023). A multifunction hydrogel-coating engineered implant for rescuing biofilm infection and boosting osseointegration by macrophage-related immunomodulation. *Adv. Healthc. Mater.* 12, 2300722. doi:10.1002/ADHM.202300722

Ding, Y., Ma, R., Liu, G., Li, X., Xu, K., Liu, P., et al. (2022). Fabrication of a new hyaluronic acid/gelatin nanocomposite hydrogel coating on titanium-based implants for treating biofilm infection and excessive inflammatory response. *ACS Appl. Mater. Interfaces* 15, 13783–13801. doi:10.1021/ACSAMI.2C23320

Finlay, B. B., and McFadden, G. (2006). Anti-Immunology: evasion of the host immune system by bacterial and viral pathogens. *Cell* 124, 767–782. doi:10.1016/J.CELL.2006.01.034

Foit, L., and Thaxton, C. S. (2016). Synthetic high-density lipoprotein-like nanoparticles potently inhibit cell signaling and production of inflammatory mediators induced by lipopolysaccharide binding Toll-like receptor 4. *Biomaterials* 100, 67–75. doi:10.1016/J.BIOMATERIALS.2016.05.021

Garcia-Orue, I., Gainza, G., Girbau, C., Alonso, R., Aguirre, J. J., Pedraz, J. L., et al. (2016). LL37 loaded nanostructured lipid carriers (NLC): a new strategy for the topical treatment of chronic wounds. *Eur. J. Pharm. Biopharm.* 108, 310–316. doi:10.1016/J.EJPB.2016.04.006

González, J. F., Hahn, M. M., and Gunn, J. S. (2018). Chronic biofilm-based infections: skewing of the immune response. *Pathogens Dis.* 76, 23. doi:10.1093/FEMSPD/FTY023

Gribova, V., Petit, L., Kocgozlu, L., Seguin, C., Fournel, S., Kichler, A., et al. (2022). Polyarginine as a simultaneous antimicrobial, immunomodulatory, and miRNA delivery agent within polyanionic hydrogel. *Macromol. Biosci.* 22, 2200043. doi:10.1002/MABI.202200043

Guzmán-Soto, I., McTiernan, C., Gonzalez-Gomez, M., Ross, A., Gupta, K., Suuronen, E. J., et al. (2021). Mimicking biofilm formation and development: recent progress in *in vitro* and *in vivo* biofilm models. *iScience* 24, 102443. doi:10.1016/J.ISCI.2021.102443

He, Y., Li, K., Yang, X., Leng, J., Xu, K., Yuan, Z., et al. (2021). Calcium peroxide nanoparticles-embedded coatings on anti-inflammatory TiO2 nanotubes for bacteria elimination and inflammatory environment amelioration. *Small* 17, 2102907. doi:10.1002/SMLL.202102907

Hou, X., Zaks, T., Langer, R., and Dong, Y. (2021). Lipid nanoparticles for mRNA delivery. *Nat. Rev. Mater.* 6, 1078–1094. doi:10.1038/s41578-021-00358-0

Hou, X., Zhang, X., Zhao, W., Zeng, C., Deng, B., McComb, D. W., et al. (2020). Vitamin lipid nanoparticles enable adoptive macrophage transfer for the treatment of multidrug-resistant bacterial sepsis. *Nat. Nanotechnol.* 15, 41–46. doi:10.1038/s41565-019-0600-1

Huang, Q., Li, X., Elkhooly, T. A., Liu, X., Zhang, R., Wu, H., et al. (2018). The Cu-containing TiO2 coatings with modulatory effects on macrophage polarization and bactericidal capacity prepared by micro-arc oxidation on titanium substrates. *Colloids Surfaces B Biointerfaces* 170, 242–250. doi:10.1016/J.COLSURFB.2018.06.020

Huang, Q., Ouyang, Z., Tan, Y., Wu, H., and Liu, Y. (2019). Activating macrophages for enhanced osteogenic and bactericidal performance by Cu ion release from micro/nano-topographical coating on a titanium substrate. *Acta Biomater.* 100, 415–426. doi:10.1016/J.ACTBIO.2019.09.030

Huo, S., Lyu, Z., Su, X., Wang, F., Liu, J., Liu, S., et al. (2023). Formation of a novel Cu-containing bioactive glass nano-topography coating with strong bactericidal capability and bone regeneration. *Compos. Part B Eng.* 253, 110521. doi:10.1016/J.COMPOSITESB.2023.110521

Ikuta, K. S., Swetschinski, L. R., Robles Aguilar, G., Sharara, F., Mestrovic, T., Gray, A. P., et al. (2022). Global mortality associated with 33 bacterial pathogens in 2019: a systematic analysis for the Global Burden of Disease Study 2019. *Lancet* 400, 2221–2248. doi:10.1016/S0140-6736(22)02185-7

Kalelkar, P. P., Riddick, M., and García, A. J. (2021). Biomaterial-based antimicrobial therapies for the treatment of bacterial infections. *Nat. Rev. Mater.* 7, 39–54. doi:10.1038/s41578-021-00362-4

Kany, S., Vollrath, J. T., and Relja, B. (2019). Cytokines in inflammatory disease. *Int. J. Mol. Sci.* 20, 6008. doi:10.3390/IJMS20236008

Kaya, E., Grassi, L., Benedetti, A., Maisetta, G., Pileggi, C., Di Luca, M., et al. (2020). *In vitro* interaction of *Pseudomonas aeruginosa* biofilms with human peripheral blood mononuclear cells. *Front. Cell. Infect. Microbiol.* 10, 187. doi:10.3389/fcimb.2020.00187

Kim, B., Pang, H. B., Kang, J., Park, J. H., Ruoslahti, E., and Sailor, M. J. (2018). Immunogene therapy with fusogenic nanoparticles modulates macrophage response to *Staphylococcus aureus*. *Nat. Commun.* 9, 1969–2013. doi:10.1038/s41467-018-04390-7

Kim, B., Yang, Q., Chan, L. W., Bhatia, S. N., Ruoslahti, E., and Sailor, M. J. (2021). Fusogenic porous silicon nanoparticles as a broad-spectrum immunotherapy against bacterial infections. *Nanoscale Horizons* 6, 330–340. doi:10.1039/D0NH00624F

Kube, S., Hersch, N., Naumovska, E., Gensch, T., Hendriks, J., Franzen, A., et al. (2017). Fusogenic liposomes as nanocarriers for the delivery of intracellular proteins. *Langmuir* 33, 1051–1059. doi:10.1021/acs.langmuir.6b04304

Kwon, J. H., and Powderly, W. G. (2021). The post-antibiotic era is here. *Science* 373, 471. doi:10.1126/SCIENCE.ABL5997

Le, K. Y., Park, M. D., and Otto, M. (2018). Immune evasion mechanisms of Staphylococcus epidermidis biofilm infection. *Front. Microbiol.* 9, 359. doi:10.3389/fmicb.2018.00359

Li, J., Liu, W., Kilian, D., Zhang, X., Gelinsky, M., and Chu, P. K. (2019). Bioinspired interface design modulates pathogen and immunocyte responses in biomaterial-centered infection combination therapy. *Mater. Horizons* 6, 1271–1282. doi:10.1039/C8MH01606B

Li, M., Ma, Z., Zhu, Y., Xia, H., Yao, M., Chu, X., et al. (2016). Toward a molecular understanding of the antibacterial mechanism of copper-bearing titanium alloys against *Staphylococcus aureus*. *Adv. Healthc. Mater.* 5, 557–566. doi:10.1002/ADHM.201500712

Li, Y., Liu, X., Li, B., Zheng, Y., Han, Y., Chen, D. F., et al. (2020). Near-infrared light triggered phototherapy and immunotherapy for elimination of methicillin-resistant *Staphylococcus aureus* biofilm infection on bone implant. *ACS Nano* 14, 8157–8170. doi:10.1021/ACSNANO.0C01486

Li, Y., Zhang, H., Chen, C., Qiao, K., Li, Z., Han, J., et al. (2022). Biomimetic immunosuppressive exosomes that inhibit cytokine storms contribute to the alleviation of sepsis. *Adv. Mater.* 34, 2108476. doi:10.1002/ADMA.202108476

Lian, Q., Zheng, S., Shi, Z., Li, K., Chen, R., Wang, P., et al. (2022). Using a degradable three-layer sandwich-type coating to prevent titanium implant infection with the combined efficient bactericidal ability and fast immune remodeling property. *Acta Biomater.* 154, 650–666. doi:10.1016/J.ACTBIO.2022.10.033

Liu, W., Gao, R., Yang, C., Feng, Z., Ou-Yang, W., Pan, X., et al. (2022). ECM-mimetic immunomodulatory hydrogel for methicillin-resistant Staphylococcus aureus-infected chronic skin wound healing. *Sci. Adv.* 8, 7006. doi:10.1126/SCIADV.ABN7006

Liu, W., Li, J., Cheng, M., Wang, Q., Qian, Y., Yeung, K. W., et al. (2019). A surface-engineered polyetheretherketone biomaterial implant with direct and immunoregulatory antibacterial activity against methicillin-resistant *Staphylococcus aureus*. *Biomaterials* 208, 8–20. doi:10.1016/J.BIOMATERIALS.2019.04.008

Lyu, Z., Zhao, Y., Huo, S., Wang, F., Meng, X., Yuan, Z., et al. (2022). Mussel-inspired dopamine-CuII coated polyetheretherketone surface with direct and immunomodulatory effect to facilitate osteogenesis, angiogenesis, and antibacterial ability. *Mater. Des.* 222, 111069. doi:10.1016/J.MATDES.2022.111069

Marshall, J. S., Warrington, R., Watson, W., and Kim, H. L. (2018). An introduction to immunology and immunopathology. *Allergy, Asthma Clin. Immunol.* 14, 49–10. doi:10.1186/s13223-018-0278-1

Murray, C. J., Ikuta, K. S., Sharara, F., Swetschinski, L., Robles Aguilar, G., Gray, A., et al. (2022). Global burden of bacterial antimicrobial resistance in 2019: a systematic analysis. *Lancet* 399, 629–655. doi:10.1016/S0140-6736(21)02724-0

Paludan, S. R., Pradeu, T., Masters, S. L., and Mogensen, T. H. (2020). Constitutive immune mechanisms: mediators of host defence and immune regulation. *Nat. Rev. Immunol.* 21, 137–150. doi:10.1038/s41577-020-0391-5

Pant, J., Goudie, M. J., Chaji, S. M., Johnson, B. W., and Handa, H. (2018). Nitric oxide releasing vascular catheters for eradicating bacterial infection. *J. Biomed. Mater. Res. Part B Appl. Biomaterials* 106, 2849–2857. doi:10.1002/JBM.B.34065

Pizarek, J. A., Fischer, N. G., and Aparicio, C. (2023). Immunomodulatory IL-23 receptor antagonist peptide nanocoatings for implant soft tissue healing. *Dent. Mater.* 39, 204–216. doi:10.1016/J.DENTAL.2023.01.001

Puthia, M., Butrym, M., Petrlova, J., Strömdahl, A. C., Andersson, M., Kjellström, S., et al. (2020). A dual-action peptide-containing hydrogel targets wound infection and inflammation. *Sci. Transl. Med.* 12, 6601. doi:10.1126/SCITRANSLMED.AAX6601

Sapkota, A., Mondal, A., Chug, M. K., and Brisbois, E. J. (2023). Biomimetic catheter surface with dual action NO-releasing and generating properties for enhanced antimicrobial efficacy. *J. Biomed. Mater. Res. Part A* 111, 1627–1641. doi:10.1002/JBM.A.37560

Super, M., Doherty, E. J., Cartwright, M. J., Seiler, B. T., Langellotto, F., Dimitrakakis, N., et al. (2021). Biomaterial vaccines capturing pathogen-associated molecular patterns protect against bacterial infections and septic shock. *Nat. Biomed. Eng.* 6, 8–18. doi:10.1038/s41551-021-00756-3

Thamphiwatana, S., Angsantikul, P., Escajadillo, T., Zhang, Q., Olson, J., Luk, B. T., et al. (2017). Macrophage-like nanoparticles concurrently absorbing endotoxins and proinflammatory cytokines for sepsis management. *Proc. Natl. Acad. Sci. U. S. A.* 114, 11488–11493. doi:10.1073/PNAS.1714267114

Vignali, D. A., and Kuchroo, V. K. (2012). IL-12 family cytokines: immunological playmakers. *Nat. Immunol.* 13, 722–728. doi:10.1038/ni.2366

Wang, C., Wang, Y., Zhang, L., Miron, R. J., Liang, J., Shi, M., et al. (2018). Pretreated macrophage-membrane-coated gold nanocages for precise drug delivery for treatment of bacterial infections. *Adv. Mater.* 30, 1804023. doi:10.1002/ADMA.201804023

Wang, F., Fang, R. H., Luk, B. T., Hu, C.-M. J., Thamphiwatana, S., Dehaini, D., et al. (2016). Nanoparticle-based antivirulence vaccine for the management of methicillin-resistant *Staphylococcus aureus* skin infection. *Adv. Funct. Mater.* 26, 1628–1635. doi:10.1002/ADFM.201505231

Wang, P., Yuan, Y., Xu, K., Zhong, H., Yang, Y., Jin, S., et al. (2021). Biological applications of copper-containing materials. *Bioact. Mater.* 6, 916–927. doi:10.1016/J.BIOACTMAT.2020.09.017

Wang, Y., and Shukla, A. (2022). Bacteria-responsive biopolymer-coated nanoparticles for biofilm penetration and eradication. *Biomaterials Sci.* 10, 2831–2843. doi:10.1039/D2BM00361A

Yao, Y., Xu, X. H., and Jin, L. (2019). Macrophage polarization in physiological and pathological pregnancy. *Front. Immunol.* 10, 792. doi:10.3389/FIMMU.2019.00792

Yousefpour, P., Ni, K., and Irvine, D. J. (2023). Targeted modulation of immune cells and tissues using engineered biomaterials. *Nat. Rev. Bioeng.* 1, 107–124. doi:10.1038/s44222-022-00016-2

Yu, Y. J., Yan, J. H., Chen, Q. W., Qiao, J. Y., Peng, S. Y., Cheng, H., et al. (2023). Polymeric nano-system for macrophage reprogramming and intracellular MRSA eradication. *J. Control. Release* 353, 591–610. doi:10.1016/J.JCONREL.2022.12.014

Zhang, P., Zhao, Q., Shi, M., Yin, C., Zhao, Z., Shen, K., et al. (2020). Fe3O4@TiO2-Laden neutrophils activate innate immunity via photosensitive reactive oxygen species release. *Nano Lett.* 20, 261–271. doi:10.1021/ACS.NANOLETT.9B03777

Zhao, Q., Wang, J., Yin, C., Zhang, P., Zhang, J., Shi, M., et al. (2019). Near-infrared light-sensitive nano neuro-immune blocker capsule relieves pain and enhances the innate immune response for necrotizing infection. *Nano Lett.* 19, 5904–5914. doi:10.1021/ACS.NANOLETT.9B01459

Zhou, J., Mei, J., Liu, Q., Xu, D., Wang, X., Zhang, X., et al. (2023). Spatiotemporal on–off immunomodulatory hydrogel targeting NLRP3 inflammasome for the treatment of biofilm-infected diabetic wounds. *Adv. Funct. Mater.* 33, 2211811. doi:10.1002/ADFM.202211811

frontiers | Frontiers in Biomaterials Science

TYPE Review
PUBLISHED 02 February 2024
DOI 10.3389/fbiom.2024.1348165

OPEN ACCESS

EDITED BY
Silviya Petrova Zustiak,
Saint Louis University, United States

REVIEWED BY
Mai Ngo,
Boston University, United States
Ian Woods,
Royal College of Surgeons in Ireland, Ireland

*CORRESPONDENCE
Rachael W. Sirianni,
rachael.sirianni@umassmed.edu
Sarah E. Stabenfeldt,
sarah.stabenfeldt@asu.edu

RECEIVED 01 December 2023
ACCEPTED 15 January 2024
PUBLISHED 02 February 2024

CITATION
Simmons A, Mihalek O, Bimonte Nelson HA, Sirianni RW and Stabenfeldt SE (2024), Acute brain injury and nanomedicine: sex as a biological variable.
Front. Front. Biomater. Sci. 3:1348165.
doi: 10.3389/fbiom.2024.1348165

Acute brain injury and nanomedicine: sex as a biological variable

Amberlyn Simmons[1], Olivia Mihalek[2], Heather A. Bimonte Nelson[3], Rachael W. Sirianni[1,2]* and Sarah E. Stabenfeldt[1]*

[1]School of Biological and Health Systems Engineering, Arizona State University, Tempe, AZ, United States, [2]Department of Neurological Surgery, UMass Chan Medical School, Worcester, MA, United States, [3]Department of Psychology, Arizona State University, Phoenix, AZ, United States

Sex as a biological variable has been recognized for decades to be a critical aspect of the drug development process, as differences in drug pharmacology and toxicity in female *versus* male subjects can drive the success or failure of new therapeutics. These concepts in development of traditional drug systems have only recently begun to be applied for advancing nanomedicine systems that are designed for drug delivery or imaging in the central nervous system (CNS). This review provides a comprehensive overview of the current state of two fields of research - nanomedicine and acute brain injury—centering on sex as a biological variable. We highlight areas of each field that provide foundational understanding of sex as a biological variable in nanomedicine, brain development, immune response, and pathophysiology of traumatic brain injury and stroke. We describe current knowledge on female *versus* male physiology as well as a growing number of empirical reports that directly address sex as a biological variable in these contexts. In sum, the data make clear two key observations. First, the manner in which sex affects nanomedicine distribution, toxicity, or efficacy is important, complex, and depends on the specific nanoparticle system under considerations; second, although field knowledge is accumulating to enable us to understand sex as a biological variable in the fields of nanomedicine and acute brain injury, there are critical gaps in knowledge that will need to be addressed. We anticipate that understanding sex as a biological variable in the development of nanomedicine systems to treat acute CNS injury will be an important determinant of their success.

KEYWORDS

sex-related, nanomedicine, nanoparticle, traumatic brain injury, stroke, sex differences

1 Introduction

The consideration of sex as a biological variable was mandated by the National Institutes of Health (NIH) in 2015 (National Institutes of Health, 2015), recognizing that health and disease processes can vary across the sexes. These differences likely impact individual variations in diagnostics, etiology, prevention, and response to health, disease, and associated therapeutic treatments. Molecular differences between the sexes are increasingly recognized to hold implications for regulation of drug pathways, with evidence that there are marked sex and gender differences in drug efficacy and adverse events; yet, even as of 2020, the majority of drugs lack sex-dependent dosing recommendations (Zucker and Prendergast, 2020; Karlsson Lind et al., 2023). Thus,

although evidence is accumulating that sex is a recognized variable influencing efficacy and outcome of traditional drug therapies, much remains unknown about how biological sex impacts development of pharmacotherapies, including the important aspect of nanoparticle systems. We focus our discussion primarily on nanoparticles, defined here as sub-micron colloidal systems. This definition includes synthetic or naturally derived particles with diameter less than 1,000 nm that are suspended within a fluid medium. Biologics, cells, antibody-drug conjugates, and injectable biomaterials are excluded from our analysis.

Several recent reviews have covered this topic from a broad perspective (Serpooshan et al., 2018; Hajipour et al., 2021; Sharifi et al., 2021; Poley et al., 2022). Here, we will focus on highlighting sex differences in both nanomedicine and acute brain injury whereby the intersection of these two areas impacts therapeutic development. We note that for the purposes of this review "sex" refers to the biological construct, rather than the social construct of "gender." Our review is structured to address the foundations of sex differences, central nervous system (CNS) barriers in health and disease, and the interplay between the CNS and the immune system. From this foundation, we will then describe what is known in the field regarding sex differences in nanoparticle delivery to the CNS, focusing on specific examples in acute brain injury. Finally, we will highlight key observations and gaps in the field which should motivate future work.

2 Absorption, distribution, metabolism, and excretion (ADME)

Biological sex is a factor that is well-understood to influence the absorption, distribution, metabolism, and excretion (ADME) of a variety of bioactive agents, including small molecules, protein therapeutics, and oligonucleotides (Farkouh et al., 2020). These differences can be highly clinically significant and are increasingly essential considerations in the drug development process (Tannenbaum et al., 2019). For example, between 1997 and 2000, 8 of the 10 drug withdrawals that occurred in the US market occurred due to greater risks of adverse events in women compared to men (Soldin and Mattison, 2009). Sex differences can originate as a function of behavior (for example, differences in dietary or activity patterns, injury or disease context, likelihood of seeking care, clinician responsiveness, or patient compliance), or they may be a result of underlying biological differences between females and males (for example, differences in organ or tissue physiology, cellular behaviors, gene expression, or organizational and activational effects of gonadal hormones). The interplay between sex, behavior, and biology is often complex. In one example, female patients undergoing treatment for hypertension were observed to be less compliant than male patients, suggesting that behavioral interventions were merited to optimize therapy; however, accumulating evidence from deeper analyses suggests that innate biological differences in response to this specific drug therapy drove differential responses to therapy as well (Consolazio et al., 2022). The impact of failing to consider sex differences in ADME is multifaceted, potentially involving unexpected toxicity or poorly optimized dosing paradigms, which leads to insufficient efficacy as well as putatively unnecessary adverse events (Madla et al., 2021). Thus, sex is an increasingly important factor understood to influence ADME to drive therapeutic development considerations. Here, we will overview the major principles of ADME and consider how these concepts may be extended for development of sex-optimized nanomedicines.

2.1 Physiological basis for sex differences in ADME

ADME refers to the process by which a molecule enters, moves through, and is ultimately cleared from the body (Figure 1). Absorption is the process by which an administered compound reaches the bloodstream. For drugs that are dosed intravenously (IV), agents will rapidly partition within the vascular compartment, which is a heterogeneous medium composed of fluid, proteins, lipids, platelets, and cells; sex-dependent interaction of drugs with these components is known to impact clinical pharmacokinetics and subsequent toxicity or efficacy (Routledge et al., 1981). For drugs that are dosed orally, absorption is initiated in the gastrointestinal tract, where sex differences in pH, enzyme secretion, gastric volume, and gut transit time have been shown to alter the uptake of bioactive agents into circulation (Stillhart et al., 2020). The microbiome also exhibits significant and well-studied sex differences, which have been proposed to impact the gut-brain axis leading to sex differences in disease phenotype and drug ADME (Jašarević et al., 2016; Hokanson et al., 2023). For intranasal dosing, drugs first encounter the nasal passageways and mucosal barriers, for which mucous pH, secretion, and clearance have been shown to be sex-dependent (England et al., 1999; Hallschmid, 2021; Luberti et al., 2021; Marjan, 2023). Additional sex differences have been observed for drug ADME through ocular (Nakamura et al., 2005), intravascular (Kunio et al., 2018), and subcutaneous (Sloan, 2000) dosing paradigms; physiological considerations for these parenteral routes of administration are reviewed elsewhere (Donovan, 2005).

Once a drug has been absorbed into systemic circulation, it will face similar physiological barriers within the vascular compartment, and it is from this source that therapeutic agents will distribute to peripheral tissues as well as the CNS. Drug distribution may depend on a multitude of factors that are sex-dependent, including the physicochemical features of the drug governing its interaction with blood components, which limits or enhances bioavailability and passive movement into tissue, or indirect impacts on physiological processes that subsequently alter distribution on the basis of sex (Figure 2). In addition to the sex-differences in the binding of drugs to plasma proteins that have been noted in the field (Soldin and Mattison, 2009), there are well appreciated sex differences in blood volume, chemistry, and physiology, as well as for organ-specific vascular features (Boese et al., 2017). Males typically have higher blood volume and cardiac output, as well as lower rates of immune activation, compared to females. Males also possess lower quantities and distinct patterns of fat deposition on the body compared to females, which yields varying distribution patterns in female *versus* male subjects (Blaak, 2001; Karastergiou et al., 2012). These differences extend to other organ systems; for example, males also have a higher glomerular filtration rate in the kidneys (McDonough et al., 2023), exhibit profound differences in lung physiology (Townsend et al., 2012), and demonstrate well-appreciated metabolic and physiological differences in the liver

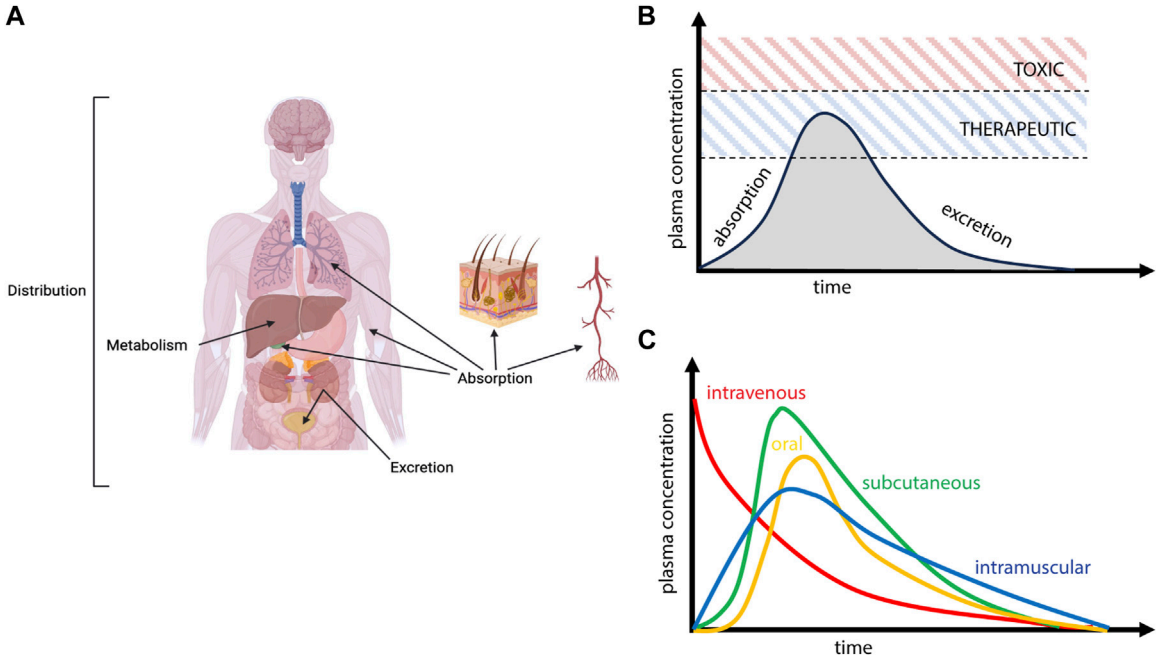

FIGURE 1
Schematic overview of Absorption, Deposition, Metabolism, and Excretion (ADME) processes. **(A)** Following administration, drugs enter the vascular compartment (absorption), distribute throughout various organs and tissues (deposition), experience biotransformation (metabolism), and ultimately clear from the body (excretion). **(B)** Circulating levels of drug reflect these competing processes of ADME, with absorption primarily defining the initial rise in plasma concentration and various deposition, metabolism, and excretion processes (elimination) defining the curve's decay. Achieving therapeutic levels of drug while avoiding toxicity is the primary driver of drug efficacy. **(C)** The time course of plasma pharmacokinetics will depend heavily on route of administration.

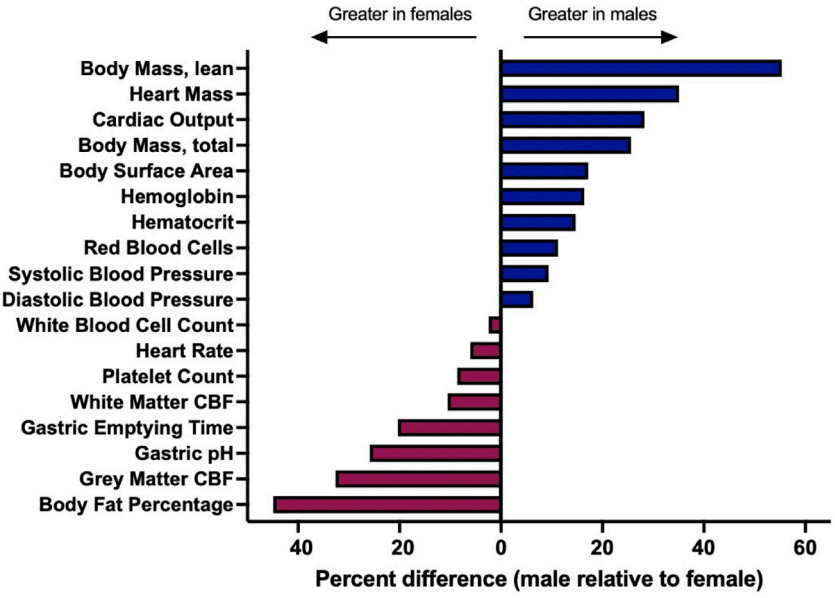

FIGURE 2
A variety of underlying physiological parameters depend on sex. Physiological parameters are described for healthy, adult populations. Percent difference was calculated by the following formula: (male-female)/female. Sources and raw data for each value are provided in Supplementary Material. Abbreviations: cerebral blood flow [CBF].

(Maggi, 2022). With respect to CNS tissues, there are known differences in blood-brain barrier (BBB) integrity and physiology as a function of sex that would be expected to influence nanomedicine delivery. This includes established differences in shear stress responses from brain endothelial cells as well as more subtle possible alterations to transendothelial electrical resistance (TEER) in *in vitro* models and drug-specific metabolism at the BBB (Weber and Clyne, 2021). Sex differences that are specific to the central nervous system will be discussed in greater detail in the sections that follow.

Once within a physiological environment, all therapeutic agents are subject to metabolism, a process or series of processes that can either enhance or inhibit activity of the compound. A significant portion of drug metabolism is driven by enzymes that are expressed in the liver and involve the cytochrome P450 (CYP) family of enzymes, although metabolism is a complex process that can occur in and involve multiple organ systems and enzyme classes. Differences in enzyme expression play a critical role in determining drug clearance from circulation, degradation within tissue compartments, and subsequent toxicity of systemically administered therapeutics. Metabolic processes are well-understood to be sex-dependent and are a primary consideration in therapeutic development for traditional drugs (Waxman and Holloway, 2009). In the case of nanoparticle-based drug delivery systems, nanoparticle distribution to organ systems is primarily driven by the properties of the nanoparticles; drug metabolism itself is outside of the scope of this review, and so we direct the reader to other abundant resources on this topic (Valodara and Johar, 2019).

Excretion is a key process governing the fate of both drugs and nanoparticles in the body, with the liver and kidneys being primary routes through which substances exit the body. Nanoparticles also clear from circulation via the reticuloendothelial/mononuclear phagocytic systems (RES and MPS, respectively), which ultimately leads to clearance and/or deposition of nanoparticle systems in lymph nodes and spleen (Tang et al., 2019). Some evidence suggests that the MPS exhibits sex differences (Varghese et al., 2022), although other works suggest there is not a sex difference (Wang et al., 2021). This mechanism of elimination is particularly important for CNS delivery, considering that rapid depletion of vascular concentration will all but prevent CNS delivery. Engineering nanoparticles to avoid the phagocytosis by circulating immune cells is thus an approach of focused interest in nanoparticle development (Wen et al., 2023).

3 Sex differences in the brain

It is evident that biological sex influences all aspects of drug delivery, including how the drug interacts with the body and how the body reacts to the drug. Keeping these critical sex differences in ADME in mind, we now highlight sex differences in the brain and discuss how these differences may impact nanomedicine delivery to the brain in the context of acute injury.

3.1 Sex determination and its effects on the brain

The phenotypic expression of sex differences is due to the effects of gonadal hormones at organizational (permanent) and activational (transient) levels, as well as the impact of sex chromosomes (Koebele and Bimonte-Nelson, 2015; Arnold, 2022). Recent advancements have led to the understanding that there are gene agents on both the X and Y chromosomes that are related to mammalian sexual differentiation, in turn driving sex differences in circulating hormone levels yielding sex differences in the brain. In early embryogenesis, the Sex-determining Region Y (*Sry*) gene on the Y chromosome, also known as the testis-determining gene, directs the bipotential gonadal ridge to differentiate into testes and inhibits ovarian development (Cabrera Zapata et al., 2022). Ovarian differentiation in XX individuals is due in part to X-linked genes, although the specific identification of these agents and their resultant functions are as-yet unclear (Arnold, 2022; Cabrera Zapata et al., 2022); deciphering these factors are critical for future directions of research. Sex chromosomes drive gonadal hormone expression, and while detailed discussion of hormonal impacts and trajectories on sex differences in the brain is beyond the scope of this review, it is important to note that gonadal steroids, including estrogens, progesterone, testosterone, dihydrotestosterone, and androstenedione, are among the key players that drive these differences (for further review and discussion see: (Koebele and Bimonte-Nelson, 2015; 2017). Notably, effects of these hormones on the brain and its functions, during development and beyond into old age, are both individual and interactive with organizational sex hormone actions setting up tissues to "activate" in a particular fashion when exposed to sex hormones at a later time.

3.2 Cerebrovasculature function

Sex differences have been observed for cardiac, vascular, and cerebrovascular physiology, and these differences could impact delivery of either drugs or nanomedicine to the CNS. Considering the cardiovascular system, females typically have smaller diameter blood vessels, reduced total blood volume, a higher heart rate, lower blood pressure, and a net lower cardiac output than males (Zaid et al., 2023). Recent literature has highlighted that differences in fluid physiology may yield distinct shear stress and vascular reactivity in females *versus* males (Pabbidi et al., 2018; James and Allen, 2021), which could be a particularly important factor influencing the interaction of circulating colloids with brain endothelial cells. Females have previously been reported to have higher cerebral blood flow compared to males, which may be largely affected by sex steroid hormones (Robison et al., 2019). Expression of sex steroid hormone receptors are established in cerebral microvasculature. Estradiol binding to its receptor on endothelial cells has previously been implicated in the maintenance of the vascular system (Cho et al., 1999; Lösel and Wehling, 2003; SenthilKumar et al., 2023). For example, *in vitro* studies have revealed estradiol binding to endothelial cell receptors activates endothelial nitric oxide synthase, which leads to elevated nitric oxide levels and changes in paracellular permeability (Cho et al., 1999). Additionally, the role of androgens in angiogenesis, reactivity, integrity, and inflammation have previously been described (Abi-Ghanem et al., 2020). For instance, Atallah and others show chronic testosterone depletion via castration of 8-week-old male mice leads to increased cerebrovascular permeability, which was evident by multiple tracers and

decreased expression of proteins that provide structural integrity (Atallah et al., 2017). They also show testosterone depletion induces increased expression of pro-inflammatory cytokines (IL-1B, TNF-a) and glial cell activation markers (IBA-1, GFAP), indicating increased inflammatory responses. Notably, they found testosterone supplementation after 5 weeks restores cerebrovascular integrity and results in no significant differences in inflammatory state between castrated and intact males. Furthermore, multiple lines of evidence support sex differences in cardiovascular health and sex-dependent risk of cardiovascular disease (CVD), which can be attributed to steroid hormone profiles (SenthilKumar et al., 2023). For example, prior to menopause, females exhibit a lower risk for developing CVD compared to males. However, alterations in sex-steriod hormone profiles associated with menopause lead to increased risk of CVD in females as compared to males.

3.3 Blood-brain barrier (BBB)

3.3.1 Healthy BBB physiology

The BBB is composed of brain endothelial cells that create a continuous, non-fenestrated microvascular network in the central nervous system (CNS) (Cho et al., 1999). A detailed review of the structure and function of the BBB was recently given by Zhang et al. (Zhang et al., 2022). In short, tight junctions, adherens junctions, and gap junctions between endothelial cells control the movement of ions, molecules, and cells from the blood to the brain parenchyma (Hawkins et al., 2006). Tight junctions are created by homotypic and heterotypic interactions between transmembrane proteins including claudins, occludins, and junction adhesion molecules (JAMs), that connect to the actin cytoskeleton via cytoplasmic scaffold proteins of the membrane-associated guanylate kinase (MAGUK) family (Yuan et al., 2020; Hashimoto et al., 2023; Sugiyama et al., 2023). Conversely, adherens junctions are formed by members of the cadherin protein family and are linked to the actin cytoskeleton by catenins (Weis and Nelson, 2006). A thin sheet of basement membrane (BM) composed of glycosaminoglycans, proteoglycans, and glycoproteins surrounds the endothelial barrier and provides structural support to the neurovascular network (Tewari et al., 2022). The composition of the brain extracellular matrix (ECM) changes with age and disease, which has effects on the integrity of the BBB (Thomsen et al., 2017); ECM composition as well as biomechanical properties have been reported to vary by sex (Batzdorf et al., 2022). Surrounding the BM are pericytes, astrocytes, and microglia that secrete ECM molecules and other signals to influence the BBB (Bisht et al., 2021; Kisler et a., 2021; Gao et al., 2023). Together, these glial cells offer homeostasis and structural support to the BBB, and any deviation can result in disease (Tewari et al., 2022). Pericytes reside within the BM and communicate with endothelial cells and astrocytes through the secretion of signals (Armulik et al., 2010; Wu et al., 2023). Astrocytes extend end foot processes into the BM, where they play major roles in the clearance of waste, regulating BBB permeability, and modulating synaptic transmission (Abbott et al., 2006; Tewari et al., 2022; Wu et al., 2023). Microglia are the brain's resident immune cells that are responsible for innate and adaptive immune responses. These glial cells, along with the endothelium and local neurons, are termed the neurovascular unit (Zlokovic, 2008; Sato et al., 2022).

Sex-related differences in the behavior of glial cells in non-disease states have previously been reported. An in-depth review conducted by Lenz and McCarthy describes the various roles microglia play in brain development, including regulation of neural stem cell populations, synaptogenesis, and sexual determination (Lenz and McCarthy, 2015). Microglia in multiple regions of the developing rodent brain show sex differences in colonization, gene expression, and cytokine secretion (Schwarz et al., 2012). Sex differences in microglia phenotypes also extend into adulthood in animal models and are retained independently from the *in vivo* steroid hormone profile (Villa et al., 2018; Doran et al., 2019). These observed differences in phenotype establish that male and female microglia behave distinctly. Additional studies are needed to determine the extent that sex-related differences in microglia phenotypes impact the BBB. Similarly, sex steroid hormones influence astrocyte function and morphology. Studies have shown that estradiol is implicated in the expansion of astrocyte processes and regulation of intracellular ion concentration (Acaz-Fonseca et al., 2014). Importantly, this may have profound sex-dependent effects on the communication between astrocytes and other cells of the BBB, which is yet to be explored. Further research is required to elucidate sex-dependent function of the neurovascular unit under normal physiological conditions.

3.3.2 Injured BBB physiology

The permeability of the BBB is tightly regulated by glial cells, which work together to sense the environment and produce signals to alter the flow of materials from the blood to the brain tissue. In the context of disease or injury, the normal signaling between glial cells and the brain endothelium is disrupted, resulting in a dysfunctional BBB (Xing et al., 2012). Microglia become activated when surface receptors come in contact with damage-associated molecular patterns (DAMPs) or pathogen-associated molecular patterns (PAMPs), which leads to the activation of pro-inflammatory machinery and induced activation of surrounding microglia (Lawrence et al., 2023). Activated microglia phagocytose cellular debris caused by the injury or disease, leading to the release of signals such as tumor necrosis factor-α (TNF-α) that act on local astrocytes. The subsequent change in gene expression and phenotype of astrocytes in response to the local environment is termed reactive astrogliosis. Reactive astrocytes promote pro-inflammatory conditions by secreting complement components and chemokines that attract circulating peripheral immune cells (Liddelow and Barres, 2017). These disease processes exacerbate oxidative stress and BBB dysfunction through the generation of pro-inflammatory signals, free radicals, and matrix metalloproteinases (MMPs) (Zhao et al., 2022). Secretion of pro-inflammatory cytokines, such as IL-1B and TNF-α, degrade tight junction proteins via multiple signaling pathways. Overproduction of free radicals by microglia and astrocytes, along with any inherent disease-induced free radical accumulation, leads to cellular damage and further disruption of the BBB. In parallel, the secretion of MMPs intensifies BBB breakdown through the direct digestion of tight junction and adherens junction proteins. In summary, the pathophysiology of the injured BBB is complex and involves all glial subtypes. Adding to this complexity, previous literature has illuminated sex-related and

hormone-related differences in glial cell response to pathological conditions. A recent study of female primary cortical astrocytes reveals estradiol and 5α-androstane-3β,17β-diol (a dihydrotestosterone metabolite) may offer protection against cytotoxic challenge with iodoacetic acid (Kim et al., 2023, p. 3). The authors speculate that the protective effects may result from steroid induced inhibition of connexin 43 gap junction opening. Specifically, this channel is important for cellular signaling and changes in channel permeability have been associated with disease states. Estradiol has also previously been implicated in pathways involved in pericyte attachment and migration in response to inflammatory stimuli (Kurmann et al., 2021). Kurmann and others show estradiol treatment prevents cultured human brain vascular pericyte migration through estrogen receptors ER-α and ER-β signaling. Furthermore, their transcriptomics analysis reveals that estradiol treatment induces changes in expression of transcripts associated with cell migration under inflammatory conditions. Since astrocytes and pericytes are involved in maintaining BBB integrity, these findings suggest a critical role of hormone-mediated protection in the context of brain injury. Additionally, previous studies reveal *ex vivo* cultures of male neonatal rat microglia stimulated with lipopolysaccharide (LPS) have increased pro-inflammatory responses compared to female cultures (Loram et al., 2012). This leads into the next section, which discusses how biological sex plays a role in peripheral immune responses to brain injury.

4 Peripheral immune response to acute brain injury

Acute brain injury leads to peripheral immune responses, which are initiated by the infiltration of peripheral immune cells into the parenchyma and transport of DAMPs and PAMPs to draining lymph nodes. Here, we review the process of peripheral immune activation, how biological sex influences immune responses and emerging sex differences in innate immune cells involved in CNS injury.

4.1 Peripheral immune cell signaling

The important players in peripheral immune responses originate from multipotent hematopoietic stem cells that undergo differentiation to become common myeloid progenitor or common lymphoid progenitor cells (Kondo et al., 1997; Akashi et al., 2000). Common myeloid progenitors give rise to innate immune cells, including granulocytes, monocytes, macrophages, and dendritic cells. Conversely, common lymphoid progenitors differentiate into adaptive immune cells including T cells, B cells, and NK cells. These peripheral immune cells use signals from other cells as a road map to reach the brain when injury or disease occurs. An in-depth review conducted by Besedovsky and Rey discussed how neural mediators, such as neurotransmitters, act on immune cells to induce a variety of responses (Besedovsky and Rey, 1996). They also examined the effects that immune-derived products have on the cells of the CNS, including neurons and astrocytes. Another important group of signals that are involved in this neuro-immune axis are chemokines, which are small proteins that initiate peripheral immune cell migration and maturation (Rostène et al., 2007). Together, neural mediators, immune-derived products, and chemokines provide a means of communication for these systems that aids in maintaining homeostasis, preventing disease, and healing injury.

4.2 Immune activation through dura and glymphatic system

The brain was once considered an immune privileged organ, however, more recent studies highlight the presence of resident immune cells within various compartments of the CNS (Buckley and McGavern, 2022; González-Hernández and Mukouyama, 2023). One major site for CNS immune surveillance is the dura mater, a collagenous membrane forming the outermost layer of the meninges. The dura mater contains fenestrated blood vessels, allowing for the trafficking of peripheral immune cells and other materials. Under inflammatory conditions, peripheral immune cells travel from the dura to the meninges via chemokines, which facilitates their access to the parenchyma. Importantly, the newly named glymphatic system provides means of waste removal and small molecule exchange between cerebral spinal fluid (CSF) and interstitial fluid (ISF) that ultimately drains to peripheral lymphatics (Iliff et al., 2012). Astrocytic aquaporin-4 (AQP4) channels enable this movement of CSF into the parenchyma, as well as removal of ISF from the parenchyma. Analogous to the peripheral lymphatic system, the glymphatic system provides means of travel for DAMPs from the CNS to peripheral immune organs such as the spleen and lymph nodes. This results in the activation of peripheral immune cells that initiate systemic immune responses.

4.3 Sex differences influence immune responses

Differences in sex steroid hormone profiles and genetics play roles in sex-specific immune responses. Innate and adaptive immune cells express a variety of hormone receptors including estrogen, progesterone, and androgen receptors. Sex hormones have a variety of implications in immune cell development and function. Generally, estrogens have been reported to promote enhanced humoral immunity, while androgens promote immunosuppression and immunomodulatory effects (Sciarra et al., 2023). Thus, differences in sex-steroid hormone profiles between males and females may have an impact on immune responses. Additionally, sex differences in immune responses have previously been linked to genetics. The human X chromosome encodes a variety of genes related to immune regulation including transcription factors, cytokine receptors, toll-like receptors (TLRs) (Klein and Flanagan, 2016). Some of these genes can escape X inactivation and show increased expression in females compared to males. In the next section we focus on emerging evidence of sex differences in innate immune cells and how it may impact acute brain injury.

4.4 Sex differences in innate inflammation

The innate immune system is rapidly activated and plays a crucial role in neuroinflammation after acute brain injury. Previous studies have revealed neutrophils and monocytes are two key innate immune cells involved in the response to brain injury (Jin et al., 2012). These cells play multiple roles in the immune response including debriding tissue, producing signaling molecules, and acting as a bridge between the innate (tissue resident) and adaptive (peripheral) immune systems (Mantovani et al., 2011; Hazeldine et al., 2014).

4.4.1 Neutrophils

Neutrophils are one of the first peripheral immune cells to reach the CNS and may persist chronically after injury (Alam et al., 2020; Mohamud Yusuf et al., 2022). Despite their initial avail, neutrophils are implicated in pathogenic processes associated with chronic neuroinflammation, such as hyperpermeability of the BBB, edema, and reactive oxygen species (ROS) metabolism (Liu et al., 2018). Notably, recent studies have revealed sex differences in neutrophil activation, function, and apoptosis. A multi-omic analysis of mouse neutrophils revealed sex differences in chromatin architecture, with male cells exhibiting increased chromatin compaction compared to female cells (Lu et al., 2021). Chromatin architecture is an important aspect of neutrophil biology due to its involvement in neutrophil extracellular traps (NETs), and the observed sex differences in chromatin architecture may contribute to sex-specific neutrophil responses and gene expression. Another study of isolated human neutrophils revealed that cells obtained from male subjects exhibit higher expression of genes associated with immature phenotypes compared to female cells (Gupta et al., 2020). Neutrophils isolated from healthy females show increased activation, as evident by female-specific gene set enrichment of pathways related to type I interferon signaling and stimulation in the absence of stimulus. It was also noted that male neutrophils treated with estradiol show similar mitochondrial metabolism compared to untreated female neutrophils, which suggests that differences in steroid hormone profile, rather than X chromosome dosage, lead to sex-specific neutrophil phenotypes. To test this hypothesis, researchers analyzed neutrophil type I interferon signaling/stimulated genes in males with Klinefelter syndrome (XXY) and prepubescent volunteers. Female (XX) neutrophils consistently exhibited higher expression of type I interferon signaling/stimulated genes compared to XY and XXY males, and no significant statistical differences in expression between the XY males and XXY males. Additionally, there were no significant differences in the maturation profile or expression of type I interferon signaling/stimulated genes of prepubescent male and female neutrophils. Together these findings suggest that sex steroid hormones contribute to determining female-specific neutrophil physiology in healthy individuals. There are also reports of sex-specific neutrophil responses to pro-inflammatory signals. For example, Pace and others demonstrated that neutrophils isolated from human male subjects exhibit increased production of prostaglandin-E2 (PGE2) upon stimulation with lipopolysaccharide compared to those isolated from female subjects (Pace et al., 2017). PGE2 is a bioactive molecule involved in homeostatic and inflammatory processes. The authors hypothesize this may be due to sex differences observed in COX2 expression, as this is the key enzyme involved in prostaglandin biosynthesis. Ultimately, these findings show there are sex differences in neutrophil biology, and additional research is needed to understand the extent of these effects. Given that neutrophils play a crucial role in inflammation after brain injury, sex differences in neutrophil function may contribute to the sex differences in CNS pathology.

4.4.2 Monocytes and macrophages

Monocytes, like neutrophils, infiltrate the CNS rapidly in the event of an injury in response to chemoattractants (Jin et al., 2012; Alam et al., 2020). Once monocytes have entered the brain tissue they mature into tissue resident macrophages and begin to perform effector functions including production of inflammatory mediators and phagocytosis of cellular debris (Yang et al., 2014; Alam et al., 2020). Recent studies have revealed hormone-related and sex-related differences in macrophage development and characteristics. Consiglio and others show androgen receptor signaling plays a role in monocyte development in male mice (Consiglio and Gollnick, 2020). They found that deletion of androgen receptors in myeloid cells leads to reduced numbers of mature monocytes and increased numbers of macrophages in bone marrow compared to controls, suggesting androgen receptor signaling increases monocyte development. Additionally, a study of isolated peritoneal macrophages from young and middle-aged rats revealed young females exhibit an increased percentage of macrophages that express activation markers toll-like receptor 4 (TLR4) and major histocompatibility complex II (MHCII) compared to young males (Ćuruvija et al., 2017). It was also reported that when stimulated with lipopolysaccharide (LPS), isolated macrophages from young female rats produced higher levels of interleukin 6 (IL-6) and interleukin 1β (IL-1β) compared to young male macrophages. These findings highlight the impact of sex and age on macrophage phenotypes and response to inflammatory stimuli in animal models. Future studies should focus on elucidating sex-related and hormone-related macrophage responses to better understand the roles they may play in CNS injury. The next section will review reported sex differences in traumatic brain injury (TBI) and stroke.

5 Sex differences in acute CNS injury

5.1 Traumatic brain injury (TBI)

5.1.1 Epidemiology

As one of the leading causes of injury-related death and disability, TBI, affects between 50 and 60 million people globally each year (Maas et al., 2022). The global economic burden of the disease is estimated to be $400 billion per year. Previous literature reveals males have higher rates of TBI compared to women (Mikolic et al., 2021; Centers for Disease Control and Prevention, 2021; Centers for Disease Control and Prevention, 2022). In 2016 and 2017, males were reported to have higher rates of TBI-related hospitalizations for all injury mechanisms including unintentional falls, motor vehicle crashes, and assault (Centers for Disease Control and Prevention, 2021). Additionally, males

were reported to have more than three times higher rates of TBI-related deaths compared to females in 2018 and 2019 (Centers for Disease Control and Prevention, 2022). Despite previous efforts to uncover sex differences in TBI outcomes in preclinical and clinical studies, this topic is still widely considered to be controversial. Remarkably, an extensive review by Gupte and others unveiled that human studies report females predominately experience poorer clinical outcomes than males following TBI (Gupte et al., 2019). They found that study parameters such as study size, stratification of TBI severity, and type of outcome measured have an impact on the extent of sex differences reported in human studies. Furthermore, similar trends extend to preclinical TBI models where the mechanism of injury, sample size, and type of outcome measured appear to have a considerable impact on reports of sex differences. Additional research in both preclinical and clinical domains is needed to decipher the etiology and magnitude of sex differences in TBI.

5.1.2 Pathophysiology

TBI is characterized by a blow, jolt, or penetration to the head that results in the disruption of brain function, leading to complex pathological processes. The acute injury phase is a direct result of the initial injury, which includes damage to neurons, glia and blood vessels. Following the acute phase is a heterogenous, secondary injury phase that encompasses neuroinflammation, heightened intracranial pressure, dysfunction of the BBB, and neuronal excitotoxicity. Neuroinflammation begins with the activation of microglia, which secrete cytokines and chemokines to attract other immune cells such as neutrophils, monocytes, and lymphocytes, to the injury penumbra (Simon et al., 2017). While the initial inflammation aids in neuroregeneration and the clearance of cellular debris, chronic inflammation in the brain can lead to neuronal cell death and further neurodegeneration (Ziebell and Morganti-Kossmann, 2010; Simon et al., 2017). Transport of DAMPs to peripheral immune organs via the glymphatic system leads to systemic immune responses. For example, preclinical studies of TBI have revealed short-term increases in myeloid cell differentiation in the bone marrow and chronic changes in circulating immune cell profiles and behaviors (Ritzel et al., 2018). Additionally, examination of the thymus has revealed chronic disturbances in T cell maturation after TBI.

Recent preclinical studies have revealed sex differences in TBI pathology. Our group previously assessed macromolecule accumulation profiles in male and female mice after experimental TBI (Bharadwaj et al., 2020). Here, horseradish peroxidase (HRP) staining revealed females experience increased macromolecule accumulation in the injured cortex 24 h post-injury compared to males, suggesting sex-dependent BBB permeability after TBI. Additionally, Schwab and others found that female mice exhibit increased DNA damage compared to males after repetitive mild TBI (Schwab et al., 2022). Female mice exhibited increases in R-loops and oxidative base damage compared to sham levels, which was not evident when comparing sham males to injured males. However, when markers for cellular senescence were examined, males and females expressed comparable increases in p21 and p16 proteins compared to their sham counterparts. The authors stated this suggests that males might be more sensitive to genotoxic stress compared to females, and additional research is needed to elucidate the mechanisms that contribute to injury-induced sex-dependent DNA damage. Furthermore, Villapol and others also report that male mice show increased microglial activation, macrophage infiltration, and cell death compared to females at acute timepoints after moderate CCI (Villapol et al., 2017). In this study biological sex and time post-injury were reported to influence cytokine production in microglia and macrophages up to 30 days post-injury. For example, male mice exhibited increased TNF expression at 3 days post-injury compared to females, whereas females exhibited increased TNF and IL-1 expression at 4 h post-injury. Similarly, a study conducted by Doran and others also reported male mice exhibited increased myeloid cell infiltration at 1 day post-injury and increased microglia count at 3 days post-injury compared to females (Doran et al., 2019). Moreover, sex differences have been reported in clinical studies. Wagner and others evaluated sex differences in CSF glutamate concentration and lactate-pyruvate ratio after severe TBI in adults ages 16–65 years (Wagner et al., 2005). Here, females had higher lactate-pyruvate ratios, indicating females experience increased oxidative stress after severe TBI compared to males. They also report sex associations with 24-h glutamate concentration using multivariate analysis, indicating sex differences in glutamate excitotoxicity post-injury. Both findings provide evidence for sex differences after injury that directly affect cells of the BBB.

5.2 Stroke

5.2.1 Epidemiology

Stroke affects approximately 12 million people worldwide each year (Feigin et al., 2021). Ischemic stroke (IS) accounted for about 60% of those cases and hemorrhagic stroke (HS) accounted for the remaining 40%. Notably, in 2019, stroke was the fifth leading cause of death for men and the third leading cause of death for women (Rexrode et al., 2022). Overall, women are considered to have a higher lifetime risk for stroke compared to men. However, age impacts the sex-related risk of stroke, with women having a higher incidence up to 30 years of age and men having a higher incidence thereafter until about age 80 (Vyas et al., 2021). There are also differences associated with the type of stroke experienced by men and women, with women having higher prevalence of subarachnoid hemorrhage and men having higher prevalence of hemorrhagic stroke (Rexrode et al., 2022). Previous studies have revealed sex-related differences in risk factors of stroke. For example, women diagnosed with diabetes have higher risk of stroke compared to men with diabetes (Peters et al., 2014). Some other factors that show sex associations include obesity, hypertension, atrial fibrillation (Vyas et al., 2021). Furthermore, there are female-specific risk factors for stroke including the use of hormone contraceptives and therapies, adverse pregnancy outcomes, and age of menopause onset. These phenomena may be due to sex and age-dependent alterations in circulating steroid hormone profiles and future investigations should lay emphasis on elucidating the causes of the sex-dependent risk of stroke.

5.2.2 Pathophysiology

IS results from reduced blood flow that disturbs the normal function of the brain, causing neurological deficits. The most common causes of IS include arterial occlusion and venous infarction. Similar to IS, HS results in reduced blood flow to the brain caused by rupture of a cerebral artery rather than occlusion. Ruptures can occur in the cerebrum or in the subarachnoid space (SAS). In cases of HS, intracranial pressure rises quickly as the hemorrhagic blood moves into the SAS, ventricles, and parenchyma (Lauzier et al., 2023). At the core of the ischemic event and downstream from the ruptured vessel, the decrease in blood flow contributes to sustained ischemic conditions leading to neuronal death and secondary injury sequelae (Arai et al., 2011). Conversely, in the surrounding penumbra, other perfusing blood vessels provide some reprieve, resulting in a much slower process of cell death. However, in more severe cases, global ischemia can occur, which causes severe oxygen deprivation to large regions of the brain (Lauzier et al., 2023). In the absence of oxygen, neurons lose the ability to generate ATP and extracellular glutamate quickly accumulates causing excitotoxicity (Arai et al., 2011; Long et al., 2023). Additionally, mitochondrial damage leads to the release of free radicals causing oxidative stress and further damage to surrounding cells (Tian et al., 2022). Resident microglia play dual roles by producing pro-inflammatory cytokines and MMPs that cause further BBB and cellular damage, while also producing growth factors that aid in neuroprotection (Jayaraj et al., 2019). Studies of the consequences of stroke have revealed both acute and chronic systemic immune responses. The disruption of the blood brain barrier after stroke allows DAMPS and cytokines to enter the bloodstream, which leads to systemic immune responses. Increases in blood plasma levels of pro-inflammatory cytokines occur as early as 4 h after experimental ischemic stroke (Offner et al., 2006; Chapman et al., 2009). Assessment of splenocytes and circulating peripheral immune cells revealed increased secretion of pro-inflammatory cytokines in experimental models. Post-stroke assessments in humans have shown similar increases in peripheral pro-inflammatory cytokine (Ferrarese et al., 1999; Landreneau et al., 2018). Despite the initial systemic inflammatory response, the immune response shifts towards immunosuppression, termed stroke-induced immunosuppression (SIIS). As emerging key contributors to SIIS, immunosuppressive neutrophils and polymorphonuclear myeloid-derived suppressor cells (PMN-MDSCs) are proposed to induce systemic immunosuppression just days after stroke (Xie et al., 2023). Increases in PMN-MDSCs are reported as early as 24 h after experimental middle cerebral artery occlusion in mice (Kawano et al., 2019). Given that these cells suppress T cell activation and proliferation in cancer, they may play similar roles in immunosuppression after stroke.

Previous studies have reported sex differences in stroke pathology, especially relating to the immune response to stroke. Here we will highlight a few examples; however, we acknowledge this topic has previously been reviewed in depth by others (Ahnstedt and McCullough, 2019; Banerjee and McCullough, 2022; Liu et al., 2022; Tariq et al., 2023). McCullough and others found sex differences in pathways leading to cell death after middle cerebral artery occlusion (MCAO) in mice (McCullough et al., 2005). Specifically, cell death as a result of poly-ADP ribose polymerase (PARP) activation and nitric oxide toxicity is mainly restricted to males, whereas cell death for females is caspase-mediated. Another group revealed that males exhibit increased macrophages and T cells within the ischemic hemisphere compared to females 2 days after MCAO (Xiong et al., 2015). Furthermore, gene expression analysis of whole blood samples from human patients revealed females express significantly more neutrophil specific transcripts up to 3 h following cardioembolic stroke (Stamova et al., 2014). Additional research is needed to elucidate the underlying cellular mechanisms that lead to sex differences in the pathological responses to stroke, including sex differences in cells of the BBB and infiltrating immune cells. Future studies should also aim to determine the extent of hormonal and chromosomal influences that impact sex specific immune responses to stroke.

6 Sex differences in nanomedicine

The study of sex differences in nanomedicine is a burgeoning field. We are not the first to consider this topic (Hajipour et al., 2021; Sharifi et al., 2021; Yang et al., 2021; Poley et al., 2022). Here, we will focus on summarizing empirical observations of sex differences in the field of nanomedicine, moving from microscopic to macroscopic length scales, with a particular focus on implications for developing nanoparticle systems in acute brain injury.

6.1 Sex differences in nanomedicine interaction with cells and fluids

Sex differences in nanoparticle interactions with cells and biological fluids have been observed in several *in vitro* contexts. Following administration of a nanoparticle to the body, proteins that are present in biological fluids will rapidly form a coating, or corona, on the surface of the nanoparticle (Bashiri et al., 2023; Jiang et al., 2023). This protein corona is a primary driver of nanoparticle distribution and elimination, mediating both desired interactions (such as uptake of the nanoparticle by target cells) as well as undesired interactions (such as nanoparticle opsonization by circulating immune cells) (Tran and Roffler, 2023). Ashkarran and others concluded that protein corona composition was distinct for silica nanoparticles exposed to female *versus* male mouse plasma (Ashkarran et al., 2023), which may be a critical finding for the field. However, it should be noted that their results are reported from experiments involving plasma that was pooled from 3 female *versus* 3 male mice, yielding a single sample of plasma for each sex. Because nanoparticles were incubated with this pooled plasma, it is difficult to ascertain whether the reported differences could be attributed to female *versus* male sex or normal biological variability. These are important early observations that merit deeper evaluation in future work.

Data regarding how sex influences the interaction of nanoparticles with cells is unfortunately sparse. However, what has been described thus far suggests that how sex influences these interactions may depend on cell type. In one example, Serpooshan and others generated human amniotic stem cell (hAMSC) cultures from the amniotic layer of placenta from female and male fetuses (Serpooshan et al., 2018). Male cells were observed to take up fewer quantum dots than female cells

in these hAMSC cultures; interestingly, this relationship was reversed in primary salivary fibroblast cells, where female cells were observed to take up fewer quantum dots than male cells. These differences in nanoparticle internalization as a function of cell sex were directly attributed to differences in arrangement and properties of actin filaments governing cytoskeletal reorganization, suggesting a cell intrinsic basis. Mahmoudi and others reported in a conference abstract that the uptake of superparamagnetic iron oxide nanoparticles (SPIONs) was threefold higher in female human inducible pluripotent stem cells (hiPSCs) compared to male hiPISCs. Similar to the work accomplished by Serpooshan, et al., these differences in nanoparticle uptake on the basis of sex were attributed to differences in actin structure and organization in female *versus* male cells (Mahmoudi, 2021). Beyond these reports, detailed analyses of NP interactions at the cellular level are otherwise lacking.

6.2 Sex differences in nanomedicine biodistribution in the periphery

When a nanoparticle system is developed for the treatment of disease, one of the most significant questions will be the extent to which the nanoparticle agent accumulates in different organ systems, i.e., biodistribution, since this will drive both efficacy and toxicity (Wei et al., 2018). The biodistribution of solid metal nanoparticles has received particular attention due to ubiquitous use of these materials in the human environment and concerns regarding potential long-term toxicity. Although these particular systems are not typically intended to deliver therapeutic agents, the studies that follow provide insight into the fundamental mechanisms that will govern distribution of nanomedicines. Of the metal nanoparticle family, silver nanoparticles (AgNPs) are well-studied in terms of potential sex differences, likely due the extensive use of AgNPs in textiles, cosmetics, and medical applications, such as wound healing (Islam et al., 2021). Multiple reports have observed that peripheral organ accumulation of AgNPs is higher in female subjects compared to male subjects for bare metal AgNPs, and this holds true for oral, IV, intraperitoneal (IP), subcutaneous, and inhaled routes of administration (Kim et al., 2009; Sung et al., 2009; Tariba Lovaković et al., 2021; Ćurlin et al., 2021; Mahdieh et al., 2022; Xue et al., 2023). There is modest evidence that steroidal hormones may drive these differences. Lovakovic and others administered AgNPs coated either with polyvinylpyrrodine (PVP) or the BBB-targeting ligand transferrin (TRF) to male and female mice. Mice were either left gonadally intact or received gonadectomy. Significant differences in AgNP deposition were observed in the liver for intact females *versus* intact males and in the lung for intact males *versus* gonadectomized males. Importantly, TRF-driven targeting effects were observed for the intact male group only, while TRF did not yield significant targeting for female or gonadectomized subjects. Differential inflammatory responses were observed in gonadectomized *versus* intact subjects, which supports the expectation that gonadotropins may influence distribution processes (Tariba Lovaković et al., 2021). For similar PVP-coated AgNPs administered orally to rats, nanoparticles were observed to accumulate to a much higher extent in female rats compared to male rats for blood, liver, kidney, heart, stomach, and duodenum (Ćurlin et al., 2021). In detailed work performed by Boudreau, et al., variously sized AgNPs (10, 75, 110 nm diameter) were observed to accumulate more effectively in female rats compared to male rats in the gastrointestinal tract and associated mesenteric lymph nodes (Boudreau et al., 2016). In contrast, aptamer-loaded gold nanostars were observed to accumulate in the spleens and liver of female mice at a five-fold lower level than male mice (Dam et al., 2015). These contrasting reports highlight the expectation that sex differences may be unique to the nanoparticle system under consideration.

Sex differences in nanomedicine circulation within the vascular compartment could be a likely explanation for sex-dependent deposition in peripheral organs. Boudreau and others concluded that there were no differences in the half-life of AgNPs in blood for female *versus* male subjects, however, the conclusion appears to have been drawn from semi-quantitative analysis (Boudreau et al., 2016). When we extracted the raw data from this report, there was modest evidence that the half-life of AgNPs for female mice is faster than for male mice (Supplementary Figure S1). Other studies have reported longer circulation time and slower elimination half-life for female *versus* male mice following administration of AgNPs (Xue et al., 2023). Yet other studies have reported no difference in half-life for female *versus* male mice following administration of ZnO nanoparticles (Choi et al., 2012), although it appears that Zn was primarily present in ionic rather than nanoparticle form in tissue, suggesting that organ deposition in that work was not driven by the colloidal system. Taking a broader view, traditional pharmacokinetic characterization of nanoparticle system via ADME approaches is critical; more detailed evaluation of the pharmacokinetic profiles of nanoparticles in blood of female *versus* male subjects, particularly in context of gonadectomy or other hormonal manipulations, would yield better understanding of the mechanisms driving differential organ distribution and may also guide eventual clinical dosing considerations.

6.3 Sex differences in the body's response to nanomedicine

Empirical evidence suggests that female *versus* male subjects exhibit different biological and physiological responses to nanoparticle administration. Here, we will focus on observational studies that have reported sex differences in serum biochemistry and complete blood counts, oxidative stress, tissue-specific toxicity, and immune activation following parenteral administration of a nanoparticle system.

6.3.1 Biochemistry and complete blood count

Whole blood is composed of both cellular (white blood cells, red blood cells) and acellular (plasma, platelets) components. Evaluation of serum biochemistry (i.e., the level of various proteins, enzymes, and lipids) or complete blood count (CBC, i.e., cellular counts and proportions) can yield insight into potential toxicity of therapeutic systems. Several recent reports suggest that biochemical and CBC responses to nanoparticle administration depend on sex (Gosselin, Ramaiah, and Earl, 2011). Lanthanum titanate nanoparticles (LT NPs) produced differing effects on both serum markers and CBC as a function of biological sex, with evidence for immunosuppression

in male mice under the same conditions in which expansion of monocytes was observed in female mice (Akram et al., 2020). Male mice were also observed to respond to nanoparticle administration with increased triglyceride levels, which was not observed in females and that may raise concerns for patients at-risk for cardiovascular disease. Sex differences were observed for female *versus* male rats after treatment with CuNPs, particularly at high doses, and these differences were not observed in the free ion Cu (non-nanoparticle) groups (Riaz et al., 2020). Complex and sex-dependent effects on serum biochemistry for female *versus* male rats following administration of CuNPs have been reported by other investigators (Kim et al., 2016). Chen et al. described differences in thymus and spleen indexes for female and male mice following administration of PEGylated AuNPs, suggesting sex-dependent immunological response (Zhang et al., 2013). These differences included distinct immunological responses, as well as differences in white blood cell, red blood cell, and platelet counts that depended on dose as well as sex. In other work, male mice that received oral administration of ZnO nanoparticles showed no change in serum biochemistry, while females showed increased bilirubin compared to their control, which could suggest sex-dependent liver toxicity (Kuang et al., 2021). Sex-dependent physiological reactions to nanoparticle treatment can involve direct impact on the endocrine system; when female rats were dosed with titanium dioxide nanoparticles, subjects exhibited transient hypoglycemia on multiple days of observation, while the same dosing regimen in male rats did not cause hypoglycemia (Chen et al., 2020). Sex differences in insulin and glucagon levels likely explain these results and could be a critical sex-dependent safety consideration for individuals with aberrant glucose metabolism (e.g., in diabetes). These data support an expectation that serum biochemistry and CBC responses to nanomedicine will depend on biological sex, which is an important consideration in toxicological evaluation of nanoparticle systems.

6.3.2 Oxidative stress

Oxidative stress is a major focus of CNS research in acute brain injury, being both a driver and potential therapeutic target for disease pathology (Allen, C. L. and Bayraktutan, U., 2009; Rodriguez-Rodriguez et al., 2014; Salim, 2017; Hakiminia et al., 2022). Oxidative stress involves an imbalance between reactive oxygen species (ROS) and antioxidant cellular machinery, leading to an accumulation of ROS that yield damage to intracellular lipids, proteins, and oligonucleotides. Increased oxidative stress has been linked causally to chronic inflammation and neurodegenerative processes in Alzheimer's disease, Parkinson's disease, amyotrophic lateral sclerosis (ALS), and multiple sclerosis (MS) (Pizzino et al., 2017). This mechanism of cellular and tissue damage is increasingly implicated in the secondary injury cascades that result from acute CNS, which is discussed in greater detail in Section 5.1.2 of this review. Early evidence suggests that oxidative responses to nanoparticle administration depend on sex, although the reported relationships are complex and are not at a stage where they can be generalized. In one study, researchers studied biocompatibility of low- and high-dose (LD and HD, respectively) PVP-coated AgNPs (Ćurlin et al., 2021). Females and males displayed distinct patterns of peroxyl radical accumulation that depended both on the particle type as well as the organ system examined. Interestingly, female liver and kidneys both showed a decrease in superoxide dismutase (SOD) levels for the LD group and a return to control values in the HD group. In contrast, levels of SOD in male rats did not show a clear pattern between liver and kidney or between HD and LD. In separate work utilizing a nanoparticle with specific intent of reducing catalase and SOD, significant reduction of oxidative stress in male mice was achieved with lower ratios of SOD1:CAT in nanoparticles, whereas the ratio was doubled in females to achieve the same effect (Tarudji et al., 2023). Complex antioxidant responses were observed to also depend on sex in specific organ systems, including heart, liver, and kidney for lanthium titanate NPs (Akram et al., 2020). Treatment with AgNPs nanoparticles yielded significant changes in oxidative stress markers, such as peroxyl radicals and superoxide radicals, in male and female mouse kidneys, livers, brains and lungs. Differences were not only observed between male and female mice, but there were also differences based on whether the mice were intact or gonadectomized, which highlights the important role that gonadotropin signaling may play (Tariba Lovaković et al., 2021). Taken in sum, these data suggest that oxidative stress responses can be sex-specific, and that these differences should be considered for the development of new therapeutics.

6.3.3 Inflammation and toxicity

Growing evidence suggests that sex differences play a role in driving phenotypic, organ-level, or cellular toxicity. In one recent and high profile example, major differences have been observed for tolerability of the solid lipid nanoparticle COVID-19 vaccine, with females reporting significantly higher adverse effects immediately following inoculation and males experience higher susceptibility to adverse cardiac events at later time points (Duijster et al., 2023); the fact that the vaccine is reported to induce cycle irregularities in menstruating individuals (Rahimi Mansour et al., 2023) suggests that endocrine or gonadotropic signaling may be involved. We note that, given the recency of these observations, sex differences in COVID-19 vaccine tolerability is an area of active clinical investigation that is evolving rapidly. Preclinically, sex differences in toxicity have been studied in various formats. Sex differences were observed for inhaled Titanium Dioxide nanoparticles (TiO_2-NPs), such that male rats exposed to TiO_2-NPs exhibited a significant increase in circulating neutrophils, while female rats were apparently more susceptible to toxicity at the organ level (Yamano et al., 2022). Phenotypic evidence of toxicity was evident as pulmonary dust foci (PDF), which presented as milky white spots on the lungs and were proposed to be agglomerations of macrophages; PDFs were seen in females at lower NP doses compared to males, which suggests that females may be more sensitive to the toxicities related to TiO_2 inhalation. Similarly, female rats were observed to be more susceptible to hepatic toxicity, with increased levels of biomarkers for oxidative stress after oral administration. In contrast to these results, a different study observed that females were less susceptible to lung toxicity than males following exposure to ZnO-NPs (Sehsah et al., 2022); although the initial experiments would have suggested a simple or generalizable dependence of toxicity on sex, their deeper analyses that examined genes regulating oxidative stress responses and inflammation-associated chemokines revealed highly complex regulation of individual pathways. Yang et al. demonstrated that there were significant changes in hormone production in the female

rats treated with copper nanoparticles (CuNPs), as well as heightened expression of caspase proteases following parenteral administration in females, although they did not compare these results to male mice (Yang et al., 2017). Other research has also shown an increase in micronucleation of immune cells, with a higher quantity of these cells in male *versus* female rats across multiple dosing groups by the oral route (Kim, Soon Yong et al., 2008). In detailed studies performed by Han and others, amorphous silica nanoparticles (ASiNPs) instilled intratracheally yielded the highest level of lung damage in female rats compared to males (Han et al., 2020). Expression of caveolin-1 and matrix metalloproteases in females were suggested to account for these differences. In separate studies, cytokine marker expression levels depended on sex. Gokulan and others reported that a T-cell marker was significantly increased in male tissues after 24 h, but the same marker was significantly decreased in females at the same time point and dose (Gokulan et al., 2020). Taken in sum, these data support an expectation that toxicity of nanoparticle systems will depend on sex, although clearly these relationships are complex and may be unique to each nanoparticle systems.

6.4 Sex differences in nanoparticle delivery to the injured brain

Nanoparticle delivery systems provide injectable, sustained release options of therapeutic intervention for various diseases and injuries. For neural applications, the largest obstacle to consider when designing drug delivery vehicles is the BBB, which larger sized particles (i.e., >20 nm) are typically unable to cross (Cook et al., 2015; Medina et al., 2017). However, the breakdown of the BBB after injury gives rise to unique opportunities to use nanoparticle drug carriers. Drug loaded nanoparticles can be tailored to suit a desired therapeutic target, which may include reducing oxidative stress, protecting against cellular apoptosis, or modulation of the immune system. While nanoparticle-based drug delivery systems for brain injury are not currently available in the clinic, these systems are clinically approved for the treatment of various diseases including cancer, hemophilia, and multiple sclerosis (Anselmo and Mitragotri, 2019; Mitchell et al., 2021). The following paragraphs discuss the preclinical reports of sex differences in systemic nanoparticle delivery to the injured brain.

Sex differences have been observed in the development of treatments for TBI. Our group has previously investigated nanoparticle accumulation profiles in male and female cerebral cortex after experimental TBI (Bharadwaj et al., 2020). Fluorescence microscopy confirmed greater nanoparticle accumulation at 24 h post-injury in the female injured cortex compared to the male injured cortex. This study also revealed sex differences in the temporal nanoparticle accumulation profile spanning up to 7 days after injury. Males exhibit a biphasic accumulation pattern with greater accumulation at 3 h and 3 days compared to 1 day after injury, however females do not share this same temporal profile. This finding is indicative of sex-dependent BBB dysfunction and is the focus of ongoing studies. Tarudji et al. reports the overall contrast extravasation rate of antioxidant enzyme loaded PLGA nanoparticles was significantly lower in female mice than male mice at 24 h after experimental TBI (Tarudji et al., 2023). Although these studies used the same injury model, this opposing finding may be due to differences in injury severity parameters, given that Bharadwaj et al. employed a 2 mm depth impact and Tarudji et al. employed a 2.5 mm impact. Previous studies characterizing the CCI model have shown that injury severity is dependent on impact depth, speed and diameter, with more severe injuries resulting from increases in these parameters (Saatman et al., 2006; Osier and Dixon, 2016). Together, these studies show that there are sex differences in nanoparticle delivery to the injured brain. Further research is needed to investigate the underlying mechanisms that cause sex-dependent pathologies seen in animal models of TBI and how these mechanisms can be harnessed to improve therapeutic delivery. Additionally, the type of injury model (cortical controlled impact, fluid percussion injury, blast-induced injury) and severity of the injury may impact the magnitude and temporal trajectory of sex differences and should be considered carefully in future research.

Similar to TBI, the dependence of efficacy on sex has been observed in preclinical studies for stroke. For example, Challa et al. explored the impact of MMP-12 slicing after ischemic stroke by delivering MMP-12 shRNA loaded nanoemulsions IV to male and female mice at different time points post-reperfusion (Challa et al., 2022). MMP-12 is a known player in amplifying local and systemic immune response as well as prolonging BBB disruption. Animals receiving the MMP-12 shRNA exhibited a significant knockdown of MMP-12 within the ipsilateral hemisphere compared to control plasmids and sham animal controls. When neuromotor behavior was assessed, a sex-dependent effect was observed with MMP-12 knockdown therapy. Specifically, a higher level of therapeutic impact for neurological motor behavior was observed in male rats compared to female rats (Challa et al., 2022). It should be noted that the stroke induced motor behavior deficit was not as significant in female rats compared to male rats (Koellhoffer and McCullough, 2013). This phenomenon is well-documented in the preclinical stroke research field, where it is hypothesized that circulating sex hormones may play a role in the molecular sequelae and thus the functional deficits that emerge. Other studies have demonstrated sex-dependent response to small molecule or antibody therapeutics, however, the PD/PK for nanoparticle systems in preclinical stroke models have yet to be fully explored and characterized (Ruddy et al., 2019; Seifert et al., 2019; Tejeda-Bayron et al., 2021). This area of research is ripe for further assessment.

7 Conclusion/call to action

The main objective of this review was to highlight the current knowledge of if and how sex-dependent biological variables impact nanomedicine within the context of acute brain injury pathologies. We can conclude from our analyses that sex is an important consideration. We also identify critical gaps and challenges for the field. This includes a lack of consideration of cell sex in *in vitro* studies, oversimplification or failure to track estrus cycles in experimental design, lack of balanced experimental designs powered for detecting sex differences, and a lack of foundational work directly evaluating nanomedicine-specific mechanisms that may drive sex differences (for example, differences in protein corona driving differences in circulation time).

We suggest the following call to action:

- Train all scientists in the distinction between gender and sex as well as the complexity of physiological factors that drive sex differences
- Elevate field-standard expectations that published work will consistently and directly provide rationale regarding
  - Inclusion or exclusion of sex as a biological variable in all experimental work
  - Inclusion or exclusion of estrus cycle tracking in preclinical experimental designs
- Deepen mechanistic rigor for nanomedicine development to account difference in sex-dependent microenvironmental factors through
  - Increased attention to foundational aspects of protein corona formation and nanoparticle distribution and clearance as a function of sex
  - Standard inclusion and description of cell sex for *in vitro* experiments
  - Utilizing preclinical manipulations such as hormone replacement, gonadectomy, or transgenic or chimeric models to better understand the mechanistic basis for sex differences
- Develop and support team science initiates that would facilitate the collaboration of diverse scientists and thought leaders capable of pursuing this complex, cross-disciplinary work

We further challenge the field to consider the real-world context for development of new nanomedicines, including addressing sex as a biological variable in clinical populations that are atypical in their sex identity or hormonal profiles as a result of typical aging processes, hormone replacement therapy, intersex conditions, non-binary gender presentation, or gender dysphoria.

Here, we address the intersection of nanomedicine and acute brain injury in the context of biological sex. This field is poised to yield new therapeutic approaches and mechanistic understanding that will positively impact human health. We are encouraged by growing recognition and incorporation of sex as a biological variable and look forward to clinical advancements in the years to come.

Author contributions

AS: Conceptualization, Writing–original draft, Writing–review and editing. OM: Conceptualization, Writing–original draft, Writing–review and editing. HBN: Writing–review and editing. RS: Conceptualization, Funding acquisition, Writing–original draft, Writing–review and editing. SS: Conceptualization, Funding acquisition, Writing–original draft, Writing–review and editing.

Funding

The author(s) declare financial support was received for the research, authorship, and/or publication of this article. Authors recognize the following funding sources: R01NS116657 (RS, SS, HBN), R01HD099543 (RS), R01NS111292 (RS), Arizona Alzheimer's Consortium (SS), and Fulton Dean's Fellowship (AS).

Acknowledgments

We thank Colin Riley for providing text editing and general feedback on this work.

Conflict of interest

The authors declare that the research was conducted in the absence of any commercial or financial relationships that could be construed as a potential conflict of interest.

Publisher's note

Supplementary material

The Supplementary Material for this article can be found online at: https://www.frontiersin.org/articles/10.3389/fbiom.2024.1348165/full#supplementary-material

References

Abbott, N. J., Rönnbäck, L., and Hansson, E. (2006). Astrocyte–endothelial interactions at the blood–brain barrier. *Nat. Rev. Neurosci.* 7 (1), 41–53. doi:10.1038/nrn1824

Abi-Ghanem, C., Robison, L. S., and Zuloaga, K. L. (2020). Androgens' effects on cerebrovascular function in health and disease. *Biol. Sex Differ.* 11 (1), 35. doi:10.1186/s13293-020-00309-4

Acaz-Fonseca, E., Sanchez-Gonzalez, R., Azcoitia, I., Arevalo, M. A., and Garcia-Segura, L. M. (2014). Role of astrocytes in the neuroprotective actions of 17β-estradiol and selective estrogen receptor modulators. *Mol. Cell. Endocrinol.* 389 (1–2), 48–57. doi:10.1016/j.mce.2014.01.009

Ahnstedt, H., and McCullough, L. D. (2019). The impact of sex and age on T cell immunity and ischemic stroke outcomes. *Cell. Immunol.* 345, 103960. doi:10.1016/j.cellimm.2019.103960

Akashi, K., Traver, D., Miyamoto, T., and Weissman, I. L. (2000). A clonogenic common myeloid progenitor that gives rise to all myeloid lineages. *Nature* 404 (6774), 193–197. doi:10.1038/35004599

Akram, I. N., Akhtar, S., Khadija, G., Awais, M. M., Latif, M., Noreen, A., et al. (2020). Synthesis, characterization, and biocompatibility of lanthanum titanate nanoparticles in albino mice in a sex-specific manner. *Naunyn-Schmiedeberg's Archives Pharmacol.* 393 (6), 1089–1101. doi:10.1007/s00210-020-01819-z

Alam, A., Thelin, E. P., Tajsic, T., Khan, D. Z., Khellaf, A., Patani, R., et al. (2020). Cellular infiltration in traumatic brain injury. *J. Neuroinflammation* 17 (1), 328. doi:10.1186/s12974-020-02005-x

Allen, C. L., and Bayraktutan, U. (2009). Oxidative stress and its role in the pathogenesis of ischaemic stroke. *Int. J. Stroke* 4 (6), 461–470. doi:10.1111/j.1747-4949.2009.00387.x

Anselmo, A. C., and Mitragotri, S. (2019). Nanoparticles in the clinic: an update. *Bioeng. Transl. Med.* 4 (3), e10143. doi:10.1002/btm2.10143

Arai, K., Lok, J., Guo, S., Hayakawa, K., Xing, C., and Lo, E. H. (2011). Cellular mechanisms of neurovascular damage and repair after stroke. *J. child neurology* 26 (9), 1193–1198. doi:10.1177/0883073811408610

Armulik, A., Genové, G., Mäe, M., Nisancioglu, M. H., Wallgard, E., Niaudet, C., et al. (2010). Pericytes regulate the blood–brain barrier. *Nature* 468 (7323), 557–561. doi:10.1038/nature09522

Arnold, A. P. (2022). X chromosome agents of sexual differentiation. *Nat. Rev. Endocrinol.* 18 (9), 574–583. doi:10.1038/s41574-022-00697-0

Ashkarran, A. A., Gharibi, H., Grunberger, J. W., Saei, A. A., Khurana, N., Mohammadpour, R., et al. (2023). Sex-specific silica nanoparticle protein corona compositions exposed to male and female BALB/c mice plasmas. *ACS Bio Med Chem Au* 3 (1), 62–73. doi:10.1021/acsbiomedchemau.2c00040

Atallah, A., Mhaouty-Kodja, S., and Grange-Messent, V. (2017). Chronic depletion of gonadal testosterone leads to blood-brain barrier dysfunction and inflammation in male mice. *J. Cereb. Blood Flow Metabolism Official J. Int. Soc. Cereb. Blood Flow Metabolism* 37 (9), 3161–3175. doi:10.1177/0271678X16683961

Banerjee, A., and McCullough, L. D. (2022). Sex-specific immune responses in stroke. *Stroke* 53 (5), 1449–1459. doi:10.1161/STROKEAHA.122.036945

Bashiri, G., Padilla, M. S., Swingle, K. L., Shepherd, S. J., Mitchell, M. J., and Wang, K. (2023). Nanoparticle protein corona: from structure and function to therapeutic targeting. *Lab a Chip* 23 (6), 1432–1466. doi:10.1039/D2LC00799A

Batzdorf, C. S., Morr, A. S., Bertalan, G., Sack, I., Silva, R. V., and Infante-Duarte, C. (2022). Sexual dimorphism in extracellular matrix composition and viscoelasticity of the healthy and inflamed mouse brain. *Biology* 11 (2), 230. doi:10.3390/biology11020230

Besedovsky, H. O., and Rey, A. D. (1996). Immune-neuro-endocrine interactions: facts and hypotheses. *Immune-Neuro-Endocrine Interact. Facts Hypotheses* 17 (1), 64–102. doi:10.1210/edrv-17-1-64

Bharadwaj, V. N., Copeland, C., Mathew, E., Newbern, J., Anderson, T. R., Lifshitz, J., et al. (2020). Sex-dependent macromolecule and nanoparticle delivery in experimental brain injury. *Tissue Eng. Part A* 26 (13–14), 688–701. doi:10.1089/ten.tea.2020.0040

Bisht, K., Okojie, K. A., Sharma, K., Lentferink, D. H., Sun, Y. Y., Chen, H. R., et al. (2021). Capillary-associated microglia regulate vascular structure and function through PANX1-P2RY12 coupling in mice. *Nat. Commun.* 12 (1), 5289. doi:10.1038/s41467-021-25590-8

Blaak, E. (2001). Gender differences in fat metabolism. *Curr. Opin. Clin. Nutr. Metabolic Care* 4 (6), 499–502. doi:10.1097/00075197-200111000-00006

Boese, A. C., Kim, S. C., Yin, K. J., Lee, J. P., and Hamblin, M. H. (2017). Sex differences in vascular physiology and pathophysiology: estrogen and androgen signaling in health and disease. *Am. J. Physiology-Heart Circulatory Physiology* 313 (3), H524–H545. doi:10.1152/ajpheart.00217.2016

Boudreau, M. D., Imam, M. S., Paredes, A. M., Bryant, M. S., Cunningham, C. K., Felton, R. P., et al. (2016). Differential effects of silver nanoparticles and silver ions on tissue accumulation, distribution, and toxicity in the sprague dawley rat following daily oral gavage administration for 13 weeks. *Toxicol. Sci.* 150 (1), 131–160. doi:10.1093/toxsci/kfv318

Buckley, M. W., and McGavern, D. B. (2022). Immune dynamics in the CNS and its barriers during homeostasis and disease. *Immunol. Rev.* 306 (1), 58–75. doi:10.1111/imr.13066

Cabrera Zapata, L. E., Garcia-Segura, L. M., Cambiasso, M. J., and Arevalo, M. A. (2022). Genetics and epigenetics of the X and Y chromosomes in the sexual differentiation of the brain. *Int. J. Mol. Sci.* 23 (20), 12288. doi:10.3390/ijms232012288

Centers for Disease Control and Prevention (2021). *Surveillance report of traumatic brain injury-related hospitalizations and deaths by age group, sex, and mechanism of injury—United States, 2016 and 2017*. Centers for Disease Control and Prevention, U.S. Department of Health and Human Services.

Centers for Disease Control and Prevention (2022). *Surveillance report of traumatic brain injury-related deaths by age group, sex, and mechanism of injury—United States, 2018 and 2019*. Centers for Disease Control and Prevention, U.S. Department of Health and Human Services.

Challa, S. R., Nalamolu, K. R., Fornal, C. A., Wang, B. C., Martin, R. C., Olson, E. A., et al. (2022). Therapeutic efficacy of matrix metalloproteinase-12 suppression on neurological recovery after ischemic stroke: optimal treatment timing and duration. *Front. Neurosci.* 16, 1012812. doi:10.3389/fnins.2022.1012812

Chapman, K. Z., Dale, V. Q., Dénes, Á., Bennett, G., Rothwell, N. J., Allan, S. M., et al. (2009). A rapid and transient peripheral inflammatory response precedes brain inflammation after experimental stroke. *J. Cereb. Blood Flow Metabolism* 29 (11), 1764–1768. doi:10.1038/jcbfm.2009.113

Chen, Z., Han, S., Zheng, P., and Zhou, S. (2020). Combined effect of titanium dioxide nanoparticles and glucose on the blood glucose homeostasis in young rats after oral administration. *J. Appl. Toxicol.* 40 (9), 1284–1296. doi:10.1002/jat.3985

Cho, M. M., Ziats, N. P., Pal, D., Utian, W. H., and Gorodeski, G. I. (1999). Estrogen modulates paracellular permeability of human endothelial cells by eNOS- and iNOS-related mechanisms. *Am. J. Physiology-Cell Physiology* 276 (2), C337–C349. doi:10.1152/ajpcell.1999.276.2.C337

Choi, S.-J., Baek, M., Chung, H. E., Yu, J., Lee, J. A., Kim, T. H., et al. (2012). Pharmacokinetics, tissue distribution, and excretion of zinc oxide nanoparticles. *Int. J. Nanomedicine* 7, 3081–3097. doi:10.2147/IJN.S32593

Consiglio, C. R., and Gollnick, S. O. (2020). Androgen receptor signaling positively regulates monocytic development. *Front. Immunol.* 11, 519383. doi:10.3389/fimmu.2020.519383

Consolazio, D., Gattoni, M. E., and Russo, A. G. (2022). Exploring gender differences in medication consumption and mortality in a cohort of hypertensive patients in Northern Italy. *BMC Public Health* 22 (1), 768. doi:10.1186/s12889-022-13052-9

Cook, R. L., Householder, K. T., Chung, E. P., Prakapenka, A. V., DiPerna, D. M., and Sirianni, R. W. (2015). A critical evaluation of drug delivery from ligand modified nanoparticles: confounding small molecule distribution and efficacy in the central nervous system. *J. Control. Release* 220, 89–97. doi:10.1016/j.jconrel.2015.10.013

Ćurlin, M., Barbir, R., Dabelić, S., Ljubojević, M., Goessler, W., Micek, V., et al. (2021). Sex affects the response of Wistar rats to polyvinyl pyrrolidone (PVP)-coated silver nanoparticles in an oral 28 days repeated dose toxicity study. *Part. Fibre Toxicol.* 18 (1), 38. doi:10.1186/s12989-021-00425-y

Ćuruvija, I., Stanojević, S., Arsenović-Ranin, N., Blagojević, V., Dimitrijević, M., Vidić-Danković, B., et al. (2017). Sex differences in macrophage functions in middle-aged rats: relevance of estradiol level and macrophage estrogen receptor expression. *Inflammation* 40 (3), 1087–1101. doi:10.1007/s10753-017-0551-3

Dam, D. H. M., Culver, K. S., Kandela, I., Lee, R. C., Chandra, K., Lee, H., et al. (2015). Biodistribution and *in vivo* toxicity of aptamer-loaded gold nanostars. *Nanomedicine Nanotechnol. Biol. Med.* 11 (3), 671–679. doi:10.1016/j.nano.2014.10.005

Donovan, M. D. (2005). Sex and racial differences in pharmacological response: effect of route of administration and drug delivery system on pharmacokinetics. *J. Women's Health* 14 (1), 30–37. doi:10.1089/jwh.2005.14.30

Doran, S. J., Ritzel, R. M., Glaser, E. P., Henry, R. J., Faden, A. I., and Loane, D. J. (2019). Sex differences in acute neuroinflammation after experimental traumatic brain injury are mediated by infiltrating myeloid cells. *J. Neurotrauma* 36 (7), 1040–1053. doi:10.1089/neu.2018.6019

Duijster, J. W., Lieber, T., Pacelli, S., Van Balveren, L., Ruijs, L. S., Raethke, M., et al. (2023). Sex-disaggregated outcomes of adverse events after COVID-19 vaccination: a Dutch cohort study and review of the literature. *Front. Immunol.* 14, 1078736. doi:10.3389/fimmu.2023.1078736

England, R. J., Homer, J. J., Knight, L. C., and Ell, S. R. (1999). Nasal pH measurement: a reliable and repeatable parameter. *Clin. Otolaryngology Allied Sci.* 24 (1), 67–68. doi:10.1046/j.1365-2273.1999.00223.x

Farkouh, A., Riedl, T., Gottardi, R., Czejka, M., and Kautzky-Willer, A. (2020). Sex-related differences in pharmacokinetics and pharmacodynamics of frequently prescribed drugs: a review of the literature. *Adv. Ther.* 37 (2), 644–655. doi:10.1007/s12325-019-01201-3

Feigin, V. L., Stark, B. A., Johnson, C. O., Roth, G. A., Bisignano, C., Abady, G. G., et al. (2021). Global, regional, and national burden of stroke and its risk factors, 1990–2019: a systematic analysis for the Global Burden of Disease Study 2019. *Lancet Neurology* 20 (10), 795–820. doi:10.1016/S1474-4422(21)00252-0

Ferrarese, C., Mascarucci, P., Zoia, C., Cavarretta, R., Frigo, M., Begni, B., et al. (1999). Increased cytokine release from peripheral blood cells after acute stroke. *J. Cereb. Blood Flow Metabolism* 19 (9), 1004–1009. doi:10.1097/00004647-199909000-00008

Gao, L., Pan, X., Zhang, J. H., and Xia, Y. (2023). Glial cells: an important switch for the vascular function of the central nervous system. *Front. Cell. Neurosci.* 17, 1166770. doi:10.3389/fncel.2023.1166770

Gokulan, K., Williams, K., Orr, S., and Khare, S. (2020). Human intestinal tissue explant exposure to silver nanoparticles reveals sex dependent alterations in inflammatory responses and epithelial cell permeability. *Int. J. Mol. Sci.* 22 (1), 9. doi:10.3390/ijms22010009

González-Hernández, S., and Mukouyama, Y. (2023). Lymphatic vasculature in the central nervous system. *Front. Cell. Dev. Biol.* 11, 1150775. doi:10.3389/fcell.2023.1150775

Gosselin, S., Ramaiah, L., and Earl, L. (2011) 'Clinical chemistry in toxicity testing: scope and methods', *general, applied, and systems toxicology* [preprint]. doi:10.1002/9780470744307.gat040

Gupta, S., Nakabo, S., Blanco, L. P., O'Neil, L. J., Wigerblad, G., Goel, R. R., et al. (2020). Sex differences in neutrophil biology modulate response to type I interferons and immunometabolism. *Proc. Natl. Acad. Sci.* 117 (28), 16481–16491. doi:10.1073/pnas.2003603117

Gupte, R., Brooks, W. M., Vukas, R. R., Pierce, J. D., and Harris, J. L. (2019). Sex differences in traumatic brain injury: what we know and what we should know. *J. Neurotrauma* 36 (22), 3063–3091. doi:10.1089/neu.2018.6171

Hajipour, M. J., Aghaverdi, H., Serpooshan, V., Vali, H., Sheibani, S., and Mahmoudi, M. (2021). Sex as an important factor in nanomedicine. *Nat. Commun.* 12 (1), 2984. doi:10.1038/s41467-021-23230-9

Hakiminia, B., Alikiaii, B., Khorvash, F., and Mousavi, S. (2022). Oxidative stress and mitochondrial dysfunction following traumatic brain injury: from mechanistic view to targeted therapeutic opportunities. *Fundam. Clin. Pharmacol.* 36 (4), 612–662. doi:10.1111/fcp.12767

Hallschmid, M. (2021). Intranasal insulin. *J. Neuroendocrinol.* 33 (4), e12934. doi:10.1111/jne.12934

Han, H.-Y., Cho, J. W., Seong, E., Park, E. J., Lee, G. H., Kim, D. W., et al. (2020). Amorphous silica nanoparticle-induced pulmonary inflammatory response depends on particle size and is sex-specific in rats. *Toxicol. Appl. Pharmacol.* 390, 114890. doi:10.1016/j.taap.2020.114890

Hashimoto, Y., Greene, C., Munnich, A., and Campbell, M. (2023). The CLDN5 gene at the blood-brain barrier in health and disease. *Fluids Barriers CNS* 20 (1), 22. doi:10.1186/s12987-023-00424-5

Hawkins, R. A., O'Kane, R. L., Simpson, I. A., and Viña, J. R. (2006). Structure of the blood-brain barrier and its role in the transport of amino acids. *J. Nutr.* 136 (1), 218S–226S. doi:10.1093/jn/136.1.218S

Hazeldine, J., Hampson, P., and Lord, J. M. (2014). The impact of trauma on neutrophil function. *Injury* 45 (12), 1824–1833. doi:10.1016/j.injury.2014.06.021

Hokanson, K. C., Hernández, C., Deitzler, G. E., Gaston, J. E., and David, M. M. (2023). Sex shapes gut–microbiota–brain communication and disease. *Trends Microbiol.* [Preprint]. doi:10.1016/j.tim.2023.08.013

Iliff, J. J., Wang, M., Liao, Y., Plogg, B. A., Peng, W., Gundersen, G. A., et al. (2012). A paravascular pathway facilitates CSF flow through the brain parenchyma and the clearance of interstitial solutes, including amyloid β. *Sci. Transl. Med.* 4 (147), 147111. doi:10.1126/scitranslmed.3003748

Islam, M. A., Jacob, M. V., and Antunes, E. (2021). A critical review on silver nanoparticles: from synthesis and applications to its mitigation through low-cost adsorption by biochar. *J. Environ. Manag.* 281, 111918. doi:10.1016/j.jenvman.2020.111918

James, B. D., and Allen, J. B. (2021). Sex-specific response to combinations of shear stress and substrate stiffness by endothelial cells *in vitro*. *Adv. Healthc. Mater.* 10 (18), 2100735. doi:10.1002/adhm.202100735

Jašarević, E., Morrison, K. E., and Bale, T. L. (2016). Sex differences in the gut microbiome–brain axis across the lifespan. *Philosophical Trans. R. Soc. B Biol. Sci.* 371 (1688), 20150122. doi:10.1098/rstb.2015.0122

Jayaraj, R. L., Azimullah, S., Beiram, R., Jalal, F. Y., and Rosenberg, G. A. (2019). Neuroinflammation: friend and foe for ischemic stroke. *J. Neuroinflammation* 16 (1), 142. doi:10.1186/s12974-019-1516-2

Jiang, K., Yu, Y., Qiu, W., Tian, K., Guo, Z., Qian, J., et al. (2023). Protein corona on brain targeted nanocarriers: challenges and prospects. *Adv. Drug Deliv. Rev.* 202, 115114. doi:10.1016/j.addr.2023.115114

Jin, X., Ishii, H., Bai, Z., Itokazu, T., and Yamashita, T. (2012). Temporal changes in cell marker expression and cellular infiltration in a controlled cortical impact model in adult male C57bl/6 mice. *PLoS ONE* 7 (7), e41892. doi:10.1371/journal.pone.0041892

Karastergiou, K., Smith, S. R., Greenberg, A. S., and Fried, S. K. (2012). Sex differences in human adipose tissues – the biology of pear shape. *Biol. Sex Differ.* 3 (1), 13. doi:10.1186/2042-6410-3-13

Karlsson Lind, L., Rydberg, D. M., and Schenck-Gustafsson, K. (2023). Sex and gender differences in drug treatment: experiences from the knowledge database Janusmed Sex and Gender. *Biol. Sex Differ.* 14 (1), 28. doi:10.1186/s13293-023-00511-0

Kawano, T., Shimamura, M., Nakagami, H., Kanki, H., Sasaki, T., and Mochizuki, H. (2019). Temporal and spatial profile of polymorphonuclear myeloid-derived suppressor cells (PMN-MDSCs) in ischemic stroke in mice. *PLOS ONE* 14 (5), 215482. doi:10.1371/journal.pone.0215482

Kim, J.-C., Lee, I. C., Ko, J. W., Park, S. H., Lim, J. O., Shin, I. S., et al. (2016). Comparative toxicity and biodistribution of copper nanoparticles and cupric ions in rats. *Int. J. Nanomedicine* 11, 2883–2900. doi:10.2147/IJN.S106346

Kim, S., Kubelka, N. K., LaPorte, H. M., Krishnamoorthy, V. R., and Singh, M. (2023). Estradiol and 3β-diol protect female cortical astrocytes by regulating connexin 43 Gap Junctions. *Mol. Cell. Endocrinol.* 578, 112045. doi:10.1016/j.mce.2023.112045

Kim, S. Y., Kim, J. S., Cho, H. S., Rha, D. S., Kim, J. M., Park, J. D., et al. (2008). Twenty-eight-day oral toxicity, genotoxicity, and gender-related tissue distribution of silver nanoparticles in Sprague-Dawley rats. *Inhal. Toxicol.* 20 (6), 575–583. doi:10.1080/08958370701874663

Kim, W.-Y., Kim, J., Park, J. D., Ryu, H. Y., and Yu, I. J. (2009). Histological study of gender differences in accumulation of silver nanoparticles in kidneys of fischer 344 rats. *J. Toxicol. Environ. Health Part A* 72 (21–22), 1279–1284. doi:10.1080/15287390903212287

Kisler, K., Nikolakopoulou, A. M., and Zlokovic, B. V. (2021). Microglia have a grip on brain microvasculature. *Nat. Commun.* 12 (1), 5290. doi:10.1038/s41467-021-25595-3

Klein, S. L., and Flanagan, K. L. (2016). Sex differences in immune responses. *Nat. Rev. Immunol.* 16 (10), 626–638. doi:10.1038/nri.2016.90

Koebele, S. V., and Bimonte-Nelson, H. A. (2015). Trajectories and phenotypes with estrogen exposures across the lifespan: what does Goldilocks have to do with it? *Hormones Behav.* 74, 86–104. doi:10.1016/j.yhbeh.2015.06.009

Koebele, S. V., and Bimonte-Nelson, H. A. (2017). The endocrine-brain-aging triad where many paths meet: female reproductive hormone changes at midlife and their influence on circuits important for learning and memory. *Exp. Gerontol.* 94, 14–23. doi:10.1016/j.exger.2016.12.011

Koellhoffer, E. C., and McCullough, L. D. (2013). The effects of estrogen in ischemic stroke. *Transl. Stroke Res.* 4 (4), 390–401. doi:10.1007/s12975-012-0230-5

Kondo, M., Weissman, I. L., and Akashi, K. (1997). Identification of clonogenic common lymphoid progenitors in mouse bone marrow. *Cell.* 91 (5), 661–672. doi:10.1016/S0092-8674(00)80453-5

Kuang, H., Zhang, W., Yang, L., Aguilar, Z. P., and Xu, H. (2021). Reproductive organ dysfunction and gene expression after orally administration of ZnO nanoparticles in murine. *Environ. Toxicol.* 36 (4), 550–561. doi:10.1002/tox.23060

Kunio, M., Wong, G., Markham, P. M., and Edelman, E. R. (2018). Sex differences in the outcomes of stent implantation in mini-swine model. *PLOS ONE* 13 (1), 192004. doi:10.1371/journal.pone.0192004

Kurmann, L., Okoniewski, M., and Dubey, R. K. (2021). Estradiol inhibits human brain vascular pericyte migration activity: a functional and transcriptomic analysis. *Cells* 10 (9), 2314. doi:10.3390/cells10092314

Landreneau, M. J., Mullen, M. T., Messé, S. R., Cucchiara, B., Sheth, K. N., McCullough, L. D., et al. (2018). CCL2 and CXCL10 are associated with poor outcome after intracerebral hemorrhage. *Ann. Clin. Transl. Neurology* 5 (8), 962–970. doi:10.1002/acn3.595

Lauzier, D. C., Jayaraman, K., Yuan, J. Y., Diwan, D., Vellimana, A. K., Osbun, J. W., et al. (2023). Early brain injury after subarachnoid hemorrhage: incidence and mechanisms. *Stroke* 54 (5), 1426–1440. doi:10.1161/STROKEAHA.122.040072

Lawrence, J. M., Schardien, K., Wigdahl, B., and Nonnemacher, M. R. (2023). Roles of neuropathology-associated reactive astrocytes: a systematic review. *Acta Neuropathol. Commun.* 11 (1), 42. doi:10.1186/s40478-023-01526-9

Lenz, K. M., and McCarthy, M. M. (2015). A starring role for microglia in brain sex differences. *Neurosci.* 21 (3), 306–321. doi:10.1177/1073858414536468

Liddelow, S. A., and Barres, B. A. (2017). Reactive astrocytes: production, function, and therapeutic potential. *Immunity* 46 (6), 957–967. doi:10.1016/j.immuni.2017.06.006

Liu, J., Sato, Y., Falcone-Juengert, J., Kurisu, K., Shi, J., and Yenari, M. A. (2022). Sexual dimorphism in immune cell responses following stroke. *Neurobiol. Dis.* 172, 105836. doi:10.1016/j.nbd.2022.105836

Liu, Y.-W., Li, S., and Dai, S.-S. (2018). Neutrophils in traumatic brain injury (TBI): friend or foe? *J. Neuroinflammation* 15 (1), 146. doi:10.1186/s12974-018-1173-x

Long, J., Sun, Y., Liu, S., Yang, S., Chen, C., Zhang, Z., et al. (2023). Targeting pyroptosis as a preventive and therapeutic approach for stroke. *Cell. Death Discov.* 9 (1), 155. doi:10.1038/s41420-023-01440-y

Loram, L. C., Sholar, P. W., Taylor, F. R., Wiesler, J. L., Babb, J. A., Strand, K. A., et al. (2012). Sex and estradiol influence glial pro-inflammatory responses to lipopolysaccharide in rats. *Psychoneuroendocrinology* 37 (10), 1688–1699. doi:10.1016/j.psyneuen.2012.02.018

Lösel, R., and Wehling, M. (2003). Nongenomic actions of steroid hormones. *Nat. Rev. Mol. Cell. Biol.* 4 (1), 46–55. doi:10.1038/nrm1009

Lu, R. J., Taylor, S., Contrepois, K., Kim, M., Bravo, J. I., Ellenberger, M., et al. (2021). Multi-omic profiling of primary mouse neutrophils predicts a pattern of sex- and age-related functional regulation. *Nat. Aging* 1 (8), 715–733. doi:10.1038/s43587-021-00086-8

Luberti, F. R., Reside, T. L., Bonin, P. L., and Carré, J. M. (2021). Development of a single-dose intranasal testosterone administration paradigm for use in men and women. *Hormones Behav.* 136, 105046. doi:10.1016/j.yhbeh.2021.105046

Maas, A. I. R., Menon, D. K., Manley, G. T., Abrams, M., Åkerlund, C., Andelic, N., et al. (2022). Traumatic brain injury: progress and challenges in prevention, clinical care, and research. *Lancet Neurology* 21, 1004–1060. doi:10.1016/S1474-4422(22)00309-X

Madla, C. M., Gavins, F. K., Merchant, H. A., Orlu, M., Murdan, S., and Basit, A. W. (2021). Let's talk about sex: differences in drug therapy in males and females. *Adv. Drug Deliv. Rev.* 175, 113804. doi:10.1016/j.addr.2021.05.014

Maggi, A. (2022). Sex and liver disease: the necessity of an overarching theory to explain the effect of sex on nonreproductive functions. *Endocrinology* 163 (1), bqab229. doi:10.1210/endocr/bqab229

Mahdieh, Z., Postma, B., Herritt, L. A., Hamilton, R. F., Harkema, J. R., and Holian, A. (2022). Hyperspectral microscopy of subcutaneously released silver nanoparticles reveals sex differences in drug distribution. *Micron* 153, 103193. doi:10.1016/j.micron.2021.103193

Mahmoudi, Serpooshan, V., Yang, P. C., and Heydarpour, M. (2021). Abstract P392: the effect of cell sex on magnetic nanoparticle uptake of human induced pluripotent stem cell-derived cardiomyocytes. *Circulation Res.* 129, AP392. doi:10.1161/res.129.suppl_1.P392

Mantovani, A., Cassatella, M. A., Costantini, C., and Jaillon, S. (2011). Neutrophils in the activation and regulation of innate and adaptive immunity. *Nat. Rev. Immunol.* 11 (8), 519–531. doi:10.1038/nri3024

Marjan, S., Sojoudi, Z., Khodagholi, F., Rahmati, H., Jameie, S. B., Eftekharzadeh, M., et al. (2023). Effect of sex differences and time of oxytocin administration on treatment of rat model of autism spectrum disorder: focused on necroptosis markers. *Int. J. Dev. Neurosci.* 83 (6), 552–570. doi:10.1002/jdn.10286

McCullough, L. D., Zeng, Z., Blizzard, K. K., Debchoudhury, I., and Hurn, P. D. (2005). Ischemic nitric oxide and poly (ADP-Ribose) polymerase-1 in cerebral ischemia: male toxicity, female protection. *J. Cereb. Blood Flow Metabolism* 25 (4), 502–512. doi:10.1038/sj.jcbfm.9600059

McDonough, A. A., Harris, A. N., Xiong, L., and Layton, A. T. (2023) 'Sex difference in renal transporters: assessment and functional consequences', *nature reviews nephrology* [preprint]. doi:10.1038/s41581-023-00757-2

Medina, D. X., Householder, K. T., Ceton, R., Kovalik, T., Heffernan, J. M., Shankar, R. V., et al. (2017). Optical barcoding of PLGA for multispectral analysis of nanoparticle fate *in vivo*. *J. Control. Release* 253, 172–182. doi:10.1016/j.jconrel.2017.02.033

Mikolic, A., Groeniger, J. O., Zeldovich, M., Wilson, L., van Lennep, J. R., van Klaveren, D., et al. (2021). Explaining outcome differences between men and women following mild traumatic brain injury. *J. Neurotrauma* 38 (23), 3315–3331. doi:10.1089/neu.2021.0116

Mitchell, M. J., Billingsley, M. M., Haley, R. M., Wechsler, M. E., Peppas, N. A., and Langer, R. (2021). Engineering precision nanoparticles for drug delivery. *Nat. Rev. Drug Discov.* 20 (2), 101–124. doi:10.1038/s41573-020-0090-8

Mohamud Yusuf, A., Hagemann, N., Ludewig, P., Gunzer, M., and Hermann, D. M. (2022). Roles of polymorphonuclear neutrophils in ischemic brain injury and post-ischemic brain remodeling. *Front. Immunol.* 12, 825572. doi:10.3389/fimmu.2021.825572

Nakamura, K., Fujiki, T., and Tamura, H. (2005). Age, gender and region-specific differences in drug metabolising enzymes in rat ocular tissues. *Exp. Eye Res.* 81 (6), 710–715. doi:10.1016/j.exer.2005.04.011

National Institutes of Health (2015). *Consideration of sex as a biological variable in NIH-funded research*. National Institutes of Health. Available at: https://grants.nih.gov/grants/guide/notice-files/NOT-OD-15-102.html.

Offner, H., Subramanian, S., Parker, S. M., Afentoulis, M. E., Vandenbark, A. A., and Hurn, P. D. (2006). Experimental stroke induces massive, rapid activation of the peripheral immune system. *J. Cereb. Blood Flow Metabolism* 26 (5), 654–665. doi:10.1038/sj.jcbfm.9600217

Osier, N. D., and Dixon, C. E. (2016). The controlled cortical impact model: applications, considerations for researchers, and future directions. *Front. Neurology* 7, 134. doi:10.3389/fneur.2016.00134

Pabbidi, M. R., Kuppusamy, M., Didion, S. P., Sanapureddy, P., Reed, J. T., and Sontakke, S. P. (2018). Sex differences in the vascular function and related mechanisms: role of 17β-estradiol. *Am. J. Physiology-Heart Circulatory Physiology* 315 (6), H1499–H1518. doi:10.1152/ajpheart.00194.2018

Pace, S., Rossi, A., Krauth, V., Dehm, F., Troisi, F., Bilancia, R., et al. (2017). Sex differences in prostaglandin biosynthesis in neutrophils during acute inflammation. *Sci. Rep.* 7 (1), 3759. doi:10.1038/s41598-017-03696-8

Peters, S. A. E., Huxley, R. R., and Woodward, M. (2014). Diabetes as a risk factor for stroke in women compared with men: a systematic review and meta-analysis of 64 cohorts, including 775 385 individuals and 12 539 strokes. *Lancet* 383 (9933), 1973–1980. doi:10.1016/S0140-6736(14)60040-4

Pizzino, G., Irrera, N., Cucinotta, M., Pallio, G., Mannino, F., Arcoraci, V., et al. (2017). Oxidative stress: harms and benefits for human health. *Oxidative Med. Cell. Longev.* 2017, 1–13. doi:10.1155/2017/8416763

Poley, M., Chen, G., Sharf-Pauker, N., Avital, A., Kaduri, M., Sela, M., et al. (2022). Sex-based differences in the biodistribution of nanoparticles and their effect on hormonal, immune, and metabolic function. *Adv. NanoBiomed Res.* 2 (12), 2200089. doi:10.1002/anbr.202200089

Rahimi Mansour, F., Keyvanfar, A., Najafiarab, H., Rajaei Firouzabadi, S., Sefidgar, S., Hooshmand Chayijan, S., et al. (2023). Menstrual disturbances following COVID-19 vaccination: a probable puzzle about the role of endocrine and immune pathways. *J. Reproductive Immunol.* 158, 103952. doi:10.1016/j.jri.2023.103952

Rexrode, K. M., Madsen, T. E., Yu, A. Y., Carcel, C., Lichtman, J. H., and Miller, E. C. (2022). The impact of sex and gender on stroke. *Circulation Res.* 130 (4), 512–528. doi:10.1161/CIRCRESAHA.121.319915

Riaz, H., Hashmi, R., Abid, S., Shareef, N., Faqir, A., Amir, A., et al. (2020). Intraperitoneal injections of copper ferrite nanoparticles disturb blood, plasma, and antioxidant parameters of Wistar rats in a sex-specific manner. *Naunyn-Schmiedeberg's Archives Pharmacol.* 393 (11), 2019–2028. doi:10.1007/s00210-020-01899-x

Ritzel, R. M., Doran, S. J., Barrett, J. P., Henry, R. J., Ma, E. L., Faden, A. I., et al. (2018). Chronic alterations in systemic immune function after traumatic brain injury. *J. Neurotrauma* 35 (13), 1419–1436. doi:10.1089/neu.2017.5399

Robison, L. S., Gannon, O. J., Salinero, A. E., and Zuloaga, K. L. (2019). Contributions of sex to cerebrovascular function and pathology. *Brain Res.* 1710, 43–60. doi:10.1016/j.brainres.2018.12.030

Rodriguez-Rodriguez, A., Egea-Guerrero, J., Murillo-Cabezas, F., and Carrillo-Vico, A. (2014). Oxidative stress in traumatic brain injury. *Curr. Med. Chem.* 21 (10), 1201–1211. doi:10.2174/09298673216613217153310

Rostène, W., Kitabgi, P., and Parsadaniantz, S. M. (2007). Chemokines: a new class of neuromodulator? *Nat. Rev. Neurosci.* 8 (11), 895–903. doi:10.1038/nrn2255

Routledge, P., Stargel, W., Kitchell, B., Barchowsky, A., and Shand, D. (1981). Sex-related differences in the plasma protein binding of lignocaine and diazepam. *Br. J. Clin. Pharmacol.* 11 (3), 245–250. doi:10.1111/j.1365-2125.1981.tb00528.x

Ruddy, R. M., Adams, K. V., and Morshead, C. M. (2019). Age- and sex-dependent effects of metformin on neural precursor cells and cognitive recovery in a model of neonatal stroke. *Sci. Adv.* 5 (9), 1912. doi:10.1126/sciadv.aax1912

Saatman, K. E., Feeko, K. J., Pape, R. L., and Raghupathi, R. (2006). Differential behavioral and histopathological responses to graded cortical impact injury in mice. *J. Neurotrauma* 23 (8), 1241–1253. doi:10.1089/neu.2006.23.1241

Salim, S. (2017). Oxidative stress and the central nervous system. *J. Pharmacol. Exp. Ther.* 360 (1), 201–205. doi:10.1124/jpet.116.237503

Sato, Y., Falcone-Juengert, J., Tominaga, T., Su, H., and Liu, J. (2022). Remodeling of the neurovascular unit following cerebral ischemia and hemorrhage. *Cells* 11 (18), 2823. doi:10.3390/cells11182823

Schwab, N., Taskina, D., Leung, E., Innes, B. T., Bader, G. D., and Hazrati, L. N. (2022). Neurons and glial cells acquire a senescent signature after repeated mild traumatic brain injury in a sex-dependent manner. *Front. Neurosci.* 16, 1027116. doi:10.3389/fnins.2022.1027116

Schwarz, J. M., Sholar, P. W., and Bilbo, S. D. (2012). Sex differences in microglial colonization of the developing rat brain: sex differences in microglial colonization. *J. Neurochem.*, no. doi:10.1111/j.1471-4159.2011.07630.x

Sciarra, F., Campolo, F., Franceschini, E., Carlomagno, F., and Venneri, M. (2023). Gender-specific impact of sex hormones on the immune system. *Int. J. Mol. Sci.* 24 (7), 6302. doi:10.3390/ijms24076302

Sehsah, R., Wu, W., Ichihara, S., Hashimoto, N., Zong, C., Yamazaki, K., et al. (2022). Protective role of Nrf2 in zinc oxide nanoparticles-induced lung inflammation in female mice and sexual dimorphism in susceptibility. *Toxicol. Lett.* 370, 24–34. doi:10.1016/j.toxlet.2022.09.004

Seifert, H. A., Zhu, W., Vandenbark, A. A., Alkayed, N. J., and Offner, H. (2019). Sex differences in the therapeutic effects of anti-PDL2 neutralizing antibody on stroke. *Metab. Brain Dis.* 34 (6), 1705–1712. doi:10.1007/s11011-019-00476-3

SenthilKumar, G., Katunaric, B., Bordas-Murphy, H., Sarvaideo, J., and Freed, J. K. (2023). Estrogen and the vascular endothelium: the unanswered questions. *Endocrinology*, bqad079. doi:10.1210/endocr/bqad079

Serpooshan, V., Sheibani, S., Pushparaj, P., Wojcik, M., Jang, A. Y., Santoso, M. R., et al. (2018). Effect of cell sex on uptake of nanoparticles: the overlooked factor at the nanobio interface. *ACS Nano* 12 (3), 2253–2266. doi:10.1021/acsnano.7b06212

Sharifi, S., Caracciolo, G., Pozzi, D., Digiacomo, L., Swann, J., Daldrup-Link, H. E., et al. (2021). The role of sex as a biological variable in the efficacy and toxicity of therapeutic nanomedicine. *Adv. Drug Deliv. Rev.* 174, 337–347. doi:10.1016/j.addr.2021.04.028

Simon, D. W., McGeachy, M. J., Bayır, H., Clark, R. S. B., Loane, D. J., and Kochanek, P. M. (2017). The far-reaching scope of neuroinflammation after traumatic brain injury. *Nat. Rev. Neurol.* 13 (3), 171–191. doi:10.1038/nrneurol.2017.13

Sloan, J. (2000). The pharmacodynamics of PK 11195 in diazepam-dependent male and female rats. *Pharmacol. Biochem. Behav.* 66 (4), 751–764. doi:10.1016/S0091-3057(00)00239-2

Soldin, O. P., and Mattison, D. R. (2009). Sex differences in pharmacokinetics and pharmacodynamics. *Clin. Pharmacokinet.* 48 (3), 143–157. doi:10.2165/00003088-200948030-00001

Stamova, B., Jickling, G. C., Ander, B. P., Zhan, X., Liu, D., Turner, R., et al. (2014). Gene expression in peripheral immune cells following cardioembolic stroke is sexually dimorphic. *PLoS ONE* 9 (7), e102550. doi:10.1371/journal.pone.0102550

Stillhart, C., Vučićević, K., Augustijns, P., Basit, A. W., Batchelor, H., Flanagan, T. R., et al. (2020). Impact of gastrointestinal physiology on drug absorption in special populations--An UNGAP review. *Eur. J. Pharm. Sci.* 147, 105280. doi:10.1016/j.ejps.2020.105280

Sugiyama, S., Sasaki, T., Tanaka, H., Yan, H., Ikegami, T., Kanki, H., et al. (2023). The tight junction protein occludin modulates blood–brain barrier integrity and neurological function after ischemic stroke in mice. *Sci. Rep.* 13 (1), 2892. doi:10.1038/s41598-023-29894-1

Sung, J. H., Ji, J. H., Park, J. D., Yoon, J. U., Kim, D. S., Jeon, K. S., et al. (2009). Subchronic inhalation toxicity of silver nanoparticles. *Toxicol. Sci.* 108 (2), 452–461. doi:10.1093/toxsci/kfn246

Tang, Y., Wang, X., Li, J., Nie, Y., Liao, G., Yu, Y., et al. (2019). Overcoming the reticuloendothelial system barrier to drug delivery with a "don't-eat-us" strategy. *ACS Nano* 13 (11), 13015–13026. doi:10.1021/acsnano.9b05679

Tannenbaum, C., Ellis, R. P., Eyssel, F., Zou, J., and Schiebinger, L. (2019). Sex and gender analysis improves science and engineering. *Nature* 575 (7781), 137–146. doi:10.1038/s41586-019-1657-6

Tariba Lovaković, B., Barbir, R., Pem, B., Goessler, W., Ćurlin, M., Micek, V., et al. (2021). Sex-related response in mice after sub-acute intraperitoneal exposure to silver nanoparticles. *NanoImpact* 23, 100340. doi:10.1016/j.impact.2021.100340

Tariq, M. B., Lee, J., and McCullough, L. D. (2023). Sex differences in the inflammatory response to stroke. *Seminars Immunopathol.* 45 (3), 295–313. doi:10.1007/s00281-022-00969-x

Tarudji, A. W., Miller, H. A., Curtis, E. T., Porter, C. L., Madsen, G. L., and Kievit, F. M. (2023). Sex-based differences of antioxidant enzyme nanoparticle effects following traumatic brain injury. *J. Control. Release* 355, 149–159. doi:10.1016/j.jconrel.2023.01.065

Tejeda-Bayron, F. A., Rivera-Aponte, D. E., Malpica-Nieves, C. J., Maldonado-Martínez, G., Maldonado, H. M., Skatchkov, S. N., et al. (2021). Activation of glutamate transporter-1 (GLT-1) confers sex-dependent neuroprotection in brain ischemia. *Brain Sci.* 11 (1), 76. doi:10.3390/brainsci11010076

Tewari, B. P., Chaunsali, L., Prim, C. E., and Sontheimer, H. (2022). A glial perspective on the extracellular matrix and perineuronal net remodeling in the central nervous system. *Front. Cell. Neurosci.* 16, 1022754. doi:10.3389/fncel.2022.1022754

Thomsen, M. S., Routhe, L. J., and Moos, T. (2017). The vascular basement membrane in the healthy and pathological brain. *J. Cereb. Blood Flow Metabolism* 37 (10), 3300–3317. doi:10.1177/0271678X17722436

Tian, H., Chen, X., Liao, J., Yang, T., Cheng, S., Mei, Z., et al. (2022). Mitochondrial quality control in stroke: from the mechanisms to therapeutic potentials. *J. Cell. Mol. Med.* 26 (4), 1000–1012. doi:10.1111/jcmm.17189

Townsend, E. A., Miller, V. M., and Prakash, Y. S. (2012). Sex differences and sex steroids in lung health and disease. *Endocr. Rev.* 33 (1), 1–47. doi:10.1210/er.2010-0031

Tran, T. T., and Roffler, S. R. (2023). Interactions between nanoparticle corona proteins and the immune system. *Curr. Opin. Biotechnol.* 84, 103010. doi:10.1016/j.copbio.2023.103010

Valodara, and Johar, S. (2019). Sexual dimorphism in drug metabolism and pharmacokinetics. *Curr. Drug Metab.* 20 (14), 1154–1166. doi:10.2174/1389200220666191021094906

Varghese, M., Clemente, J., Lerner, A., Abrishami, S., Islam, M., Subbaiah, P., et al. (2022). Monocyte trafficking and polarization contribute to sex differences in meta-inflammation. *Front. Endocrinol.* 13, 826320. doi:10.3389/fendo.2022.826320

Villa, A., Gelosa, P., Castiglioni, L., Cimino, M., Rizzi, N., Pepe, G., et al. (2018). Sex-specific features of microglia from adult mice. *Cell. Rep.* 23 (12), 3501–3511. doi:10.1016/j.celrep.2018.05.048

Villapol, S., Loane, D. J., and Burns, M. P. (2017). Sexual dimorphism in the inflammatory response to traumatic brain injury. *Glia* 65 (9), 1423–1438. doi:10.1002/glia.23171

Vyas, M. V., Silver, F. L., Austin, P. C., Yu, A. Y., Pequeno, P., Fang, J., et al. (2021). Stroke incidence by sex across the lifespan. *Stroke* 52 (2), 447–451. doi:10.1161/STROKEAHA.120.032898

Wagner, A. K., Chen, X., Kline, A. E., Li, Y., Zafonte, R. D., and Dixon, C. E. (2005). Gender and environmental enrichment impact dopamine transporter expression after experimental traumatic brain injury. *Exp. Neurol.* 195 (2), 475–483. doi:10.1016/j.expneurol.2005.06.009

Wang, L., Butcher, N. J., Minchin, R. F., and Kaminskas, L. M. (2021). Monocytes do not contribute to sex differences seen in the pharmacokinetics of pegylated liposomal doxorubicin. *J. Pharm. Sci.* 110 (8), 3099–3101. doi:10.1016/j.xphs.2021.05.009

Waxman, D. J., and Holloway, M. G. (2009). Sex differences in the expression of hepatic drug metabolizing enzymes. *Mol. Pharmacol.* 76 (2), 215–228. doi:10.1124/mol.109.056705

Weber, C. M., and Clyne, A. M. (2021). Sex differences in the blood–brain barrier and neurodegenerative diseases. *Apl. Bioeng.* 5 (1), 011509. doi:10.1063/5.0035610

Wei, Y., Quan, L., Zhou, C., and Zhan, Q. (2018). Factors relating to the biodistribution and clearance of nanoparticles and their effects on *in vivo* application. *Nanomedicine* 13 (12), 1495–1512. doi:10.2217/nnm-2018-0040

Weis, W. I., and Nelson, W. J. (2006). Re-Solving the cadherin-catenin-actin conundrum. *J. Biol. Chem.* 281 (47), 35593–35597. doi:10.1074/jbc.R600027200

Wen, P., Ke, W., Dirisala, A., Toh, K., Tanaka, M., and Li, J. (2023). Stealth and pseudo-stealth nanocarriers. *Adv. Drug Deliv. Rev.* 198, 114895. doi:10.1016/j.addr.2023.114895

Wu, D., Chen, Q., Chen, X., Han, F., Chen, Z., and Wang, Y. (2023). The blood–brain barrier: structure, regulation, and drug delivery. *Signal Transduct. Target. Ther.* 8 (1), 217. doi:10.1038/s41392-023-01481-w

Xie, W., Simats, A., Guo, Y., Huang, T., Sun, X., Chen, W., et al. (2023). Perspective review of myeloid immune cell responses and poststroke immunosuppression. *Stroke* 54 (7), 1920–1929. doi:10.1161/STROKEAHA.122.042075

Xing, C., Hayakawa, K., Lok, J., Arai, K., and Lo, E. H. (2012). Injury and repair in the neurovascular unit. *Neurological Res.* 34 (4), 325–330. doi:10.1179/1743132812Y.0000000019

Xiong, X., Xu, L., Wei, L., White, R. E., Ouyang, Y. B., and Giffard, R. G. (2015). IL-4 is required for sex differences in vulnerability to focal ischemia in mice. *Stroke* 46 (8), 2271–2276. doi:10.1161/STROKEAHA.115.008897

Xue, Y., Zhang, S., Huang, Y., Zhang, T., Liu, X., Hu, Y., et al. (2023). Acute toxic effects and gender-related biokinetics of silver nanoparticles following an intravenous injection in mice. *J. Appl. Toxicol.* 32 (11), 890–899. doi:10.1002/jat.2742

Yamano, S., Goto, Y., Takeda, T., Hirai, S., Furukawa, Y., Kikuchi, Y., et al. (2022). Pulmonary dust foci as rat pneumoconiosis lesion induced by titanium dioxide nanoparticles in 13-week inhalation study. *Part. Fibre Toxicol.* 19 (1), 58. doi:10.1186/s12989-022-00498-3

Yang, J., Hu, S., Rao, M., Hu, L., Lei, H., Wu, Y., et al. (2017). Copper nanoparticle-induced ovarian injury, follicular atresia, apoptosis, and gene expression alterations in female rats. *Int. J. Nanomedicine* 12, 5959–5971. doi:10.2147/IJN.S139215

Yang, J., Zhang, L., Yu, C., Yang, X. F., and Wang, H. (2014). Monocyte and macrophage differentiation: circulation inflammatory monocyte as biomarker for inflammatory diseases. *Biomark. Res.* 2 (1), 1. doi:10.1186/2050-7771-2-1

Yang, J.-L. J., Narayanamurthy, R., Yager, J. Y., and Unsworth, L. D. (2021). How does biological sex affect the physiological response to nanomaterials? *Nano Today* 41, 101292. doi:10.1016/j.nantod.2021.101292

Yuan, S., Liu, K. J., and Qi, Z. (2020). Occludin regulation of blood–brain barrier and potential therapeutic target in ischemic stroke. *Brain Circ.* 6 (3), 152–162. doi:10.4103/bc.bc_29_20

Zaid, M., Sala, L., Despins, L., Heise, D., Popescu, M., Skubic, M., et al. (2023). Cardiovascular sex-differences: insights via physiology-based modeling and potential for noninvasive sensing via ballistocardiography. *Front. Cardiovasc. Med.* 10, 1215958. doi:10.3389/fcvm.2023.1215958

Zhang, S., Gan, L., Cao, F., Wang, H., Gong, P., Ma, C., et al. (2022). The barrier and interface mechanisms of the brain barrier, and brain drug delivery. *Brain Res. Bull.* 190, 69–83. doi:10.1016/j.brainresbull.2022.09.017

Zhang, X.-D., Chen, Song, Wang, Shen, Wu, , et al. (2013). Sex differences in the toxicity of polyethylene glycol-coated gold nanoparticles in mice. *Int. J. Nanomedicine* 8, 2409–2419. doi:10.2147/IJN.S46376

Zhao, Y., Gan, L., Ren, L., Lin, Y., Ma, C., and Lin, X. (2022). Factors influencing the blood-brain barrier permeability. *Brain Res.* 1788, 147937. doi:10.1016/j.brainres.2022.147937

Ziebell, J. M., and Morganti-Kossmann, M. C. (2010). Involvement of pro- and anti-inflammatory cytokines and chemokines in the pathophysiology of traumatic brain injury. *Neurotherapeutics* 7 (1), 22–30. doi:10.1016/j.nurt.2009.10.016

Zlokovic, B. V. (2008). The blood-brain barrier in health and chronic neurodegenerative disorders. *Neuron* 57 (2), 178–201. doi:10.1016/j.neuron.2008.01.003

Zucker, I., and Prendergast, B. J. (2020). Sex differences in pharmacokinetics predict adverse drug reactions in women. *Biol. Sex Differ.* 11 (1), 32. doi:10.1186/s13293-020-00308-5

frontiers | Frontiers in Biomaterials Science

TYPE Review
PUBLISHED 03 April 2024
DOI 10.3389/fbiom.2024.1358508

OPEN ACCESS

EDITED BY
Silviya Petrova Zustiak,
Saint Louis University, United States

REVIEWED BY
Arul Prakash Francis,
Saveetha Dental College And Hospitals, India
Nathaniel Huebsch,
Washington University in St. Louis, United States
Dilip Thomas,
Stanford University, United States

*CORRESPONDENCE
Janet Zoldan,
zjanet@utexas.edu

†These authors have contributed equally to this work

RECEIVED 19 December 2023
ACCEPTED 21 March 2024
PUBLISHED 03 April 2024

CITATION
Kalkunte N, Cisneros J, Castillo E and Zoldan J (2024), A review on machine learning approaches in cardiac tissue engineering. *Front. Front. Biomater. Sci.* 3:1358508. doi: 10.3389/fbiom.2024.1358508

A review on machine learning approaches in cardiac tissue engineering

Nikhith Kalkunte†, Jorge Cisneros†, Edward Castillo and Janet Zoldan*

Department of Biomedical Engineering, The University of Texas at Austin, Austin, TX, United States

Cardiac tissue engineering (CTE) holds promise in addressing the clinical challenges posed by cardiovascular disease, the leading global cause of mortality. Human induced pluripotent stem cells (hiPSCs) are pivotal for cardiac regeneration therapy, offering an immunocompatible, high density cell source. However, hiPSC-derived cardiomyocytes (hiPSC-CMs) exhibit vital functional deficiencies that are not yet well understood, hindering their clinical deployment. We argue that machine learning (ML) can overcome these challenges, by improving the phenotyping and functionality of these cells via robust mathematical models and predictions. This review paper explores the transformative role of ML in advancing CTE, presenting a primer on relevant ML algorithms. We focus on how ML has recently addressed six key address six key challenges in CTE: cell differentiation, morphology, calcium handling and cell-cell coupling, contraction, and tissue assembly. The paper surveys common ML models, from tree-based and probabilistic to neural networks and deep learning, illustrating their applications to better understand hiPSC-CM behavior. While acknowledging the challenges associated with integrating ML, such as limited biomedical datasets, computational costs of learning data, and model interpretability and reliability, we examine suggestions for improvement, emphasizing the necessity for more extensive and diverse datasets that incorporate temporal and imaging data, augmented by synthetic generative models. By integrating ML with mathematical models and existing expert knowledge, we foresee a fruitful collaboration that unites innovative data-driven models with biophysics-informed models, effectively closing the gaps within CTE.

KEYWORDS

cardiac tissue engineering, machine learning, hiPSC-CM, cardiac maturation, deep learning

1 Introduction

Cardiac tissue engineering (CTE) is poised to improve clinical outcomes of cardiovascular disease (CVD), the leading cause of death worldwide. Affecting over 80 million Americans every year (Benjamin et al., 2018), the impact of cardiovascular disease is magnified by the heart's inability to repair and self-regenerate. Cardiomyocytes (CMs) have a limited ability to proliferate and generate new tissue after birth (Laflamme and Murry, 2011). Thus, infarction events that cause the death of cardiac tissue commonly result in permanent cardiac output deficiencies (Anderson and Morrow, 2017). Current treatment strategies for CVD seek to resolve infarction triggers, like coronary artery atherosclerosis,

and prevent future events (Reddy et al., 2015). While effective, these strategies do not repair or regenerate already-damaged cardiac tissue.

Human induced pluripotent stem cells (hiPSCs) are pivotal in realizing the potential of cardiac regeneration therapy. They address immunogenicity concerns associated with allogeneic cell sources and, more importantly, facilitate the achievement of high cell densities essential for restoring the over one billion cardiac cells damaged during myocardial infarction. hiPSCs are derived from patient tissue, minimizing the immunogenicity of implanted engineered tissues. Additionally, the self-renewal and proliferative behavior of hiPSCs ensure a theoretically limitless supply of CMs, enabling the engineering of patient-specific cardiac macrotissues at physiological cell densities. Yet, hiPSC differentiated cardiomyocytes (hiPSC-CM) exhibit abnormal morphology and decreased functionality compared to adult CMs with regards to contraction force and electrochemical coupling (Feric and Radisic, 2016). These deficiencies compound to significantly increase the potential for arrhythmias when hiPSC-CMs are implanted *in vivo* (Chong et al., 2014). Numerous groups have demonstrated the role of electrical (Nunes et al., 2013; Ruan et al., 2016), mechanical (McCain and Parker, 2011; Ruan et al., 2016), and biochemical stimuli (Horikoshi et al., 2019) on hiPSC-CM development and functionality, working to close the gap between hiPSC-CMs and *in vivo* cardiac tissues (Ronaldson-Bouchard et al., 2018). Even so, the discovery and optimization of these stimuli requires complex experimental methods and extended timelines, greatly slowing the rate of progress. Artificial intelligence, and more specially machine learning, has recently emerged to be a powerful tool, poised to accelerate experimental methods and parallel, even predict, *in vitro* work.

Herein we provide a primer on relevant machine learning algorithms, review current work applying machine learning to CTE and trends of focus, and discuss key ideas for further development. Specifically, we identify the following six challenges of CTE: cell differentiation, morphology, calcium handling and cell-cell coupling, cell contraction, and tissue assembly. Historically, biomedical applications of ML have primarily focused on processing large quantitative sets like RNA sequencing data or MRI imaging datasets (Wang et al., 2018; Cascianelli et al., 2020; Petegrosso et al., 2020). Here we discuss how this work have been translated to the field of tissue engineering to resolve the challenges related to hiPSC-CM maturity. It is worth noting others have sought to review the applications of machine learning in stem cell therapies (Coronnello and Francipane, 2022), cardiovascular pathology and treatment (Bizopoulos and Koutsouris, 2019; Glass et al., 2022; Kresoja et al., 2023), 3D bioprinting (An et al., 2021), organ-on-a-chip methodologies (Koyilot et al., 2022), and biomedical engineering as a whole (Shajun Nisha and Nagoor Meeral, 2021), yet few focus on the specific challenges of CTE and provide an in-depth review of how machine learning may be leveraged to improve the maturation of hiPSC-CMs.

It is important to note that ML remains a highly dynamic field of research, particularly within tissue engineering. In our literature review, we specifically targeted research articles that employ ML models to enhance the comprehension of hiPSC-CM behavior. We deliberately excluded studies that integrate ML into the use of hiPSC-CMs as models, like drug cardiotoxicity or disease progression (Heylman et al., 2015; Lee et al., 2017; Maddah et al., 2020; Grafton et al., 2021; Juhola et al., 2021; Kowalczewski et al., 2022; Yang et al., 2023). To assemble the cohort of research papers, a comprehensive literature search was conducted using the PubMed-NCBI database with the following search terms:

1) cardiac tissue engineering[MeSH:noexp] AND artificial intelligence[MeSH:noexp];
2) cardiac tissue engineering[MeSH:noexp] AND machine learning[MeSH:noexp];
3) cardiac maturation[MeSH:noexp] AND machine learning [MeSH:noexp]; and
4) scaffold optimization hiPSC-CM machine learning.

Other searches with relevant key terms yielded no results; therefore, they were omitted from this list. By selecting papers from the last decade that align with our specific focus, we curated a cohort of 23 research papers spanning 2013–2023.

In review, we observe that efforts within each challenge of CTE work to 1) improve the functionality of hiPSC-CMs and 2) improve physiological phenotyping and characterization of tissues to accelerate innovation. This distinction is made in our discussion of each implementation of ML in hiPSC-CM immaturity.

2 Artificial intelligence and machine learning

Artificial intelligence (AI) has become a transformative force across numerous disciplines, promising groundbreaking advancements and technological revolutions. Within the expansive landscape of AI, machine learning (ML) emerges as a pivotal subset, fundamentally reshaping problem-solving and decision-making processes. In our exploration of recent ML methods in the realm of CTE, it is imperative to navigate through the layers of AI and ML, grasping their core principles and understanding their relevance in the broader field of biomedical engineering (BME).

At its essence, AI strives to emulate intelligent behavior and decision-making in computers, pushing the boundaries of what machines can achieve. AI systems are designed to undertake tasks requiring human-like intelligence, including learning, reasoning, problem-solving, perception, and language understanding. Within this multifaceted field, ML stands out as an integral component as it falls within the vast data science umbrella of AI, empowering systems to learn patterns and make decisions from data without explicit programming. The hallmark of ML lies in its capacity to enhance performance iteratively through learning from experience and statistical inferences. This computationally expensive learning process is a crucial feature, especially in addressing the complex challenges posed by CTE, where the interplay of biological components demands robust and well-guided solutions. The intersection of ML and BME has exposed unprecedented possibilities in healthcare, diagnostics, and therapeutic interventions (Jovel and Greiner, 2021; Strzelecki and Badura, 2022). In the context of CTE, ML algorithms offer the potential to decipher intricate relationships within biological systems. Mathematical or physics-based models traditionally

attempt to decipher systems like cellular interactions and tissue behavior, yet many times fall short (Park et al., 2018). To supplement these efforts, researchers have begun to harness ML in the recent decade to further analyze and explore novel avenues in CTE. Within the broader ML landscape lies deep learning (DL) with its neural network architectures, showing remarkable success in 2D and 3D image and signal processing (Litjens et al., 2017; Zhou et al., 2017). DL models with multiple layers (usually more than one hidden layer between the input and output layers) excel in capturing intricate hierarchical representations and features from complex data, when enough data is provided (Cybenko, 1989; Hornik et al., 1989; Yarotsky, 2017). Within CTE, this translates to enhanced capabilities in biomedical image analysis, signal processing, and predictive modeling, offering a deeper understanding of cardiac dynamics and responses to various perturbations.

The integration of AI and its subfields is not without challenges. Biomedical data, either in signals or images, is often complex, heterogeneous, and characterized by high dimensionality (Dinov, 2016; Hulsen et al., 2019). Ensuring the robustness and generalizability of ML models across diverse datasets is a persistent challenge. Additionally, ML models are often viewed as "black boxes," which naturally creates distrust regarding the transparency and interpretability of decision-making processes in critical biomedical applications and healthcare, specifically in clinical settings with diagnoses and treatment plans. The challenges of ML in CTE are further amplified by the intricate nature of cardiac tissue. Modeling the dynamic and multifaceted aspects of cardiac function and response requires sophisticated ML approaches. Furthermore, DL models are known for their demand for substantial amounts of labeled data, posing challenges in scenarios where obtaining sufficiently large training sets may be difficult or impractical. Nevertheless, as this review explores, ML methods, including DL architectures, prove to be successful in CTE, especially in cases where mathematical models are limited. It is noteworthy that these physics-based models demand extensive time and computational resources for numerically solving complex systems of equations spanning multiple scales, all the while data-driven methods often fall short in achieving high accuracy and generalization capabilities (Peek et al., 2014; Rueckert and Schnabel, 2020; Regazzoni et al., 2022). We expect the balancing of these trade-offs will expedite the evaluation and accuracy of mathematical models and tackle issues associated with many-query problems in CTE applications. By understanding these challenges, researchers and practitioners can harness the potential of ML methodologies and advance the frontiers of cardiac tissue research and engineering.

3 Common machine learning models

In the last decade, ML has become integral to BME, particularly in CTE, by providing powerful tools to extract meaningful insights from complex data. We first discuss common ML models and then delve into how these are used to tackle the CTE challenges we have identified in this review.

3.1 Linear models

Two of the most intuitive and straightforward supervised ML models are linear and logistic regression (James et al., 2023). Linear regression learns the relationship between the dependent variable and one or more independent variables by fitting a linear equation to observed data. It is widely used in CTE for tasks, such as predicting cell culture properties based on a set of initial parameters. Despite its simplicity, linear regression provides interpretable insights into the impact of individual features on the outcome. Applying a threshold to the output classifies data into multiple categories, such as different types of tissue structures or cell types. Similarly, logistic regression is for binary classification tasks, making use of the logistic or sigmoid function to map the linear combination of input features into a probability distribution between 0 and 1 (Fukunaga and Hostetler, 1975). Logistic regression is valuable in scenarios like cell-type classification, where it is essential understanding the likelihood of a cell culture having a specific content of successfully differentiated cells or having specific types of cell phenotypes, as we will discuss in forthcoming sections.

3.2 Tree-based models

More involved, but well-established supervised ML models are decision trees and random forests, both of which serve for both regression and classification tasks. Decision trees partition the feature space into regions based on feature thresholds, making decisions by traversing the tree from the root to the leaves (Quinlan, 1986). They are susceptible to overfitting, but standard techniques like pruning and ensemble methods mitigate this. Decision trees are intuitive and interpretable, while capturing complex decision boundaries, making them valuable for feature selection and identifying critical factors. Random forest models build an ensemble of decision trees, each trained on a subset of the data and features (Breiman, 2001). They leverage the diversity among trees to improve generalization and robustness, favored for its ability to handle high-dimensional data and nonlinear relationships. The aggregation of multiple trees enhances predictive performance and provides insights into feature importance.

3.3 Probabilistic models

Naïve Bayes is a probabilistic classification algorithm based on Bayes' theorem, which describes the probability of an event based on prior knowledge of conditions that might be related to the event (Manning, 2008; Witten et al., 2011). The "naïve" assumption is that features are conditionally independent given the class label, which simplifies the computation of probabilities, but may not hold in all cases. Thanks to its framework that is computationally efficient, simple to implement, and often requires smaller amounts of training data, naïve Bayes performs well in tasks with high-dimensional data, like predicting diseases or drugs based on cellular features. Gaussian Processes (GPs) are one of the most flexible models for regression tasks, providing a probabilistic framework for learning relationships in data by considering entire distributions of functions (Rasmussen

and Williams, 2006). Unlike traditional regression models, GPs offer a non-parametric approach, making them suitable for capturing complex patterns and uncertainties in diverse datasets. The strength of GPs lies in their ability to provide not only predictions, but also estimates of prediction uncertainty, valuable in CTE scenarios where uncertainty quantification is crucial for cell maturation. Linear discriminant analysis (LDA) and its variants, like quadratic discriminant analysis (QDA), are dimensionality reduction and classification techniques (Izenman, 2008; Hastie et al., 2009). These models find combinations of features that maximize the distance between class means and minimize the spread within each class, making them valuable for task in biomedical signal processing and imaging, like feature extraction and cell-type classification.

3.4 Other models

Support vector machines (SVMs) aim to find the hyperplane that maximally separates data points of different classes (Cortes and Vapnik, 1995). They operate effectively in high-dimensional spaces and are applicable for tasks such as classifying cell cultures based on complex profiles. An SVM uses kernels to compute the similarity between pairs of data points, enabling it to handle nonlinear relationships and making it versatile in capturing intricate patterns in biomedical data. It is mostly used in classification tasks, but it can be extended to regression. As it implies, k-nearest neighbors (kNN) classifies data points based on the majority class among their k-nearest neighbors (Cover and Hart, 1967). kNN is valued for its simplicity and effectiveness, especially in scenarios where data points form well-defined clusters. kNN is sensitive to the choice of distance metric and the number of neighbors, making careful parameter selection crucial in achieving optimal results.

3.5 Neural networks and deep learning

Artificial neural networks (ANN) vary significantly from the mentioned models, consisting of interconnected nodes organized in layers that are trained using backpropagation (Haykin, 1998, 2008; Bishop and Nasrabadi, 2006). The input layer receives the initial data, usually preprocessed, and computations take place within intermediate "hidden" layers, helping the network learn complex patterns and representations. The output layer produces the final output or prediction. Each connection between neurons or "nodes" in different layers is associated with a weight. The network learns by adjusting these weights during training, where the activation of neurons in the hidden and output layers is determined by applying certain activation functions, like sigmoidal, hyperbolic tangent, or leaky rectified linear unit (ReLu). Fully-connected or "dense" layers are those that have each neuron connected to every neuron in the adjacent layer, creating a dense network of connections and, hence, more unknowns to solve for. A common ANN is a feedforward neural network, where information flows from the input layer through one or more hidden layers to the output layer without forming cycles or loops (Rumelhart et al., 1986; Haykin, 2008). Feedforward neural networks are foundational and used in various machine learning tasks like cell-type classification or bioprinting parameter regression based on multimodal data.

While feedforward networks are powerful and can be considered DL with several hidden layers, more complex architectures, such as convolutional neural networks (CNNs) and recurrent neural networks (RNNs), have been developed to address specific challenges in different types of data through either supervised or unsupervised learning (Goodfellow et al., 2016). CNNs are designed for grid-like data, leveraging convolutional layers for spatial feature extraction (Szegedy et al., 2015; Venkatesan and Li, 2017; Shanmugamani, 2018). CNNs excel in medical image analysis, detecting patterns and structures, by applying filters to learn hierarchical representations that identify localized features critical in tasks, such as cell detection and quality assessment of maturing hiPSC-CMs. RNNs maintain hidden states to capture temporal dependencies in sequential data with feedback loops and are commonly applied to time-series data, allowing tasks like physiological signal analysis and predicting disease progression (Rumelhart et al., 1986; Pascanu et al., 2013). However, traditional RNNs face challenges in capturing long-term dependencies, leading to the development of more advanced architectures like Long Short-Term Memory (LSTM). LSTM networks are a type of RNN designed to address the vanishing gradient problem, modeling long-range dependencies in sequential data (Gers et al., 2000). These networks are crucial for tasks requiring an understanding of temporal relationships across even irregular intervals, such as subtleties of cellular interactions and tissue development and analyzing dynamic physiological signals. Their ability to capture context over extended sequences makes them well-suited for time-sensitive medical data.

These handful of models collectively form a diverse toolkit for addressing various challenges in BME, offering solutions tailored to different data types, complexities, and desired outcomes. Other models found in the literature that are more tailored to specific CTE challenges will be discussed in the following sections. Although the field of ML can be overwhelming, numerous resources exist to support researchers from diverse backgrounds in acquiring the skills to program, implement, and utilize ML models in Python, R, and MATLAB (Conway and White, 2012; Murphy, 2012; Kelleher et al., 2015; Theodoridis, 2015; Müller and Guido, 2016; Raschka and Mirjalili, 2017; Géron, 2019).

4 ML in cardiac cell differentiation

Numerous protocols for CM differentiation exist that result in varying degrees of purity and functionality. Post differentiation purification schemes leveraging metabolic selection have become a standard part of cardiac differentiation to ensure high percentages of CMs and to prime lipid metabolism seen in adult CMs (Sharma et al., 2015). These strategies are inherently reactive and cannot proactively ensure efficient differentiation. Given that cardiac differentiation is a multifactor process with complex interactions, experimental optimization can be expensive both in time and resources. ML techniques have been leveraged to identify important factors in driving efficient cardiac differentiation and predict the purity of differentiating hiPSC-CMs at early timepoints.

Williams et al. were among the first to leverage ML techniques to identify the most influential experimental variables that may be controlled during cardiac differentiation and sought to establish a robust classification and prediction of CM purity during differentiation in advanced stirred tank bioreactors (STBRs) (Williams et al., 2020). STBRs facilitate scale-up of differentiation protocols and continuous monitoring of environmental conditions (such as media dissolved oxygen and pH level) and have been used extensively for tissue culture over the last decade (Kehoe et al., 2010; Kempf et al., 2016; Halloin et al., 2019). Manual sampling can also enable evaluation of cell viability and proliferation. During the differentiation process, spanning up to 5 days after initiation, 39 variables were measured relating to dissolved oxygen, pH, cell density, aggregate size, nutrient concentration, and preculture conditions. Post differentiation, CM purity was analyzed via flow cytometry using canonical CM markers cardiac troponin T and myosin heavy chain. Cultures yielding >90% CMs were coded to be successful or insufficient otherwise. Data from 58 unique cardiac differentiations were split into training ($n = 42$) and testing ($n = 16$) datasets and applied to random forest, GP regression, and multivariate adaptive regression splines (MARS) algorithms. The latter is a non-parametric regression technique for modeling complex relationships between input features and output variables, well-suited for data with underlying nonlinear interactions and discontinuities (Friedman, 1991). Random forest and GP regression models yielded 90% accuracy and 90% precision in identifying experiments that would yield sufficient CM purity, while random forest models yielded 84% accuracy at identifying if an experiment would have an insufficient final CM content. Importantly, this work details how ML may be used to predict CM purity after only 5 days of differentiation, using less than 16% of collected data.

Similarly, Mohammadi et al. studied random forest, GP classification, and SVM methods to identify important differentiation factors and conduct quality checks on hiPSC-CM embedded PEG-fibrinogen microspheres (Mohammadi et al., 2022). While extruded cardiac microspheres enhance 3D culture and differentiation efficiency, potentially facilitating scalable hiPSC-CM production, they may affect CM purity due to variations in physical properties. By tuning variables such as CHIR concentration, fibrinogen concentration, differentiation media, size and shape of extruded microspheres, and cells seeding density, this group aimed to develop predictive models for resulting CM purity. Principal component analysis (PCA) was first employed to determine features that correlate strongly with efficient CM differentiation (65% CM or higher). PCA is a method commonly used to transform high-dimensional data into a lower-dimensional space by identifying the principal components that capture the most variance (Pearson, 1901; Hotelling, 1936). This uncovers latent patterns in datasets with numerous correlated features while retaining as much information as possible. In this case, random forest, GP classification, and SVMs were trained on select input features including postfreeze passage number, PGE-fibrinogen concentration, and the ratio between the CHIR concentration and microsphere surface to volume ratio with CM purity as output. GP classification models yielded 70% accuracy with 56% precision at classifying high purity cultures. It should be noted that the principal components used in the best-performing model explained only 18% of the input data variance. This suggests that the variance of the input set did not entirely account for the variance in the output data, indicating the need for more features and indicators within a larger dataset.

One year later, the same supervised classification task was tested, this time employing CNNs (Mohammadi et al., 2023). Two models were created to predict the percentage of CM content on Day 10 of differentiation, using pre-differentiation experimental features and nondestructive images from Days 3 or 5. One CNN utilized only phase-contrast image, while another incorporated a combination of both images and the features identified in earlier work (Mohammadi et al., 2022). With an accuracy of 85% and precision of 92%, the best-performing model was the combination CNN using images from Day 5, outperforming the other ML models, including GP with features only, SVM with images only, and SVM with a combination of images and features. Although successful on only about 300 images, the model developed a dependence on the specific cell line used. Evaluation on another cell line yielded a significantly lower accuracy of 46%, emphasizing the substantial challenges in generalizing predictions across diverse cell lines.

5 ML in morphology

CMs exhibit a strong structure-function relationship, causing morphological differences to have significant impact on cardiac function. Healthy, adult CMs exhibit elongated, rod-shaped, and anisotropic morphologies with high aspects ratios (7:1 to 9.5:1) (Gerdes et al., 1992). hiPSC-CMs instead exhibit round, polygonal morphologies with significantly smaller aspect ratios, trending more to isotropic orientations (Feric and Radisic, 2016). Morphological assessment has historically required extensive time and resources to execute and is prone to user bias. ML methods trained on images of CMs have accelerated and standardized morphological assessment of hiPSC-CMs.

Pasquilini et al. were among the first to bring ML to analyze hiPSC-CM morphology and intracellular structure (Pasqualini et al., 2015). After gathering fluorescent images of rat primary ventricular monocytes (rpCMs) and hiPSC-CMs, stained for sarcomeric α-actinin and fibronectin, 11 metrics were assessed. Among others, metrics included sarcomere length, sarcomeric packing density, and Z-disk relative coherence. Naïve Bayes, a feedforward neural network, and a bootstrap aggregation of decision trees were trained to classify rat primary cardiomyocytes (rpCMs) as mature or immature using the 11 metrics as prediction elements and a user-defined maturity label as output elements. All models, trained with the same dataset, yielded similar degrees of hiPSC-CMs immaturity accuracy, with the naïve Bayes classifier yielding 70%, the neural network yielding 71%, and the tree bagging classifier yielding 77%.

Orita et al. addressed the variability in the viability of cultured hiPSC-CMs through a CNN, emphasizing the need for accurate and high-throughput screening methods due to limitations in manual inspection (Orita et al., 2019). A VGG16 architecture, pretrained with the ImageNet dataset for transfer learning, was further trained on experimental images labeled as ‘normal’ or ‘abnormal’ by an expert, however, the authors did not elaborate on what parameters

warranted normal or abnormal classification. The VGG16 architecture used contained a total of 16 layers: 13 convolutional layers and 3 fully connected layers. The former are used for extracting image features, such as edges and colors, while the latter are used for image classification through nonlinear combination of the extracted features. All convolutional layers of VGG16 were frozen and used as fixed feature extractors, except for the eighth fully connected layer, which was modified from 1000 nodes to 2 nodes for binary classification. After implementing data augmentation methods to expand the dataset to 18,000 images, the model successfully reached 90% accuracy, showcasing its capability for automating quality control. Nevertheless, the study acknowledges the necessity for a more extensive dataset, especially given the trade-off between calculation speed and performance. The findings suggest that full retraining of VGG16 or exploring more advanced pretrained models could further enhance performance and robustness in classifying hiPSC-CM cultures.

Khadangi et al. introduced CardioVinci, a deep-learning framework combining a U-net and GAN for unsupervised segmentation and synthesis of 3D electron microscopy (EM) datasets of cardiac cells (Khadangi et al., 2022). 3D Electron microscopy datasets excel in providing high resolution images of intracellular organelles and extracellular matrix organization. But their large data size cause processing and analysis steps to be time and energy intensive. Generative adversarial networks (GANs) excel in biomedical imaging by generating realistic synthetic data through adversarial training of a generator and discriminator network, fostering advancements in image synthesis, data augmentation, and disease simulation for enhanced machine learning model training (Goodfellow et al., 2014). U-net, a versatile convolutional neural network, proves indispensable in biomedical image segmentation, effectively delineating and identifying structures with its distinctive U-shaped architecture, thereby contributing to precise and efficient medical image analysis and diagnosis (Ronneberger et al., 2015). The U-net segments mitochondria, myofibrils, and Z-discs, achieving notable accuracy as confirmed by niche evaluation metrics, like compactness, flatness, sphericity, elongation, and surface area to volume ratio (SA:V). Next in the CardioVinci pipeline, a GAN is encoded as a probabilistic model of CM architecture to extract morphological metrics and spatial distributions of mitochondria, myofibrils, and Z-discs in semantic segmentations. StyleGAN is popular type of GAN architecture with densely connected convolutions motivated by style transfer problems (Karras et al., 2019). Here, StyleGAN was used to minimize the Fréchet inception distance and was trained on experimentally collected 3D EM datasets of left ventricular cardiomyocyte extracted from a type 1 diabetic rat tissue sample to generate a probability distribution of 2D CM structures found within the image slices of the 3D EM segmented volume datasets, offering a novel approach to generative modeling of CM ultrastructure. Despite its ability to generate statistically similar geometries, CardioVinci requires an initial segmentation step and accurate stacking of 2D images into 3D volumes, posing challenges for large tissue samples. Nevertheless, it represents a notable advancement in automating the analysis of cardiac ultrastructure.

6 ML in calcium handling and cell-cell coupling

Functional adult CMs exhibit mature intracellular and efficient intercellular calcium handing. Effective intracellular calcium handling is dictated by high expression of voltage-gated Ca^{2+}, Na^{+}, and K^{+} ion channels in adult CMs (Bodi et al., 2005; Sartiani et al., 2007). Responding to varying membrane potentials, these channels trigger intracellular calcium release and take-up, allowing for efficient contraction cycles. Relative expressions of these ion channels are significantly lower in hiPSC-CMs vs. adult CMs, resulting in deficient function action potential and contraction cycling (Feric and Radisic, 2016). Similarly, hiPSC-CMs exhibit lower levels of gap junction proteins, preventing efficient intercellular transduction of cardiac action potentials between neighboring CMs. Significant work has been conducted to accurately classify calcium transient signals into normal or abnormal to study the contributions of calcium handling to cardiac disorders and overall disfunction. Application of these methods in characterizing calcium transients of hiPSC-CMs may help identify the root causes of deficient calcium cycling and improve the electrophysiology of hiPSC-CMs to match adult CMs.

Through spectral clustering, Gorospe et al. (2014) automatically classified a population of hESC-CMs into different phenotypes based on electrophysiology signals. Spectral clustering is a ML technique that utilizes the eigenvalues and eigenvectors of the data matrix to project the data into a lower-dimensional space for the purpose of clustering data points (Ng et al., 2001). Heterogeneity of differentiated CMs may be characterized by electrophysiology as action potential (AP) waveforms differ significantly across pacemaker, atrial, and ventricular phenotypes. The classification task is based on the hypothesis that APs of the same phenotype exhibit more similar shapes than those of different phenotypes. This distinction is captured via spectral clustering in an experimentally collected dataset comprising 6940 APs from nine cardiac clusters, analyzed using Euclidean distance to quantify the similarity between APs. Then, these similarities were fed as inputs to a simple spectral grouping algorithm with the aim to objectively distinguish populations of cardiac APs with distinct phenotypes. The best grouping fitness was achieved when identifying 2 phenotypes, as indicated by normalized cut cost and Davies-Bouldin Index metrics. However, due to the simplicity of the clustering algorithm and diversity in waveforms, the strength of this method diminished when attempting to identify three and four phenotypes per cell cluster. Notably, grouping the population based on standard AP features, like duration at 30% (APD30) and 80% (APD80) repolarization, and their differential, was effective for two groups, while using the entire AP waveform was effective for two, three, or four groups.

Researchers often use microelectrode arrays (MEAs) to measure APs in cardiac cells. This technique enables simultaneous recordings from multiple locations, allowing researchers to capture the spatiotemporal dynamics of electrical activity across the entire cell population. However, simultaneous recordings from multiple locations generate a

large amount of data, and the interpretation of such complex datasets may pose challenges. To tackle this, Jurkiewicz et al. (2021) implemented an SVM to analyze signals recorded from hiPSC-CMs on MEAs. Within MEA readings, intracellular APs can be directly measured via electroporation or indirectly via extracellular field potentials (FPs). The SVM was used to filter MEA recorded signals into APs and FPs, classify signals as usable or unusable, and extract AP features from the signals. Collected signals were first split into APs and FPs based on time of electroporation. Signals collected prior to electroporation were identified as FPs, while signal collected after electroporation were classified as action potentials. APs and FPs were then sorted into usable and unusable signals based on deterministic noise and signal fidelity rules. The SVM was then trained on AP and FPs signal as predictive inputs to identify usable and unusable signals. The classifier achieved 100% accuracy on the training set due to linear separability. Finally, once AP signals were identified, 3 classical features were computed - basic cycle length (BCL), APD30 and APD80. This analysis facilitated an in-depth investigation of cardiac restitution, exploring the relationship between APD for a given beat to the diastolic interval (DI) of the preceding beat, DI = BCL − APD. The application of an SVM with MEA readings accelerates the location and classification of APs and allows for quick extraction of AP features within MEA datasets, but is limited in its translatability to patch clamp experimental data.

Juhola et al. (2015) extended the analysis to calcium cycling signals, using ML techniques to characterize and classify hiPSC-CMs based on calcium cycling signals. Calcium cycling, downstream of cardiac action potentials, provides insight into cardiac calcium handing and contraction. In this study, calcium-reporting fluorescent images of hiPSCs-CMs derived from patients with catecholaminergic polymorphic ventricular tachycardia (CVPT) were collected. After pre-processing, calcium waveforms were generated by plotting the average intensity in regions of interest within calcium images, resulting in 280 unique signals. Peaks within each waveform were identified and classified as normal or abnormal via deterministic rules associated with changes in absolute fluorescence, peak amplitude, and symmetry. Next, seven peak parameters, including left/right side amplitude, duration, and time interval between peaks were calculated for each identified peak. These seven predictive elements were reduced via PCA, which yielded a first principal component explaining 95% of sample variance and a second principal component explaining 5%. After testing a variety of ML models, including kNN and SVMs, QDA was found to perform the best with an 80% accuracy compared to human expert assessment. It should be noted that the deterministic rules guiding classification were rooted in identifying at least one abnormal peak in waveforms, i.e., abnormal waveforms were classified as such if they contain at least one abnormal peak. In a follow-up study, Juhola et al. (2018) then applied this method to discriminate specific genetic diseases. Applying previous methods to hiPSC-CMs derived from patients with catecholaminergic polymorphic ventricular tachycardia (CPVT), long QT syndrome (LQT), and hypertrophic cardiomyopathy (HCM), yielded classification accuracies of 79%–88%.

Building on this work, Hwang et al. (2020) incorporated expert determined ground truths, leveraging shared characteristics of normal and abnormal Ca^{2+} transient peaks and signals across all samples. The peaks in 200 training calcium transients were identified and characterized according to 14 peak characteristics similar to Juhola et al. (2015). Notably, the peak detection algorithm was improved by using derivatives of calcium transient over raw amplitudes and additional peak characteristics were calculated, such as nearby peak distance varying peak amplitude, and peak asymmetry. A peak-level SVM classifier was then trained using the 14 peak variables as predictive features and expert normal/abnormal assessment as outcome variables. Taking the outcomes of peak-level classification, overall calcium transient signals were classified as normal/abnormal using a cell-level SVM. For training, peak normality assessments along with additional cell variables, like proportion of abnormal peaks per signal, variance of peak amplitude per signal, variance of peak distances per signal, and variance of peak areas per signal, were taken as predictive features, while human-expert assessments were taken as outcomes. This two-tiered signal analysis pipeline results in an 88% training accuracy and 87% test accuracy, but these models were trained and tested on similar signals potentially overfitting or biasing the model. In general, training and testing on more varied data sets is recommended.

Yang et al. (2022) introduced an alternative ML method to identify drug treatment of hiPSC-CMs, of 63 unique compounds, using calcium waveforms. The custom CardioWave pipeline extracts 38 parameters from waveforms, including metrics on rise/decay time, number of peaks, peak frequency, amplitude, and shoulder characteristics. With 303 samples across 63 compounds, PCA was used to project all samples parameters into a 2D space. Next, a random forest model was trained with calcium waveforms as predictive elements and the identity of the dosed compound as ground truth elements. Employing leave-one-compound-out cross-validation to evaluate the random forest model yielded an overall accuracy rate of 86%. Gaps in the experimental data set, notably varying drug concentrations and forced hyper-parameterization of training inputs, may be reducing the accuracy of this model.

Aghasafari et al. (2021) introduced a multitask network that simultaneously classifies iPSC-CM AP traces into categories representing drugged CMs and drug-free CMs and translates them into adult-CM AP waveforms. Action potentials of drug-free iPSC-CM and adult human CMs were generated via pacing *in silico* models using the Kernik iPSC-CMs *in silico* model (Kernik et al., 2020) and the O'Hara–Rudy human adult-CMs *in silico* model (O'Hara et al., 2011). Drugged action potentials were collected via simulation of the above models modified with a simple drug-induced IKr block model of hERG channel conduction, reducing conductance by 1%–50%, and complex Markov model of conformation-state dependent IKr block in the presence of hERG blocking drug dofetilide. A deep learning algorithm was built on an RNN architecture with LSTM layers, where the layers remember the most important iPSC-CM AP features needed for the synchronized classification and translation tasks. The model used preprocessed iPSC-CM APs

as the network input and adult-CM APs along with corresponding drug-free and drugged labels as network outputs. The supervised tasks of classification and translation were achieved independently of each other through individual fully-connected layers. Addressing the challenge of immature hiPSC-CM models, the algorithm navigates the translation task by learning from synthetic data, exhibiting proficiency in predicting drug-free and drugged states with approximately 90% accuracy. Although the model also successfully translates hiPSC-CM APs into adult-CM APs with less than 0.003 mean-squared error, it requires multiple high-quality datasets for effective training, with potential improvements including addressing data sparsity and exploring diverse approaches beyond supervised learning. The LSTM-based multitask network showcases the capability to discern and translate cardiac APs, offering promise for applications in drug testing and disease modeling.

7 ML in cell contraction

Contraction is intricately tied to intracellular calcium handling in CMs. Thus, the abnormal calcium cycling seen in hiPSC-CMs further diminishes contractile force generation and contributes to a large functionality gap between hiPSC-CMs and adult, and even neonatal, CMs. The active stress generated by freshly isolated contracting human ventricular CMs was measured to be >50 mN/mm2 (van der Velden et al., 1998) and neonatal (<2 weeks) ventricular CMs generated of 0.8–1.7 mN/mm2 (Wiegerinck et al., 2009). hiPSC-CMs, by comparison are measured to produce 0.15–0.30 mN/mm2 (Kita-Matsuo et al., 2009; Hazeltine et al., 2012). Numerous mechanical and electrical stimuli such as static and cyclic mechanical stretch (Kensah et al., 2011; Turnbull et al., 2014; Ribeiro et al., 2019), electrical stimulation (Nunes et al., 2013; Ruan et al., 2016), and supporting cell co-cultures (Richards et al., 2017; Beauchamp et al., 2020), have been noted to improve contractile properties of hiPSCs. Given the multitude of factors influencing cardiac contraction development, machine learning emerges as a powerful tool for accelerating the characterization and optimization of hiPSC-CMs' contraction.

Lee et al. (2015) provided one of the first applications of ML to evaluate the contraction of CMs. Leveraging an SVM, brightfield image sequences of beating CMs were classified as normal or abnormal. Brightfield images were first processed with optimal flow algorithms to generate matrices of x- and y-directional vectors that describe CM motion. PCA summarized vector information into a singular variable that described bulk cardiac contraction over time. Using user-identified contraction and relaxation peaks, 12 contraction parameters were calculated including peak duration, amplitude, rise time, area under curve, and frequency. An SVM was then trained with over 200 unique samples to classify samples as normal or abnormal using the contraction parameters as predictive variables and known experimental conditions as the outcome variable. The trained model achieved an accuracy rate of 83%–99% in identifying cells treated with known contraction modulators, E-4031, verapamil, and blebbistatin, at higher concentrations. Notably, the model faced challenges in predicting outcomes for drug dosing concentrations lower than 10 nM.

Orita et al. (2020) automated the process of contraction identification and employed a trained SVM to classify hiPSC-CM cultures as normal (experimentally usable) or abnormal (experimentally unusable). 556 brightfield image sequences of beating hiPSC-CMs were captured and classified by experts as abnormal (n = 190) or normal (n = 366). The contraction properties of the imaged CMs were calculated to be the 200-frame simple moving average (SMA) around the frame of interest. Data augmentation, via the sliding window method, enabled each contraction profile to be split into individual contraction waves, increasing the data set six-fold. Then, a fast Fourier transform converted contraction waves (n = 3,336) to the frequency domain and UMAP was employed to reduce the dimensionality of contraction waves to two dimensions. Uniform manifold approximation and projection (UMAP) is a nonlinear dimensionality reduction technique that is particularly effective for preserving both local and global structures in high-dimensional data (McInnes et al., 2020). Finally, an SVM was trained, using UMAP reduced dimensions as inputs and expert-assessment as ground truths, yielding an 89% accuracy and 92% precision rate. Notably, this pipeline was trained on global features within image sequences, potentially overlooking important local features that could impact accuracy negatively.

Similarly, Teles et al. (2021) employed ML to differentiate healthy CMs from CMs derived from patients with Timothy syndrome (TS). Cardiomyocytes were differentiated from healthy iPSC lines (WTC-11 and BS2) and from iPSCs derived from patients with TS. Brightfield videos of contracting hiPSC-CMs were collected and processed using custom MATLAB software to assess contractility parameters like beat frequency, peak-to-peak time, interbeat variability, and rise time. Contractility parameters and experimentally defined ground truths were trained on kNN, decision trees, naive Bayes classifier, QDA, and SVM. QDA and decision trees yielded a 92% accuracy when discriminating TS and healthy WTC-11s, while decision trees and SVM were best preforming at differentiating TS and healthy BS2 cells with 88% and 87% accuracy respectively. Finally, WTC-11 and BS2 derived cardiomyocytes were differentiated from each other with accuracies above 90% using decision trees, naïve Bayes with normal kernel, and SVM with quadratic and cubic kernel. Given the strongest predictive parameter was unable to be identified due to dimension reduction pre-processing, the authors argue for the generation of more diverse datasets of contractility, varying race, ethnicity, sex, and disease of donor cells.

Another automated approach for assessing drug-induced effects on CM electrophysiology used a feed-forward neural network that processes mechanical beating signals from hiPSC-CMs (Ouyang et al., 2022). A custom feature extraction program was applied to partition CM beating signals into distinct beating patterns and extract specific features in the time domain. These features were then manually analyzed to identify various drugs and predict their cardiotoxic concentrations. A multi-labeled neural network (MLNN) was constructed to identify different drugs and drug

concentrations based on the specialized features of individual CM beating patterns. Nodes with dual labels in the output layers were designed to represent both binary drug types and numeric drug concentrations. This approach aimed to reduce the number of output classes in the classifier, preventing overfitting, especially when training with a limited dataset. By combining automatic feature extraction and MLNN, the model accurately classified six different drugs as either cardiotoxic or not and predicted their cardiotoxic concentrations, achieving 98% and 96% for training and testing accuracies, respectively. Despite the introduction of noise, the MLNN demonstrated robust performance, maintaining accuracy, precision, and recall at approximately 96%. Although the MLNN outperforms other DL methods like CNN and RNN frameworks at low concentrations, there is a need for more extensive datasets to enable a comprehensive comparison with other deep-learning methods.

8 ML in tissue assembly

The assembly of *in vitro* differentiated CMs into functional tissue is hindered by the complex nature of healthy myocardium, characterized by the high cell density, multicellularity, ordered structural composition. While the self-assembly of hiPSC-CMs into engineered heart tissues has produced largely functional 3D myocardium, its scalability and lack of vasculature pose limitations (Ronaldson-Bouchard et al., 2018). Various approaches, including scaffold or scaffold free systems (Feinberg et al., 2013; Nunes et al., 2013; Kobayashi et al., 2019; Qasim et al., 2019) such as bioprinting have been explored for 3D cardiac tissue assembly (Ong et al., 2018; Esser et al., 2023; Finkel et al., 2023). ML offers a potential avenue to expedite the optimization of scaffold and bioink parameters for supporting multicellular culture and facilitating functional tissue assembly.

Rafieyan et al. (2023) provide one of the few direct applications of ML to hiPSC-CM scaffold optimization. Their main objective was to overcome limitations created by small experimental datasets. To address this, they first developed a comprehensive, multi-cell line, muti-fabrication method dataset through an extensive literature review that connected material properties to CM function. Subsequently, they identified the most accurate algorithm to predict cell behavior on CTE scaffolds. Briefly, scaffold materials in this dataset included synthetic and natural materials like polycaprolactone and Fibroblasts-derived ECM. Fabrication methods in the dataset were comprised of electrospinning, hydrogel encapsulation, and 3D printing among others. Finally, cell lines ranged from cardiac progenitor cells to hiPSCs. Cellular response with these materials was categorized into 4 classes: (0) no evaluation of cellular behavior preformed, (1) poor cell viability, growth, and proliferations, (2) cell viability, growth, and proliferation seen up to 3 days, and (3) cell viability, growth, and proliferation seen past 3 days. The dataset, encompassing 33 different materials, 16 different cell lines, and 6 different fabrication methods, was used to train 23 algorithms using material parameters as predictive inputs and the 4 classifications of cell response as outcomes. XGBoost, a gradient boosting machine for regression and classification problems, yielded the highest classification accuracy (87%), while quadratic discriminant analysis yielded the lowest (33%). XGBoost also indicated bioactive ECM as a defining feature driving CM function. This study demonstrates the importance of comprehensive datasets in achieving high accuracy in ML methods and illustrates an example wherein ML may help identify important contributors of CM behavior, leveraging a diverse and disparate dataset.

Among various cardiac tissue assembly methods, bioprinting stands out as particularly promising. Not surprisingly, there is a notable emphasis on the application of hierarchical machine learning (HML) to optimizing bioprinting parameters specifically addressing the complexities of bioprinting for cardiac tissues, where achieving precise and accurate spatial arrangements of cells is crucial for functional outcomes. HML, a hybrid approach integrating physical and statistical methodologies, is particularly designed for small experimental datasets (Menon et al., 2017). In this approach, predictors are linked to the system response through an intermediary layer with variables parameterized by established physiochemical relationships. Regression techniques are then employed to establish connections between the middle layer and the system response, enabling effective prediction and optimization. Bone et al. (2020) used HML to optimize ink-related variables and printer settings for improved print fidelity in the Freeform Reversible Embedding of Suspended Hydrogels (FRESH) bioprinting modality. FRESH printing, while successfully employed for assembling 3D cardiac tissues, is plagued by print fidelity issues difficult to optimize (Finkel et al., 2023). With 48 prints generated and assessed for print fidelity by varying normalized flow rate, nozzle speed, alginate concentration, and nozzle diameter, an HML model was constructed. The model included a bottom layer composed of predictor system variables, a middle layer leveraging known physical relationships of the flow-gelation process of alginate, and a top layer representing print fidelity rating. Despite the low sample size, the model revealed that faster nozzle speed and higher alginate concentrations were the primary factors contributing to print fidelity. The model was then used to predict print scores based on synthetic parameters yielding R^2 = 0.5 for the fidelity of lines and corners. Although exhibiting low accuracy, this model primary leverages physical knowledge to enhance predictive power and achieve interpretability of the results for downstream analysis, even with limited training data.

Another innovative ML approach to optimize bioprinting fidelity was employed by Conev et al. (2020), taking one step further by training a regression ML model to estimate the printing quality metric based on given material and printing parameters. Utilizing a previously collected data set that varied weight percent of poly(propylenefumarate) (PPF) composition, fiber spacing, printing speed, and printing pressure, two ML models were explored for their accuracy in predicting print fidelity. The first approach involved a classification-based model, using random forests with user defined high and low print fidelity ground truths. The second approach tested a regression-based model to circumvent the need for user-defined thresholds for print fidelity. A random forest model was trained to predict machine precision and material

accuracy, followed by applying a threshold to characterize the printing as either "low" or "high" quality. These models were compared to a standard linear regression model that predicts material accuracy based on printing speed and printing pressure. The random forest classifier and regressor models yielded accuracies of 74% and 75%, respectively. The high performance of this model should be weighted by the limited scope of this study. Only one polymer, PPF, made up the entire training and testing data set, albeit at varying weight percentages.

Lee et al. (2020) focused on optimizing bioink composition, particularly for CTE, with a keen consideration of properties like elastic modulus and yield stress that are crucial for efficient 3D printing. For the optimization process, they employed inductive logic programming (ILP), a ML technique that learns general rules or patterns from specific instances by combining logic programming with inductive reasoning (Muggleton and de Raedt, 1994). Concentrations of type 1 collagen, fibrin, and hyaluronic acid as components of the bioink were varied to create 19 unique bioink formulations. By training a model using the fidelity of these formulations, the authors can predict rheological parameters and printing results. The ML analysis revealed that the main contributing factor determining shape fidelity is the bioink's elastic modulus, accounting for 85% accuracy, while the dominant factor determining extrusion efficiency was the bioink's yield stress, accounting for 90% accuracy. To validate the model's findings, the study successfully produced 3D structures of fibroblast-laden hydrogels with high shape fidelity, maintaining the shape for 28 days without collapsing or contracting. Confocal microscopy observations showed an increase in the number of living cells over time, emphasizing the bioink's potential for sustained cell culture. While the predictive model demonstrated effectiveness, the study underscores the need for a more comprehensive understanding of the complex relationships among bioink variables and parameters in the context of 3D bioprinting for CTE applications.

Similarly, Ruberu et al. (2021) utilized Bayesian optimization (BO) to identify the optimal printing parameters of gelatin methacryloyl (GelMA) and hyaluronic acid methacrylate (HAMA) bioinks with minimal experimentation. Notably, this pipeline leveraged ML to adaptively inform sampling during the experimentation process, surpassing classical Design of Experiment (DoE) methods that determine a sampling pattern prior to taking observations. This enables development of a database to predict printability and to make recommendations to the experimenter. A data set of score prints were generated varying GelMA and GelMA/HAMA composition, ink reservoir temperature, print pressure, print speed, and platform temperature. This seed data set was used to initialize the Bayesian optimizer. Within the optimizer, a probabilistic model of the system was built and used to recommend the next batch of experiments (printer settings) to be conducted. After executing the recommended experiments, prints were scored and fed again into optimizer in a continuous loop until optimal print conditions were reached. Optimal prints were achieved in 4-47 experiments, depending on the concentration of GelMA, drastically under the 6,000 to 10,000 possible combinations in the Bayesian algorithm. Here, BO efficiently navigates the complex parameter space of 3D bioprinting via theoretical convergence guarantees and collaborative adaptability. However, there is still a significant reliance on trial-and-error experimentation, and larger batch sizes potentially encompassing experiments with lower confidence.

9 Discussion

The lack of effective curative treatments for CVD generates a large need that hiPSC-CMs may fill if their functionality can be better understood and improved. Traditional brute-force methods at improving cardiac maturity have yielded some results, but there still exists a large gap between engineered cardiac tissue and the tissue they aim to repair or replace. The high experimental costs of cardiac optimization create opportunities for the utilization of ML.

Several groups have employed mathematical and numerical modeling of cardiac systems to help guide future areas of focus. Sobie and Wehrens (2009) reviewed computational and experimental models that may be used to explain the mechanisms of Ca^{2+}-dependent arrythmias, like CPVT. Montero-Calle et al. (2022) have utilized computational modeling to guide the fabrication of biomaterials to support the assembly of cardiac microtissues. Furthermore, other researchers have generated *in silico* mathematical models of hiPSC-CMs to estimate adult-CM behavior (Koivumäki et al., 2018; Tveito et al., 2018). These methods, while effective, are inherently deterministic as they require extensive model parameter definition and incorporate assumptions on relationships and system operation. The computational challenges of traditional models are summarized in long response times to solve the equations at hand, high monetary costs for computational resources for every evaluation with a new set of parameters, and a high environmental footprint precisely due to the repeated long response times. On the other hand, training a ML model is the most arduous computational step that is done once, while response times are typically 1 s or less for a new input or set of parameters.

Table 1 summarizes the ML methods reviewed here in connection to the functional deficiencies of hiPSC-CM they aim to address. Methods are implemented primarily in Python using experimental data (Figures 1A, C). The top three common models are SVMs, random forests, and kNNs, successful at learning from limited datasets with relatively low training times. However, these supervised models require the selection of specialized features that may make-or-break the task at hand. Meanwhile, deep convolutional networks benefit from the ability to process images and signals without such careful selection of features, since they learn the features themselves, but they require significantly more data than the supervised models. This yields higher computation costs with the longer training times, leading to their lower utilization (Figure 1D). The frequency of model usage within each CTE challenge show the utility of SVMs within various problem cases and the specialization of neural networks for the analysis of image data sets within CM morphology (Figure 2). A handful of studies emphasize the potential of DL for automating quality control, while acknowledging the trade-off between calculation speed and performance compared to the more common ML methods cited in this review. Two of the more critical items that should be measured for all ML models are the

TABLE 1 Summary of machine learning application in cardiac tissue engineering.

CTE Challenge Addressed	Model(s) used	Type of prediction	Evaluation metrics	Data availability	Citation
Purity	RFs, GPR, and MARS	Supervised (classification)	90% accuracy	Training/Testing Dataset only	Williams et al. (2020)
	RFs, GPs, SVM	Supervised (classification)	70% accuracy	Available upon request	Mohammadi et al. (2022)
	CNN	Supervised (classification)	85% accuracy	None	Mohammadi et al. (2023)
Morphology	Naïve Bayes, NN, tree bagging	Supervised (classification)	Not provided	Training/Testing Dataset only	Pasqualini et al. (2015)
	CNN	Supervised (classification)	90% accuracy	None	Orita et al. (2019)
	U-Net, StyleGAN	Unsupervised (segmentation and synthesis)	N/A	Code + training and testing datasets	Khadangi et al. (2022)
Calcium Handling or EP	spectral grouping	Supervised (classification)	NCC = 0.14 DBI = 1.16	None	Gorospe et al. (2014)
	kNN, LDA, QDA, NNB, classification tree, SVM	Supervised (classification)	80% accuracy	None	Juhola et al. (2015)
	kNN, RFs, SVM	Supervised (classification)	88% accuracy	None	Juhola et al. (2018)
	SVM	Supervised (classification)	87% accuracy	Code + training and testing datasets	Hwang et al. (2020)
	RNN	Supervised (classification and translation)	90% accuracy	Code + training and testing datasets	Aghasafari et al. (2021)
	SVM	Supervised (classification)	100% accuracy	None	Jurkiewicz et al. (2021)
	RFs	Supervised (classification)	86% accuracy	Code + training and testing datasets	Yang et al. (2022)
Contraction	SVM	Supervised (classification)	83%–99% accuracy	None	Lee et al. (2015)
	UMAP, SVM	Supervised (classification)	89% accuracy	None	Orita et al. (2020)
	Feed Forward -NN	Supervised (classification and regression)	96% accuracy	None	Ouyang et al. (2022)
	kNN, decision trees, Naive Bayes classifier, QDA, SVM	Supervised (classification)	>90% accuracy	None	Teles et al. (2021)
Tissue Assembly	hierarchical ML	Supervised (regression)	$R^2 = 0.5$	datasets and model equations	Bone et al. (2020)
	RFs	Supervised (classification and regression)	75% accuracy	None	Conev et al. (2020)
	Inductive Logic	Supervised (classification)	90% accuracy	None	Lee et al. (2020)
	Bayesian Optimization	Supervised (regression)	N/A	Training/Testing Dataset only	Ruberu et al. (2021)
	decision trees, logistic regression, kNN, XGBoost, SVM	Supervised (classification)	87% accuracy	Code + training and testing datasets	Rafieyan et al. (2023)

Acronyms used: RFs, random forests; GPR, gaussian process regression; LDA, linear discriminant analysis; QDA, quadratic discriminant analysis; MARS, multivariate adaptive regression splines; SVM, support vector machine; CNN, convolutional neural network; NN, neural network; kNN, k-nearest-neighbors; NNB, normal naïve Bayes; RNNs, recurrent neural networks; and UMAP, Uniform manifold approximation and projection.

computational resources and the amount of time required for successful implementation and training. However, many authors do not provide this. Finally, there exists a distinct focus on physiological phenotyping in the field, and that is reflected in this review. These studies are critical to inform the necessary interventions that may improve hiPSC-CM functionality. This need places further emphasis on the importance of training data bias, for if bias exists in phenotyping methods, it may skew the results of interventions designed to these parameters.

In addition, the training size itself is a crucial factor for almost every AI approach. Notably, the studies reviewed here rely on experimental data, particularly from cardiac differentiation experiments, as a primary data source. The experimental data consists of variables related to cell density, bioprinting

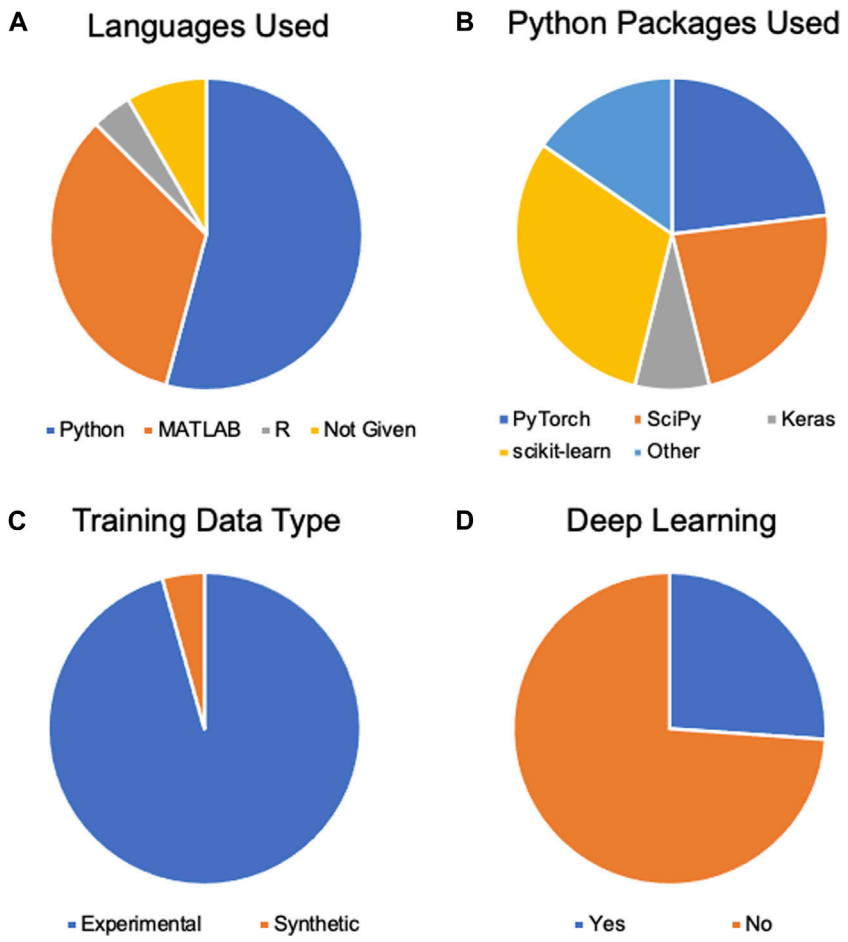

FIGURE 1
Of the 23 papers reviewed, we describe the frequency of programming language used **(A)**, the specific python package used **(B)**, the source of training data **(C)**, and if deep learning methods were used **(D)**.

parameters, drug concentrations, and preculture conditions. While these datasets capture various aspects of the differentiation process, they remain low in sample sizes. Researchers often choose to focus on different variables, even when addressing the same challenges, such that this variability poses a barrier when attempting to join datasets across studies (Rafieyan et al., 2023). This review highlights the need for more features and larger datasets to comprehensively explain the variance in output data. Closing this gap is vital for understanding the complete set of factors influencing cardiac differentiation.

The lack of proper training data sets could be addressed by incorporating more temporal data, integrating diverse types of data from imaging and variable cell sources, and implementation of generative models to synthesize larger datasets. Firstly, long-term dependencies and variations in cardiac differentiation need to be considered, especially when aiming for clinically relevant outcomes. Although binary classification tasks are proactive ways to quantify if a particular environment will be successful or not, how the environment succeeds or fails over time can lead to new insights for early correction approaches. These insights can also aid in more accurate mathematical modeling, emphasizing the symbiotic relationship between data-driven and physics-based techniques. Secondly, collecting data from diverse cell lines and experimental conditions, like 3D bioprinting settings, is crucial to improving the robustness and generalizability of ML models. Consistent data collection across the field is needed to compare and combine disparate datasets. Integrating various features and modalities, including imaging data, can enhance the predictive power of nowadays pragmatic ML models. However, prioritizing or even measuring the vast possible number of features is overwhelming. There is a gradual shift toward unsupervised or semi-supervised learning to capture nuanced information, especially now that these approaches are more practical. The ultimate goal is to generate digital twins (An et al., 2021; Zimmermann et al., 2021) of hiPSC-CMs, producing robust and diverse datasets spanning various configurations. Although this goal is still out of reach, we anticipate that ML coupled with mathematical modeling will play a crucial role in achieving it. In the meantime, generative models can close the gap, augmenting existing data with tailored synthetic data. Some emerging approaches rely on DL frameworks, like GANs and autoencoders (Goodfellow et al., 2014; Goodfellow et al., 2016), but with sufficient modeling and understanding of the task at hand, non-DL approaches many times are sufficient, particularly

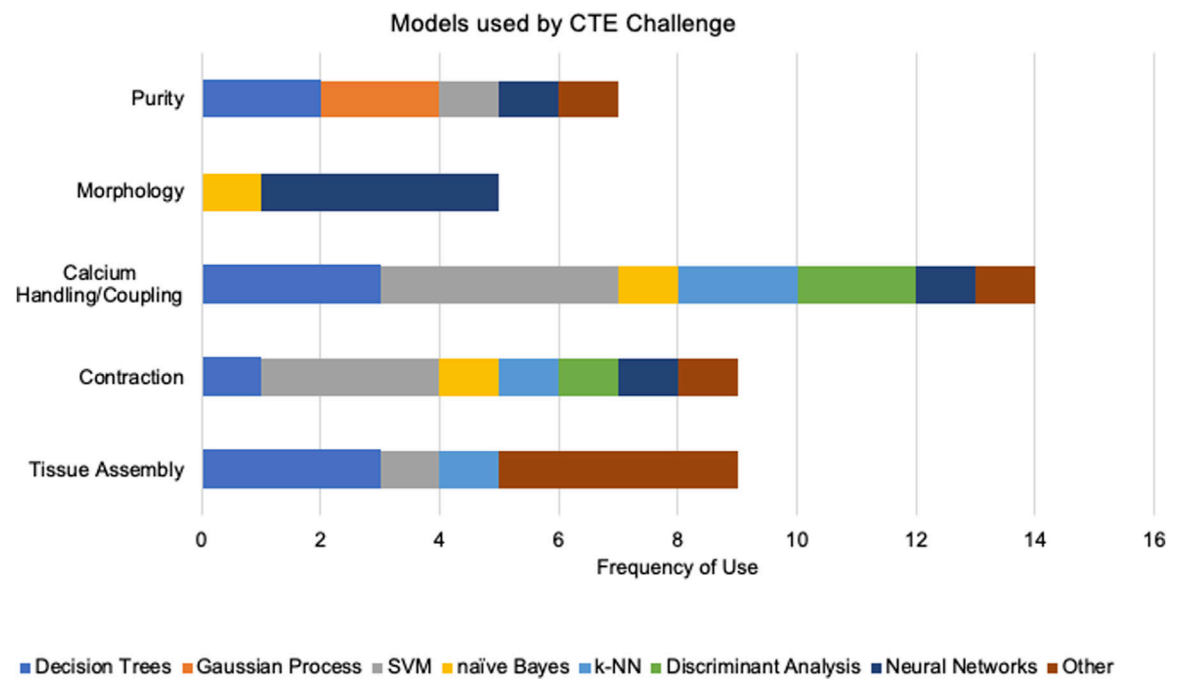

FIGURE 2
We segment the frequency of models used within each cardiac tissue engineering challenge. We categorized models as "decision trees" (RF, tree bagging, classification tree, XGBoost), "Gaussian processes" (GPR, GP), "SVM", "naïve Bayes", "kNN", "discriminant analysis" (LDA, QDA), "neural networks" (CNN, NN, U-net, StyleGAN, RNN, feed forward NN, hierarchical machine learning), and "other" (MARS, spectral grouping, UMAP, hierarchical ML, inductive logic, Bayesian optimization, logistic regression).

hidden Markov models and Gaussian mixture models (Bishop and Nasrabadi, 2006).

10 Conclusion

The application of ML in CTE is progressing toward more sophisticated frameworks capable of handling diverse data types. These observations underscore the multidimensional nature of CTE challenges, the innovative integration of ML with computational models, and the ongoing need for refining ML frameworks to balance accuracy, interpretability, and computational efficiency. Through combining ML with mathematical models and expert knowledge, we envision a rich collaboration between novel data-driven and biophysics-informed models to bridge knowledge and computational gaps.

Author contributions

NK: Conceptualization, Formal Analysis, Methodology, Project administration, Writing–original draft. JC: Conceptualization, Formal Analysis, Methodology, Writing–original draft. EC: Funding acquisition, Supervision, Writing–review and editing. JZ: Funding acquisition, Supervision, Writing–review and editing.

Funding

The author(s) declare that financial support was received for the research, authorship, and/or publication of this article. We gratefully acknowledge the support of the National Science Foundation (2002652, awarded to JZ) and National Institutes of Health (R01CA236857, awarded to JC and EC).

Conflict of interest

The authors declare that the research was conducted in the absence of any commercial or financial relationships that could be construed as a potential conflict of interest.

Publisher's note

All claims expressed in this article are solely those of the authors and do not necessarily represent those of their affiliated organizations, or those of the publisher, the editors and the reviewers. Any product that may be evaluated in this article, or claim that may be made by its manufacturer, is not guaranteed or endorsed by the publisher.

References

Aghasafari, P., Yang, P. C., Kernik, D. C., Sakamoto, K., Kanda, Y., Kurokawa, J., et al. (2021). A deep learning algorithm to translate and classify cardiac electrophysiology. *eLife* 10, e68335. doi:10.7554/eLife.68335

An, J., Chua, C. K., and Mironov, V. (2021). Application of machine learning in 3D bioprinting: focus on development of big data and digital twin. *Int. J. Bioprinting* 7 (1), 342. doi:10.18063/ijb.v7i1.342

Anderson, J. L., and Morrow, D. A. (2017). Acute myocardial infarction. *N. Engl. J. Med.* 376 (21), 2053–2064. doi:10.1056/NEJMra1606915

Beauchamp, P., Jackson, C. B., Ozhathil, L. C., Agarkova, I., Galindo, C. L., Sawyer, D. B., et al. (2020). 3D Co-culture of hiPSC-derived cardiomyocytes with cardiac fibroblasts improves tissue-like features of cardiac spheroids. *Front. Mol. Biosci.* 7, 14. doi:10.3389/fmolb.2020.00014

Benjamin, E. J., Virani, S. S., Callaway, C. W., Chamberlain, A. M., Chang, A. R., Cheng, S., et al. (2018). Heart disease and stroke statistics—2018 update: a report from the American heart association. *Circulation* 137 (12), e67–e492. doi:10.1161/CIR.0000000000000558

Bishop, C. M., and Nasrabadi, N. M. (2006). *Pattern recognition and machine learning*. Springer.

Bizopoulos, P., and Koutsouris, D. (2019). Deep learning in cardiology. *IEEE Rev. Biomed. Eng.* 12, 168–193. doi:10.1109/RBME.2018.2885714

Bodi, I., Mikala, G., Koch, S. E., Akhter, S. A., and Schwartz, A. (2005). The L-type calcium channel in the heart: the beat goes on. *J. Clin. Investigation* 115 (12), 3306–3317. doi:10.1172/JCI27167

Bone, J. M., Childs, C. M., Menon, A., Póczos, B., Feinberg, A. W., LeDuc, P. R., et al. (2020). Hierarchical machine learning for high-fidelity 3D printed biopolymers. *ACS Biomaterials Sci. Eng.* 6 (12), 7021–7031. doi:10.1021/acsbiomaterials.0c00755

Breiman, L. (2001). Random forests. *Mach. Learn.* 45, 5–32. doi:10.1023/a:1010933404324

Cascianelli, S., Molineris, I., Isella, C., Masseroli, M., and Medico, E. (2020). Machine learning for RNA sequencing-based intrinsic subtyping of breast cancer. *Sci. Rep.* 10 (1), 14071. doi:10.1038/s41598-020-70832-2

Chong, J. J. H., Yang, X., Don, C. W., Minami, E., Liu, Y. W., Weyers, J. J., et al. (2014). Human embryonic-stem-cell-derived cardiomyocytes regenerate non-human primate hearts. *Nature* 510 (7504), 273–277. doi:10.1038/nature13233

Conev, A., Litsa, E. E., Perez, M. R., Diba, M., Mikos, A. G., and Kavraki, L. E. (2020). Machine learning-guided three-dimensional printing of tissue engineering scaffolds. *Part A* 26 (23–24), 1359–1368. doi:10.1089/ten.tea.2020.0191

Conway, D., and White, J. (2012). *Machine learning for hackers: case studies and algorithms to get you started*. First Edition. Sebastopol, CA: O'Reilly.

Coronnello, C., and Francipane, M. G. (2022). Moving towards induced pluripotent stem cell-based therapies with artificial intelligence and machine learning. *Stem Cell Rev. Rep.* 18 (2), 559–569. doi:10.1007/s12015-021-10302-y

Cortes, C., and Vapnik, V. (1995). Support-vector networks. *Mach. Learn.* 20, 273–297. doi:10.1007/bf00994018

Cover, T., and Hart, P. (1967). Nearest neighbor pattern classification. *IEEE Trans. Inf. theory* 13 (1), 21–27. doi:10.1109/tit.1967.1053964

Cybenko, G. (1989). Approximation by superpositions of a sigmoidal function. *Math. Control, Signals Syst.* 2 (4), 303–314. doi:10.1007/BF02551274

Dinov, I. D. (2016). Volume and value of big healthcare data. *J. Med. Statistics Inf.* 4, 3. doi:10.7243/2053-7662-4-3

Esser, T. U., Anspach, A., Muenzebrock, K. A., Kah, D., Schrüfer, S., Schenk, J., et al. (2023). Direct 3D-bioprinting of hiPSC-derived cardiomyocytes to generate functional cardiac tissues. *Adv. Mater.* 35, 2305911. doi:10.1002/adma.202305911

Feinberg, A. W., Ripplinger, C., van der Meer, P., Sheehy, S., Domian, I., Chien, K., et al. (2013). Functional differences in engineered myocardium from embryonic stem cell-derived versus neonatal cardiomyocytes. *Stem Cell Rep.* 1 (5), 387–396. doi:10.1016/j.stemcr.2013.10.004

Feric, N. T., and Radisic, M. (2016). Maturing human pluripotent stem cell-derived cardiomyocytes in human engineered cardiac tissues. *Adv. Drug Deliv. Rev.* 96, 110–134. doi:10.1016/j.addr.2015.04.019

Finkel, S., Sweet, S., Locke, T., Smith, S., Wang, Z., Sandini, C., et al. (2023). FRESH™ 3D bioprinted cardiac tissue, a bioengineered platform for *in vitro* pharmacology. *Apl. Bioeng.* 7 (4), 046113. doi:10.1063/5.0163363

Friedman, J. H. (1991). Multivariate adaptive regression splines. *Ann. Statistics* 19 (1), 1–67. doi:10.1214/aos/1176347963

Fukunaga, K., and Hostetler, L. (1975). The estimation of the gradient of a density function, with applications in pattern recognition. *IEEE Trans. Inf. Theory* 21 (1), 32–40. doi:10.1109/TIT.1975.1055330

Gerdes, A. M., Kellerman, S. E., Moore, J. A., Muffly, K. E., Clark, L. C., Reaves, P. Y., et al. (1992). Structural remodeling of cardiac myocytes in patients with ischemic cardiomyopathy. ', *Circ.* 86 (2), 426–430. doi:10.1161/01.CIR.86.2.426

Géron, A. (2019). *Hands-on machine learning with scikit-learn, keras, and TensorFlow: concepts, tools, and techniques to build intelligent systems*. 2nd edition. Beijing China ; Sebastopol, CA: O'Reilly Media.

Gers, F. A., Schmidhuber, J., and Cummins, F. (2000). Learning to forget: continual prediction with LSTM. *Neural Comput.* 12 (10), 2451–2471. doi:10.1162/089976600300015015

Glass, C., Lafata, K. J., Jeck, W., Horstmeyer, R., Cooke, C., Everitt, J., et al. (2022). The role of machine learning in cardiovascular pathology. *Can. J. Cardiol.* 38 (2), 234–245. doi:10.1016/j.cjca.2021.11.008

Goodfellow, I., Bengio, Y., and Courville, A. (2016). *Deep learning*. Illustrated edition. Cambridge, Mass: The MIT Press.

Goodfellow, I. J., Pouget-Abadie, J., Mirza, M., Xu, B., Warde-Farley, D., Ozair, S., et al. (2014). Generative adversarial networks. *arXiv*. doi:10.48550/arXiv.1406.2661

Gorospe, G., Zhu, R., Millrod, M. A., Zambidis, E. T., Tung, L., and Vidal, R. (2014). Automated grouping of action potentials of human embryonic stem cell-derived cardiomyocytes. *IEEE Trans. Biomed. Eng.* 61 (9), 2389–2395. doi:10.1109/TBME.2014.2311387

Grafton, F., Ho, J., Ranjbarvaziri, S., Farshidfar, F., Budan, A., Steltzer, S., et al. (2021). Deep learning detects cardiotoxicity in a high-content screen with induced pluripotent stem cell-derived cardiomyocytes. *eLife* 10, e68714. doi:10.7554/eLife.68714

Halloin, C., Coffee, M., Manstein, F., and Zweigerdt, R. (2019). Production of cardiomyocytes from human pluripotent stem cells by bioreactor technologies. *Methods Mol. Biol.* 1994, 55–70. doi:10.1007/978-1-4939-9477-9_5

Hastie, T., Tibshirani, R., and Friedman, J. (2009). *The elements of statistical learning*. New York, NY: Springer (Springer Series in Statistics. doi:10.1007/978-0-387-84858-7

Haykin, S. (1998). *Neural networks: a comprehensive foundation*. Subsequent edition. Upper Saddle River, N.J: Prentice Hall.

Haykin, S. (2008). *Neural networks and learning machines*. 3rd edition. New York Munich: Pearson.

Hazeltine, L. B., Simmons, C. S., Salick, M. R., Lian, X., Badur, M. G., Han, W., et al. (2012). Effects of substrate mechanics on contractility of cardiomyocytes generated from human pluripotent stem cells. *Int. J. Cell Biol.* 2012, 1–13. doi:10.1155/2012/508294

Heylman, C., Datta, R., Sobrino, A., George, S., and Gratton, E. (2015). Supervised machine learning for classification of the electrophysiological effects of chronotropic drugs on human induced pluripotent stem cell-derived cardiomyocytes. *PLOS ONE* 10 (12), e0144572. doi:10.1371/journal.pone.0144572

Horikoshi, Y., Yan, Y., Terashvili, M., Wells, C., Horikoshi, H., Fujita, S., et al. (2019). Fatty acid-treated induced pluripotent stem cell-derived human cardiomyocytes exhibit adult cardiomyocyte-like energy metabolism phenotypes. *Cells* 8 (9), 1095. doi:10.3390/cells8091095

Hornik, K., Stinchcombe, M., and White, H. (1989). Multilayer feedforward networks are universal approximators. *Neural Netw.* 2 (5), 359–366. doi:10.1016/0893-6080(89)90020-8

Hotelling, H. (1936). Simplified calculation of principal components. *Psychometrika* 1 (1), 27–35. doi:10.1007/bf02287921

Hulsen, T., Jamuar, S. S., Moody, A. R., Karnes, J. H., Varga, O., Hedensted, S., et al. (2019). From big data to precision medicine. *Front. Med.* 6, 34. doi:10.3389/fmed.2019.00034

Hwang, H., Liu, R., Maxwell, J. T., Yang, J., and Xu, C. (2020). Machine learning identifies abnormal Ca 2+ transients in human induced pluripotent stem cell-derived cardiomyocytes. *Sci. Rep.* 10 (1), 16977. doi:10.1038/s41598-020-73801-x

Izenman, A. J. (2008). *Modern multivariate statistical techniques*. New York, NY: Springer (Springer Texts in Statistics). doi:10.1007/978-0-387-78189-1

James, G., Witten, D., Hastie, T., Tibshirani, R., and Taylor, J. (2023). *An introduction to statistical learning: with applications in pyth*. Cham: Springer International Publishing (Springer Texts in Statistics). doi:10.1007/978-3-031-38747-0

Jovel, J., and Greiner, R. (2021). An introduction to machine learning approaches for biomedical research. *Front. Med.* 8, 771607. doi:10.3389/fmed.2021.771607

Juhola, M., Joutsijoki, H., Penttinen, K., and Aalto-Setälä, K. (2018). Detection of genetic cardiac diseases by Ca 2+ transient profiles using machine learning methods. *Sci. Rep.* 8 (1), 9355–9410. doi:10.1038/s41598-018-27695-5

Juhola, M., Penttinen, K., Joutsijoki, H., and Aalto-Setälä, K. (2021). Analysis of drug effects on iPSC cardiomyocytes with machine learning. *Ann. Biomed. Eng.* 49 (1), 129–138. doi:10.1007/s10439-020-02521-0

Juhola, M., Penttinen, K., Joutsijoki, H., Varpa, K., Saarikoski, J., Rasku, J., et al. (2015). Signal analysis and classification methods for the calcium transient data of stem cell-derived cardiomyocytes. *Comput. Biol. Med.* 61, 1–7. doi:10.1016/j.compbiomed.2015.03.016

Jurkiewicz, J., Kroboth, S., Zlochiver, V., and Hinow, P. (2021). Automated feature extraction from large cardiac electrophysiological data sets. *J. Electrocardiol.* 65, 157–162. doi:10.1016/j.jelectrocard.2021.02.003

Karras, T., Laine, S., and Aila, T. (2019). A style-based generator architecture for generative adversarial networks. *arXiv*. doi:10.48550/arXiv.1812.04948

Kehoe, D. E., Jing, D., Lock, L. T., and Tzanakakis, E. S. (2010). Scalable stirred-suspension bioreactor culture of human pluripotent stem cells. *Tissue Eng. Part A* 16 (2), 405–421. doi:10.1089/ten.tea.2009.0454

Kelleher, J. D., Namee, B. M., and D'Arcy, A. (2015). *Fundamentals of machine learning for predictive data analytics: algorithms, worked examples, and case studies*. 1st edition. Cambridge, Massachusetts: The MIT Press.

Kempf, H., Andree, B., and Zweigerdt, R. (2016). Large-scale production of human pluripotent stem cell derived cardiomyocytes. *Adv. Drug Deliv. Rev.* 96, 18–30. doi:10.1016/j.addr.2015.11.016

Kensah, G., Gruh, I., Viering, J., Schumann, H., Dahlmann, J., Meyer, H., et al. (2011). A novel miniaturized multimodal bioreactor for continuous *in situ* assessment of bioartificial cardiac tissue during stimulation and maturation. *Methods* 17 (4), 463–473. doi:10.1089/ten.tec.2010.0405

Kernik, D. C., Yang, P. C., Kurokawa, J., Wu, J. C., and Clancy, C. E. (2020). A computational model of induced pluripotent stem-cell derived cardiomyocytes for high throughput risk stratification of KCNQ1 genetic variants. *PLOS Comput. Biol.* 16 (8), e1008109. doi:10.1371/journal.pcbi.1008109

Khadangi, A., Boudier, T., Hanssen, E., and Rajagopal, V. (2022). CardioVinci: building blocks for virtual cardiac cells using deep learning. *Philosophical Trans. R. Soc. B Biol. Sci.* 377 (1864), 20210469. doi:10.1098/rstb.2021.0469

Kita-Matsuo, H., Barcova, M., Prigozhina, N., Salomonis, N., Wei, K., Jacot, J. G., et al. (2009). Lentiviral vectors and protocols for creation of stable hESC lines for fluorescent tracking and drug resistance selection of cardiomyocytes. *PLOS ONE* 4 (4), e5046. doi:10.1371/journal.pone.0005046

Kobayashi, J., Kikuchi, A., Aoyagi, T., and Okano, T. (2019). Cell sheet tissue engineering: cell sheet preparation, harvesting/manipulation, and transplantation. *J. Biomed. Mater. Res. Part A* 107 (5), 955–967. doi:10.1002/jbm.a.36627

Koivumäki, J. T., Naumenko, N., Tuomainen, T., Takalo, J., Oksanen, M., Puttonen, K. A., et al. (2018). Structural immaturity of human iPSC-derived cardiomyocytes: *in silico* investigation of effects on function and disease modeling. *Front. Physiology* 9, 80. doi:10.3389/fphys.2018.00080

Kowalczewski, A., Sakolish, C., Hoang, P., Liu, X., Jacquir, S., Rusyn, I., et al. (2022). Integrating nonlinear analysis and machine learning for human induced pluripotent stem cell-based drug cardiotoxicity testing. *J. Tissue Eng. Regen. Med.* 16 (8), 732–743. doi:10.1002/term.3325

Koyilot, M. C., Natarajan, P., Hunt, C. R., Sivarajkumar, S., Roy, R., Joglekar, S., et al. (2022). Breakthroughs and applications of organ-on-a-chip technology. *Cells* 11 (11), 1828. doi:10.3390/cells11111828

Kresoja, K.-P., Unterhuber, M., Wachter, R., Thiele, H., and Lurz, P. (2023). A cardiologist's guide to machine learning in cardiovascular disease prognosis prediction. *Basic Res. Cardiol.* 118 (1), 10. doi:10.1007/s00395-023-00982-7

Laflamme, M. A., and Murry, C. E. (2011). Heart regeneration. *Nature* 473 (7347), 326–335. doi:10.1038/nature10147

Lee, E. K., Kurokawa, Y. K., Tu, R., George, S. C., and Khine, M. (2015). Machine learning plus optical flow: a simple and sensitive method to detect cardioactive drugs. *Sci. Rep.* 5 (1), 11817. doi:10.1038/srep11817

Lee, E. K., Tran, D. D., Keung, W., Chan, P., Wong, G., Chan, C. W., et al. (2017). Machine learning of human pluripotent stem cell-derived engineered cardiac tissue contractility for automated drug classification. *Stem Cell Rep.* 9 (5), 1560–1572. doi:10.1016/j.stemcr.2017.09.008

Lee, J., Oh, S. J., Kim, W. D., and Kim, S. H. (2020). Machine learning-based design strategy for 3D printable bioink: elastic modulus and yield stress determine printability. *Biofabrication* 12 (3), 035018. doi:10.1088/1758-5090/ab8707

Litjens, G., Kooi, T., Bejnordi, B. E., Setio, A. A. A., Ciompi, F., Ghafoorian, M., et al. (2017). A survey on deep learning in medical image analysis. *Med. Image Anal.* 42, 60–88. doi:10.1016/j.media.2017.07.005

Maddah, M., Mandegar, M. A., Dame, K., Grafton, F., Loewke, K., and Ribeiro, A. J. (2020). Quantifying drug-induced structural toxicity in hepatocytes and cardiomyocytes derived from hiPSCs using a deep learning method. *J. Pharmacol. Toxicol. Methods* 105, 106895. doi:10.1016/j.vascn.2020.106895

Manning, C. D. (2008). *Intro to information retrieval*. Cambridge, UNITED KINGDOM: Cambridge University Press Textbooks. Available at: http://ebookcentral.proquest.com/lib/utxa/detail.action?docID=5119897 (Accessed December 15, 2023).

McCain, M. L., and Parker, K. K. (2011). Mechanotransduction: the role of mechanical stress, myocyte shape, and cytoskeletal architecture on cardiac function. *Pflügers Archiv - Eur. J. Physiology* 462 (1), 89–104. doi:10.1007/s00424-011-0951-4

McInnes, L., Healy, J., and Melville, J. (2020). UMAP: Uniform manifold approximation and projection for dimension reduction. *arXiv*. doi:10.48550/arXiv.1802.03426

Menon, A., Gupta, C., Perkins, K. M., DeCost, B. L., Budwal, N., Rios, R. T., et al. (2017). Elucidating multi-physics interactions in suspensions for the design of polymeric dispersants: a hierarchical machine learning approach. *Mol. Syst. Des. Eng.* 2 (3), 263–273. doi:10.1039/c7me00027h

Mohammadi, S., Hashemi, M., Finklea, F., Williams, B., Lipke, E., and Cremaschi, S. (2022). Classification of cardiac differentiation outcome, percentage of cardiomyocytes on day 10 of differentiation, for hydrogel-encapsulated hiPSCs. *J. Adv. Manuf. Process.* 5 (2), e10148. doi:10.1002/amp2.10148

Mohammadi, S., Hashemi, M., Finklea, F. B., Lipke, E. A., and Cremaschi, S. (2023). Differentiating engineered tissue images and experimental factors to classify cardiomyocyte content. *Tissue Eng. Part A* 29 (1–2), 58–66. doi:10.1089/ten.tea.2022.0122

Montero-Calle, P., Flandes-Iparraguirre, M., Mountris, K., S de la Nava, A., Laita, N., Rosales, R. M., et al. (2022). Fabrication of human myocardium using multidimensional modelling of engineered tissues. *Biofabrication* 14 (4), 045017. doi:10.1088/1758-5090/ac8cb3

Muggleton, S., and de Raedt, L. (1994). Inductive logic programming: theory and methods. *J. Log. Program.* 19–20, 629–679. doi:10.1016/0743-1066(94)90035-3

Müller, A. C., and Guido, S. (2016). *Introduction to machine learning with Python: a guide for data scientists*. Sebastopol, CA: O'Reilly Media, Inc.

Murphy, K. P. (2012). *Machine learning: a probabilistic perspective*. MIT press.

Ng, A., Jordan, M., and Weiss, Y. (2001). "On Spectral Clustering: Analysis and an algorithm," in (Editors) D. Dietterich, S. Becker, and Z. Ghahramani *Advances in Neural Information Processing Systems*. MIT Press. Available at: https://proceedings.neurips.cc/paper_files/paper/2001/file/801272ee79cfde7fa5960571fee36b9b-Paper.pdf.

Nunes, S. S., Miklas, J. W., Liu, J., Aschar-Sobbi, R., Xiao, Y., Zhang, B., et al. (2013). Biowire: a platform for maturation of human pluripotent stem cell–derived cardiomyocytes. *Nat. Methods* 10 (8), 781–787. doi:10.1038/nmeth.2524

O'Hara, T., Virág, L., Varró, A., and Rudy, Y. (2011). Simulation of the undiseased human cardiac ventricular action potential: model formulation and experimental validation. *PLOS Comput. Biol.* 7 (5), e1002061. doi:10.1371/journal.pcbi.1002061

Ong, C. S., Nam, L., Ong, K., Krishnan, A., Huang, C. Y., Fukunishi, T., et al. (2018). 3D and 4D bioprinting of the myocardium: current approaches, challenges, and future prospects. *BioMed Res. Int. Hindawi* 2018, 1–11. doi:10.1155/2018/6497242

Orita, K., Sawada, K., Koyama, R., and Ikegaya, Y. (2019). Deep learning-based quality control of cultured human-induced pluripotent stem cell-derived cardiomyocytes. *J. Pharmacol. Sci.* 140 (4), 313–316. doi:10.1016/j.jphs.2019.04.008

Orita, K., Sawada, K., Matsumoto, N., and Ikegaya, Y. (2020). Machine-learning-based quality control of contractility of cultured human-induced pluripotent stem-cell-derived cardiomyocytes. *Biochem. Biophysical Res. Commun.* 526 (3), 751–755. doi:10.1016/j.bbrc.2020.03.141

Ouyang, Q., Yang, W., Wu, Y., Xu, Z., Hu, Y., Hu, N., et al. (2022). Multi-labeled neural network model for automatically processing cardiomyocyte mechanical beating signals in drug assessment. *Biosens. Bioelectron.* 209, 114261. doi:10.1016/j.bios.2022.114261

Park, K. M., Shin, Y. M., Kim, K., and Shin, H. (2018). Tissue engineering and regenerative medicine 2017: a year in review. *Tissue Eng. Part B Rev.* 24 (5), 327–344. doi:10.1089/ten.teb.2018.0027

Pascanu, R., Mikolov, T., and Bengio, Y. (2013). "On the difficulty of training recurrent neural networks," in International conference on machine learning (Atlanta, Georgia, USA: Pmlr), 1310–1318.

Pasqualini, F. S., Sheehy, S., Agarwal, A., Aratyn-Schaus, Y., and Parker, K. (2015). Structural phenotyping of stem cell-derived cardiomyocytes. *Stem Cell Rep.* 4 (3), 340–347. doi:10.1016/j.stemcr.2015.01.020

Pearson, K. (1901). LIII. On lines and planes of closest fit to systems of points in space. *Lond. Edinb. Dublin philosophical Mag. J. Sci.* 2 (11), 559–572. doi:10.1080/14786440109462720

Peek, N., Holmes, J. H., and Sun, J. (2014). Technical challenges for big data in biomedicine and Health: data sources, infrastructure, and analytics. *Yearb. Med. Inf.* 23 (1), 42–47. doi:10.15265/IY-2014-0018

Petegrosso, R., Li, Z., and Kuang, R. (2020). Machine learning and statistical methods for clustering single-cell RNA-sequencing data. *Briefings Bioinforma.* 21 (4), 1209–1223. doi:10.1093/bib/bbz063

Qasim, M., Arunkumar, P., Powell, H. M., and Khan, M. (2019). Current research trends and challenges in tissue engineering for mending broken hearts. *Life Sci.* 229, 233–250. doi:10.1016/j.lfs.2019.05.012

Quinlan, J. R. (1986). Induction of decision trees. *Mach. Learn.* 1 (1), 81–106. doi:10.1007/BF00116251

Rafieyan, S., Vasheghani-Farahani, E., Baheiraei, N., and Keshavarz, H. (2023). MLATE: machine learning for predicting cell behavior on cardiac tissue engineering scaffolds. *Comput. Biol. Med.* 158, 106804. doi:10.1016/j.compbiomed.2023.106804

Raschka, S., and Mirjalili, V. (2017). *Machine learning and deep learning with Python, scikit-learn, and TensorFlow*. Python Machine Learning, Second Edition. Birmingham Mumbai: Packt Publishing.

Rasmussen, C. E., and Williams, C. K. (2006). *Gaussian processes for machine learning*. Springer.

Reddy, K., Khaliq, A., and Henning, R. J. (2015). Recent advances in the diagnosis and treatment of acute myocardial infarction. *World J. Cardiol.* 7 (5), 243–276. doi:10.4330/wjc.v7.i5.243

Regazzoni, F., Salvador, M., Dede', L., and Quarteroni, A. (2022). A machine learning method for real-time numerical simulations of cardiac electromechanics. *Comput. Methods Appl. Mech. Eng.* 393, 114825. doi:10.1016/j.cma.2022.114825

Ribeiro, A. J. S., Guth, B. D., Engwall, M., Eldridge, S., Foley, C. M., Guo, L., et al. (2019). Considerations for an *in vitro*, cell-based testing platform for detection of drug-induced inotropic effects in early drug development. Part 2: designing and fabricating microsystems for assaying cardiac contractility with physiological relevance using human iPSC-cardiomyocytes. *Front. Pharmacol.* 10, 934. doi:10.3389/fphar.2019.00934

Richards, D. J., Coyle, R. C., Tan, Y., Jia, J., Wong, K., Toomer, K., et al. (2017). Inspiration from heart development: biomimetic development of functional human cardiac organoids. *Biomaterials* 142, 112–123. doi:10.1016/j.biomaterials.2017.07.021

Ronaldson-Bouchard, K., Ma, S. P., Yeager, K., Chen, T., Song, L., Sirabella, D., et al. (2018). Advanced maturation of human cardiac tissue grown from pluripotent stem cells. *Nature* 556 (7700), 239–243. doi:10.1038/s41586-018-0016-3

Ronneberger, O., Fischer, P., and Brox, T. (2015). U-net: convolutional networks for biomedical image segmentation. *arXiv*. doi:10.48550/arXiv.1505.04597

Ruan, J.-L., Tulloch, N. L., Razumova, M. V., Saiget, M., Muskheli, V., Pabon, L., et al. (2016). Mechanical stress conditioning and electrical stimulation promote contractility and force maturation of induced pluripotent stem cell-derived human cardiac tissue. *Circulation* 134 (20), 1557–1567. doi:10.1161/CIRCULATIONAHA.114.014998

Ruberu, K., Senadeera, M., Rana, S., Gupta, S., Chung, J., Yue, Z., et al. (2021). Coupling machine learning with 3D bioprinting to fast track optimisation of extrusion printing. *Appl. Mater. Today* 22, 100914. doi:10.1016/j.apmt.2020.100914

Rueckert, D., and Schnabel, J. A. (2020). Model-based and data-driven strategies in medical image computing. *Proc. IEEE* 108 (1), 110–124. doi:10.1109/JPROC.2019.2943836

Rumelhart, D. E., Hinton, G. E., and Williams, R. J. (1986). Learning representations by back-propagating errors. *Nature* 323 (6088), 533–536. doi:10.1038/323533a0

Sartiani, L., Bettiol, E., Stillitano, F., Mugelli, A., Cerbai, E., and Jaconi, M. E. (2007). Developmental changes in cardiomyocytes differentiated from human embryonic stem cells: a molecular and electrophysiological approach. *Stem Cells Dayt.* 25 (5), 1136–1144. doi:10.1634/stemcells.2006-0466

Shajun Nisha, S., and Nagoor Meeral, M. (2021). "9 - applications of deep learning in biomedical engineering," in *Handbook of deep learning in biomedical engineering*. Editors V. E. Balas, B. K. Mishra, and R. Kumar (Academic Press), 245–270. doi:10.1016/B978-0-12-823014-5.00008-9

Shanmugamani, R. (2018). *Deep learning for computer vision: expert techniques to train advanced neural networks using TensorFlow and keras*. Birmingham Mumbai: Packt Publishing.

Sharma, A., Li, G., Rajarajan, K., Hamaguchi, R., Burridge, P. W., and Wu, S. M. (2015). Derivation of highly purified cardiomyocytes from human induced pluripotent stem cells using small molecule-modulated differentiation and subsequent glucose starvation. *J. Vis. Exp. JoVE Prepr.* (97), 52628. doi:10.3791/52628

Sobie, E. A., and Wehrens, X. H. T. (2009). Computational and experimental models of Ca2+-dependent arrhythmias. *Drug Discov. Today Dis. Models* 6 (3), 57–61. doi:10.1016/j.ddmod.2010.04.002

Strzelecki, M., and Badura, P. (2022). Machine learning for biomedical application. *Appl. Sci.* 12 (4), 2022. doi:10.3390/app12042022

Szegedy, C., Liu, W., Jia, Y., Sermanet, P., Reed, S., Anguelov, D., et al. (2015). "Going deeper with convolutions," in Proceedings of the IEEE conference on computer vision and pattern recognition, 1–9.

Teles, D., Kim, Y., Ronaldson-Bouchard, K., and Vunjak-Novakovic, G. (2021). Machine learning techniques to classify healthy and diseased cardiomyocytes by contractility profile. *ACS biomaterials Sci. Eng.* 7 (7), 3043–3052. doi:10.1021/acsbiomaterials.1c00418

Theodoridis, S. (2015). *Machine learning: a Bayesian and optimization perspective*. Academic Press.

Turnbull, I. C., Karakikes, I., Serrao, G. W., Backeris, P., Lee, J., Xie, C., et al. (2014). Advancing functional engineered cardiac tissues toward a preclinical model of human myocardium. *FASEB J.* 28 (2), 644–654. doi:10.1096/fj.13-228007

Tveito, A., Jæger, K. H., Huebsch, N., Charrez, B., Edwards, A. G., Wall, S., et al. (2018). Inversion and computational maturation of drug response using human stem cell derived cardiomyocytes in microphysiological systems. *Sci. Rep.* 8 (1), 17626. doi:10.1038/s41598-018-35858-7

van der Velden, J., Klein, L., van der Bijl, M., Huybregts, M., Stooker, W., Witkop, J., et al. (1998). Force production in mechanically isolated cardiac myocytes from human ventricular muscle tissue. *Cardiovasc. Res.* 38 (2), 414–423. doi:10.1016/s0008-6363(98)00019-4

Venkatesan, R., and Li, B. (2017). *Convolutional neural networks in visual computing: a concise guide*. Boca Raton: CRC Press.

Wang, L., Xi, Y., Sung, S., and Qiao, H. (2018). RNA-seq assistant: machine learning based methods to identify more transcriptional regulated genes. *BMC Genomics* 19 (1), 546. doi:10.1186/s12864-018-4932-2

Wiegerinck, R. F., Cojoc, A., Zeidenweber, C. M., Ding, G., Shen, M., Joyner, R. W., et al. (2009). Force frequency relationship of the human ventricle increases during early postnatal development. *Pediatr. Res.* 65 (4), 414–419. doi:10.1203/PDR.0b013e318199093c

Williams, B., Löbel, W., Finklea, F., Halloin, C., Ritzenhoff, K., Manstein, F., et al. (2020). Prediction of human induced pluripotent stem cell cardiac differentiation outcome by multifactorial process modeling. *Front. Bioeng. Biotechnol.* 8, 851. doi:10.3389/fbioe.2020.00851

I. H. Witten, E. Frank, and M. A. Hall (2011). "Front matter," *Data mining: practical machine learning tools and techniques*. Third Edition (Boston: Morgan Kaufmann (The Morgan Kaufmann Series in Data Management Systems), i–iii. doi:10.1016/B978-0-12-374856-0.00018-3

Yang, H., Obrezanova, O., Pointon, A., Stebbeds, W., Francis, J., Beattie, K. A., et al. (2023). Prediction of inotropic effect based on calcium transients in human iPSC-derived cardiomyocytes and machine learning. *Toxicol. Appl. Pharmacol.* 459, 116342. doi:10.1016/j.taap.2022.116342

Yang, H., Stebbeds, W., Francis, J., Pointon, A., Obrezanova, O., Beattie, K. A., et al. (2022). Deriving waveform parameters from calcium transients in human iPSC-derived cardiomyocytes to predict cardiac activity with machine learning. *Stem Cell Rep.* 17 (3), 556–568. doi:10.1016/j.stemcr.2022.01.009

Yarotsky, D. (2017). Error bounds for approximations with deep ReLU networks. *Neural Netw.* 94, 103–114. doi:10.1016/j.neunet.2017.07.002

Zhou, S. K., Greenspan, H., and Shen, D. (2017). "Front matter," *Deep learning for medical image analysis* (Academic Press), i–iii. doi:10.1016/B978-0-12-810408-8.00026-2

Zimmermann, J., Budde, K., Arbeiter, N., Molina, F., Storch, A., Uhrmacher, A. M., et al. (2021). Using a digital twin of an electrical stimulation device to monitor and control the electrical stimulation of cells *in vitro*. *Front. Bioeng. Biotechnol.* 9, 765516. doi:10.3389/fbioe.2021.765516

frontiers | Frontiers in Biomaterials Science

TYPE Original Research
PUBLISHED 09 May 2024
DOI 10.3389/fbiom.2024.1365781

OPEN ACCESS

EDITED BY
Jenny Robinson,
University of Washington, United States

REVIEWED BY
Sushma Venkata Mudigunda,
Harvard Medical School, United States
Zalike Keskin Erdogan,
Imperial College London, United Kingdom

*CORRESPONDENCE
Kaitlin C. Fogg,
kaitlin.fogg@oregonstate.edu

RECEIVED 04 January 2024
ACCEPTED 15 April 2024
PUBLISHED 09 May 2024

CITATION
Cadena IA, Adhikari G, Almer A, Jenne M, Obasi N, Soria Zurita NF, Rochefort WE, Mueller JL and Fogg KC (2024), Development of a 3D *in vitro* human-sized model of cervical dysplasia to evaluate the delivery of ethyl cellulose-ethanol injection.
Front. Biomater. Sci. 3:1365781.
doi: 10.3389/fbiom.2024.1365781

Development of a 3D *in vitro* human-sized model of cervical dysplasia to evaluate the delivery of ethyl cellulose-ethanol injection

Ines A. Cadena[1], Gatha Adhikari[2], Alyssa Almer[1], Molly Jenne[1], Ndubuisi Obasi[1], Nicolas F. Soria Zurita[3], Willie E. Rochefort[1], Jenna L. Mueller[2,4,5] and Kaitlin C. Fogg[1]*

[1]School of Chemical, Biological, and Environmental Engineering, Oregon State University, Corvallis, OR, United States, [2]Department of Bioengineering, University of Maryland, College Park, MD, United States, [3]School of Engineering Design and Innovation, College of Engineering, Pennsylvania State University, University Park, PA, United States, [4]Department of OB-GYN and Reproductive Science, University of Maryland School of Medicine, Baltimore, MD, United States, [5]Marlene and Stewart Greenebaum Cancer Center, University of Maryland School of Medicine, Baltimore, MD, United States

Introduction: Cervical cancer, the second leading cause of cancer-related death for women worldwide, remains a preventable yet persistent disease that disproportionately affects women in low and middle-income countries (LMICs). While existing therapies for treating cervical dysplasia are effective, they are often inaccessible in LMICs. Ethanol ablation is an alternative low-cost, accessible therapy that we previously enhanced into ethyl cellulose (EC)-ethanol gel formulation to improve efficacy.

Methods: To evaluate the efficacy of EC-ethanol, in this study, we developed a 3D *in vitro* model of cervical dysplasia featuring a central lesion of cervical cancer cells surrounded by fibroblasts and keratinocytes. Using a GelMA hydrogel formulation (8.7% w/v), we successfully built a 3D model that captured the architectural complexity of cervical dysplasia. We evaluated changes in cell coverage and cell viability. Then, we compared the viscoelastic properties of the GelMA hydrogels to human cervical tissue and using micro-CT imaging, we assessed EC-ethanol injection deposition in the hydrogel, revealing retention of virtually the entire injected volume near the injection site. Finally, we measured changes in cell viability and cell coverage after the EC-ethanol injection.

Results: The developed 3D in vitro model successfully replicated the architectural complexity of cervical dysplasia, demonstrating high cell viability and capturing cell responses effectively. The GelMA hydrogel formulation (8.7% w/v) exhibited viscoelastic properties akin to human cervical tissue. Micro-CT imaging revealed efficient deposition of EC-ethanol within the hydrogel, with retention of the injected volume near the injection site. Furthermore, the EC-ethanol injection significantly reduced cervical cancer cell viability and cell coverage while preserving healthy cells within the model.

Conclusion: Our findings indicate that our 3D *in vitro* model mirrored the architecture of cervical dysplasia and demonstrated the potential of EC-ethanol for localized treatment of cervical dysplasia.

KEYWORDS

hydrogel, cervical dysplasia, triculture, GelMA, ethanol ablation, ethyl cellulose

1 Introduction

Cervical cancer is a preventable disease, yet it remains the second leading cause of cancer-related death for women worldwide (Ferlay et al., 2015). Mortality is projected to rise to 400,000 annual deaths by 2030, and 90% of those deaths will be in low and middle-income countries (LMICs) if no additional action is taken (Ferlay et al., 2015). Cervical cancer is highly preventable through vaccination against the human papillomavirus (HPV) (Human papillomavirus vaccines, 2015), as well as screening, diagnosis, and treatment of cervical dysplasia before it progresses to cervical cancer (Comprehensive Cervical Cancer Control, 2014). While considerable efforts have been made to increase access to vaccination, screening, and diagnosis (Jeronimo et al., 2005; Huchko et al., 2014; Huchko et al., 2015; Lam et al., 2015; Mueller et al., 2017; Mueller et al., 2018), up to 80% of women who have been diagnosed with cervical dysplasia in LMICs never receive treatment, largely due to treatment being inaccessible at the point of care (Gage et al., 2003). Thus, there is a need to develop novel therapies for cervical dysplasia that are accessible in LMICs.

In light of the above, ethanol ablation is a form of clinical tissue ablation well-suited for LMICs (Path, 2013). Ethanol ablation entails directly injecting ethanol into the region of interest to induce necrosis through protein denaturation and cytoplasmic dehydration (Tsu et al., 2013). It is a standard treatment option for small, unresectable liver tumors and has low complication rates (Abdul-Karim et al., 1982). However, its direct injection into tissue leads to fluid leakage outside of the lesion, which decreases efficacy and can lead to side effects (Seki et al., 1989). To address this limitation, we develop a new formulation that includes a low-cost, biocompatible polymer called ethyl cellulose (EC) that forms a gel when injected into tissue. Previous studies have shown promising results in the use of EC-ethanol ablation to safely and effectively treat tumors in a variety of preclinical models, including a chemically induced hamster cheek pouch model of squamous cell carcinoma (Morhard et al., 2017) and subcutaneous flank tumor induced by injecting a murine breast cancer cell line (Nief et al., 2021). While we are most interested in applications in the cervix, these other models were used as no xenograft models of cervical dysplasia currently exist (Larmour et al., 2015). Most recently, we scaled up to swine cervices, which are comparable in size to human cervices (Lorenzen et al., 2015). However, currently, no swine model of cervical dysplasia exists—thus, our previous study was limited to normal anatomy. Taken together, none of these widely used animal models recapitulate the microenvironment of cervical dysplasia or cervical cancer, limiting our ability to investigate how to tune EC-ethanol ablation such that it kills precancerous and cancerous cells and leaves the surrounding healthy cells alone.

Three-dimensional (3D) *in vitro* models offer potential avenues for investigating the therapeutic application of EC-ethanol ablation in the context of cervical dysplasia. However, current models, including a 3D printed model (Larmour et al., 2015) and an organotypic raft culture (De Gregorio et al., 2020), lack suitability for testing EC-ethanol injection due to their inability to capture cervical dysplasia's histology and size. In a prior study, we successfully demonstrated that using gelatin methacrylate (GelMA) as the main component in a 3D *in vitro* model allowed phenotypic cell responses that captured the histology of the tumor microenvironment (Cadena et al., 2023). The motivation for using GelMA in designing a 3D *in vitro* model for cervical dysplasia is inspired by its favorable characteristics established in previous studies, showing its biocompatibility, tunable mechanical properties, and support for cell adhesion, proliferation, and differentiation (Nichol et al., 2010). Previous studies have demonstrated the efficacy of GelMA hydrogels in facilitating the growth and function of various cell types (Van Den Bulcke et al., 2000), including fibroblasts and epithelial cells, which are crucial components of the cervical microenvironment. Additionally, their suitable rheological properties enable the fabrication of complex 3D structures, mimicking the architectural complexity of cervical dysplasia *in vitro* (Bogorad et al., 2015). Moreover, GelMA hydrogels possess good transport properties, allowing for the diffusion of essential nutrients and oxygen necessary for cell viability and function in 3D culture systems (Belair and Abbott, 2017). Owing to these properties, the use of GelMA in constructing a 3D *in vitro* model for cervical dysplasia offers a promising approach to mimic the ECM environment and cellular interactions characteristic of the disease, thus facilitating the evaluation of potential therapeutic interventions. In our previous 3D model for cervical cancer, GelMA was observed to support cervical cancer progression after 48 h of coculture with endothelial cells (Cadena et al., 2023). Despite its success in modeling cervical cancer, our 3D model reflected characteristics of metastatic cancer and is, therefore, unsuitable for studying cervical dysplasia. Additionally, the model's construction in a 96-well plate restricted its size, rendering it ill-suited for testing treatments such as the EC-ethanol injection. Nevertheless, considering GelMA's mechanical properties (Yue et al., 2015), it remains a promising scaffold for developing a 3D *in vitro* model specifically tailored for cervical dysplasia with some tuning for the test of therapies involving EC-ethanol injection.

The overall goal of the present study was to develop a 3D *in vitro* model of cervical dysplasia that shows an initial stage of cervical cancer invasion for the application of an EC-ethanol injection to target cervical cancer growth and viability over time. We developed a 3D triculture model that is the approximate size of a human cervix, captured cell responses, and resembled the mechanical properties of human cervical tissue. We then administered EC-ethanol to the 3D model and demonstrated that we could cause necrosis of the cancer cells in the center of the model while leaving the noncancerous cells (fibroblasts and keratinocytes) on the outside of the model alive. Overall, this study demonstrated that our 3D model captured the architecture and geometry of the cervical disease and could be used to evaluate the potential of EC-ethanol (and, in the future, other novel therapies) for localized treatment of cervical dysplasia.

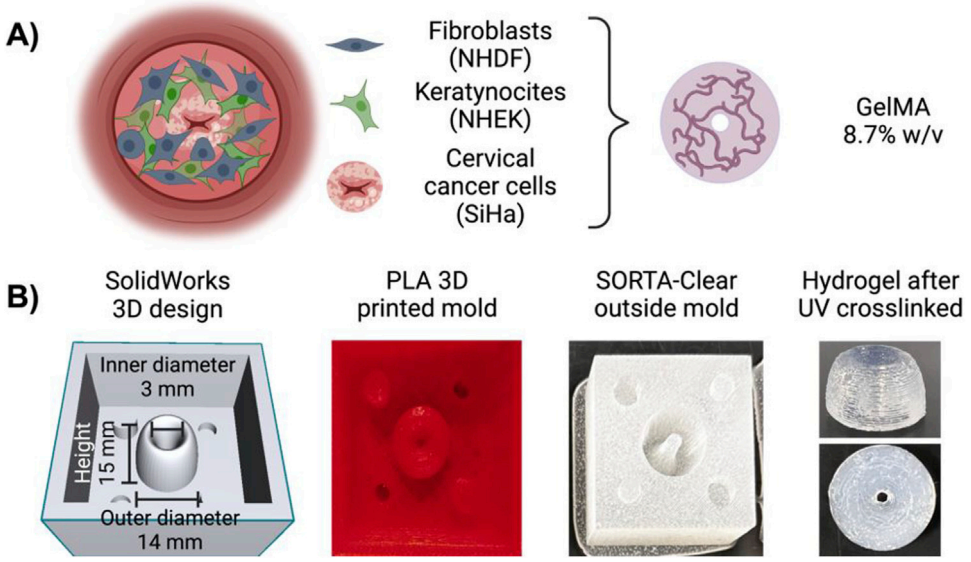

FIGURE 1
Three-dimensional (3D) mold for a tri-coculture model of cervical dysplasia. **(A)** Schematic representation of the 3D model with cervical cancer cells (SiHa) in the center encapsulated in Ge1MA (8.7%w/v with LAP), surrounded by fibroblasts (NHDF) cells suspended in Ge1MA (8.7%w/v with LAP), and covered with keratinocytes (NHEK) cells suspended in culture media. **(B)** The outside mold was created in SolidWorks, printed in PLA with a 10% infill, and built with SORTA-Clear 40 silicone rubber. Diagram created in BioRender.com.

2 Materials and methods

2.1 Cell lines and reagents

Normal adult human dermal fibroblasts (NHDF-Ad) and human epidermal keratinocytes-adult (NHEK-Ad) were purchased from Lonza (CC-2511 Walkerville, MD), and SiHa cells were purchased from ATCC (ATCC® HTB-35™, Manassas, VA). All cell lines were used without additional characterization. NHDF cells were cultured in FBM fibroblast basal media (supplemented with FGM-2 SingleQuot supplements: insulin, hEGF-B, GA-1000, and FBS) (Lonza). NHEK cells were expanded in KBM gold basal medium (KGM gold supplemented with Lonza's SingleQuot supplements: hydrocortisone, transferrin, epinephrine, GA-1000, BPE low protein-nonspecific, hEGF, and recombinant human insulin 0.5%) (Lonza). Human cervical cancer cell line SiHa from ATCC (ATCC® HTB-35™, Manassas, VA) was used without additional characterization. SiHa cells were expanded in Eagle's Minimum Essential Medium (EMEM, ATCC), supplemented with 10% FBS (Sigma-Aldrich, St. Louis, MO) and 1% Penicillin-Streptomycin (P/S, Sigma-Aldrich). All cell lines were expanded in standard cell culture conditions (37°C, 21% O_2, 5% CO_2) until passage 5. Cells were recovered at 80% confluency.

2.2 Cell staining and evaluation of cell response

All reagents were purchased from ThermoFisher (Waltham, MA) unless stated. The cell area was evaluated by taking images of the cells over time. NHDF cells, NHEK cells, and SiHa cells were stained with fluorescent dyes. CellTracker Green CMFDA (C7025), CellTracker Blue CMF2HC (C12881), and CellTracker Red CMTPX (C34552) were used to visualize and quantify the cell area over time. Three channels (469/525 nm, 628/685 nm, and 377/447 nm excitation/emission) with 9 z-stack images were taken every 12 h for 48 h using a Cytation 5 cell imaging multimode reader (Agilent Technologies). The distance between the z-stack is described in each experiment. Images were processed with NIH Fiji- ImageJ, and cell coverage was measured by calculating the area within the well covered by cells and dividing it by the total well area (NIH, Bethesda, MD). Cell viability was quantified by adding Calcein AM (2M, eBioscience™ Calcein AM Viability Dye, 65-0853-39, San Diego, CA) and Propidium Iodide (5M Propidium Iodide Ready Flow™ Reagent, R37169) to the cell cultures. Following the manufacturer's instructions, the staining solution was added on top of the wells at either 24 h or 48 h post-cultured or post-treatment. Two-channel (469/525 nm and 586/647 excitation/emission) 54.8 µm z-stack and 180 µm z-stack images in a 4 × 4 and 4 × 5 montage were taken to image the 3D *in vitro* models. Images were stitched to facilitate the image analysis and quantification of live/dead cells. The mean fluorescent intensity (MFI) of live cells (stained with calcein AM) and dead cells (stained with propidium iodide) were quantified using Fiji ImageJ, and the number of cells that were alive or dead was quantified using Gen 5 software (Agilent Technologies).

2.3 Design of a 3D mold

We employed SolidWorks (Dassault Systèmes SolidWorks Corporation) to create a customized 3D mold that mirrors the size and histology of cervical dysplasia, featuring cancer cells on the inside and surrounded by healthy cells on the outside (Figure 1A).

TABLE 1 Cell density in the 10 mm and 15 mm constructs. The cells' pellet was dissolved in culture media, and then cells were suspended in GelMA (8.7%w/v) hydrogels.

Model thickness (mm)	NHDF (cells/well)	NHEK (cells/well)	SiHa (cells/well)
10	53,333	83,160	26,667
15	1,33,333	277,200	106,667

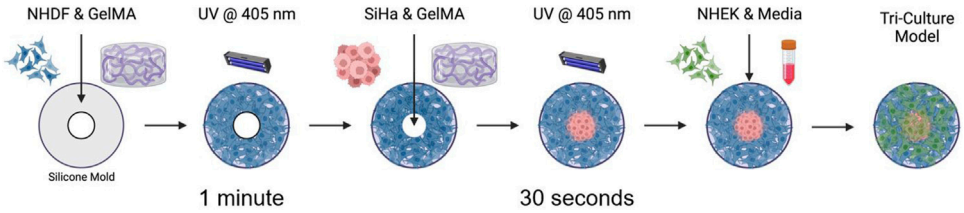

FIGURE 2
Fabrication of a 3D triculture hydrogel model for cervical dysplasia. Schematic illustrating fabrication process of the 3D tri-culture model. Fibroblasts (NHDF), are first recovered from the culture plates and suspended in Ge1MA (8.7% w/v with LAP). 1.5 mL of cell: hydrogel solution is added to the silicone mold and UV form 1 min. Then the construct is carefully added to the 24-well plate ibidi, immediately after cervical cancer cells (SiHa) are recovered from culture plates and suspended in GelMA (8.7% w/v with LAP). Cancer cell-hydrogel solution is pipetted in the center of the 3D model (–200 !IL), and UV cured for about 30 s. Finally, keratinocytes (NHEK) are recovered from the culture plates, the cell pellet is mixed with culture media and added on top of the final 3D model. Constructs are incubated at 37°C for the duration of the experiment. Diagram created in BioRender.com.

Using polylactic acid (PLA) material with 10% infill, the mold was 3D printed at the Valley Library at Oregon State University. Subsequently, we filled the PLA mold with SORTA-Clear 40 silicone rubber (Smooth-ON, Inc., Macungie, PA 18062). Following the manufacturer's guidelines, the mold was then cured and sterilized (Figure 1B). This was done for two sizes, one with a height of 10 mm, and inner diameter of cervical dysplasia of 2 mm, and another with a height of 15 mm and inner diameter of 3 mm. Both models had an outside diameter of 14 mm (Supplementary Figure S1).

2.4 Assembly of 3D tri-culture model of cervical dysplasia

We have previously reported a multilayer model of cervical cancer that used 7% w/v gelatin methacrylate (GelMA) to promote cervical cancer invasion over time (Cadena et al., 2023). Previous viscoelastic experiments showed a closer mimic of the elastic properties of GelMA at 8.7% to the human cervix compared to our previous model (GelMA 7%w/v) (Supplementary Figure S2). GelMA at 8.7% w/v also gives us the possibility to improve the hydrogel formulation for future studies where the inclusion of extracellular matrix components is possible at this GelMA concentration. We prepared the GelMA hydrogels at a final concentration of 8.7% w/v following manufacturer instructions (GelMA, AdvancedBiomatrix, San Diego, CA). We used lithium phenyl-2,4,6-trimethylbenzoylphosphinate (LAP) as a photoinitiator (17 mg/mL, Advanced Biomatrix), as it has been reported to improve cell viability compared to irgacure (Xu et al., 2020; Montazerian et al., 2021). NHDF cells were suspended in an 8.7% w/v GelMA with LAP solution to the desired cell density for each model (1.5 mL of cell: hydrogel solution, 400 µL of NHDF cells were suspended in 1.5 mL of GelMA) (Table 1). For the 10 mm construct, we use approximately 500 µL of the final solution, and for the 15 mm construct, we use 1.5 mL of the solution. The solution was pipetted into the silicone mold and UV-cured using a 405 nm light for 1 min, following the protocol specified by the manufacturer. The hydrogel was then removed from the mold and carefully added to a black-walled 24-µ plate (IBIDI, Fitchburg, WI). Following a similar procedure, SiHa cells were suspended in a GelMA hydrogel (8.7% w/v) at the desired cell density (Table 1). The mixture was then pipetted in the center of the well and UV crosslinked for 30 s using the same light source as before (10 mm construct used about 100 µL, and 15 mm construct 250 µL of cell-hydrogel solution, 400 µL of SiHa cells were suspended in 1.5 mL of GelMA). Lastly, 120 µL (10 mm) or 300 µL (15 mm) NHEK cells suspended in KBM-KGM culture media were added on top to simulate normal epithelium. Constructs were covered in 100 µL of culture media comprised of a 1:1:1 ratio of FBM-FGM-2, KBM-KGM, and EMEM. The media was changed every 24 h, and the plate was incubated at 37°C and 5% CO_2 in a BioSpa live cell analysis system (Agilent Technologies, Santa Clara, CA) for 48 h (Figure 2).

2.5 Tissue preparation and comparison of material properties between human cervix samples and GelMA hydrogel

Supplied by the University of Maryland School of Medicine (UMSOM) post-autopsy, human cervix samples were dissected to remove excess fat and residual tissue (Supplementary Figure S3). For rheometric testing, the cervix was sectioned laterally to obtain samples that fit the 25 mm circular plate of the AR-G2 rheometer (TA Instruments, New Castle, DE). They were stored

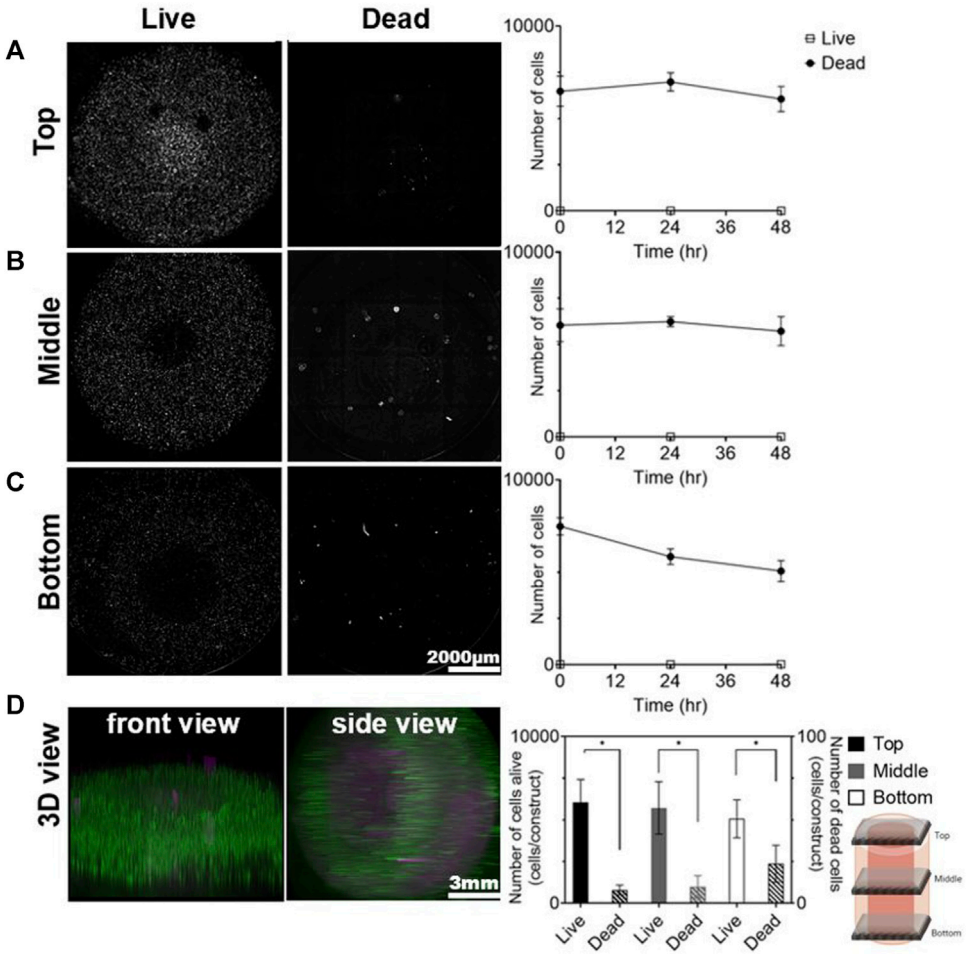

FIGURE 3
Cell viability in the 3D model for cervical dysplasia. Cell viability was measured by quantifying the number of live and dead cells in the **(A)** top, **(B)** middle, and **(C)** bottom layers of the construct at 0, 24, and 48 h of culturing. Cells were stained with a Calcein and Propidium Iodide solution at every time point. Top layer corresponded to the images at the z-stacks = 493.2-274 gm, the middle layer the z-stacks = 109.6–219.2 gm, and the bottom layer were at a z-stacks = -54.8-54.8 gm. Z-projections of the top, middle, and bottom layer were created to quantify the number of cells per construct. One z-stack image was added below the focused point and 8 slices were added above the focus point. Distance between z-stack layers was defined as 54.8 gm. **(D)** A 3D view of the live cells (green-calcein) and dead cells (magenta-propidium iodide) was created using Fiji ImageJ. Images represent 48 h after culturing. A montage of 4 × 4 (rows x columns) with 9 z-stacks were taken to capture the 3D model. The sample thickness was 493.2 gm, and the scale bar was set at 2000 gm. Images were created using Gen5 V3.14 software and Fiji-ImageJ. The data represent the mean ± SEM (n = 4). *$p < 0.05$, analyzed using 2-Way ANOVA with Tukey post-test.

in 10% PBS and incubated at 37°C for 1 h before experiments. Likewise, the GelMA hydrogels were crosslinked with LAP using a 405 nm light source for about 1 min; then, they were also incubated at 37°C for 1 h to accurately depict the mechanical properties of the model. We characterized the mechanical properties of our GelMA hydrogels relative to human cervical tissue using a previously described method (Cadena et al., 2023). Briefly, a dynamic oscillatory shear measurement was used to evaluate the rheological properties of GelMA at 8.7% w/v (Supplementary Figure S3). GelMA was kept in the incubator at 37°C before reading. Rheological characterization was evaluated using an AR-G2 rheometer (TA Instruments, New Castle, DE) equipped with a 20 mm standard steel parallel top plate with a bottom standard Peltier plate. 150 grit (120 μm particle size) sandpaper was attached to the top and bottom to prevent hydrogel from slipping. Frequency sweeps were set from 0.01 to 10 rad/s within the linear viscoelastic (LVE) region. The temperature of 37°C and a strain amplitude of 5% were kept constant during analysis. The hydrogels were allowed to equilibrate to the plate temperature for 15 min before frequency sweeps. The rheological parameters (storage moduli (G′), loss moduli (G") and their ratio (G'/G") were determined from these experiments.

2.6 EC-ethanol formulation and contrast agent for visualization

Mixtures of ethyl cellulose (Sigma Aldrich, St. Louis, MO) and ethanol (200 proof, Koptec, King of Prussia, PA) were prepared at room temperature using a hotplate stirrer (VWR Hotplate/Stirrer). The ethyl cellulose and ethanol mixture (EC-ethanol) were continuously stirred

until the ethyl cellulose was completely dissolved. In all experiments, EC concentrations of 12% (EC to ethanol, % weight: volume) were used, as previous studies indicated significant increases in distribution volume for ≥6% EC (Adhikari et al., 2023). To contrast the CT image between the injectate and surrounding cell construct, iohexol (Omnipaque, GE Healthcare, Chicago IL) was added to EC-ethanol. Iohexol was chosen for its high solubility in ethanol. The EC-ethanol-iohexol solutions were injected into the cell constructs and imaged using micro-CT (Bruker SkyScan 1276, Billerica, MA) as previously described (Adhikari et al., 2023). An 80 mg/mL concentration of iohexol was used for all experiments based on previous study results that maximized the signal-to-background ratio.

2.7 Micro-CT imaging

The Bruker SkyScan 1276 micro-CT was employed for imaging to visualize the EC-ethanol distribution. Samples were positioned upright during imaging, with the needle insertion site oriented at the 12 o'clock position. The images had a pixel size of 81.072 μm, a field of view of 9.31 × 158.75 cm, and were acquired in full rotation (360°) in a 504 × 336 matrix. After image acquisition and reconstruction, post-alignment correction and appropriate ring correction were applied. EC-ethanol distribution volume was then quantified within the hydrogel by loading the images onto 3Dslicer software (Kitware, Clifton Park, NY) and maximum entropy auto-thresholding was applied to the data to segment EC-ethanol-iohexol (Muñoz et al., 2021).

2.8 EC-ethanol injection in 3D triculture hydrogel model

We evaluated the effect of an EC-ethanol injection (EC to ethanol, weight to weight, i.e., 12% EC to 88% pure ethanol) on cell viability and cancer cell area in the 3D *in vitro* model. Using the 15 mm thickness construct, we cocultured the 3 cell lines for 24 h at 37°C and 5% CO_2 in the BioSpa. Then, 50 μL of 12% EC-ethanol was injected into the 3D *in vitro* model at a needle depth of 7 mm using a 22 G syringe. Culture media was changed every 24 h, and images were taken using the same procedure described above. Two-channel and three-channel 180 μm z-stack images were taken every 12 h for 48 h post-injection to evaluate changes in cell viability and cancer cell area over time. Finally, to examine the accurate placement of the ethyl-cellulose drug within the 3D *in vitro* model, we employed bright-field imaging using a Cytation 5 cell imaging multimode reader (Agilent Technologies). Images were stitched and z-projected prior to analysis of the MFI and SiHa cell area. As a control for cell viability, the 3D models were submerged in ethanol (99% v/v) for 48 h.

2.9 Statistical analysis

All quantitative measures are expressed as mean ± standard deviation or as median and interquartile range (if an approximate normal distribution was not achieved after an appropriate transformation). Statistical analysis was performed using a two-way analysis of variance (ANOVA) with Tukey correction for multiple comparisons or one-way ANOVA when appropriate. The same analysis was used to compare human cervices samples to the GelMA hydrogels. All statistical analyses were performed using Prism 8.2.1 software (GraphPad, San Diego, CA); *p*-values less than 0.05 were considered statistically significant. Replicates are specified in each experiment, and asterisks denote significance.

3 Results

3.1 Cell viability and cell coverage in 3D *in vitro* models of cervical dysplasia

We quantified the number of live *versus* dead cells in the 3D model during 48 h of culture and saw that, over time, cell viability was maintained throughout the 3D model (Figure 3). There were no significant differences in cell viability as a function of z-position. However, there was a slight decrease in the number of viable cells in the bottom layer at 24 h (Figure 3C). The 15 mm construct followed similar trends (Supplementary Figure S4).

Our 3D model captured the architecture and geometry of cervical dysplasia, with SiHa cells in the center and healthy fibroblasts and keratinocytes surrounding them. We evaluated changes in cell area over time (Figure 4; Supplementary Figure S4). At time 0 h, cell coverage was highest for SiHa cells on the inside, and the outside had higher coverage of NHDF cells and NHEK cells. After 48 h of culturing, there was an increase in NHEK coverage on the inside, and NHDF cells moved slightly to the inside. However, at 48 h, SiHa cells remained the predominant cell type in the inside region, and NHDF cells were predominant in the outside region (Figure 4B). NHEK and NHDF cells increased their cell coverage over time, while SiHa cells maintained constant cell coverage throughout the construct after 48 h (Figure 4C). The 15 mm model has demonstrated the same trends (Supplementary Figure S4). Overall, these results showed that after 48 h of culturing, the cells were viable throughout the model and mimicked the size and architecture of cervical dysplasia.

3.2 Comparison of material properties between the human cervix and GelMA hydrogels

To ensure that the biophysical properties of our 3D model matched the tissue we were trying to recapitulate, we characterized the mechanical properties of our GelMA hydrogels relative to human cervical tissue (Figure 5). Our 8.7% w/v GelMA had very similar storage moduli compared to human cervices, indicating that it captured the elastic contribution of cervical tissue's resistance to deformation (Figure 5C). The loss moduli of the GelMA were lower, suggesting that we may need to add in additional ECM proteins or explore a wider range of GelMA hydrogel formulations to capture elastic and viscous contributions (Figure 5D). Our results had a higher G'/G″ value for the GelMA hydrogels, suggesting its greater elasticity than the human cervical tissue (Figure 5E).

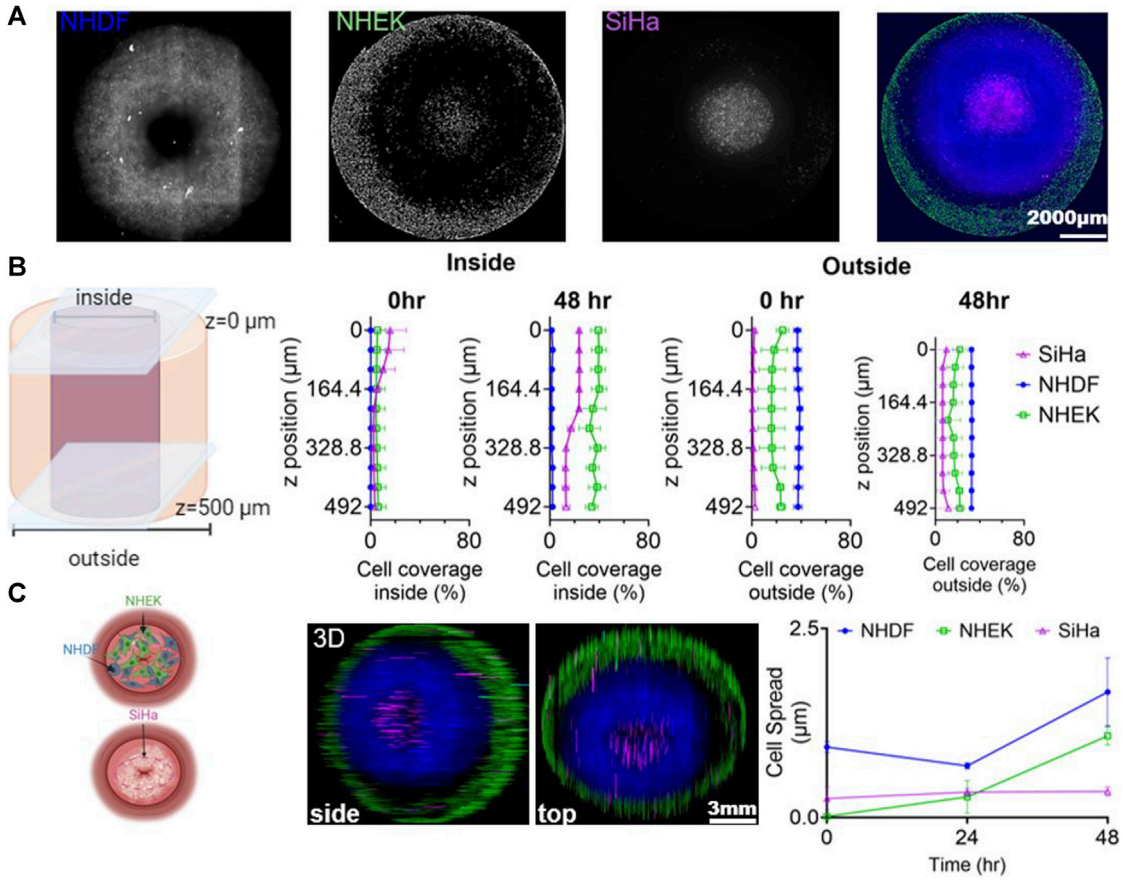

FIGURE 4
Phenotypic Cell Response in Cervical Dysplasia 3D *in vitro* Model. **(A)** Representative z-projection of the images of the 3 cell lines (NHDF (blue), NHEK (green), and SiHa (magenta)) after 48 h of culturing in the 3D model. **(B)** Representation of the outer and inner regions of the 3D model, with cell coverage quantification along the *z*-axis. **(C)** Schematic representation of the 3D model with a view of the cells after 48 h of co-culture. Cell spread was tracked by staining NHDF cells with CellTracker Green CMFDA (C7025), SiHa were tracked using CellTracker Red CMTPX (C34552), and NHEK cells with CellTracker Blue CMF2HC (C 12881). Cell spread was measured as the area covered by each cell line. Data was normalized to the time 0 and showed as a fraction. The 3D hydrogel model was cultured in a 24-well ibidi plate for 48 h, with media changed every 24 h. A montage of 4 x 4 with 54.8 z-stacks was taken to capture the 3D model. Images were created and processed with GenS V3.14 software. 3D z-projections and color of the images were defined and generated using Fiji ImageJ (showing the side and bottom view). Cell area was measured using Fiji ImageJ. Data represent the mean ± SD (n = 3). Schemes created in BioRender.com.

3.3 Micro-CT imaging to visualize the distribution of the injectate

GelMA hydrogels (8.7% w/v) were injected with EC-ethanol-iohexol (using injection parameters optimized in a previous study) (Adhikari et al., 2023). Using Micro-CT imaging, we evaluated if iohexol (Figure 6B) correlated with where the EC-ethanol injectate went, which could be visualized by its white color against the translucent GelMA background (once the GelMA was sectioned in half) (Figure 6A). We demonstrated that there were no statistical differences between the two visualization methods (Figure 6D), which in the future will enable us to track where the gel forms in our intact 3D *in vitro* models without the need for sectioning. Moreover, our results indicated that for injected volumes of 50 uL, virtually the entire injected volume was retained near the site of injection (Figure 6C). This not only facilitates comprehensive visualization but also empowers precise quantitative analysis of the distribution of EC-ethanol in our *in vitro* constructs.

3.4 Effect of ethyl cellulose-ethanol injection on cell viability and cell area in 3D *in vitro* model

In our 3D *in vitro* model, we evaluated the efficacy of the EC-ethanol injection in reducing the cell viability of the SiHa cells and preserving the viability of the surrounding healthy cells (Figure 7). We injected 50 μL of EC-ethanol and evaluated cell viability in the 3D model compared to positive and negative controls. The 3D models cultured in media had viable cells throughout the construct with very few dead cells (Figure 7A). In contrast, the 3D models submerged in ethanol had only dead cells (Figure 7B). Finally, the 3D models injected with the EC-ethanol had higher cell viability outside the EC-injection and higher cell death in the injection area (Figure 7C).

We then evaluated the ability of the EC-ethanol injection to reduce the SiHa cell area, as the goal in patients would be to eliminate the spread of cancer cells to the surrounding healthy tissue (Figure 8). NHDF, NHEK and SiHa cells were stained with cell tracker dies and cultured in the 3D model for 24 h prior to

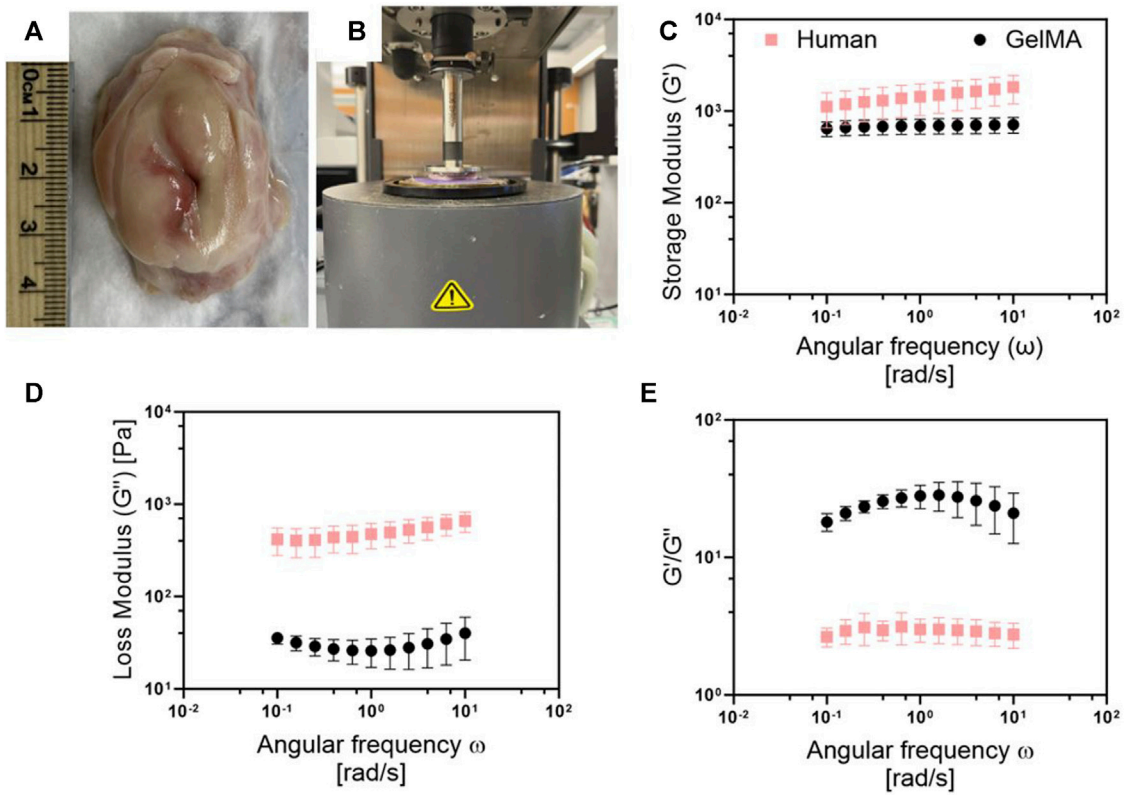

FIGURE 5
Comparison of the viscoelastic properties between the human cervix and Ge1MA. **(A)** Picture of human cervix obtained after autopsy from UMSOM. **(B)** Set up for rheornetric testing with AR-G2 rheometer. Comparison of **(C)** storage and **(D)** loss modulus, and **(E)** G′/G″ ratio of human cervices and Ge1MA hydrogel (8.7% w/v). Frequency sweeps were conducted from 0.1 to 100 rad/sec within the linear viscoelastic (LVE) region at a constant strain amplitude of 5%, and temperature of 37°C. Human cervix samples were stored in 10% PBS and incubated at 37°C for 1 h before experiments. Ge1MA hydrogels were crosslinked with LAP using a 405 nrn UV light source for about 1 min, then hydrogels were incubated at 37°C for 1-h prior measurement. Data represent the mean +SD (n = 5).

injection; as control, we cultured the 3D models in culture media (Figure 8A). After injection there was a significant decrease in cancer cell area in the 3D models treated with the EC-ethanol injection (Figure 8B), and 48 h post-injection the cancer cells were completely eliminated. In contrast, the SiHa cell area increased in the untreated control group. The cell area of fibroblasts and keratinocytes was also evaluated post-EC-ethanol injection. The area where the injection was applied caused a decrease in cell spread in all cell lines (Supplementary Figure S5). Outside the injection, we saw an increase in keratinocytes spreading, and the cell area for fibroblasts did not show a significant difference with the control group. Excitingly, there was no increase in SiHa cells outside of the injection site (Supplementary Figure S5). Taken together, these findings highlight the capacity of our model to provide a more comprehensive understanding of cellular reactions to the EC-ethanol injection and its efficacy in treating disease while preserving the surrounding healthy tissue.

4 Discussion

Current animal models face significant limitations in accurately replicating the intricate microenvironment characteristics of cervical dysplasia observed in humans (Larmour et al., 2015). *In vivo* models vary in human anatomy, physiology, and immune response, leading to disparities in disease modeling (Matchett et al., 2018). Animal models are often used due to the scarcity of human cervical tissue samples, but they fail to accurately represent the human cervical microenvironment. Additionally, animal models are unable to capture the complexity of human immune responses adequately, which is crucial to cervical dysplasia development, and variations in hormonal regulation between species can further impact disease progression (Ntuli et al., 2022). However, technical challenges in recreating the intricate microenvironment of cervical dysplasia in animal models result in oversimplified representations of the disease, further limiting their translational relevance to human patients (Malinowski, 2007). Recognizing this significant knowledge gap, we developed a 3D *in vitro* model to mimic the architectural complexity of cervical dysplasia, featuring a central region with cancer cells surrounded by healthy fibroblasts and keratinocytes. The development of our 3D *in vitro* model adds to the growing field of GelMA-based tissue-engineered models (Bupphathong et al., 2022). Our study represents a significant advancement in the field of cervical dysplasia research by introducing a novel 3D *in vitro* model that mimics the cellular and architectural complexity of cervical dysplasia. Furthermore, our work addresses several limitations of existing animal models, such as species differences and limited access to human samples, by providing a more accessible and reproducible experimental platform. Our innovative model aimed to

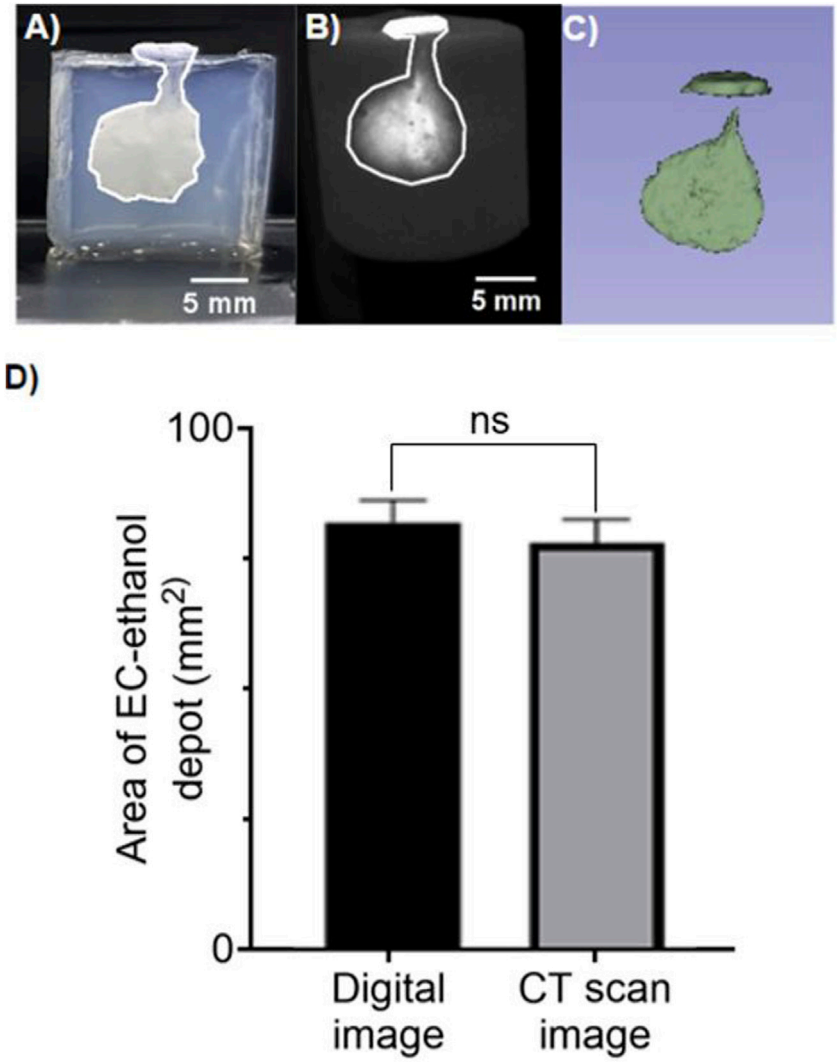

FIGURE 6
CT imaging to visualize distribution volume achieved with EC-Ethanol injection. Representative images of 12% EC- ethanol injections on 15 mm tall 8.7% GelMA hydrogels with Iohexol as a contrast agent. **(A)** Digital image of the EC-Ethanol gel depot with area of 86.93 mm^2. **(B)** Image acquired from CT imaging with area of 83.36 mm^2. **(C)** Coin shaped 3D projection of the depot acquired using 3D slicer. The following parameters were used: 22G - 25 mm-long beveled needles, 7 mm needle insertion depth, manual injection, 12% EC-ethanol, 80 mg/mL Iohexol. Images are shown as a side view. Scale bar = 5 mm. **(D)** Quantification of the cell area calculated from digital image vs. CT scan image. GelMA hydrogels were crosslinked with LAP using a 405 nm UV light source for about 1 min prior imaging. No statically significant differences were observed across the two group. Unpaired t-test. Data represent the mean ± SD (n = 5).

recapitulate the microenvironment of cervical lesions for evaluating the efficacy of ethyl cellulose (EC)-ethanol injection in mitigating cancer cell viability while preserving healthy tissue. Our 3D *in vitro* model is the first coculture system for cervical dysplasia in the literature and is the first to use an *in vitro* model to demonstrate EC-ethanol efficacy.

GelMA was selected as the supportive matrix for human fibroblast cells and cancer cells due to its biocompatibility and wide application in tissue engineering (Kim et al., 2022). We conducted a rheological characterization of the GelMA hydrogel formulation used in our model and compared its mechanical properties with human cervical tissue. It was confirmed that the GelMA hydrogel-based model demonstrated compatibility with human cervical tissue in terms of mechanical properties, and their values range in similar magnitudes to those observed in the literature (Dewall et al., 2010). Our results showed an average G′ of 1,453 Pa and a G″ of 494 Pa in the human cervix. Meanwhile, the GelMA hydrogel had a G′ of 686 Pa and a G″ of 30 Pa. Differences in the mechanical properties between our material and the human cervix are likely due to the ECM-components constituting the cervical tissue (Shi et al., 2022). However, the GelMA hydrogel has enough flexibility in its mechanical properties that allows the incorporation of more ECM components to approximate the human cervix better, a focus of future work (Nagaraj et al., 2022; Cadena et al., 2023).

Our GelMA-hydrogel model had high cell viability and promoted cell growth over 48 h. GelMA has proven to have good transport of nutrients and oxygen that enables cell response over time (Dong et al., 2022; Barros et al., 2023). A recent model showed

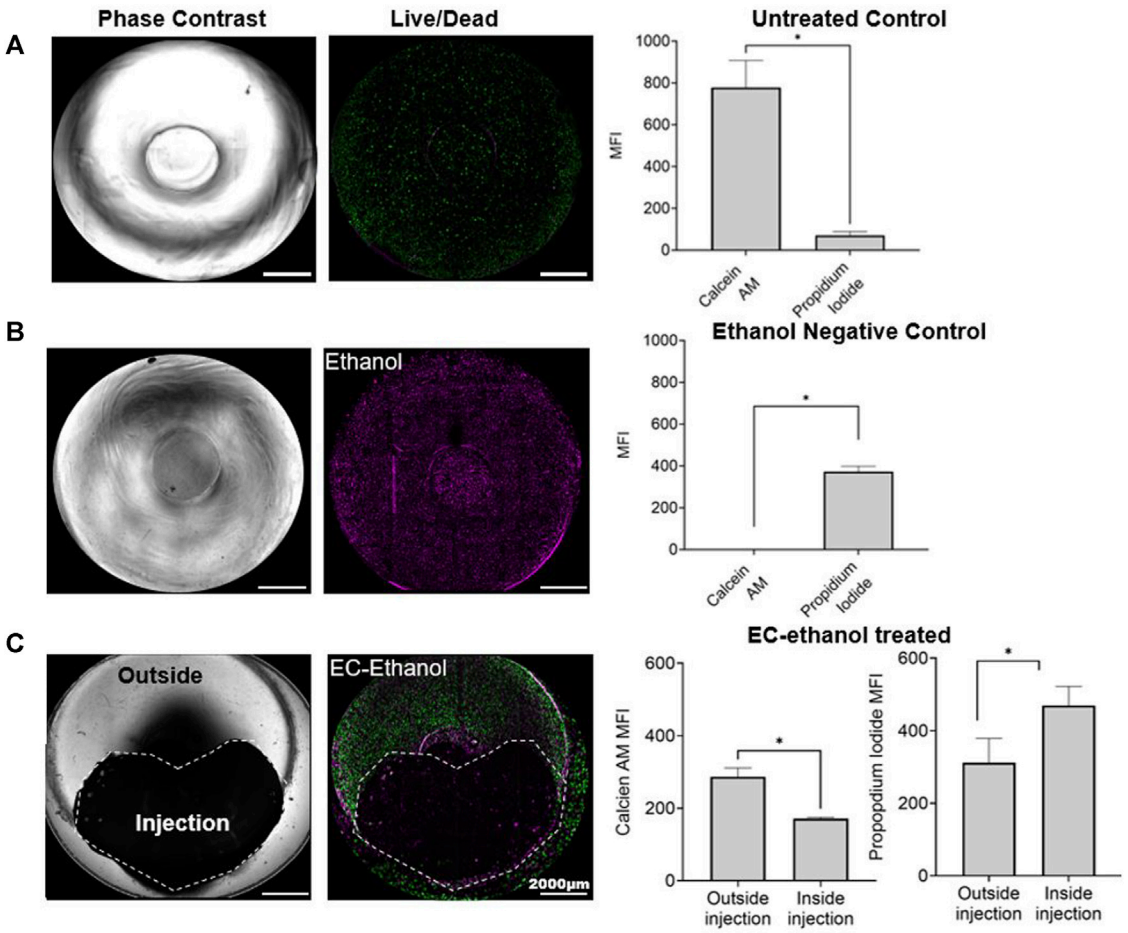

FIGURE 7
Effect of EC-ethanol on cell viability. 3D *in vitro* models **(A)** untreated and treated with **(B)** ethanol (99% v/v), and with **(C)** EC-ethanol injection. Representative images in bright field and with the fluorescent dies representing the live cells in green (Calcein AM) and the dead cells in magenta (propidium iodide). Data represent at 48 h post treatment. As control we culture the 3D *in vitro* model in **(A)** culture media, and **(B)** in ethanol for 48 h. The mean fluorescent intensity (MFI) of live cells (stained with calcein AM) and dead cell (stained with propidium iodide) was quantified using Fiji ImageJ. The scale bar was set at 2000 µm. Images were created and processed with Gen5 V3.14 software. 3D z-projections were generated using Fiji ImageJ. * $p < 0.05$, compared with the mean of each group. Paired t-test. Data represent the mean ± SD (n = 3).

the encapsulation of human pancreatic cells and stromal fibroblasts in GelMA (8% w/v) with the photoinitiator LAP could mimic cell-ECM interactions and is proven to have a good diffusion of nutrients and oxygen, which allowed the cells to proliferate in the GelMA beads (Huang et al., 2023). Using the GelMA hydrogel, we were able to increase the thickness of our first model and still have a higher number of live cells compared to dead cells. Moreover, in this study, we observed that cell viability and function were maintained in both models (10 mm and 15 mm), with the presence of healthy cells mostly on the outside and cancer cells on the inside. Over time, there was a slight spread of the cancer cells to the outside and an increase in cell area for the keratinocytes that were found in all the regions at 48 h.

To demonstrate a potential application of our 3D *in vitro* model, we evaluated the distribution area achieved with our EC-ethanol gel (through micro CT imaging) and the resulting region of cell viability and SiHa cell area post-injection. A critical finding of this work is that cell viability drastically decreased in the injection area while the outer region remained unaffected, suggesting the targeted, localized impact of EC-ethanol. As previously reported, studies suggested that a concentration higher than 6% of EC-ethanol gave a localized injection with minimal leakage and highlighted the potential of EC-ethanol in precisely targeting diseased areas (Morhard et al., 2020). The complement analysis on cell viability and cell area gave a better understanding of cell response to the EC-ethanol treatment in comparison with previous studies that have reported only the effect of the volume distribution of EC-ethanol (Morhard et al., 2020; Mueller et al., 2021). These findings highlight the nuanced and comprehensive understanding that our model offers regarding cellular reactions to EC-ethanol, emphasizing its promise as an ideal model in which to study the relationship between EC-ethanol distribution and cellular response. Moreover, our study demonstrates the efficacy of EC-ethanol in reducing cancer cell viability while preserving healthy tissue, highlighting the potential of this treatment approach for cervical dysplasia. In comparison to previous *in vitro* studies, which lack the 3D microenvironment or the interaction of healthy and disease cells in a complex coculture system (Aasen et al., 2003; Bonartsev et al., 2022), our 3D *in vitro* model better mimicked the cervical microenvironment and uniquely enabled visualization of the EC-ethanol treatment in 3D. We observed a significant decrease in the SiHa cell area following the

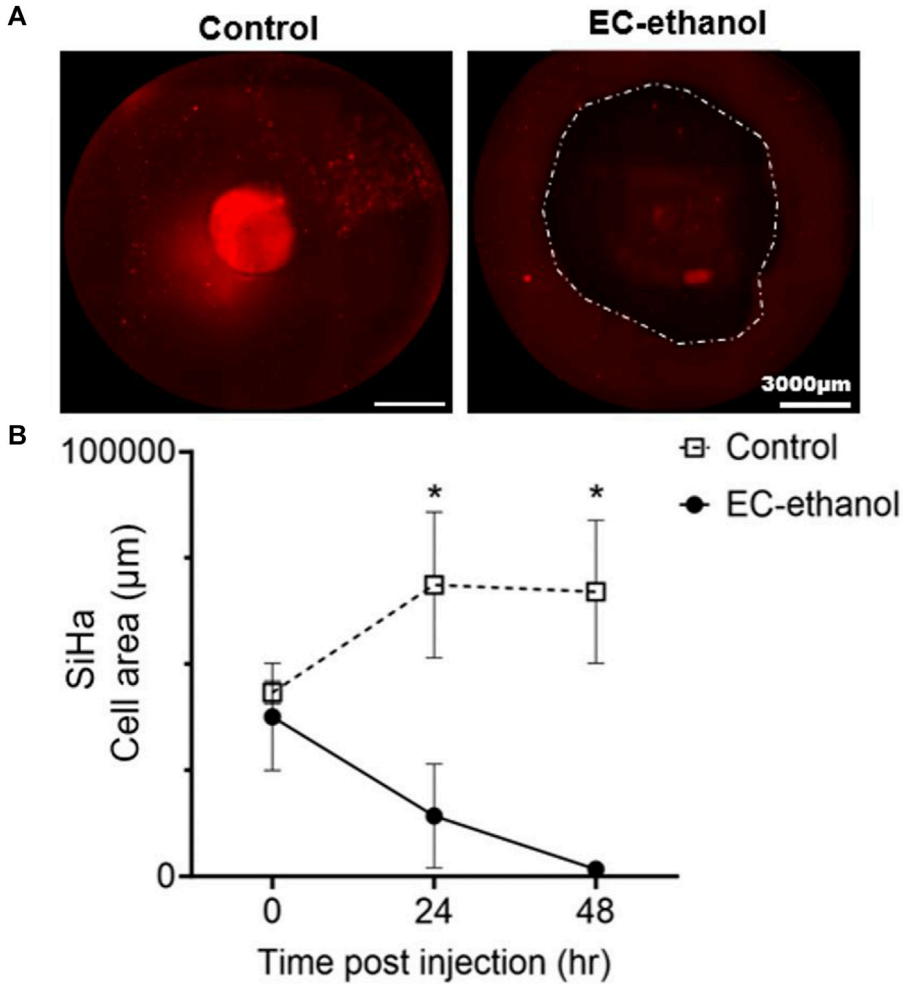

FIGURE 8
Effect of EC-ethanol on SiHa cell area. **(A)** Representative images of SiHa cells (CellTracker Red-labeled) cultured in 3D *in vitro* model at 48 h with and without EC- ethanol injection. A 2D z-projection of full construct was created using Gen5 V3.14 software to quantify the SiHa cell area post- EC ethanol treatment. Dash line shows the area were the EC-ethanol injection was applied after 48 h of cocultured. **(B)** SiHa cell area at all time points pre (time 0) and post injection (24 h and 48 h). Cell area was tracked by staining SiHa cells with CellTracker Red CMTPX (C34552). The scale bar was set at 3000 μm. Images were created and processed with Gen5 V3.14 software. SiHa cell area was quantified using Fiji ImageJ. * $p < 0.05$, compared to the EC-ethanol group. Control group had only culture media. Two-way ANOVA with Tukey post-test. Data represent the mean ± SD (n = 4).

injection of EC-ethanol. However, the surroundings of the injection preserved or maintained healthy cell growth while decreasing the spread of SiHa cells. Due to the paucity of animal models of cervical dysplasia, we had previously evaluated EC-ethanol in a normal swine cervix model, which was not diseased. These *in vitro* results mirror those observed in the swine model in terms of local delivery (Quang et al., 2023). However, here, for the first time, we are able to assess whether or not the diseased lesions were removed in a human-sized model of cervical dysplasia. Our study showed that the 3D model was able to capture the target cancer cell effect while preserving the healthy cells that were outside the site of injection. Overall, our study has the potential to significantly impact the field of cervical dysplasia research and to pave the way for the development of more effective therapeutic strategies.

Our study presents an innovative approach to address the drawbacks of existing animal models for studying cervical dysplasia. However there were several limitations of this study. While our 3D *in vitro* model mimics the architectural complexity of cervical dysplasia, it may still lack some key features of the *in vivo* microenvironment, such as immune cell infiltration, interactions with surrounding tissues and the addition of ECM components involved in disease progression (Sobel et al., 2005). Incorporating additional components, such as immune cells and endothelial cells, into the 3D *in vitro* model can better simulate the complex interactions present in the disease. Additionally, although GelMA hydrogel has shown good biocompatibility and mechanical properties comparable to human cervical tissue, its composition may not fully replicate the ECM components present in cervical tissue, potentially influencing cellular behavior and response to treatment. We have previously reported changes in mechanical properties by combining GelMA with collagen type I and fibronectin. Our hydrogel formulation significantly enhanced cervical cancer invasion over time compared to Matrigel and GelMA alone (Cadena et al., 2023). Adding similar components to the presented 3D model, but in a concentration range for cervical dysplasia, could open the opportunity to better mimic cell adhesion and cell-ECM crosstalk in the 3D *in vitro* model. Moreover,

further studies with the inclusion of ECM components could delve into the molecular mechanisms underpinning these observed effects, further advancing our understanding of how to best deliver EC-ethanol to treat cervical dysplasia. One issue that may be encountered with scaling up the 3D *in vitro* model with more ECM components is the hypoxia effect for cells located in the core in the long-term utilization of the model, which can be addressed by modulating the cell density and incorporating vascularization within the model to enhance oxygen transport and nutrient delivery. Although our study demonstrated the efficacy of EC-ethanol in reducing cancer cell viability in the injected area while preserving healthy tissue, the long-term effects and potential systemic impact of this treatment are yet to be studied. Future studies aim to address these limitations by incorporating additional components of the cervical microenvironment and investigating the broader physiological implications of EC-ethanol treatment.

5 Conclusion

We developed a 3D *in vitro* model of cervical dysplasia that demonstrated the successful elimination of cervical dysplasia following EC-ethanol injection while leaving the surrounding healthy cells intact. These results show the promise of using our 3D *in vitro* model to study localized interventions in cervical dysplasia, and the insights gained from EC-ethanol ablation in the 3D *in vitro* model will inform its future *in vivo* applications. While our initial findings are promising for treating lesions, critical questions remain regarding optimal delivery parameters, particularly as lesions progress from low-grade to high-grade dysplasia to early invasive disease. These parameters are pivotal for the effective delivery of EC-ethanol into the cervix, ensuring comprehensive coverage of precancerous lesions and early invasive disease within deeper tissue layers. Further investigation of these delivery parameters is essential for the successful translation of EC-ethanol and similar therapeutic solutions for treating cervical dysplasia in LMICs.

Data availability statement

The datasets presented in this study can be found in online repositories. The names of the repository/repositories and accession number(s) can be found in the article/Supplementary Material.

Author contributions

IC: Conceptualization, Data curation, Project administration, Resources, Supervision, Visualization, Writing–original draft, Writing–review and editing, Formal Analysis, Investigation, Methodology, Software, Validation. GA: Conceptualization, Data curation, Formal Analysis, Investigation, Methodology, Project administration, Resources, Software, Supervision, Validation, Visualization, Writing–original draft, Writing–review and editing. AA: Formal Analysis, Methodology, Validation, Writing–original draft, Writing–review and editing. MJ: Formal Analysis, Writing–original draft, Writing–review and editing, Data curation. NO: Data curation, Formal Analysis, Writing–original draft, Writing–review and editing. NS: Writing–original draft, Writing–review and editing, Investigation, Software. WR: Writing–original draft, Writing–review and editing, Data curation. JM: Methodology, Project administration, Resources, Supervision, Visualization, Writing–original draft, Writing–review and editing, Conceptualization, Formal Analysis, Funding acquisition. KF: Conceptualization, Funding acquisition, Project administration, Resources, Supervision, Visualization, Writing–original draft, Writing–review and editing, Data curation.

Funding

The author(s) declare that financial support was received for the research, authorship, and/or publication of this article. This work was supported by Oregon State University startup funds (KF), and the University of Maryland startup funds (JM).

Conflict of interest

IC, GA, JM, and KF have filed a provisional patent related to this work. The remaining authors declare that the research was conducted in the absence of any commercial or financial relationships that could be construed as a potential conflict of interest.

Publisher's note

Supplementary material

The Supplementary Material for this article can be found online at: https://www.frontiersin.org/articles/10.3389/fbiom.2024.1365781/full#supplementary-material

References

Aasen, T., Hodgins, M. B., Edward, M., and Graham, S. V. (2003). The relationship between connexins, gap junctions, tissue architecture and tumour invasion, as studied in a novel *in vitro* model of HPV-16-associated cervical cancer progression. *Oncogene* 22, 7969–7980. doi:10.1038/sj.onc.1206709

Abdul-Karim, F. W., Fu, Y. S., Reagan, J. W., and Wentz, W. B. (1982). Morphometric study of intraepithelial neoplasia of the uterine cervix. *Obstet. Gynecol.* 60 (2), 210–214.

Adhikari, G., Sarojasamhita, V. P., Richardson-Powell, V., Farooqui, A., Budzinski, M., Garvey, D. T., et al. (2023). Impact of injection-based delivery parameters on local

distribution volume of EthylCellulose ethanol gel in tissue and tissue mimicking phantoms. *IEEE Trans. Biomed. Eng.*, 1–11. doi:10.1109/tbme.2023.3340613

Belair, D. G., and Abbott, B. D. (2017). Engineering epithelial-stromal interactions in vitro for toxicology assessment. *Toxicology* 382, 93–107. doi:10.1016/j.tox.2017.03.007

Barros, N. R., Gomez, A., Ermis, M., Falcone, N., Haghniaz, R., Young, P., et al. (2023). Gelatin methacryloyl and Laponite bioink for 3D bioprinted organotypic tumor modeling. *Biofabrication* 15 (4), 045005. doi:10.1088/1758-5090/ace0db

Bogorad, M. I., Karlsson, J., Wong, A. D., Gerecht, S., and Searson, P. C. (2015). Review: in vitro microvessel models. *Lab Chip* 15, 4242–4255. doi:10.1039/C5LC00832H

Bonartsev, A. P., Lei, B., Kholina, M.S., Menshikh, K. A., Svyatoslavov, D. S., Samoylova, S. I., et al. (2022). Models of head and neck squamous cell carcinoma using bioengineering approaches. *Crit Rev Oncol Hematol* 175, 103724. doi:10.1016/j.critrevonc.2022.103724

Cadena, I. A., Buchanan, M. R., Harris, C. G., Jenne, M. A., Rochefort, W. E., Nelson, D., et al. (2023). Engineering high throughput screening platforms of cervical cancer. *J. Biomed. Mater. Res. Part A* 111 (6), 747–764. doi:10.1002/jbm.a.37522

Comprehensive Cervical Cancer Control (2014). *Comprehensive cervical cancer control: a guide to essential practice*. 2nd ed. Geneva: World Health Organization. Available at: http://www.ncbi.nlm.nih.gov/books/NBK269619/.

De Gregorio, V., Urciuolo, F., Netti, P. A., and Imparato, G. (2020). *In vitro* organotypic systems to model tumor microenvironment in human papillomavirus (HPV)-Related cancers. *Cancers* 12 (5), 1150. doi:10.3390/cancers12051150

Dewall, R. J., Varghese, T., Kliewer, M. A., Harter, J. M., and Hartenbach, E. M. (2010). Compression-dependent viscoelastic behavior of human cervix tissue. *Ultrason. Imaging* 32 (4), 214–228. doi:10.1177/016173461003200402

Dong, Y., Zhang, M., Han, D., Deng, Z., Cao, X., Tian, J., et al. (2022). A high-performance GelMA-GelMA homogeneous double-network hydrogel assisted by 3D printing. *J. Mater Chem. B* 10 (20), 3906–3915. doi:10.1039/d2tb00330a

Ferlay, J., Soerjomataram, I., Dikshit, R., Eser, S., Mathers, C., Rebelo, M., et al. (2015). Cancer incidence and mortality worldwide: sources, methods and major patterns in GLOBOCAN 2012. *Int. J. Cancer* 136 (5), E359–E386. doi:10.1002/ijc.29210

Gage, J. C., Ferreccio, C., Gonzales, M., Arroyo, R., Huivín, M., and Robles, S. C. (2003). Follow-up care of women with an abnormal cytology in a low-resource setting. *Cancer Detect Prev.* 27 (6), 466–471. doi:10.1016/j.cdp.2003.09.004

Huang, B., Wei, X., Chen, K., Wang, L., and Xu, M. (2023). Bioprinting of hydrogel beads to engineer pancreatic tumor-stroma microtissues for drug screening. *Int. J. Bioprint* 9 (3), 676. doi:10.18063/ijb.v9i3.676

Huchko, M. J., Sneden, J., Leslie, H. H., Abdulrahim, N., Maloba, M., Bukusi, E., et al. (2014). A comparison of two visual inspection methods for cervical cancer screening among HIV-infected women in Kenya. *Bull. World Health Organ* 92 (3), 195–203. doi:10.2471/blt.13.122051

Huchko, M. J., Sneden, J., Zakaras, J. M., Smith-McCune, K., Sawaya, G., Maloba, M., et al. (2015). A randomized trial comparing the diagnostic accuracy of visual inspection with acetic acid to visual inspection with lugol's iodine for cervical cancer screening in HIV-infected women. *PLoS One* 10 (4), e0118568. doi:10.1371/journal.pone.0118568

Human papillomavirus vaccines (2015). Human papillomavirus vaccines: WHO position paper, October 2014-Recommendations. *Vaccine* 33 (36), 4383–4384. doi:10.1016/j.vaccine.2014.12.002

Jeronimo, J., Morales, O., Horna, J., Pariona, J., Manrique, J., Rubiños, J., et al. (2005). Visual inspection with acetic acid for cervical cancer screening outside of low-resource settings. *Rev. Panam. Salud Publica* 17 (1), 1–5. doi:10.1590/s1020-49892005000100001

Kim, Y. H., Dawson, J. I., Oreffo, R. O. C., Tabata, Y., Kumar, D., Aparicio, C., et al. (2022). Gelatin methacryloyl hydrogels for musculoskeletal tissue regeneration. *Bioeng. (Basel)* 9 (7), 332. doi:10.3390/bioengineering9070332

Lam, C. T., Krieger, M. S., Gallagher, J. E., Asma, B., Muasher, L. C., Schmitt, J. W., et al. (2015). Design of a novel low-cost point of care tampon (POCkeT) colposcope for use in resource-limited settings. *PLOS ONE* 10 (9), e0135869. doi:10.1371/journal.pone.0135869

Larmour, L. I., Jobling, T. W., and Gargett, C. E. (2015). A review of current animal models for the study of cervical dysplasia and cervical carcinoma. *Int. J. Gynecol. Cancer* 25 (8), 1345–1352. doi:10.1097/igc.0000000000000525

Lorenzen, E., Follmann, F., Jungersen, G., and Agerholm, J. S. (2015). A review of the human vs. porcine female genital tract and associated immune system in the perspective of using minipigs as a model of human genital Chlamydia infection. *Veterinary Res.* 46 (1), 116. doi:10.1186/s13567-015-0241-9

Malinowski, D. P. (2007). Multiple biomarkers in molecular oncology. I. Molecular diagnostics applications in cervical cancer detection. *Expert Rev Mol Diagn* 7, 117–131. doi:10.1586/14737159.7.2.117

Matchett, W. E., Anguiano-Zarate, S. S., and Barry, M. A. (2018). Comparison of systemic and mucosal immunization with replicating Single cycle Adenoviruses. *Glob Vaccines Immunol* 3, doi:10.15761/GVI.1000128

Montazerian, H., Baidya, A., Haghniaz, R., Davoodi, E., Ahadian, S., Annabi, N., et al. (2021). Stretchable and bioadhesive gelatin methacryloyl-based hydrogels enabled by *in situ* dopamine polymerization. *ACS Appl. Mater Interfaces* 13 (34), 40290–40301. doi:10.1021/acsami.1c10048

Morhard, R., Mueller, J. L., Tang, Q., Nief, C., Chelales, E., Lam, C. T., et al. (2020). Understanding factors governing distribution volume of ethyl cellulose-ethanol to optimize ablative therapy in the liver. *IEEE Trans. Biomed. Eng.* 67 (8), 2337–2348. doi:10.1109/tbme.2019.2960049

Morhard, R., Nief, C., Barrero Castedo, C., Hu, F., Madonna, M., Mueller, J. L., et al. (2017). Development of enhanced ethanol ablation as an alternative to surgery in treatment of superficial solid tumors. *Sci. Rep.* 7 (1), 8750. doi:10.1038/s41598-017-09371-2

Mueller, J. L., Asma, E., Lam, C. T., Krieger, M. S., Gallagher, J. E., Erkanli, A., et al. (2017). International image concordance study to compare a point-of-care tampon colposcope with a standard-of-care colposcope. *J. Low. Genit. Tract. Dis.* 21 (2), 112–119. doi:10.1097/lgt.0000000000000306

Mueller, J. L., Lam, C. T., Dahl, D., Asiedu, M. N., Krieger, M. S., Bellido-Fuentes, Y., et al. (2018). Portable Pocket colposcopy performs comparably to standard-of-care clinical colposcopy using acetic acid and Lugol's iodine as contrast mediators: an investigational study in Peru. *BJOG* 125 (10), 1321–1329. doi:10.1111/1471-0528.15326

Mueller, J. L., Morhard, R., DeSoto, M., Chelales, E., Yang, J., Nief, C., et al. (2021). Optimizing ethyl cellulose-ethanol delivery towards enabling ablation of cervical dysplasia. *Sci. Rep.* 11 (1), 16869. doi:10.1038/s41598-021-96223-9

Muñoz, N. M., Williams, M., Dixon, K., Dupuis, C., McWatters, A., Avritscher, R., et al. (2021). Influence of injection technique, drug formulation and tumor microenvironment on intratumoral immunotherapy delivery and efficacy. *J. Immunother. Cancer* 9 (2), e001800. doi:10.1136/jitc-2020-001800

Nagaraj, A., Etxeberria, A. E., Naffa, R., Zidan, G., and Seyfoddin, A. (2022). 3D-Printed hybrid collagen/GelMA hydrogels for tissue engineering applications. *Biol. (Basel).* 11 (11), 1561. doi:10.3390/biology11111561

Nichol, J. W., Koshy, S., Bae, H., Hwang, C. M., Yamanlar, S., Khademhosseini, A., et al. (2010). Cell-laden microengineered gelatin methacrylate hydrogels. *Biomaterials* 31, 5536–5544. doi:10.1016/j.biomaterials.2010.03.064

Nief, C., Morhard, R., Chelales, E., Alvarez, D. A., Bs, I. B., Lam, C. T., et al. (2021). Polymer-assisted intratumoral delivery of ethanol: preclinical investigation of safety and efficacy in a murine breast cancer model. *PLOS ONE* 16 (1), e0234535. doi:10.1371/journal.pone.0234535

Ntuli, L., Mtshali, A., Mzobe, G., Liebenberg, L. J., and Ngcapu, S. (2022). Role of Immunity and Vaginal Microbiome in Clearance and Persistence of Human Papillomavirus Infection. *Front. Cell. Infect. Microbiol.* 12. doi:10.3389/fcimb.2022.927131

Path (2013). Cervical cancer screening and treatment in low-resource settings: practical experience from PATH. Available at: https://www.path.org/resources/cervical-cancer-screening-and-treatment-in-low-resource-settings-practical-experience-from-path/.

Quang, T. T., Yang, J., Kaluzienski, M. L., Parrish, A., Farooqui, A., Katz, D., et al. (2023). *In Vivo* Evaluation of Safety and Efficacy of Ethyl Cellulose-Ethanol Tissue Ablation in a Swine Cervix Model. *Bioengineering (Basel)* 10, 1246. doi:10.3390/bioengineering10111246

Seki, T., Nonaka, T., Kubota, Y., Mizuno, T., and Sameshima, Y. (1989). Ultrasonically guided percutaneous ethanol injection therapy for hepatocellular carcinoma. *Am. J. Gastroenterol.* 84 (11), 1400–1407.

Shi, L., Hu, L., Lee, N., Fang, S., and Myers, K. (2022). Three-dimensional anisotropic hyperelastic constitutive model describing the mechanical response of human and mouse cervix. *Acta Biomater.* 150, 277–294. doi:10.1016/j.actbio.2022.07.062

Sobel, G., Szabó, I., Páska, C., Kiss, A., Kovalszky, I., Kádár, A., et al. (2005). Changes of cell adhesion and extracellular matrix (ECM) components in cervical intraepithelial neoplasia. *Pathol Oncol Res* 11, 26–31. doi:10.1007/BF03032402

Tsu, V. D., Jeronimo, J., and Anderson, B. O. (2013). Why the time is right to tackle breast and cervical cancer in low-resource settings. *Bull. World Health Organ* 91 (9), 683–690. doi:10.2471/blt.12.116020

Van Den Bulcke, A. I., Bogdanov, B., De Rooze, N., Schacht, E. H., Cornelissen, M., and Berghmans, H. (2000). Structural and rheological properties of methacrylamide modified gelatin hydrogels. *Biomacromolecules* 1, 31–38. doi:10.1021/bm990017d

Xu, H., Casillas, J., Krishnamoorthy, S., and Xu, C. (2020). Effects of Irgacure 2959 and lithium phenyl-2,4,6-trimethylbenzoylphosphinate on cell viability, physical properties, and microstructure in 3D bioprinting of vascular-like constructs. *Biomed. Mater* 15 (5), 055021. doi:10.1088/1748-605x/ab954e

Yue, K., Trujillo-de Santiago, G., Alvarez, M. M., Tamayol, A., Annabi, N., and Khademhosseini, A. (2015). Synthesis, properties, and biomedical applications of gelatin methacryloyl (GelMA) hydrogels. *Biomaterials* 73, 254–271. doi:10.1016/j.biomaterials.2015.08.045

frontiers | Frontiers in Biomaterials Science

TYPE Original Research
PUBLISHED 22 May 2024
DOI 10.3389/fbiom.2024.1399448

OPEN ACCESS

EDITED BY
Silviya Petrova Zustiak,
Saint Louis University, United States

REVIEWED BY
Koyal Garg,
Saint Louis University, United States
Era Jai,
Syracuse University, United States

*CORRESPONDENCE
April M. Kloxin,
akloxin@udel.edu
Catherine A. Fromen,
cfromen@udel.edu

†These authors have contributed equally to this work and share last authorship

RECEIVED 11 March 2024
ACCEPTED 19 April 2024
PUBLISHED 22 May 2024

CITATION
Graf J, Bomb K, Trautmann-Rodriguez M, Jarai BM, Gill N, Kloxin AM and Fromen CA (2024), Macrophage variance: investigating how macrophage origin influences responses to soluble and physical cues with immortalized vs. primary cells in 2D and 3D culture. *Front. Biomater. Sci.* 3:1399448. doi: 10.3389/fbiom.2024.1399448

Macrophage variance: investigating how macrophage origin influences responses to soluble and physical cues with immortalized vs. primary cells in 2D and 3D culture

Jodi Graf[1], Kartik Bomb[1], Michael Trautmann-Rodriguez[1], Bader M. Jarai[1], Nicole Gill[1], April M. Kloxin[1,2*†] and Catherine A. Fromen[1*†]

[1]Department of Chemical and Biomolecular Engineering, University of Delaware, Newark, DE, United States, [2]Department of Materials Science and Engineering, University of Delaware, Newark, DE, United States

Macrophages are phagocytic innate immune cells capable of phenotypical switching in response to the local microenvironment. Studies often use either primary macrophages or immortalized cell lines for hypothesis testing, therapeutic assessment, and biomaterial evaluation without carefully considering the potential effects of cell source and tissue of origin, which strongly influence macrophage response. Surprisingly, limited information is available about how, under similar stimuli, immortalized cell lines and primary cells respond in both phenotypical and functional changes. To address this need, in this work, we cultured immortalized macrophage cell lines derived from different origins (*i.e.,* blood, lung, peritoneal) to understand and compare macrophage phenotypical responses, including polarization and plasticity, morphological changes, and phagocytic functionalities, as well as compared primary macrophages extracted from peritoneal and bone marrow to their immortalized cell line counterparts. We found significant differences in baseline expression of different markers (e.g., CD86, MHCII, CD206, and EGR2) amongst different cell lines, which further influence both polarization and repolarization of the cells, in addition to their phagocytic functionality. Additionally, we observed that, while RAW 264.7 cells behave similarly to the primary bone marrow-derived macrophages, there are noticeable phenotypical and functional differences in cell line (IC-21) and primary peritoneal macrophages, highlighting tissue-specific differences in macrophage response amongst cell lines and primary cells. Moving to three-dimensional (3D) culture in well-defined biomaterials, blood-derived primary and cell line macrophages were encapsulated within hydrogel-based synthetic extracellular matrices and their polarization profiles and cell morphologies were compared. Macrophages exhibited less pronounced polarization during 3D culture in these compliant, soft materials compared to two-dimensional (2D) culture on rigid, tissue culture

plastic plates. Overall, our findings highlight origin-specific differences in macrophage response, and therefore, careful considerations must be made to identify the appropriate cell source for the application of interest.

KEYWORDS

macrophage, hydrogel, biomaterials, innate immune cell, polarization, 3D culture

1 Introduction

Macrophages are chief immune effector cells that are the first responders upon pathogen entry and are responsible for neutralizing the invading pathogen by engulfing it through phagocytosis (Park et al., 2022). Additionally, macrophages can activate differently based on their microenvironment through a process called polarization, adopting transient phenotypes classically characterized as pro-inflammatory activation (M1) or anti-inflammatory (M2) activation (Sreejit et al., 2020). Furthermore, macrophages exhibit plasticity, allowing them to repolarize in response to alternate stimuli, which is an interesting approach to addressing immune dysfunction and imbalance in diseased states. Indeed, recent studies have highlighted that macrophage polarization goes beyond the linear M1-M2 paradigm and is often influenced by tissue origin, disease states, and polarization stimuli (Sreejit et al., 2020; Park et al., 2022; Strizova et al., 2023). For example, Lavin *et al.* performed a comprehensive analysis on tissue-derived macrophages from different sources, including brain, lung, liver, spleen, peritoneal, colon, ileal, and monocytes, and showed marked differences in the base expression level in the markers for macrophages from different tissue origin (Lavin et al., 2014). Yet, many *in vitro* studies, including in the design and application of biomaterials, do not consider macrophage origin in cell type selection.

An increasing number of studies have utilized immune engineering approaches (*e.g.*, protein-based therapies, engineered particles, and polymer scaffolds) to drive phenotypical and functional responses of macrophages (Mao et al., 2022; Zarubova et al., 2022; Zheng et al., 2022). Biomaterial properties, such as surface topography, stiffness, and dynamic mechanical forces, in addition to bioactive cues, have been shown to have a profound effect on modulating macrophage phenotype. Recent advances in particle-based drug delivery have shown that material composition, size, shape, charge, and targeting ligands impact macrophage phagocytosis and polarization (Sylvestre et al., 2020; Mao et al., 2022). Researchers continue to evaluate biomaterial design rules in macrophages from varied sources, including both immortalized cell lines (Wu et al., 2020; Tu et al., 2022) and primary cells (Chen et al., 2020; Jarai et al., 2021). Macrophages are powerful models to understand the innate immune system, but further consideration into cell choice and origin are needed to contextualize experimental data.

Some of the commonly used murine cell lines for *in vitro* investigation include RAW 264.7 (monocyte-derived) (Kim et al., 2019), MH-S (alveolar macrophages) (Ruge et al., 2012), and IC-21 (peritoneal macrophages) (Ullah et al., 2019) cells. Common *ex vivo* murine primary cells include bone-marrow derived macrophages (BMMs) (Palomba et al., 2021), which are hematopoietic precursors differentiated *ex vivo* into macrophages, or terminally differentiated macrophages from different tissues, such as lung (alveolar macrophages, AM) (Bobba et al., 2021) and peritoneal cavity (peritoneal macrophages, PM) (Tran et al., 2016). Despite known differences between macrophages from different tissues, macrophages used for *in vitro* applications often have a discrepancy between the application of interest and the macrophage origin, which limits the understanding of macrophage response in a disease- and tissue-specific context. There remains limited understanding of how cells from these different locations will polarize and repolarize in the presence of different stimuli, or what inherent differences exist in their phagocytic capacity. Comparing immortalized cell lines and primary cells from the same source and in the same culture conditions is also important for informing the desired cell type for application of interest.

While 2D culture on tissue-culture plastic (TCP) remains the standard of practice, the field is shifting toward 3D culture models for both fundamental and applied studies of cell function and fate inspired by native cellular microenvironments (Liu and Segura, 2020). For well-defined 3D cultures, synthetic hydrogels have shown relevance as 3D cell culture platforms for testing hypotheses about cell-microenvironment interactions, including with the extracellular matrix (ECM), and for providing well-defined, tunable, and robust properties. For example, previous work has shown that the stiffness of hydrogel-based synthetic ECMs, presence of specific adhesive ligands, and degradability significantly affect macrophage responses in both 2D and 3D culture (Cha et al., 2017; Kim et al., 2019; Bomb et al., 2022; Bomb et al., 2023). Researchers have also shown that biomaterial properties, such as porosity, topography, geometry, hydrophobicity, applied forces, and viscoelasticity, also impact cellular response (Rayahin et al., 2015; Zhou et al., 2021). The microenvironment, as well as the cell choice, will dictate polarization and functionality of macrophages, and both should be carefully considered for *in vitro* immune modeling. Amongst synthetic systems, poly (ethylene glycol) (PEG)-based hydrogels linked and modified with peptides are widely used for their tunability and biocompatibility. PEG is bioinert; therefore, bioactive ligands can be integrated to allow cell adhesion and present biochemical cues relevant to the tissue of interest, and concentration and crosslinking of the polymer and peptide building blocks can be used to control stiffness (Lou and Mooney, 2022; Wiley et al., 2022; Brady et al., 2023). Recently, bioprinting has emerged with the potential to replace manual preparation of hydrogels for creating 3D cultures with consistency and high-throughput and facilitating studies of cellular interactions within physiologically relevant microenvironments (Sun et al., 2021; Du et al., 2022). As these biomaterials-based tools enable ECM mimicry, their coupled role

in understanding macrophage response as a function of cell origin and tissue-specific response remains an important area of research, from understanding design rules to elucidating underlying biological mechanisms.

In this work, we examined the phenotypical and functional profile of different macrophage cell lines (*i.e.,* RAW 264.7, MH-S, and IC-21) and primary cells (*i.e.,* BMMs and PMs) for insights into their similarities and differences. In traditional 2D culture, we first investigated the marker expression of untreated or naïve macrophage cell lines and primary cells, then evaluated the polarization profile upon M1 and M2 stimulation, phagocytic profile, and repolarization with alternative stimuli in TCP culture conditions. To characterize the phenotype of the cell, we focused on traditional surface and intracellular markers (CD86, MHCII, CD206, and EGR2), quantified by flow cytometry to provide a cell-by-cell analysis. Our observations highlighted the differences in macrophage response obtained from different sources (Figure 1). We then further explored the behavior of primary versus immortalized macrophages encapsulated in bioprinted PEG-peptide synthetic ECMs, specifically focusing on cells that were bone-marrow derived (BMMs and RAW 264.7) as prototypical macrophages often used in general studies of immune cell responses. We employed the RASTRUM™ bioprinter for creating well-defined 3D cultures of immune cells within in a multiwell plate format, where the RASTRUM™ is capable of synthesizing synthetic ECMs with combinations of adhesive peptides (*e.g.*, RGD, GFOGER, and DYIGSR), whole proteins, and enzyme-degradable linkers inspired by the native ECM (Mahmodi et al., 2021; Du et al., 2022). Overall, our results can inform the macrophage choice for 3D cell culture or more broadly to assess the immune response to emerging biomaterial technologies.

2 Materials and methods

2.1 Cell culture

MH-S, IC-21, and RAW 264.7 murine cell lines were purchased from American Type Culture Collection (ATCC, Manassas, Virginia, United States). All the cells were cultured between passages 2–10 in complete media, RPMI 1640 Medium (ThermoFisher Scientific) supplemented with 10% heat-inactivated fetal bovine serum (certified Gibco heat inactivated, USA origin) and 1% penicillin/streptomycin. Primary BMMs and PMs were isolated from healthy BALB/c and C57BL/6 mice (6–12 weeks old, Jackson Laboratories, Bar Harbor, Maine, United States), respectively, following the approved Institutional Animal Care and Use Committee (IACUC) protocol at the University of Delaware. Bone marrow was extracted from femurs and tibias, and cells were cultured in BMM differentiation media (complete media supplemented with 30% L929 conditioned media) until confluent in a T-75 flask before using for the experiments. PMs were isolated using a peritoneal lavage. Cells were isolated and cultured per standard techniques (Gonçalves and Mosser, 2015). The cells were centrifuged (500 g for 5 min) and resuspended in complete media and allowed to attach overnight before using for the experiments.

2.2 Macrophage polarization

Cells were seeded, allowed to adhere for 24 h, then stimulated with M1 or M2 stimuli for 24 h. Immortalized cell lines (seeded at 10e5 cells/well in a 6-well plate) were polarized with M1 and M2 stimuli for 24 h to compare the polarization profile of the cell line. The polarization profile of primary cells was determined by treating the cells (seeded at 50e5 cells/well in a 6-well plate) with M1 or M2 stimuli for 24 h. Cell lines were seeded at a lower density to account for their higher proliferation rates, assuming the cells lines would double approximately twice between seeding and flow cytometry analysis while primary cells would exhibit limited proliferation and potentially lower viability within the same timeframe.

Lipopolysaccharides (LPS) (20 ng/mL, *Escherichia coli* O111: B4 [Millipore Sigma, Rockville, MD, United States]) and interferon (IFN)-γ (20 ng/mL, PeproTech®) were used as M1 stimuli. Interleukin (IL)4/IL13 (10 ng/mL each, PeproTech®) was used as M2 stimuli. IL4/IL13 (10 ng/mL each) supplemented with 50% tumor-conditioned media (TCM) from A549 cells (IL4/IL13/TCM) was used as a tumor-conditioned stimuli. The cytokine concentration was decided based on values found in previous literature, where concentrations between 10 ng/mL to 100 ng/mL are typical for polarization stimuli (Andreakos et al., 2004; Edwards et al., 2006; Genin et al., 2015; Bomb et al., 2022).

To compare the plasticity of different cell lines, pre-polarized macrophages (M1 or M2) receiving 24 h of dose 1 were repolarized with either the same stimuli or a different stimulus for an additional 24 h with dose 2 (Supplementary Figure S1). The polarization profile was quantified using flow cytometry.

2.3 Plasticity index quantification

The plasticity index (PI) was defined to assess the relative polarization of macrophages to alternative stimuli compared to the polarization with the same stimuli. PI was quantified separately for each marker using median fluorescence intensity (MFI) using Eqs 1, 2 (for M1 markers) and Eqs 3, 4 (for M2 markers), where subscripts indicate either dose 1 (initial polarization) or dose 2 (plastic change). A (+) sign convention was adopted for when the repolarization would be expected to align with upregulation of the marker type (*i.e.*, + for M1 markers of CD86 and MHCII when M2→M1; (−) for M1 markers when M1→M1). Absolute values >1 indicate that cells were plastic and experienced repolarization upon secondary stimuli based on the respective marker.

M1 Markers (CD86, MHCII)

$$PI_{M1}\,(\mathrm{M1} \rightarrow \mathrm{M2}) = (-)\frac{IFN\gamma_1 \rightarrow IFN\gamma_2}{IFN\gamma_1 \rightarrow IL4/13_2} \tag{1}$$

$$PI_{M1}\,(\mathrm{M2} \rightarrow \mathrm{M1}) = (+)\frac{IL4/13_1 \rightarrow IFN\gamma_2}{IL4/13_1 \rightarrow IL4/13_2} \tag{2}$$

M2 Markers (CD206, EGR2)

$$PI_{M2}\,(\mathrm{M1} \rightarrow \mathrm{M2}) = (+)\frac{IFN\gamma_1 \rightarrow IL4/13_2}{IFN\gamma_1 \rightarrow IFN\gamma_2} \tag{3}$$

$$PI_{M2}\,(\mathrm{M2} \rightarrow \mathrm{M1}) = (-)\frac{IL4/13_1 \rightarrow IL4/13_2}{IL4/13_1 \rightarrow IFN\gamma_2} \tag{4}$$

2.4 Phagocytosis assay

The phagocytic ability of cell lines was determined by quantifying the uptake of fluorescent (FITC) phosphatidylcholine (PC) coated lipid microparticles (3 µm diameter, Echelon Biosciences, Salt Lake City, Utah, United States). Uniform PC particle suspension (achieved by sonication and vortexing) was seeded (~2 particles per cell) on polarized cell lines (20 ng/mL IFNγ or 10 ng/mL each IL4/13). The particle uptake was determined after 6 h by quantifying particle positive cell population [% PC positive (+ve)] and MFI of the internalized particles using flow cytometry on FITC channel.

2.5 Flow cytometry

Cells on TCP were detached using Accutase (Innovative Cell Technologies, Inc.) for 30 min and washed with phosphate buffered saline (PBS), followed by staining with Zombie Yellow (10 min). Cells were blocked with anti-CD16/32 (Fc block) and immunostained with anti-CD86 and anti-MHCII (30 min). Cells were then fixed with 4% paraformaldehyde (PFA) in PBS (15 min), permeabilized using Intracellular Staining Permeabilization Wash Buffer (BioLegend), and immunostained with anti-CD206 and EGR2 (30 min). Further information on antibodies can be found in Supplementary Table S1. BMMs and PMs were gated on CD11b and F4/80 double positive. For internalization studies, cells were washed twice with FACS buffer (2% FBS in PBS) to remove unbound particles and quenched with 0.4% Trypan Blue dye to quantify internalized particles. Samples were analyzed using ACEA NovoCyte Flow Cytometer. The gates were set using untreated samples and MFI was plotted for each marker (Supplementary Figures S2–S4).

2.6 2D immunostaining

Cell lines (seeded at 10e4 cells/well) and primary cells (seeded at 50e4 cells/well) were washed with PBS and fixed with 4% PFA (15 min). Note, higher cell seeding density was selected for terminally differentiated primary cells given their lack of proliferation over time. Cells were permeabilized by washing with 0.2% Triton-X (5 min) and stained with 2:250 Phalloidin-Rhodamine (ActinRed™ 555 ReadyProbes™ Reagent, Invitrogen™) for 20 min. Cells were washed with PBS and incubated with 70 nM 4',6-diamidino-2-phenylindole (DAPI) (Invitrogen™) for 10 min to stain nuclei. Cells were imaged on BioTek Cytation 5 Multimode Imager. Cell area and circularity were analyzed using Fiji imaging package for the ImageJ2 1.53q software. For morphological analysis, the area selection tool was used to trace the macrophage area and determine the cell spread manually. Circularity for each macrophage was then quantified using the built-in circularity analysis tool.

2.7 3D cell encapsulation within hydrogel-based synthetic ECM

Bioinks and activators (Cat. no. Px02.29PH, 1.1 kPa with RGD, GFOGER, YIGSR, and HA) were generously provided by Inventia Life Science (Sydney, Australia). The 3D cultures were printed using the RASTRUM™ bioprinter (Inventia Life Science) following protocols previously described for breast cancer cell lines (Engel et al., 2022). Briefly, the printing protocol was created via RASTRUM™ Cloud (Inventia Life Science). Cells were seeded in the F177 activator at a density of 20e6 cells/mL (BMMs) and 5e6 cells/mL (RAW 264.7) and printed within Large Plug model in a 96-well plate (Corning—#CLS3904). The Large Plug model (0.5 mm in height) fills the whole surface of a well in a standard 96 well plate (surface area ~0.32 cm^2) as shown in previous literature (Gomila Pelegri et al., 2023). Seeding densities were varied to account for differences in proliferation between the cell types, as shown in Supplementary Figure S6. A lower seeding density of RAW 264.7 cells allowed for proliferation over the experiment time course with the aim of having the number of RAW 264.7 cells be similar to the number of BMMs after 7 days; the initial cell densities also provided a mix of cell-cell and cell-matrix interactions with single cells/small clusters of encapsulated cells throughout the 3D culture upon printing. RAW 264.7 cells were maintained in Dulbecco's Modified Eagle's Medium (DMEM) complete media (10% heat-inactivated fetal bovine serum and 1% penicillin/streptomycin) and BMMs were maintained in BMM culture media (DMEM with 10% heat-inactivated fetal bovine serum and 1% penicillin/streptomycin supplemented with 30% L929 conditioned media).

2.8 Assessment of cell viability

The viability of macrophages in 3D culture was assessed by a LIVE/DEAD Viability/Cytotoxicity Kit (ThermoFisher Scientific). The LIVE/DEAD kit contained calcein-AM to indicate viable cells (live cells fluoresce green; excitation [ex.] 494 nm, emission [em.] 517 nm) and ethidium homodimer-1 to label dead cells (dead cells fluoresce red; ex. 528 nm, em. 617 nm). Hydrogels were washed 3x with PBS + 3 min PBS incubation, then incubated (37°C, 5% CO_2) for 10 min in a solution of calcein-AM (2 µM) and ethidium homodimer-1 (4 µM). After incubation, hydrogels were washed 3x with PBS + 3 min PBS incubation. Hydrogels were imaged with a confocal microscope (LSM 800, Zeiss; ×10 objective and frame size of 1,024 × 1,024, 180 µm z-stack, 8.38 µm/stack, three images per sample). Cell viability was quantified with Imaris 9.9.1 imaging software (Oxford Instruments) using Find Surfaces for AF488 (green) channel and Rhoda (red) channel functions. The percentage of viable cells was calculated by the number of green cells/total number of cells × 100%.

2.9 3D immunostaining

For 3D Immunostaining, cells were washed with PBS and fixed with 4% PFA (15 min). Cells were permeabilized by washing with 0.2% Triton-X (5 min) and stained with Phalloidin-Rhodamine (2:50, 20 min). Cells were washed with PBS and incubated with Hoechst 33342 solution (ThermoFisher Scientific) (1:200) to stain nuclei. Hydrogels were imaged with a confocal microscope (LSM 800, Zeiss; ×20 objective and frame size of 1,024 × 1,024, 200 µm z-stack, 2 µm/slice, three images per sample). Cell area and circularity were analyzed using Fiji imaging package for the

ImageJ2 1.53q software. For morphological analysis, the area selection tool was used to trace the macrophage area and determine the cell spread manually. Circularity for each macrophage was then quantified using the built-in circularity analysis tool.

2.10 Hydrogel cell retrieval

All centrifugation steps and washes were complete at 500 g for 5 min. Cells were retrieved from hydrogel matrix to complete downstream flow cytometry analysis. Here, 75 µL of cell retrieval solution (F235, Inventia Life Science) was added to each well for 45 min to enzymatically degrade the hydrogel matrix followed by addition of 100 µL of PBS. To remove contents from the well, 3x PBS washes were performed, passed through a 70 µm cell strainer, and centrifuged and washed 2x with 2% FBS in PBS buffer. Cells were used for flow cytometry analysis as described in Section 2.5.

2.11 Statistical analysis

GraphPad Prism 9 was used to perform statistical analyses. All quantitative data are represented as mean ± standard error of the mean. Tukey's multiple-comparison test was used to generate *p*-values in ANOVA multiple comparisons unless stated otherwise. Three or more biological replicates were used for statistical analysis.

3 Results and discussion

3.1 Phenotypical and morphological differences between untreated cell types

We first investigated the baseline expression of M1 and M2 markers and morphology for both untreated cell lines and primary cells to understand basal profiles. RAW 264.7 (BALB/c origin, monocyte-derived), IC-21 (C57BL/6 origin, peritoneum), and MH-S (BALB/c origin, lungs) cells were selected as immortalized cell lines. BMMs (BALB/c and C57BL/6 origin) and PMs (C57BL/6 origin) were selected as primary cells. Cells were seeded for 24 h before analyzing M1 (CD86 and MHCII) and M2 (CD206 and EGR2) markers using flow cytometry. M1 and M2 markers were selected based on our previous work (Jarai and Fromen, 2022), where we showed the specific marker expression strongly correlated with polarization stimuli.

Statistically significant differences were observed for all the markers between different cell lines (Figure 2A). RAW 264.7 cells showed the lowest marker expression for both M1 and M2 markers compared to MH-S and IC-21 cells. We hypothesize that the low marker expression for RAW 264.7 cells is due to the monocyte-derived origin of the cell line, while both MH-S and IC-21 are sourced from tissue-resident macrophage cell lines, where the baseline expression differs depending on the tissue type. This is also reported in previous literature where BMMs showed differences in marker expression compared to tissue-resident macrophage counterparts both in the lung and the peritoneal cavity (Misharin et al., 2017; Zhao et al., 2017). IC-21 cells showed the highest basal M2 marker expression of both CD206 and EGR2. This basal phenotypical skewing is somewhat counterintuitive to the genetic background of the strain used to isolate the cells; RAW 264.7 and MH-S cells are derived from BALB/c mice, which is characterized as a more Th2 strain, whereas IC-21 cells are derived from C57BL/6 mice, which is characterized as a more Th1 strain (Santos et al., 2006; Jones et al., 2013). However, we speculate these basal M1 and M2 dispositions are attributed to the extent of macrophage differentiation. This is also highlighted in previous studies, which showed a higher M2 marker expression on cells correlated with macrophage differentiation marker expression (F4/80) irrespective of the genetic background of the mice (Chamberlain et al., 2009; Chamberlain et al., 2015). Furthermore, MH-S cells had the lowest surface area and a statistically higher circular morphology compared to both IC-21 to RAW 264.7 cells. This may be due to the increased surface tension observed for AMs resulting in a more circular morphology. Also, F-actin staining of MH-S cells showed that actin structure was diffuse in the cytoplasm, whereas for both IC-21 and RAW 264.7 cells, increased formation of cytoplastic protrusions was observed.

Next, we looked at the marker expression and morphology for untreated *ex vivo* primary cells and again observed statistically significant differences between PMs and BMMs of two strains (Figure 2B). Like the cell lines, PMs showed statistically higher MHCII expression than both BMMs (C57BL/6 and BALB/c); however, contrary to cell lines, PMs showed statistically lower CD206 expression compared to BMMs. BMMs from C57BL/6 origin (Th1 skewed) showed higher CD206 and EGR2 expression compared to those from BALB/c origin (Th2 skewed), which again is counterintuitive. However, we hypothesize the hyper-physiological conditions of TCP may contribute to this basal expression and, as shown in our later evaluations, basal expression levels do not directly correlate to polarization potential. Unlike the cell lines, PMs and BMMs (C57BL/6 and BALB/c) showed similar elongated cell morphology. C57BL/6 BMMs had lowest mean cell area (218.7 μm^2) compared to BALB/c BMMs (357 μm^2) and PMs (362 μm^2). These findings highlight the differences in marker expressions and cell morphology between the cell lines and the primary cells from similar tissue origin.

3.2 Phenotypical and morphological comparison of polarized cell lines

Next, we studied the response of M1 and M2 stimuli on macrophage cell lines. Cells were polarized for 24 h with M1 (LPS or IFNγ) or M2 (IL4/13 or IL4/3/13/TCM) stimuli for 24 h before analyzing the phenotypical profile using flow cytometry and normalizing MFI to the untreated (UT) condition of each cell type, where upregulation of a particular marker is indicated by a normalized MFI greater than 1. For M1 markers (CD86 and MHCII, Figures 3A, B, respectively), IFNγ promoted a robust marker expression across all the cell lines; however, LPS only resulted in increased M1 marker expression for RAW 264.7 cells. MHCII, an antigen presentation marker, was highly upregulated in M1-stimulated RAW 264.7 cells, followed by MH-S and IC-21 cells

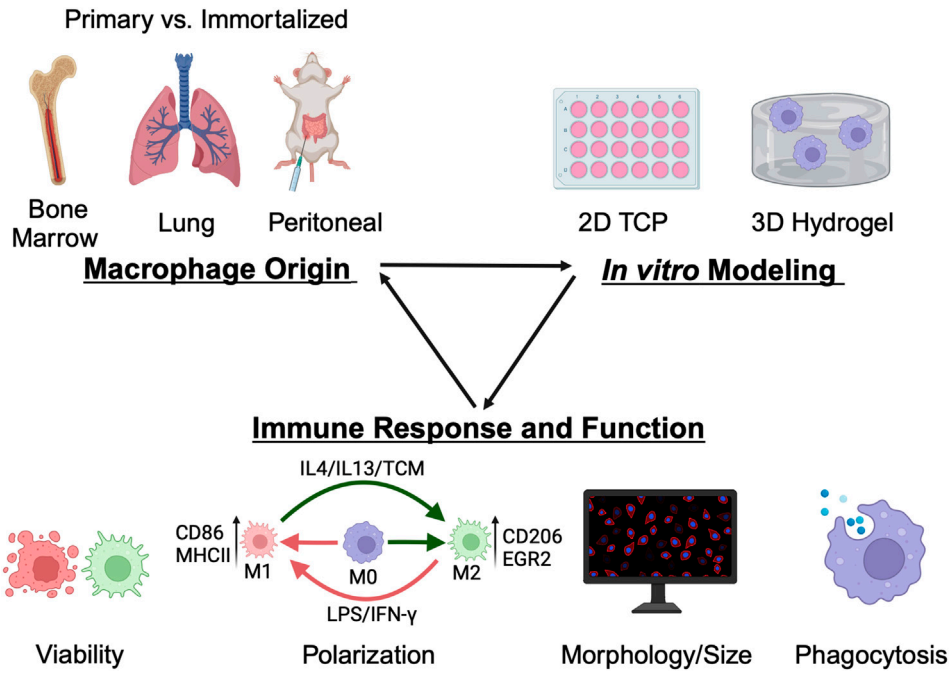

FIGURE 1
Overview of methodology. Common macrophage sources, both immortalized and primary, from various tissue origins (lung, peritoneal, and bone-marrow) were analyzed for functional and phenotypic differences in both traditional tissue-culture plastic and in 3D hydrogel culture to inform cell choice for *in vitro* applications in biomaterial evaluation, hypothesis testing, and therapeutic screening. Figure created using BioRender.com.

(Figure 3B). RAW 264.7 cells are of monocyte-derived origin that has been shown to closely resemble primary BMMs (Berghaus et al., 2010). Furthermore, Zajd *et al.* reported that compared to PMs, primary BMMs (C57BL/6) are skewed more toward a M1 phenotype when stimulated, which may explain both increased MHCII and CD86 marker expression in RAW 264.7 cells (Zajd et al., 2020). Reduced M1 marker expression upon M1 stimulation in IC-21 cells may be attributed to the origin of tissue-resident macrophages. This was also reported by Stevens *et al.*, who showed that PMs show a lower M1 response to mycobacterial infection compared to AMs (Stevens et al., 2021). Interestingly, for IC-21 cells, M2 stimuli downregulated the expression for M1 markers (statistically significant for CD86), whereas, for other cell lines, no such difference in the expression levels was observed.

For M2 markers, we observed interesting trends. CD206 expression was upregulated by both M2 stimuli in IC-21 and RAW 264.7 cells, while no changes were observed in MH-S cells (Figure 3C). Surprisingly, for EGR2, both M2 stimuli failed to upregulate EGR2 expression (Figure 3D). These data indicate that different cell lines upregulate M2 marker expressions to different levels. A higher dose of M2 stimuli or a repeated dose of M2 stimuli might be required to effectively polarize cells and generate persistent M2 marker expression. Furthermore, M1 stimuli of LPS and IFNγ upregulated the marker expression of both CD206 and EGR2. While LPS and IFNγ are thought to be only M1 stimuli, macrophages exist on a spectrum and therefore can express both inflammatory and anti-inflammatory markers at the same time (Mosser and Edwards, 2008; Smith et al., 2016). Further, macrophages generally progress from inflammatory to anti-inflammatory over time (Risser et al., 2023). Previous works have shown that LPS led to increased expressed of M2-like markers and cytokines, (such as IL-10, Arg1, CD206) (Ci et al., 2010; Zhang et al., 2019; Zhen et al., 2023). Further, immortalized cells lines have chromosomal abnormalities or mutations that allow their propagation, which may also affect polarization markers; therefore, the choice to use a cell line should be carefully considered.

For M1 stimuli, compared to IFNγ stimulation, LPS-stimulated cells showed reduced M1 marker expression across the cell lines. IFNγ stimulation is modulated by JAK-STAT pathway, which promotes the upregulation of pro-inflammatory genes leading to immediate response to IFNγ (Sikorski et al., 2012). In addition to pro-inflammatory genes, interferon regulatory factors are also secreted, which helps sustain IFNγ induced response. On the other hand, LPS stimulation is modulated by Toll Like Receptor 4 (TLR4) signaling to promote upregulation of pro-inflammatory genes and induce an M1 response. However, due to a lack of sustained pro-inflammatory response, LPS stimulation might generate a weaker M1 stimulation compared to IFNγ at equivalent mass dosages. Furthermore, IFNγ stimulation also regulates the transcription of interferon-stimulated gene, which contributes to the upregulation of MHC molecules (Ivashkiv, 2018). Our results follow this trend where MHCII expression is upregulated more by IFNγ compared to LPS across all the cell lines.

For M2 stimuli, IL4 and IL13 were used together for M2 stimulation because both IL4 and IL13 have been shown to involve phosphorylation of STAT6, which promotes STAT6 translocation to the nucleus to regulate the transcription of M2 genes and promote M2 polarization (Gordon and Martinez, 2010). Further, adding tumor-conditioned stimuli with IL4 and IL13 yielded a similar phenotypical profile as IL4/13 stimulation.

10.3389/fbiom.2024.1399448

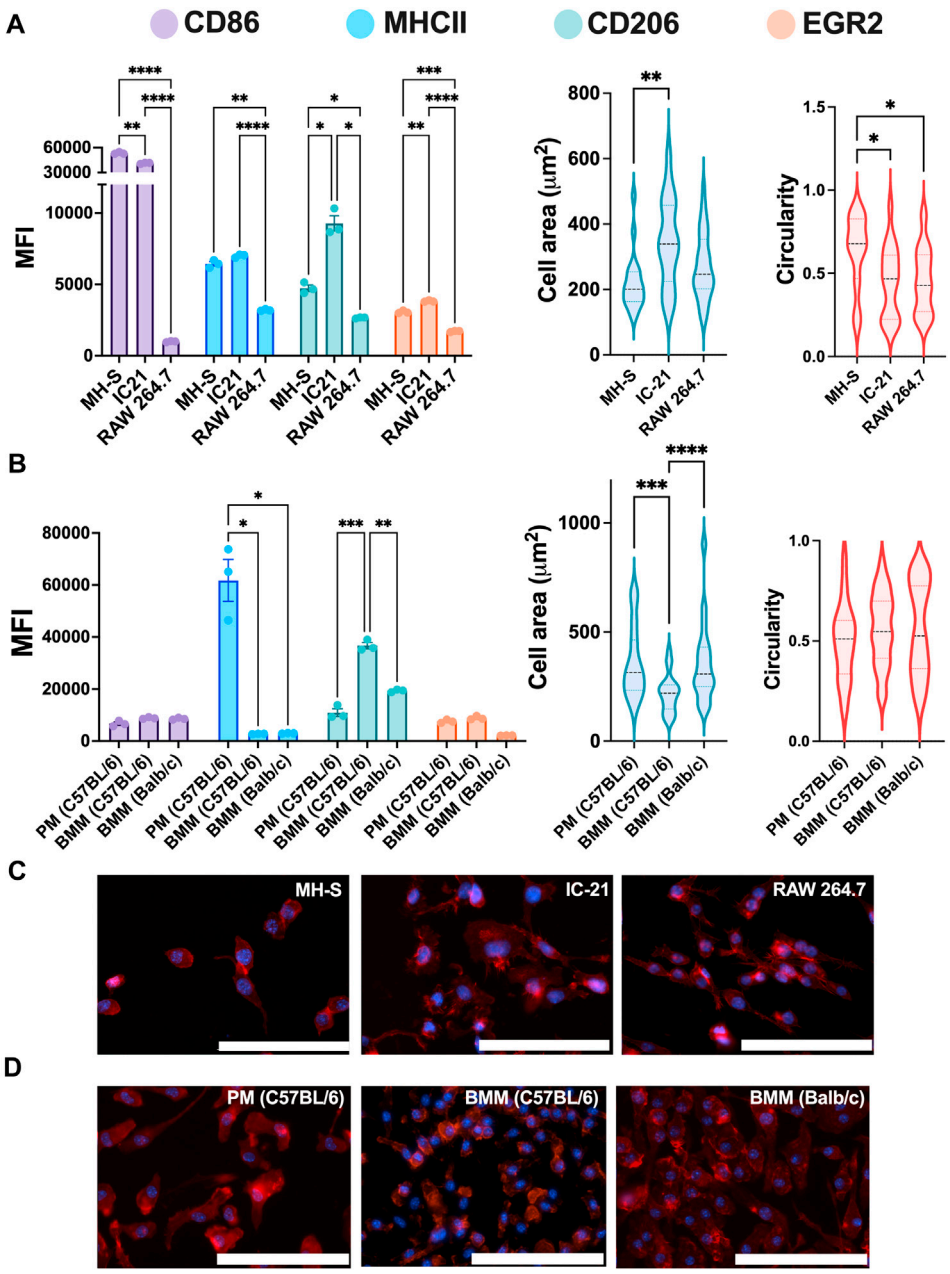

FIGURE 2
Phenotypical characterization of macrophages from different origins. The Phenotypical characterization and morphology of **(A)** untreated macrophage cell lines (n = 3) and **(B)** untreated primary macrophages (n = 3). CD86 and MHCII were used to characterize M1 phenotype, while CD206 and EGR2 were used for M2 phenotype assessment. Cells were immunostained **(C–D)** for nuclei (blue) and F-actin (red), and cell morphology was quantified using cell spread and circularity characterization. Statistics were performed using Tukey's post-hoc test with one-way ANOVA for comparing marker expression for cell lines and primary cells and cell area and circularity analysis for cell lines, *$p < 0.05$, **$p < 0.01$, ***$p < 0.001$, ****$p < 0.0001$. Scale bar: 100 μm.

This may be due to the heterogeneous source of tumor-conditioned stimuli, which in our study was obtained from A549 cells (human-derived lung cancer cells) for use with murine macrophages. Previous studies have successfully shown differences in the phenotypical profile of macrophages using tumor-conditioned stimuli from homogenous sources for both mice and human models (Benner et al., 2019; Little et al., 2019). Based on these observations, we selected IFNγ and IL4/13 for further evaluation.

Overall, our results indicate that the RAW 264.7 cell line is the most responsive to both M1 and M2 stimuli compared to both MH-S and IC-21 cells. This robust response, as well as quick proliferation, may be a reason why these cells are extensively used within *in vitro* characterizations in the literature.

Next, we assessed the effect of these stimuli on the cell morphology of different cell lines by quantifying cell area and cell circularity (Figure 4A). In general, MH-S cells exhibited a trend of lower cell spread and higher circular morphology

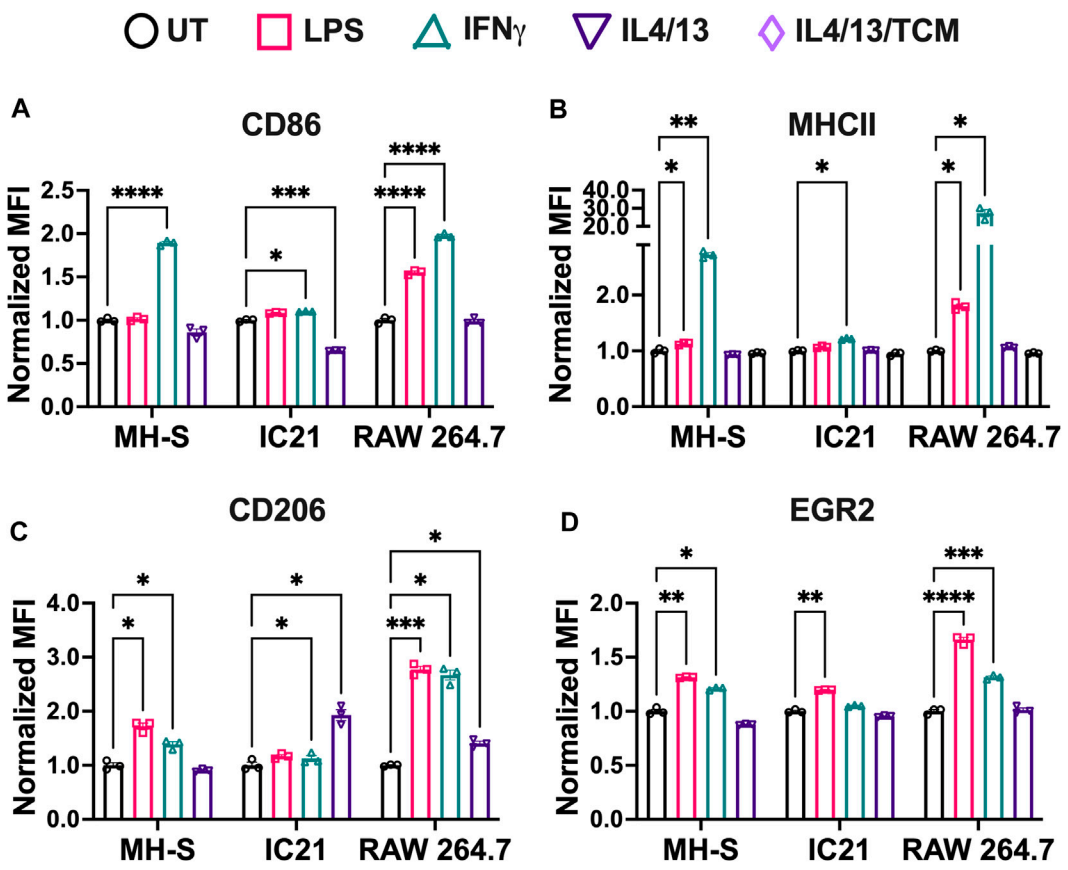

FIGURE 3
Phenotypical responses of macrophages from different origins stimulated with soluble factors. The phenotypical profile of macrophage cell lines was quantified by characterizing both M1 and M2 markers upon stimulation with different M1 and M2 stimuli using flow cytometry. **(A)** CD86 and **(B)** MHCII were used as M1 markers. **(C)** CD206 and **(D)** EGR2 were used as M2 markers. Statistics were performed using Tukey's post-hoc test with one-way ANOVA. *$p < 0.05$, **$p < 0.01$, ***$p < 0.001$, ****$p < 0.0001$.

compared to both IC-21 and RAW 264.7 cells (Figures 4B, C). This difference could arise from the cell origins, where AMs reside at the air-liquid interface in the lung and face increased surface tension resulting in a more circular morphology with compact actin fiber assembly. The area of both MH-S and IC-21 cells was independent of M1 and M2 stimuli, while LPS significantly increased the area of RAW 264.7 cells, highlighting differences in stimuli-dependent morphology changes amongst different cell lines (Figure 4B). Next, we quantified the circularity of the cells to determine cell elongation upon stimuli treatment (Figure 4C), where McWhorter *et. al* have reported a higher circularity upon M1 stimuli treatment and lower circularity or increased cell elongation upon M2 stimuli treatment (McWhorter et al., 2013). We observed that cell morphology, like cell spreading, exhibited trends of dependence on tissue of origin. For example, MH-S cells showed a more circular morphology independent of the stimuli, while IC-21 cells showed a higher circularity with M1 stimuli and a more elongated morphology upon M2 stimuli treatment, as previously reported in the literature. For IC-21 cells, morphological changes correlated well with phenotypical changes, where M1 marker expression (CD86) was increased with M1 stimulation and decreased with M2 stimulation (Figure 3A). Interestingly, for RAW 264.7 cells, IL4/13 treatment significantly increased cell circularity.

Overall, we report cell line-specific differences in morphology in response to different stimuli. Except for RAW 264.7 cells, we did not observe statistically significant changes in morphology upon stimuli treatment. We hypothesize this may be due to the stiff TCP substrate used in the experiments. The stiffness of many body tissues is in the kilopascal (kPa) range, while the stiffness of these culture dishes is in the gigapascal range, which may negate the effect of soluble stimuli on cell morphology. We, along with others, have shown an increased morphological response to stimuli treatment when cultured on a more physiologically relevant substrate (Sridharan et al., 2019; Bomb et al., 2022).

3.3 PC phagocytosis by macrophage cell lines

Phagocytosis is a critical macrophage function responsible for the uptake and removal of foreign pathogens to maintain homeostasis and is often impaired in diseased conditions (Allard et al., 2018). We investigated the effect of polarization stimuli on phagocytosis in different cell lines by using fluorescent lipid

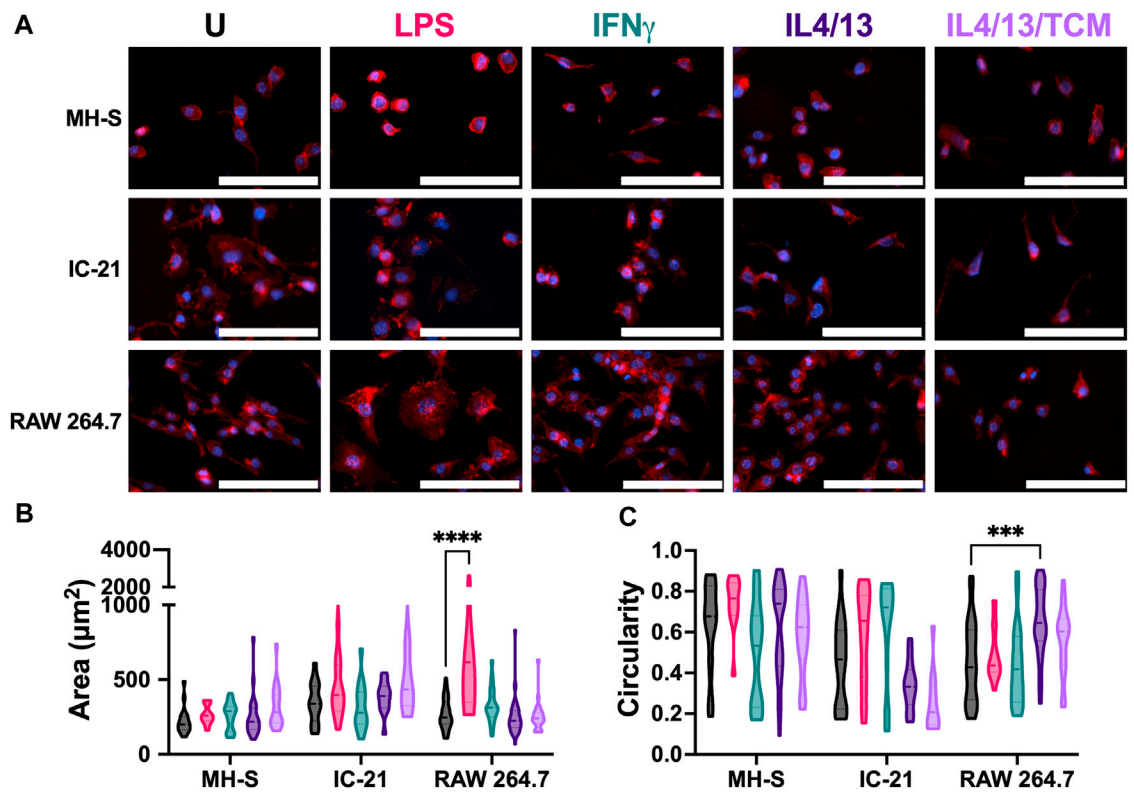

FIGURE 4
Morphological responses of macrophages from different origins stimulated with soluble factors. The effect of polarization stimuli on cell morphology of different cell lines was determined. **(A)** Representative image of cells with nuclei (blue) and F-actin (red) qualitatively show morphological differences between different cell lines across all the treatment groups. **(B)** Cell area and **(C)** circularity were quantified for all the cell lines across different conditions. Statistics were performed using Tukey's post-hoc test with one-way ANOVA. ***$p < 0.001$, ****$p < 0.0001$. Scale bar: 100 μm.

microparticles coated with PC as phagocytic mimics and allowed the cells to internalize the particles for 6 h. Uptake of the PC microparticles was confirmed in all the cell lines with the presence of a second peak (Figure 5A, gray), which is quantified in Figure 5B. For the untreated condition, RAW 264.7 cells showed the highest particle uptake, followed by IC-21 cells and MH-S cells. This trend was observed for both the M1 and M2 polarization conditions as well. Wang *et al.* reported similar observation in primary cells, where BMMs showed increased uptake compared to PMs, highlighting phagocytic similarities between primary cells and immortalized cell lines (Wang et al., 2013). Quantitative analysis of % PC + ve cells further confirmed the uptake profile (Figure 5B). For all the experimental conditions, MH-S cells (~30% UT, ~34% IFNγ, ~34% IL4/13) showed the lowest uptake, followed by IC-21 (~37% UT, ~36% IFNγ, ~41% IL4/13) and RAW 264.7 cells (~45% UT, ~45% IFNγ, ~45% IL4/13). Furthermore, stimuli-related effects on phagocytosis were cell-line dependent. While RAW 264.7 cells did not show changes in phagocytosis on polarization, phagocytosis by both MH-S and IC-21 cells was sensitive to stimuli treatment in different ways. For MH-S cells, the polarization with both M1 and M2 stimuli increased the uptake compared to untreated cells; however, for IC-21 cells, only M2 stimuli increased the uptake, again highlighting the impact of tissue origin differences.

We also evaluated uptake via the normalized MFI (Figure 5C), where a higher normalized MFI value indicates a higher number of average internalized particles. For MH-S cells, we observed a significantly higher normalized MFI with IFNγ stimulation, while the normalized MFI was significantly reduced with IL4/13 stimulation compared to the untreated condition. A similar trend was observed for RAW 264.7 cells but was non-significant. This suggests that, for different cell lines, the polarization of macrophages not only impacts how many cells uptake particles but also influences how active individual cells are in their ability to internalize multiple particles.

Overall, we highlight that different cell lines have different propensities to internalize particles, which are further influenced by the polarization stimuli. Both the proportion of phagocytic cells and normalized MFI yield differential insights and are important considerations in investigating the phagocytic capacity of the macrophages.

3.4 Repolarization of macrophage cell lines

We next investigated the relative repolarization capacity of different cell lines. Pre-polarized cells were treated with either IFNγ or IL4/13 (dose 2), and the phenotype of the repolarized macrophages after 24 h with dose 2 was quantified using flow

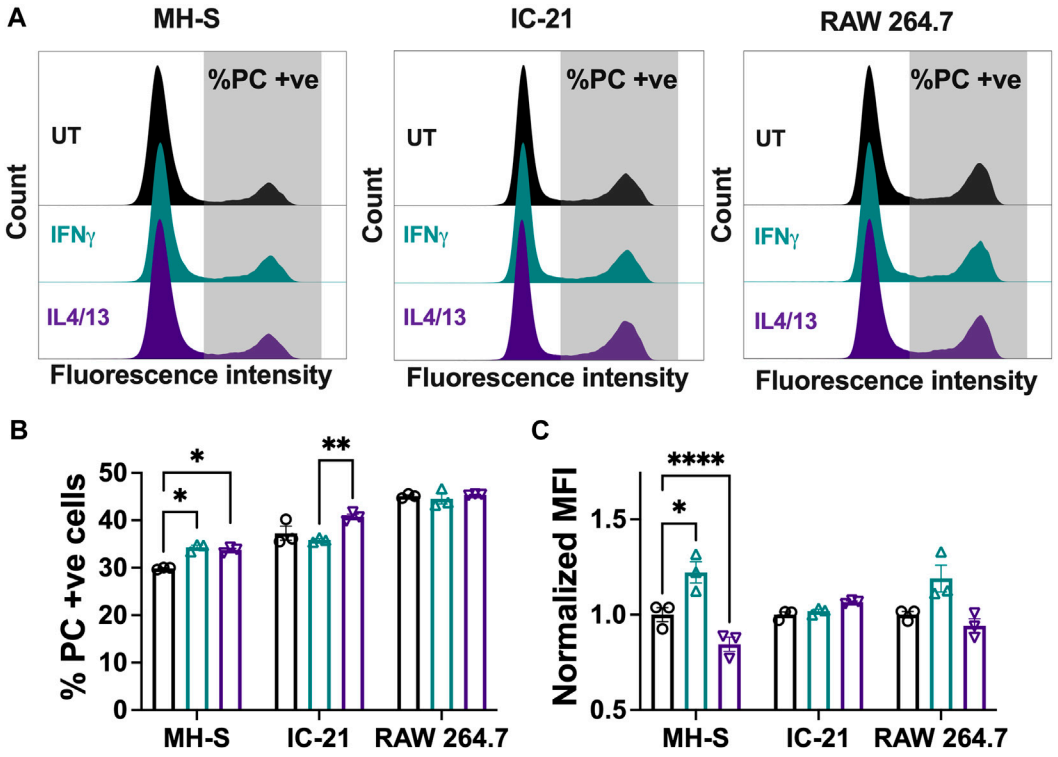

FIGURE 5
Phagocytic responses of macrophages from different origins stimulated with soluble factors. The effect of polarization stimuli on phagocytosis of phosphatidylcholine (PC) coated fluorescent microparticles by different cell lines was determined. **(A)** Representative histograms of population of cells that internalized PC microparticles. **(B)** Quantification of population of cells (%) that internalized PC microparticles and **(C)** normalized median fluorescence intensity (MFI) of the internalized particles. Statistics were performed using Tukey's post-hoc test with one-way ANOVA. *$p < 0.05$, ***$p < 0.001$, ****$p < 0.0001$.

cytometry. Repolarization of macrophages was determined by quantifying the PI for each marker, which normalizes the change in expression of final phenotype to the initial phenotype (Figure 6). A negative PI value indicates: 1) a decrease in M1 marker expression for (M1 to M2) repolarized macrophages compared to M1 macrophages and 2) a decrease in M2 marker expression for (M2 to M1) repolarized macrophages compared to M2 macrophages. In contrast, a positive PI value indicates: 1) an increase in the M1 marker expression for the (M2 to M1) repolarized macrophages compared to the M2 macrophages and 2) an increase in the M2 marker expression for (M1 to M2) repolarized macrophages compared to M1 macrophages. We compared PI for (M1 to M2) polarization (black bars) with (M2 to M1) polarization (pink bars). If the magnitude of the PI for (M1 to M2) polarization is higher than (M2 to M1) polarization, then it is easier to polarize cells to M2 phenotype, and *vice versa*. Similar values of the PI highlight that the cells can be repolarized to either stimulus effectively.

For example, for RAW 264.7 cells, PI for MHCII (M1 marker) was ~ (−) 12.07 for (M1 to M2) repolarized macrophages and ~ (+) 2.74 for (M2 to M1) repolarized macrophages; similarly, for IC-21 cells, PI for EGR2 (M2 marker) was ~ (+)17.04 for M1 to M2 repolarized macrophages and ~ (−)4.09 for M2 to M1 repolarized macrophages, highlighting changes in the individual marker expression upon repolarization (Figure 6). Overall, for MH-S cells, (M1 to M2) polarized cells had a higher PI for EGR2; (M2 to M1) polarized cells had higher PI for CD86. At the same time, both MHCII and CD206 showed similar PI values, indicating a similar level of plasticity. For IC-21 cells, (M1 to M2) polarized cells had a higher PI for MHCII and EGR2, while (M2 to M1) polarized cells had a higher PI for CD86 and CD206. For RAW 264.7 cells, (M1 to M2) polarized cells had a higher PI for CD86, MHCII, and EGR2. In contrast, CD206 had a higher PI for (M2 to M1) polarized cells.

These results suggest that not all macrophage cell lines respond similarly to repolarization. For example, for RAW 264.7 cells, it is easier to repolarize M1 polarized cells to M2, whereas the M2 polarized cells dampen the repolarization response to M1 stimuli. This observation is in-line with their strain background of Th2, indicating a preference towards M2-phenotypes. On the other hand, MH-S cells were more plastic and responded similarly to M1 and M2 repolarization. IC-21 cells showed a relatively higher EGR2 PI than other markers, suggesting an increased propensity to repolarize towards the M2 phenotype. Previous literature, to our knowledge, has investigated either M1 or M2 repolarization of macrophages, which limits our understanding of macrophage plasticity to either phenotype. For example, PMs have been shown to repolarize to either M1 or M2 macrophage phenotype in the presence of different therapeutic modalities (Farajzadeh et al., 2018; Moradi-Chaleshtori

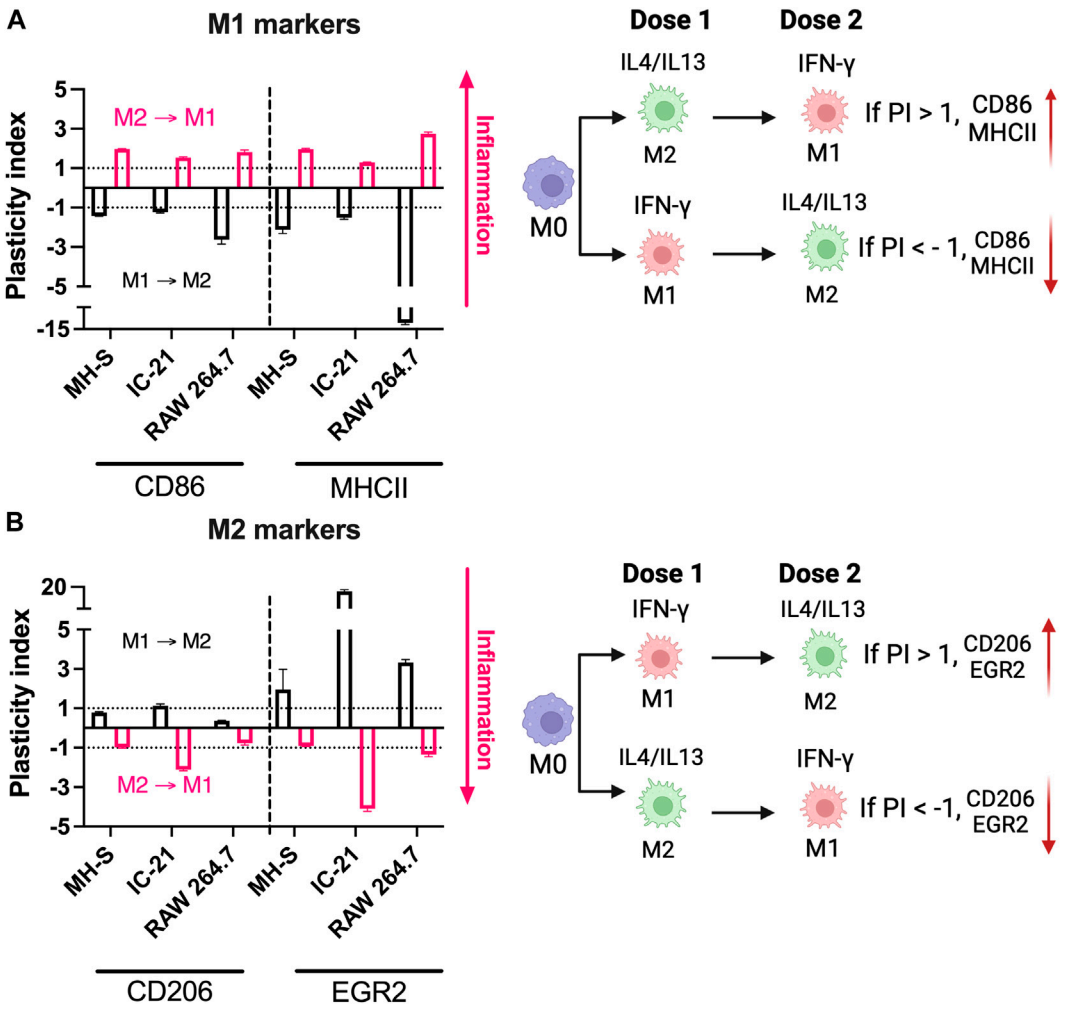

FIGURE 6
Repolarization responses of macrophages from different origins stimulated with soluble factors. Relative repolarization of different macrophage cell lines was determined by quantifying the PI for both **(A)** M1 and **(B)** M2 markers. The M1 to M2 PI was calculated by repolarizing IFNγ-treated cells to IL4/13 treated cells, and M2 to M1 PI was calculated by repolarizing IL4/13 treated cells to IFNγ.

et al., 2021). However, to determine plasticity, the repolarization of macrophages should be investigated using both M1 and M2 stimuli simultaneously. This was previously demonstrated by Smith *et al.* where BMMs increasingly repolarize from the M1 to M2 phenotype; however, the M2 phenotype inhibits repolarization to the M1 phenotype (Smith et al., 2016). These observations, along with our results, are important for immune-engineering applications reliant on repolarization paradigms (Jarai et al., 2023).

3.5 Phenotypical profile and morphology of primary macrophages

Analogous to Figures 2, 3, we next assessed the phenotypical profile and morphology of primary macrophages extracted from mice of relevant genetic background and cultured *ex vivo*. As mentioned, macrophage phenotypes vary among strains; therefore, we assessed BMMs from both BALB/c and C57BL/6 mice. For both types of BMMs, M1 stimuli of IFNγ significantly upregulated both CD86 (Figure 7A) and MHCII (Figure 7B) marker expression. Notably, C57BL/6 BMMs had higher upregulation of both M1 markers (MHCII and CD86), which is consistent with previous literature that shows macrophages from C57BL/6 mice are more responsive to inflammatory stimuli (Santos et al., 2006). While M2 stimuli IL4/13 significantly upregulated CD206 (Figure 7C) for both strains, IL4/13 upregulated EGR2 for only BMMs from BALB/c mice, not C57BL/6 mice (Figure 7D), again consistent with the genetic background. Further, CD206 was more strongly increased in BALB/c BMMs compared to C57BL/6 BMMs. These data further align with BALB/c being a predominantly Th2 strain (Watanabe et al., 2004; Santos et al., 2006; Jones et al., 2013). This point is further illustrated by calculating the ratio of M1 and M2 markers (Supplementary Figure S5). C57BL/6 BMMs exhibited higher M1/M2 when stimulated with IFNγ. BALB/c BMMs exhibited higher M2/M1 when stimulated with IL4/IL13. For PMs, IFNγ significantly upregulated MHCII (Figure 7B) and CD206 (Figure 7C), while IL4/13 significantly upregulated MHCII (Figure 7B) and EGR2

10.3389/fbiom.2024.1399448

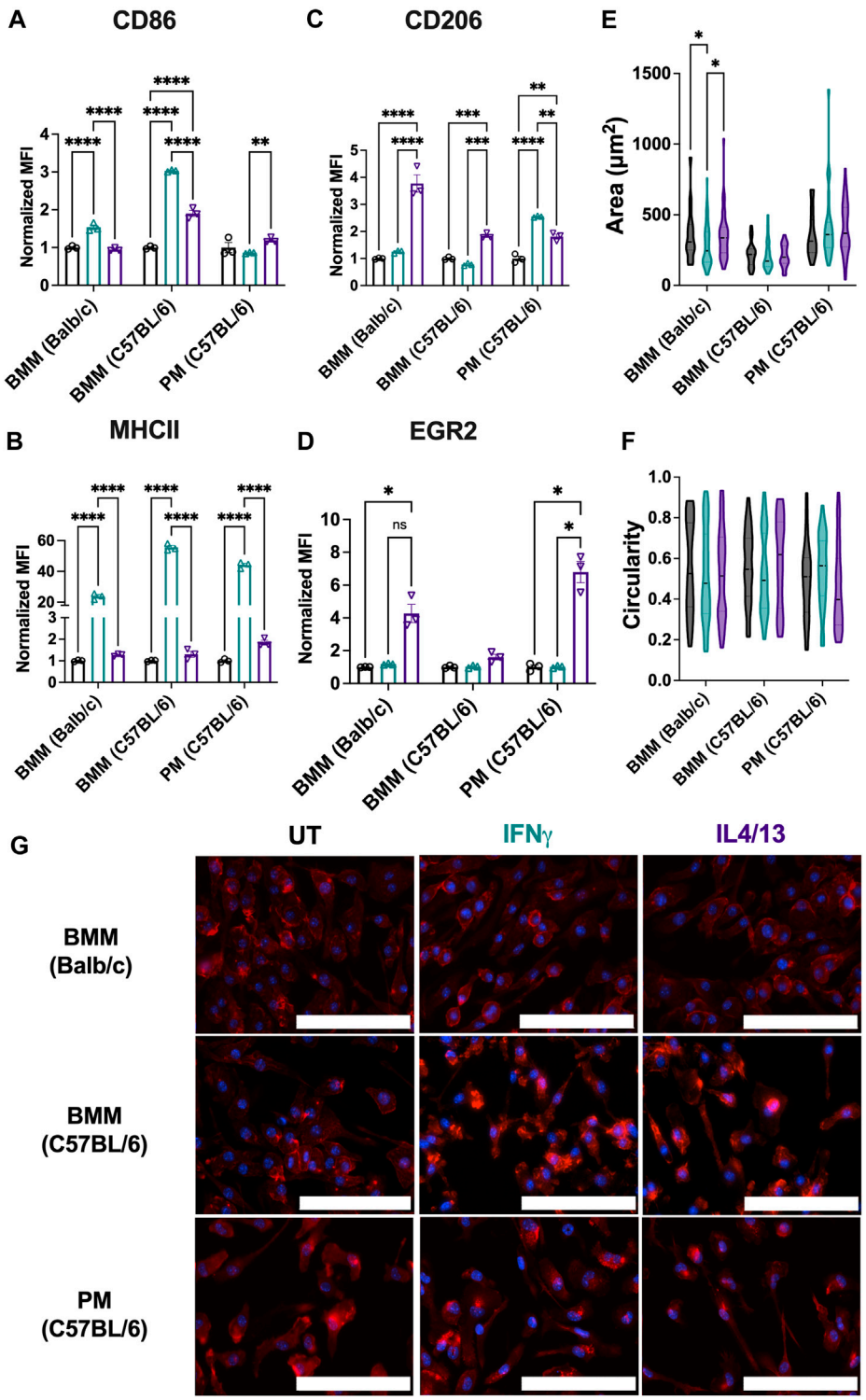

FIGURE 7
Phenotypical and phagocytic responses of macrophages from different origins upon repolarization. The effect of polarization stimuli on macrophage polarization and phagocytosis was determined for primary bone marrow-derived macrophages (BMMs) and peritoneal macrophages (PMs). **(A)** CD86 and **(B)** MHCII were used as M1 markers. **(C)** CD206 and **(D)** EGR2 were used as M2 markers **(E)** Cell area and **(F)** circularity were quantified for all the primary cells across different conditions. **(G)** Representative images of cells with nuclei (blue) and F-actin (red) qualitatively show morphological changes between different cell lines across all the treatment groups. Statistics were performed using one-way ANOVA. *$p < 0.05$, **$p < 0.01$, ***$p < 0.001$, ****$p < 0.0001$. Scale bar: 100 µm.

(Figure 7D). Unlike BMMs from the same strain (C57BL/6), IL4/13 strongly upregulated EGR2 in PMs but not CD206. Upregulation of MHCII holds across all PMs and BMMs tested in response to IFNγ, while only PMs did show not an increase in CD86 when treated with either M1 or M2 stimuli.

Comparing cell lines to their primary cell counterparts (Figures 3, 7), some differences in the marker expression in the primary cells were observed: these include 1) IL4/13 stimulation upregulated EGR2 marker expression in BMMs (BALB/c) and PMs, whereas no change in the marker expression was observed for the cell line counterparts (RAW 264.7 and IC-21); 2) for IFNγ stimulation, the MHCII expression was similar for both RAW 264.7 and BMMs (BALB/c), whereas PMs showed a much higher increase in the fold change (~44.1X) compared to IC-21 cells (~1.2X). We hypothesize this is due to the transcriptional and genetic changes (Ben-David et al., 2018) introduced by the immortalization of primary cells, which has previously been reported for multiple cell types including macrophages (Levenson et al., 2018) and endothelial cells (Deng et al., 2020).

Next, we assessed the morphological changes of primary cells under both M1 and M2 stimulation. BMMs from both strains and PMs showed similar cell area (Figure 7E), and circularity (Figure 7F), and elongated morphology (Figure 7G), irrespective of the stimuli. Only BALB/c BMMs showed differences in cell area due to stimuli; IFNγ treated cells had lower cell area compared to the other conditions. Similar morphology was observed for both RAW 264.7 and IC-21 cell lines compared to BMMs (BALB/c) and PMs (C57BL/6), respectively, suggesting both primary cells and cell lines show similar morphology under different activation conditions. Non-significant differences in the morphology are again attributed to the hyper-physiological stiffness of the TCP culture substrate, which promotes a more elongated morphology. Overall, our results indicate that notable phenotypical differences exist in the primary macrophages obtained from different tissues and between the cell lines and the primary cells from the same origin.

3.6 Comparison of immortalized and primary macrophages in well-defined 3D cultures

Although 2D cell culture on TCP is the standard of practice, cell function and fate are dictated by a range of biochemical and biophysical cues in their multi-dimensional microenvironments. Bioinspired 3D culture models provide opportunities for understanding immune responses in more physiologically relevant environments that are specific to the tissue of interest. Among the cell types analyzed above in 2D culture, the most widely used immortalized (RAW 264.7) and primary (C57BL/6) murine bone-marrow macrophages were chosen for culture in three dimensions for probing similarities and differences in responses of immortalized and primary cells in 3D culture. Here, we used the RASTRUMTM bioprinter to create well-defined 3D cultures in a multi-well plate format (Figure 8A), providing rigor, reproducibility, and accessibility and enabling facile imaging and cell harvesting for downstream assays. We selected a bioprinted synthetic ECM composition (1.1-kPa cell-degradable PEG-peptide hydrogel with RGD, GFOGER, YIGSR, and HA) with properties inspired by tissues from which macrophages were derived (e.g., stiffness and ligands from ECM proteins [fibronectin, collagen, laminin] relevant to lung, peritoneal cavity) (Yen et al., 1997; Bomb et al., 2022; Wodzanowski et al., 2022).

Cell viability up to 7 days was confirmed using Live/Dead™ staining. The results suggest that cells maintain viability >70% after 7 days (Figure 8), showing that RASTRUM™ printed hydrogels are suitable for 3D culture of both immortalized and primary macrophages. As expected, RAW 264.7 cells exhibited increased cell number and metabolic activity that are indicative of proliferation (Supplementary Figure S6). As seen in Figure 8B, RAW 264.7 cells also formed large clusters over time, consistent with reports of their behavior in other 3D applications (Kim et al., 2019; Fang et al., 2020). However, cell clustering and proliferation may make RAW 264.7 cells undesirable for future 3D culture applications, limiting single cell analysis. Notably, unlike RAW 264.7 cells, BMMs remained mainly single cells (Figure 8C), with greater uniformity of cells throughout the hydrogel. Lack of cell clustering with BMM cultures is likely attributed to their limited proliferation, as expected and supported by the total cell counts and metabolic data over the 7-day period (Supplementary Figure S6). To the best of our knowledge, these results represent the first use of the RASTRUM™ bioprinter for 3D culture of macrophages, presenting future opportunities for tuning of cell-matrix and cell-cell interactions using the features of this platform (Du et al., 2022; Engel et al., 2022; Jung et al., 2022; Sullivan et al., 2023).

3.7 Phenotypical profiles of primary and immortalized macrophages in 3D culture

To probe any differences between immortalized and primary macrophage responses now in 3D culture, we examined the polarization of RAW 264.7 cells and BMMs encapsulated within the synthetic ECM upon the application of soluble stimuli. Analogous to Figure 7, M1 (CD86/MHCII) and M2 markers (CD206/EGR2) were quantified using flow cytometry after 24-h polarization with M1 stimuli (IFNγ) or M2 stimuli (IL4/IL13). IFNγ significantly upregulated M1 markers (CD86/MHCII) for RAW 264.7 cells (Figures 9A, B). Although not statistically significant, BMMs treated with IFNγ also showed slight upregulation of CD86 and MHCII compared to IL4/13 treated cells (Figures 9A, B). Neither cell line showed significant upregulation of M2 markers (Figures 9C, D).

Analogous to analyses on TCP, we assessed morphological differences (area and cell circularity) based on stimuli (IFNγ and IL4/13) (Figure 9E). Only BMMs were quantitatively analyzed for morphology; single cell statistics cannot be determined accurately with large cell clusters, and therefore, RAW 264.7 cells were not analyzed for volume and sphericity. We observed similar mean cell areas (350–400 μm^2) and circularities (~0.8) of BMMs across conditions (Figure 9F, G). Similarities across treatment groups are expected based on flow cytometry results, which suggest that polarization across conditions was insignificant. We observed the largest ranges of circularity and area of cells in the untreated condition, with lower circularity and larger cell areas in the untreated condition compared to the other conditions. Unlike on TCP, we observed mainly rounded morphologies, which is expected

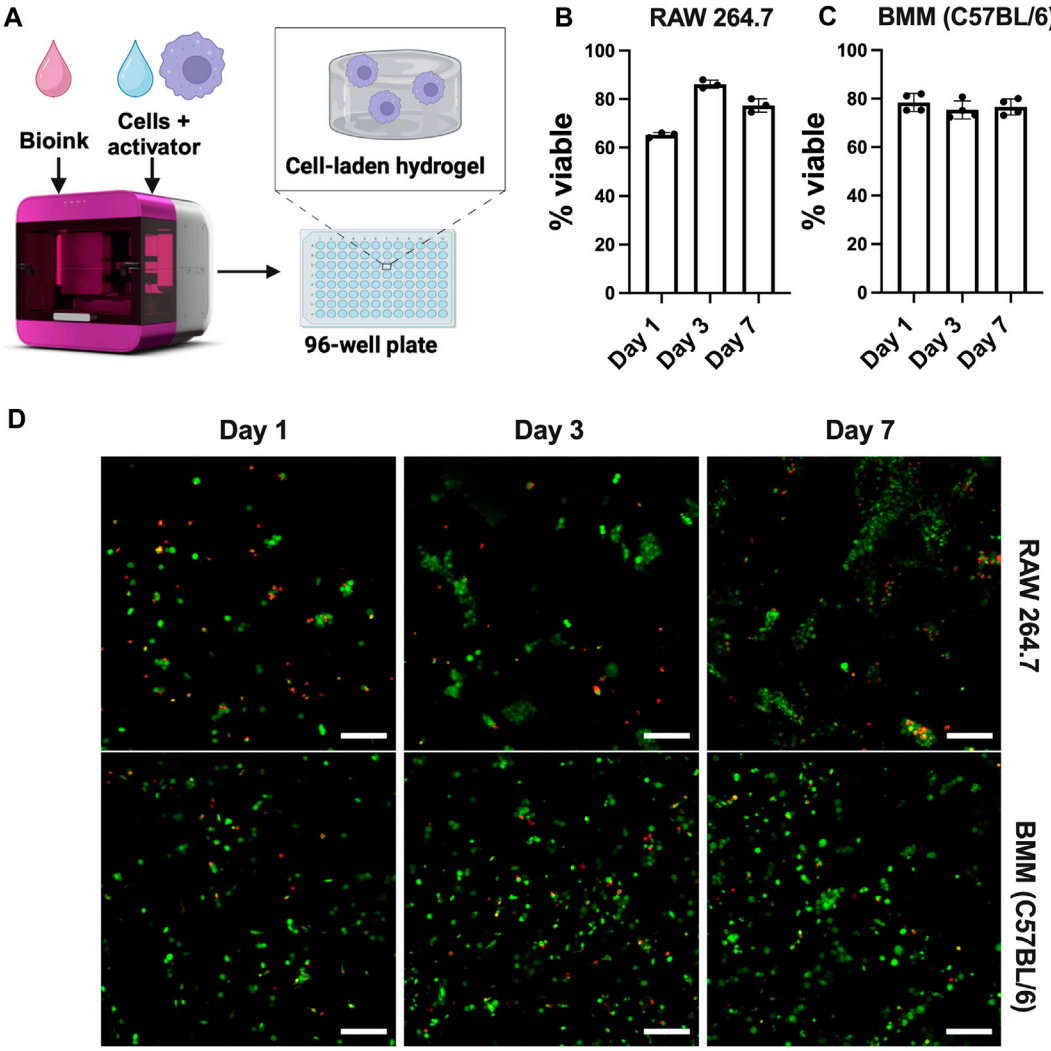

FIGURE 8
Well-defined, bioprinted 3D cultures of macrophages from different origins. **(A)** Schematic of Inventia™ bioprinter for 3D cell encapsulation. Viability of **(B)** RAW 264.7 cells (5E6 cells/mL) and **(C)** BMMs (C57BL/6, 20E6 cells/mL) encapsulated in 1.1 kPa PEG-peptide hydrogels with RGD, GFOGER, YIGSR, and HA was confirmed using **(D)** LIVE/DEAD™ kit ($n \geq 3$). Scale bar: 100 μm. Figure created using BioRender.com.

for macrophages encapsulated within soft materials (Cha et al., 2017; Chen et al., 2020; Bomb et al., 2022; Wodzanowski et al., 2022).

Compared to TCP, macrophages cultured in hydrogels were less responsive to external stimuli (IFNγ and IL14/IL13) when compared to the untreated condition for the respective cell type. This observation aligns with previous literature. For example, Lee *et al.* found that RAW 264.7 cells cultured in 3D hydrogels were less responsive to stimuli (LPS) (Lee and Ki, 2020). The biophysical properties of the microenvironment (e.g., matrix stiffness, density, degradability, structure) as well as biochemical cues (e.g., ligand type, density) all influence cellular responses (Bomb et al., 2022). We hypothesize that the lack of significant upregulation of M1 or M2 markers relative to TCP is due to culture in compliant materials relative to culture on rigid TCP. Soft materials have been shown to activate inflammatory responses in macrophages (Cha et al., 2017; Chen et al., 2020), where Cha *et al.* showed higher levels of CD86 expression in PEG diacrylate (PEGDA) hydrogels compared to gelatin methacrylate hydrogels (Cha et al., 2017). Kim *et al.* also noted that the 3D environment itself can induce inflammation compared to TCP (Kim et al., 2019). Further, Lee *et al.* found that RAW 264.7 cell response to an immunomodulatory polysaccharide was less in 3D culture in PEG-based hydrogels relative to 2D culture on TCP, potentially owing to the low availability of receptors in 3D culture like in tissues (Lee and Ki, 2020).

Hydrogel compliance also plays an important role in polarization; however, exactly how the modulus correlates to polarization remains unclear based on the current literature. Some researchers have noted that cells seeded on top of hydrogels display a more M2-like phenotype with stiffer gels (Chen et al., 2020; Bomb et al., 2022) while others have found that increased stiffness promotes M1-like phenotype (Sridharan et al., 2019; Bu et al., 2022). This trend can change based on the range of stiffnesses tested and the chemistry of the hydrogel. Further, 3D cultures and 2D hydrogel culture trends do not always align. Several researchers noted that larger pores size and lower modulus

10.3389/fbiom.2024.1399448

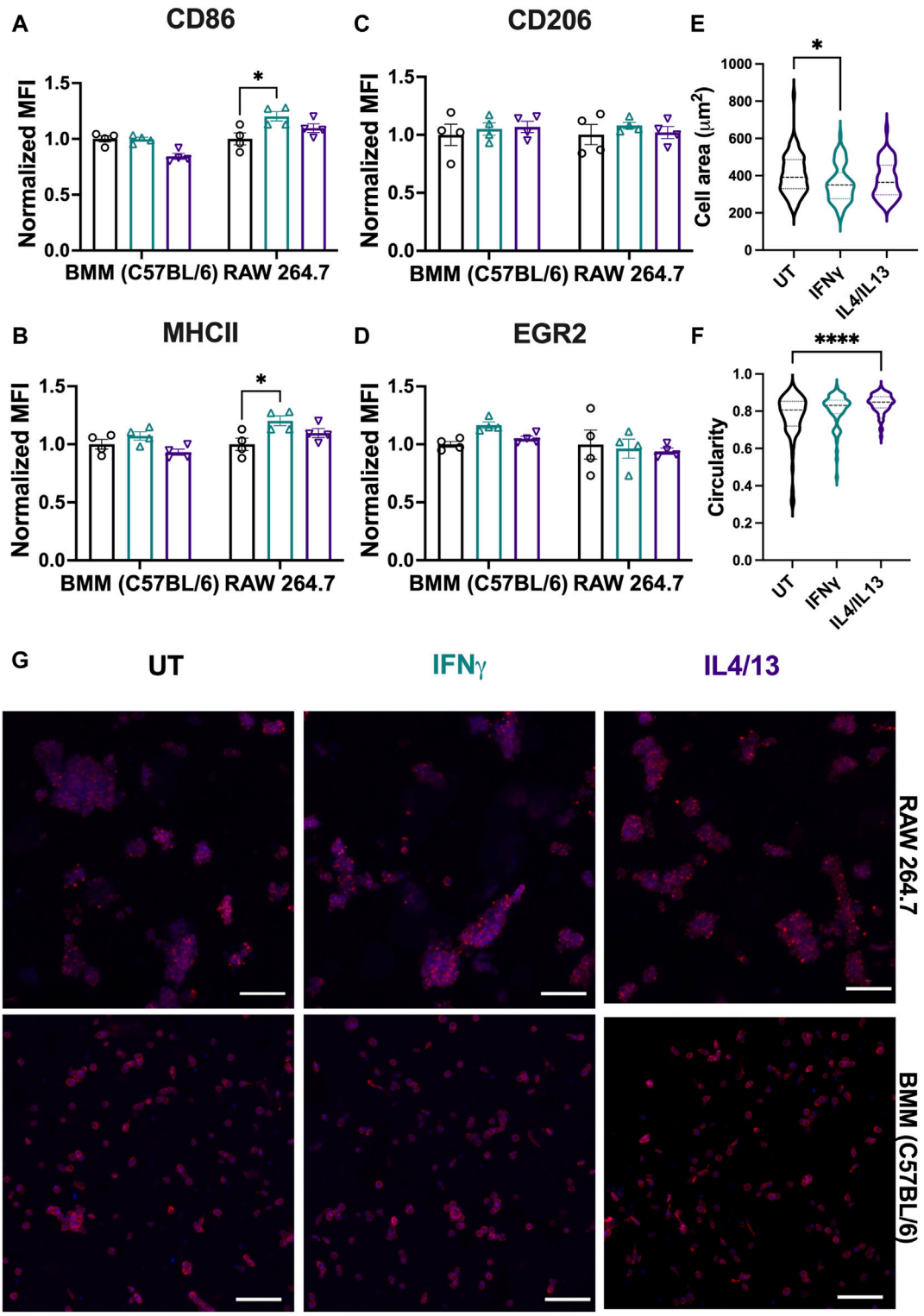

FIGURE 9
Effect of soluble stimuli on macrophage polarization in well-defined, bioprinted 3D cultures. Effect of polarization stimuli on macrophage polarization was determined for RAW 264.7 cells and primary BMMs (C57BL/6) in 3D culture (1.1 kPa PEG-peptide hydrogels with RGD, GFOGER, YIGSR, and HA). **(A)** CD86 and **(B)** MHCII were used as M1 markers. **(C)** CD206 and **(D)** EGR2 were used as M2 markers. All data are normalized to the UT control for the respective cell type. **(E)** Cell area and **(F)** circularity were quantified for all the cell types across different conditions. **(G)** Representative images of BMMs with nuclei (blue) and F-actin (red) qualitatively show morphology of BMMs across all the treatment groups. Statistics were performed using Tukey's *post hoc* test with one-way ANOVA. *$p < 0.05$, **$p < 0.01$, ***$p < 0.001$, ****$p < 0.0001$." Scale bar: 100 μm.

promote more M2-like phenotypes (He et al., 2018; Bu et al., 2022; Cicuéndez Maroto et al., 2024). Others also have reported that RAW 264.7 cells in PEG-based hydrogels increase baseline expression of both M1 and M2 markers in 3D culture in both compliant and stiff cell-degradable PEG-peptide hydrogels relative to 2D culture on TCP (Kim et al., 2019). Future work is needed to address how stiffness impacts the phenotype in such well-defined 3D cultures alongside synergistic effects of stiffness and external stimuli.

Based on previous literature as noted above (Cha et al., 2017; Kim et al., 2019; Lee and Ki, 2020), we speculate that higher base level expression of inflammatory markers prior to stimulation may hinder subsequent polarization with external stimuli when compared to the untreated control. There may also be less availability of receptors in 3D culture for binding to applied ligands or nonspecific interactions between the hydrogel components and cytokines that impact ligand-receptor binding. Note, the diffusion of cytokines through the full hydrogel thickness is expected to occur within an hour, based on the literature and assuming one-dimensional Fickian diffusion ($t_d = L^2/D$, where the length (L) is 0.055 cm and the diffusion coefficient (D) of the proteins through a PEG-hydrogel is estimated to be ~1E-6 cm^2/s) (Weber et al., 2009). In this context, we do not expect cytokine diffusion to be limiting the macrophage response in these studies. Macrophages may need higher concentrations of cytokines and longer incubation times, or repeated exposures to see pronounced responses to stimuli. Opportunities for future studies include probing tissue-specific responses within such culture systems for their validation and application. Overall, our results establish the relevance of a bioprinted synthetic ECM for well-defined 3D culture of both immortalized and primary macrophages and provide insights into differences in their function in 3D culture toward informing cell type selection in both fundamental and applied studies, from biological mechanisms to biomaterials designs.

4 Conclusion

Our findings demonstrate that macrophages from different cell lines display marked differences in phenotypical and morphological profile, phagocytosis function, and repolarization with alternative stimuli. Both immortalized and primary cells vary in polarization based on the tissue origin and mouse strain. Macrophages are less sensitive to stimuli in 3D hydrogel culture and have notably different morphologies than on TCP. While limited to the specific cell lines and markers addressed here, through this analysis, we aim to provide researchers with an important baseline for selecting a macrophage cell line or primary cells for biomaterial applications. Our results further showcase bioprinted well-defined 3D cultures for studies of immortalized or primary macrophages in bioactive hydrogel-based synthetic ECMs with high throughput; future work with such systems has the potential to bridge an important gap between *in vitro* and *in vivo* systems for probing tissue-relevant responses of macrophages and other innate immune cells. Here, we focused on cell-by-cell analysis to understand the phenotype and function of the cell. In future work, phenotypic characterization of selected cell lines or primary cells of interest in a specific application should also include gene expression and functional differences in cytokine release profiles to fully elucidate differences between these macrophage research tools.

Data availability statement

The raw data supporting the conclusion of this article will be made available by the authors, without undue reservation.

Ethics statement

Primary BMMs and PMs were isolated from healthy BALB/c and C57BL/6 mice (6–12 weeks old, Jackson Laboratories, Bar Harbor, Maine, USA), respectively, following the approved Institutional Animal Care and Use Committee (IACUC) protocol at the University of Delaware. The study was conducted in accordance with the local legislation and institutional requirements.

Author contributions

JG: Writing–original draft, Writing–review and editing, Conceptualization, Data curation, Formal Analysis, Investigation, Methodology, Project administration, Supervision, Visualization. KB: Conceptualization, Data curation, Formal Analysis, Investigation, Methodology, Project administration, Visualization, Writing–original draft, Writing–review and editing. MT-R: Conceptualization, Formal Analysis, Investigation, Writing–original draft, Writing–review and editing. BJ: Conceptualization, Formal Analysis, Investigation, Writing–original draft, Writing–review and editing. NG: Formal Analysis, Investigation, Writing–original draft, Writing–review and editing. AK: Writing–original draft, Writing–review and editing, Conceptualization, Funding acquisition, Project administration, Resources, Supervision. CF: Writing–original draft, Writing–review and editing, Conceptualization, Funding acquisition, Project administration, Resources, Supervision.

Funding

The author(s) declare that financial support was received for the research, authorship, and/or publication of this article. Research reported in this work was supported by a National Institutes of Health (NIH) Director's New Innovator Award with grant number DP2HL152424 (AK), a NIH National Institute of General Medicine (NIGMS) Award with grant number R35GM142866A (CF), by the National Science Foundation (NSF) through the University of Delaware Materials Research Science and Engineering Center (DMR-2011824), and by the Institute for Engineering Driven Health at the University of Delaware with support from a NSF Accelerating Research Translation grant (2331440). Additionally, the authors acknowledge the use of facilities and instrumentation supported by the NSF through the University of Delaware Materials Research Science and Engineering Center (DMR-2011824) and NIH NIGMS through the Delaware COBRE (P20GM104316). Microscopy access, through the Delaware Biotechnology Institute (DBI) BioImaging, was supported by grants from the NIH-NIGMS (P20GM103446), the NIGMS (P20 GM139760), and the State of Delaware. Additional student support was obtained from the Collins fellowship (KB and JG), National Science Foundation (NSF) Graduate Research Fellowship Program (GRFP) Award number

1940700 (JG), and Department of Education (DOE) Graduate Assistance in Areas of National Need (GAANN): Inclusive Teaching in Chemical Engineering (ITChE) fellowship (MT-R).

Conflict of interest

The authors declare that the research was conducted in the absence of any commercial or financial relationships that could be construed as a potential conflict of interest.

Publisher's note

All claims expressed in this article are solely those of the authors and do not necessarily represent those of their affiliated organizations, or those of the publisher, the editors and the reviewers. Any product that may be evaluated in this article, or claim that may be made by its manufacturer, is not guaranteed or endorsed by the publisher.

Author disclaimer

The content of this article is solely the responsibility of the authors and does not necessarily represent the official views of the National Institutes of Health or National Science Foundation.

Supplementary material

The Supplementary Material for this article can be found online at: https://www.frontiersin.org/articles/10.3389/fbiom.2024.1399448/full#supplementary-material

References

Allard, B., Panariti, A., and Martin, J. G. (2018). Alveolar macrophages in the resolution of inflammation, tissue repair, and tolerance to infection. *Front. Immunol.* 9, 1777. doi:10.3389/fimmu.2018.01777

Andreakos, E., Sacre, S. M., Smith, C., Lundberg, A., Kiriakidis, S., Stonehouse, T., et al. (2004). Distinct pathways of LPS-induced NF-κB activation and cytokine production in human myeloid and nonmyeloid cells defined by selective utilization of MyD88 and Mal/TIRAP. *Blood* 103, 2229–2237. doi:10.1182/blood-2003-04-1356

Ben-David, U., Siranosian, B., Ha, G., Tang, H., Oren, Y., Hinohara, K., et al. (2018). Genetic and transcriptional evolution alters cancer cell line drug response. *Nature* 560, 325–330. doi:10.1038/s41586-018-0409-3

Benner, B., Scarberry, L., Suarez-Kelly, L. P., Duggan, M. C., Campbell, A. R., Smith, E., et al. (2019). Generation of monocyte-derived tumor-associated macrophages using tumor-conditioned media provides a novel method to study tumor-associated macrophages *in vitro*. *J. Immunother. cancer* 7, 140–214. doi:10.1186/s40425-019-0622-0

Berghaus, L. J., Moore, J. N., Hurley, D. J., Vandenplas, M. L., Fortes, B. P., Wolfert, M. A., et al. (2010). Innate immune responses of primary murine macrophage-lineage cells and RAW 264.7 cells to ligands of Toll-like receptors 2, 3, and 4. *Comp. Immunol. Microbiol. Infect. Dis.* 33, 443–454. doi:10.1016/j.cimid.2009.07.001

Bobba, C. M., Fei, Q., Shukla, V., Lee, H., Patel, P., Putman, R. K., et al. (2021). Nanoparticle delivery of microRNA-146a regulates mechanotransduction in lung macrophages and mitigates injury during mechanical ventilation. *Nat. Commun.* 12, 289. doi:10.1038/s41467-020-20449-w

Bomb, K., Pradhan, L., Zhang, Q., Jarai, B. M., Bhattacharjee, A., Burris, D. L., et al. (2022). Destructive fibrotic teamwork: how both microenvironment stiffness and profibrotic interleukin 13 impair alveolar macrophage phenotype and function. *Biomaterials Sci.* 10, 5689–5706. doi:10.1039/d2bm00828a

Bomb, K., Zhang, Q., Ford, E. M., Fromen, C. A., and Kloxin, A. M. (2023). Systematic d-amino acid substitutions to control peptide and hydrogel degradation in cellular microenvironments. *ACS Macro Lett.* 12, 725–732. doi:10.1021/acsmacrolett.3c00144

Brady, S. R., Gohsman, S. B., Sepulveda, K., and Weaver, J. D. (2023). Engineering synthetic poly(ethylene) glycol-based hydrogels compatible with injection molding biofabrication. *J. Biomed. Mater. Res. Part A* 111, 814–824. doi:10.1002/jbm.a.37523

Bu, W., Wu, Y., Ghaemmaghami, A. M., Sun, H., and Mata, A. (2022). Rational design of hydrogels for immunomodulation. *Regen. Biomater.* 9, rbac009. doi:10.1093/rb/rbac009

Cha, B. H., Shin, S. R., Leijten, J., Li, Y. C., Singh, S., Liu, J. C., et al. (2017). Integrin-mediated interactions control macrophage polarization in 3D hydrogels. *Adv. Healthc. Mater.* 6, 1700289. doi:10.1002/adhm.201700289

Chamberlain, L. M., Godek, M. L., Gonzalez-Juarrero, M., and Grainger, D. W. (2009). Phenotypic non-equivalence of murine (monocyte-) macrophage cells in biomaterial and inflammatory models. *J. Biomed. Mater. Res. Part A* 88, 858–871. doi:10.1002/jbm.a.31930

Chamberlain, L. M., Holt-Casper, D., Gonzalez-Juarrero, M., and Grainger, D. W. (2015). Extended culture of macrophages from different sources and maturation results in a common M2 phenotype. *J. Biomed. Mater. Res. Part A* 103, 2864–2874. doi:10.1002/jbm.a.35415

Chen, M., Zhang, Y., Zhou, P., Liu, X., Zhao, H., Zhou, X., et al. (2020). Substrate stiffness modulates bone marrow-derived macrophage polarization through NF-κB signaling pathway. *Bioact. Mater* 5, 880–890. doi:10.1016/j.bioactmat.2020.05.004

Cicuéndez Maroto, M., García-Lizarribar, A., Casarrubios Molina, L., Feito Castellano, M. J., Fernández San Argimiro, F. J., García Urkia, N., et al. (2024). *Functionality of macrophages encapsulated in porcine decellularized adipose matrix hydrogels and interaction with Candida albicans.*

Ci, X., Ren, R., Xu, K., Li, H., Yu, Q., Song, Y., et al. (2010). Schisantherin A exhibits anti-inflammatory properties by down-regulating NF-κB and mapk signaling pathways in lipopolysaccharide-treated raw 264.7 cells. *Inflammation* 33, 126–136. doi:10.1007/s10753-009-9166-7

Deng, L., Pollmeier, L., Zhou, Q., Bergemann, S., Bode, C., Hein, L., et al. (2020). Gene expression in immortalized versus primary isolated cardiac endothelial cells. *Sci. Rep.* 10, 2241. doi:10.1038/s41598-020-59213-x

Du, E. Y., Jung, M., Skhinas, J., Tolentino, M. K., Jamshidi, N., Houng, J., et al. (2022). A 3D bioprintable hydrogel with tuneable stiffness for exploring cells encapsulated in matrices of differing stiffnesses. *ACS Applied Bio Materials* 6, 4603–4612. doi:10.1021/acsabm.3c00334

Edwards, J. P., Zhang, X., Frauwirth, K. A., and Mosser, D. M. (2006). Biochemical and functional characterization of three activated macrophage populations. *J. Leukoc. Biol.* 80, 1298–1307. doi:10.1189/jlb.0406249

Engel, M., Belfiore, L., Aghaei, B., and Sutija, M. (2022). Enabling high throughput drug discovery in 3D cell cultures through a novel bioprinting workflow. *SLAS Technol.* 27, 32–38. doi:10.1016/j.slast.2021.10.002

Fang, J. Y., Yang, Z., and Han, B. (2020). Switch of macrophage fusion competency by 3D matrices. *Sci. Rep.* 10, 10348. doi:10.1038/s41598-020-67056-9

Farajzadeh, R., Zarghami, N., Serati-Nouri, H., Momeni-Javid, Z., Farajzadeh, T., Jalilzadeh-Tabrizi, S., et al. (2018). Macrophage repolarization using CD44-targeting hyaluronic acid–polylactide nanoparticles containing curcumin. *Artif. cells, nanomedicine, Biotechnol.* 46, 2013–2021. doi:10.1080/21691401.2017.1408116

Genin, M., Clement, F., Fattaccioli, A., Raes, M., and Michiels, C. (2015). M1 and M2 macrophages derived from THP-1 cells differentially modulate the response of cancer cells to etoposide. *BMC Cancer* 15, 577. doi:10.1186/s12885-015-1546-9

Gomila Pelegri, N., Stanczak, A. M., Bottomley, A. L., Milthorpe, B. K., Gorrie, C. A., Padula, M. P., et al. (2023). Adipose-derived stem cells spontaneously express neural markers when grown in a PEG-based 3D matrix. *Int. J. Mol. Sci.* 24, 12139. doi:10.3390/ijms241512139

Gonçalves, R., and Mosser, D. M. (2015). The isolation and characterization of murine macrophages. *Curr. Protoc. Immunol.* 111, 14.1. 1–14.1. 16. doi:10.1002/0471142735.im1401s111

Gordon, S., and Martinez, F. O. (2010). Alternative activation of macrophages: mechanism and functions. *Immunity* 32, 593–604. doi:10.1016/j.immuni.2010.05.007

He, X.-T., Wu, R.-X., Xu, X.-Y., Wang, J., Yin, Y., and Chen, F.-M. (2018). Macrophage involvement affects matrix stiffness-related influences on cell osteogenesis under three-dimensional culture conditions. *Acta Biomater.* 71, 132–147. doi:10.1016/j.actbio.2018.02.015

Ivashkiv, L. B. (2018). IFNγ: signalling, epigenetics and roles in immunity, metabolism, disease and cancer immunotherapy. *Nat. Rev. Immunol.* 18, 545–558. doi:10.1038/s41577-018-0029-z

Jarai, B. M., Bomb, K., and Fromen, C. A. (2023). Nanoparticle pre-treatment for enhancing the survival and activation of pulmonary macrophage transplant. *Drug Deliv. Transl. Res.* 13, 1955–1966. doi:10.1007/s13346-023-01319-6

Jarai, B. M., and Fromen, C. A. (2022). Nanoparticle internalization promotes the survival of primary macrophages. *Adv. NanoBiomed Res.* 2, 2100127. doi:10.1002/anbr.202100127

Jarai, B. M., Stillman, Z., and Fromen, C. A. (2021). Hydrogel nanoparticle degradation influences the activation and survival of primary macrophages. *J. Mater. Chem. B* 9, 7246–7257. doi:10.1039/d1tb00982f

Jones, S. W., Roberts, R. A., Robbins, G. R., Perry, J. L., Kai, M. P., Chen, K., et al. (2013). Nanoparticle clearance is governed by Th1/Th2 immunity and strain background. *J. Clin. Investigation* 123, 3061–3073. doi:10.1172/jci66895

Jung, M., Skhinas, J. N., Du, E. Y., Tolentino, M. A. K., Utama, R. H., Engel, M., et al. (2022). A high-throughput 3D bioprinted cancer cell migration and invasion model with versatile and broad biological applicability. *Biomaterials Sci.* 10, 5876–5887. doi:10.1039/d2bm00651k

Kim, M., Lee, S., and Ki, C. S. (2019). Cellular behavior of RAW264.7 cells in 3D poly(ethylene glycol) hydrogel niches. *ACS Biomaterials Sci. Eng.* 5, 922–932. doi:10.1021/acsbiomaterials.8b01150

Lavin, Y., Winter, D., Blecher-Gonen, R., David, E., Keren-Shaul, H., Merad, M., et al. (2014). Tissue-resident macrophage enhancer landscapes are shaped by the local microenvironment. *Cell* 159, 1312–1326. doi:10.1016/j.cell.2014.11.018

Lee, S., and Ki, C. S. (2020). Inflammatory responses of macrophage-like RAW264.7 cells in a 3D hydrogel matrix to ultrasonicated schizophyllan. *Carbohydr. Polym.* 229, 115555. doi:10.1016/j.carbpol.2019.115555

Levenson, E. A., Martens, C., Kanakabandi, K., Turner, C. V., Virtaneva, K., Paneru, M., et al. (2018). Comparative transcriptomic response of primary and immortalized macrophages to murine norovirus infection. *J. Immunol.* 200, 4157–4169. doi:10.4049/jimmunol.1700384

Little, A. C., Pathanjeli, P., Wu, Z., Bao, L., Goo, L. E., Yates, J. A., et al. (2019). IL-4/IL-13 stimulated macrophages enhance breast cancer invasion via rho-GTPase regulation of synergistic VEGF/CCL-18 signaling. *Front. Oncol.* 9, 456. doi:10.3389/fonc.2019.00456

Liu, Y., and Segura, T. (2020). Biomaterials-Mediated regulation of macrophage cell fate. *Front. Bioeng. Biotechnol.* 8, 609297. doi:10.3389/fbioe.2020.609297

Lou, J., and Mooney, D. J. (2022). Chemical strategies to engineer hydrogels for cell culture. *Nat. Rev. Chem.* 6, 726–744. doi:10.1038/s41570-022-00420-7

Mahmodi, H., Piloni, A., Utama, R., and Kabakova, I. (2021). Mechanical mapping of bioprinted hydrogel models by brillouin microscopy. *bioRxiv* 23, e00151. 2021.02.18.431535. doi:10.1016/j.bprint.2021.e00151

Mao, J., Chen, L., Cai, Z., Qian, S., Liu, Z., Zhao, B., et al. (2022). Advanced biomaterials for regulating polarization of macrophages in wound healing. *Adv. Funct. Mater.* 32, 2111003. doi:10.1002/adfm.202111003

Mcwhorter, F. Y., Wang, T., Nguyen, P., Chung, T., and Liu, W. F. (2013). Modulation of macrophage phenotype by cell shape. *Proc. Natl. Acad. Sci.* 110, 17253–17258. doi:10.1073/pnas.1308887110

Misharin, A. V., Morales-Nebreda, L., Reyfman, P. A., Cuda, C. M., Walter, J. M., Mcquattie-Pimentel, A. C., et al. (2017). Monocyte-derived alveolar macrophages drive lung fibrosis and persist in the lung over the life span. *J. Exp. Med.* 214, 2387–2404. doi:10.1084/jem.20162152

Moradi-Chaleshtori, M., Shojaei, S., Mohammadi-Yeganeh, S., and Hashemi, S. M. (2021). Transfer of miRNA in tumor-derived exosomes suppresses breast tumor cell invasion and migration by inducing M1 polarization in macrophages. *Life Sci.* 282, 119800. doi:10.1016/j.lfs.2021.119800

Mosser, D. M., and Edwards, J. P. (2008). Exploring the full spectrum of macrophage activation. *Nat. Rev. Immunol.* 8, 958–969. doi:10.1038/nri2448

Palomba, R., Di Francesco, M., Di Francesco, V., Piccardi, F., Catelani, T., Ferreira, M., et al. (2021). Boosting nanomedicine performance by conditioning macrophages with methyl palmitate nanoparticles. *Mater. Horizons* 8, 2726–2741. doi:10.1039/d1mh00937k

Park, M. D., Silvin, A., Ginhoux, F., and Merad, M. (2022). Macrophages in health and disease. *Cell* 185, 4259–4279. doi:10.1016/j.cell.2022.10.007

Rayahin, J. E., Buhrman, J. S., Zhang, Y., Koh, T. J., and Gemeinhart, R. A. (2015). High and low molecular weight hyaluronic acid differentially influence macrophage activation. *ACS Biomater. Sci. Eng.* 1, 481–493. doi:10.1021/acsbiomaterials.5b00181

Risser, G. E., Machour, M., Hernaez-Estrada, B., Li, D., Levenberg, S., and Spiller, K. L. (2023). Effects of Interleukin-4 (IL-4)-releasing microparticles and adoptive transfer of macrophages on immunomodulation and angiogenesis. *Biomaterials* 296, 122095. doi:10.1016/j.biomaterials.2023.122095

Ruge, C. A., Schaefer, U. F., Herrmann, J., Kirch, J., Canadas, O., Echaide, M., et al. (2012). The interplay of lung surfactant proteins and lipids assimilates the macrophage clearance of nanoparticles. *PloS one* 7, e40775. doi:10.1371/journal.pone.0040775

Santos, J. L., Andrade, A. A., Dias, A. A. M., Bonjardim, C. A., Reis, L. F. L., Teixeira, S. M. R., et al. (2006). Differential sensitivity of C57BL/6 (M-1) and BALB/c (M-2) macrophages to the stimuli of IFN-γ/LPS for the production of NO: correlation with iNOS mRNA and protein expression. *J. Interferon & Cytokine Res.* 26, 682–688. doi:10.1089/jir.2006.26.682

Sikorski, K., Chmielewski, S., Olejnik, A., Wesoly, J. Z., Heemann, U., Baumann, M., et al. (2012). STAT1 as a central mediator of IFNγ and TLR4 signal integration in vascular dysfunction. *Jak-Stat* 1, 241–249. doi:10.4161/jkst.22469

Smith, T. D., Tse, M. J., Read, E. L., and Liu, W. F. (2016). Regulation of macrophage polarization and plasticity by complex activation signals. *Integr. Biol. (Camb)* 8, 946–955. doi:10.1039/c6ib00105j

Sreejit, G., Fleetwood, A. J., Murphy, A. J., and Nagareddy, P. R. (2020). Origins and diversity of macrophages in health and disease. *Clin. Transl. Immunol.* 9, e1222. doi:10.1002/cti2.1222

Sridharan, R., Cavanagh, B., Cameron, A. R., Kelly, D. J., and O'Brien, F. J. (2019). Material stiffness influences the polarization state, function and migration mode of macrophages. *Acta Biomater.* 89, 47–59. doi:10.1016/j.actbio.2019.02.048

Stevens, M. T., Nagaria, B. D., Britton, W. J., and Saunders, B. M. (2021). Macrophages of different tissue origin exhibit distinct inflammatory responses to mycobacterial infection. *Immunol. Cell Biol.* 99, 1085–1092. doi:10.1111/imcb.12493

Strizova, Z., Benesova, I., Bartolini, R., Novysedlak, R., Cecrdlova, E., Foley, LILY K., et al. (2023). M1/M2 macrophages and their overlaps – myth or reality? *Clin. Sci.* 137, 1067–1093. doi:10.1042/cs20220531

Sullivan, M. A., Lane, S., Volkerling, A., Engel, M., Werry, E. L., and Kassiou, M. (2023). Three-dimensional bioprinting of stem cell-derived central nervous system cells enables astrocyte growth, vasculogenesis, and enhances neural differentiation/function. *Biotechnol. Bioeng.* 120, 3079–3091. doi:10.1002/bit.28470

Sun, X., Ma, Z., Zhao, X., Jin, W., Zhang, C., Ma, J., et al. (2021). Three-dimensional bioprinting of multicell-laden scaffolds containing bone morphogenic protein-4 for promoting M2 macrophage polarization and accelerating bone defect repair in diabetes mellitus. *Bioact. Mater.* 6, 757–769. doi:10.1016/j.bioactmat.2020.08.030

Sylvestre, M., Crane, C. A., and Pun, S. H. (2020). Progress on modulating tumor-associated macrophages with biomaterials. *Adv. Mater.* 32, 1902007. doi:10.1002/adma.201902007

Tran, T.-H., Krishnan, S., and Amiji, M. M. (2016). MicroRNA-223 induced repolarization of peritoneal macrophages using CD44 targeting hyaluronic acid nanoparticles for anti-inflammatory effects. *PloS one* 11, e0152024. doi:10.1371/journal.pone.0152024

Tu, P.-C., Pan, Y.-L., Liang, Z.-Q., Yang, G.-L., Wu, C.-J., Zeng, L., et al. (2022). Mechanical stretch promotes macrophage polarization and inflammation via the RhoA-ROCK/NF-κB pathway. *BioMed Res. Int.* 2022, 1–9. doi:10.1155/2022/6871269

Ullah, S., Seidel, K., Türkkan, S., Warwas, D. P., Dubich, T., Rohde, M., et al. (2019). Macrophage entrapped silica coated superparamagnetic iron oxide particles for controlled drug release in a 3D cancer model. *J. Control. Release* 294, 327–336. doi:10.1016/j.jconrel.2018.12.040

Wang, C., Yu, X., Cao, Q., Wang, Y., Zheng, G., Tan, T. K., et al. (2013). Characterization of murine macrophages from bone marrow, spleen and peritoneum. *BMC Immunol.* 14, 6–10. doi:10.1186/1471-2172-14-6

Watanabe, H., Numata, K., Ito, T., Takagi, K., and Matsukawa, A. (2004). Innate immune response in th1- and th2-dominant mouse strains. *Shock* 22, 460–466. doi:10.1097/01.shk.0000142249.08135.e9

Weber, L. M., Lopez, C. G., and Anseth, K. S. (2009). Effects of PEG hydrogel crosslinking density on protein diffusion and encapsulated islet survival and function. *J. Biomed. Mater Res. A* 90, 720–729. doi:10.1002/jbm.a.32134

Wiley, K. L., Sutherland, B. P., Ogunnaike, B. A., and Kloxin, A. M. (2022). Rational design of hydrogel networks with dynamic mechanical properties to mimic matrix remodeling. *Adv. Healthc. Mater* 11, e2101947. doi:10.1002/adhm.202101947

Wodzanowski, K. A., Caplan, J. L., Kloxin, A. M., and Grimes, C. L. (2022). Multiscale invasion assay for probing macrophage response to gram-negative bacteria. *Front. Chem.* 10, 842602. doi:10.3389/fchem.2022.842602

Wu, Z., Chen, C., Luo, J., Davis, J. R., Zhang, B., Tang, L., et al. (2020). EGFP-EGF1-conjugated poly (lactic-co-glycolic acid) nanoparticles as a carrier for the delivery of CCR2– shRNA to atherosclerotic macrophage *in vitro*. *Sci. Rep.* 10, 19636. doi:10.1038/s41598-020-76416-4

Yen, C. J., Fang, C. C., Chen, Y. M., Lin, R. H., Wu, K. D., Lee, P. H., et al. (1997). Extracellular matrix proteins modulate human peritoneal mesothelial cell behavior. *Nephron* 75, 188–195. doi:10.1159/000189530

Zajd, C. M., Ziemba, A. M., Miralles, G. M., Nguyen, T., Feustel, P. J., Dunn, S. M., et al. (2020). Bone marrow-derived and elicited peritoneal macrophages are not created equal: the questions asked dictate the cell type used. *Front. Immunol.* 11, 269. doi:10.3389/fimmu.2020.00269

Zarubova, J., Hasani-Sadrabadi, M. M., Ardehali, R., and Li, S. (2022). Immunoengineering strategies to enhance vascularization and tissue regeneration. *Adv. Drug Deliv. Rev.* 184, 114233. doi:10.1016/j.addr.2022.114233

Zhang, W., Zhang, Y., He, Y., Wang, X., and Fang, Q. (2019). Lipopolysaccharide mediates time-dependent macrophage M1/M2 polarization through the Tim-3/Galectin-9 signalling pathway. *Exp. Cell Res.* 376, 124–132. doi:10.1016/j.yexcr.2019.02.007

Zhao, Y.-L., Tian, P.-X., Han, F., Zheng, J., Xia, X.-X., Xue, W.-J., et al. (2017). Comparison of the characteristics of macrophages derived from murine spleen, peritoneal cavity, and bone marrow. *J. Zhejiang University-SCIENCE B* 18, 1055–1063. doi:10.1631/jzus.b1700003

Zheng, Y., Han, Y., Sun, Q., and Li, Z. (2022). Harnessing anti-tumor and tumor-tropism functions of macrophages via nanotechnology for tumor immunotherapy. *Exploration* 2, 20210166. doi:10.1002/exp.20210166

Zhen, H., Hu, H., Tan, C., Yu, X., Gan, X., and Huang, X. (2023). Regulation of M1/M2 polarization in LPS-stimulated macrophages by 1,25(OH)2D3. *Altern. Ther. Health Med.* 29, 501–505.

Zhou, H., Xue, Y., Dong, L., and Wang, C. (2021). Biomaterial-based physical regulation of macrophage behaviour. *J. Mater. Chem. B* 9, 3608–3621. doi:10.1039/d1tb00107h

frontiers | Frontiers in Biomaterials Science

TYPE Correction
PUBLISHED 17 July 2024
DOI 10.3389/fbiom.2024.1458672

OPEN ACCESS

APPROVED BY
Frontiers Editorial Office,
Frontiers Media SA, Switzerland

*CORRESPONDENCE
April M. Kloxin,
akloxin@udel.edu
Catherine A. Fromen,
cfromen@udel.edu

†These authors have contributed equally to this work and share last authorship

RECEIVED 02 July 2024
ACCEPTED 03 July 2024
PUBLISHED 17 July 2024

CITATION
Graf J, Bomb K, Trautmann-Rodriguez M, Jarai BM, Gill N, Kloxin AM and Fromen CA (2024), Corrigendum: Macrophage variance: investigating how macrophage origin influences responses to soluble and physical cues with immortalized vs. primary cells in 2D and 3D culture.
Front. Biomater. Sci. 3:1458672.
doi: 10.3389/fbiom.2024.1458672

Corrigendum: Macrophage variance: investigating how macrophage origin influences responses to soluble and physical cues with immortalized vs. primary cells in 2D and 3D culture

Jodi Graf[1], Kartik Bomb[1], Michael Trautmann-Rodriguez[1], Bader M. Jarai[1], Nicole Gill[1], April M. Kloxin[1,2*†] and Catherine A. Fromen[1*†]

[1]Department of Chemical and Biomolecular Engineering, University of Delaware, Newark, DE, United States, [2]Department of Materials Science and Engineering, University of Delaware, Newark, DE, United States

KEYWORDS

macrophage, hydrogel, biomaterials, innate immune cell, polarization, 3D culture

A Corrigendum on
Macrophage variance: investigating how macrophage origin influences responses to soluble and physical cues with immortalized vs. primary cells in 2D and 3D culture

by Graf J, Bomb K, Trautmann-Rodriguez M, Jarai BM, Gill N, Kloxin AM and Fromen CA (2024). Front. Biomater. Sci. 3:1399448. doi: 10.3389/fbiom.2024.1399448

In the published article, there was an error in Figure 9G as published. The labels on the images "BMM" and "Raw264.7" were inadvertently switched**.** The corrected figure and its caption appear below.

The authors apologize for this error and state that this does not change the scientific conclusions of the article in any way. The original article has been updated.

Publisher's note

All claims expressed in this article are solely those of the authors and do not necessarily represent those of their affiliated organizations, or those of the publisher, the editors and the reviewers. Any product that may be evaluated in this article, or claim that may be made by its manufacturer, is not guaranteed or endorsed by the publisher.

10.3389/fbiom.2024.1458672

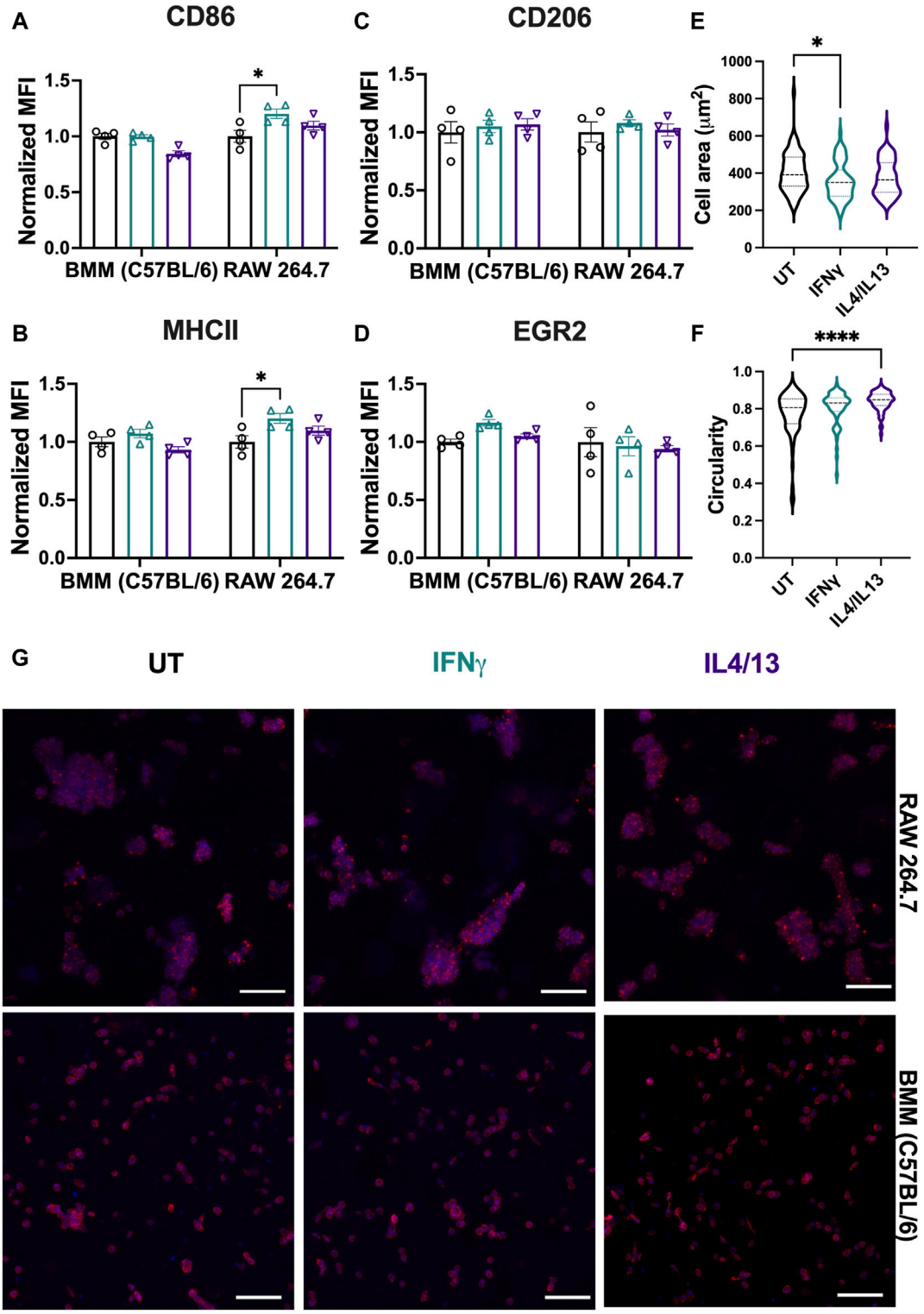

FIGURE 9
Effect of soluble stimuli on macrophage polarization in well-defined, bioprinted 3D cultures. Effect of polarization stimuli on macrophage polarization was determined for RAW 264.7 cells and primary BMMs (C57BL/6) in 3D culture (1.1 kPa PEG-peptide hydrogels with RGD, GFOGER, YIGSR, and HA). **(A)** CD86 and **(B)** MHCII were used as M1 markers. **(C)** CD206 and **(D)** EGR2 were used as M2 markers. All data are normalized to the UT control for the respective cell type. **(E)** Cell area and **(F)** circularity were quantified for all the cell types across different conditions. **(G)** Representative images of BMMs with nuclei (blue) and F-actin (red) qualitatively show morphology of BMMs across all the treatment groups. Statistics were performed using Tukey's *post hoc* test with one-way ANOVA. *$p < 0.05$, **$p < 0.01$, ***$p < 0.001$, ****$p < 0.0001$." Scale bar: 100 μm.

frontiers | Frontiers in Biomaterials Science

TYPE Original Research
PUBLISHED 25 June 2024
DOI 10.3389/fbiom.2024.1362599

OPEN ACCESS

EDITED BY
Jenny Robinson,
University of Washington, United States

REVIEWED BY
John Clegg,
University of Oklahoma, United States
Gemma Palazzolo,
Italian Institute of Technology (IIT), Italy
M. Tyler Nelson,
Wright-Patterson Air Force Base, United States

*CORRESPONDENCE
Chiara Tonda-Turo,
chiara.tondaturo@polito.it

†These authors have contributed equally to this work

RECEIVED 28 December 2023
ACCEPTED 06 June 2024
PUBLISHED 25 June 2024

CITATION
Licciardello M, Traldi C, Bortolameazzi M, Testore D, Ciardelli G and Tonda-Turo C (2024), Aligned polycaprolactone/polyaniline electrospun nanofibers for directing neural stem cell differentiation and neuron arrangement.
Front. Biomater. Sci. 3:1362599.
doi: 10.3389/fbiom.2024.1362599

Aligned polycaprolactone/polyaniline electrospun nanofibers for directing neural stem cell differentiation and neuron arrangement

Michela Licciardello[1,2,3†], Cecilia Traldi[1,2,3†], Matteo Bortolameazzi[1,2,3], Daniele Testore[1,2,3], Gianluca Ciardelli[1,2,3,4] and Chiara Tonda-Turo[1,2,3*]

[1]Department of Mechanical and Aerospace Engineering, La.Di.Spe Bioengineering, Politecnico di Torino, Turin, Italy, [2]POLITO BIOMedLAB, Politecnico di Torino, Turin, Italy, [3]Interuniversity Center for the Promotion of the 3Rs Principles in Teaching and Research, Pisa, Italy, [4]National Research Council-Institute for Chemical and Physical Processes (CNR-IPCF), Pisa, Italy

The use of engineered biomimetic substrates combined with neural stem cells (NSCs) constitutes a promising approach to develop reliable *in vitro* models of the nervous tissue. The fabrication of scaffolds with suitable compositional, topographical, and electrical properties is crucial for directing neural cell adhesion, differentiation, and arrangement. Herein, we propose the development of electroconductive polycaprolactone/polyaniline (PCL/PANI) electrospun mats as functional substrates for NSC culture. A rotating drum collector was employed to obtain fibers with aligned geometry. According to the results, the increase in alignment contributed to the reduction of fiber diameter and the increase of scaffold mechanical properties in terms of elastic modulus and tensile strength. *In vitro* experiments demonstrated the ability of PCL/PANI membranes to support NSC attachment and growth, as well as significantly foster neuronal differentiation. Furthermore, the presence of an aligned pattern was shown to effectively influence the arrangement of NSC-derived neurons, confirming the potential of this substrate for the design of a physiologically relevant culture platform for *in vitro* investigation of the nervous tissue.

KEYWORDS

electrospinning, electrical activity, topographical cue, ECM-like scaffolds, biomimetic substrates, *in vitro* nervous system modeling

1 Introduction

The nervous system is commonly considered one of the most complex systems in the human body. Due to its unique structural and functional characteristics, its pathophysiology is yet poorly understood, making the treatment of neurological disorders extremely challenging (Lu et al., 2022). Nervous tissue damage, caused by neurodegenerative conditions or traumatic injuries, often results in the progressive loss of neuronal cells and disruption of axonal bundles, leading to the interruption of nervous signal transmission below the injured segments. Indeed, the restoration of neuronal connectivity and the recovery of tissue functionality are significantly hampered by the

highly neurotoxic environment proper of chronic neurodegeneration and the poor regenerative potential of neurons, especially in the case of the central nervous system. Additionally, efficient clinical treatments are still lacking in this field, as existing therapies are limited to preventing secondary injury effects and are proving to be ineffective in curing neuronal dysfunction (Kaplan and Levenberg, 2022). Recently, neural tissue engineering has provided novel strategies for the *in vitro* modeling of the nervous system, contributing to the understanding of many mechanisms involved in neurological disorders, and the development of innovative regeneration approaches (Qiu et al., 2020). Indeed, the development of physiologically relevant *in vitro* systems is crucial for the identification of molecular pathways linked to tissue regeneration and holds great potential in drug screening. Therefore, significant efforts have been made by neural researchers to develop functional biomimetic platforms, able to recreate *in vitro* the distinctive properties of the nervous tissue (Rouleau et al., 2023). A wide range of biomaterials and biofabrication methods have been explored to replicate the native extracellular composition and structure and provide appropriate stimuli for directing neural cell behavior and maturation *in vitro*.

Among the numerous techniques exploited for the fabrication of bioengineered substrates (Babaliari et al., 2018; Cadena et al., 2021; Traldi et al., 2023), electrospinning technology has attracted considerable attention in neural tissue engineering and *in vitro* modeling, thanks to its ability to simply fabricate fibrous substrates resembling fiber-shaped cellular assemblies specific to nervous tissue structures (Hu et al., 2022). Electrospinning is a versatile technique that exploits the application of a high voltage between the needle of a syringe (containing the solution) and the collector plate (for the fiber deposition) (Isaac et al., 2021), to produce micro or nanofibrous substrates with a high surface-to-volume ratio and an interconnected porous structure. An appealing aspect of this approach is the possibility to obtain structures with different compositions, topography, and, consequently, properties by tuning the solution and process parameters (Giannitelli et al., 2018). Several studies have reported the use of electrospinning for the development of fibrous substrates that guide neural cell activity and nervous tissue regeneration, by providing several stimuli, such as biochemical (Cheong et al., 2019; Zhu et al., 2020), topographical (Gnavi et al., 2015b; 2015a; Karimi et al., 2018; Wu et al., 2020), or electrical (Zha et al., 2020; Zhang et al., 2021) cues.

Substrate conductivity is a key factor for electro-active tissue such as nervous tissue (Keshvardoostchokami et al., 2021). Indeed, electrical activity is a distinguishing feature of nervous tissue that can be exploited to guide tissue regeneration and enhance the biomimicry of tissue graft and *in vitro* models (Bierman-Duquette et al., 2022). Conductive polymers, such as poly (pyrrole) and PANI, have been used to confer electrical activity to nervous tissue-engineered scaffolds (Farkhondehnia et al., 2018; Zhao et al., 2018; Garrudo et al., 2019; Guo et al., 2023) thereby promoting neural cell differentiation and the formation of longer neurites (Jin and Li, 2015). In particular, PANI is widely selected for the preparation of electrospun scaffolds (Razak et al., 2015; Garrudo et al., 2019).

In the work of Garrudo et al. (2021), the author described the optimization of PANI and PCL ratio to obtain random nanofibers with ideal electroconductive properties and high biocompatibility for NSC culture.

However, due to its brittle nature and low processability, the blending of PANI with natural or synthetic polymers is required to obtain effective scaffolds for tissue engineering approaches (Palaniappan and John, 2008; Balint et al., 2014; Peidavosi et al., 2022). For instance, Peidavosi et al. (2022) reported the potential application of blending PANI with PCL and Barium Titanate to fabricate electrospun random mats as biocompatible substrates for bone cell culture.

In addition to electrical activity, the alignment of ECM and cells is a distinctive feature of nervous tissue (Chen et al., 2019). Then, many attempts have been made to produce scaffolds with an anisotropic pattern, intended to guide neural cell migration, differentiation, and out-growth by influencing the distribution of focal adhesion and the arrangement of actin filaments (Gnavi et al., 2015a; Kennedy et al., 2017; Ferraris et al., 2020; Hu et al., 2022). Electrospun substrates with aligned patterns have been successfully obtained by using different strategies (Jha et al., 2011; Amores de Sousa et al., 2020; Asheghali et al., 2020; Li et al., 2022). For instance, Amores de Sousa et al. (2020) produced aligned PCL nanofibers through a parallel plate-based collector to investigate the role of substrate morphology in directing NSC fate DSL. Differently, a touch-spun method was used in the work of Asheghali et al., who fabricated PCL nanofibrous mats with high control of fiber alignment, crystallinity, and diameter. The authors demonstrated the preferential orientation of NSCs according to the fiber main direction (Asheghali et al., 2020). Rotating drum collectors have been widely used to obtain aligned fibers through electrospinning technology, thanks to the possibility of tailoring scaffold properties by changing collection speed (Gnavi et al., 2015a; Zhu et al., 2015; Nitti et al., 2018; He et al., 2020). For example, Zhu et al. reported the fabrication of a highly aligned PCL electrospun substrate by using a rotating drum collector. Aligned fibers better promoted axonal growth and extension compared to random substrates (Zhu et al., 2015).

Furthermore, several groups demonstrated that the combination of electrical and topographical cues promotes and enhances neural cell growth and differentiation (Yang et al., 2016; Farkhondehnia et al., 2018; Qing et al., 2018; Eftekhari et al., 2020). As previously reported by Yang et al. (2016) the synergic effect of substrate anisotropy and conductivity enhanced the differentiation of rat pheochromocytoma PC12-L cells into neurons. Qing et al. (2018) fabricated an aligned electrospun silk mat functionalized with conductive reduced graphene paper that promoted neuronal differentiation of SH-SY5Y cells and the establishment of an interconnected neural network. In another work, Farkhondehnia et al. (2018) prepared aligned electrospun conductive nanofibers, composed of PANI/PCL/poly lactic-co-glycolic acid and explored the effect of topography and electrical stimulation on the proliferation and morphology of glioblastoma cells (A-172 cell line).

Recently, we described the preparation of biocompatible PCL/PANI electrospun mats as a promising substrate for tissue engineering applications (Licciardello et al., 2021). Herein, we explored the potential of PCL/PANI blend to obtain an electroconductive nanofibrous scaffold with aligned geometry by employing a rotating drum collector to mimic the anisotropic structure and electroactive properties of nervous tissue. The collector speed was optimized to obtain nanofibers with defect-free and highly oriented morphology. PCL/PANI nanofibrous membranes were characterized in terms of morphology, mechanical behavior, and wettability to evaluate the influence of

fiber alignment on scaffold physical properties. Then, we explored the feasibility of using PCL/PANI mats to establish a biomimetic neural cell culture system and create an optimal microenvironment for the growth and maturation of neural cells. In particular, we evaluate the effect of substrate composition and topography on NSC differentiation and arrangement. Indeed, *in vitro* experiments demonstrated that the fabricated scaffold effectively supports the growth and differentiation of NSCs in both neuronal and glial phenotypes recapitulating the *in vivo* multi-cellular composition. Immunofluorescence analysis underlined the ability of ECM-like nanofibrous mats to steer neuronal differentiation rather than standard 2D culture. In addition, when cultured on aligned PCL/PANI mats, the arrangement and neurite outgrowth of NSC-derived neurons were strongly influenced by the morphological cue of the substrate.

2 Materials and methods

2.1 Fabrication and characterization of PCL/PANI electrospun membranes

2.1.1 Formulation of solution

A PCL/PANI blended solution was formulated as previously described by authors (Licciardello et al., 2021). Briefly, 19 mg of (1S)-(+)-10-camphorsulfonic acid (CSA, 99%, Sigma Aldrich, Italy) were dispersed in 3 mL of 1,1,1,3,3,3-Hexafluoroisopropanol-d2 (HFP, 99% purity, Carlo Erba Reagents, Italy). After complete solubilization, 15 mg of PANI (emeraldine base, Mw = 100 kDa, Sigma Aldric, Italy) was added. The solution was sonicated for 3 min at 20 kHz and then stirred for 4 h, obtaining the PANI-doped solution (PANI:CSA). Meanwhile, a solution of PCL was prepared by dispersing 500 mg of PCL (Mn = 80 kDa, Sigma Aldrich, Italy) in 2 mL of HFP for 3 h under magnetic stirring. The PANI:CSA and PCL solution were mixed and left under stirring overnight, obtaining the PCL/PANI blended solution.

2.1.2 Evaluation of electroconductive properties of PCL/PANI

The conductivity of PCL/PANI blend was evaluated using a four-point probe instrument (Ossila, United Kingdom). The measurements were first performed on PCL/PANI films in a dry state to evaluate the effect of PANI on the electroconductive properties of PCL/PANI blend. Hence, PCL/PANI solution was evenly spread on a glass petri dish and left to dry overnight at room temperature (RT). In addition, a film of pure PCL was also prepared from a 10% w/v PCL solution in HFP. The conductivity of PCL/PANI electrospun nanofibers was measured in a wet state after incubating the membranes in deionized water overnight. The analysis was also conducted on electrospun PCL mats as controls. Before analysis, the obtained films and membranes were cut into small square specimens and their thickness (t) was measured through a digital caliber. The sheet resistance (R_s) was detected for each sample (n = 3 for each condition). Subsequently, resistivity (ρ) and conductivity (σ) of the samples were also calculated according to the following equations:

$$\rho = R_s{}^{*}t$$

$$\sigma = \frac{1}{\rho}$$

The conductivity values were reported as mean ± standard deviation (std dev).

2.1.3 Electrospinning of PCL/PANI membrane

The electrospun membranes were obtained using Novaspider instrument (CIC nanoGUNE, Spain) in vertical configuration, using the previously optimized parameters (20 kV voltage, 1,000 μL h^{-1} flow rate and 20 cm distance) (Licciardello et al., 2023). The electrospun fibers were collected on a plane collector or rotating drum, obtaining random (coded as PCL/PANI_RDN) or aligned (coded as PCL/PANI_ALG) fibers, respectively. To assess the influence of speed on fiber orientation and morphology, two drum speeds were tested: 800 rpm (coded as ALG_low speed) and 3,200 rpm (ALG_high speed). After fabrication, the resulting membranes were dried overnight at RT.

2.1.4 Scanning electron microscopy analysis (SEM)

The morphological features of PCL/PANI_RDN and PCL/PANI_ALG electrospun mats were investigated through scanning electron microscopy (SEM, Tescan Vega). Before analysis, all the samples were cut into 1 cm^2 pieces and coated with a thin platinum layer using the sputtering instrument. ImageJ software was used to quantify the average diameter (n = 100 measurements for each sample). Moreover, the fiber alignment was evaluated by ImageJ Directionality plugin analyzing the orientation of both aligned and random fibers and quantifying the percentage of fibers oriented in the preferential direction.

2.1.5 Uniaxial tensile tests

The mechanical properties of membranes were evaluated using the uniaxial tensile instruments MTS QTestTM/10 equipped with a fixed lower crossbar and an upper mobile crossbar. Before tests, the samples were cut in dog-bone shape and then mounted between the grips of the instruments. The samples (n = 3 samples for each membrane type) were tested at a displacement of 2 mm/min using a 10 N load cell. The stress-strain curves of PCL/PANI_RND and PCL/PANI_ALG samples were plotted and used to calculate Young's modulus (E), ultimate tensile strength (UTS) and strain at failure (ε %).

2.1.6 Transwell insert modification

Transwell inserts (CellQART®, SABEU GmbH & Co. KG, Germany) were modified to lodge the electrospun mats, as previously described (Licciardello et al., 2023). Briefly, the poly (ethylene terephthalate) (PET) membranes were removed from the inserts. Sylgard 184 Polydimethylsiloxane base (PDMS, VWR) and the curing agent were mixed in a ratio of 10:1 wt./wt obtaining a viscous PDMS solution. A thin layer of PDMS was applied on the outer walls of the plastic inserts and a first incubation was performed at 90°C for 10 min to allow a pre-curing of PDMS. The PCL/PANI_RND and PCL/PANI_ALG mats were cut into 3 cm × 3 cm pieces and then positioned on the support. The complete crosslinking of PDMS was promoted by maintaining

the inserts at 70°C for 2 min, thus obtaining the modified transwell systems (coded as PCL/PANI TWs).

2.1.7 Cold atmospheric plasma treatment

The electrospun mats were treated with the Argon cold atmospheric plasma process using Stylus Plasma Noble (Nadir S. r.l, Italy) under the previously optimized conditions (Licciardello et al., 2021): 10 kV_{pp} high voltage, 9 W of radiofrequency power and 7.5 slm argon flux. PCL/PANI TWs were positioned on the flat support of the instruments and then treated with plasma by manually moving the stylus on the apical and basolateral surfaces of the mats.

2.1.8 Water contact angle (WCA) measurement

The water contact angle of atmospheric plasma untreated and treated samples of electrospun membranes was evaluated using the Drop Shape Analyzer apparatus equipped with Advance software (Krüss Gmbh, Germany) for data acquisition. A drop of 2 µL of milliQ water was applied on the basolateral side of the PCL/PANI TWs and the WCA measurements (n = 3 for each sample) were recorded using the ellipse fitting method of the data acquisition software.

2.2 *In vitro* cell cultures

2.2.1 NSC culture on PCL/PANI electrospun membranes

Mouse NSCs (NE-4C, ATCC) were cultured in a growth medium composed of Eagle's Minimum Essential Medium (EMEM, ATCC), supplemented with 10% fetal bovine serum (FBS, Gibco) and 1% L-glutamine (L-Glu, Gibco). Cells were maintained at 37°C in a humidified atmosphere of 5% CO_2 on tissue culture flasks. Before NSC seeding, PCL/PANI TWs were subjected to atmospheric plasma treatment to enhance their wettability. Then, PCL/PANI TWs were sterilized through incubation in 2% antibiotic-antimycotic solution (Sigma Aldrich) overnight, followed by UV light irradiation for 1 h. NSCs were seeded at a density of 2×10^5 cells/cm^2 on the apical side of PCL/PANI TWs after conditioning the membranes with the growth medium for an hour. NE-4C cells (2×10^5 cells/cm^2) were also cultured on aligned PCL TWs and glass coverslips as controls. For NSC differentiation, cells were cultured in the growth medium for 3 days (until reaching 80%–90% of confluency), and then they were treated with a differentiation medium comprising the growth medium supplemented by 10^{-6} M retinoic acid (RA, Sigma Aldrich) for 4°days. The culture medium was changed every 2 days. NE-4C cells (2×10^5 cells/cm^2) were also cultured on glass coverslips as a control. CellTiter-Blue® assay was used to evaluate NSC viability on PCL/PANI electrospun membranes and to assess the influence of both cold atmospheric plasma treatment and fiber alignment on cell attachment and proliferation. Four different conditions were tested: cells seeded on untreated random membranes (RND_untreated), plasma-treated random membranes (RND_treated), untreated aligned membranes (ALG_untreated), and plasma-treated aligned membranes (ALG_treated). CellTiter-Blue® assay was performed at 1 day and 3 days of culture according to manufacturer protocol. Briefly, the culture medium was removed from PCL/PANI TWs (n = 3 for each condition) and samples were incubated in CellTiter-Blue® reagent solution (1:6 dilution in culture medium) at 37°C for 1 h. Fluorescence intensity values were recorded by using SYNERGYTM HTX multimode plate reader (BioTeK, Winooski, VM, United States) with a 530 nm excitation/590 nm emission filter set.

2.2.2 Fluorescence and immunofluorescence staining

Fluorescence staining of cell nuclei and cytoskeletons was performed on NSCs seeded on random (RND) and aligned (ALG) membranes after 3 days of culture. This test was performed to analyze NSC behavior on untreated and plasma-treated mats and qualitatively attest the cell confluency required before starting cell differentiation. For cell fixing, PCL/PANI TWs were rinsed with PBS, and incubated in paraformaldehyde 4% in PBS (PFA, Alfa Aesar) at RT. After 30 min, samples were washed twice with PBS and permeabilized with 0.5% v/v Triton X-100 solution in PBS for 10 min. Then, Flash Phalloidin Green 488 (Phalloidin, BioLegend) was added to the apical compartment of PCL/PANI TWs as 1:60 diluted solution in 1% v/v bovine serum albumin (BSA, Sigma Aldrich) in PBS and incubated for 40 min at RT, avoiding exposure to light. Lastly, 4′,6-Diamidino-2-Phenylindole, Dihydrochloride (DAPI, Invitrogen) was used to stain nuclei by incubation in 1:1,000 DAPI solution in PBS in the dark for 10 min.

For NSC differentiation, NE-4C cells were cultured on RND and ALG membranes for up to 14°days after RA induction. Immunofluorescence staining was carried out to investigate the expression of neuron- and astrocyte-specific markers on days 0, 7, and 14 from RA induction. PCL/PANI TWs were fixed with PFA 4% in PBS for 40 min at RT and permeabilized with 0.2% v/v Triton X-100 solution in PBS for 10 min. 2% BSA solution in PBS was used as blocking buffer and incubated for 1 h at RT. Later, primary antibody (Table 1) solutions (diluted in PBS with 1% v/v BSA and 0.1% v/v Tween 20) were added to the apical compartment of PCL/PANI TWs and maintained at 4°C overnight. After washing with 1% v/v BSA and 0.1% v/v Tween 20 solution in PBS, samples were incubated in secondary antibody solutions (Table 1) at RT for 1 h. Then, samples were rinsed with PBS and cell nuclei were stained with DAPI as detailed above.

Before the imaging, the PCL/PANI membranes were separated from the TW inserts and mounted on glass coverslips by using Fluoromount™ Aqueous Mounting Medium (Sigma Aldrich). All images were acquired with the Eclipse Ti2 confocal microscope (Nikon). ImageJ software and the Directionality plugin were used for image analysis. The expression levels of differentiation markers were evaluated and reported as mean ± std dev of the fluorescence intensity of MAP2 and GFAP-related signals for NSC-derived neurons and astrocytes, respectively. In addition, the percentages of neuronal and astroglial cells were calculated considering MAP2 and GFAP stain-positive areas. Lastly, the assessment of neuron cytoskeleton orientation on aligned nanofibers was conducted by processing MAP2 images for NSC-derived neurons. Specifically, the alignment level of neurons was calculated as the difference in degrees between the main orientation angles of nanofibers and neurofilaments, obtained by Fourier spectrum analysis. For each experimental condition (n = 3), three image fields of each sample were considered.

TABLE 1 List of primary and secondary antibodies used for neural cell labeling in immunofluorescence staining.

Antibody	IgG subclass	Source	Dilution
Primary mouse anti-MAP2 (clone AP20)	IgG	Sigma Aldrich	1:500
Primary rabbit anti-GFAP (Polyclonal)	—	Agilent	1:500
Secondary Alexa Fluor 488 goat anti-mouse	IgG (H + L)	Invitrogen	1:1,000
Secondary Alexa Fluor 555 goat anti-rabbit	IgG (H + L)	Invitrogen	1:500

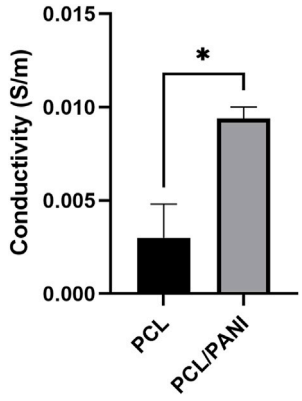

FIGURE 1
Analysis of the electroconductive properties of PCL/PANI electrospun membrane. Comparison of the conductivity values detected for PCL/PANI mats (PCL/PANI) and pure PCL mats (PCL) in wet conditions. Data are presented as mean ± std dev (n = 3). Statistical difference (*p < 0.1).

2.3 Statistical analysis

Statistical analyses were performed using GraphPad software (San Diego, CA, United States). A t-test analysis was used to evaluate differences in electroconductivity analysis, membrane mechanical properties, and cell alignment over time. A one-way ANOVA was conducted to record statistical differences in mat morphological properties and neural cell differentiation, while a two-way ANOVA was performed for the analysis of data from WCA, cell viability on the different substrates, and neural marker relative expressions.

3 Results

3.1 Electroconductive properties of PCL/PANI

The effect of PANI on the electroconductive properties of PCL/PANI was evaluated through the four-point probe method. According to the results, the PCL/PANI blend displayed a conductivity of 66 ± 15 S/m. As expected, the conductivity of pristine PCL was found to be undetectable due to the non-conductive nature of the material. Moreover, the electroconductive properties of PCL/PANI nanofibers were measured in wet conditions following overnight incubation in deionized water. As shown in Figure 1, the detected conductivity value of PCL/PANI mats was 0.009 ± 0.001 S/m. This value was significantly higher compared to PCL mats, which display a conductivity of 0.003 ± 0.002 S/m (0.01). These results demonstrated the strong contribution of PANI in conferring electroconductive properties to the PCL/PANI membranes, creating electrically conductive domains on the substrate surface, useful for electrical signal transmission (Chen et al., 2013).

3.2 Morphological characterization of PCL/PANI membranes

The morphology and the arrangement of fibers were evaluated through SEM analysis. As shown in Figure 2, all the obtained mats presented a defect-free nanofibrous morphology. In particular, fibers collected onto the flat collector presented a random orientation with an average diameter of 355 ± 90 nm. Interestingly, fibers produced using a low speed (800 rpm) had no preferential orientation and an average diameter of 342 ± 50 nm while membranes generated using high speed (3,200 rpm) consisted of aligned fibers with an average diameter of 224 ± 53 nm (p < 0.0001). Indeed, according to the analysis of fiber distribution, the orientation of ALG_high speed (Figure 2F) fibers resulted to be more pronounced in a preferred direction rather than RND (Figure 2D) and ALG_low speed samples (Figure 2E). Moreover, as shown in Figure 2F, the amount of fibers oriented in the same direction was significantly higher in ALG_high speed mats (about 80%) than RND and ALG_low speed which instead displayed comparable values. In particular, the high variability of the amount values for RND and ALG_low speed could be attributed to the absence of preferential orientation of the fibers. According to these results, the high speed of 3,200 rpm was used to produce mats for further characterization.

3.3 Mechanical characterization of PCL/PANI membranes

The mechanical characterization of the electrospun mats was performed through uniaxial tensile test. Figure 3A shows the stress-strain curves of PCL/PANI_RND and PCL/PANI_ALG. Both the curves exhibited a near-linear elastic trend until the electrospun samples broke. As shown in the histograms, the UTS and E of aligned fibers were found to be higher than the random counterparts. In particular, E increased from 14.33 ± 1.81 MPa for the PCL/PANI_RND fibers to 35.06 ± 5.06 MPa for PCL/PANI_ALG fibers (p < 0.001). Moreover, the increase in fiber alignment led to an increase in UTS from 10.31 ± 0.56 MPa for PCL/PANI_RND to 17.73 ± 3.04 MPa for PCL/PANI_ALG (p <

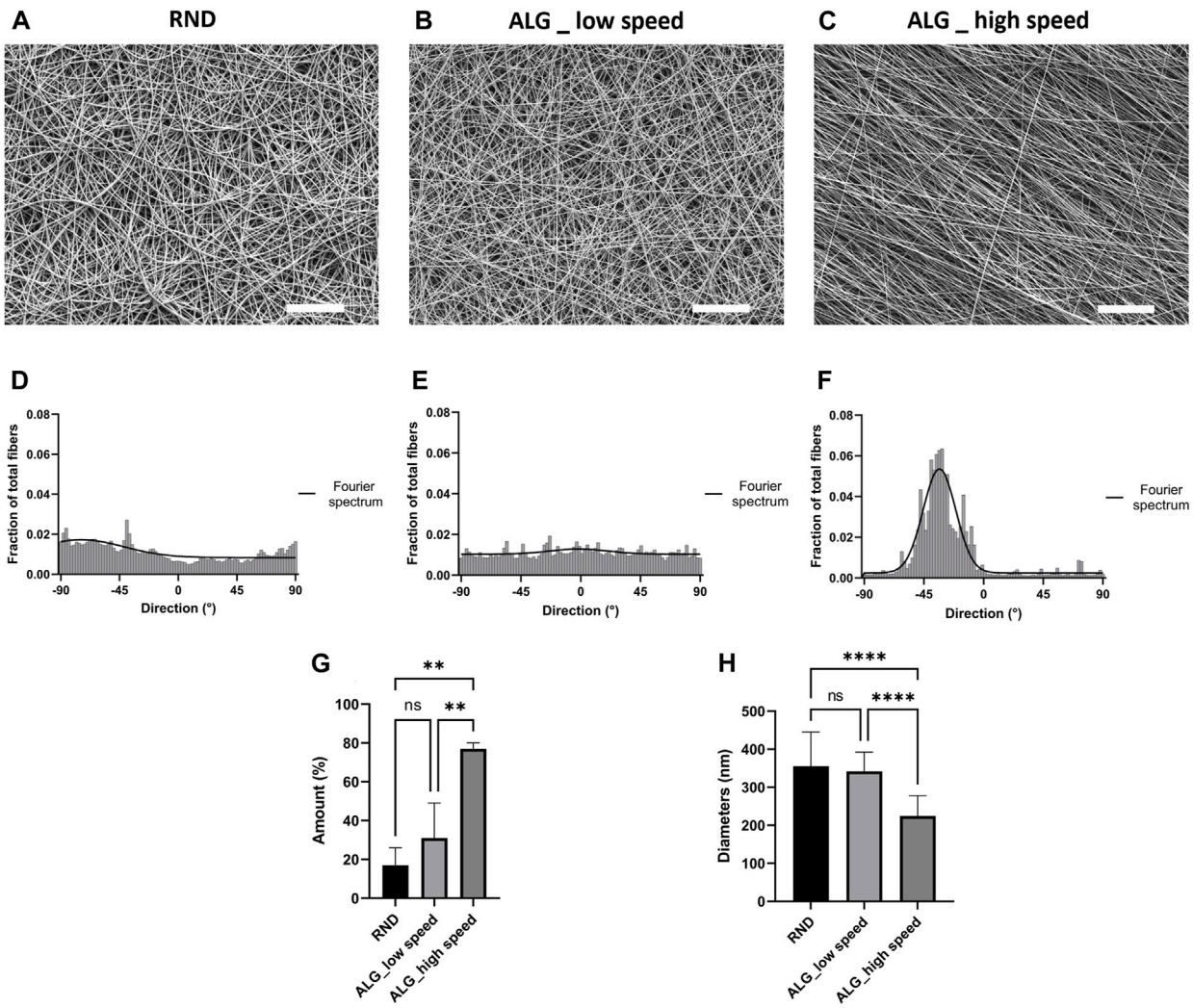

FIGURE 2
Morphological characterization of the electrospun membranes. **(A–C)** Representative SEM micrographs of RND **(A)**, ALG_low speed (800 rpm) **(B)** and ALG_high speed (3,200 rpm) **(C)** PCL/PANI nanofibers (scale bar = 20 μm). Quantification of fiber direction and Fourier spectrum of RND **(D)**, ALG_low speed (800 rpm) **(E)** and ALG_high speed (3,200 rpm) **(F)** PCL/PANI nanofibers. **(G)** Quantification of the amount of fibers oriented in the preferential direction. Data are presented as mean ± std dev (n = 3) **(H)** Comparison between RND, ALG_low speed and ALG_high speed fiber diameters Data are presented as mean ± std dev (n = 100). Statistical difference (**p < 0.01; ****p < 0.0001).

0.0001). Conversely, the ε% increased from 65.6 ± 8.2% for PCL/PANI_ALG fibers to 93.35% ± 11% for PCL/PANI_RND (p < 0.1).

3.4 Water contact angle and atmospheric plasma treatment of PCL/PANI membranes

The evaluation of the contact angle of the electrospun membranes was performed to investigate the influence of fiber topography and plasma treatment on the surface wettability of the electrospun mats. As shown in Figure 4, untreated PCL/PANI_RND and PCL/PANI_ALG displayed hydrophobic properties, presenting a water contact angle of 105.5° ± 6.6° and 119° ± 7.2° (p < 0.1), respectively. Thus, an atmospheric plasma treatment was performed to improve the surface wettability. The effective modification of the mat surface was confirmed by observing a reduction in water contact angle to 52.9° ± 19.3° and 76.3 ± 6.7 for PCL/PANI_RND (p < 0.0001) and PCL/PANI_ALG (p < 0.001), respectively. In addition, after plasma treatment, PCL/PANI_ALG presented higher mean values of water contact angles compared to PCL/PANI_RND, demonstrating that the topography slightly affects the surface properties of the substrate. In addition, a slight difference in WCA was detected between random and aligned samples, as the values of PCL/PANI_ALG were higher than PCL/PANI_RND, with a relevant statically difference after the plasma treatment.

3.5 NSC growth and viability on aligned PCL/PANI electrospun membranes

To validate the use of PCL/PANI electrospun membranes as culture substrates for neural cells, NE-4C cells were seeded on PCL/PANI TWs and cell viability was quantified after days 1 and 3 of

10.3389/fbiom.2024.1362599

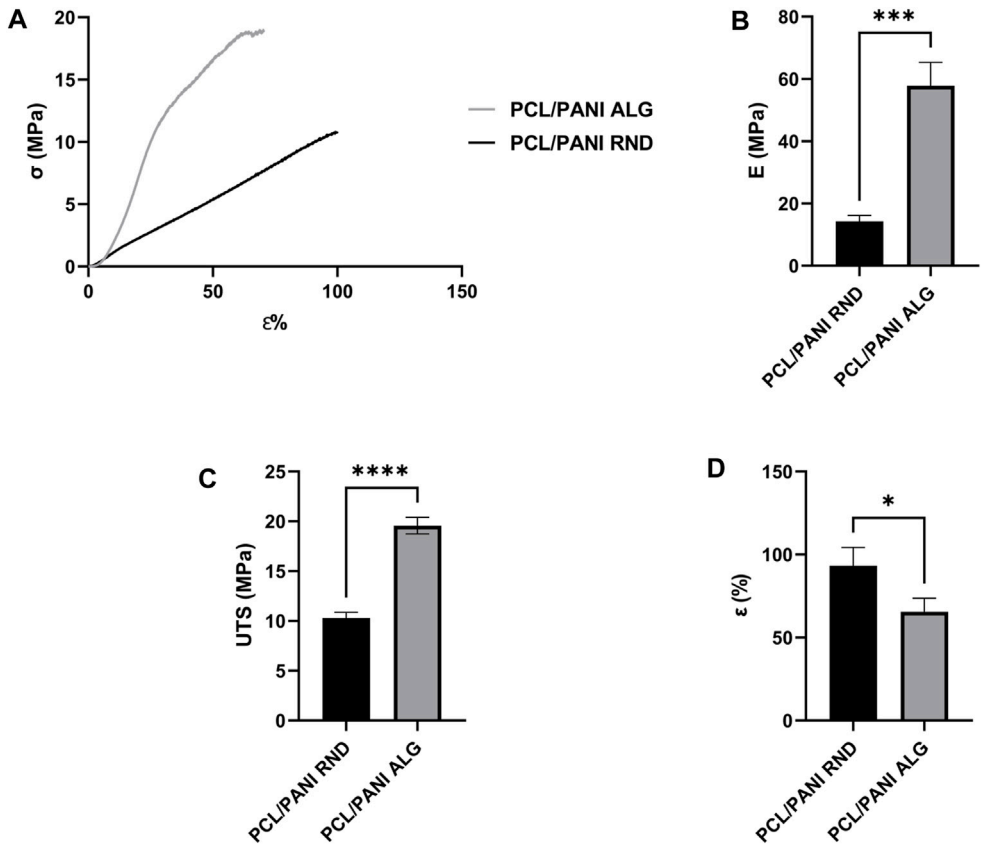

FIGURE 3
Mechanical characterization of the electrospun membranes. **(A)** Stress-strain curves of PCL/PANI_RND and PCL/PANI_ALG. Comparison between Young's modulus (E) **(B)**, ultimate tensile strength (UTS) **(C)** and strain at failure (ε %) **(D)**. Data are presented as mean ± std dev (n = 3). Statistical difference (*p < 0.1; ***p < 0.001 ****p < 0.0001).

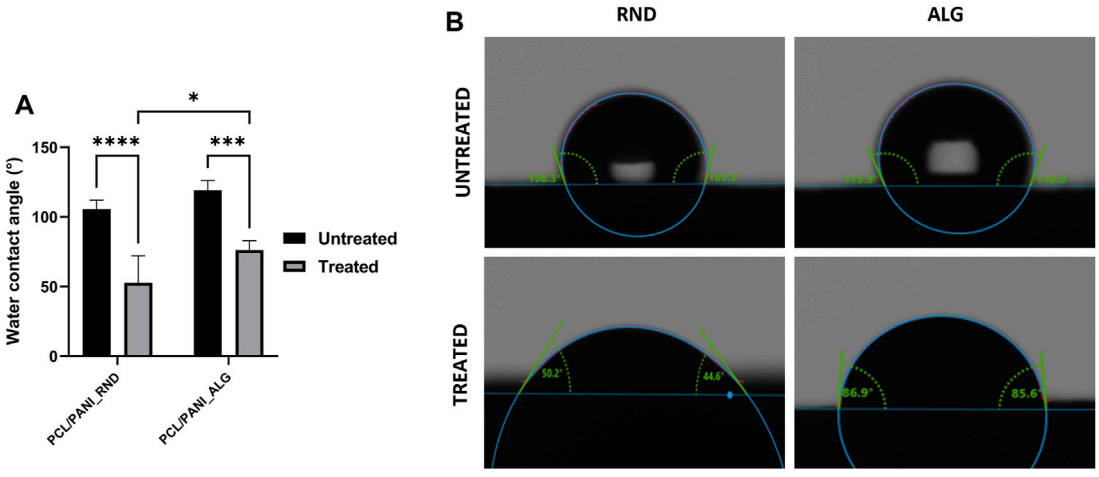

FIGURE 4
Characterization of surface wettability of the electrospun membranes. **(A)** Comparison of water contact angle values of RND and ALG mats before and after plasma treatment. **(B)** Representative contact angle images for droplets of water on RND and ALG mats before and after plasma treatment. Data are presented as mean ± std dev (n = 3). Statistical difference (*p < 0.1; ***p < 0.001 ****p < 0.0001).

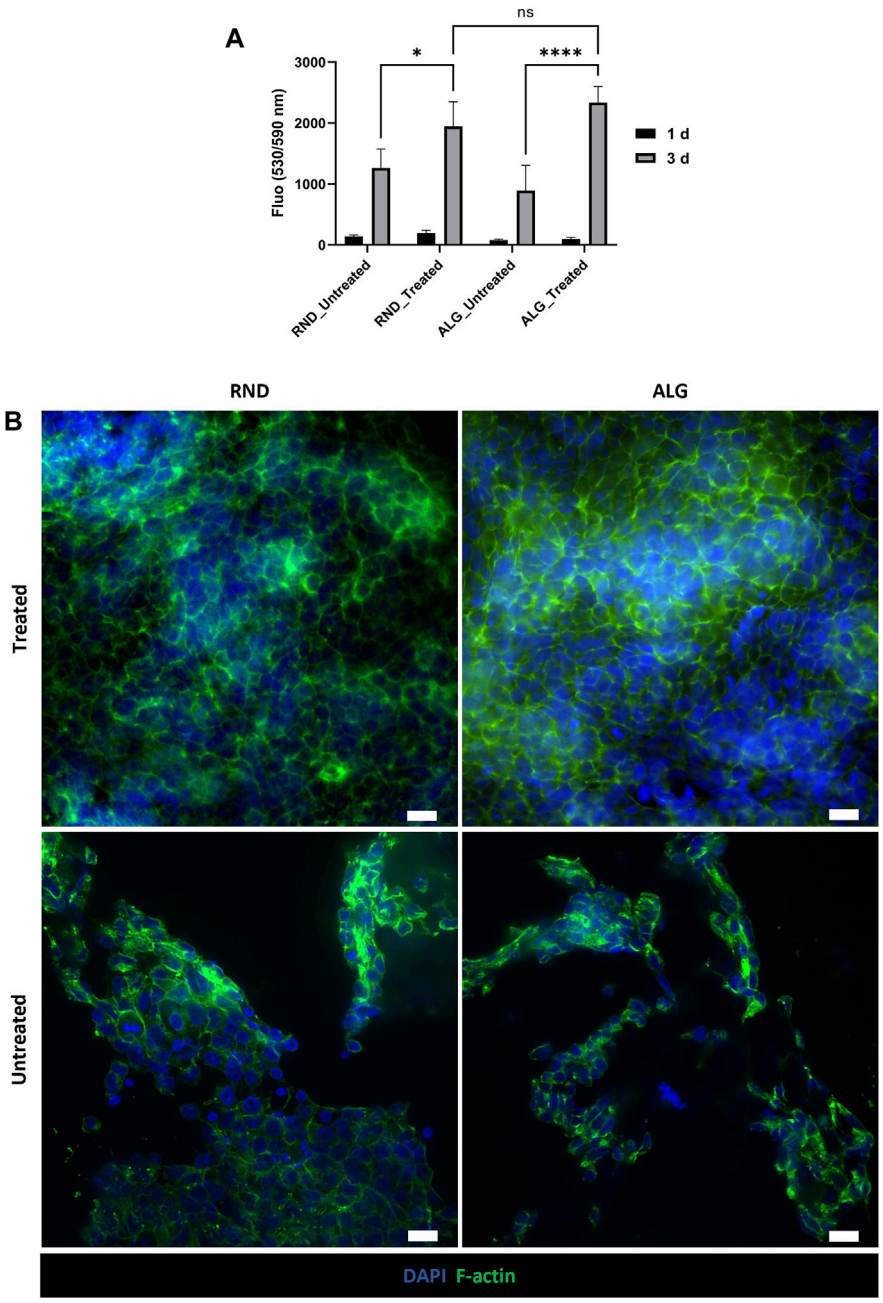

FIGURE 5
Evaluation of NSC behavior on PCL/PANI electrospun membranes. **(A)** Cell viability of NE-4C cells cultured on different substrates (plasma-treated or untreated, randomly oriented or aligned membranes). Data are presented as mean ± std dev (n = 3 biological replicates). Statistical difference (*p < 0.1; ****p < 0.0001). **(B)** Representative fluorescence images of cytoskeleton staining in NE-4C cell cultures on plasma-treated and untreated random and aligned membranes for 3 days (scale bar = 20 μm).

culture by using CellTiter-Blue® assay (Figure 5A). An increment in the recorded fluorescence values was detected after 3°days of culture in all the groups with slight differences among different samples, indicating cell proliferation over time. After 3°days, cell viability was significantly higher for cells seeded on plasma-treated membranes compared to untreated ones, while no statistically significant differences were observed between random and aligned fibrous membranes (Figure 5A). In addition, NSC morphology and distribution on plasma-treated and untreated membranes were evaluated by the fluorescence staining of cell nuclei and actin filaments (Figure 5B). At 3°days of culture, NSCs formed a uniform monolayer on both random and aligned fibers, showing characteristic epithelial-like morphology. On the contrary, cells cultured on untreated mats displayed a different behavior, as they tended to agglomerate in separated clusters, suggesting a reduction of initial cell adhesion thus inducing the formation of aggregates over time. According to these results, plasma-treated PCL/PANI TWs were selected for the subsequent studies.

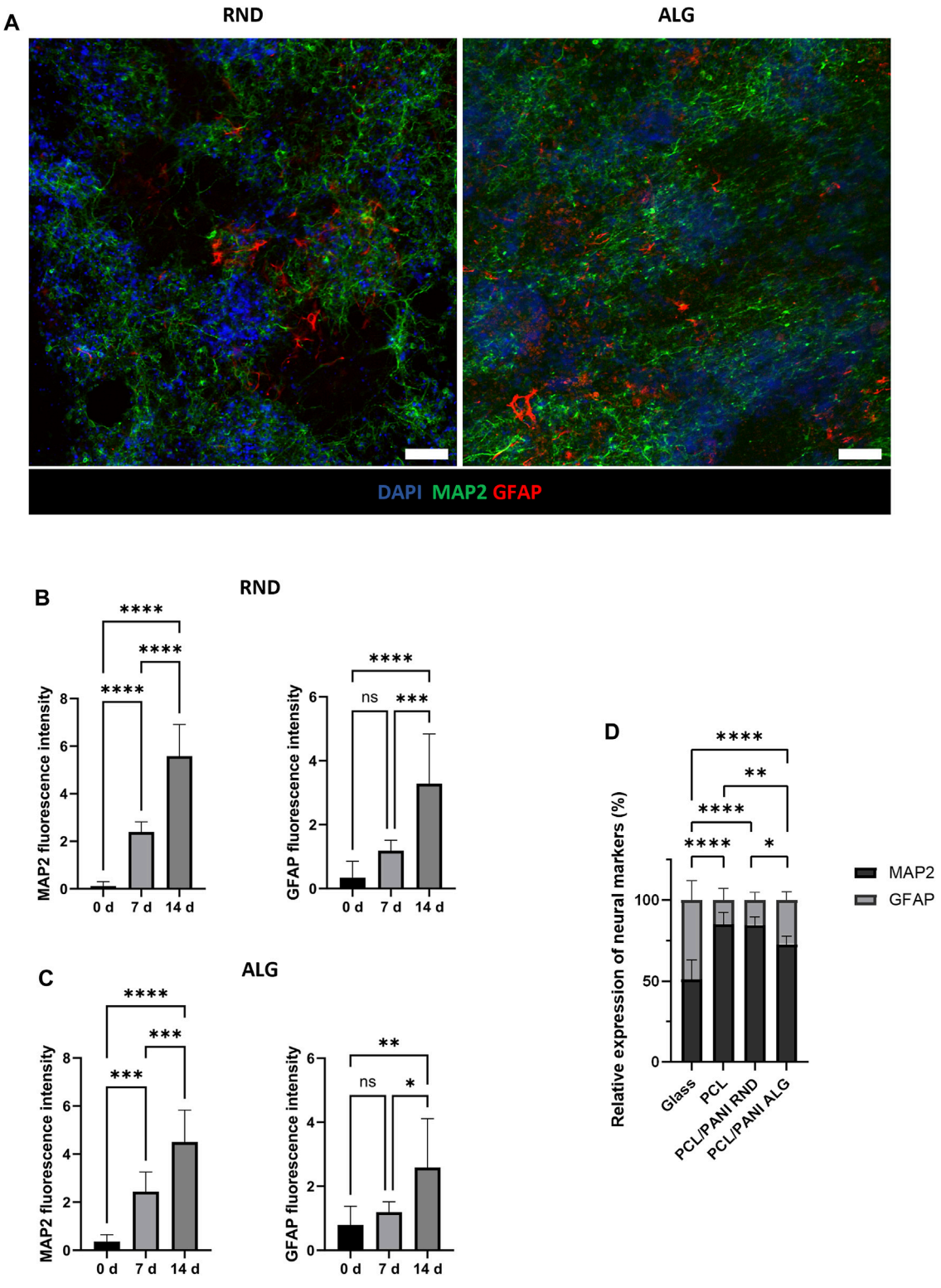

FIGURE 6
NSC differentiation on PCL/PANI electrospun membranes. **(A)** Representative immunofluorescence images for neuronal and astroglial markers in NE-4C cell cultures on both random (RND) and aligned (ALG) mats at 14°days after RA induction. Scale bar = 100 μm. **(B, C)** Expression levels of differentiation markers over time for NE-4C cells cultured on PCL/PANI random **(B)** and aligned **(C)** membranes. **(D)** Comparison of the percentages of MAP2 and GFAP stain-positive cells in NSC cultures on glass (Glass), aligned PCL mats (PCL), random PCL/PANI mats (PCL/PANI RND) and aligned PCL/PANI mats (PCL/PANI ALG) at 14°days after RA induction. Data are presented as mean ± std dev (n = 3 biological replicates; n = 3 technical replicates). Statistical difference (*p < 0.1; **p < 0.01; ***p < 0.001; ****p < 0.0001).

3.6 NSC differentiation on PCL/PANI electrospun membranes

The differentiation behavior of NSCs was evaluated by immunofluorescence analysis (Figure 6; Supplementary Figures S1, S2). The phenotypic characterization was conducted over 14°days after RA induction to assess the presence of different cell phenotypes and examine the effect of scaffold topography on NSC fate. Immunofluorescence staining revealed the presence of GFAP-expressing cells and MAP2-expressing cells after 14°days from RA induction, thus indicating NSC differentiation into astrocytes and mature neurons, respectively. In addition, MAP2-positive cells extended numerous neurites and interconnections all over the membranes (Figure 6A), suggesting high cell interaction with the substrate. It is noticed that MAP2 expression was upregulated already at 7°days compared to day 0 and it increased over the days, as confirmed by the greater fluorescence intensity (Figures 6B, C; Supplementary Figures S1, S2A). On the contrary, GFAP expression resulted to be not detectable at 0°days and 7°days, and GFAP-positive cells were stained only at 14°days (Figures 6B, C; Supplementary Figure S2B). Similar trends were observed in cells cultured on both aligned and random PCL/PANI TWs. For both the tested conditions, the number of MAP2-expressing cells was higher than GFAP ones, in contrast to cells seeded on glass. Indeed, the percentage of neurons exceeded over two times the percentage of astrocytes at 14°days, while it was quite comparable in the case of glass (Figure 6D; Supplementary Figure S3). NSCs cultured on PCL mats showed similar behavior, as no statistically significant differences were observed in the ratio of MAP2 to GFAP stain-positive cells between PCL fibers and random PCL/PANI fibers, while the ratio value was slightly higher compared to aligned PCL/PANI mats (Figure 6D; Supplementary Figure S3). Interestingly, the percentage of neurons was higher than that of astrocytes when NSCs were cultured on random PCL-PANI fibers (Figure 6D). Overall, these results revealed that PCL/PANI fibrous membranes can support NSC differentiation and promote the growth of mature neuron populations.

3.7 Influence of scaffold topography on neuronal cell alignment

The influence of fiber alignment on the behavior of neuronal cells was investigated by seeding NSCs on random and aligned PCL/PANI TWs. Differences in cell morphology and orientation were underlined by analyzing the arrangement of neuron-specific cytoskeletal protein on cells cultured in the two different conditions. According to the analysis of MAP2 staining, NSC-derived neurons exhibited directional neurite outgrowth along aligned fibers (Figures 7A, B, D), while they did not show a preferential orientation in the case of random membranes (Figure 7C). Indeed, the average difference between the orientation angles of MAP2-positive cells and aligned electrospun fibers was calculated to be around 11° at 7°days from RA induction (Supplementary Figure S4) and it is reduced by half in the late-stage differentiation (Figures 7D, E).

4 Discussion

Electrospun nanofibrous scaffolds have been extensively employed in nerve tissue engineering. Indeed, it is well known that the presence of topographical cues at the nanoscale level could play a pivotal role in influencing neural cell behavior, in terms of cell adhesion, proliferation, and maturation (Farrukh et al., 2018). On the other hand, electrical signals are crucial stimuli for electroactive tissue regeneration such as nerves (Rivers et al., 2002). Thus, the cell culture substrate should be specifically engineered to mediate electrical signaling between cells and respect the anisotropic structure of the native tissue.

In this work, an electroconductive substrate was obtained by blending PCL with PANI. To the best of our knowledge, electroconductive nanofibers have been obtained by using several synthetic polymers (alone or blended), however the use of electrospun aligned PCL/PANI nanofibers has not been reported for the fabrication of scaffolds for neural cell culture. Therefore, a detailed investigation of the effect of scaffold composition and anisotropy was conducted in this work, highlighting the contribution of the different substrate properties on guiding NSC fate.

Firstly, the analysis of surface conductivity on PCL/PANI films demonstrated that the presence of PANI conferred electroconductive properties to the PCL/PANI blend recording a conductivity of 66 ± 15 S/m. This value is in line with the conductivity achieved for PANI-based substrates as reviewed by Bierman-Duquette et al. (2022). Moreover, the inclusion of PANI into PCL nanofibers was shown to enhance the electroconductive properties of the electrospun membranes in wet conditions. PCL mats showed conductivity of 0.003 ± 0.002 S/m which is related to the presence of ions in the aqueous medium absorbed and retained by the nanofibrous substrate. The addition of the conductive dopant PANI in PCL/PANI nanofibers resulted in an overall increased conductivity (Figure 1), which is a combination of ionic-based conductivity of the absorbed medium and electron-based conductivity of the conductive polymer (Roshanbinfar et al., 2018). Indeed, PCL/PANI mats showed a conductivity of 0.009 ± 0.001 S/m which is in line with the values measured for PANI-based electrospun fibers reported in the literature (Garrudo et al., 2019, 2021).

Although previous studies evidenced that the combination of electrical and topographical features of the cell culture support can be an effective strategy to promote neural cell adhesion and neurite outgrowth, none of them have reported the ability of these substrates of modulating the co-differentiation of precursor cells in both neurons and astrocytes (Ghasemi-Mobarakeh et al., 2011). Anisotropic substrates have been shown to play a key role in providing topographical cues for neural cell body alignment along the fiber's axes (Wang et al., 2009; Badrossamay et al., 2014). To induce the fiber alignment, a drum collector was used during the electrospinning process. The influence of drum speed on fiber orientation was evaluated. In particular, the results of SEM analysis demonstrated that electrospun nanofibers became more aligned with increasing drum speed. Moreover, the Fourier spectrum analysis (Figure 2) revealed the presence of a sharper and higher peak of alignment for ALG_high speed mats compared to ALG_low speed that confirmed as the increase of collection speed

10.3389/fbiom.2024.1362599

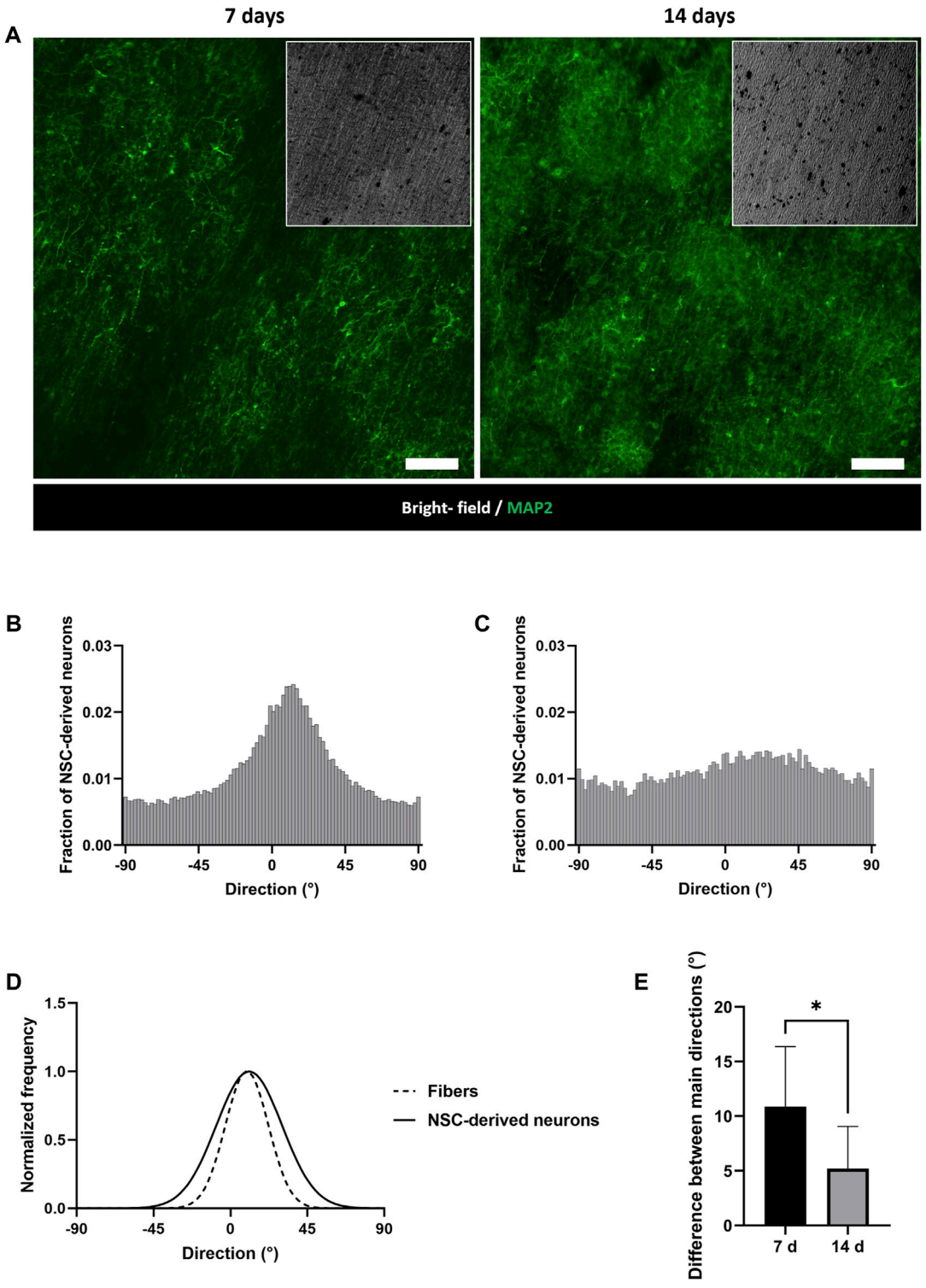

FIGURE 7
Evaluation of NSC-derived neuron orientation on PCL/PANI membranes. **(A)** Representative immunofluorescence images of MAP2-expressing cells on aligned mats at 7 and 14 days after RA induction. Scale bar = 100 μm. **(B, C)** Distribution of NSC-derived neuron directions on aligned **(B)** and random **(C)** PCL/PANI membranes at 14 days after RA induction. **(D)** Comparison between the main directions of NSC-derived neurons and fibers at 14 days after RA induction by Fourier spectrum analysis. **(E)** Comparison between the alignment levels of NSC-derived neurons at 7 and 14 days. Data are presented as mean ± std dev (n = 3 biological replicates; n = 3 technical replicates). Statistical difference (*p < 0.1).

led to a higher percentage of nanofibers oriented in a preferential direction. These findings are in line with previous reports (Nitti et al., 2018; He et al., 2020). In particular, the improvement of fiber alignment was previously ascribed to the increase in the difference between the drum surface speed and the final fiber speed, which is enhanced in the case of high collection speeds (Sadrjahani et al., 2010). Based on our results, the optimal fiber alignment was achieved with a speed of 3,200 rpm, allowing for the fabrication of highly oriented nanofibrous mats. The uniaxial tensile test demonstrated that fiber alignment led to an enhancement of scaffold mechanical properties in terms of Young's modulus and tensile strength. Several studies have investigated the effect of fiber alignment on the mechanical properties of electrospun mats, demonstrating that nanofiber orientation towards a preferential direction can lead to increased tensile strength and Young's modulus in electrospun mats (El-hadi and Al-Jabri, 2016; Merighi et al., 2019; Chen et al., 2021). Indeed, since the fiber orientation is in the direction of the load, the fiber's uniaxial orientation allows for the equal distribution of the tensile force to all fibers. Thus, the increase in tensile strength and Young's modulus was ascribed to the orientation of the molecular chains in the axis of the fiber. In particular, when aligned fibers are obtained through a rotating collector, its rotational speed leads to the application of mechanical forces to the polymeric jet, thus inducing the stretching of the polymer chains along the fiber axis. In addition, the morphological analysis highlighted a correlation between the fiber diameter and the drum speed, revealing that the fiber diameter decreased as the collector speed increased due to the higher stretching level imposed on fibers during the drum rotation (Medeiros et al., 2008). Several studies reported the correlation between fiber diameter and mechanical properties of the electrospun mats (Baji et al., 2010). The electrospun mats presented thinner diameters at higher collection speeds, leading to an increase in the membrane's strength (Shin et al., 2006; Pai et al., 2011; Yao et al., 2014; Pham et al., 2021). The surface properties of PCL/PANI membranes were improved by treating electrospun mats with atmospheric argon plasma. Indeed, PCL/PANI mats were found to be highly hydrophobic, displaying a contact angle higher than 100° regardless of fiber orientation. After plasma exposure, the detected values of wettability decreased to around 53° and 76°, for random and aligned fibers, respectively (Figure 4). The argon plasma treatment causes the formation of polar groups on fiber surfaces, allowing water to more easily enter the scaffold pores (Ivanova et al., 2018; Miroshnichenko et al., 2019; Licciardello et al., 2021). Additionally, the WCA was slightly higher in the case of aligned fibers, suggesting that fiber morphology also influences the wettability of PCL/PANI mats. Indeed, the presence of an aligned pattern results in changes in mat porosity and fiber diameter and consequently in the surface properties of the membranes. By comparing the results of the morphological analysis between random and aligned membranes, a reduction of fiber diameter was found with the increased level of alignment. These findings are consistent with the investigation of Sivan et al., who suggested that the value of the contact angle of PCL nanofibrous mats is inversely proportional to the diameter of the fibers, as it determines the extent of the contact area (Sivan et al., 2020).

The influence of scaffold anisotropy on cell viability and differentiation has been investigated *in vitro* using PCL/PANI membranes as culture substrates for neural cells. NSCs were successfully cultured on the electroconductive nanofibrous mats and differentiated into mature neuronal and astroglial cells. Viability analysis and fluorescence staining demonstrated that PCL/PANI membranes are able to support NSC attachment and growth, as confirmed by the formation of a confluent cell monolayer within 3 days of seeding (Figure 5B). A significant increase of viable cells was detected in the case of plasma-treated samples, confirming that the surface modification can improve scaffold hydrophilicity and then cell adhesion, reducing the formation of cell aggregates (Figures 5A, B). Indeed, it has been reported that surface wettability considerably affects the absorption and conformation of proteins from the culture medium, which subsequently mediate cell binding (Cai et al., 2020). Beyond scaffold surface properties, many other features such as scaffold topography and alignment are known to influence cell attachment and outgrowth. However, no significant differences have been noticed between random and aligned fibers in terms of NSC viability, as comparable values of fluorescence were reached at 3°days (Figure 5A). Additionally, the cell nuclei and F-actin staining did not show any changes in cell morphology and cytoskeleton arrangement according to fiber orientation (Figure 5B). It is reported in the literature that the effect of fiber alignment is strictly correlated with fiber diameters. Indeed, fibers displaying average diameters lower than around 700 nm were shown to promote the proliferation of NSCs, by forming uniform mats and minimizing the effects of topography in growth conditions (Christopherson et al., 2009; Garrudo et al., 2019). Accordingly, the calculated fiber diameters in our work were 224 ± 53 nm and 355 ± 90 nm, for aligned and random fibers, respectively, which are both included in the range cited above. These results suggest that plasma-treated PCL/PANI mats can support neural cell adhesion and growth without affecting their stemness state, as confirmed by the maintenance of NSC proper morphology and highly proliferative behavior.

Secondly, the differentiation of NSCs was performed by culturing them on PCL/PANI electrospun membranes to investigate the influence of scaffold anisotropy on NSC fate and maturation. NE-4C cells are known to have the capability of differentiating into neurons and astrocytes under RA treatment (Schlett and Madarász, 1997). After 14°days after RA induction, cells seeded on both random and aligned fibers expressed neuronal and astroglial markers and created interconnected neural networks on the entire membrane (Supplementary Figure S5; Supplementary Video S1). By analyzing the time course of marker expressions, the formation of neural aggregates displaying neuron characteristics was observed on day 7 after RA induction, while GFAP-expressing astrocytes appeared at 14°days (Figure 6; Supplementary Figure S2). This is in line with NE-4C neurogenesis stages described in the literature, where the onset of astroglia cells follows the main neuronal differentiation. Indeed, different studies reported that GFAP-positive cells were noted not sooner than the ninth day of RA treatment (Schlett and Madarász, 1997; Varga et al., 2008; Hádinger et al., 2009). Moreover, according to immunofluorescence images, the morphology and arrangement of differentiated NE-4C cells respected the characteristics reported in the literature, as interconnected neuronal aggregates were observed on a cell monolayer, while astrocytes were located inside and around the clusters (Figure 6A) (Varga et al., 2008). In addition, marker

stain-positive areas were calculated to estimate the number of cells undergoing neuronal and glial differentiations. According to the analysis, the percentage of cells expressing MAP2 was significantly higher than GFAP-labeled cells, confirming that NSCs preferentially differentiate into neurons on PCL/PANI mats. Indeed, neuronal cells resulted to be more than 70% of cells expressing neural markers, either in the case of random or aligned mats (Figure 6D). The same trend was also observed in cells cultured on PCL mats. Differently, the number of neurons and astrocytes was comparable when NE-4C cells were seeded on glass. In general, these results suggest that fiber-based substrates promoted neuronal differentiation, providing a biomimetic environment for neural cells. Indeed, although the values of Young's modulus in PCL-PANI mats are significantly higher than that of brain tissue, whose elastic modulus ranges from 0.1 to 1 kPa (Tarricone et al., 2022), they can be considered more similar to the one of native tissue compared to glass (~GPa) (Ford and Rajagopalan, 2018).

Interestingly, the ratio of neurons to astrocytes was higher for PCL/PANI random mats than aligned ones (Figure 6D). This aspect is apparently in contrast to what was reported in the work of Ashegali and colleagues, who showed a correlation between higher alignment and increased ratio of TUJ1-labeled neurons to GFAP-labeled astrocytes (Asheghali et al., 2020). Several studies underlined the importance of anisotropy in enhancing neuronal differentiation (Lim et al., 2010; Mohtaram et al., 2015; Eftekhari et al., 2020). However, it is well-documented that the mechanical properties of scaffolds are equally important in directing NSC fate (Farrukh et al., 2018). It is reported that NSCs preferentially differentiate into neurons on substrates having low elastic modulus while stiffer materials induce their differentiation into astrocytes (Saha et al., 2008; Ali et al., 2015). In this work, a higher percentage of astrocytes was detected on aligned fibers, which presented both a biomimetic aligned orientation and enhanced mechanical properties in terms of Young's modulus and tensile strength compared to random counterparts. Accordingly, the GFAP stain-positive area was higher in the case of NSC culture on glass, as cells were differentiated on stiff substrates (~GPa) (Ford and Rajagopalan, 2018). In summary, the capability of PCL/PANI nanofibrous mats in boosting the differentiation of cultured NSCs into neurons was demonstrated, in contrast to traditional over differentiation in glial cells, also evidencing the possibility of modulating the ratio between the two cell populations depending on substrate physical properties.

Lastly, the use of PCL/PANI mats in modulating neuron arrangement and neurite outgrowth was assessed. Several studies have shown the potential of aligned structures in directing neurite extension (Wang et al., 2009; Mohtaram et al., 2015; Hyysalo et al., 2017; Amores de Sousa et al., 2020). This aspect has been proven to be a very important factor for regulating *in vitro* neuronal activity (Hajiali et al., 2018) and significantly contributes to the maturation of *in vitro* neural tissues, especially in combination with exogenous electrical stimulation (Eftekhari et al., 2020). In our study, the effect of aligned fiber configuration was investigated on NSC-derived neurons. Specifically, neuronal morphology was evaluated by analyzing the localization of cytoskeleton protein with respect to fiber orientations. According to immunofluorescence imaging, cells cultured on aligned mats were arranged in a preferential direction, following fiber main orientation angles (Figures 7A, D). Indeed, by comparing the Fourier spectra of angle distributions, a difference lower than 5° was observed between the primary directions of neurons and fibers at 14°days (Figure 7E). On the contrary, a wide distribution was found in the case of neurons seeded on random mats, where no trend in cell orientation can be identified (Figure 7C). These results confirmed that the presence of aligned patterns in the PCL/PANI nanofibrous mats directly influenced neuronal cell spreading and neurite attachment and could provide contact guidance for axonal elongation towards a preferential direction.

5 Conclusion

In this work, the use of electroconductive PCL/PANI nanofibrous membranes was proposed to develop functional scaffolds for neural stem cell culture and nervous tissue modeling. The electrospinning process was employed to fabricate nanofibers in both random and aligned configurations, to mimic the typical nanofibrous and anisotropic architecture of the neural ECM. The interaction of NSCs with substrates having different physical and morphological properties was shown to stimulate specific cell responses in terms of cell differentiation and arrangement. The results of this work demonstrated that the nanofibrous structure of PCL/PANI mats significantly promoted the differentiation of NSCs into neurons compared to traditionally used glass substrates, supporting the establishment of an extended and interconnected neural network. Additionally, the presence of aligned patterns was proven to guide neuron orientation toward a preferential direction, providing biomimetic topographical cues for neurite outgrowth. The capability of this system to replicate some essential features of the *in vivo* microenvironment, such as tissue anisotropy and multi-cellular composition, makes it an attractive platform for the *in vitro* investigation of neuronal injuries and neurodegeneration, as well as the exploration of novel regenerative approaches. A step forward in model biomimicry would be the combined use of this platform with human induced pluripotent stem cell (hiPSCs) culture. Moreover, the electroactive properties of such nanofibrous substrates expand their applicability within dynamic systems for electrical stimulation or signal recordings, thus offering new opportunities for the creation of functional engineered tissue analogs.

Data availability statement

The original contributions presented in the study are included in the article/Supplementary Material, further inquiries can be directed to the corresponding author.

Author contributions

ML: Conceptualization, Data curation, Formal Analysis, Investigation, Methodology, Validation, Writing–original draft. CT: Conceptualization, Data curation, Formal Analysis, Investigation, Methodology, Validation, Writing–original draft. MB: Data curation, Investigation, Methodology, Writing–review and editing. DT: Methodology, Writing–review and editing. GC: Conceptualization, Funding acquisition, Resources, Writing–review

and editing. CT-T: Conceptualization, Data curation, Funding acquisition, Investigation, Methodology, Resources, Supervision, Writing–original draft, Writing–review and editing.

The author(s) declared that they were an editorial board member of Frontiers, at the time of submission. This had no impact on the peer review process and the final decision.

Funding

The author(s) declare that financial support was received for the research, authorship, and/or publication of this article. This project was carried out with the support of Fondazione Compagnia di San Paolo—Trapezio Call for Proposals-Target 1-project "Human multi-tissue platform for comprehensive evaluation of chemical toxicology on a chip."

Publisher's note

Conflict of interest

The authors declare that the research was conducted in the absence of any commercial or financial relationships that could be construed as a potential conflict of interest.

Supplementary material

The Supplementary Material for this article can be found online at: https://www.frontiersin.org/articles/10.3389/fbiom.2024.1362599/full#supplementary-material

References

Ali, S., Wall, I. B., Mason, C., Pelling, A. E., and Veraitch, F. S. (2015). The effect of Young's modulus on the neuronal differentiation of mouse embryonic stem cells. *Acta Biomater.* 25, 253–267. doi:10.1016/j.actbio.2015.07.008

Amores de Sousa, M. C., Rodrigues, C. A. V., Ferreira, I. A. F., Diogo, M. M., Linhardt, R. J., Cabral, J. M. S., et al. (2020). Functionalization of electrospun nanofibers and fiber alignment enhance neural stem cell proliferation and neuronal differentiation. *Front. Bioeng. Biotechnol.* 8, 580135–580216. doi:10.3389/fbioe.2020.580135

Asheghali, D., Lee, S. J., Furchner, A., Gruzd, A., Larson, S., Tokarev, A., et al. (2020). Enhanced neuronal differentiation of neural stem cells with mechanically enhanced touch-spun nanofibrous scaffolds. *Nanomedicine Nanotechnol. Biol. Med.* 24, 102152. doi:10.1016/j.nano.2020.102152

Babaliari, E., Kavatzikidou, P., Angelaki, D., Chaniotaki, L., Manousaki, A., Siakouli-Galanopoulou, A., et al. (2018). Engineering cell adhesion and orientation via ultrafast laser fabricated microstructured substrates. *Int. J. Mol. Sci.* 19, 2053. doi:10.3390/ijms19072053

Badrossamay, M. R., Balachandran, K., Capulli, A. K., Golecki, H. M., Agarwal, A., Goss, J. A., et al. (2014). Engineering hybrid polymer-protein super-aligned nanofibers via rotary jet spinning. *Biomaterials* 35, 3188–3197. doi:10.1016/j.biomaterials.2013.12.072

Baji, A., Mai, Y. W., Wong, S. C., Abtahi, M., and Chen, P. (2010). Electrospinning of polymer nanofibers: effects on oriented morphology, structures and tensile properties. *Compos. Sci. Technol.* 70, 703–718. doi:10.1016/j.compscitech.2010.01.010

Balint, R., Cassidy, N. J., and Cartmell, S. H. (2014). Conductive polymers: towards a smart biomaterial for tissue engineering. *Acta Biomater.* 10, 2341–2353. doi:10.1016/j.actbio.2014.02.015

Bierman-Duquette, R. D., Safarians, G., Huang, J., Rajput, B., Chen, J. Y., Wang, Z. Z., et al. (2022). Engineering tissues of the central nervous system: interfacing conductive biomaterials with neural stem/progenitor cells. *Adv. Healthc. Mater.* 11, 21015777–e2101628. doi:10.1002/adhm.202101577

Cadena, M., Ning, L., King, A., Hwang, B., Jin, L., Serpooshan, V., et al. (2021). 3D bioprinting of neural tissues. *Adv. Healthc. Mater.* 10, e2001600. doi:10.1002/adhm.202001600

Cai, S., Wu, C., Yang, W., Liang, W., Yu, H., and Liu, L. (2020). Recent advance in surface modification for regulating cell adhesion and behaviors. *Nanotechnol. Rev.* 9, 971–989. doi:10.1515/ntrev-2020-0076

Chen, C. H., Li, D. L., Chuang, A. D. C., Dash, B. S., and Chen, J. P. (2021). Tension stimulation of tenocytes in aligned hyaluronic acid/platelet-rich plasma-polycaprolactone core-sheath nanofiber membrane scaffold for tendon tissue engineering. *Int. J. Mol. Sci.* 22, 11215–11220. doi:10.3390/ijms222011215

Chen, M. C., Sun, Y. C., and Chen, Y. H. (2013). Electrically conductive nanofibers with highly oriented structures and their potential application in skeletal muscle tissue engineering. *Acta Biomater.* 9, 5562–5572. doi:10.1016/j.actbio.2012.10.024

Chen, Y., Taskin, M. B., Zhang, Z., Su, Y., Han, X., and Chen, M. (2019). Bioadhesive anisotropic nanogrooved microfibers directing three-dimensional neurite extension. *Biomater. Sci.* 7, 2165–2173. doi:10.1039/c8bm01603h

Cheong, H., Kim, J., Kim, B. J., Kim, E., Park, H. Y., Choi, B. H., et al. (2019). Multi-dimensional bioinspired tactics using an engineered mussel protein glue-based nanofiber conduit for accelerated functional nerve regeneration. *Acta Biomater.* 90, 87–99. doi:10.1016/j.actbio.2019.04.018

Christopherson, G. T., Song, H., and Mao, H. Q. (2009). The influence of fiber diameter of electrospun substrates on neural stem cell differentiation and proliferation. *Biomaterials* 30, 556–564. doi:10.1016/j.biomaterials.2008.10.004

Eftekhari, B. S., Eskandari, M., Janmey, P. A., Samadikuchaksaraei, A., and Gholipourmalekabadi, M. (2020). Surface topography and electrical signaling: single and synergistic effects on neural differentiation of stem cells. *Adv. Funct. Mater.* 30, 1–17. doi:10.1002/adfm.201907792

El-hadi, A. M., and Al-Jabri, F. Y. (2016). Influence of electrospinning parameters on fiber diameter and mechanical properties of poly(3-Hydroxybutyrate) (PHB) and polyanilines (PANI) blends. *Polym. (Basel)* 8, 97. doi:10.3390/polym8030097

Farkhondehnia, H., Amani Tehran, M., and Zamani, F. (2018). Fabrication of biocompatible PLGA/PCL/PANI nanofibrous scaffolds with electrical excitability. *Fibers Polym.* 19, 1813–1819. doi:10.1007/s12221-018-8265-1

Farrukh, A., Zhao, S., and del Campo, A. (2018). Microenvironments designed to support growth and function of neuronal cells. *Front. Mater.* 5, 1–22. doi:10.3389/fmats.2018.00062

Ferraris, S., Spriano, S., Scalia, A. C., Cochis, A., Rimondini, L., Cruz-Maya, I., et al. (2020). Topographical and biomechanical guidance of electrospun fibers for biomedical applications. *Polym. (Basel)* 12, 2896–2932. doi:10.3390/polym12122896

Ford, A. J., and Rajagopalan, P. (2018). Measuring cytoplasmic stiffness of fibroblasts as a function of location and substrate rigidity using atomic force microscopy. *ACS Biomater. Sci. Eng.* 4, 3974–3982. doi:10.1021/acsbiomaterials.8b01019

Garrudo, F. F. F., Chapman, C. A., Hoffman, P. R., Udangawa, R. W., Silva, J. C., Mikael, P. E., et al. (2019). Polyaniline-polycaprolactone blended nanofibers for neural cell culture. *Eur. Polym. J.* 117, 28–37. doi:10.1016/j.eurpolymj.2019.04.048

Garrudo, F. F. F., Mikael, P. E., Rodrigues, C. A. V., Udangawa, R. W., Paradiso, P., Chapman, C. A., et al. (2021). Polyaniline-polycaprolactone fibers for neural applications: electroconductivity enhanced by pseudo-doping. *Mater. Sci. Eng. C* 120, 111680. doi:10.1016/j.msec.2020.111680

Ghasemi-Mobarakeh, L., Prabhakaran, M. P., Morshed, M., Nasr-Esfahani, M. H., Baharvand, H., Kiani, S., et al. (2011). Application of conductive polymers, scaffolds and electrical stimulation for nerve tissue engineering. *J. Tissue Eng. Regen. Med.* 5, e17–e35. doi:10.1002/term.383

Giannitelli, S. M., Costantini, M., Basoli, F., Trombetta, M., and Rainer, A. (2018). "8 - electrospinning and microfluidics: an integrated approach for tissue engineering and cancer," in *Woodhead publishing series in biomaterials*. Editors V. Guarino and M. D. Ambrosio (Germany: Woodhead Publishing), 139–155. doi:10.1016/B978-0-08-101745-6.00008-6

Gnavi, S., Elena Fornasari, B., Tonda-Turo, C., Laurano, R., Zanetti, M., Ciardelli, G., et al. (2015a). The effect of electrospun gelatin fibers alignment on schwann cell and

axon behavior and organization in the perspective of artificial nerve design. *Int. J. Mol. Sci.* 16, 12925–12942. doi:10.3390/ijms160612925

Gnavi, S., Fornasari, B. E., Tonda-Turo, C., Ciardelli, G., Zanetti, M., Geuna, S., et al. (2015b). The influence of electrospun fibre size on Schwann cell behaviour and axonal outgrowth. *Mater. Sci. Eng. C* 48, 620–631. doi:10.1016/j.msec.2014.12.055

Guo, Y., Ghobeira, R., Aliakbarshirazi, S., Morent, R., and De Geyter, N. (2023). Polylactic acid/polyaniline nanofibers subjected to pre- and post-electrospinning plasma treatments for refined scaffold-based nerve tissue engineering applications. *Polym. (Basel)* 15, 72. doi:10.3390/polym15010072

Hádinger, N., Varga, B. V., Berzsenyi, S., Környei, Z., Madarász, E., and Herberth, B. (2009). Astroglia genesis *in vitro*: distinct effects of retinoic acid in different phases of neural stem cell differentiaion. *Int. J. Dev. Neurosci.* 27, 365–375. doi:10.1016/j.ijdevneu.2009.02.004

Hajiali, H., Contestabile, A., Mele, E., and Athanassiou, A. (2018). Influence of topography of nanofibrous scaffolds on functionality of engineered neural tissue. *J. Mater. Chem. B* 6, 930–939. doi:10.1039/c7tb02969a

He, H., Wang, Y., Farkas, B., Nagy, Z. K., and Molnar, K. (2020). Analysis and prediction of the diameter and orientation of AC electrospun nanofibers by response surface methodology. *Mater. Des.* 194, 108902–108909. doi:10.1016/j.matdes.2020.108902

Hu, Y., Zhang, H., Wei, H., Cheng, H., Cai, J., Chen, X., et al. (2022). Scaffolds with anisotropic structure for neural tissue engineering. *Eng. Regen.* 3, 154–162. doi:10.1016/j.engreg.2022.04.001

Hyysalo, A., Ristola, M., Joki, T., Honkanen, M., Vippola, M., and Narkilahti, S. (2017). Aligned poly(ε-caprolactone) nanofibers guide the orientation and migration of human pluripotent stem cell-derived neurons, astrocytes, and oligodendrocyte precursor cells *in vitro*. *Macromol. Biosci.* 17, 1–8. doi:10.1002/mabi.201600517

Isaac, B., Taylor, R. M., and Reifsnider, K. R. (2021). Mechanical and dielectric properties of aligned electrospun fibers. *Fibers* 9, 114–122. doi:10.3390/fib9010004

Ivanova, A. A., Syromotina, D. S., Shkarina, S. N., Shkarin, R., Cecilia, A., Weinhardt, V., et al. (2018). Effect of low-temperature plasma treatment of electrospun polycaprolactone fibrous scaffolds on calcium carbonate mineralisation. *RSC Adv.* 8, 39106–39114. doi:10.1039/c8ra07386d

Jha, B. S., Colello, R. J., Bowman, J. R., Sell, S. A., Lee, K. D., Bigbee, J. W., et al. (2011). Two pole air gap electrospinning: fabrication of highly aligned, three-dimensional scaffolds for nerve reconstruction. *Acta Biomater.* 7, 203–215. doi:10.1016/j.actbio.2010.08.004

Jin, G., and Li, K. (2015). The electrically conductive scaffold as the skeleton of stem cell niche in regenerative medicine. *Mater. Sci. Eng. C* 45, 671–681. doi:10.1016/j.msec.2014.06.004

Kaplan, B., and Levenberg, S. (2022). The role of biomaterials in peripheral nerve and spinal cord injury: a review. *Int. J. Mol. Sci.* 23, 1244. doi:10.3390/ijms23031244

Karimi, A., Karbasi, S., Razavi, S., and Zargar, E. (2018). Poly(hydroxybutyrate)/chitosan aligned electrospun scaffold as a novel substrate for nerve tissue engineering. *Adv. Biomed. Res.* 7, 44. doi:10.4103/abr.abr_277_16

Kennedy, K. M., Bhaw-Luximon, A., and Jhurry, D. (2017). Cell-matrix mechanical interaction in electrospun polymeric scaffolds for tissue engineering: implications for scaffold design and performance. *Acta Biomater.* 50, 41–55. doi:10.1016/j.actbio.2016.12.034

Keshvardoostchokami, M., Majidi, S. S., Huo, P., Ramachandran, R., Chen, M., and Liu, B. (2021). Electrospun nanofibers of natural and synthetic polymers as artificial extracellular matrix for tissue engineering. *Nanomaterials* 11, 21–23. doi:10.3390/nano11010021

Li, Y., Dong, T., Li, Z., Ni, S., Zhou, F., Alimi, O. A., et al. (2022). Review of advances in electrospinning-based strategies for spinal cord regeneration. *Mater. Today Chem.* 24, 100944. doi:10.1016/j.mtchem.2022.100944

Licciardello, M., Ciardelli, G., and Tonda-Turo, C. (2021). Biocompatible electrospun polycaprolactone-polyaniline scaffold treated with atmospheric plasma to improve hydrophilicity. *Bioengineering* 8, 24–18. doi:10.3390/bioengineering8020024

Licciardello, M., Sgarminato, V., Ciardelli, G., and Tonda-Turo, C. (2023). Development of biomimetic co-culture and tri-culture models to mimic the complex structure of the alveolar-capillary barrier. *Biomater. Adv.* 154, 213620. doi:10.1016/j.bioadv.2023.213620

Lim, S. H., Liu, X. Y., Song, H., Yarema, K. J., and Mao, H. Q. (2010). The effect of nanofiber-guided cell alignment on the preferential differentiation of neural stem cells. *Biomaterials* 31, 9031–9039. doi:10.1016/j.biomaterials.2010.08.021

Lu, D., Yang, Y., Zhang, P., Ma, Z., Li, W., Song, Y., et al. (2022). Development and application of three-dimensional bioprinting scaffold in the repair of spinal cord injury. *Tissue Eng. Regen. Med.* 19, 1113–1127. doi:10.1007/s13770-022-00465-1

Medeiros, E. S., Mattoso, L. H. C., Ito, E. N., Gregorski, K. S., Robertson, G. H., Offeman, R. D., et al. (2008). Electrospun nanofibers of poly(vinyl alcohol) reinforced with cellulose nanofibrils. *J. Biobased Mater. Bioenergy* 2, 231–242. doi:10.1166/jbmb.2008.411

Merighi, S., Mazzocchetti, L., Benelli, T., Maccaferri, E., Zucchelli, A., D'Amore, A., et al. (2019). A new wood surface flame-retardant based on poly-m-aramid electrospun nanofibers. *Polym. Eng. Sci.* 59, 2541–2549. doi:10.1002/pen.25235

Miroshnichenko, S., Timofeeva, V., Permykova, E., Ershov, S., Kiryukhantsev-Korneev, P., Dvořaková, E., et al. (2019). Plasma-coated polycaprolactone nanofibers with covalently bonded platelet-rich plasma enhance adhesion and growth of human fibroblasts. *Nanomaterials* 9, 637. doi:10.3390/nano9040637

Mohtaram, N. K., Ko, J., King, C., Sun, L., Muller, N., Jun, M. B. G., et al. (2015). Electrospun biomaterial scaffolds with varied topographies for neuronal differentiation of human-induced pluripotent stem cells. *J. Biomed. Mater. Res. - Part A* 103, 2591–2601. doi:10.1002/jbm.a.35392

Nitti, P., Gallo, N., Natta, L., Scalera, F., Palazzo, B., Sannino, A., et al. (2018). Influence of nanofiber orientation on morphological and mechanical properties of electrospun chitosan mats. *J. Healthc. Eng.* 2018, 1–12. doi:10.1155/2018/3651480

Pai, C. L., Boyce, M. C., and Rutledge, G. C. (2011). Mechanical properties of individual electrospun PA 6(3)T fibers and their variation with fiber diameter. *Polym. Guildf.* 52, 2295–2301. doi:10.1016/j.polymer.2011.03.041

Palaniappan, S., and John, A. (2008). Polyaniline materials by emulsion polymerization pathway. *Prog. Polym. Sci.* 33, 732–758. doi:10.1016/j.progpolymsci.2008.02.002

Peidavosi, N., Azami, M., Beheshtizadeh, N., and Ramazani Saadatabadi, A. (2022). Piezoelectric conductive electrospun nanocomposite PCL/Polyaniline/Barium Titanate scaffold for tissue engineering applications. *Sci. Rep.* 12, 20828–20913. doi:10.1038/s41598-022-25332-w

Pham, L. Q., Uspenskaya, M. V., Olekhnovich, R. O., and Baranov, M. A. (2021). The mechanical properties of PVC nanofiber mats obtained by electrospinning. *Fibers* 9, 1–12. doi:10.3390/fib9010002

Qing, H., Jin, G., Zhao, G., Huang, G., Ma, Y., Zhang, X., et al. (2018). Heterostructured silk-nanofiber-reduced graphene oxide composite scaffold for SH-SY5Y cell alignment and differentiation. *ACS Appl. Mater. Interfaces* 10, 39228–39237. doi:10.1021/acsami.8b12562

Qiu, B., Bessler, N., Figler, K., Buchholz, M. B., Rios, A. C., Malda, J., et al. (2020). Bioprinting neural systems to model central nervous system diseases. *Adv. Funct. Mater.* 30, 1910250. doi:10.1002/adfm.201910250

Razak, S. I. A., Wahab, I. F., Fadil, F., Dahli, F. N., Khudzari, A. Z., and Adeli, H. (2015). A review of electrospun conductive polyaniline based nanofiber composites and blends: processing features, applications, and future directions. *Adv. Mater. Sci. Eng.* 2015, 1–19. doi:10.1155/2015/356286

Rivers, T. J., Hudson, T. W., and Schmidt, C. E. (2002). Synthesis of a novel, biodegradable electrically conducting polymer for biomedical applications. *Adv. Funct. Mater.* 12, 33–37. doi:10.1002/1616-3028(20020101)12:1<33::AID-ADFM33>3.0.CO;2-E

Roshanbinfar, K., Vogt, L., Greber, B., Diecke, S., Boccaccini, A. R., Scheibel, T., et al. (2018). Electroconductive biohybrid hydrogel for enhanced maturation and beating properties of engineered cardiac tissues. *Adv. Funct. Mater.* 28. doi:10.1002/adfm.201803951

Rouleau, N., Murugan, N. J., and Kaplan, D. L. (2023). Functional bioengineered models of the central nervous system. *Nat. Rev. Bioeng.* 1, 252–270. doi:10.1038/s44222-023-00027-7

Sadrjahani, M., Hoseini, S. A., Mottaghitalab, V., and Haghi, A. K. (2010). Development and characterization of highly oriented pan nanofiber. *Braz. J. Chem. Eng.* 27, 583–589. doi:10.1590/S0104-66322010000400010

Saha, K., Keung, A. J., Irwin, E. F., Li, Y., Little, L., Schaffer, D. V., et al. (2008). Substrate modulus directs neural stem cell behavior. *Biophys. J.* 95, 4426–4438. doi:10.1529/biophysj.108.132217

Schlett, K., and Madarász, E. (1997). Retinoic acid induced neural differentiation in a neuroectodermal cell line immortalized by p53 deficiency. *J. Neurosci. Res.* 47, 405–415. doi:10.1002/(SICI)1097-4547(19970215)47:4<405::AID-JNR6>3.0.CO;2-I

Shin, M. K., Kim, S. I., Kim, S. J., Kim, S. K., Lee, H., and Spinks, G. M. (2006). Size-dependent elastic modulus of single electroactive polymer nanofibers. *Appl. Phys. Lett.* 89, 2004–2007. doi:10.1063/1.2402941

Sivan, M., Madheswaran, D., Asadian, M., Cools, P., Thukkaram, M., Van Der Voort, P., et al. (2020). Plasma treatment effects on bulk properties of polycaprolactone nanofibrous mats fabricated by uncommon AC electrospinning: a comparative study. *Surf. Coatings Technol.* 399, 126203. doi:10.1016/j.surfcoat.2020.126203

Tarricone, G., Carmagnola, I., and Chiono, V. (2022). Tissue-engineered models of the human brain: state-of-the-art analysis and challenges. *J. Funct. Biomater.* 13, 146. doi:10.3390/jfb13030146

Traldi, C., Chiappini, V., Menduti, G., Tonda-turo, C., and Boido, M. (2023). Advanced materials and biofabrication technologies to design *in vitro* functional central nervous system models. *Front. Med. Eng.* 1, 1–21. doi:10.3389/fmede.2023.1270943

Varga, B. V., Hádinger, N., Gócza, E., Dulberg, V., Demeter, K., Madarász, E., et al. (2008). Generation of diverse neuronal subtypes in cloned populations of stem-like cells. *BMC Dev. Biol.* 8, 89–18. doi:10.1186/1471-213X-8-89

Wang, H. B., Mullins, M. E., Cregg, J. M., Hurtado, A., Oudega, M., Trombley, M. T., et al. (2009). Creation of highly aligned electrospun poly-L-lactic acid fibers for nerve regeneration applications. *J. Neural Eng.* 6, 016001. doi:10.1088/1741-2560/6/1/016001

Wu, T., Xue, J., and Xia, Y. (2020). Engraving the surface of electrospun microfibers with nanoscale grooves promotes the outgrowth of neurites and the migration of schwann cells. *Angew. Chem.* 132, 15756–15762. doi:10.1002/ange.202002593

Yang, H., Zhu, G., Huang, Y., Shi, X., and Wang, Y. (2016). The stimulation of the differentiation of pheochromocytoma (PC12-L) cells into neuron-like cells by electrically conductive nanofibre mesh. *Appl. Mater. Today* 5, 215–222. doi:10.1016/j.apmt.2016.09.017

Yao, J., Bastiaansen, C. W. M., and Peijs, T. (2014). High strength and high modulus electrospun nanofibers. *Fibers* 2, 158–186. doi:10.3390/fib2020158

Zha, F., Chen, W., Hao, L., Wu, C., Lu, M., Zhang, L., et al. (2020). Electrospun cellulose-based conductive polymer nanofibrous mats: composite scaffolds and their influence on cell behavior with electrical stimulation for nerve tissue engineering. *Soft Matter* 16, 6591–6598. doi:10.1039/D0SM00593B

Zhang, J., Zhang, X., Wang, C., Li, F., Qiao, Z., Zeng, L., et al. (2021). Conductive composite fiber with optimized alignment guides neural regeneration under electrical stimulation. *Adv. Healthc. Mater.* 10, e2000604–e2000612. doi:10.1002/adhm.202000604

Zhao, Y. H., Niu, C. M., Shi, J. Q., Wang, Y. Y., Yang, Y. M., and Wang, H. B. (2018). Novel conductive polypyrrole/silk fibroin scaffold for neural tissue repair. *Neural Regen. Res.* 13, 1455–1464. doi:10.4103/1673-5374.235303

Zhu, L., Jia, S., Liu, T., Yan, L., Huang, D., Wang, Z., et al. (2020). Aligned PCL fiber conduits immobilized with nerve growth factor gradients enhance and direct sciatic nerve regeneration. *Adv. Funct. Mater.* 30. doi:10.1002/adfm.202002610

Zhu, W., Masood, F., O'Brien, J., and Zhang, L. G. (2015). Highly aligned nanocomposite scaffolds by electrospinning and electrospraying for neural tissue regeneration. *Nanomedicine Nanotechnol. Biol. Med.* 11, 693–704. doi:10.1016/j.nano.2014.12.001

frontiers | Frontiers in Biomaterials Science

TYPE Original Research
PUBLISHED 15 July 2024
DOI 10.3389/fbiom.2024.1408748

OPEN ACCESS

EDITED BY
Monica Boffito,
Polytechnic University of Turin, Italy

REVIEWED BY
Santosh Phuyal,
University of Oslo, Norway
Sharda Yadav,
Griffith University, Australia
Qiang Wei,
Sichuan University, China

*CORRESPONDENCE
Silviya Petrova Zustiak,
silviya.zustiak@slu.edu

RECEIVED 28 March 2024
ACCEPTED 24 June 2024
PUBLISHED 15 July 2024

CITATION
Ferchichi E, Stealey S, Bogert P and Zustiak SP (2024), Tunable gelatin methacrylate polyethylene glycol diacrylate hydrogels for cell mechanosensing applications.
Front. Biomater. Sci. 3:1408748.
doi: 10.3389/fbiom.2024.1408748

Tunable gelatin methacrylate polyethylene glycol diacrylate hydrogels for cell mechanosensing applications

Eya Ferchichi, Samuel Stealey, Paige Bogert and Silviya Petrova Zustiak*

Department of Biomedical Engineering, School of Science and Engineering, Saint Louis University, St Louis, MO, United States

Three-dimensional (3D) tissue-engineered scaffolds mimic the physiological environment of cells by providing essential structural support, biochemical cues, and the mechanical strength needed for cell adhesion, proliferation, migration, and differentiation. Hydrogels like polyethylene glycol diacrylate (PEGDA) are commonly used biomaterials for cell culture due to their affordability, tunable stiffness, and ability to efficiently transport nutrients and gases. However, PEGDA lacks cell adhesion sites essential for cell proliferation and migration and has limited degradability. Methacrylated gelatin (GelMA) produced from denatured bovine collagen, crosslinks under ultraviolet light (UV) resulting in a degradable hydrogel with cell adhesion sites. Here, we synthesized GelMA with variable degree of methacrylation and crosslinked it with PEGDA to produce cell scaffolds with independently tunable mechanical and biochemical properties by varying the ratios of the two polymers. We determined polymer ratios that resulted in scaffolds with different mechanical properties but the same gelatin concentrations (providing cell adhesion and degradation sites) as well as different gelatin concentrations but the same mechanical properties. With the developed scaffold library, we further used a design of experiments approach to probe the parameter space and perform detailed analysis on chemical composition-scaffold properties as well as scaffold properties-cell behavior correlations. Our findings showed that hydrogel properties such as modulus, swelling, pore size, and permeability, strongly depended on total polymer concentration and not on the GelMA fraction. GelMA significantly influenced cell spreading, while addition of any amount of PEGDA delayed cell spreading significantly. We suggest that such analysis will broaden the utility of the GelMA/PEGDA hydrogels, presenting a versatile platform for mechanosensing research in 3D environments.

KEYWORDS

cell scaffold, mechanosensing, mechanobiology, stiffness, compliance, hydrogel

1 Introduction

The extracellular matrix (ECM) is a complex 3D network composed of proteins and other molecules that surround cells in tissues throughout the body (Theocharis et al., 2016). The ECM includes structural proteins such as collagen, elastin, and fibronectin, as well as proteoglycans and glycosaminoglycans that form a hydrated gel-like substance (Lepedda et al., 2021). Decades ago, research revealed that the ECM supports and regulates cell growth and behaviors (Kim et al., 1999; Dutta and Dutta, 2009). It provides physical support to cells, allows for cellular movement and communication, and regulates cell signaling and

behavior, which makes it crucial for physiological processes such as tissue repair and regeneration as well as pathological processes such as cancer metastasis, fibrosis, and inflammation (Walker et al., 2018). Since then, multiple studies have focused on developing physiologically relevant 3D hydrogel microenvironments that mimic the structure, properties, and function of the native ECM (Tibbitt and Anseth, 2009). Cell–scaffold interactions and scaffold mechanical properties are essential for cell fate and for the regulation of cellular behavior (Caliari and Burdick, 2016). Thus, the chemical composition of the scaffold is an important factor in biomaterial development because it dictates the material physical, mechanical, and biochemical properties. These material properties in turn, influence cell survival, spreading, proliferation, migration, and differentiation (Kim et al., 1999; Dutta and Dutta, 2009; Huang et al., 2017).

Gelatin, which is denatured collagen, is naturally found in most tissues which makes it an excellent biomaterial for many applications. Gelatin promotes cell adhesion and proliferation due to the presence of cell-binding domains such as the arginine-lysine-aspartate (RGD) sequence that interacts with cell surface receptors (Hoch et al., 2012; Huang et al., 2017). To address the limitations of using gelatin alone, Van Den Bulk et al. (2000) chemically modified gelatin with methacrylic anhydride by substituting the available amino groups with methacrylate functional groups and obtained gelatin methacrylate, also referred to as methacryloyl (GelMA). GelMA has since become widely used in tissue engineering and regenerative medicine due to its easy-to-use crosslinking chemistry, stability under physiological conditions, and support of cell attachment (Van Den Bulcke et al., 2000; Hoch et al., 2012; Loessner et al., 2016; Huang et al., 2017; Sun M. et al., 2018). GelMA has been shown as an excellent scaffold for mechanosensing applications in particular, because the polymer fibers possess both high deformability and modulus, which maximize cell adhesive forces due to fiber recruitment (Dong et al., 2024). The addition of methacrylate groups to the gelatin backbone enables gelatin to undergo photocrosslinking in response to light exposure, which can be used to control the properties (e.g., mechanical and biochemical) of the resulting hydrogel (Loessner et al., 2016). However, to achieve diverse mechanical properties one has to either: i) modify the degree of methacrylation, which offers somewhat limited tunability due to the finite number of modifiable groups (Pepelanova et al., 2018; O'Connell et al., 2018), ii) adjust the UV exposure resulting in uncoupled reactive groups and with possible implications for cell function due to UV exposure (O'Connell et al., 2018), or iii) modify the polymer concentration (Sun Y. et al., 2018), which leads to both increase in mechanical and biochemical properties (i.e., prevents independent tunability) and could also result in an impractically viscous precursor solution. Hence, a different strategy might be desired for achieving GelMA hydrogels with varying properties, such as mechanical and biochemical, for use in applications such as mechanosensing.

The objective of this study was to assess the utility and explore the structure-property relationships for GelMA/poly (ethylene glycol) diacrylate (PEGDA) hydrogel scaffolds for mechanosensing applications. The addition of PEGDA introduces key features: modulation of mechanical properties independently of biochemical ones for mimicking native tissue mechanics and enhanced hydrophilicity for a well-hydrated microenvironment conducive to cell survival (Hutson et al., 2011). Further, while others have shown changes in porosity and pore size with PEGDA addition, the GelMA/PEGDA gels have been shown to retain their porous structure (Mamaghani et al., 2018; Wang et al., 2018), facilitating nutrient and oxygen diffusion while aiding in waste product removal. This mass transport is crucial for supporting cell viability and functionality within the 3D hydrogel matrix.

GelMA/PEGDA hydrogels, compared to GelMA-only hydrogels, demonstrate enhanced mechanical properties and prolonged degradation rates of up to several weeks (Xiao et al., 2019a), making them suitable for prolonged cell mechanosensting studies (Jiang et al., 2019). For example, *in vitro* experiments have shown that osteoblasts adhere and proliferate effectively on the hydrogels' surface, indicating excellent cell viability and biocompatibility and positioning the GelMA/PEGDA hydrogel as a suitable material for guided bone regeneration applications (Wang et al., 2018). GelMA/PEGDA hydrogels have also been utilized in 3D *in vitro* models of intestinal mucosa, accurately mimicking the intestinal barrier's function and permeability, thus enabling predictions of drug absorption and understanding intestinal function related diseases (Vila et al., 2020). Another study showed breast cancer cells seeded in GelMA/PEGDA hydrogels formed either spherical tumor-like clusters or exhibited spindle-shaped morphology, indicative of invasive behavior, where cell spreading was guided primarily by the GelMA content (Peter et al., 2019).

Because many recent studies have shown the utility of the GelMA/PEGDA hydrogels as cell scaffolds (Hutson et al., 2011; Duan et al., 2022), here we sought to perform detailed structure-property analysis of the hydrogels and their effect on cell spreading, viability, and drug responsiveness. Our detailed analysis focused on the effect of total polymer content as well as GelMA fraction (correlating with number of adhesive sites and enzymatic gel degradability) on the gels' mechanical and physical properties (i.e., modulus, swelling, pore size, and permeability) and subsequently the effect of those properties on cell viability, spreading and drug responsiveness over 7–14 days of culture. Through varying the PEGDA and GelMA concentrations, we were able to identify gel conditions with the same modulus but different number of adhesive ligands and different modulus but the same number of adhesive ligands, positioning the GelMA/PEGDA gels as excellent scaffolds in mechanosensing applications.

2 Materials and methods

2.1 Materials

Poly (ethylene glycol) diacrylate (PEGDA, MW 5,000 g/mol) was obtained from Laysan Bio, Inc (Arab, AL). Gelatin from bovine skin type B (bloom strength 257), methacrylic anhydride (MAA), trypsin, ethylenediaminetetraacetic acid (EDTA), and Ribonuclease A (RNase) were obtained from Millipore Sigma (St. Louis, MO). Phosphate buffered saline (PBS), Atto 655-NHS ester, fluorescence dye removal columns, and SnakeSkin™ dialysis tubing (10K MWCO) were obtained from ThermoFisher Scientific (Waltham, MA). Irgacure 2,959 was obtained from BASF Corporation (Florham Park, NJ) and silicone spacers were obtained from Grace Bio-Labs (Bend, OR). Roswell Park Memorial Institute (RPMI) 1,640 medium and fetal bovine serum (FBS) were obtained from Hyclone (Logan,

UT). Penicillin/streptomycin (pen/strep) was obtained from MP Biomedicals (Santa Ana, CA). Propidium iodide (PI), acridine orange (AO), Cell Tracker Green CMFDA Dye, dimethyl sulfoxide (DMSO), temozolomide (TMZ), and four-chambered coverglass were obtained from Fisher Scientific (Hamptom, NH). U-87 human glioblastoma and NIH 3T3 fibroblast cells were obtained from American Type Culture Collection (Manassas, VA).

2.2 GelMA preparation

GelMA of low and high degree of modification (DM) was synthesized following a protocol developed by Van Den Bulcke et al. (Van Den Bulcke et al., 2000) with some modifications. Briefly, 5 g gelatin was dissolved by gently mixing it in 50 mL of 1X PBS pH 7.4 at 60 °C. After the gelatin was fully dissolved, MAA was added (2.50 mL for the high DM and 0.25 mL for the low DM GelMA) dropwise via a syringe pump at a rate of 0.5 mL/min under vigorous stirring (500 rpm). For the high DM, a 1:10 M ratio of free amine groups in gelatin to MAA was used and for the low DM, a 1:1 M ratio was used. The molar concentration of amine groups was assumed to be 0.335 mmol amine groups per gram of gelatin as determined previously by Ven Den Bulcke et al. (Van Den Bulcke et al., 2000) for bovine gelatin (type B) with bloom strength of 257 (the gelatin used here). After 2 h of reaction under stirring at 60 °C, 250 mL of PBS was added to neutralize the reaction. The mixture was dialyzed for 7 days against deionized water at 50 °C using 10K MWCO dialysis tubing with daily change of the dialysate buffer, then lyophilized for 5 days. The collected GelMA powder was stored at −20 °C until use.

To confirm the successful methacrylation of gelatin and quantify the DM, ^{1}H-nuclear magnetic resonance (NMR) spectroscopy was used. For the analysis, 0.8 mg of GelMA or gelatin was dissolved in 600 µL deuterium oxide and analyzed on a HDTM 700 MHz NMR spectrometer (Bruker, Billerica, MA). The DM was defined as the percentage of lysine methylene groups (2.8–2.95 ppm) of the gelatin that were modified in the GelMA (Hoch et al., 2012). The ^{1}H NMR spectra were normalized to the signal at 0.8 ppm corresponding to the proton of the methyl group. DM was calculated from the integration of the ^{1}H-NMR spectra to determine the area, A, of the lysine signal in both GelMA and gelatin as:

$$DM\,(\%) = 1 - [A\,(lysine\,methylene\,of\,GelMA)/ (A\,(lysine\,methylene\,of\,gelatin) \times 100 \quad (1)$$

2.3 GelMA/PEGDA hydrogel fabrication

Stocks solution of PEGDA and lyophilized high or low DM GelMA were made by gently mixing each polymer in PBS at 30% w/v until both polymers were completely dissolved. High DM was used for all experiments unless specified otherwise. The hydrogels were prepared by radical crosslinking of different ratios of GelMA and PEGDA in the presence of the photoinitiator Irgacure 2959 at 0.1% w/v final concentration. Irgacure 2959 (<2 wt% at 25 °C water solubility (Tomal and Ortyl, 2020) stock solution was first prepared at 1% w/v in deionized (DI) water via sonication for 8 h and stored up to 14 days under constant stirring and protected from light.

TABLE 1 Hydrogel composition and abbreviations used.

Abbreviation	GelMA [% w/v]	PEGDA [% w/v]
G2P3	2	3
G2P5	2	5
G2P10	2	10
G5P2	5	2
G5P5	5	5
G5P10	5	10
G10	10	0
G10P2	10	2
G10P5	10	5
G10P10	10	10

Table 1 summarizes the different concentrations of GelMA and PEGDA used and the associated hydrogel abbreviations. Dissolved GelMA and PEGDA were mixed and diluted in PBS to the desired final concentration. Once Irgucure 2959 was added, the solution was placed between two glass plates with two silicone spacers (1 mm thickness) and placed under 365 nm UV light for 10 min at 10 cm distance to the UV light (4.81 mW/cm^2) to form a gel.

2.4 Rheology and swelling ratio

Rheological measurements were performed using an AR-2000ex rheometer (TA Instruments, New Castle, DE) with a 20 mm parallel plate geometry. Storage modulus, G', and loss modulus, G'', were measured at a constant strain of 0.1%, which was within the linear viscoelastic region of all hydrogels tested, at a frequency of 1–10 Hz and an axial force of 0.2 N (Vila et al., 2020). For testing, 500 µL gels of 1 mm thickness were equilibrium swollen for 24 h at room temperature in DI water and cut into 20 mm discs. Before measurements, excess water from the gel surface was wicked away carefully using KimWipe. The measured G' was converted to Young's modulus, E, using the following equation:

$$E = G'2\,(1 + \upsilon) \quad (2)$$

where υ is the Poisson's ratio which was approximated to 0.5 for the GelMA/PEGDA hydrogels.

For swelling ratio measurements, hydrogels were prepared as 6 mm × 1 mm slabs and equilibrium swollen in DI water for 24 h at 37 °C. Their swollen mass (M_s) was measured. Hydrogels slabs were then dried for 24 h at 60 °C to obtain the dry mass (M_d). The swelling ratio (Q_M) was calculated as the ratio of M_s to M_d (M_s/M_d).

2.5 Scanning electron microscopy

Hydrogels were soaked in DI water overnight and were then frozen at −80 °C for 30 min and lyophilized for 24 h. The samples were sputter coated with gold for 240 s at 20 mA (SCD 005, BAL-TEC, Liechtenstein). The samples were imaged via Scanning

Electron Microscopy (SEM, EVO LS15) under high vacuum at ×5 kV and ×500 magnification. Pore size and wall thickness were measured using ImageJ software (50 pores were measured per image from three images per hydrogel type).

2.6 Fluorescence correlation spectroscopy

Fluorescence correlation spectroscopy (FCS) was used to investigate the effect of polymer concentration on hydrogel mesh size and diffusivity. Ribonuclease A (RNase A) was used as a model protein and was fluorescently labeled with Atto 655-NHS ester, according to the manufacturer's protocol. Briefly, Atto 655-NHS ester and RNase were dissolved in PBS and reacted under gentle mixing for 2 h while protected from light to avoid photobleaching. Unbound dye was removed using dye removal columns with >95% removal efficiency. Labeling efficiency was measured to be 64% and was calculated by measuring the bound fraction of Atto 655 using a two-component autocorrelation function fit. Next, fluorescently labeled RNase was added to hydrogels of varying GelMA and PEGDA concentration by mixing with the hydrogel precursor solution for a final RNase concentration of 1 μg/mL. Gels were placed in an 8-chambered coverglass, crosslinked as previously described and swollen in a solution of 1X PBS with 1 μg/mL fluorescent RNase to maintain constant protein concentration within each hydrogel.

FCS measurements were performed using Microtime 200 software (PicoQuant, Berlin, Germany). Atto 655-NHS ester (0.2 nM) in PBS was used to calibrate the illuminated confocal volume. A 640 nm ps pulsed laser was used at an optical power of 11 μW for at least five measurements of 120 s for each sample. An autocorrelation function $G(\tau)$ was obtained for each measurement:

$$G(\tau) = \frac{1}{N}\frac{1}{\left[1+\left(\frac{\tau}{\tau_D}\right)\right]}\frac{1}{\left[1+p\left(\frac{\tau}{\tau_D}\right)\right]^{0.5}} \quad (3)$$

where N is the number of fluorescent particles, $p = r_o/z_o$ is an instrumental constant, r_o is the radius and z_o is the axial length of the focused laser beam spot, and τ_D is the solute diffusion time. A one component autocorrelation function fit was used for all samples as protein interaction with the polymer was not expected. Additionally, a triplet model was used to account for possible excitation of molecular triplet states at higher laser intensities. Autocorrelation functions for labeled RNase A were normalized as follows:

$$\text{Normalized } G(\tau) = \frac{(G(\tau_D))}{(G(\tau 0))} \quad (4)$$

where $G(\tau_D)$ is the value of Eq. (3) at each time point and $G(\tau_0)$ is the value of Eq. (3) at the initial time point.

2.7 Cell maintenance

Human glioblastoma cells U87 were cultured in RPMI-1640 medium supplemented with 10% v/v FBS and 1% v/v pen/strep in a humidified incubator at 37 °C and 5% CO_2 in a T-75 flask. NIH 3T3 cells were cultured in DMEM medium supplemented with 10% FBS and 1% pen/strep in a humidified environment at 37 °C and 5% CO_2 in a T-75 flask. Once at 80% confluency, cells were harvested with 0.1 M Trypsin/EDTA at an exposure time of 5 min and used for experiments. Only cells between passages 10 and 14 were used for experiments.

2.8 Cell encapsulation in GelMA/PEGDA hydrogels

For cell encapsulation, hydrogels were prepared as described above except that cells were added to the gel precursor solution at a concentration of 10^6 cells/mL. Then, 20 μL hydrogel precursor solution droplets were pipetted between two glass plates separated by 1 mm silicone spacers and placed under UV light (365 nm) for 10 min at 10 cm distance from the light. The hydrogels containing encapsulated cells were cultured in a humidified incubator at 37 °C and 5% CO_2 for up to 14 days with a change in media every other day.

2.9 Cell viability measurement

Live/dead (AO/PI) staining was used to assess cell viability. At specified time points, hydrogel encapsulated cells were incubated with PI (2 μg/mL) and AO (2 μg/mL) for 30 min, rinsed with PBS and soaked in complete cell culture medium for imaging. Images were taken using a confocal microscope (Leica Confocal SP8, Leica Microsystems, Wetlzar, Germany) at ×10 magnification. Cell viability was calculated using a MATLAB code that counts individual cells stained with AO (all cells) and with PI (dead) and then calculates the ratio:

$$\text{Viability } (\%) = \frac{\#\text{ of all cells } - \#\text{ of dead cells}}{\#\text{ of all cells}} * 100\% \quad (5)$$

2.10 Drug screening

For drug screening, U87 cells were first encapsulated in the hydrogels at a density of 10^6 cells/mL and cultured for 3 days in a 48-well plate. On day 3, the encapsulated cells were treated with 0, 1, 2, 3, and 4 mM TMZ in 4% DMSO and incubated for an additional 3 days. On the third day following TMZ addition, cells were stained with 2 μg/mL PI (dead cells) and 1 μM Cell Tracker Green (live cells) for 30 min at 37 °C. Z-stack images were captured using a Leica SP8 confocal microscope at ×10 magnification. Cell viability was calculated for each hydrogel condition and TMZ concentration as previously described.

2.11 Quantification of number of cells spreading

To assess cell spreading, cells encapsulated in GelMA/PEGDA hydrogels were stained with Cell-Tracker Green at a concentration of 1 μM for 30 min at 37 °C. The staining medium was then exchanged with fresh complete medium. Images were captured using a confocal microscope at ×10 and ×20 magnification and

analyzed on ImageJ via the Shape Descriptor and Area software plug-ins. For the four conditions G2P3, G10, G10P2, and G10P10, cell spreading area was determined by generating a mask to delineate the perimeter of each individual cell. Cell shape (circularity) was then calculated from the following relationship:

$$\text{Shape factor} = \frac{4\pi(\text{area})}{\text{Perimeter}^2} \quad (6)$$

Circularity was measured on a scale of 0–1, where values of 0.6-1 were taken to designate rounded cells and values of 0–0.5 were taken to designate elongated cells. Cell spreading was also quantified for all hydrogel types by assessing the number of cells that were spreading (had protrusions and were not round in shape) to the total cell count in the image. Analysis involved examining >100 cells for each data point across a minimum of three independent experiments. However, for G10P10 gels, analysis was based on >30 cells from three separate experiments due to the low cell number in these gels.

2.12 Dynamic data visualization with JMP

JMP (version 16.0.0) statistical software (SAS Institute, Cary, NC) was used for dynamic data visualization as well as statistical analysis. We leveraged the software's capabilities to generate contour plots, allowing us to effectively visualize trends and patterns within our data. Contour plots assist in identifying regions of interest, boundaries, or thresholds where specific outcomes occur or where variables exhibit notable changes. To derive regression models and obtain predictive expressions, we employed the method of least squares within JMP. This statistical technique was applied with default emphasis on effect leverage. By emphasizing effect leverage, we aimed to prioritize influential factors and better understand their impact within our experimental setup. By weighing these influential factors, we aimed to enhance the robustness of our models and better understand variable relationships in our analyses conducted using JMP.

2.13 Statistics

GraphPad Prism software was used to express results as average ± standard deviation (SD) from three independent experiments, where 3–10 samples were used per experiment. Multiple groups were compared using single factor analysis of variance (ANOVA) with a Tukey's *post hoc* test. Two-tailed Student's t-test was used to compare between two groups. A value of $p < 0.05$ was considered significant. The coefficient of variance (%CV) was calculated as the standard deviation divided by the mean.

3 Results

3.1 Methacrylation of gelatin

Here, we synthesized GelMA with varying degrees of methacrylation. In this process, the amino groups in gelatin are functionalized through methacrylation using methacrylic anhydride (MAA), resulting in the formation of GelMA. Upon exposure to UV light in the presence of a photoinitiator, the methacrylate groups within GelMA can covalently bond, resulting in the crosslinking of GelMA chains and the formation of a stable hydrogel. This study followed a protocol established by Van den Bulcke et al. (Van Den Bulcke et al., 2000) with the degree of methacrylation adjusted by controlling the quantity of MAA, as illustrated in Figure 1A. ^{1}H NMR spectroscopy confirmed the methacrylation (Figure 1B). The NMR signal at 1.9 ppm corresponds to the methylene protons (CH_2) adjacent to the carbonyl group of the methacrylate and the signals at 5.4 and 5.7 ppm correspond to the protons of the vinyl group (CH = CH_2) in the methacrylate (Van Den Bulcke et al., 2000). The lysine signal at 2.9 ppm, highlighted in green, nearly disappeared when using higher molar ratios of MAA to gelatin but changed only minimally for the lower molar ratio of MAA to gelatin (Yue et al., 2015; Claaßen et al., 2018). We calculated 80% degree of methacrylation for the high DM GelMA and 16% degree of methacrylation for the low DM GelMA. GelMA with a high DM was used for subsequent experiments unless otherwise indicated.

3.2 Mechanical and physical properties of GelMA and GelMA/PEGDA hydrogels

We used a combination of GelMA and PEGDA polymers to fabricate hydrogels with different stiffness, as governed primarily by the PEGDA concentration, or different biochemical composition (e.g., RGD and MMP moieties), as governed primarily by the GelMA concentration. We tested various ratios of GelMA/PEGDA hydrogels as follows: 2%, 5%, and 10% w/v GelMA combined with 0%, 2%, 3%, 5%, and 10% w/v PEGDA (Table 1). We tested GelMA alone as a control, but not PEGDA alone as it lacks binding sites for cell attachment and spreading. The chosen compositions were based on prior literature (Mahdavi et al., 2021; Liu et al., 2024) as well as on our preliminary work establishing the lower and upper polymer concentration boundaries. For example, G10P10 was the highest concentration used because the hydrogel precursor solution became too viscous to pipette at higher polymer concentrations. G10 was the only control tested because G2 did not gel and G5 resulted in a very soft gel, which was difficult to handle. Similarly, G2P3 was used instead of G2P2, as G2P2 did not gel. Hence, G2P3 was the lowest and G10P10 the highest practical polymer concentration which resulted in a stable hydrogel that was easy to handle. These compositions resulted in a range of stiffness from Young's modulus of ~3.7 kPa–~45.0 kPa (Figures 2A–C). Overall, within each group (for the same GelMA concentration), Young's modulus increased with an increase in PEGDA concentration. Furthermore, we were able to fabricate gels with the same stiffness but different biochemical properties as well as gels with the same biochemical properties but different stiffness. Specifically, we fabricated both soft and stiff gel pairs with the same Young's modulus but varying biochemical composition due to different GelMA concentration: soft G2P3 and G10 gels (Young's modulus of ~4 kPa) and stiff G2P10 and G10P10 gels (Young's modulus of ~30 kPa). At the same time, we achieved gels with the same biochemical properties (i.e., GelMA concentration) but varying Young's modulus (e.g., G2P3 vs. G2P10 and G10 vs. G10P10). We also noted that hydrogel swelling showed inverse

10.3389/fbiom.2024.1408748

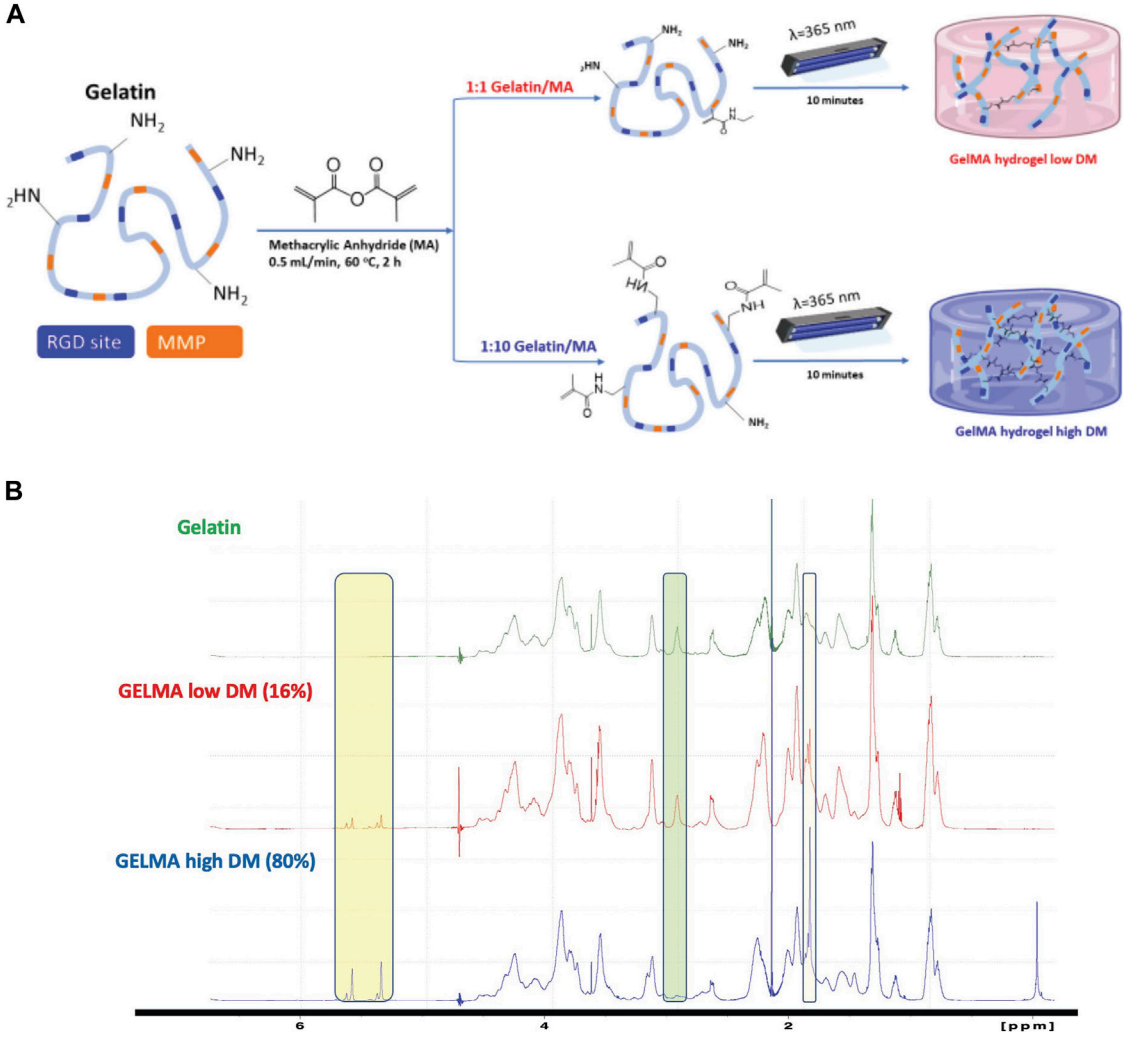

FIGURE 1
(A) Synthesis of GelMA. High and low degree of modification (DM) of the amino groups on gelatin with MAA to form GelMA without affecting the RGD adhesion and MMP degradation moieties. **(B)** ^{1}H-NMR spectra for gelatin and GelMA with high and low DM. Yellow highlights the chemical shifts around 5.35 and 5.65 ppm to confirm the presence of acrylic protons of the methacrylate group, the green highlights at 2.9 ppm confirm the reduction of lysine methylene protons with increase of DM, and the blue highlights the new signal at 1.8 ppm assigned to the methyl moiety of the methacrylate.

trends to the hydrogel modulus and varied from ~7 (for G10P10) to ~28 (for G2P3) (Figure 2D). We saw a decrease in hydrogel swelling with increase in PEGDA concentration for the same GelMA concentration. The effect of PEGDA addition was more pronounced for the lower GelMA concentrations (G2 and G5) than the highest GelMA concentration (G10), where gels made with G10 also swelled less overall (Q_M of ~7–11) compared to gels made with G2 (Q_M of ~10–27) and G5 (Q_M of ~9–25).

We also investigated the stiffness of hydrogels made from GelMA of low DM (Supplementary Figure S1). As mentioned above, we classified G2P3 and G10 as soft hydrogels, while G2P10 and G10P10 were deemed stiff. It is worth noting that the low DM G2P3 was so soft that it presented difficulties when handling it during experiments. Our results showed that G10 of low DM had a Young's modulus of ~1 kPa. In contrast, both G10P10 and G2P10 showed a modulus of ~25 kPa, with no significant difference observed between them ($p > 0.05$). This data implies that the stiffness primarily arises from the PEGDA content, rather than the GelMA. Our results indicated that the degree of modification could be a useful strategy to manipulate hydrogel mechanical properties within a narrow range. For example, the same G10 gels were ~4 kPa for the high DM vs. ~1 kPa for the low DM GelMA and G10P10 gels were ~30 kPa for the high and ~25 kPa for the low DM GelMA (due to the overpowering effect of PEGDA on mechanical properties). Only high DM gels were used for further experiments as they allowed a broader range of mechanical properties and easier gel handling overall.

3.3 Hydrogel pore size and morphology

Figure 3A shows SEM images that highlight the structure of both the pure GelMA hydrogel (G10) and hybrid GelMA/PEGDA

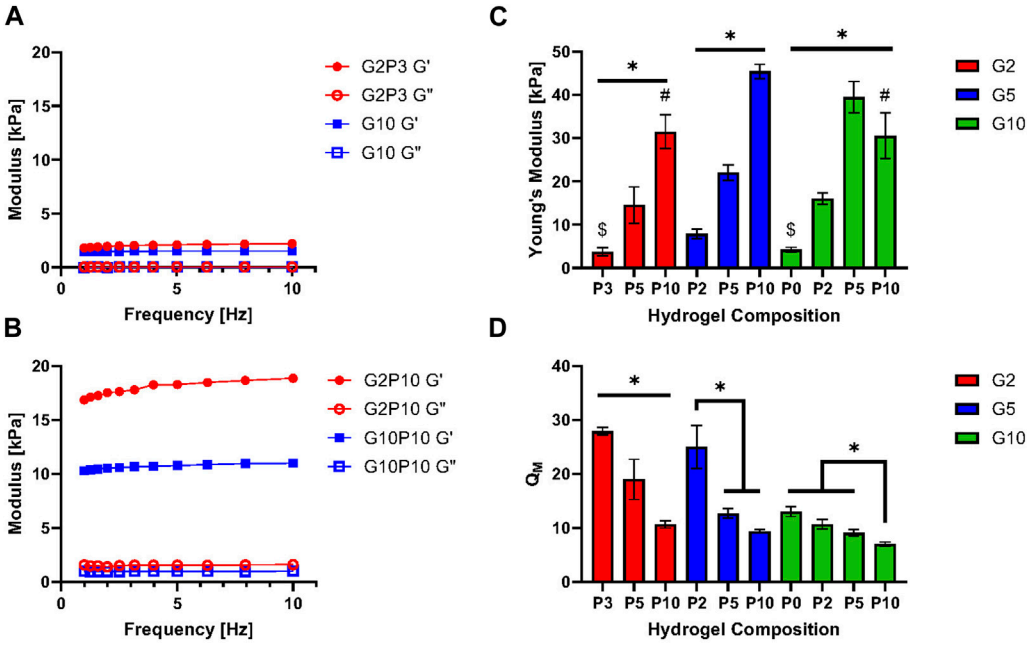

FIGURE 2
(A) Storage and loss moduli for the soft G2P3 and G10 GelMA/PEGDA hydrogels as a function of oscillation frequency. **(B)** Storage and loss moduli for stiff G2P10 and G10P10 GelMA/PEGDA hydrogels as a function of oscillation frequency. **(C)** Young's Modulus of GelMA/PEGDA hydrogels as a function of hydrogel composition. **(D)** Swelling ratio of GelMA/PEGDA hydrogels as a function of hydrogel composition. * Designates significant difference; one-way ANOVA test, $p < 0.05$, n = 3. # and $ designate no significant difference between denoted hydrogel pairs.

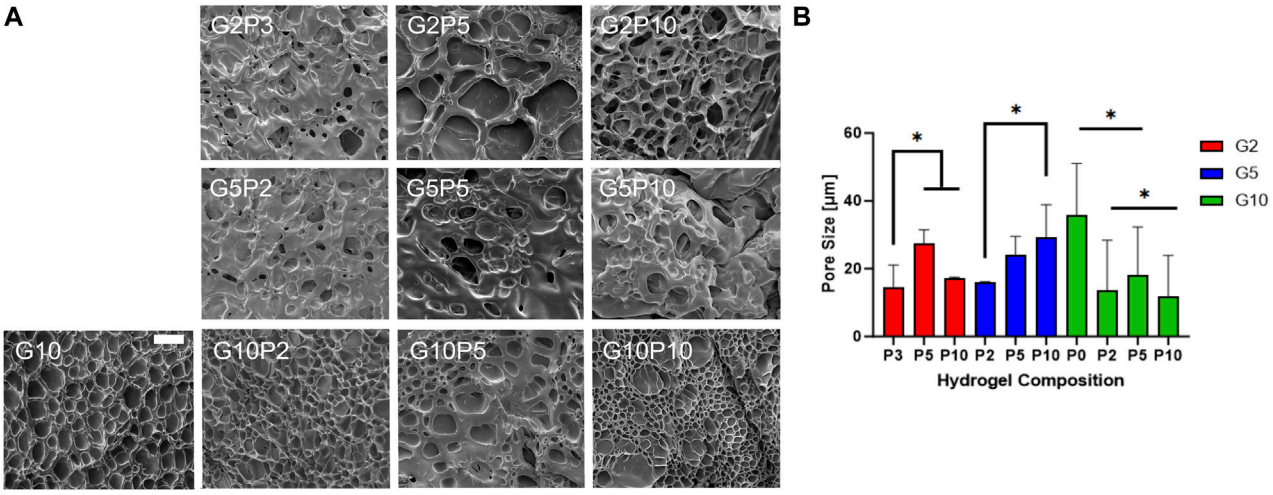

FIGURE 3
Characterization of hydrogel porosity. **(A)** Scanning electron microscope (SEM) images of all GelMA/PEGDA hydrogels. Scale bar = 50 μm. **(B)** Pore size measured from SEM images with the software ImageJ. * designates significant difference; one-way ANOVA test, $p < 0.05$, n = 3.

hydrogels. All gels exhibited an interconnected porous structure, where the pore size varied between ~9 (for G10P10)—~37 μm (for G10) (Figure 3B). Overall, the G10 gels appeared to have the most defined porous structure, while the addition of PEGDA seemed to lead to lower overall number of pores (for P2 and P3) or thicker walls (for P5 and P10), which could be attributed to higher crosslinking and is consistent with a higher gel modulus. Looking at the average pore size, G10 also seemed to have the highest pore size of all conditions of ~37 μm, suggesting the PEGDA addition led to a decrease in pore size. Further, the average pore size seemed to be higher for P5 gels than P2 or P3 gels for each GelMA concentration, suggesting that there might be an optimal PEGDA concentration that could lead to higher stiffness than GelMA gels alone, while also not compromising hydrogel porosity, where porosity is important for supporting cell growth.

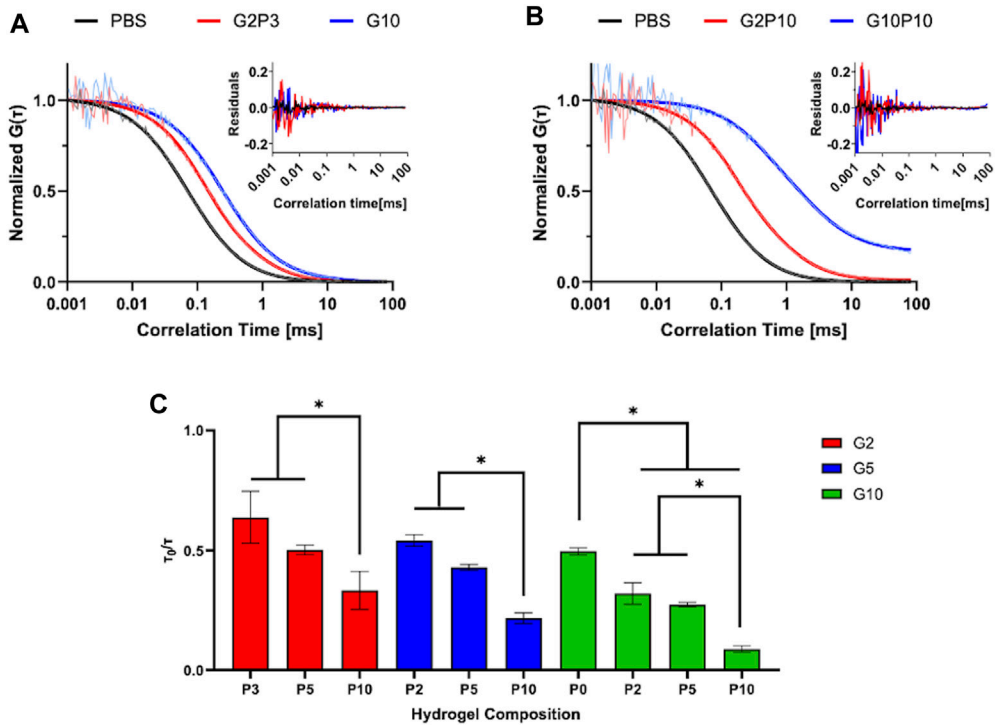

FIGURE 4
FCS Measurement of Diffusivity. Normalized autocorrelation curves of soft **(A)** and stiff **(B)** hydrogel pairs. Insets represent residuals of plotted data. **(C)** Measured normalized diffusivity of tested hydrogel conditions. * designates statistically significant difference between indicated groups. N = 4, $p < 0.05$.

3.4 Protein diffusivity in hydrogels as measured by fluorescence correlation spectroscopy

Fluorescence correlation spectroscopy (FCS) was used to measure diffusivity of a model protein RNase A as an indirect measure of hydrogel mesh size and porosity (Figure 4). As mesh size decreases, diffusivity would also be expected to decrease due to a more tortuous path through which the solute must diffuse. Hydrogels of varying compositions of GelMA and PEGDA were tested. Figures 4A,B show representative normalized autocorrelation functions and residuals (highlighting the goodness of the fit) for the soft and stiff hydrogel pairs of different GelMA concentrations. For all gels tested, we saw a shift of the autocorrelation function to the right compared to buffer only, indicative of slower solute diffusion in the hydrogels due to physical obstruction from polymer chains. Further, even though the soft and stiff gel pairs highlighted had the same modulus, they showed different protein diffusivity indicative of different porosity, corroborating the SEM observations of different pore structure between the gel pairs. For all tested conditions, protein diffusivity decreased (τ_0/τ decreased from ~0.5 to ~0.08) with increase in PEGDA concentration for the same GelMA concentration (Figure 4C). The diffusivity of the different hydrogels varied from τ_0/τ of 0.08 (for G10P10) to τ_0/τ of 0.64 (for G2P3). Overall, protein diffusivity trends tracked stiffness and swelling trends, where stiffer, less swollen gels showed lower diffusivity, indicative of higher crosslinking.

3.5 Detailed correlations of hydrogel composition and properties

We next aimed to clearly delineate the effect of PEGDA and GelMA independently as well as the total polymer concentration on the resultant hydrogel properties. To do so, we looked both at the total polymer concentration (Figures 5A–D) and at the GelMA fraction (Figures 5E–H). Overall, the hydrogel physical and mechanical properties showed a strong dependence on total polymer concentration and little to no correlation on the relative GelMA fraction. As expected, diffusivity and swelling decreased as total polymer concentration increased, while stiffness increased as a function of total polymer concentration. Pore size did not show nearly as strong of a correlation with total polymer concentration, potentially due to the sample preparation for SEM imaging. The relative amount of GelMA appeared to have no influence on hydrogel physical and mechanical properties, with R^2 values all less than 0.2. However, there was a weak correlation between GelMA fraction and hydrogel stiffness, where stiffness seemed to decrease with increase in GelMA fraction; however, there was a large data fluctuation (resulting in a low R^2 value) due to the pronounced effect of PEGDA on gel stiffness.

3.6 U87 cell viability and spreading in GelMA/PEGDA hydrogels

We first focused most of our analysis on two pairs of gels, the soft G10 and G2P3 and the stiff G2P10 and G10P10, representing the same

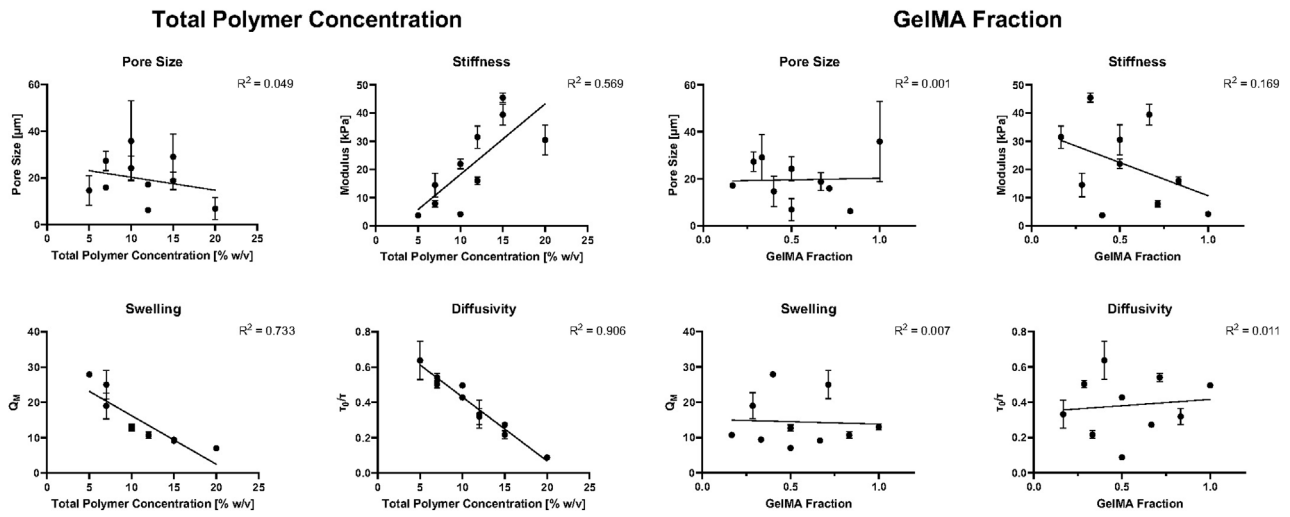

FIGURE 5
Hydrogel mechanical and physical properties as a function of total polymer concentration **(A–D)** and GelMA fraction **(E–H)**. A straight-line fit was used for all plots to show correlation.

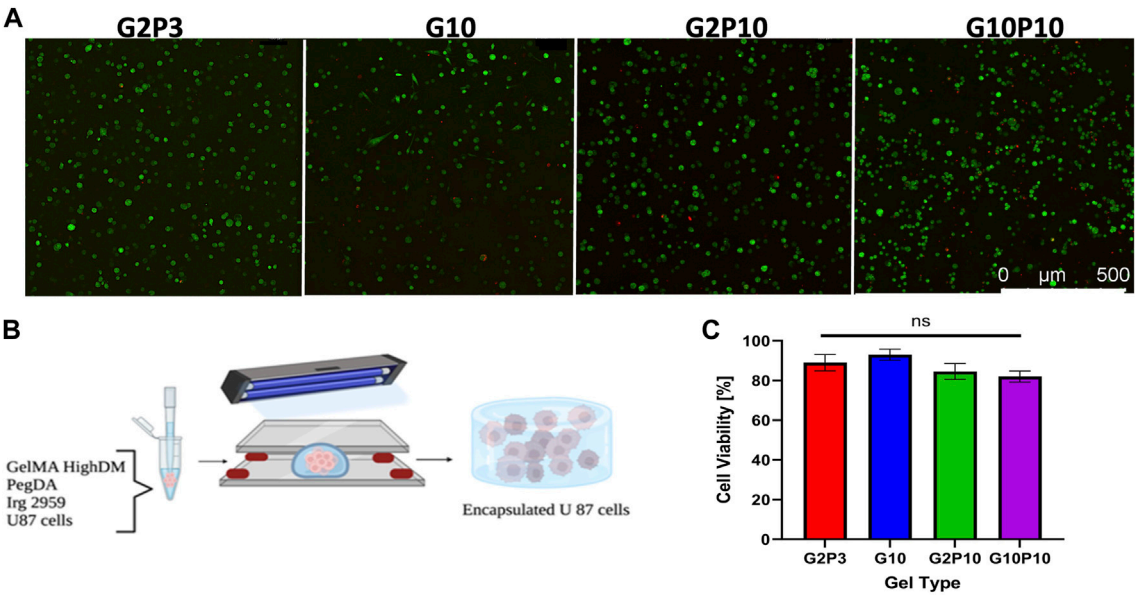

FIGURE 6
U87 Cell Viability within GelMA/PEGDA Hydrogels. **(A)** Representative confocal live/dead images of cells encapsulated in G2P3, G2P10, G10, and G10P10 hydrogels for 24 h. Acridine orange, AO (green stain) shows all cells and PI (red stain) shows dead cells. Scale bar = 100 μm. **(B)** Schematic of encapsulation of U87 cells in GelMA/PEGDA hydrogels. **(C)** Cell viability in the different hydrogel conditions on day 1 of culture (n = 3, $p < 0.5$).

stiffness but different biochemical properties. The gels also encompassed the 'extreme' of the tested gel formulations - from no PEGDA to maximum PEGDA and from minimum to maximum GelMA, to ascertain that the effect of both polymers is adequately represented. However, cell growth data are available for all gel conditions (Supplementary Figure S2 for images) and will be discussed further below. Here, we used U87 human glioblastoma cells as a model cell line because these cells are adhesion dependent, grow well in 3D culture and cell spreading upon adhesion is guided by the mechanical properties of the substrate as shown by us and others (Wang et al., 2014; Bruns et al., 2023). To further show that the gels are suitable for a variety of cell types, we also used NIH 3T3 normal mouse fibroblast cells, which have been used extensively in mechanosensing studies (Yu et al., 2020). For all conditions, cells were encapsulated during gelation and, hence, exposed to UV light (at 365 nm for 10 min) (Figure 6B). Consistent with our previous findings and those of others (Jung and Oh, 2014; Yue et al., 2015; Wang et al., 2018; Peter et al., 2019), the encapsulation procedure demonstrated no adverse effects on cell viability after 24 h (Figure 6A). In fact, we observed over 95% cell viability at the 24 h mark for both U87 cells (Figure 6C) and NIH 3T3 cells (Supplementary Figure S3),

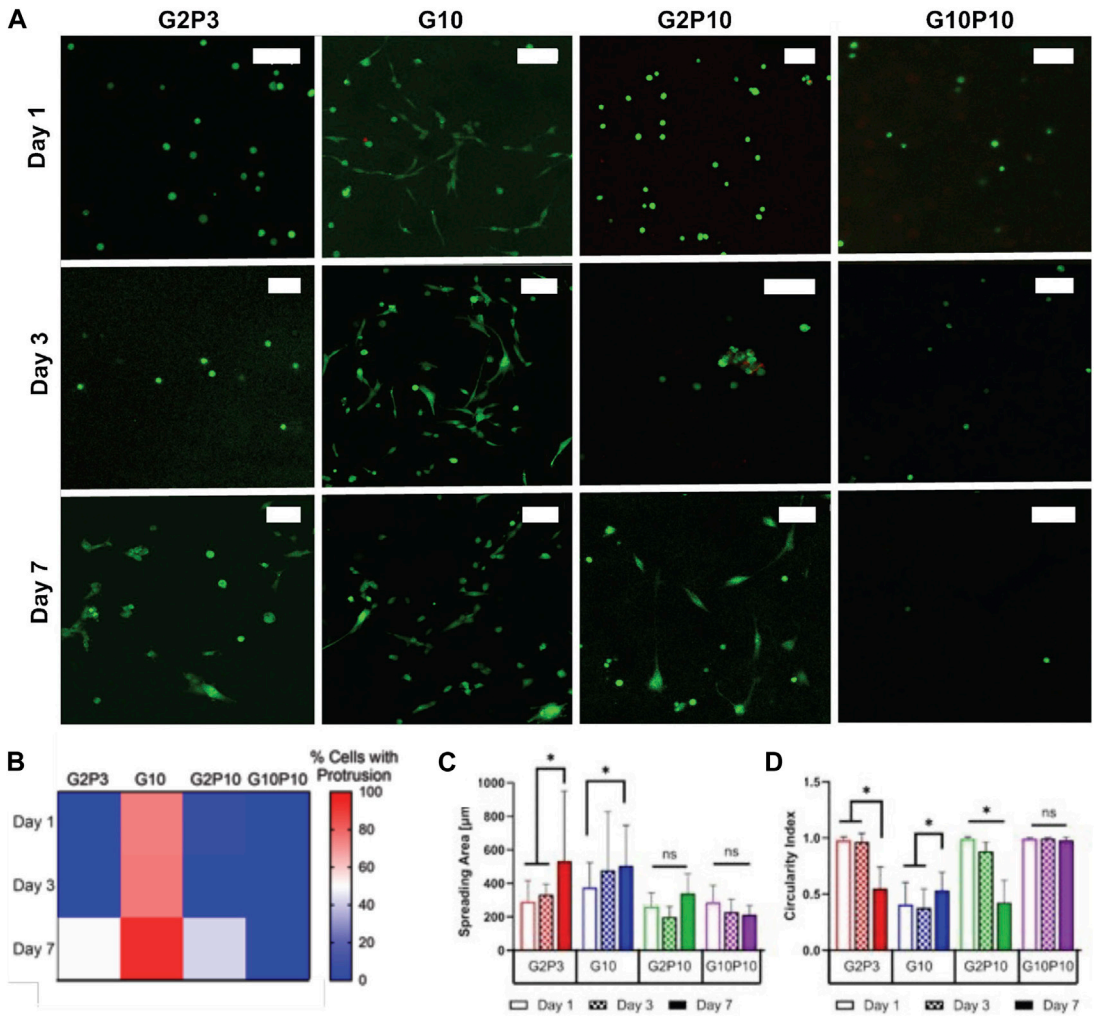

FIGURE 7
U87 glioblastoma cell spreading within GelMA/PEGDA hydrogels. **(A)** Fluorescent confocal z-stack images for tested conditions on Days 1, 3, and 7. Green cell tracker stains all cells. Scale bar represents 100 µm. **(B)**. Heat map of quantification of the percentage of cells that exhibited spreading on Day 1, 3, or 7. In this map, blue indicates areas where no spreading was observed (0% cells with protrusions), white corresponds to 50% spreading, and red signifies majority spreading. The color gradient allows for easy visualization of the distribution and extent of cell spreading over time. **(C)** Measured spreading area of cells within each condition as a function of time. **(D)** Calculated circularity index of measured conditions. * Indicates statistical significance between indicated groups (>120 cells/condition $p < 0.05$).

indicating the suitability of the developed materials as scaffolds for cell culture. Additionally, confocal imaging conducted at day 14 of culture revealed that the cells successfully infiltrated the entire hydrogel for both U87 cells (Supplementary Figure S4) and NIH 3T3 cells (Supplementary Figure S3).

We further evaluated cell spreading as a function of time for U87 cells only (Figure 7). Representative images of cells stained with cell tracker on days 1, 3 and 7 are shown in Figure 7A. We cultured all cells for 14 days (Supplementary Figure S4) but chose not to analyze individual cells for cell spreading area at day 14. However, qualitative observations showed that cells that did not spread by day 7 (e.g., cells in G10P10 gels) stayed round even on day 14. On the other hand, cells which spread early on (e.g., cells in G10 gels), had fully infiltrated the whole gel by day 14 (hence, it was technically difficult to quantify the spreading area of individual cells).

To better understand the time course of cells extending protrusions in the gels, we quantified the percentage of cells extending protrusions in each gel as a function of time (Supplementary Figure S2; Figure 7B). Overall, we noted that the pure GelMA gels (G10) allowed some cells to spread even at 24 h, while the addition of PEGDA in both the G2P3 and G2P10 gels delayed cell spreading until about day 7. Specifically, cells started to spread by day 6 in the G2P3 gels and by day 7 in the G2P10 gels (data now shown for all days for brevity). Cells were not able to extend protrusions in the G10P10 gels even at day 7 (and even at day 14 as shown in Supplementary Figure S3). Quantification of cell spreading area and circularity index corroborated our observations (Figures 7C,D). In G10 hydrogels cell area increased (from 375 to 477 µm^2) from day 1 to day 3, but did not change further by day 7, due to most cells being fully elongated by day 3. For cells in the G2P3 and G2P10 gels we noted an increase in cell spreading area and decrease in circularity at day 7 compared to days 1 and 3. No change was observed for cells in the G10P10 gels, where circularity was ~1 even at day 7, indicating lack of spreading.

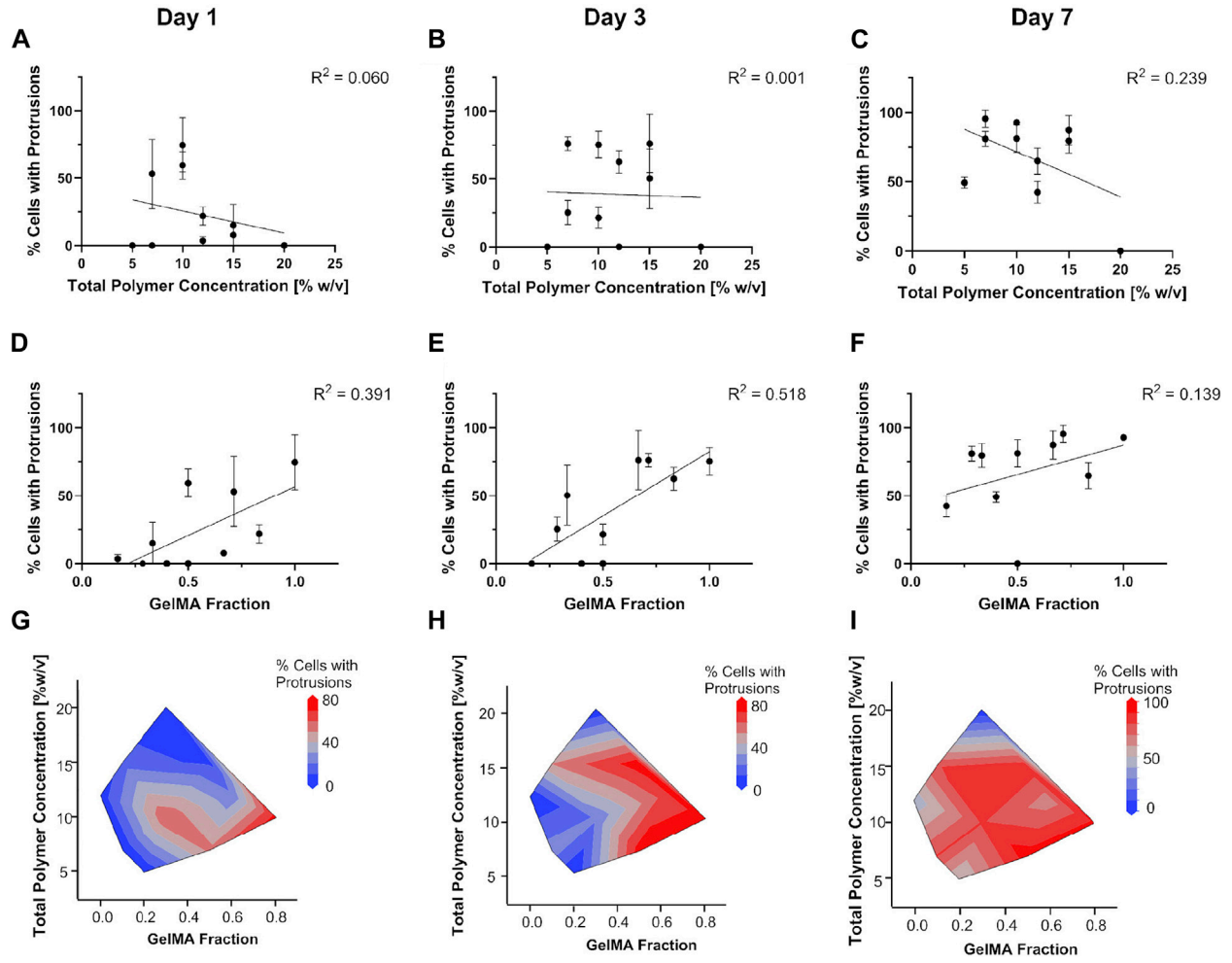

FIGURE 8
Dependence of U87 cell spreading on total polymer concentration **(A–C)** or GelMA fraction **(D–F)**. Contour plots in **(G–I)** detail the interplay in hydrogel stiffness and biochemical cues on cell spreading.

3.7 Detailed correlations of hydrogel composition/properties and cell spreading

To better understand cell spreading as a function of hydrogel composition and properties, we drew correlations between percentage of cells with protrusions and the total polymer concentration (which contributes to hydrogel stiffness) or GelMA fraction (which contributes to adhesion and degradation sites for cells) (Figure 8). For this analysis we looked at U87 cell spreading in all gel conditions (see cell images in Supplementary Figure S2). Our data showed that cell spreading was overall more dependent on the GelMA fraction as opposed to the total polymer concentration. The percentage of cells that exhibited spreading showed no correlation with total polymer concentration on Days 1 or 3. At day 7 total polymer concentration showed a weak correlation with cell spreading ($R^2 > 0.2$) (Figures 8A–C). On the other hand, GelMA fraction showed relatively clear correlation with cell spreading especially for days 1 and 3, with hydrogels with a higher proportion of GelMA exhibiting more spreading (Figures 8D–F). The trend was not as clear on Day 7 at which point cells were spread in most hydrogels. The data indicates that having a higher GelMA fraction (or concentration) leads to faster cell spreading independent of the total polymer concentration. Contour plots of the same data aided visualization (Figures 8G–I). They showed that initial cell spreading at day 1 was most pronounced for a high GelMA fraction (adhesion sites) and low total polymer concentration (gel stiffness). By day 3, the total polymer concentration (gel stiffness) did not show a pronounced impact, but GelMA fraction (adhesion sites) was still important. By day 7, the effect of both was masked as all cells, except for cells in G10P10, had spread.

3.8 Cell response to chemotherapeutics in GelMA/PEGDA hydrogels

We tested the effect of hydrogel composition on cell responsiveness to a chemotherapeutic. TMZ was chosen because it is the standard chemotherapy used for the treatment of glioblastoma. TMZ concentrations of 1–4 mM were chosen based on our preliminary work showing the IC_{50} (inhibitory concentration needed to kill 50% of cells) for U87 cells in 3D cell culture to be ~2 mM (Hill et al., 2021). The analysis of U87 cells' response to TMZ treatment demonstrated significant variability in cell viability across different hydrogel compositions. The confocal images in Supplementary Figure S5

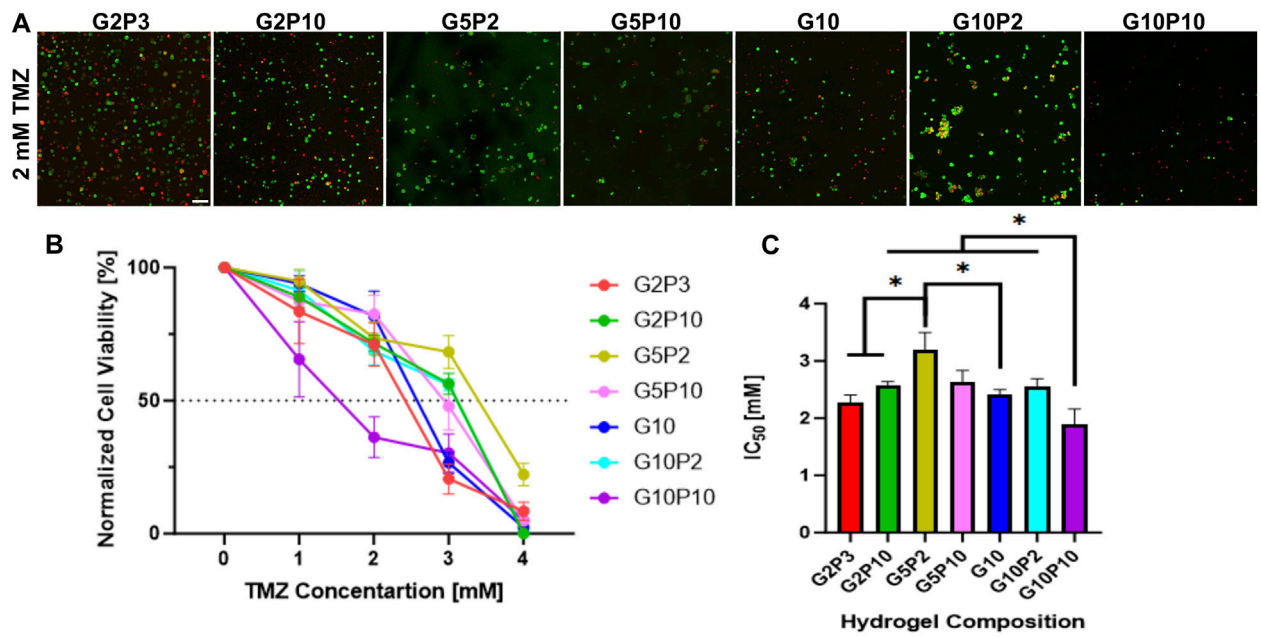

FIGURE 9
U87 cell response to TMZ treatment across various hydrogel compositions. **(A)** Fluorescent confocal Z stack images for all tested hydrogel compositions at 2 mM TMZ, the average IC_{50} concentration. Green fluorescence is cell tracker green, which stains all cells, while red fluorescence is propidium iodide, which stains dead cells. Scale bar is 100 μm. **(B)** Normalized percent cell viability across all hydrogel compositions at all tested TMZ concentrations (from 0 to 4 mM TMZ). Data points represent mean value with standard error. **(C)** Concentration of TMZ required to achieve 50% reduction in cell viability (IC_{50}) for each hydrogel composition tested. * Indicates statistical significance between indicated groups (n = 3, $p < 0.05$).

display all hydrogel compositions tested with TMZ concentrations ranging from 1 to 4 mM. 2 mM TMZ (Figure 9A) show a noticeable increase in the number of dead cells (red fluorescence) in certain hydrogel compositions compared to others. This observation was quantitatively supported by the cell viability data (Figure 9B), which illustrated a dose-dependent reduction in cell viability, with notable differences between the hydrogel compositions at higher TMZ concentrations. Figure 9C highlights the IC_{50} values for each hydrogel composition. The G5P2 hydrogel exhibited the highest IC_{50} value (~3.2 mM), indicating the least sensitivity to TMZ, whereas the G10P10 hydrogel had the lowest IC_{50} (~1.9 mM), indicating the highest sensitivity to TMZ. The results indicate that the response to TMZ did not correlate with PEGDA concentration. The IC_{50} concentration for the G5 hydrogel conditions was higher than that for both the G2 and G10 hydrogel conditions tested, irrespective of the PEGDA concentration. The IC_{50} showed a weak negative correlation with the total polymer concentration and no correlation with the GelMA fraction (Supplementary Figure S6).

4 Discussion

Here, we fabricated and characterized a library of GelMA/PEGDA hydrogels with the goal of achieving a highly tunable hydrogel system that allowed for the independent manipulation of hydrogel biochemical (i.e., cell adhesive and MMP-degradable sites) and mechanical (i.e., Young's modulus) properties for use in mechanosensing applications. The change in biochemical properties was achieved by varying the concentration of GelMA and the change in mechanical properties was achieved by varying the concentration of PEGDA. However, in varying the concentration of both polymers we also affected the total polymer concentration, which was expected to influence hydrogel pore size and permeability; hence, these properties were also measured. The effect of the gel properties on cell viability, spreading and drug responsiveness was then investigated. As a result, here we present a detailed analysis on the interplay between hydrogel composition-properties and their collective effect on cell viability, spreading and drug responsiveness. We used adhesion dependent cancerous U87 glioblastoma cells and normal NIH 3T3 fibroblast cells and focused on cell spreading since it is facilitated by integrin binding with adhesive ligands (e.g., RGD) present on GelMA, but not on PEGDA.

GelMA was synthesized in-house. When modifying gelatin with MAA to synthesize GelMA, the primary reaction is methacrylation of amino groups. However, at high MAA concentrations, esterification with hydroxyl groups may also occur, potentially altering GelMA properties (Shirahama et al., 2016). Despite the high MAA concentration used here, our ^{1}H NMR spectrum showed the absence of a peak at 4.0–4.5 ppm, indicating no esterification, and a visible vinyl proton at 5.5–6.5 ppm, confirming methacrylation. While most studies of GelMA hydrogels cite 50% degree of methacrylation (Nichol et al., 2010), we opted for a higher degree of 80%, aiming to enhance the stiffness of the resultant hydrogel (Figure 1). The selection of an 80% degree of methacrylation was influenced by studies indicating that higher degrees of methacrylation result in increased crosslink density and, consequently, a stiffer hydrogel network (Billiet et al., 2012; Malda et al., 2013). However, we confirmed that even a low degree of modification (i.e. 16%) could lead to gel formation but did not enable the same wide range of mechanical properties

(Supplementary Figure S1). We were concerned that while the methacrylation process does not directly modify cell binding sites (e.g., RGD), the overall conformational changes induced by methacrylation may impact the accessibility or functionality of RGD motifs and hence might negatively impact cell spreading (Xiao et al., 2019b). However, we noted excellent cell spreading in G10 only gels and with increase in GelMA concentration overall (as discussed below), negating these concerns. To obtain a wide range of stiffness with the high degree of modification GelMA, we combined GelMA at 2%–10% w/v with PEGDA at 2%–10% w/v, giving Young's moduli in the range of ~3–43 kPa (Figure 2).

The change in polymer concentration affected other hydrogel properties such as porosity as measured via SEM (Figure 3). We did not observe an overall correlation between modulus and porosity and noted that all gels exhibited a porous structure necessary for cell growth. However, at least for the 5% w/v GelMA we noted an increase in pore size with increase in PEGDA concentration (despite a corresponding increase in modulus and decrease in swelling). Corroborating this observation, a prior study by Wang et al. found that adding 5% PEGDA to a GelMA gel substantially increased the gel pore diameter (Wang et al., 2018). This observation was also consistent with our findings in the G2 and G5 samples for all PEGDA concentrations, but inconsistent with our observation of the highest overall porosity for the G10 gels containing no PEGDA.

The change in polymer concentration affected hydrogel swelling (Figure 2D) and permeability as estimated via FCS measurement of diffusivity of a fluorescent protein in the gels (Figure 4). Both properties, swelling and permeability, were inversely correlated with gel modulus. The decrease in diffusivity with increase in polymer concentration could be attributed to a higher degree of crosslinking, which appeared driven predominantly by the addition of PEGDA and minimally affected by the GelMA concentration. Similar trends were noted by Dogan et al., who noted that the diffusivity of solutes inside GelMA hydrogels was influenced more strongly by the degree of methacrylation (i.e., crosslinking density) as opposed to the total GelMA concentration for the same degree of crosslinking (Dogan et al., 2023). However, Pedron et al. showed that both degree of methacrylation and total polymer content led to changes in diffusivity, with a more pronounced drop in diffusivity for the high GelMA concentration of 10% w/v (compared to 5% or 7% w/v) (Pedron and Harley, 2013).

Gel permeability (i.e., diffusivity measured via FCS) correlated with gel pore size with some exceptions, such as, for example, G10P2 compared to G10P5, which had similar diffusivity even though G10P2 had smaller pore size compared to G10P5. We suggest that this seeming discrepancy is related to the hydrogels' morphology and the nature of the SEM vs. FCS measurements. SEM provides valuable data of gel morphology, but requires gel freezing and freeze-drying, which could disrupt the gel structure and result in pore sizes higher than those observed in the gel hydrated state (Bruns et al., 2018). FCS measures diffusivity of gels in their natural equilibrium hydrated state, where diffusivity would depend on pore size, pore number, pore interconnectivity and wall thickness. Lower pore number and interconnectivity and higher wall thickness would all lead to a higher tortuosity of the path length for a diffusing molecule, leading to lower diffusivity. Our quantitative data shows a lower pore size for G10P2 compared to G10P10, which should have resulted in lower diffusivity for G10P2. However, qualitatively we noted lower wall thickness and higher number of pores in the G10P2 compared to G10P5 gels, possibly negating the effect of the smaller pore size and resulting in similar diffusivity.

Our results indicate that for each GelMA concentration, the addition of PEGDA led to a higher degree of crosslinking and a higher modulus. For example, in Figure 5, we showed a strong correlation between total polymer concentration and modulus, where the modulus increased with increase in total polymer concentration. At the same time, there was a weak negative correlation between GelMA fraction and modulus, showing that as the GelMA concentration increased, modulus decreased. Hence, the hydrogel modulus was governed primarily by the PEGDA concentration. Overall, while a strong correlation was found between gel mechanical and physical properties and total polymer concentration, the fraction of GelMA used in the composite gels did not have a pronounced effect on gel properties (Figure 5).

The GelMA/PEGDA encapsulation process ensured uniform cell distribution, with consistently high >90% cell viability for different cell types (Figures 6, 9; Supplementary Figure S3). However, cell spreading was dependent on hydrogel composition, where it increased with increase in GelMA and decreased with increase in total polymer concentration (Figure 9). These variations in cell spreading dynamics across different hydrogel formulations suggest that distinct matrix properties influence cellular behaviors (Figure 7). Cell spreading dynamics proved to be more dependent on the relative GelMA to PEGDA fraction than on total polymer concentration. Cell spreading exhibited no correlation with total polymer concentration on Days 1 or 3, while GelMA fraction demonstrated a clear correlation with increased cell spreading. Although less distinct on Days 3 and 7, the data suggests that higher GelMA fractions led to faster cell spreading. Overall, our results showed that when the PEGDA concentration was kept at or below 10% w/v (except for G10P10), all gels were able to support cell spreading, albeit at different times. However, adding any PEGDA led to slower cell spreading with just a few cells showing protrusions at 24 h even for the lowest PEGDA concentrations tested, compared to most cells showing protrusions in the GelMA only gels. Similar results were observed by Mahdavi et al. (2021), where the authors reported that adding PEGDA might delay cell proliferation and growth compared to GelMA alone for 3D encapsulation of corneal stromal cells. However, Wang et al. (2018) showed that 2D cultures of mouse osteoblast MC23T3-E1 cells exhibited high viability, adhesion, and proliferation in both GelMA alone at concentrations of 10%, 20%, and 30%, as well as in the same concentrations of GelMA with an additional 5% PEGDA, indicating that the effect of PEGDA on cell spreading might be specific to 3D cell culture. Others have also shown that cell spreading correlates with GelMA concentration and that a high amount of polymer and crosslinking (as in G10P10) could prevent spreading. For example, Peter et al. have shown that MDA-MB-231 breast cancer cells develop a spindle-shaped morphology in GelMA-rich hydrogels, but retain a spheroidal morphology in PEGDA rich gels (PEGDA >15% w/v) (Peter et al., 2019).

Overall, the higher concentration of cell-adhesion (e.g., RGD) and MMP-degradable moieties in G10 gels (except for G10P10) promoted cell attachment. For example, although G2P3 and G10 gels shared similar stiffness, G10, with five times more binding sites, promoted

better cell attachment and spreading. In G2P3, while cells could adhere, they required additional time to remodel the scaffold and access sparser binding sites compared to G10. G2P10, although stiffer than G2P3, contained an equivalent number of binding sites. The increased PEGDA content in G2P10 reduced pore size and lowered the diffusion coefficient by two-fold, yet cells were able to spread within a comparable timeframe in both conditions. These findings underscore the nuanced interplay between hydrogel composition, stiffness, binding sites, and diffusion properties, influencing cell spreading dynamics in 3D culture systems. The only hydrogel that did not support cell spreading at 7 days and even at 14 days was the G10P10 gel (Supplementary Figures S2, S3, S4), which was attributed to its low diffusivity and smaller pore size. Qualitative observations showed that cells did not increase in number over time in those gels, indicative of impeded cell proliferation and possibly cell death after 24 h. One limitation for those gels was the high viscosity of the gel precursor solution due to the high total polymer concentration, which led to difficulties in pipetting and sometimes resulted in air bubbles being trapped in the gel (where the high surface tension of the air bubbles could explain a lower cell viability). Hence, the G10P10 gel was the upper limit of total polymer concentration that was practical for cell encapsulation.

Lastly, we tested the effect of hydrogel composition on U87 cell responsiveness to TMZ treatment. TMZ is the chemotherapeutic of choice for the treatment of GBM, although it has limited effectiveness and high toxicity (Janjua et al., 2021). 3D cell culture, and hydrogels in particular, have emerged as promising *in vitro* platforms for drug screening applications because they can be adapted to existing high-throughout screening technologies, while mimicking the physiological environment more faithfully than a standard 2D cell culture (Zustiak, 2015). Our results showed that within the conditions tested here, there was no clear correlation between cell responsiveness to TMZ and total polymer concentration or GelMA fraction (Figure 9; Supplementary Figures S5, S6). However, the condition G5P2 showed significantly higher IC_{50} than all other conditions, while the condition G10P10 showed significantly lower IC_{50} than all other conditions. G5P2 has a medium GelMA concentration and low PEGDA and total polymer concentration and G10P10 had the highest total polymer concentration tested. While more studies are needed, our data suggest that there might be an optimal number of adhesive sites and hydrogel properties such as swelling, stiffness and diffusivity (Figure 5) that confer resistance to TMZ treatment. Our findings suggest that hydrogel composition could influence the therapeutic effectiveness of TMZ in U87 GBM cells, which could inform future design strategies for hydrogel-based drug screening platforms.

Collectively, our results indicate that the developed hydrogel formulations are suitable for mechanosensting applications with some limitations. Among the design parameters important for hydrogels used in mechanosensing studies, are a wide range of mechanical properties and independent tunability of mechanical, biochemical and physical properties. The latter is an especially important consideration for 3D cell cultures, where cells are embedded inside the hydrogels. The GelMA/PEGDA hydrogels described here cover a wide range of moduli, from ~3 to ~45 kPa, which encompasses the moduli of most soft tissues in the body (Levental et al., 2007). Further, they allow for independent tuning of mechanical and biochemical properties, where formulations of similar modulus but different biochemical properties and similar biochemical properties but different modulus were identified. While porosity and diffusivity of the hydrogels were also affected by the chemical composition, we saw a ~15-fold change in modulus (for the tested formulations) compared to only a ~3-fold change in pore size and diffusivity. Further, the average pore size was >10 μm for all hydrogel compositions and even hydrogels with high PEGDA concentrations and high modulus (e.g., G5P10, E = 45.7 ± 1.6 kPa) exhibited some of the highest pore sizes of ~30 μm. Pore sizes greater than the typical cell size (~10 μm) are optimal to allow for cell spreading and proliferation (Loh and Choong, 2013). The diffusivity of macromolecules in the hydrogels was linearly dependent on total polymer concentration, but it was impeded by up to 70% even at the highest polymer concentration used. Lastly, while the addition of PEGDA delayed cell spreading, cell spreading and protrusions were seen for all hydrogel formulations by day 3 (except for G10P10 as described earlier). The gels retained their integrity over a long period, but cell culture was terminated at 14 days because most gels were fully infiltrated with cells by that time point. However, longer time points could be pursued if needed for different applications.

5 Conclusion

This study explores the intricate interplay of biochemical and mechanical properties within GelMA/PEGDA hydrogels, offering insights into the influence of total polymer concentration and the GelMA/PEGDA ratio, with a specific focus on their impact on hydrogel properties and subsequent cell spreading and drug responsiveness. Our findings reveal a robust dependence of hydrogel properties, such as modulus, swelling, pore size, and permeability, on total polymer concentration, while indicating minimal correlation with the relative GelMA/PEGDA ratio. At the same time, the amount of GelMA had a more profound effect on cell spreading than the total polymer concentration and any addition of PEGDA delayed cell spreading until about day 3 of culture. Drug responsiveness showed a weak negative correlation with total polymer concentration and no correlation with the GelMA fraction, although one condition, namely, G5P2, exhibited the highest IC_{50}. Further, we showcased GelMA/PEGDA composition pairs, namely, the soft G2P3 and G10, ~3 kPa in Young's modulus, vs. the stiff G2P10 and G10P10, ~35 kPa in Young's modulus, which exhibited similar stiffness but different number of adhesive sights or different stiffness but the same number of adhesive sites. This diversity in properties emphasizes the versatility of the GelMA/PEGDA hydrogel system, suggesting its potential suitability for mechanosensing studies.

Data availability statement

The raw data supporting the conclusions of this article will be made available by the authors, without undue reservation.

Author contributions

EF: Conceptualization, Methodology, Writing–original draft, Writing–review and editing, Data curation, Formal Analysis,

Investigation. SS: Data curation, Formal Analysis, Investigation, Writing–review and editing. PB: Data curation, Formal Analysis, Writing–review and editing, Software. SZ: Writing–review and editing, Conceptualization, Funding acquisition, Methodology, Project administration, Resources, Supervision, Writing–original draft.

Funding

The author(s) declare that financial support was received for the research, authorship, and/or publication of this article. Funding for this work was partially provided by major research infrastructure grant 1920251 from the National Science Foundation awarded to SPZ. Funding was also partially provided by a graduate assistantship awarded to EF by the School of Science and Engineering, Saint Louis University.

Acknowledgments

We would like to thank Nathaniel Huebsch and Harper Jiang for advice on GelMA synthesis. We thank Fahu He for help and training on the nuclear magnetic resonance.

Conflict of interest

The authors declare that the research was conducted in the absence of any commercial or financial relationships that could be construed as a potential conflict of interest.

The author(s) declared that they were an editorial board member of Frontiers, at the time of submission. This had no impact on the peer review process and the final decision.

Publisher's note

Supplementary material

The Supplementary Material for this article can be found online at: https://www.frontiersin.org/articles/10.3389/fbiom.2024.1408748/full#supplementary-material

References

Billiet, T., Vandenhaute, M., Schelfhout, J., Van Vlierberghe, S., and Dubruel, P. (2012). A review of trends and limitations in hydrogel-rapid prototyping for tissue engineering. *Biomaterials* 33 (26), 6020–6041. doi:10.1016/j.biomaterials.2012.04.050

Bruns, J., Egan, T., Mercier, P., and Zustiak, S. P. (2023). Glioblastoma spheroid growth and chemotherapeutic responses in single and dual-stiffness hydrogels. *Acta Biomater.* 163, 400–414. doi:10.1016/j.actbio.2022.05.048

Bruns, J., McBride-Gagyi, S., and Zustiak, S. P. (2018). Injectable and cell-adhesive polyethylene glycol cryogel scaffolds: independent control of cryogel microstructure and composition. *Macromol. Mater. Eng.* 303 (10), 1800298. doi:10.1002/mame.201800298

Caliari, S. R., and Burdick, J. A. (2016). A practical guide to hydrogels for cell culture. *Nat. methods* 13 (5), 405–414. doi:10.1038/nmeth.3839

Claaßen, C., Claaßen, M. H., Truffault, V., Sewald, L., Tovar, G. E., Borchers, K., et al. (2018). Quantification of substitution of gelatin methacryloyl: best practice and current pitfalls. *Biomacromolecules* 19 (1), 42–52. doi:10.1021/acs.biomac.7b01221

Dogan, E., Holshue, C., Bhusal, A., Shukla, R., and Miri, A. K. (2023). Cell encapsulation in gelatin methacryloyl bioinks impairs microscale diffusion properties. *Front. Bioeng. Biotechnol.* 11, 1193970. doi:10.3389/fbioe.2023.1193970

Dong, X., Sun, Q., Geng, J., Liu, X., and Wei, Q. (2024). Fiber flexibility reconciles matrix recruitment and the fiber modulus to promote cell mechanosensing. *Nano Lett.* 24 (13), 4029–4037. doi:10.1021/acs.nanolett.4c00923

Duan, J., Cao, Y., Shen, Z., Cheng, Y., Ma, Z., Wang, L., et al. (2022). 3D bioprinted GelMA/PEGDA hybrid scaffold for establishing an *in vitro* model of melanoma. *J. Microbiol. Biotechnol.* 32 (4), 531–540. doi:10.4014/jmb.2111.11003

Dutta, R. C., and Dutta, A. K. (2009). Cell-interactive 3D-scaffold; advances and applications. *Biotechnol. Adv.* 27 (4), 334–339. doi:10.1016/j.biotechadv.2009.02.002

Hill, L., Bruns, J., and Zustiak, S. P. (2021). Hydrogel matrix presence and composition influence drug responses of encapsulated glioblastoma spheroids. *Acta Biomater.* 132, 437–447. doi:10.1016/j.actbio.2021.05.005

Hoch, E., Schuh, C., Hirth, T., Tovar, G. E., and Borchers, K. (2012). Stiff gelatin hydrogels can be photo-chemically synthesized from low viscous gelatin solutions using molecularly functionalized gelatin with a high degree of methacrylation. *J. Mater. Sci. Mater. Med.* 23 (11), 2607–2617. doi:10.1007/s10856-012-4731-2

Huang, G., Li, F., Zhao, X., Ma, Y., Li, Y., Lin, M., et al. (2017). Functional and biomimetic materials for engineering of the three-dimensional cell microenvironment. *Chem. Rev.* 117 (20), 12764–12850. doi:10.1021/acs.chemrev.7b00094

Hutson, C. B., Nichol, J. W., Aubin, H., Bae, H., Yamanlar, S., Al-Haque, S., et al. (2011). Synthesis and characterization of tunable poly (ethylene glycol): gelatin methacrylate composite hydrogels. *Tissue Eng. Part A* 17 (13-14), 1713–1723. doi:10.1089/ten.tea.2010.0666

Janjua, T. I., Rewatkar, P., Ahmed-Cox, A., Saeed, I., Mansfeld, F. M., Kulshreshtha, R., et al. (2021). Frontiers in the treatment of glioblastoma: past, present and emerging. *Adv. drug Deliv. Rev.* 171, 108–138. doi:10.1016/j.addr.2021.01.012

Jiang, T., Zhao, J., Yu, S., Mao, Z., Gao, C., Zhu, Y., et al. (2019). Untangling the response of bone tumor cells and bone forming cells to matrix stiffness and adhesion ligand density by means of hydrogels. *Biomaterials* 188, 130–143. doi:10.1016/j.biomaterials.2018.10.015

Jung, J., and Oh, J. (2014). Swelling characterization of photo-cross-linked gelatin methacrylate spherical microgels for bioencapsulation. *e-Polymers* 14 (3), 161–168. doi:10.1515/epoly-2014-0025

Kim, B.-S., Nikolovski, J., Bonadio, J., Smiley, E., and Mooney, D. J. (1999). Engineered smooth muscle tissues: regulating cell phenotype with the scaffold. *Exp. Cell Res.* 251 (2), 318–328. doi:10.1006/excr.1999.4595

Lepedda, A. J., Nieddu, G., Formato, M., Baker, M. B., Fernandez-Perez, J., and Moroni, L. (2021). Glycosaminoglycans: from vascular physiology to tissue engineering applications. *Front. Chem.* 9, 680836. doi:10.3389/fchem.2021.680836

Levental, I., Georges, P. C., and Janmey, P. A. (2007). Soft biological materials and their impact on cell function. *Soft Matter* 3 (3), 299–306. doi:10.1039/b610522j

Liu, Y., Zhang, J., Jin, Y., and Yin, M. (2024). Gelatin methacrylate based liquid dressing with antibacterial and hemostasis properties. *Colloids Surfaces A Physicochem. Eng. Aspects* 689, 133749. doi:10.1016/j.colsurfa.2024.133749

Loessner, D., Meinert, C., Kaemmerer, E., Martine, L. C., Yue, K., Levett, P. A., et al. (2016). Functionalization, preparation and use of cell-laden gelatin methacryloyl–based hydrogels as modular tissue culture platforms. *Nat. Protoc.* 11 (4), 727–746. doi:10.1038/nprot.2016.037

Loh, Q. L., and Choong, C. (2013). Three-dimensional scaffolds for tissue engineering applications: role of porosity and pore size. *Tissue Eng. Part B Rev.* 19, 485–502. doi:10.1089/ten.teb.2012.0437

Mahdavi, S. S., Abdekhodaie, M. J., Mashayekhan, S., Baradaran-Rafii, A., and Kim, K. (2021). Development and *in vitro* evaluation of photocurable GelMA/PEGDA hybrid hydrogel for corneal stromal cells delivery. *Mater. Today Commun.* 27, 102459. doi:10.1016/j.mtcomm.2021.102459

Malda, J., Visser, J., Melchels, F. P., Jüngst, T., Hennink, W. E., Dhert, W. J., et al. (2013). 25th anniversary article: engineering hydrogels for biofabrication. *Adv. Mater.* 25 (36), 5011–5028. doi:10.1002/adma.201302042

Mamaghani, K. R., Naghib, S. M., Zahedi, A., and Mozafari, M. (2018). Synthesis and microstructural characterization of GelMa/PEGDA hybrid hydrogel containing graphene oxide for biomedical purposes. *Mater. Today Proc.* 5 (7), 15635–15644. doi:10.1016/j.matpr.2018.04.173

Nichol, J. W., Koshy, S. T., Bae, H., Hwang, C. M., Yamanlar, S., and Khademhosseini, A. (2010). Cell-laden microengineered gelatin methacrylate hydrogels. *Biomaterials* 31 (21), 5536–5544. doi:10.1016/j.biomaterials.2010.03.064

O'Connell, C. D., Zhang, B., Onofrillo, C., Duchi, S., Blanchard, R., Quigley, A., et al. (2018). Tailoring the mechanical properties of gelatin methacryloyl hydrogels through manipulation of the photocrosslinking conditions. *Soft matter* 14 (11), 2142–2151. doi:10.1039/c7sm02187a

Pedron, S., and Harley, B. (2013). Impact of the biophysical features of a 3D gelatin microenvironment on glioblastoma malignancy. *J. Biomed. Mater. Res. Part A* 101 (12), 3404–3415. doi:10.1002/jbm.a.34637

Pepelanova, I., Kruppa, K., Scheper, T., and Lavrentieva, A. (2018). Gelatin-methacryloyl (GelMA) hydrogels with defined degree of functionalization as a versatile toolkit for 3D cell culture and extrusion bioprinting. *Bioengineering* 5 (3), 55. doi:10.3390/bioengineering5030055

Peter, M., Singh, A., Mohankumar, K., Jeenger, R., Joge, P. A., Gatne, M. M., et al. (2019). Gelatin-based matrices as a tunable platform to study *in vitro* and *in vivo* 3D cell invasion. *ACS Appl. Bio Mater.* 2 (2), 916–929. doi:10.1021/acsabm.8b00767

Shirahama, H., Lee, B. H., Tan, L. P., and Cho, N.-J. (2016). Precise tuning of facile one-pot gelatin methacryloyl (GelMA) synthesis. *Sci. Rep.* 6 (1), 31036. doi:10.1038/srep31036

Sun, M., Sun, X., Wang, Z., Guo, S., Yu, G., and Yang, H. (2018a). Synthesis and properties of gelatin methacryloyl (GelMA) hydrogels and their recent applications in load-bearing tissue. *Polymers* 10 (11), 1290. doi:10.3390/polym10111290

Sun, Y., Deng, R., Ren, X., Zhang, K., and Li, J. (2018b). 2D gelatin methacrylate hydrogels with tunable stiffness for investigating cell behaviors. *ACS Appl. Bio Mater.* 2 (1), 570–576. doi:10.1021/acsabm.8b00712

Theocharis, A. D., Skandalis, S. S., Gialeli, C., and Karamanos, N. K. (2016). Extracellular matrix structure. *Adv. drug Deliv. Rev.* 97, 4–27. doi:10.1016/j.addr.2015.11.001

Tibbitt, M. W., and Anseth, K. S. (2009). Hydrogels as extracellular matrix mimics for 3D cell culture. *Biotechnol. Bioeng.* 103 (4), 655–663. doi:10.1002/bit.22361

Tomal, W., and Ortyl, J. (2020). Water-soluble photoinitiators in biomedical applications. *Polymers* 12 (5), 1073. doi:10.3390/polym12051073

Van Den Bulcke, A. I., Bogdanov, B., De Rooze, N., Schacht, E. H., Cornelissen, M., and Berghmans, H. (2000). Structural and rheological properties of methacrylamide modified gelatin hydrogels. *Biomacromolecules* 1 (1), 31–38. doi:10.1021/bm990017d

Vila, A., Torras, N., Castaño, A. G., García-Díaz, M., Comelles, J., Pérez-Berezo, T., et al. (2020). Hydrogel co-networks of gelatine methacrylate and poly (ethylene glycol) diacrylate sustain 3D functional *in vitro* models of intestinal mucosa. *Biofabrication* 12 (2), 025008. doi:10.1088/1758-5090/ab5f50

Walker, C., Mojares, E., and del Río Hernández, A. (2018). Role of extracellular matrix in development and cancer progression. *Int. J. Mol. Sci.* 19 (10), 3028. doi:10.3390/ijms19103028

Wang, C., Tong, X., and Yang, F. (2014). Bioengineered 3D brain tumor model to elucidate the effects of matrix stiffness on glioblastoma cell behavior using PEG-based hydrogels. *Mol. Pharm.* 11 (7), 2115–2125. doi:10.1021/mp5000828

Wang, Y., Ma, M., Wang, J., Zhang, W., Lu, W., Gao, Y., et al. (2018). Development of a photo-crosslinking, biodegradable GelMA/PEGDA hydrogel for guided bone regeneration materials. *Materials.* 11 (8), 1345. doi:10.3390/ma11081345

Xiao, S., Zhao, T., Wang, J., Wang, C., Du, J., Ying, L., et al. (2019a). Gelatin methacrylate (GelMA)-based hydrogels for cell transplantation: an effective strategy for tissue engineering. *Stem Cell Rev. Rep.* 15, 664–679. doi:10.1007/s12015-019-09893-4

Xiao, S., Zhao, T., Wang, J., Wang, C., Du, J., Ying, L., et al. (2019b). Gelatin methacrylate (GelMA)-based hydrogels for cell transplantation: an effective strategy for tissue engineering. *Stem Cell Rev. Rep.* 15, 664–679. doi:10.1007/s12015-019-09893-4

Yu, L., Hou, Y., Xie, W., Camacho, J. L. C., Cheng, C., Holle, A., et al. (2020). Ligand diffusion enables force-independent cell adhesion via activating α5β1 integrin and initiating rac and RhoA signaling. *Adv. Mater.* 32 (29), 2002566. doi:10.1002/adma.202002566

Yue, K., Trujillo-de Santiago, G., Alvarez, M. M., Tamayol, A., Annabi, N., and Khademhosseini, A. (2015). Synthesis, properties, and biomedical applications of gelatin methacryloyl (GelMA) hydrogels. *Biomaterials* 73, 254–271. doi:10.1016/j.biomaterials.2015.08.045

Zustiak, S. P. (2015). The role of matrix compliance on cell responses to drugs and toxins: towards predictive drug screening platforms. *Macromol. Biosci.* 15 (5), 589–599. doi:10.1002/mabi.201400507

Frontiers in
Biomaterials Science

Probes into the science and technology of biomaterials

An interdisciplinary journal that advances our understanding of old and new biomaterials at the interface of chemistry, physics, biology, materials science, and biomedical engineering.

Discover the latest Research Topics

See more →

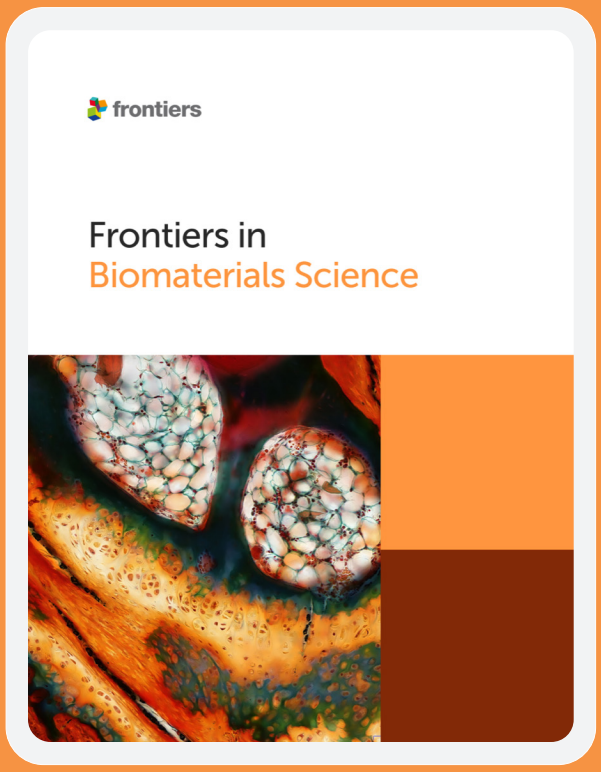

Frontiers

Avenue du Tribunal-Fédéral 34
1005 Lausanne, Switzerland
frontiersin.org

Contact us

+41 (0)21 510 17 00
frontiersin.org/about/contact